Exploring New Paths Towards Biological Anion Recognition by Lanthanide Complexes

Carlson Alexander

St Cross College, University of Oxford



A thesis submitted for the degree of

Doctor of Philosophy in Inorganic Chemistry

Michaelmas Term **2022**

Abstract

Exploring new paths towards biological anion recognition by lanthanide complexes

Anions are ubiquitous in nature. In order to understand them in their natural setting, this thesis focusses on developing lanthanide complexes as hosts for the recognition of biologically relevant anions, particularly chloride and sialic acid. Chapter-I introduces lanthanide chemistry encompassing macrocyclic complexes, luminescence, and MRI. An account of anion recognition and lanthanide complexes used as hosts for biologically relevant anions are reviewed.

Chapter-II focuses on developing receptors for chloride recognition. The concept of binuclear lanthanide complexes, bridged by flexible ethane/propane spacer, for chloride recognition is envisioned. The proposed complexes are synthesised, and their anion binding properties are studied by luminescence, NMR spectroscopy, and X-ray crystallography. The study demonstrates the versatility of these binuclear complexes as the strongest chloride binding receptor to function in water and buffers to date. Thus, the work described here, hits a new milestone in anion coordination chemistry, ameliorating detailed exploration. Chapter-III builds on the drawbacks from these neutral complexes towards anion binding, and proposes tryptophan-conjugated cationic binuclear complexes for halide recognition. Initial studies show promising results towards halide recognition in water from this cationic coordination complex.

Chapter-IV revisits a ditopic approach of arylboronate-conjugated lanthanide chelates for sialic acid recognition, a tumour biomarker. However, the complexes suffer from protodeboronation, leading to the cleavage of boronic acid which is reported for the first time with structural evidence. The resulting boron free

complex binds to L-lactate and D-gluconate. Chapter-V employs the ditopic approach, but with the incorporation of rigid anthracene and dansyl spacers between them, to improve the stability of the arylboronate during complexation. However, the anthracene-based receptor proved synthetically challenging. The success in making the dansyl-functionalised ligand extents the possibility of investigating sialic acid binding.

Chapter-VI summarises the work embodied in this thesis and Chapter-VII describes the complete experimental procedures followed in accomplishing the results reported in Chapters II-V.

Acknowledgements

It has been a little over four years since I left home and moved to Oxford. Little did I know back then that these four plus years would leave a huge impact in my life. First of all, I pray and thank my Lord and Our Lady for taking care of me at all times, helping me during the pandemic and when I was in distress.

I consider it an absolute honour to work under the supervision of Prof. Steve Faulkner. When I applied to several universities for a doctoral study, Prof. Steve was the only one who had faith in me and welcomed me into his group. He is a man of pure class and I always look up to him. His unwavering support and guidance was always reassuring even when my confidence hit rock-bottom. Thank you for Stevemas, Faulksmas, and the summer barbeque which was an absolute treat to me. There is no one else who I could have worked for. I also thank my College advisor, Prof. Gavin Dalton for his constant reassurance and support. I extend a huge thanks to the NMR Manager, Dr. Nick Rees, for guiding me throughout with the NMR measurements, and for all the useful interactions we had. I thank the Mass Spec facility, especially Dr. Victor and Dr. John-Walsby Tickle, without whom I would not have got any high-resolution mass spec data. I also thank Dr. Kirsten Christensen for looking at my army of crystal submissions and salvaging them as much as possible. This thesis has some richness only because of your help and skill.

Outside Oxford, I would first like to thank Prof. Thomas Sørensen from the University of Copenhagen. Although I was in contact with you only in my final year of study, your knowledge and support took my work to a better level and I am indebted to you on that. Thank you for making time for me in your busy schedule. I thank Prof. Robert Pal and Dr. Lewis MacKenzie for taking care of me during my Durham visit, teaching me CPL and its tricks, and allowing me to record some

samples which was very kind of you. I thank Drs. Ben Tickner and Djordje Toljic for all the fruitful discussions on Yttrium NMR and Gd-based MRI relaxivity measurements. I gratefully acknowledge the inputs on NMR spectroscopy in lanthanides from Dr. Alan Kenwright who answered all my concerns comprehensively, even after his retirement from academia.

A major part of my life in Oxford was memorable because of the past and present members of the Faulkner group. A huge shout to Grace, Debs, Agnes, Cameron, Dani, Qidian, Daohe, Marie, Kezi, Louis, Charlie Simms, Carlos, Zepeng, Xuejian, Tom, Clara, Xiaofan, Laura, Charlotte Ball and others for all the support I received. I learned a lot from all of you which shaped me into a better person than I was when I first joined in. Special mention to Grace, Debs, Agnes, Cameron, Kezi, Qidian, and Dani for being very nice to me and supportive (and made sure I was not home sick). I am glad to have you guys and I am so happy to work with all of you. Special mention to Leila Hill for helping me with titrations and data plotting from Australia and never shied away from my emails.

Outside the lab, I thank Shiny for being a good friend to rant about everything, for constant support which I gratefully acknowledge, and the best cooking partner that I can ask for. I thank Drs. Priyanka Vincent, Wilson, Irudaya Jyothi, Amudhan, and Nithya Kumar for all the useful guidance and support, and I am benefitted a lot from it. I also thank Vihanga and Dilhan for all the help and fruitful discussions on anion recognition and molecular modelling.

Finally, I wish to acknowledge my parents. Life outside India was different than expected. The steadfast love and support I received from both of you, ensured me to try everything I possibly could. I cannot ask any better from both of you. I shall never let you both down. To my beloved dad and mum, *I dedicate this thesis.*

“I alone know the plans I have for you, plans to bring you prosperity and not disaster, plans to bring about the future you hope for”

Jeremiah 29:11 (The Holy Bible)

“We will get there, goooott!”

Prof. Steve Faulkner (Beloved Mentor)

Publication and Presentations

Publication

1. Alexander, C.; Thom, J. T.; Kenwright, A. M.; Christensen, K. E.; Sørensen, T. J.; Faulkner, S. *Chelating chloride using binuclear lanthanide complexes in water*, *Chem. Sci*., 2022, Accepted Manuscript, DOI:10.1039/D2SC05417E.

Presentations

4. Alexander, C.; Sørensen, T. J.; Christensen, K. E.; Faulkner, S. *Binuclear lanthanide(III) complexes for the detection of fluoride in water*, 44th International Conference on Coordination Chemistry (ICCC-44), Rimini, Italy, August 28-September 02, 2022.
3. Alexander, C.; Sørensen, T. J.; Faulkner, S. *Ditopic lanthanide complexes for fluoride recognition*; Early Career Researcher Macrocyclic and Supramolecular Chemistry (ECR-MASC) by RSC, Loughborough University, UK, July 28, 2022.
2. Alexander, C.; Faulkner, S. *Photophysical processes in homobinuclear lanthanide(III) complexes for ratiometric detection of fluoride*; 30th International Conference on Photochemistry, University of Geneva (virtual conference), July 19-23, 2021.
1. Alexander, C.; Faulkner, S. *Fluoride and sialic acid responsive smart lanthanide agents*, 3 Minute Research Presentation Prize at St Cross College, University of Oxford, competed among other projects in other scientific areas to academic audience and won the first place (virtual competition), March 05, 2021.

Table of Contents

Abstract ..... **iii**

Acknowledgements ..... **v**

Publication and Presentations ..... **viii**

Abbreviations ..... **xiv**

Chapter-I: Introduction **2**

1.1. Coordination Chemistry of Lanthanides 2

1.2. Lanthanide Photophysics 3

1.2.1. Electronic Transitions in Lanthanides 3

1.2.2. Lanthanide Emission 4

1.2.3. Induced Electric Dipole Transitions and Their Intensity-Judd-Ofelt Theory 6

1.2.4. Hypersensitive Transitions 7

1.2.5. Sensitisation of Lanthanide Emission 8

1.2.6. Efficiency of Sensitised Emission 11

1.2.7. Ligand to Metal Ion Energy Transfer-*Mechanisms* 13

1.2.8. Quenching of Lanthanide Luminescence 15

1.2.8.1. Photoinduced electron transfer (PeT) 15

1.2.8.2. Non-radiative quenching (multiphonon relxation) 15

1.2.9. Circularly Polarised Luminescence 20

1.2.9.1. Factors that govern CPL 21

1.3. Macrocyclic Complexes of Lanthanides 22

1.3.1. Lanthanide(III) Complexes of Macrocyclic Polyaminocarboxylates: *Thermodynamic Stability and Metal Ion Selectivity* 23

1.3.2. Thermodynamic Stability and Kinetic Inertness of Ln(III) Macrocyclic Complexes 24

1.3.3. Dissociation Kinetics of Ln(III) Macrocyclic Complexes 25

1.3.4. Lanthanide Complexes of the Ubiquitous DOTA and its Derivatives 25

1.3.5. NMR Studies of Solution Structures and Conformations of Lanthanide Macrocyclic Complexes 28

1.4. Paramagnetism in Lanthanides 31

1.4.1. Paramagnetism and Magnetic Susceptibility by NMR 32

1.5. Magnetic Resonance Imaging 34

1.5.1. Relaxation Time and MR Image Intensity and Resolution 35

1.5.2. Gadolinium(III) Complexes as Contrast Agents for MRI 36

1.5.3. Clinically Approved Gadolinium(III) Chelates as Contrast Agents 38

1.5.4. Relaxation Theory for GBCAs 39

1.5.4.1. Inner-Sphere Relaxation 41
1.5.4.2. Electronic Relaxation 43
1.5.4.3. Outer-Sphere Relaxation 43
1.5.5. Parameters of Relaxivity Optimisation 44
1.5.6. New Strategies in the Design of MRI Contrast Agents 45
1.5.7. Targeted GBCAs 46
1.5.8. Bioresponsive GBCAs 47
1.5.9. Chemical Exchange Saturation Transfer (CEST) Agents 47
1.5.9.1. Categories of Exogenous CEST Contrast Agents 49
1.5.9.2. ParaCEST Contrast Agents 50
1.6. Development of receptors for Anion Recognition in Water 51
1.6.1. Approaches to Anion Receptor Design for Anion Recognition 53
1.6.2. Anion Binding by Receptors and Signalling Mechanisms 54
1.6.3. Engineering Electron-Deficient Lewis Acid-Containing Binding Sites on Anion Receptors 55
1.6.4. Luminescent Lanthanide Complexes for Anion Binding and Sensing 55
1.6.4.1. Luminescent Ln(III) Complexes for Binding and Sensing Anions-Design Considerations 56
1.6.4.2. Anion Binding at Ln(III) Centres and Signalling Mechanisms 57
1.6.4.3. Tuning Anion Affinity of Lanthanide-Based Receptors and Gaining Selectivity 61
1.6.4.4. Constitution and Configuration of Anion Adducts Formed at Ln(III) Centres 63
1.6.5. Luminescent Lanthanide(III)-Based Receptors for Anion Sensing: *Bioimaging Applications* 63
1.6.5.1. Selective Recognition of Phosphate in Water 63
1.6.5.2. Lanthanide Complexes as Receptors for Hydroxy Acids (lactate, malate, and citrate) 68
1.6.5.3. Luminescent Lanthanide Receptors for Bicarbonate 74
1.6.5.4. Interaction of anions with Lanthanides: innocent versus non-innocent anions 77
1.7. Aim and Scope of this Thesis 78
1.7.1. Aim of the Thesis 79
1.7.2. Scope of the Thesis 83
1.8. References 84
Chapter-II: Binuclear Lanthanide Complexes for Halide Chelation in Water 101
2.1. Supramolecular Assemblies for Chloride Recognition in Water 103
2.2. Lanthanide Complexes as Hosts for Halide Recognition 106
2.3. Design Inspiration for Halide Recognition 112
2.4. Aim of Chapter-II 114

2.5. Results and Discussion 115
2.5.1. Synthesis of the Proposed Binuclear Complexes 115
2.5.2. Photophysics of the Binuclear and Mononuclear Eu(III) Complexes 121
2.5.2.1. Electronic, excitation, and emission spectra of binuclear Eu(III) complexes 121
2.5.2.2. Effect of pH on binuclear Eu(III) complexes 123
2.5.2.3. Chloride chelation on the binuclear Eu(III) complexes 125
2.5.2.4. Fluoride chelation on the binuclear Eu(III) complexes 131
2.5.2.5. Chelation of heavier halides to the binuclear Eu(III) complexes 144
2.5.2.6. Halide chelation on [Eu(pDO3A)] 145
2.5.2.7. Luminescence lifetime of binuclear and mononuclear complexes with halides 149
2.5.3. NMR Studies on Lanthanide Complexes 150
2.5.3.1. NMR studies at basic pD 150
2.5.3.2. Fluorine NMR studies to explore fluoride binding 154
2.5.3.3. Chlorine NMR studies to explore chloride binding 158
2.5.4. Mass Spectral Studies of Halide Binding with Lanthanide Complexes 160
2.5.5. X-Ray Crystal Structures of Anions-Bound Lanthanide Complexes 162
2.5.6. MRI Longitudinal Relaxivity Studies on Halide Binding to Binuclear Gd(III) Complexes 166
2.6. Conclusion 168
2.7. References 169
Chapter-III: Binuclear Lanthanide Complex Bearing Tryptophan Pendant Arm for Halide Chelation in Water 175
3.1. Results and Discussion 177
3.1.1. Synthesis of the Proposed Complexes 177
3.1.1.1. Alternative Approaches Attempted to Make the Proposed Binuclear Complexes 180
3.1.2. Photophysics of $[Tb_2(DO3AM\text{-}L\text{-}TrpOMe)_2C\text{-}3]^{6+}$ 184
3.1.2.1. Electronic, excitation, and emission spectra 184
3.1.2.2. Luminescence of the Binuclear Tb Complex upon Halide Addition 186
3.1.2.3. Luminescence Lifetime of the Binuclear Complex 189
3.2. Conclusion 190
3.3. References 190
Chapter-IV: Revisiting Lanthanide Complexes of PBA-Conjugated DO3A Towards Sialic Acid Recognition 193
4.1. The Biology of Glycans 193
4.1.1. Sialic Acids (*Sias*) 194
4.1.2. *Sia* Modifications 195

4.1.3. *Sia* as a Tumour Marker 195

4.2. Changes in Glycosylation During Cancer Progression 196

4.3. Boronic Acid-Based Molecular Receptors for Monosaccharides 197

4.4. *Sia* Sensing and Imaging by Lanthanide(III) Complexes 200

4.5. Bioorthogonal Chemistry-*An Introduction* 205

4.6. Aim of Chapter-IV 206

4.7. Results and Discussion 207

4.7.1. Synthesis of the Ditopic Complexes 207

4.7.1.1. Attempts to make the DO3A-PBA ligands 210

4.7.1.2. Protodeboronation of PBA-conjugated ligands by Eu(III) and Tb(III) 211

4.7.2. Electronic, Excitation, and Emission Spectra 215

4.7.3. Luminescence Titrations of [Eu(DO3A)benzyl] with Monosaccharides 216

4.7.4. Circularly Polarised Luminescence Study for the Detection of Monosaccharides 220

4.7.5. NMR Binding Studies of Monosaccharides with [Eu(DO3A)benzyl] 223

4.8. Conclusion 224

4.9. References 225

Chapter-V: Towards Molecular Recognition of Sialic Acid by [Ln(DO3A)] Tethered to Anthracene and Dansyl-Conjugated Phenylboronic Acid 231

5.1. Design Inspiration 231

5.2. Towards the Synthesis of [Ln(DO3A)anth-*o*-PBA] 234

5.3. Towards the Synthesis of [Ln(DO3A)dansyl-*m*-PBA] 236

5.4. Conclusion 240

5.5. *References* 240

Chapter-VI: Summary and Conclusion 243

Chapter-VII: Experimental Procedures 251

7.1. Reagents and Solvents 251

7.2. Vacuum Processing, Dialysis, Centrifugation, Filtration, TLC, and Column Chromatography 253

7.3. Preparation of Buffers and Standard Solutions 253

7.4. Physical Methods 255

7.5. Software details 264

7.6. Synthesis of Ligands and Complexes 265

7.6.1. Synthesis and characterisation of compounds in Chapter-II 265

7.6.2. Synthesis and characterisation of compounds in Chapter-III 278

7.6.3. Synthesis and characterisation of compounds in Chapter-IV 289

7.6.4. Synthesis and characterisation of compounds in Chapter-V 299

7.7. References 311
Appendix A: Additional information for Chapter-II **314**
Appendix-B: HPLC conditions used in Chapter-IV **329**
Appendix C: X-ray Crystal Data **334**
Appendix D: DYNAFIT input scripts **354**

Abbreviations

ISC	intersystem crossing
η_{isc}	intersystem crossing efficiency
Fl	fluorescence
Ph	phosphorescence
NR	non-radiative processes
ILCT	intra ligand charge transfer state
MLCT	metal-to-ligand charge transfer
CD	circular dichroism
CPL	circularly polarised luminescence
ΔE	energy gap
ΔI	luminescence intensity
I_L	left circularly polarised light
I_R	right circularly polarised light
g_{lum}	luminescence dissymmetric ratio (or factor)
g_{abs}	Kuhn dissymmetric ratio
LIS	lanthanide induced shift
m_J	total angular momentum
B_q^k	crystal field parameters
B_0^2 B_2^2	second order crystal field parameters
O_q^k	Stevens operators
δ_ω	lanthanide induced shift
δ_d	diamagnetic shift
δ_c	contact shift
δ^{pcs}	pseudocontact shift
δ'	magnetic anisotropy factor
δ	chemical shift
μ_B	Bohr magneton
μ_0	Permeability of free space
C_J	Bleaney′s constant
MRI	magnetic resonance imaging
NMR	nuclear magnetic resonance
MTR	magnetisation transfer ratio
RF	radiofrequency
Δ_{RF}	off-resonance frequency
Δ_{CS}	separation in chemical shifts beween two pools
DFT	density functional theory
EPR	electron paramagnetic resonance
FID	free induction decay
T_1	longitudinal relaxation time
T_2	transverse relaxation time

CAs	contrast agents
GBCAs	Gd(III)-based contrast agents
FDA	Federal Drug Administration
HSA	human serum albumin
PRE	paramagnetic relaxation enhancement
$1/T_{id}$	diamagnetic relaxation rate enhancement
$1/T_{ip}$	paramagnetic relaxation rate enhancement
r_1/r_{1p}	longitudinal relaxivity
r_2/r_{2p}	transverse relaxivity
τ_m	residence lifetime of water molecules in the inner-coordination sphere
τ_R	rotational correlation time
T_{1e}	longitudinal electronic relaxation time
T_{2e}	transverse electronic relaxation time
$A/\hbar$	electron-nuclear hyperfine coupling constant
μ_{eff}	effective magnetic moment of the paramagnetic metal ion.
H_O	applied field strength (in Gauss)
N_A	Avogadro′s number
D	diffusion constants for the solvent
q	number of water molecules in the inner-coordination sphere
ZFS	zero field splitting
ω_H	proton Larmor frequency
ω_s	electron Larmor frequency
$\Delta\omega$	frequency separation between the exchangeable protons and the bulk water resonances
sh	shoulder
D	donor
A	acceptor
C-2	ethane spacer
C-3	propane spacer
Calc	calculated
CI	confidence interval
Ln	lanthanide
br	broad
s	singlet
d	doublet
t	triplet
dd	doublet of doublets
ddd	doublet of doublet of doublets
dddd	doublet of doublet of doublet of doublets
dt	doublet of triplets
m	multiplet
K_1	first binding event (constant)

K_2	second binding event (constant)
K_3	third binding event (constant)
$K/K_a/K_{eq}$	binding constants
$K_{Ln\text{-}L}$	binding strength of lanthanide to ligand
a.u.	arbitrary units
Da	daltons
λ	wavelength
λ_{ex}	excitation wavelength
λ_{em}	emission wavelength
υ	wavenumber
nm	nanometer
MHz	megahertz
ppm	parts per million
τ	luminescence lifetime
A	inner-sphere contribution
B	outer-sphere contribution
PeT	photoinduced electron transfer
HOMO	highest occupied molecular orbital
LUMO	lowest unoccupied molecular orbital
S_0	ground state singlet level
S_1	excited state singlet level
T_1	triplet level
ADP	adenosine diphosphate
ATP	adenosine triphosphate
GTP	guanosine-5'-triphosphate
NPP	nucleoside polyphosphate
PAPS	adenosine-3'-phosphate-5'-phosphosulfate
PAP	adenosine-3'-5'-diphosphate
A^-	anion
e^{-r}	distance dependance between donor and acceptor
Fl	fluorescence
Ph	phosphorescence
BET	back energy transfer
ISC	intersystem crossing
ED	electric dipole
MD	magnetic dipole
ms	millisecond
o	ortho
m	meta
p	para
m/z	mass to charge ratio
TOF	time of flight

OTf	trifluoromethane sulfonate
Anal.	elemental analysis
J	coupling constant
Hz	hertz
mL	millilitre
mM	millimolar
μM	micromolar
M^{-1}	per mole
v/v	volume by volume
h	hours
min	minutes
°C	degree Celsius
mp	melting point
RB	round bottom
T	temperature
l	path length of cell
c	concentration of the sample
α	observed rotation
[α]	specific rotation
eq	equation
equiv	equivalents
D	dextrorotarory
L	levorotatory
Ar, *Ar*	aryl
aq.	aqueous
Pd/C	palladium on carbon
UV	Ultraviolet
Vis	visible
DAD	diode-array detector
R_f	retention factor
en	ethylenediamine
pH	potential of hydrogen (negative logarithm of hydrogen ion activity in solution)
DPA	dipicolinic acid
DCM	dichloromethane
DMF	*N*,*N*-dimethylformamide
DMSO	dimethylsulfoxide
TFA	trifluoroacetic acid
SAP	square antiprismatic
TSAP	twisted-square antiprismatic
TLC	thin layer chromatography
UPLC	ultra performance liquid chromatography

HRMS	high resolution mass spectrometry
LRMS	low resolution mass spectrometry
ICP-MS	inductively coupled plasma-mass spectrometry
MALDI-TOF	matrix assisted laser desorption ionisation-time of flight
DCTB	2-[(2*E*)-3-(4-*tert*-butylphenyl)-2-methylprop-2-enylidene]malononitrile
NMRD	nuclear magnetic relaxation dispersion
LD_{50}	median lethal dose
CEST	chemical exchange saturation transfer
DiaCEST	diamagnetic chemical exchange saturation transfer
ParaCEST	paramagnetic chemical exchange saturation transfer
lipoCEST	liposomal chemical exchange saturation transfer
hyperCEST	hyperpolarised chemical exchange saturation transfer
RIME	receptor induced magnetisation enhancement
HEDTA	*N*-(hydroxyethyl)ethylenediamine triacetic acid
DTPA	diethylenetriamine pentaaacetic acid
BOPTA	4-carboxy-5,8,11-*tris*(carboxymethyl)-1-phenyl-2-oxa-5,8,11-triazatridecane-13-oic acid
EDTA	ethylenediamine tetraacetic acid
DTPA-BMA	diethylenetriamine pentaaacetic acid-*N,N′*-*bis*(methylamide)
cyclen	1,4,7,10-tetraazacyclododecane
cycl	cyclen ring
DOTA	1,4,7,10-tetraazacyclododecane-*N,N′,N″,N‴*-tetraacetic acid
DO3A	1,4,7,10-tetraazacyclododecane-1,4,7-triacetic acid
pDO3A	2,2',2"-(10-(prop-2-yn-1-yl)-1,4,7,10-tetraazacyclododecane-1,4,7-triyl)triacetic acid
HP-DO3A	10-(2-hydroxypropyl)-1,4,7,10-tetraazacyclododecane-1,4,7-triacetic acid
DOTP	1,4,7,10-tetraazacyclododecane-*N,N′,N″,N‴*-*tetrakis*-(methylene phosphonate)
DOTAM	1,4,7,10-*tetrakis*(2-carbamoylethyl)-1,4,7,10-tetraazacyclododecane
OBETA	2,2′-oxy*bis*(ethylamine)-*N,N,N′,N′*-tetraacetic acid
TCMC	1,4,7,10-*tetrakis*(carbamoylmethyl)-1,4,7,10-tetraazacyclododecane
dacda	1,10-diaza-4,7,13,16-tetraoxacyclooctadecane-*N,N′*-diacetic acid
THP	1,4,7,10-*tetrakis*(2-hydroxypropyl)-1,4,7,10-tetraazacyclododecane
DOTPBz	1,4,7,10-tetraazacyclododecane*tetrakis*(methylenebenzylphosphinic acid)
DO3MA	(1*R*,4*R*,7*R*)-*α,α′,α″*-trimethyl-1,4,7,10-tetraazacyclododecane-1,4,7-triacetic acid
MS-325	trisodium{4-(*R*)-[(4,4′-diphenylcyclohexyl)phosphanooxymethyl]-3,6,9-triaza-3,6,9-*tris*(methoxycarbonyl)undecanedioato}gadolinium(III)
PFC	perfluorocarbon
HFB	hexafluorobenzene
PFCE	perfluoro-15-crown-5-ether
PERFECTA	tetra(perfluoro-*tert*-butyl)pentaerythritol

DIPEA	*N*,*N*-diisopropylethylamine (Hünig's base)
PBS	phosphate buffered saline
CHES	2-(cyclohexylamino)ethanesulfonic acid
Tris-HCl	*tris*(hydroxymethyl)aminomethane hydrochloride
HEPES	2-[4-(2-hydroxyethyl)piperazin-1-yl]ethanesulfonic acid
HATU	hexafluorophosphate azabenzotriazole tetramethyl uronium
HOBt	hydroxybenzotriazole
Trp	L-tryptophan
BOC	*tert*-butyloxycarbonyl
CBzCl	benzyloxycarbonyl chloride
PDB	dibenzoyl preoxide
Sia	sialic acid
Neu5Gc	*N*-glycolylneuraminic acid
Neu5Ac	5-acetylneuraminic acid
KDN	2-keto-3-deoxy-D-glycero-D-galacto-nononic acid
MeNeu5Ac	2-*α*-*O*-methyl-5-acetylneuraminic acid
GBPs	glycan-binding proteins
PBA	phenylboronic acid
PAPBA	3-(propionamido)phenylboronic acid
sLex	sialyl Lewis X
NRC	national research council
CNS	central nervous system
EPA	environment protection agency
WHO	world health organisation
$[Cl^-]_e$	extracellular chloride concentration
$[Cl^-]_i$	intracellular chloride concentration

CHAPTER-I

Chapter-I: Introduction

1.1. Coordination Chemistry of Lanthanides

The coordination chemistry of lanthanides (Ln = Ce to Lu) is unique from other elements. The high charge density of Ln(III) ions make them hard Lewis acids and tend to form complexes with ligands which are hard Lewis bases. The coordination numbers vary from 8 to 12 (depending on the ligand type) and the interaction with the surrounding ligand is predominantly electrostatic in nature.[1] Owing to lanthanide contraction, the size of lanthanide ions decreases across the 4*f*-row of the periodic table, resulting in higher coordination numbers for the early lanthanides and smaller coordination numbers for those towards the end of the series. Since they form complexes with higher coordination numbers than the transition metal ions, ligand binding sites and metal coordination geometries play an important role in determining and controlling the overall structure of the resulting complexes. In the coordination complexes of rare earths, coordination number between 6 and 11 have been observed, with coordination numbers of 9 and 10 being perhaps the most common. The steric bulk and flexibility of the ligands play a key role in determining the resultant coordination number and geometry. Crystal structures[2] of $[Ln(\mathbf{H_2O})_9](EtSO_4)_3$ (Ln = Y, La, Ce, Pr, Nd, Sm, Gd, or Dy) and $[Nd(H_2O)_9](BrO_3)_3$ showed the presence of 9-coordinate metal ions in a tricapped trigonal prisms (C_{3h}) geometry.[3]

In 1963,[4] 12-coordination in the $[Ce(\mathbf{NO_3})_6]^{3-}$ units in $Ce_2Mg_3(NO_3)_{12}.24H_2O$ and in 1965,[5] 10-coordination in $[La(\mathbf{HEDTA})(H_2O)_4].3H_2O$ were reported. Subsequently, it was shown that a hindered aryl ligand gave 4-coordination in $[Li(thf)_4][Lu(\mathbf{2,6\text{-}dimethylphenyl})_4]$,[6] while the bulky *bis*(trimethylsilyl)amide ligand forms 3-coordinate $[Ln\{\mathbf{N}(\mathbf{SiMe_3})_2\}_3]$ (Ln = Y, La, Ce, Pr, Nd, Sm, Eu, Gd,

Ho, Yb, or Lu) complexes,[7] and 2-coordination was achieved by a very bulky ligand in [Yb{**C**(**SiMe**$_3$)$_3$}$_2$].[8] Further, owing to the inner nature of the 4*f*-valence orbitals, ligand field effects for the trivalent lanthanide ions are very small, on the order of 500 cm^{-1} (6 kJ mol^{-1}), while these effects for *d*-transition metal ions are commonly in the range of 10-30,000 cm^{-1} (0.120-360 kJ mol^{-1}). Raymond[9] has described this situation as "*The coordination chemistry of the lanthanides shows much structural diversity. However, there is often only a limited degree of predictability because of the absence of strong ligand field effects, resulting in small energy differences between different geometric arrangements and/or coordination numbers*".

The coordination chemistry of rare earth elements gained renewed momentum during the past four decades, stimulated by emerging applications in a wide range of areas through the rise of several exciting areas linked to the coordination chemistry of 4*f*-elements. The advancement made in the development of complexes with macrocyclic and anionic polydentate chelating ligands, self-assembled supramolecular edifices, heterometallic *d-f* compounds, new extraction processes, organometallic compounds, coordination in ionic liquids, lanthanidomesogens, nanoparticles, coordination polymers, host-guest hybrid materials, single-molecule magnets, and luminescent devices make coordination chemistry of the 4*f*-elements a mature and attractive field of research with almost unlimited perspectives.[1,10-12]

1.2. Lanthanide Photophysics

1.2.1. Electronic Transitions in Lanthanides

The electronic transitions within 4*f*-shell of lanthanides arise owing to the interaction of the electric- and magnetic components of the electromagnetic radiation with the *f*-electrons, leading to electric dipole (ED) or magnetic dipole

(MD) transitions. Allowed and forbidden transitions are determined by selection rules.[10] According to the parity or Laporte rule, for an electronic transition to be allowed, the parity between the final and initial states must change.[10a] In the case of ED transitions both the operator and the *f*-orbitals have *u* (*ungerade*, odd) symmetry and hence these transitions are forbidden by the parity rule. In the case of MD transitions, the magnetic dipole operator and the *f*-orbitals have *g* (*gerade*, even) symmetry, and therefore these transitions are allowed in lanthanide complexes. However, weak induced ED transitions can occur because of the interaction of the central ion with the surrounding ligand-field mixing into the f^n configuration states from configurations of opposite parity and thus relaxing the parity restriction. ED transitions may also be induced because of the asymmetries produced by means of the vibronic coupling of the central ion with its ligands. In contrast, MD transitions within the f^n configuration are parity-allowed. For spin allowed transitions, spins of ground and excited states should be the same. In the case of several *f-f* transitions of the lanthanide ions, these are accompanied by a change in spin and therefore strictly forbidden. However, due to the spin-orbit coupling, the total spin quantum number *S* is not completely valid, and therefore this rule is relaxed. The selection rules $\Delta J = 0, \pm 1$ (except $0 \leftrightarrow 0$) is followed and a few magnetic dipole transitions are known which are mentioned in Table 1.1.[10b] The energy level diagram of the common lanthanide ions is shown in Figure 1.1.[11]

1.2.2. Lanthanide Emission

Most lanthanide(III) ions are luminescent and their emission covers the entire spectrum from UV (Gd^{III}) to visible (orange Sm^{III}, red Eu^{III}, green Tb^{III}, yellow Dy^{III}, and blue Tm^{III}) and near-infrared (Pr^{III}, Nd^{III}, Ho^{III}, Er^{III}, and Yb^{III}) ranges. Some ions are fluorescent ($\Delta S = 0$), some are phosphorescent ($\Delta S > 0$), and

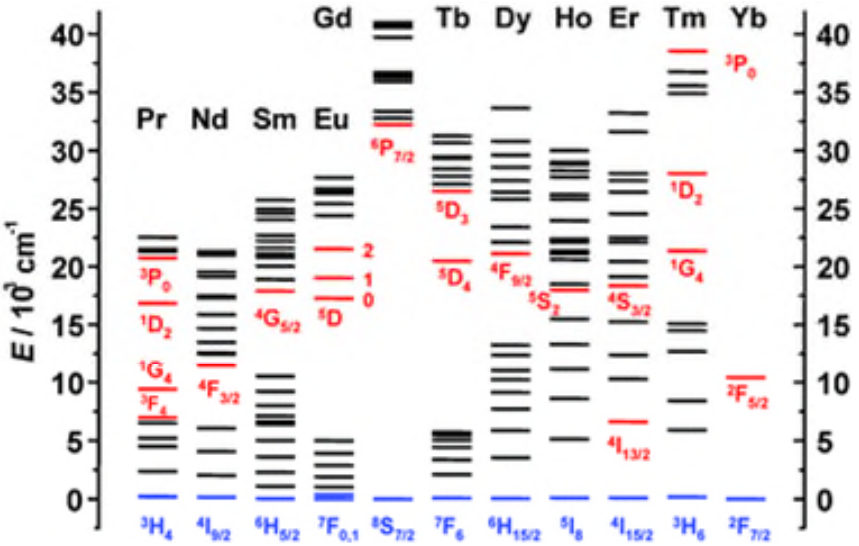


Figure 1.1. Energy level diagram of lanthanide aquo ions. The main luminescent levels are drawn in red, while the fundamental level is indicated in blue (reproduced with permission from Ref 11a).

some exhibit both. Lanthanide emission is due to two main types of transitions, the parity allowed MD and the parity forbidden ED transitions. When a Ln(III) ion is inserted into a chemical environment, non-centrosymmetric interactions allow the mixing of electronic states of opposite parity into the 4*f*-wave functions and ED transitions become partly allowed, termed induced ED transitions. Most of the absorption and emission lines of the lanthanides are induced ED transitions. The intensity of these transitions is particularly sensitive to the nature of the metal ion environment and they can be either completely absent or very intense depending upon the ligand field and these transitions are called "hypersensitive". A typical example is the $^5D_0 \rightarrow {}^7F_2$ transition of Eu(III). Some emission lines acquire strength both by MD and ED transitions. For instance, the emission spectrum of Tb(III) is dominated by mixed ED and MD transitions.[12]

1.2.3. Induced Electric Dipole Transitions and Their Intensity-Judd-Ofelt Theory

ED transitions are allowed only between states of different parity. Therefore, the electric dipole operator must be combined with other odd-parity operators to enable transitions within the *f*-shell.[13] When the metal is present in a

Table 1.1. Selected magnetic dipole allowed transitions in Ln(III) ions*

Ln(III) ion	Transition	Approx. wavelength (nm)
Sm	$^4G_{5/2} \rightarrow {}^6H_{7/2}$	580
	$^4G_{5/2} \rightarrow {}^6H_{5/2}$	560
Eu	$\mathbf{^5D_0 \rightarrow {}^7F_1}$	**590**
Gd	$^8S_{7/2} \rightarrow {}^6P_{7/2}$	312
Tb	$^5D_4 \rightarrow {}^7F_3$	625
	$^5D_4 \rightarrow {}^7F_4$	580
	$^5D_4 \rightarrow {}^7F_5$	540
Dy	$^4F_{9/2} \rightarrow {}^6H_{11/2}$	650
Yb	$^2F_{5/2} \rightarrow {}^2F_{7/2}$	980

* The highlighted transition is extensively studied in this thesis.

symmetry site without inversion symmetry, the parity rule is no longer applicable and therefore ED transitions can be observed. Furthermore, even in lanthanide complexes of centrosymmetric point groups, ED transitions can be observed due to vibronic coupling which lifts the site symmetry. MD transitions follow the selection rules $\Delta J \leq 1$, $\Delta L = 0$, $\Delta S = 0$, and $\Delta l = 0$ in the Russell-Saunders approximation. Given the eigenvectors of the states involved, the intensities of the MD transitions may be readily calculated.[14] The observed intensities of the ED transitions are the result of mixing of electronic states of opposite parity (such as *d*-orbitals) into the states of the f^n configuration, mediated by the electrostatic ligand field, proposed independently by Brian Judd[15] and George Ofelt.[16] The Judd-Ofelt theory is discussed in detail.[10b] Judd-Ofelt parameters for aqueous Ln(III) ions are reported.[12]

This theory does not estimate well for Pr(III), probably due to the significant perturbation between two wavefunctions under consideration. The electronic energy levels of trivalent lanthanide aqua ions across the lanthanide series have been determined from their absorption spectra and energy-level assignments made on the basis of correlations between calculated and observed band intensities.[17] Carnall *et al.*[14,18] determined the intensities of the solution absorption spectra in hydrated trivalent lanthanides and correlated with the theoretically calculated oscillator strength, *P*, using the expressions derived by Judd and Ofelt.

1.2.4. Hypersensitive Transitions

Hypersensitive transitions are ED transitions whose form/shape and intensity display large dependence on the point group symmetry of the metal ion, pH, temperature, and the type of ligand chelating the metal (leading to crystal-filed effects). These transitions obey the selection rules: $|\Delta S| = 0$, $|\Delta L| \leq 2$, $|\Delta J| \leq 2$.[15,16,19] Over the years, several explanations have been proposed for hypersensitivity.[12,20] The most successful one to date is the dynamic coupling mechanism proposed by Mason *et al.*[21] According to these authors, the intensity of the hypersensitive *f-f* transitions in Ln(III) complexes arises principally from the induced electric dipoles in the ligands by the transition quadrupole moment of the metal ion. Intensity calculations on the hypersensitive *f-f* transitions in noncentrosymmetric lanthanide complexes was reported by Richardson *et al.*[22] by incorporating both the Judd-Ofelt static coupling and Mason, Peacock, and Stewart dynamic coupling (or ligand polarisation) contributions to the electric dipole strengths. The hypersensitivity phenomenon has been exploited as a spectroscopic probe of lanthanide-ligand interactions, lanthanide-anion interactions, and complex formation in solution. The

hypersensitive transitions observed for different Ln(III) metals are presented in Table 1.2.

Table 1.2. Selected hypersensitive transitions of the Ln(III) ions observed in absorption and emission spectra*

Ln(III) ion	Transition	Approx. wavelength (nm)
Sm	$^4F_{1/2}$, $^4F_{3/2} \rightarrow {}^6H_{5/2}$	1560
	$^4G_{5/2} \rightarrow {}^6H_{5/2}$	560
Eu	$^5D_2 \rightarrow {}^7F_0$	465
	$^5D_1 \rightarrow {}^7F_1$	535
	$^5D_0 \rightarrow {}^7F_2$	**613**
Gd	$^6P_{5/2}$, $^6P_{7/2} \rightarrow {}^8S_{7/2}$	308
Dy	$^6F_{11/2} \rightarrow {}^6H_{15/2}$	1300
	$^4G_{11/2}$, $^4I_{15/2} \rightarrow {}^6H_{15/2}$	427
Ho	$^3H_6 \rightarrow {}^5I_8$	361
	$^5G_6 \rightarrow {}^5I_8$	452

* The highlighted transition is extensively studied in this thesis.

1.2.5. Sensitisation of Lanthanide Emission

The shielding of the 4*f*-orbitals by the filled $5p^6$,$6s^2$ orbitals results in special spectroscopic properties with parity forbidden 4*f*-4*f* transitions. As a result, the absorption coefficients are very low (typically 1-10 L mol^{-1} cm^{-1}), the lifetimes of the excited states are relatively long (microsecond to millisecond), and the emissive rates are slow which result in long-lived and narrow line-like emission bands. As a consequence, direct excitation of Ln ions is more demanding and requires intense (laser) sources at precise wavelengths. In 1942, Weissman[23] discovered "the antenna effect" in a series of organo-Eu(III) complexes of ligands such as salicylaldehyde, benzoylacetonates, and nitrosalicylaldehydes by observing the characteristic Eu(III) fingerprint emission spectra by irradiation with light absorbed

only by the organic ligands. The efficiency of excitation varies greatly with the nature of the ligand, temperature, and solvent. This paved the way for the sensitised emission of lanthanides which circumvent the shortcomings of direct excitation of Ln(III) complexes. Since then, a variety of ligands have been designed by employing two general strategies to sensitise the lanthanide ions: (1) *chromophoric chelates* which contain aromatic groups and coordinate to the metal ions (weak) and absorb incident light and (2) the *pendant chromophore* design, in which chromophores are appended onto a multidentate ligand which strongly coordinates to the Ln(III) ion. Both strategies allow the incorporation of multiple chromophores which increases the overall absorbance of the complex.[24] The sensitisation of Ln(III) cations by the antenna effect using the pendant chromophore ligand designs is illustrated in Figure 1.2. Crosby and Kasha[25] in 1958 established that lanthanide luminescence is sensitised by the ligand centered triplet excited state and that singlet state does not play any role in the sensitisation process. Although Weissman discovered the antenna effect, it was named as such only in 1993 by Lehn.[26]

The antenna effect (illustrated by the modified Jablonski diagram, Figure 1.3) relies on a sensitiser (which is typically an organic chromophore or transition

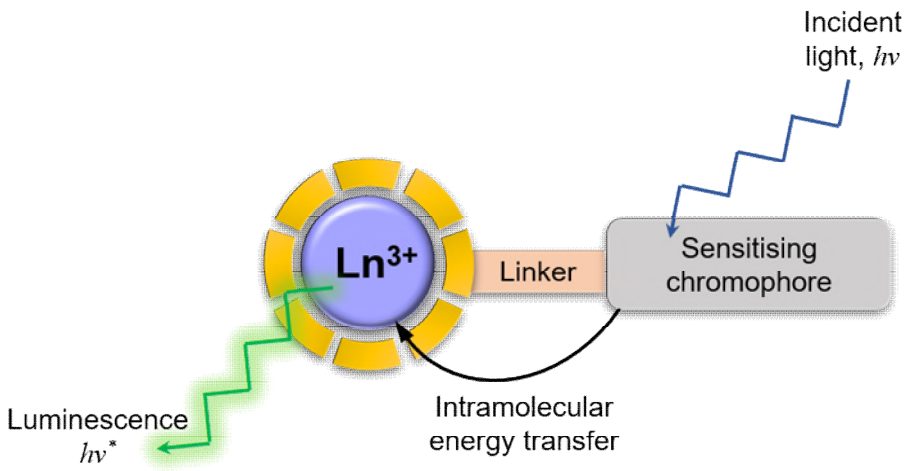


Figure 1.2. Cartoon illustration of sensitised lanthanide luminescence at the molecular level.

metal complex) to harvest energy through photon absorption, leading to the population of its excited singlet state (S_1). The population of the excited triplet state of the sensitiser (T_1) from S_1 is facilitated by intersystem crossing (ISC) through heavy atom (Franck-Condon overlap) effect.[27] T_1 being a long-lived state, can funnel its energy (energy transfer) to the emissive state of the lanthanide ion (*f**) in the complex which decays to the ground state in the form of narrow and sharp emission lines which characterise lanthanide luminescence. Since sensitisation typically occurs via the excited triplet state, the antenna should possess a high

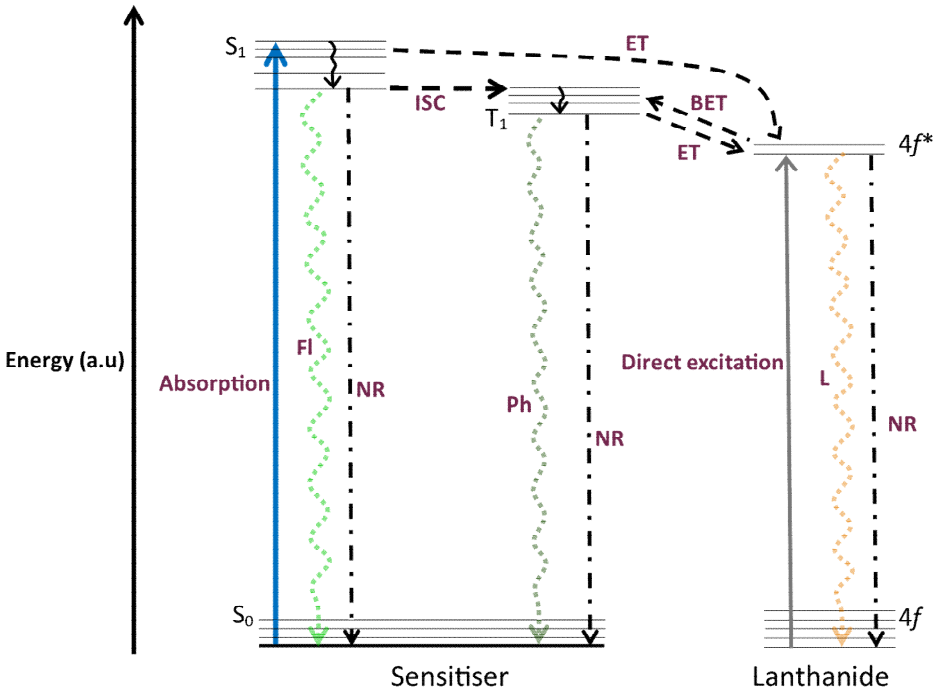


Figure 1.3. Jablonski diagram demonstrating the photophysics of lanthanide luminescence: Fl, fluorescence; ISC, intersystem crossing; BET, back energy transfer; ET, energy transfer; NR, non-radiative quenching; Ph, phosphorescence; L, luminescence (adapted from Ref 10b). Only one emission possibility of L shown, others omitted for clarity.

intersystem crossing efficiency (η_{isc}). If T_1 is closer in energy to *f**, back energy transfer takes place. Fluorescence (Fl) and phosphorescence (Ph) compete for deactivation of S_1 and T_1 states, respectively, while non-radiative processes (NR) deactivate all excited states. Sensitisation of lanthanide luminescence occurs

through different excited states of the sensitiser such as singlet states[28] triplet states,[29] ILCT state,[30] and MLCT states.[31] However, the most favoured pathway is the energy transfer from the triplet states of ligands to the excited states of Ln(III) ions. From spectroscopic studies on over 50 chelates of trivalent lanthanides, Crosby *et al*.[32] observed that the intramolecular energy transfer efficiency is a sensitive function of the relative positions on the resonance energy levels in lanthanide ions and the triplet states of the complexes. Therefore, in order to make energy transfer effective, the match in energy is one of the most important factors for designing highly luminescent lanthanide complexes.

1.2.6. Efficiency of Sensitised Emission

In the case of lanthanide emission via direct excitation, its overall efficiency (ϕ_{Ln}^{Ln}) is described by eq 1.1.

$$\phi_{Ln}^{Ln} = \frac{k_R}{k_R + k_{NR}} = \frac{k_R}{k_{\exp}} = \frac{\tau_{\exp}}{\tau_R} \qquad (1.1)$$

Where ϕ_{Ln}^{Ln} is related to the overall rate of depopulation of the emissive state through radiative and non-radiative pathways ($k_{\exp} = k_R + k_{NR}$), the radiative rate constant (k_R) or their corresponding lifetimes (τ_{exp}), and τ_R.[10b] Contributions to non-radiative rate (k_{NR}) include back-energy transfer to the ligand and quenching by the high energy oscillators of the ligands.[33] In contrast, radiative rates (k_R) are related to the geometry.[34] If there is no inversion symmetry at the lanthanide ion sites, ED transitions that are forbidden by odd parity become partially allowed by mixing 4*f*- and 5*d*-states through ligand field effects.[12]

The overall efficiency of sensitised emission (ϕ_{Ln}^{L}) is given by eq 1.2.

$$\phi_{Ln}^{L} = \phi_{ISC} \times \phi_{ET} \times \phi_{Ln}^{Ln} = \phi_{sens} \times \phi_{Ln}^{Ln} \qquad (1.2)$$

The efficiency of sensitisation (ϕ_{sens}) depends on the efficiency of intersystem crossing (ϕ_{ISC}) and energy transfer (ϕ_{ET}). For an efficient energy transfer toward Ln luminescence, the relative positions of S_1 and T_1 states of the sensitiser are important as they influence the efficiency of ISC and energy transfer alongside the magnitude of back energy transfer.[10b] The energy transfer from ligand to Ln(III) ion occurs from the lowest triplet state energy level of the ligand to the emissive level of Ln(III). Furthermore, the ligand should saturate the Ln(III) coordination sphere to prevent solvent molecule from coordinating to the metal ion since bound solvent effectively quenches luminescence (due to O-H and N-H oscillators from the solvent).[33] The basic rule of thumb for sensitised lanthanide luminescence is to have ΔE (*D*–Ln*) > 0, ΔE (^{1}S – ^{3}T) ~ 5,000 cm^{-1}, ΔE (^{3}T–Ln*) in the 2,000-3,500 cm^{-1} range (*D* = donor), and ΔE (ILCT*–Ln*) in the 2,000-3,500 cm^{-1} range and to avoid thermally active back energy transfer (BET) from *f** to T_1 level.[30a]

Luminescence properties of Eu(III) and Tb(III) complexes of 41 ligands, studied by Latva *et al.*,[35] indicate that chelated Eu(III) and Tb(III) ions are able to accept energy by all their ^5D_J levels depending on the energy of the lowest triplet state of the ligand, and the Ln(III) luminescence quantum yield is highest when the energy is transferred from the lowest triplet state level of the ligand directly to the lowest excited level of the Ln(III). The authors have given an empirical rule that the optimal ligand to metal energy transfer process takes place when the energy difference between the excited level of Ln(III) and the lowest triplet state of the ligand is > 2,500 cm^{-1}. The Tb(III) luminescence quantum yields decrease due to the back energy transfer from excited Tb(III)* to the ligand when the energy difference between the $^5D_4$ level of Tb(III) and the lowest triplet state energy level of the ligand is less than 1,850 cm^{-1}. Along these lines, Yuster and Weissman[36] studied the sensitised

luminescence of non-emissive trivalent La, Lu, and Gd ions in their complexes of dibenzoylmethane derivatives. In the quest toward the design of bright lanthanide luminescent complexes as bioprobes, Raymond *et al.*[37] have reported sensitisation of Ln(III) luminescence by 2-hydroxyisophthalamide-based chelating ligand, Parker *et al.*[38] have developed Eu(III) complexes of NOTA-based ligands that stain cellular mitochondria, and Borbas *et al.*[39] have developed a series of complexes containing coumarin and carboxystril chromophores for multiplex detection.

1.2.7. Ligand to Metal Ion Energy Transfer-*Mechanisms*

Sensitised lanthanide luminescence is due to the absorption of light by a coordinated ligand and the subsequent energy transfer to the metal ion. Generally, energy transfer between a donor (*D*) and an acceptor (*A*) will follow one of two mechanisms: one involves electron transfer, known as Dexter energy transfer[40] and the other involving dipole-dipole interaction, known as Förster energy transfer.[41] Owing to the lack of the overlap of 4*f*-orbitals with the ligand orbitals, energy transfer primarily occurs through the Dexter exchange in lanthanides. In the case of Eu(III) and Yb(III) ions which are easily reduced, electron transfer and phonon-assisted mechanisms are also possible.[42]

Dexter energy transfer (Figure 1.4) is a double electron exchange interaction and is a through-bond mechanism. It depends on distance between donor and accept with a dependance on e^{-r} where r is the distance between *D* and *A*.[31a] It requires short donor-acceptor separations of < 10-15 Å as its distance dependence is e^{-r}.[43] Lanthanide luminescence is most effectively sensitised through the Dexter process as it is the ligand-based triplet excited state that transfers energy to the lanthanide centre over distances of ~ 50 pm, although distances up to 2000 pm are possible by superexchange.[10b,44] However, this energy transfer relies on a pathway which is

offered through covalent bonds. Spin selection rule does not apply here, therefore the transition can be singlet-singlet or triplet-triplet.[45]

Förster or dipole-dipole energy transfer (Figure 1.4) is a through-space interaction based on coulombic dipole-dipole interaction between the antenna and

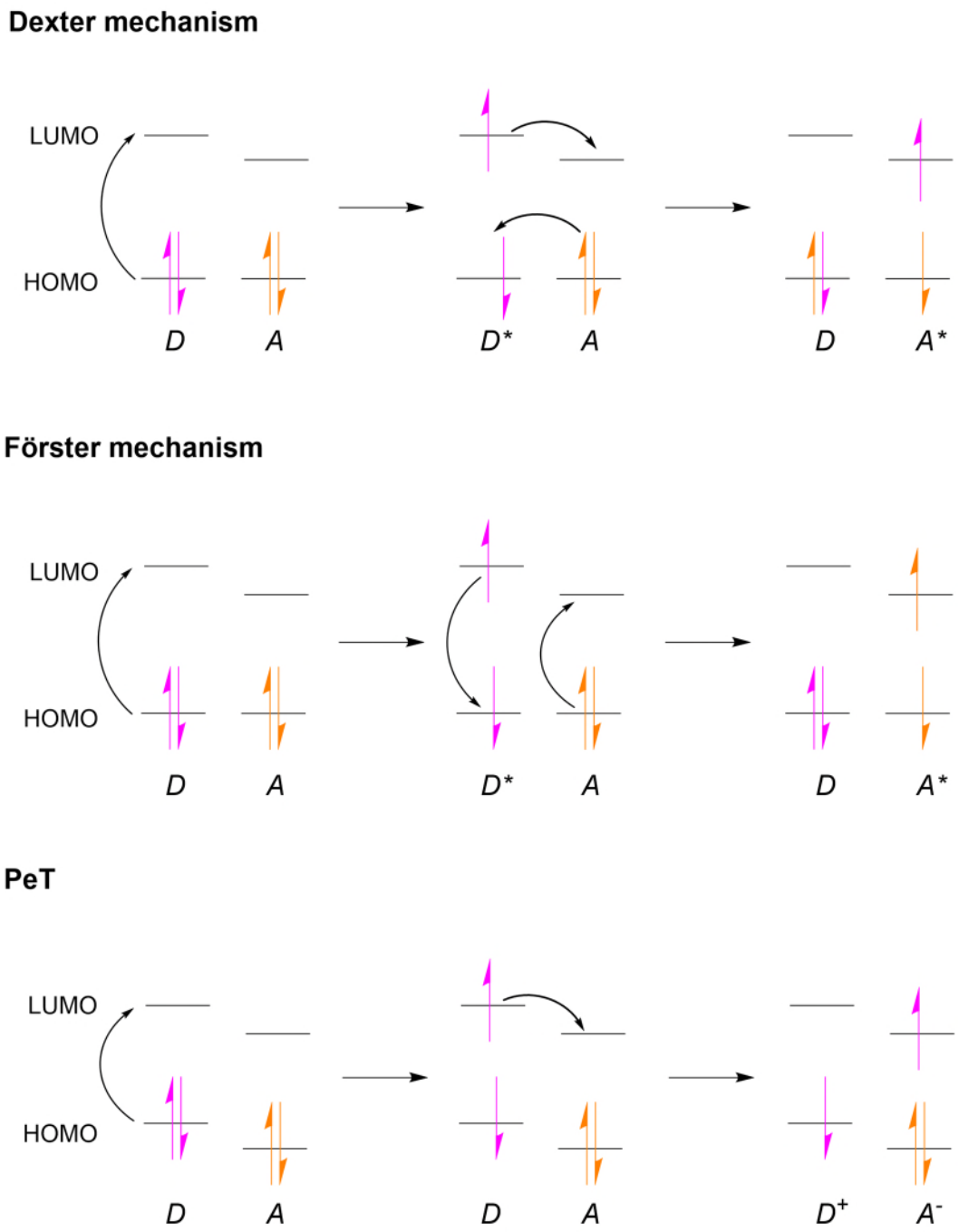


Figure 1.4. Pictorial representation of energy transfer between donor (*D*) and acceptor (*A*) through Dexter, Förster, and PeT mechanism. HOMO (Highest Occupied Molecular Orbital), LUMO (Lowest Unoccupied Molecular Orbital). Redrawn from ref 10b and 47c.

the metal center. Since it is electric-field dependent, distance between the donor and acceptor is crucial for this process. With a distance dependence of r^{-6}, it can operate over 100 Å distance.[43] It is noteworthy that no spin change can occur during this process.[44]

1.2.8. Quenching of Lanthanide Luminescence

1.2.8.1. Photoinduced electron transfer (PeT)

Photoinduced electron transfer (PeT) (Figure 1.4) is a process that occurs between the excited antenna and the highest emitting level of lanthanides.[45] Although it resembles the Dexter mechanism, electron transfer happens only in one direction. In Eu(III) complexes, PeT is observed from the chromophore to the metal contributing to diminished lanthanide luminescence. However, in Yb(III), PeT happens from the excited antenna to the metal and a back electron transfer from the transient Yb(II) to the antenna radical cation.[46] Borbas *et al.*[39,45,47] have extensively studied the PeT effect in Eu(III) and Yb(III) complexes. Kovacs *et al.*[39] have reported a study of 61 Ln complexes based on 14 ligands carrying either coumarin or carbostyril sensitisers and identified multiple sensitisation pathways contributing to Ln-emission in most of the metals. The role of PeT in the quenching of sensitised Eu(III) emission and the strategy for diminishing this quenching pathway is reviewed.[45] Some of the ways to control PeT include Ln-antenna distance, antenna and Ln redox properties, and Ln coordinating environment.[39,45,47a,c] The effect of PeT is also prevalent in the complexes of anions such as sugars and halides which contribute to quenching of lanthanide luminescence.[48]

1.2.8.2. Non-radiative quenching (multiphonon relxation)

As shown in the Jablonski diagram (Figure 1.3), non-radiative quenching pathways exist at several stages of the sensitisation process leading to overall low efficiency

of lanthanide luminescence. High energy molecular vibrations of ligands that encapsulate the Ln(III) ion, in particular C–H, N–H, and O–H, are good quenchers of lanthanide luminescence.[33] The energy gap law states that the smaller the energy gap, the smaller the number of phonon and higher the quenching (eq 1.3).[49]

$$\Delta k_{nr}^{Ln}(OH) = \frac{1}{\tau_{OH}^{obs}} - \frac{1}{\tau_{OD}^{obs}} \qquad (1.3)$$

Where τ_{OH}^{obs} is the observed luminescence lifetime in protic solvent and τ_{OD}^{obs} is the observed luminescence lifetime in deuterated solvent.[49]

Quenching can occur when vibrational harmonics of nearby oscillators overlap with the lanthanide excited state, inducing energy transfer (Figure 1.5).[10] Accordingly, in intrinsic Ln(III) emission, smaller the energy gap between the emissive state and the highest sub-level of ground state manifold, easier it is to non-radiatively quench the emission. Eu(III) and Yb(III) have relatively small energy gap (12,300 and 10,250 cm^{-1}, respectively) and are efficiently quenched by

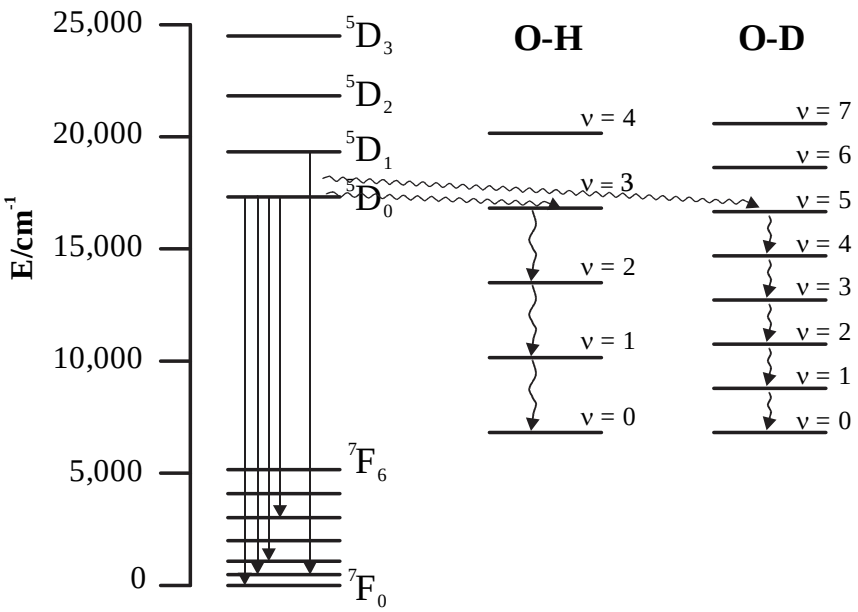


Figure 1.5. Radiative transitions of Eu(III) and non-radiative quenching through O–H and O–D bonds (adapted from Ref 10b).

coupling to the third vibrational overtone of nearby O–H oscillators.[33a] In Eu(III), the quenching of the emissive state is achieved through three vibrational quanta of the O–H bond, with a vibrational energy of 3,600 cm^{-1}. Tb(III) with a larger energy gap (15,000 cm^{-1}), couples to the fourth overtone with a poor Franck-Condon overlap, resulting in less effective quenching. O–D oscillator with a low vibrational energy of 2,200 cm^{-1} alongside its higher reduced mass relative to the O–H oscillator proves inefficient in quenching of lanthanide luminescence. The higher vibrational states which match the lanthanide emissive state have poor Franck-Condon overlap and are less populated at room temperature. This leads to inefficient vibronic quenching and longer luminescence lifetimes for Ln(III) ions in deuterated solvents.[10b,31a,33a] Vibrational bridging of different energy gap in lanthanide metals by O–H and O–D bonds is presented in Table 1.3.

Table 1.3. Vibrational bridging of different energy gap in lanthanide metals by O–H and O–D bonds

Ln(III)	$\Delta E/cm^{-1}$	No of phonons	
		OH	OD
Gd($^6P_{7/2}$)	32,100	9	15
Tb ($^5D_4$)	14,800	4	7
Eu ($^5D_0$)	12,200	3-4	5-6
Yb ($^4F_{5/4}$)	10,300	3	4.5
Dy ($^4F_{9/2}$)	7,850	2-3	3-4
Sm ($^4G_{5/2}$)	7,400	2	3
Er ($^4I_{11/2}$)	6,600	2	3
Nd ($^4F_{3/2}$)	5,400	1-2	2-3

Horrocks *et al.*[50] derived an empirical equation which allows the determination of the number of water molecules coordinated to the metal by comparing the emission lifetimes in water and deuterated water. This was later

modified by Parker *et al.*[33a] in order to account for N–H (3,300 cm^{-1}), C–H (2,900 cm^{-1}), and C=O oscillators and to extend the Horrocks′ equation for the quenching of Ln(III) luminescence in methanol and deuterated methanol. It is noteworthy that C-H oscillators play a crucial role in quenching Nd(III) luminescence due to its energy level matching the emissive level of the metal.[33a]

The rate constant for the depopulation of a Ln(III) emissive state in water can be expressed as a sum of different quenching contributions (eq 1.4).

$$k_{H_2O} = k_R + k_{NR} + \sum k_{X-H} + \sum k_{C=O} \quad (1.4)$$

Where $\sum k_{X-H}$ and $\sum k_{C=O}$ are the sum of rate constants for the energy transfer to X-H and C=O oscillators, respectively.

For deuterated solvents, exchangeable X–H oscillators contribute negligibly to quenching so the rate constant in deuterium oxide can be calculated using eq 1.5.

$$k_{D_2O} = k_R + k_{NR} + \sum k_{C=O} \quad (1.5)$$

The difference between k_{H_2O} and k_{D_2O} corresponds to Δk (eq 1.6) which is related to the number of bound water molecules (q) on the lanthanide ion.

$$\Delta k = k_{H_2O} - k_{D_2O} \approx \sum k_{X-H} \quad (1.6)$$

The value of q is described by the Horrocks′ equation 1.7

$$q = A(k_{H_2O} - k_{D_2O}) \quad (1.7)$$

where, A is a proportionality constant which refers to the sensitivity of each lanthanide to O–H vibronic quenching. To account for additional sources of quenching such as N–H oscillators in polyamines and outer-sphere O–H contributions, the modified Horrocks′ equation **1.8** containing the constant B is introduced. It is assumed that these contributions are the same for all lanthanide

complexes, hence *B* is a constant. This makes quenching more efficient and increases *q*.

$$q = A(k_{H_2O} - k_{D_2O} - B) \quad \textbf{(1.8)}$$

This equation can be further simplified to eq 1.9.

$$q = A(\frac{1}{\tau_{OH}^{obs}} - \frac{1}{\tau_{OD}^{obs}} - B) \quad (1.9)$$

This equation works well when there are fewer than three bound water molecules. *q* is rarely an integer and has a standard error of ±10%. Non-integer values arise since A and B are defined for an average water separation. Small changes to the Ln–O distance are amplified as quenching occurs through space which follows an r^{-6} dependency. The parameters that determine *q* are presented in Table 1.4.

Table 1.4. Parameters that determine *q* for selected Ln(III) metals

Lanthanide	Solvent	A (ms)*	B (ms)*
Eu(III)	water	1.2	$0.25 + 0.44n_{OH} + 0.075n_{CONH}$
	methanol	2.4	$0.125 + 0.44n_{OH} + 0.075n_{CONH}$
Tb(III)	water	5.0	0.06
Yb(III)	water	1.0	0.1

* A = inner-sphere contribution, B = outer-sphere contribution. A and B are determined using a series of complexes of known *q* value from X-ray crystal structures.

Eq 1.8 is good in predicting the inner-sphere water in ionic metals and in mononuclear complexes, but it becomes associated with very large errors in multimetallic lanthanide systems as they tend to quench each other proving it hard to establish the hydration number. Although there are other equations and techniques to predict the hydration number,[10b] eq 1.8 is the one that is widely used to determine the number of inner-sphere water molecules in lanthanide complexes.[51]

1.2.9. Circularly Polarised Luminescence

Molecular chirality is a unique property where two mirror images of a molecule cannot be superimposed on each other. For a given chiral molecule, its chirality is preliminarily determined through optical rotations using a polarimeter where the plane polarised light is turned left or right depending on the enantiomeric excess of the given molecule. Circular Dichroism (CD) (which is a chiral UV spectroscopy) allows one to probe the chirality of the ground state. Therefore, in CD spectroscopy, all absorbing chromophores which are chiral contribute and affect the observed differential absorption measurements. However, in the case of Circularly Polarised Luminescence (CPL) (which is a chiral luminescence spectroscopy), chirality of the excited state is probed. CPL is restricted to luminescent species where it reflects local chiral structural changes associated with the local environment surrounding the emitting species. The measurement of net circular polarisation in luminescence is referred to as of Circularly Polarised Luminescence. Nonetheless, lanthanides dominate the world of CPL based luminescent probes due to their greater luminescence dissymmetric factor (g_{lum}) in comparison to other compounds.[10b,50b,52] The dissymmetric factors of selected chiral species are presented in Table 1.5.[53]

Table 1.5. Luminescence dissymmetric factors of selected chiral species[53]

Chiral molecular system	g_{lum} **Representative maximum**
Lanthanide complexes	~10^{-1}
Helicenes	~10^{-2}
Ketones	~10^{-2}
Helical polymers	~10^{-2}
Proteins	~10^{-2}
BODIPYs	~10^{-3}
Self-assembled chiral nanoparticles	~10^{-3}
Quantum dots	~10^{-3}

1.2.9.1. Factors that govern CPL

From a chiral non-racemic luminescent molecule, CPL spectroscopy measures the difference in luminescence intensity (ΔI) of left circularly polarised light (I_L) versus the right circularly polarised light (I_R). This is represented as $\Delta I = I_L - I_R$. Owing to the difficulty in measuring the absolute emission intensities, the degree of CPL is reported (quantified) as luminescence dissymmetric ratio (or factor), g_{lum} by equation 1.10. This represents the ratio of the difference is emission intensity to the average total luminescence intensity.

$$g_{lum} = \frac{\Delta I}{\frac{1}{2} I} = \frac{I_L - I_R}{\frac{1}{2}(I_L - I_R)} \tag{1.10}$$

The extra factor of one-half in this equation is used to establish consistency with the related quantity in CD, the Kuhn dissymmetric ratio g_{abs} (eq 1.11)

$$g_{abs} = \frac{\Delta \varepsilon}{\varepsilon} = \frac{\varepsilon_L - \varepsilon_R}{\frac{1}{2}(\varepsilon_L - \varepsilon_R)} \tag{1.11}$$

ε is explicitly defined as an average quantity, while ε_L and ε_R indicate the molar absorption coefficients of left and right-circularly polarised light, respectively. Further, it is demonstrated that for a case of a randomly oriented emitting distribution, the orientational average yields eq 1.12 where μ^{gn} and m^{gn} refer to the electric dipole transition moment and the imaginary MD transition moment, respectively.

$$g_{lum}(\lambda) = 4Re\left[\frac{\mu^{gn} \cdot m^{gn}}{\left|\mu^{gn}\right|^2 + \left|m^{gn}\right|^2}\right] \tag{1.12}$$

From the above equation, it is conceivable that the measurement of larger g_{lum} values occurs when the transition considered is ED forbidden, but MD allowed.

Due to the typically much smaller MD transition moments than the ED terms, the denominator in the above equation will be dominated by the first term, $|\mu|^2$. Hence, CPL is dominated by Ln(III) complexes in which large g_{lum} values are achieved from the MD allowed intraconfigurational *f-f* transitions of the lanthanide ions. However, g_{lum} can be large (up to 1.38) for MD transitions,[230] but they have usually low intensity and as a result, more difficult to measure. A value of 0 for g_{lum} corresponds to no circular polarisation, while the absolute maximum is 2.

1.3. Macrocyclic Complexes of Lanthanides

For many applications of the Ln(III) ions, ligands are required to chelate these ions to control and modify their chemical properties and to maintain their solution stability. Luminescent Ln(III) complexes of chelating organic ligands conjugated with a chromophore can exhibit sensitised Ln(III) luminescence.[1b,24,48,54] For these reasons, strongly absorbing antenna must be incorporated in ligands that chelate the metal.[48,55] Polyazacarboxylate macrocyclic ligands with eight or nine donor atoms are well suited to form stable Ln(III) complexes as has been demonstrated by the studies on Gd(III) chelates of DOTA and its derivatives. Such complexes are currently used as contrast agents for MRI and these chelating ligands made a significant impact on major biomedical imaging modalities, including PET, SPECT, and fluorescence imaging.[56] The availability of a range of chelating ligands with different affinities and selectivity patterns for the Ln(III) ions, measured by the stability constant K_{LnL}, is valuable for the development of Ln(III) complexes for many applications.[57]

1.3.1. Lanthanide(III) Complexes of Macrocyclic Polyaminocarboxylates: *Thermodynamic Stability and Metal Ion Selectivity*

In general, most ligands possess a higher affinity for the heavier, smaller Ln(III) ions because the increased charge density on these smaller ions enhances metal-ligand electrostatic interactions. Macrocyclic ligands, however, have some additional features, including internal cavity size, conformation, and preorganisation properties which affect the stability and their acid-assisted dissociation rates. Four types of Ln(III) selectivity patterns for macrocyclic ligands have been identified. The most common trend shows a systematic increase in K_{LnL} across the lanthanide series (type I). This type I behavior is observed for many well-known ligands including EDTA, DOTA, and DTPA.[58] Another less frequently observed trend, type II, has the stability reach a maximum prior to dropping again. The ligands OBETA[59] and TCMC[60] follow this pattern. The rarely observed trend, type III, occurs with ligands having reverse-size selectivity, an unusual thermodynamic preference for large over small Ln(III) ions. This pattern has been observed in ligands containing the large diaza-18-crown-6 macrocycle such as macropa[61] and dacda.[62] A common feature of these three selectivity patterns is that they all have a maximum affinity for only one Ln(III) ion.

Wilson *et al.*[63] have studied the size-selectivity pattern of 18-membered macrocyclic ligands macrodipa and macrotripa bearing two or three pendent picolinate donors, respectively, for Ln(III) ions and found that the ligands undergo dramatic conformational changes upon binding large versus small Ln(III) ions. These conformational changes manifest in a type IV selectivity pattern, revealed from a plot of log K_{LnL} versus the Ln(III) ionic radius,[64] with one minimum and two maxima of stability (K_{LnL}) across the Ln(III) series. Incorporation of conformational

flexibility in ligands can be used to satisfy the coordination environments of different lanthanide ions, a principle of great value for chelator design efforts.

1.3.2. Thermodynamic Stability and Kinetic Inertness of Ln(III) Macrocyclic Complexes

The thermodynamic stability is quantitatively defined as the stability constant log K_{LnL} (eq 1.13) of the complex formation equilibrium between a Ln(III) ion and a ligand (L) and it provides the affinity of Ln(III) for a given ligand.

$$Ln + L = LnL \qquad K_{LnL} = \frac{[LnL]}{[Ln][L]} \qquad (1.13)$$

The thermodynamic selectivity is quantitatively defined as the difference (Δlog K) of the log K_{ML} values of two different metal complexes (eq 1.14). Thus, for a Ln(III) complex, [LnL],

$$\Delta\log K_{Ln/M} = \log K_{LnL} - \log K_{ML} \qquad (1.14)$$

where ML is a different metal complex. A positive value of Δlog K indicates ligand selectivity in favour of the Ln(III) ion and a negative value indicates selectivity in favour of the other metal ion, M. The structural, thermodynamics, and kinetics aspects of macrocyclic complexes of lanthanides are described by Chang.[65] The linear correlation between the sum of the ligand protonation constants (Σ log K_{1-n}) and thermodynamic stability (log K_{GdL}) was reported.[66] For instance, DOTA is much more basic than DTPA-BMA (sum of ligand protonation constants: Σ log K_{1-4} = 30.94 versus Σ log K_{1-4} = 19.3, respectively)[67] and forms a thermodynamically much more stable complex with Gd(III) (log K_{GdL} = 24.7 versus log K_{GdL} = 16.85, respectively). Under all applied conditions, the macrocyclic Ln(III) complexes are the kinetically most inert, which is in line with what has been observed in *in vivo* studies where Gd(III) release was examined in animal models. The rigidity of the

macrocyclic Ln(III) complexes leads to considerably slower dissociation rates in comparison to the linear Ln(III) chelates.

1.3.3. Dissociation Kinetics of Ln(III) Macrocyclic Complexes

In general, linear DTPA-type Ln(III) chelates are kinetically more labile than the macrocyclic DOTA-type complexes. At physiological pH, the dissociation of linear chelates proceeds mainly via transmetalation, which mainly takes place via the acid-assisted pathway. In contrast, the dissociation of macrocyclic chelates is much slower and independent of the exchanging metal ion concentration, showing that it occurs through proton-assisted pathways.[68] The thermodynamic stability constants for cyclen-based macrocyclic Ln(III) complexes follow the order: [Ln(**ODO2A**)]$^{+}$ < [Ln(**DO2A**)]$^{+}$ < [Ln(**DO3A**)] < [Ln(**DOTA**)]$^{-}$. In general, at a given pH, for a given Ln(III) ion such as Eu(III) ion, the dissociation rates follow the order: [Eu(**DOTA**)]$^{-}$ < [Eu(**DO3A**)] < [Eu(**DO2A**)]$^{+}$ < [Eu(**ODO2A**)]$^{+}$ which is the reverse trend of their formation stability.

1.3.4. Lanthanide Complexes of the Ubiquitous DOTA and its Derivatives

The macrocyclic ligand DOTA was first reported as a chelate in 1976[69] and the first lanthanide complex was published by Bryden *et al.*[70] in 1981. It exhibits a very strong complexing ability toward Ln(III) ions because it provides a preformed internal cavity of eight donor sites well suited to wrap around the metal ions. This results in tightly packed complexes with high thermodynamic stability, conformational rigidity, and kinetic inertia.[71] The X-ray crystal structures of [Ln(**DOTA**)]$^{-}$ complexes (Ln = Eu(III),[72] Gd(III),[73] and Lu(III)[74]) show that DOTA acts as an octadentate ligand with four nitrogen and four oxygen donor atoms arranged in a square-antiprismatic geometry around the lanthanide ion with a ninth axial coordination site, at a capping position above the plane of the four oxygens,

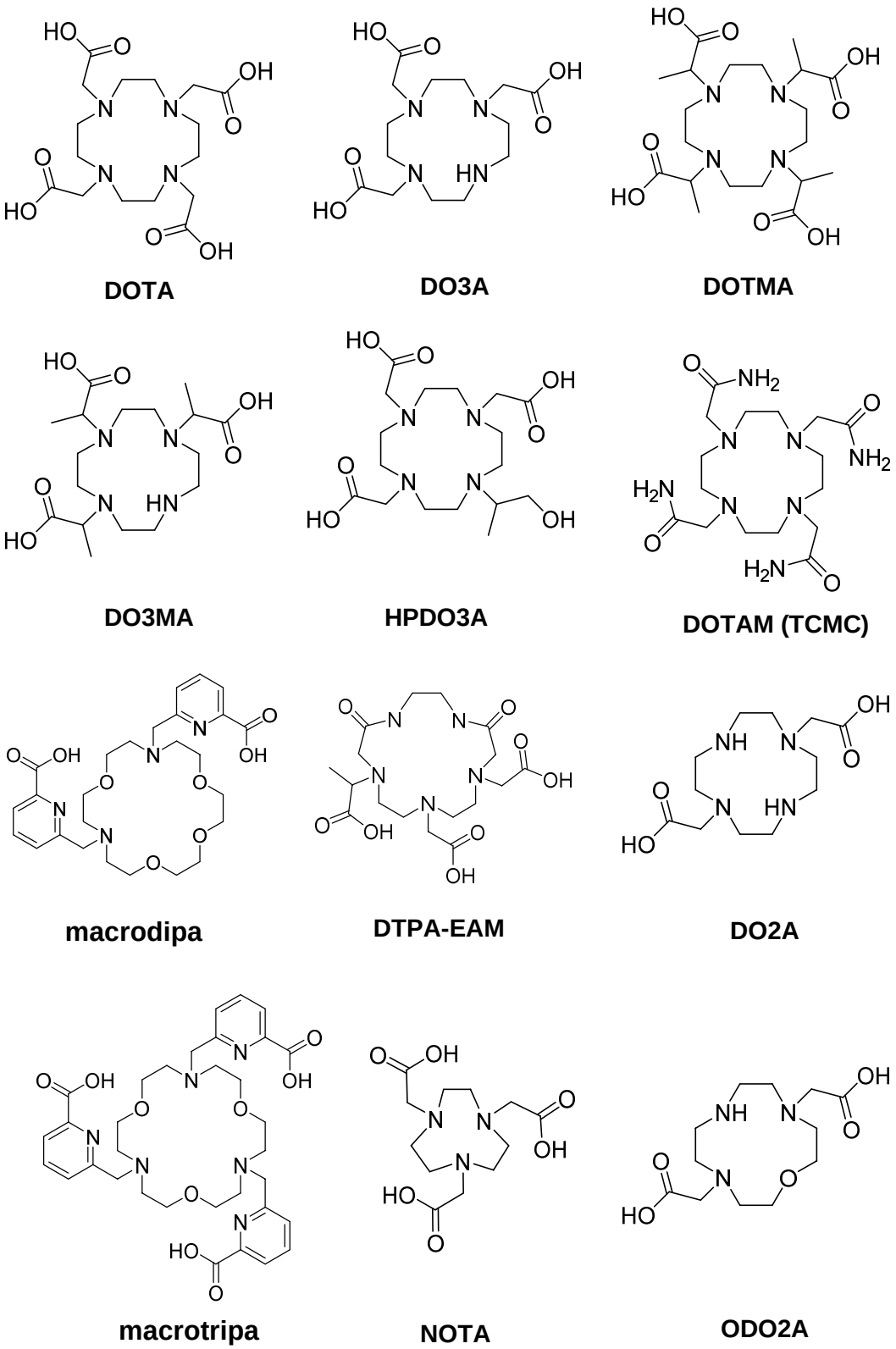


Figure 1.6. Macrocyclic polyaminocarboxylate ligands used in chelating Ln(III) metals.

occupied by one water molecule. [Gd(**DOTA**)(H_2O)]$^-$ exhibits the highest thermodynamic stability constant of 24.7.[58b] An alternate value sometimes reported is pM (-log[M]) which refers to the unchelated metal ion under a given set of conditions, where higher the pM value, the more stable the complex.

DOTA became the parent molecule of an ever-growing family of macrocyclic Ln(III) chelating ligands. By replacing one of the acetate arms in DOTA with a different moiety, the ligand becomes a derivative of DO3A. Such heptadentate ligands yield coordinatively unsaturated Ln(III) chelates with lower thermodynamic stability and kinetic inertness than the chelates of DOTA.[66] A wide range of DOTA- and DO3A-based macrocyclic ligands have been developed by substituting chemical groups on the macrocyclic ring and/or on the pendant arms. Modification of the substituent pendant arms of DOTA has led to the creation of functional-, targeted-, and dual-modal imaging agents.[56] Functionalisation of the nitrogen atoms of cyclen by pendant arms containing donor groups is crucial in order to ensure thermodynamically stable and kinetically inert Ln(III) chelates. Several functional groups such as carboxylates, phosphonates, phosphinates, amides, or alcohols have been used. Derivatives containing more than one type of pendant arm have also been synthesised. Bifunctional chelating agents have also been designed in order to broaden the fields of application of the DOTA derivatives. The synthetic strategies used for the preparation of bifunctional chelators for MRI applications is reviewed.[75]

The stabilities of Gd(III) complexes of DOTA, HPDO3A, DO3A, and DO2A follow the order: [Gd(**DOTA**)]$^-$ > [Gd(**HPDO3A**)] > [Gd(**DO3A**)] > [Gd(**DO2A**)]$^+$ with log K_{GdL} values of 24.6, 23.8, 21.0, and 13.06 (25 °C, I = 0.1 M NaCl or $(CH_3)_4NCl$, respectively.[66,76] The respective log K_{LnL} values of [Ce(**DO3A**)],

[Lu(**DO3A**)], [Ce(**HPDO3A**)], and [Lu(**HPDO3A**)] are 19.7 ± 0.4, 23.0 ± 0.2, 21.2, and 23.3 ± 0.3.[66] This indicates that the stability of the complexes increases with the ligand basicity, increasing number of coordinating atoms, and chelate rings on the complex as well as decreasing ionic radii or increasing charge density of the lanthanide ions. Substitution of nitrogen donors by oxygen atoms decreases the overall basicity of the ligand, resulting in reduced Ln(III) complex stability. For example, the log K_{LnL} values for [Gd(**ODO2A**)]$^{+}$ (~12.0) is less than that of [Gd(**DO2A**)]$^{+}$ (~13.1).

1.3.5. NMR Studies of Solution Structures and Conformations of Lanthanide Macrocyclic Complexes

Trivalent lanthanides form stable but highly fluxional chelates with a variety of ligands. Their lability results in the appearance of one set of NMR peaks for a large number of geometries in fast exchange. The ^{1}H NMR spectra of [Ln(**DOTA**)]$^{-}$ complexes (Ln = La(III), Lu(III), Eu(III), and Yb(III)), reported by Desreux in 1980,[71a] showed that DOTA forms highly symmetric and exceedingly rigid lanthanide complexes and the rigidity of the macrocycle ring is lost as the temperature is increased. This rigidity is due to the strong preference of the 12-membered tetraazacyclododecane ring of DOTA, enforcing a square [3.3.3.3] geometry. The low-temperature limiting ^{1}H and ^{13}C NMR spectra of [Ln(**DOTA**)]$^{-}$ complexes (Ln = La(III), Pr(III), Nd(III), Sm(III), Eu(III), Tb(III), Dy(III), Ho(III), Er(III), Tm(III), Yb(III), and Lu(III)), reported by Aime *et al.*,[77] show that the complexes in solution exist in two diastereomeric forms in slow exchange at room temperature, one with larger shifts (due to larger magnetic anisotropic susceptibility) than the other. The structures of these isomers were determined from the analysis of the dipolar shifts in the ^{1}H NMR spectrum of [Yb(**DOTA**)]$^{-}$ and are called M (major) and m (minor). The relative abundance of the two isomers changes

markedly along the lanthanide series and it is found that the structure of the major isomer of [La(**DOTA**)]$^{-}$ corresponds to that of the minor isomer of [Lu(**DOTA**)]$^{-}$. These isomers differ in the layout of the acetate arms, while the cyclododecane ring conformation being identical in both species. The structure found for the M isomer closely resembles those observed in the X-ray crystal structures of DOTA complexes of Eu(III), Gd(III), Dy(III), Ho(III), Lu(III), and Y(III) complexes, displaying regular antiprismatic geometry of the DOTA ligand around the lanthanide ion.[72-74,78]

Conversely, a less regular coordination geometry, envisaged as an inverted antiprism, strongly distorted toward a regular prism, has been found for the m isomer.[77] This m-type structure is found in the X-ray crystal structures of other macrocyclic complexes such as [La(**DOTAM**)],[79] [Eu(**THP**)],[80] [Y(**DOTPBz$_4$**)],[81] and [Gd(**DO3MA**)].[82] The intra- and intermolecular exchanges within and between the two isomeric forms of [Yb(**DOTA**)]$^{-}$ have been investigated by a quantitative analysis of the EXSY spectra.[83] The square-antiprismatic geometry of [Ln(**DOTA**)]$^{-}$ complexes implies the occurrence of two helicities, one belonging to the cyclen ($\lambda\lambda\lambda\lambda$ and $\delta\delta\delta\delta$) and one associated with the layout of the acetate arms (Δ and Λ), which may give rise to two enantiomeric pairs of diastereoisomers (Figure 1.7).

Aime *et al.*[84] have reported the isomer equilibrium for the [Ln(**DOTA**)]$^{-}$ complexes along the lanthanide series from the detailed ^{1}H, ^{13}C, and ^{17}O NMR study of the effects of temperature, pressure, and ionic strength of the aqueous solutions of DOTA complexes of all trivalent rare earth cations (Sc(III), Y(III), La(III), Ce(III)-Lu(III)). In order explain the observed apparent reversal of the isomer ratio at the end of the lanthanide series, the authors have proposed a model where a coordination equilibrium, arising from the loss of inner-sphere water

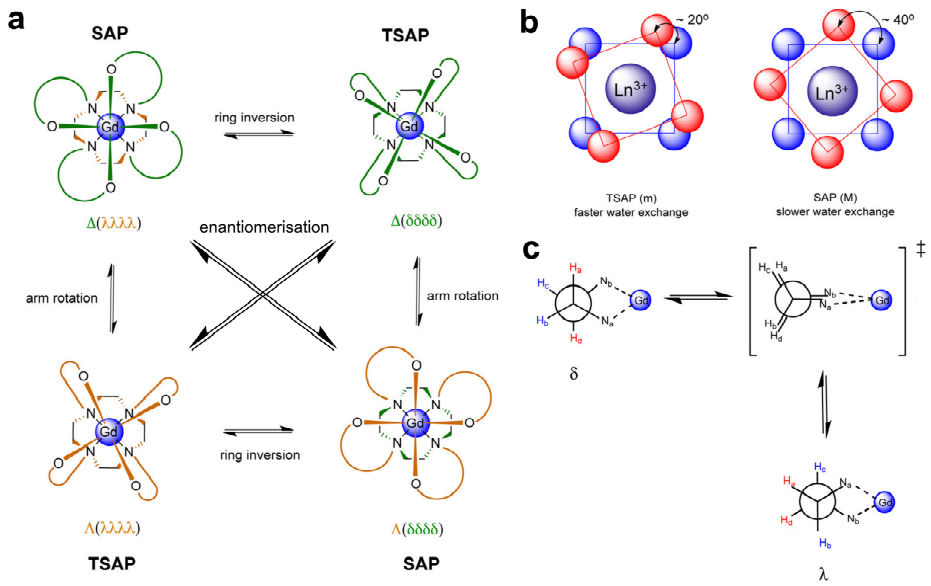


Figure 1.7. Dynamics of [Ln(**DOTA**)]⁻ in solution. (a) SAP/TSAP interconversion occurs by either arm rotation or ring inversion. Sequential application of both processes leads to enantiomerisation. (b) The SAP (M) and TSAP (m) isomers of macrocyclic lanthanide chelates differ in the twist angle between the planes defined by the chelating nitrogen and oxygen atoms. It is proposed that the TSAP isomer is more sterically crowded about the water binding site, weakening the Gd–O_w bond and leading to faster water exchange. (c) During the ring inversion process, the axial and equatorial protons of the two isomers exchange with one another; conversely, during the arm rotation process, the axial protons of one isomer exchange only with the axial protons of the other (adapted with permission from Ref 191a).

molecule by both conformers, is superimposed on this conformational equilibrium. Thus, in solution two diastereomeric forms, the majuscule M and M′ assign the Δ(*λλλλ*)/Λ(*δδδδ*) pair, with (M) and without (M′) inner-sphere water, and the minuscule m and m′ the Λ(*δδδδ*)/Δ(*λλλλ*) pair, with (m) and without (m′) inner-sphere water, occur (Figure 1.7). The transformations between M and M′ or between m and m′ species, which differ in the coordination of one water molecule, appear to be fast on the proton NMR time scale and thus not distinguishable by this technique.

The isomers predominate in this order as the Ln(III) ion radius decreases: the m structure is observed from the La(III) to the Dy(III) complex, but predominates

until Nd(III), the M structure is present from La(III) to Lu(III) and is most stable at Ho(III), the m′ form appears from Er(III) to Lu(III), and the M′ structure is not observed for the Ln(III) complexes, but observed its presence in the [Sc(**DOTA**)]$^{-}$ complex. In the cases of all paramagnetic chelates of the lanthanides, except Tm(III), the M isomer has the larger susceptibility anisotropy relative to the other isomer (m or m′). The abnormally high paramagnetic shifts for the Tm(III) m′ isomer could be related to changes in the crystal field parameter (B_0^2), which have been reported for the [Ln(**DOTP**)]$^{5-}$ chelates (Tb-Yb), where this parameter has the largest value for Tm(III).[85] The dynamics of [Ln(**DOTA**)]$^{-}$ in solution is shown in Figure 1.7.

1.4. Paramagnetism in Lanthanides

The unique chemical and physical properties of lanthanide complexes arise from the electronic structure of these metal ions. Electrostatic shielding of 4*f*-orbitals by the occupied 5*s*- and 5*p*-orbitals reduces their interactions with ligands and neighbouring molecules. Interelectron repulsion and spin-orbit coupling can become on the same order of magnitude as ligand-field effects. Due to these differences, electronic transitions in Ln(III) complexes are often independent of the ligand environment, and the ligand field splitting can be considered on the basis of the ground-state total angular momentum, *J*. For a given *J* multiplet, the model Hamiltonian is represented by eq 1.15.

$$\hat{H} = \sum_{k=2,4,6} \theta_k \sum_{q=-k}^{k} B_q^k \hat{O}_k^q \qquad (1.15)$$

where B_q^k are crystal field parameters, O_q^k are Stevens operators, and θ_k are operator equivalent coefficients. *k* is the rank label with the possible value from 0 to 7. The interactions between electrons in different orbitals contribute to the even numbers of the rank label (2, 4, and 6), whereas the electrical dipole transition is responsible for the odd rank labels. The component label, *q* is related to the symmetry elements.

The magnitude of this parameter is increased when the symmetry is reduced. Thus, for a complex with low symmetry, this parameter has a significant effect on paramagnetism.[86]

1.4.1. Paramagnetism and Magnetic Susceptibility by NMR

Magnetic susceptibility plays an important role in the paramagnetism of lanthanide containing systems. The magnetic susceptibility becomes anisotropic when there is residual orbital magnetic moment (as a consequence of spin-orbit coupling).[87] In paramagnetic lanthanide complexes, the anisotropy of magnetic susceptibility causes direct changes to the chemical shifts of a given nucleus in a coordinated ligand compared to the corresponding diamagnetic analogue; this effect is known as the lanthanide induced shift (LIS) which is also called the hyperfine shift (δ_ω, expressed in ppm). The LIS for a nucleus of a ligand arises via three mechanisms: contact (δ_c) (through bond), pseudocontact (δ_{pcs}) (through space), and diamagnetic (δ_d) mechanisms (eq 1.16).[88]

$$\delta_\omega = \delta_d + \delta_c + \delta_{pcs} \qquad (1.16)$$

Diamagnetic shifts are usually small, as a result of modulating the electronics of the ligand. The contact (or Fermi) contribution (δ_c) results from a through-bond transmission of unpaired electron spin density of Ln(III) to the ligand nucleus. The distance between the paramagnetic metal center and the nucleus can be several chemical bonds away, or even longer if the chemical bonds contain π-character. Therefore, the contact shift implies structural information of bonding. The contact shift contribution by a paramagnetic Ln(III) ion in complexes can be calculated using eq 1.17.[88]

$$\delta_c = \langle S_z \rangle F = \langle S_z \rangle \frac{\beta}{3kT\gamma_1}\frac{A}{\hbar}10^6 \qquad (1.17)$$

The pseudocontact shift is the result of a through-space dipolar interaction between the magnetic moments of the unpaired electrons in Ln(III) and the nucleus under study. In most lanthanide-containing complexes, the pseudocontact term (δ_{pcs}) is the dominant factor in determining the observed shift for a given nucleus. This is due to the unpaired electron spin density which largely resides on the Ln^{3+} ion. Since the dipolar shift depends on the orientation of the resonating nucleus with respect to the Ln^{3+} ion, useful structural information may be gained. δ_{pcs} induced by lanthanide complexes are described by McConnell′s long-range relation (SI units) (eq 1.18),[89]

$$\delta^{PCS} = \frac{1}{12\pi r^3}\left[\chi_{ax}\left(3\cos^2\theta - 1\right) + 3\chi_{rh}\sin^2\theta\cos 2\varphi\right] \qquad (1.18)$$

where θ, φ, and r are the polar coordinates of the nucleus relative to the lanthanide in the eigenframe of the molar magnetic susceptibility tensor and χ_{ax} and χ_{rh} are axiality and rhombicity of the susceptibility tensor.[90] The interpretation and control of δ_{pcs} often rely on Bleaney′s theory[91] which connects axiality and rhombicity with the ligand field parameters with different lanthanide metals for a well-isolated ground state when the magnitude of the *J*-states split by the ligand field is smaller than *k*T (eq 1.19).[92]

$$\chi_{ax} = -\frac{\mu_0\mu_B^2 C_J B_0^2}{10(kT)^2} \qquad \chi_{rh} = -\frac{\mu_0\mu_B^2 C_J B_2^2}{30(kT)^2} \qquad (1.19)$$

Where μ_B is the Bohr magneton, C_J is Bleaney′s constant, defined for each Ln, and B_0^2 and B_2^2 are second order ligand field parameters. Bleaney′s theory of magnetic anisotropy shows that for a well-isolated *J* multiplet in the high temperature approximation, the anisotropy of the susceptibility tensor depends only on the second rank ligand field parameters.[86,90,91] Subtracting δ_d, δ_w is expressed as magnetic anisotropy factor (δ') which is

$$\delta' = \delta_c + \delta^{pcs} \quad (1.19.1)$$

Most lanthanide complexes have a magnetic easy axis where it is energetically favourable to be spontaneously magnetised. Lanthanide complexes are prolate if their ground state aligns with the magnetic easy axis, and oblate if their ground state is perpendicular to it.[93] As a result of these effects created by *f*-elements from LIS to magnetic anisotropy, the NMR shift induced by these metals when chelated to organic ligands extend over a wide range of NMR spectral window. In the case of anion binding, chelation of anions to the coordinatively unsaturated lanthanide ion alters LIS and magnetic anisotropy.

Bleaney′s theory worked well in understanding the solution state dynamics of these complexes. However, both Judd-Ofelt theory[15,16] and Bleaney′s theory[91,92] fail to give an accurate picture of the optical properties and paramagnetic pseudocontact shift of lanthanide complexes. Thus, it is important to consider the relationship between molecular structure, electric and magnetic susceptibilities, as well as their anisotropies to design new complexes with desired optical properties for sensing-related applications.[86]

1.5. Magnetic Resonance Imaging

Magnetic resonance imaging (MRI) has evolved into one of the most powerful diagnostic techniques in modern clinical medicine and biomedical research.[94] It is used to obtain information on the physicochemical status of tissues and to monitor biological processes and functional changes *in vivo*, blood flow, and organ function.[94,95] Practical medical imaging is restricted to protons of the *in vivo* water molecules because of its high sensitivity and abundance. The specimen is placed in a magnetic field gradient, by using pulses of radio frequency radiation to induce nuclear spin transitions, one can image the specimen under study. After the

data collection from various field gradients, computational processing gives a three-dimensional computer reconstructed signal intensity map of the spatially encoded proton signal of the *in vivo* water molecules in a given volume element (*voxel*).

1.5.1. Relaxation Time and MR Image Intensity and Resolution

In MRI, the signal intensity comes from the proton of the water molecules in the body fluids and tissues. The signal intensity arising from any volume element is a function of the water concentration and other NMR parameters like the longitudinal relaxation time, T_1 and transverse relaxation time, T_2.

Most human soft tissues contain the same amount of water and therefore, do not allow tissue discrimination on the basis of water content.[96] However, the longitudinal and transverse relaxation times of water protons vary markedly depending on the tissue type and therefore, may be used as a source for a contrast in MR. The signal intensity depends on the longitudinal and transverse relaxation rates of water protons. The rapid movement of protons from one position to another during the relaxation experiment affects the signal intensity and for this reason moving blood usually has no detectable signals. It is common to increase the contrast of the images by increasing the relaxation rates of water protons by administering pharmacological products, called contrast agents. They are paramagnetic metal complexes which alters the longitudinal and/or transverse relaxation rates of water protons in the immediate surroundings of the tissue in which they localise, which contributes to the intensity of the MRI signal and thus to the contrast of the image.[88,94,97]

Tissues with short T_1 values generally give higher image intensity than those with longer T_1 values. On the other hand, short T_2 values are always associated with

lower signal intensity since this diminishes the net transverse magnetisation available for detection. The recent advancements in MRI demonstrates the feasibility of a true three-dimensional MR image at cellular resolution (10 μm).[95,98] A typical MRI scanner has spatial resolution in the hundreds of micrometers with 1 mm slice thickness, while ultra-high-field MRI can reach resolutions in the tens of micrometers (approximately the diameter of a mammalian cell). As a result, MRI can be used to detect at nearly single cell resolution, albeit requiring extremely "bright" contrast agents.[99]

1.5.2. Gadolinium(III) Complexes as Contrast Agents for MRI

Paramagnetic contrast agents are by far the most prominent MRI contrast agents. Paramagnetic metal ions such as Mn(II), Mn(III), Fe(II), Fe(III), Cr(III), and Gd(III) alter the relaxation of water protons.[100] Among these metal ions, Gd(III) with its half-filled f^7 shell (S = 7/2) and high spin Mn(II)- and Fe(III) complexes with their half-filled d^5 shells (S = 5/2) all exhibit a large magnetic susceptibility compared to other metal ions. Paramagnetic induced T_1 relaxation directly depends on the spin quantum number (as a function of $S(S+1)$) and inversely on the distance (r_{MH}) between the metal ion and the proton of the water as a function of $1/r_{MH}$. The shortest r_{MH} distance can be achieved through direct coordination of water molecule to the metal ion in the inner-coordination sphere (Figure 1.8). In order to transmit the relaxation effect to the bulk water, the exchange rate of the coordinated water molecule must be fast ($> 10^6$ s^{-1}). The absence of ligand field stabilisation energy of Gd(III) makes its complexes quite labile, thus favouring the fast-chemical exchange of the bound water molecule.[94,95]

Paramagnetic Gd(III)-based contrast agents (GBCAs) due to their Brownian motion in aqueous solution generates fluctuating magnetic fields that accelerate the

T_1- and T_2 relaxations of nearby water protons. This phenomenon is known as paramagnetic relaxation enhancement (PRE). In the body, water T_2 is generally 5–20 times shorter than T_1. As a result, the effect of a GBCA will be much more pronounced on T_1 and act predominantly as T_1 relaxation agents of water protons resulting in signal enhancement and 'positive' contrast.[94,95]

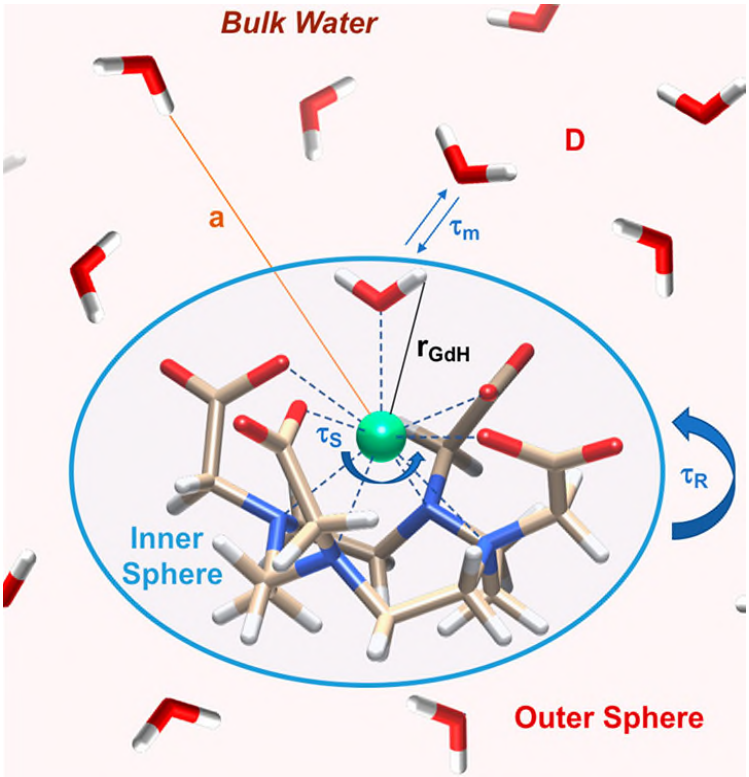


Figure 1.8. Physical parameters that govern relaxivity for a Gd(III)-based contrast agent. r_{GdH} is the metal ion to water hydrogen distance, rotational correlation time (τ_R), and the water residency time (τ_m), interaction of metal to outer sphere water (a), the electronic relaxation time (T_{1e} and T_{2e}, referred as τ_s) (reproduced with permission from Ref 94b).

Free Gd(III) ions are highly toxic (intravenous LD_{50} ~ 0.2 mmol/kg in mice) and therefore it must be administered as a complex with exceptionally high thermodynamic stability and kinetic inertia, thus rendering the paramagnetic metal biologically tolerable.[101] The *in vitro* and *in vivo* chemical results reported by Tweedle *et al.*[102] support the usefulness of strongly chelated Gd(III) complexes as contrast agents. The diagnostic potential of paramagnetic agents in patients was

studied by Carr *et al.*[103] by administering the FDA approved contrast agent [Gd(**DTPA**)(H_2O)]$^{2-}$ to patients with cerebral tumour. Since these early reports, Gd(III) has become the most widely used metal ion for the production of paramagnetic contrast agents.[94,95] Various measurements such as the thermodynamic stability constant, the conditional stability, and the kinetic inertness[100,104] are used to assess the stability of the chelates. The efficiency of a contrast agent is quantified by its relaxivity, which is the enhancement of the measured longitudinal relaxation rate of the water protons per millimole of added complex. The conventional units for relaxivity is $mM^{-1}s^{-1}$. Of all the potential metal complexes, discrete Gd(III) chelates have been the most successful paramagnetic contrast agents so far and dominate their use in the clinic.[94] The use of Gd(III) based contrast agents (GBCAs) further enhances anatomical resolution and improves diagnostic accuracy.[94,95,105] Clinically used GBCAs have an excellent safety profile with severe adverse events in only 1 in 40,000 injections.[106] As a result, approximately 40% of clinical MR scans employ Gd(III) chelates for contrast-enhanced MRI (> 20 million/year).[94]

1.5.3. Clinically Approved Gadolinium(III) Chelates as Contrast Agents

Clinically used GBCAs utilise an octadentate poly(aminocarboxylate) based ligand and have a ninth coordination site available for water coordination. The coordinated water can be rapidly exchanged with bulk water molecules. The first MR contrast agent was made available in 1988 for imaging blood-brain barrier abnormalities, and since then, contrast enhanced MRI has played an increasingly important role is diagnostic medicine.[107] Today, there have been some FDA approved MR contrast agents.

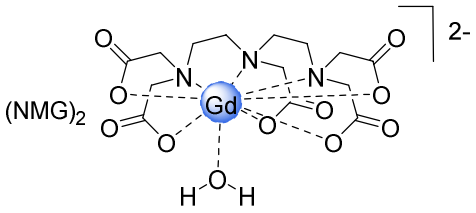
The clinically approved GBCAs are:[108] $(NMG)_2$[Gd(**DTPA**)(H_2O)] (**1**) (gadopentetate dimeglumine, Magnevist, Schering, Germany),[109]

[Gd(**DTPA-BMA**)(H_2O)] (**2**) (gadodiamide, Omniscan, Amersham-Nycomed),[109] [Gd(**DTPA-BMEA**)(H_2O)] (**3**) (gadoversetamide, OptiMark, Tyco Healthcare),[110] (NMG)[Gd(**DOTA**)(H_2O)] (**4**) (gadoterate meglumine, Dotarem, Clariscan, Guerbet, France), [Gd(**HP-DO3A**)(H_2O)] (**5**) (gadoteridol, ProHance, Bracco Diagnostics Inc.),[76,111] [Gd(**DO3A-butrol**)(H_2O)] (**6**) (gadobutrol, Gadovist, Schering), $(NMG)_2$[Gd(**EOB-DTPA**)(H_2O)] (**7**) (Eovist, primovist, Schering), MS-325 (**8**) (AngioMark, Vasovist BSP), $(NMG)_2$[Gd(**BOPTA**)(H_2O)] (**9**) (gadobenate dimeglumine, MultiHance, Bracco Diagnostics Inc.),[112] and Na_3[Mn(**DPDP**)] (**10**) (Figure 1.9). To date, only two manganese-based contrast agents have been approved: Na_3[Mn(**DPDP**)] and an orally administered contrast agent that consists of liposomal encapsulated manganese chloride (LumenHance).[113]

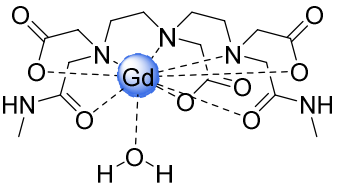
The first six complexes shown in Figure 1.9 act as nonspecific extracellular agents.[114] Seven of the commercially available agents received their primary indication for imaging lesions of the central nervous system which are classified as extracellular fluid (ECF) contrast agents. The complex $(NMG)_2$[Gd(**EOB-DTPA**)(H_2O)] received FDA approval for liver imaging applications, while MS-325 was approved for angiographic (blood vessel) imaging. A Mn(II) complex Na_3[Mn(**DPDP**)] and a superparamagnetic iron-oxide nanoparticle (SPION) formulation (ferumoxide) were approved for liver imaging, and an oral SPION formulation was approved for gastrointestinal imaging (ferumoxsil).[94]

1.5.4. Relaxation Theory for GBCAs

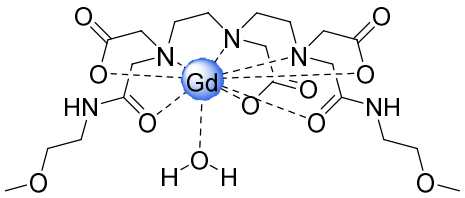
Nuclear relaxation rate of water protons is the result of the efficient dipolar magnetic coupling between the unpaired electrons of the metal ions and the nuclear spins of water proton. The general theory of nuclear relaxation in the presence of



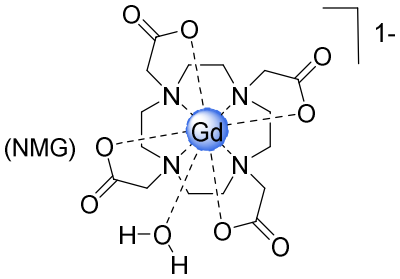
(NMG)$_2$[Gd(**DTPA**)(H$_2$O) (**1**)



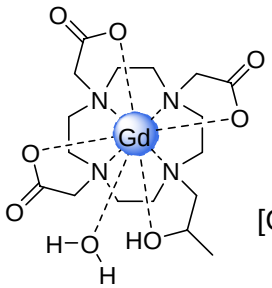
[Gd(**DTPA-BMA**)](H$_2$O) (**2**)



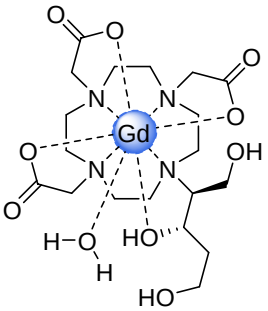
[Gd(**DTPA-BMEA**)](H$_2$O) (**3**)



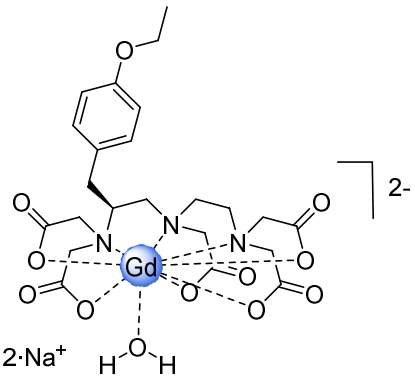
(NMG)[Gd(**DOTA**)](H$_2$O) (**4**)



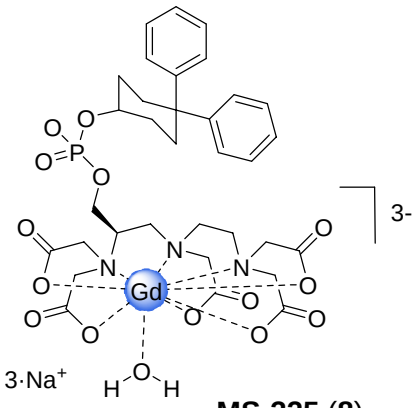
[Gd(**HP-DO3A**)](H$_2$O) (**5**)



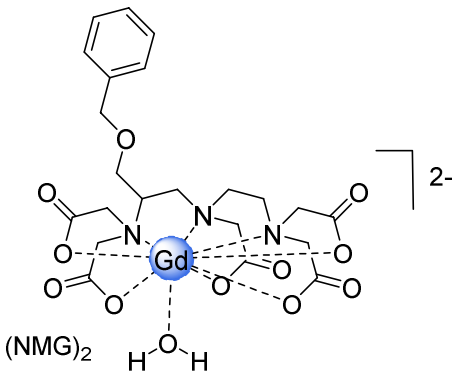
[Gd(**DO3A-butrol**)](H$_2$O) (**6**)



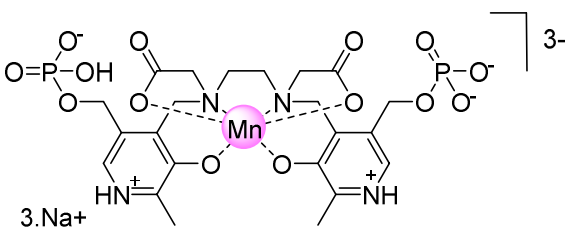
(NMG)$_2$[Gd(**EOB-DTPA**)](H$_2$O) (**7**)



MS-325 (**8**)



(NMG)$_2$[Gd(**BOPTA**)](H$_2$O) (**9**)



Na$_3$[Mn(**DPDP**)] (**10**)

Figure 1.9. Commercially approved T_1 contrast agents for MRI (NMG = meglumine).

paramagnetic substance was developed by Solomon, Bloembergen, and others.[115] Theory of proton relaxation pertaining to the GBCAs is reviewed.[94] The observed relaxation rate $(1/T_i)_{obs}$ is the sum of a diamagnetic term $(1/T_i)_d$ corresponding to the relaxation rate of the solvent nuclei without the paramagnetic solute and a paramagnetic term $(1/T_i)_p$ due to the relaxation rate enhancement caused by a paramagnetic compound (eq 1.20). In the absence of solute-solute interactions, the solvent relaxation rates are linearly dependent on the concentration of the paramagnetic complex. Thus, a plot of $(1/T_i)_{obs}$ versus concentration of the CA would give the relaxivity as the slope in units of $mM^{-1}\,s^{-1}$ (eq 1.21).

$$\left(\frac{1}{T_i}\right)_{obs} = \left(\frac{1}{T_i}\right)_d + \left(\frac{1}{T_i}\right)_p \quad i = 1,2 \tag{1.20}$$

$$\left(\frac{1}{T_i}\right)_{obs} = \left(\frac{1}{T_i}\right)_d + r_i[CA] \quad i = 1,2 \tag{1.21}$$

Relaxivity can be factored into inner-sphere and outer-sphere contributions. In the case of monomeric GBCAs, the inner-sphere relaxation contributes a major component of the observed proton relaxivity. It is the inner-sphere term that can be considerably augmented, whereas the outer-sphere contribution can hardly be modified.

1.5.4.1. Inner-Sphere Relaxation

The parameters that influence the relaxation efficiency of Gd(III)-based MRI contrast agent at the molecular level is pictorially depicted in Figure 1.8. The inner-sphere relaxivity is described by equations **1.22** and **1.23** by combining the definition of relaxivity with the Bloch equations for a system which is in fast exchange between two sites, where one pool (bulk water) is present at much higher concentration than the other pool (metal bound water).

$$r_1^{IS} = \frac{q/[H_2O]}{T_{1m} + \tau_m} \tag{1.22}$$

$$r_1^{IS} = \frac{q}{[H_2O]}\frac{1}{\tau_m}\left(\frac{T_{2m}^{-1}(\tau_m^{-1}+T_{2m}^{-1})+\Delta\omega_m^2}{(T_{2m}^{-1}+\tau_m^{-1})^2+\Delta\omega_m^2}\right) \quad (1.23)$$

$T_{i\mathrm{m}}$ is the T_i (i = 1 or 2) of the coordinated water molecule and is described by the Solomon-Bloembergen-Morgan eqs 1.24 and 1.25 of paramagnetic relaxation theory.[115a-d]

$$\frac{1}{T_{1m}} = \frac{2}{15}\left(\frac{\mu_0}{4\pi}\right)\frac{\gamma_H^2 g_e^2 \mu_B^2 S(S+1)}{r_{MH}^6}\left[\frac{7\tau_{c_2}}{1+\omega_s^2\tau_{c_2}^2}+\frac{3\tau_{c_1}}{1+\omega_H^2\tau_{c_2}^2}\right] \quad (1.24)$$

$$\frac{1}{T_{2m}} = \frac{1}{15}\left(\frac{\mu_0}{4\pi}\right)\frac{\gamma_H^2 g_e^2 \mu_B^2 S(S+1)}{r_{MH}^6}\left[4\tau_{c_1}+\frac{13\tau_{c_2}}{1+\omega_s^2\tau_{c_2}^2}+\frac{3\tau_{c_1}}{1+\omega_H^2\tau_{c_1}^2}\right]+\frac{S(S+1)}{3}\left(\frac{A}{\hbar}\right)^2\tau_{sc} \quad (1.25)$$

where r_{MH} is the metal ion to water hydrogen distance, γ_{H} is the proton magnetogyric ratio, g is the electronic g-factor, μ_{B} is the Bohr magneton, μ_0 is the vacuum permeability, and ω_s and ω_H are the Larmor frequencies of the electron and proton, respectively. There is also a correlation time for the magnetic fluctuation (τ_c), that is the shorter of the rotational correlation time (τ_R), the electronic relaxation time (T_{1e} or T_{2e}), and the water residency time (τ_m), defined by eq **1.26**. The scalar contribution depends on the hyperfine coupling constant between the metal ion and the water proton and a correlation time τ_{sc} for that interaction, eq 1.27.

$$\frac{1}{\tau_{ci}} = \frac{1}{\tau_R}+\frac{1}{\tau_m}+\frac{1}{T_{ie}} \quad i=1,2 \quad (1.26)$$

$$\frac{1}{\tau_{sc}} = \frac{1}{\tau_m}+\frac{1}{T_{1e}} \quad (1.27)$$

For simple metal complexes, inner-sphere relaxivity can be approximated to eq 1.28 and depends on only q and τ_R.

$$r_1^{IS} = C \times q \times \tau_R \quad (1.28)$$

1.5.4.2. Electronic Relaxation

At very low fields (< 0.1 T) electronic relaxation is the dominant correlation time for Gd(III) complexes. At low proton Larmor frequencies (e.g., 10 kHz) the Zeeman energy may be lower than the zero-field splitting (ZFS) and in such instances, the widely used SBM relaxation theory does not apply.[116] In addition to this static ZFS, solvent collisions can induce distortions in the molecule resulting in a transient ZFS which can serve as an efficient relaxation mechanism. The electronic relaxation rates are given by eqs 1.29 and 1.30, where τ_v is a correlation time that describes the modulation of the transient ZFS, and Δ^2 is the square of the trace of the ZFS tensor.[116]

$$\left(\frac{1}{T_{1e}}\right)=\frac{12}{5}\Delta^2\tau_v\left(\frac{1}{1+\omega_S^2\tau_v^2}+\frac{4}{1+4\omega_S^2\tau_v^2}\right) \tag{1.29}$$

$$\left(\frac{1}{T_{2e}}\right)=\frac{12}{10}\Delta^2\tau_v\left(3+\frac{5}{1+\omega_S^2\tau_v^2}+\frac{2}{1+4\omega_S^2\tau_v^2}\right) \tag{1.30}$$

1.5.4.3. Outer-Sphere Relaxation

Outer-sphere contribution to relaxivity is due to the long-range through space dipolar interactions between the paramagnetic metal ion and the bulk water and arises from translational diffusion.[117] The outer-sphere contribution to the longitudinal proton relaxivity may be calculated from the Freed′s equation (1.31).[117c]

$$\frac{1}{T_1^{OS}}=C\left[3j(\omega_I)+7j(\omega_S)\right] \tag{1.31}$$

$$\frac{1}{T_2^{OS}}=C\left[2+1.5j(\omega_I)+6.5j(\omega_S)\right] \tag{1.32}$$

$$C=\left(\frac{32\pi}{405}\right)\gamma_I^2\gamma_S^2\hbar^2S(S+1)\frac{N_AM}{1000aD} \tag{1.33}$$

The spectral density function $j(\omega)$ is given by the eq 1.34.

$$j(\omega) = \mathrm{Re}\frac{1+\frac{1}{4}\left[i\omega\tau_D + \left(\frac{\tau_D}{T_{1e}}\right)\right]^{\frac{1}{2}}}{1+\left[i\omega\tau_D + \left(\frac{\tau_D}{T_{1e}}\right)\right]^{\frac{1}{2}} + \frac{4}{9}\left[i\omega\tau_D + \left(\frac{\tau_D}{T_{1e}}\right)\right] + \frac{1}{9}\left[i\omega\tau_D + \left(\frac{\tau_D}{T_{1e}}\right)\right]^{\frac{3}{2}}} \qquad (1.34)$$

where N_A is Avagadro's number, M is the concentration of the complex, a is the distance of closest approach of the outer-sphere water molecule and the complex, D is the relative diffusion coefficient of the outer-sphere water and the complex, and τ_D is a diffusional correlation time which is given by the eq 1.35.

$$\tau_D = \frac{\alpha^2}{D} \qquad (1.35)$$

1.5.5. Parameters of Relaxivity Optimisation

The relaxivity of GBCAs can be considerably increased through the simultaneous optimisation of mainly six molecular properties: (a) the number of water molecules (q) coordinated to Gd(III), (b) the exchange rate k_{ex} of a coordinated water molecule with bulk water, (c) metal-water proton distance (r), (d) the rotational correlation time (τ_R) of the complex, and (e) the longitudinal relaxation time (T_{1e}) of the Gd(III) electronic spin. The inner-sphere proton relaxivity is directly proportional to the hydration number q (eq 1.22 and 1.23), thus a higher q would result in increased relaxivities. However, ligands that leave coordination sites for more than one water molecule in the inner-coordination sphere form complexes of lower stability. (f) τ_m, the residency time of the coordinated water, is related to the water exchange mechanism and/or with changes in the population of the geometrical isomers (TSAP versus SAP) present in solution.[118]

The water exchange rate k_{ex}, where another approach to gain higher relaxivity of a T_1 agent is increasing τ_R, which results in a longer correlation time for the dipole-dipole interaction between the electron spin and proton spin at low

field strength. It is achieved by increasing the size and molecular weight of the Gd(III) complex or by immobilising the complex, covalently or noncovalently, on a macromolecule.[119] For low molecular weight spherical molecules, τ_R can be estimated from the Debye-Stokes equation (1.36).

$$\tau_R = \frac{4\pi\eta r_{eff}^3}{3k_BT} \qquad (1.36)$$

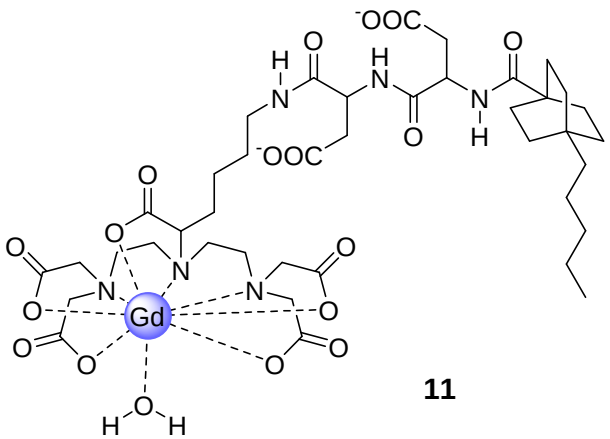
Where r_{eff} is the effective radius of the spherical molecules and η is the microviscosity.

1.5.6. New Strategies in the Design of MRI Contrast Agents

In general, the use of GBCAs is considered to be very safe. However, in 2006, incidence of adverse drug reactions associated with the GBCAs, a disease termed nephrogenic systemic fibrosis (NSF), was identified in renally impaired patients.[120] It has since been recognised that Gd(III) ion must be bound in a chelate possessing both high thermodynamic stability and high kinetic inertness to be safe for *in vivo* use. This is achieved with octadentate polyaminocarboxylate chelators mainly based on two structural types: macrocyclic DOTA and acyclic DTPA. Studies comparing MR probes *in vitro*,[66,111b,121] in animal models,[111b,122] as well as in human subjects[123] consistently demonstrated that kinetic inertness of macrocyclic chelates is superior to that of acyclic structures. On the basis of these results, it is believed that octadentate macrocyclic ligands derived from DO3A[124] provide Gd(III) chelates with the highest kinetic inertness and are therefore most suitable for *in vivo* applications. The coordination chemistry approach in designing high relaxivity MRI contrast agents is highlighted by Desreux *et al*.[127] and Raymond *et al*.[128]

1.5.7. Targeted GBCAs

Targeted GBCAs involve conjugating a Gd(III) chelate to a targeting moiety, which imparts selectivity for biomarkers which are more abundant in the disease state than in the healthy state. These targeting moieties are commonly proteins.[129] The targeting strategy increases the MR signal via the differential accumulation of the GBCAs. The receptor-bound GBCA usually has increased r_{1p} compared to the unbound GBCA as a result of increased τ_R, further enhancing the MR signal. This binding-induced MR signal enhancement is referred to as the receptor-induced magnetisation enhancement (RIME) effect.[130] The RIME concept was articulated in 1991 and the first molecule designed for this concept is MS-325 (AngioMark) which interacts noncovalently with the abundant blood protein, Human Serum Albumin (HSA). When MS-325 binds to HSA, its relaxivity increases nine-fold to 51 mM^{-1} s^{-1} (37 °C and 20 MHz).[130b] MP-2269 (**11**) is another example of blood pool agent which binds to HSA and exhibits enhanced relaxivity and demonstrates the RIME concept.[131] Since the sensitivity of ^1H MRI is in the range of μM, biomarkers that are in the pM-nM range may not be imaged with targeted GBCAs.[95] The multipurpose agent $[Gd(BOPTA)(H_2O)]^{2-}$ is the first RIME agent approved for human use.



11

1.5.8. Bioresponsive GBCAs

In order to expand the capability of MRI into the molecular imaging regime, a specialised class of CAs known as bioresponsive GBCAs have been developed.[132] These agents have the potential to noninvasively probe and investigate essential physiological and pathological processes at the molecular level by MRI. This can be through changes in pH, metal ion concentration, and enzyme activity.[133] These CAs conditionally respond to a biochemical event of interest by altering the MR signal through either selective binding (targeted GBCAs) or biorthogonal chemical transformations (activatable GBCAs). The use of macrocyclic ligands such as DOTA and DO3A gained popularity over linear ligands such as DTPA due to their superior stability as well as ease of functionalisation. The design strategies of bioresponsive probes and the key advances made in recent years are reviewed.[132g] For both targeted and activatable GBCAs, choosing the appropriate biomarker is of utmost importance. In general, biomarkers that are extracellular and abundant are preferred targets. Imaging intracellular targets can be accomplished with activatable GBCAs.

1.5.9. Chemical Exchange Saturation Transfer (CEST) Agents

In a seminal paper, Balaban *et al*.[134] proposed a new class of contrast agents for MRI based on proton chemical exchange dependent saturation transfer (CEST) for generating image contrast. The authors have proposed that non-metal based contrast agents that operate by CEST would offer an advantage over conventional metal-based T_1- or T_2-shortening agents in that the effect of the contrast agent could be turned on and off by a presaturation pulse. CEST agents contain a pool of labile protons such as N−H, O−H, and H_2O, that are frequency shifted well away from the bulk water NMR frequency, which can be exchanged with the protons of the bulk water.[135] For a CEST agent to be effective, there needs to be good frequency

separation between the exchangeable protons and the bulk water resonances ($\Delta\omega$), with an intermediate to slow exchange rate on the NMR time scale ($k_{ex} \leq \Delta\omega$).[136] In a CEST experiment, the exchangeable protons of the CEST agent are irradiated with an off-resonance RF saturation pulse at the frequency of the exchangeable protons. Their magnetisation (i.e., spin polarisation) is spontaneously transferred to the protons of the bulk water pool by chemical exchange between both pools, which attenuates the signal of the bulk water.[137] This in turn generates an MRI contrast. The CEST signal is typically reported as the ratio of the bulk water magnetisation after application of a long pre-saturation pulse (Ms) relative to the water intensity without saturation (Mo). A plot of Ms/Mo versus pre-saturation frequency is referred to as a CEST or a *Z*-spectrum.[134] The CEST process is illustrated in Figure 1.10.

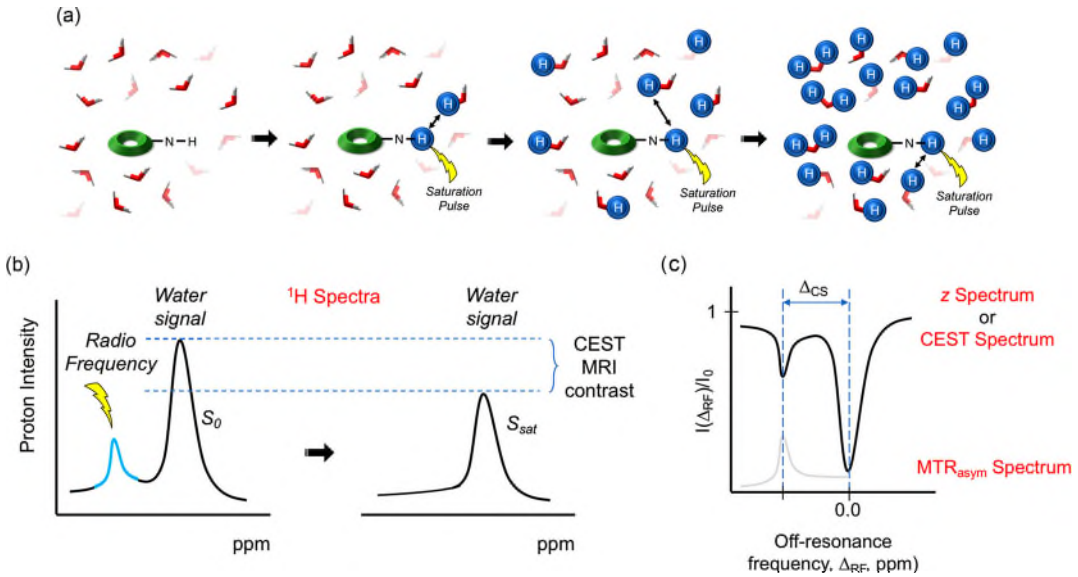


Figure 1.10. Illustration of a CEST process: (a) exchangeable amine protons of a CEST agent are selectively saturated using RF irradiation, leading to a reduction of the amine ^{1}H signal intensity. Because of chemical exchange, the saturated protons (blue spheres) are transferred to the bulk water pool. Continuous chemical exchange during the saturation experiment leads to the amplification of the water signal reduction. (b) Continuous application of RF pulses leads to the saturation of more bulk water protons, thereby decreasing the ^{1}H NMR signal. (c) Z-spectrum of normalised water intensity (I/I_0) versus off-resonance frequency (Δ_{RF}); Δ_{CS} is the separation in chemical shift between the two proton pools; (reproduced with permission from Ref 94b).

One of the major advantages of this technique is that despite the small concentration of the solute molecules (micromolar to millimolar range), the signal can be amplified several orders of magnitude through the transmission of the magnetisation to the bulk water.[138] CEST offers multiplex detection that is not permitted with classical relaxation enhancers based on Gd(III) complexes. Another important advantage that CEST agents have over conventional relaxation agents is the possibility of designing responsive agents whose MRI signal can be made independent of the probe concentration.[139]

1.5.9.1. Categories of Exogenous CEST Contrast Agents

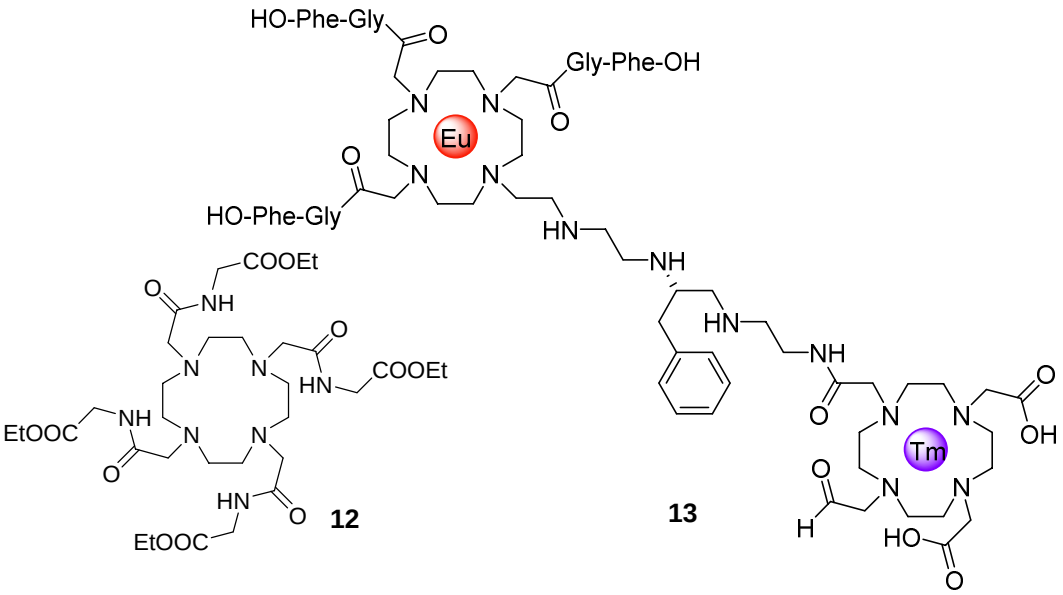
There are four categories of exogenous CEST contrast agents: diamagnetic (diaCEST), paramagnetic (paraCEST), liposomal (lipoCEST), and hyperpolarised gas (hyperCEST).[137b,140] In the case of diaCEST agents, the exchangeable protons usually belong to −NH and −OH groups, and the chemical shift difference ($\Delta\omega$) with the bulk water protons is less than 6 ppm which limits the magnitude of the CEST effect. In the case of paraCEST agents, the chemical shift difference ($\Delta\omega$) of the labile protons with the bulk water protons can be much larger, up to a few hundred ppm leading to a much faster proton exchange.[138b] LipoCEST agents are composed of liposomes that encapsulate a chemical shift agent in the inner-cavity, thus shifting the resonating frequency of intraliposomal water protons by 1 to 5 ppm from that of extraliposomal water protons.[141] By introducing a lanthanide shift agent inside the liposome, the resonance of the intraliposomal water is shifted relative to the water outside the liposome. HyperCEST is a technique that combines CEST with hyperpolarised MRI and has been typically performed with ^{129}Xe. ^{129}Xe is soluble in aqueous solutions (including blood plasma) and possesses a highly polarisable electron cloud and can be easily hyperpolarised using spin-exchange optical

pumping (SEOP) from electronically polarised rubidium atoms in the vapour state.[142]

1.5.9.2. ParaCEST Contrast Agents

The use of paraCEST agents endowed with markedly different chemical-shift values of the exchangeable protons allows them to be visualised at will by a selection of the proper irradiation frequency. The paramagnetic complex [Eu(**12**)(H_2O)]Cl_3, with a bound water resonance at 49.7 ppm at 25 °C, exchange lifetime of 351 ± 12 μs, and a bulk water relaxation time (T_{1sat}) of 537 ± 23 ms, shows a novel CEST effect in water.[143] Sherry *et al*.[144] have reported Yb(III) complex of DOTAM, which has eight exchangeable, hyperfine-shifted amide protons, as a prototype high-sensitivity MT agent. Aime *et al*.[145] have reported Eu(III) and Tb(III) complexes of DOTAM-Gly which contain two pools of exchangeable protons: the metal-coordinated water protons and the amide protons. The presence of Eu(III) complex was visualised by irradiating at 50 ppm downfield from the resonance of bulk water protons and the Tb(III) complex was identified by irradiating -600 ppm from the bulk water. *In vitro* cell labeling study indicates internalisation of these paraCEST agents, sufficient for CEST-MRI detection. The CEST spectrum of the heterobimetallic complex **13** shows a marked reduction in the signal due to bound water at the Eu(III) center (45 ppm). ParaCEST agents have been designed for specific detection of enzyme activity,[146] as pH[147] and temperature[148] reporters, and for the sensing of glucose,[149] lactate,[150] poly L-arginine,[151] and zinc.[152] A frequency-selective pH-responsive paraCEST agent is reported by Ratnakar *et al*.[153] for detecting changes in blood pH in rodents. Several paraCEST agents have shown utility as responsive agents for reporting physiological information by MRI.[154]

Paramagnetic lanthanide complexes as paraCEST agents for medical imaging is reviewed by Sherry *et al.*[154]



1.6. Development of receptors for Anion Recognition in Water

Anions are ubiquitous in nature and fundamentally important to a range of biological processes. DNA, which carries genetic information, is a polyanion; lactate, citrate, and key metabolites in the intermediary metabolism of the cell, are essential oxy-anions in nature. Anions play important roles in a wide range of chemical, biological, medical, environmental, and industrial arenas, while pollutant anions have been linked to eutrophication of surface water[155] and carcinogenesis.[156] In nature, anion binding is achieved through multiple hydrogen bonding interactions to a well-defined site within a hydrophobic protein cavity in which directed hydrogen bonds complement the shape of the target anion.[157] The development of potent anion receptors to recognise and sense biologically and environmentally important anionic species in aqueous conditions has emerged as a significant area of research in the field of chemical sensors.[158]

The design of receptors for anion recognition in water is particularly challenging for several reasons: anions are larger than isoelectronic cations with a lower charge to radius ratio. Consequently, the electrostatic binding interactions are less effective than they would be for the smaller cation; anions may be pH sensitive, thus receptors must function within the pH window of their target anion; anions have a range of geometries and therefore a higher degree of design may be required to make receptors complementary to their anionic guest; solvent effects also play a crucial role in controlling anion binding strength and selectivity.

Water is a highly competitive polar solvent due to its ability to act as both a hydrogen bond donor and acceptor. Anions possess intrinsic properties that make them difficult to bind effectively in aqueous solution. This is because anions are more heavily solvated in water than analogous cations of the same charge and similar size,[159] they also display a much greater range of hydrophilicity/ hydrophobicity,[160] and their recognition is further complicated by the multiple protonation equilibria. Anion recognition in water requires sufficient binding free energy to overcome the high hydration energies of anions in water. Hydrogen bonding interactions alone are usually not sufficient to displace the water molecules surrounding an anion. Strong electrostatic and metal-ligand interactions are required to overcome the anion hydration energy and allow binding in aqueous conditions. The hydrophobic effect in particular has attracted much interest in the context of anion recognition in water by electroneutral hosts. Design and synthesis of hydrophobic host systems capable of strongly binding anions in water is aided by the relationship among the hydrophobic effect, the Hofmeister series,[161] ion-solute interactions, and the thermodynamic contributions that dominate these phenomena. Selectivity for a target anion may be achieved by integrating additional binding sites

within the receptor, creating a structured binding pocket with high geometric complementarity.[158a,162] The nature and abundance of potentially interfering species such as competing anions, cations, and complex ionic biomolecules (e.g. proteins and nucleic acids) define the requirements for selectivity of the receptor.[163] Synthetic receptors for the recognition and sensing of anionic substrates[164] and anion recognition by supramolecular and macromolecular host systems[165] in water are reviewed.

1.6.1. Approaches to Anion Receptor Design for Anion Recognition

In the design of selective hosts for anions the geometry and basicity of the anion and the nature of the solvent medium play important roles. Complementarity between the receptor and anion is crucial in determining selectivities. Anion receptors are categorised on the basis of nature of interactions such as electrostatic, hydrogen bonding, hydrophobicity, coordination to a metal ion, and combination of these interactions involved in binding the anionic guests to the hosts. Hydrogen bonds are directional, which allows the design of receptors with specific shapes that are capable of differentiating between anionic guests with different geometries or hydrogen bonding requirements in nonpolar solvents, but the hydrogen bonding interaction is much weaker in water. However, some promising systems are being examined in predominantly aqueous media.[166]

Charged receptors for the recognition of anions in water by nondirectional electrostatic interactions result in poor anion selectivity. Thus, in order to achieve selective anion binding by synthetic receptors, recognition features such as electrostatic or hydrophobic interactions, hydrogen bonding or electron-deficient binding sites must be incorporated to the molecular receptors to complement the chemical characteristics of the anions. In addition to the N–H hydrogen-bond donor for anion recognition, the C–H hydrogen bonding motifs are also incorporated in

anion receptor design capable of operating in aqueous solution.[167] Elegant examples of neutral and charged anion receptors that are able to operate in water have been reported by exploiting both complementary hydrogen-bonding interactions and the hydrophobic effect to enhance the overall complex stability.[165-167] The different mechanisms and systems that have been employed to sense anions in solution using small molecules and molecular ensembles is reviewed.[167] Developments in anion receptors based on noncovalent interactions such as hydrogen bonding, anion-π, and halogen bonding are reviewed.[158b,167] Engineering a hydrophobic binding site on a receptor based on complementarity of charge and shape, emulating the binding sites found in sulfate binding proteins and phosphatase enzymes is an elegant anion receptor design.[157] Early examples were based on macropolycyclic systems including positively charged polyaza-cryptands that bind spherical anions in aqueous solution. Each anion was encapsulated within a rigid molecular cavity and held by an array of hydrogen bond donors, typically involving protonated nitrogens.

1.6.2. Anion Binding by Receptors and Signalling Mechanisms

The anion binding event should be signalled by modulation of a parameter that can be measured rapidly independent of local probe concentration and can be calibrated to the target anion concentration range. Optical methods that signal anion binding offer great advantages over insensitive magnetic resonance methods and invasive electroanalytical analyses.[163] The design of receptors that have the ability to selectively bind and sense the anion recognition event through a macroscopic electrochemical or optical response has been an active area of research in recent years.[164a,168] Sensors based on anion-induced changes in fluorescence appear particularly attractive. They offer the potential for high sensitivity at low analyte concentration coupled with obvious ease of use.[168b,169] The high sensitivity of

fluorescence used for sensing guest species has stimulated interest in the covalent attachment of organic and inorganic luminophores in proximity to guest-recognition sites.[169b] Luminescent anion-responsive receptors have been developed by conjugating anthracene fluorophore(s) with polyammonium,[170] guanidinium,[171] zinc(II) amine,[172] and calixpyrrole[173] anion recognition sites. The "chemodosimeter approach" for the design of chemosensors involves specific anion-induced chemical reactions coupled with selective changes in fluorescence or colour changes in the sample from its host.[174]

1.6.3.Engineering Electron-Deficient Lewis Acid-Containing Binding Sites on Anion Receptors

Anion binding by receptors which incorporate positively charged or electron-deficient binding sites is accomplished by Lewis acid-containing receptors,[175] quaternary ammonium macropolycycles,[176] protonated macrobicyclic anion receptors,[177] polyammonium macrocycles,[178] macrobicycles,[179] and macrotricycles,[180] cryptands,[180a,181] and macrocyclic guanidinium-based receptors.[182] The ammonium group is the most frequently employed motif to bind anions through electrostatic and hydrogen-bonding interactions in aqueous solution.[183]

1.6.4. Luminescent Lanthanide Complexes for Anion Binding and Sensing

The strongest interaction that can be used for anion binding in water is direct coordination to a metal cation.[163] Metal-containing receptors are typically designed around an organic scaffold that binds metal cations with high kinetic and thermodynamic stability such that at least one coordination site on the metal centre remains vacant or coordinated to a weakly bound ligand and thus available for anion binding. The metal can induce a geometrical pre-organisation of the complex that

results in a better host-guest complementarity. In certain cases, anion selectivity can be enhanced by positioning two metal centres in proximity, allowing the anion to interact with each metal ion. The use of luminescent lanthanide complexes is established as an effective approach to anion binding and sensing in water and has been reviewed.[163] The long luminescence lifetimes (up to milliseconds) enable time-gated or time-resolved measurements to distinguish the lanthanide-centred emission from the background short-lived autofluorescence.[184] Time-gating methods offer enhanced signal-to-noise and very low limits of anion detection. This feature is particularly advantageous if the complex is to be used as a probe in complex aqueous media such as in biological and environmental samples.[185] The sharp, line-like emission spectra enables accurate ratiometric analyses by measuring the change in intensity of one emission band relative to the almost stationary intensity of a second band and a luminescence response that is fast and sensitive, offering the high spatial and temporal resolution required for biological imaging applications.[163]

1.6.4.1. Luminescent Ln(III) Complexes for Binding and Sensing Anions-*Design Considerations*

Well-defined and kinetically stable Ln(III) complexes of polydentate ligands based on DO3A and DOTA offer significant scope for the design of selective anion receptors with one or two coordinated water molecules; the affinity and selectivity may be modulated by permuting the ligand or the lanthanide ion and varying the ligand structure, geometry, and conformational flexibility. When designing such receptors, the ligand should incorporate a sufficient number (6-8) of hard donor atoms such as oxygen and nitrogen to ensure high kinetic inertness and thermodynamic stability of the Ln(III) complex, both in the absence and presence of anions. The coordinated water molecules can be displaced rapidly and reversibly by anions leading to the formation of ternary adducts.[186] In addition to the structural

requirements for anion binding, a strongly absorbing chromophore (or antenna), which can be excited by UV/visible light, should be integrated into the ligand structure to create emissive Ln(III) probes for anion sensing.[1b,24,187]

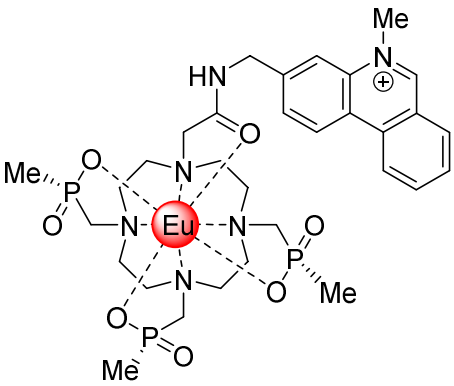
Emissive Ln(III) complexes, particularly Eu(III) and Tb(III) which emit in the red and green spectral region, respectively, offer unique photophysical properties that are valuable for anion recognition in aqueous and biological media.[185a,b,188] The excited states of Eu(III) and Tb(III) ions lie 206 and 244 kJ mol^{-1} above the ground state and possess a radiative lifetime in the order of a millisecond.[189] By careful design of ligand, Ln(III) complexes capable of rapid and reversible anion binding can be created, providing a luminescence response that is fast and sensitive, offering high spatial resolution required for biological imaging applications.[190,185a] A variety of Ln(III) complexes have been developed for binding and sensing anions, cations, and biomolecules in aqueous media and have been reviewed.[163,188b,191,192]

1.6.4.2. Anion Binding at Ln(III) Centres and Signalling Mechanisms

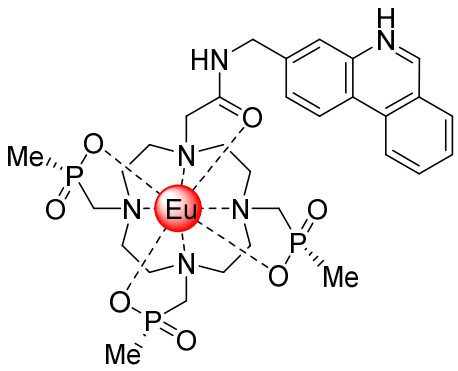
Anion binding and signalling at Ln(III) complexes may be achieved through a variety of mechanisms. Primarily, anion binding is explored directly at the metal centre by the displacement of one or more inner-sphere water molecules. This in turn, alters the Ln(III) coordination environment and the local ligand field, resulting in changes in the emission intensity, spectral form, and lifetime of the complex.[169a,186,187a,193] These properties readily enable determination of the mode by which the lanthanide receptor binds anion as well as the stoichiometery of the receptor:host complex. This is best reported by changes in the emission spectra of Eu(III) complexes.[163,192] The absence of degeneracy in the emissive $^5D_0$ excited state of Eu simplifies its emission spectral form. The intensity of the MD allowed $\Delta J = 1$ transitions at ~ 590 nm is relatively unaffected by any coordination change,

whereas the hypersensitive ED allowed $\Delta J = 2$ transitions at ~ 615 nm are strongly perturbed.[48] This causes differences in the relative intensity of this pair of emission bands allowing ratiometric analysis.[194] This strategy has been utilised effectively by Parker *et al.*,[186a] wherein a range of DO3A-based heptadentate ligands were designed to generate emissive Eu(III) and Tb(III) complexes with one or two available anion binding sites, occupied by water molecules in aqueous solution.[48,163]

Several Ln(III) receptors have been developed into practical assays for the selective and ratiometric detection of anions in biological fluids, including lactate,



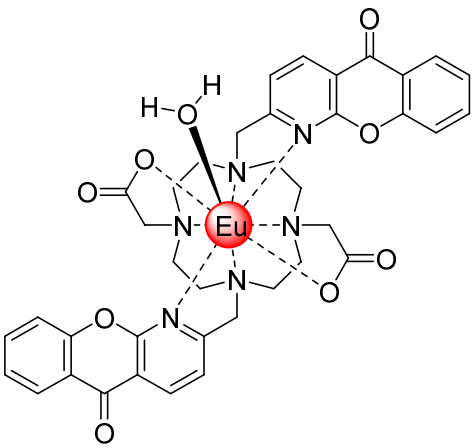
14



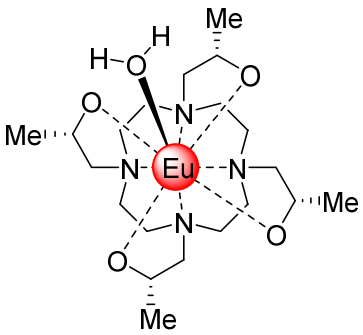
15

bicarbonate, and citrate. Such an analysis can also be undertaken with mixtures of Eu(III) and Tb(III) complexes of a common ligand and analysing the change in the red-green emission intensity ratio that accompanies anion binding.[194b,c,195] Reversible anion binding may also take place at a ligand based anion recognition site, perturbing the ground state of the chromophore. For example, reversible attack of hydroxide α to the sensitiser nitrogen in the phenanthridinium complex **14** can be used to assess hydroxide concentration in the pH range 10-12 (K_d = 16 mM).[193a] The Eu and Tb complexes have been shown to sense halide and hydroxide ions in water.[193a,196] The Eu(III) complex **15**[196] shows a pH dependent luminescence enhancement of over 500 by comparing the Eu emission intensity at 594 nm ($\Delta J = 1$).

Anion binding at the lanthanide centre is reversible: an example is binding of bicarbonate by the displacement of one of the coordinated azaxanthone nitrogens in the Eu(III) complex **16** which is signalled by a 200% increase in emission intensity at 615 nm as the local coordination environment at Eu changes.[193d] Similarly, addition of citrate to (*S*)-[Eu(**THP**)]$^{3+}$ (**17**) displaces a weakly bound ligand hydroxyl group. In this case, the metal ion was excited directly using laser excitation.[197]



16



17

In the second case of anion binding, at the Ln centre, reversible anion binding involves the 'switching on′ of Ln(III) emission upon binding an anion that possesses a sensitising chromophore (Figure 1.11a). This requires matching of the triplet excited state energy of the anion with the Ln(III) excited state such that back energy transfer is not competitive. While this approach can lead to high levels of selectivity for a target anion, it is limited in scope due to the requirement of the anion to possess a suitable chromophore.

In the third case, an anion encounters the sensitiser excited state and modulates the observed lanthanide emission. Usually, this process is signalled by

quenching of the longer-lived sensitiser triplet excited state by either charge or energy transfer (Figure 1.11b). With electron poor sensitising groups such as tetraazatriphenylenes and azaxanthones, a long-lived excited state complex (exciplex) can form involving charge transfer with electron rich anions. For example, halide quenching of the phenanthridinium singlet excited state in **14** (λ_{exc} 385 nm; $I^- > Br^- > Cl^-$) occurs over the chloride concentration range of 10-100 mM leading to a reduction in emission intensity. The electron rich phosphates such as ATP and GTP can bind to a Eu(III) centre in aqueous media and perturb the Eu(III) excited state. This behaviour has allowed the selective quantification of ATP in mixtures with ADP, AMP, cyclic AMP, and inorganic phosphate, enabling kinase activity to be tracked.[198] The relatively hydrophobic anion urate forms a much more stable exciplex than ascorbate. Urate can be determined selectively in urine and serum using mixtures of Eu(III) and Tb(III) complexes (**18** and **19**) measuring its differential quenching effect on Eu and Tb emission (λ_{exc} 355 nm).[199] These two

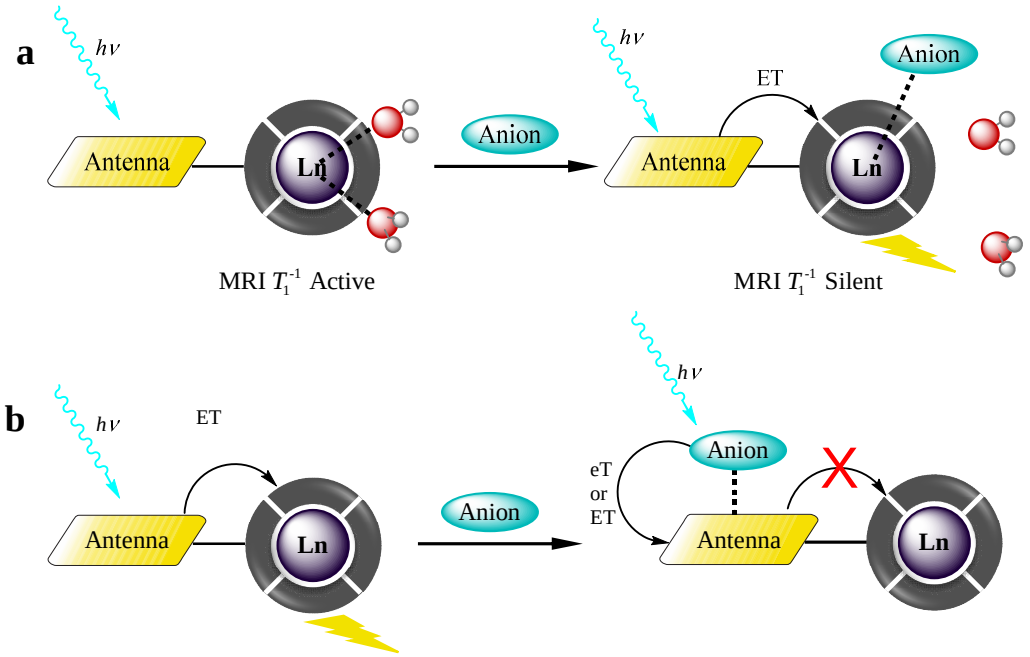


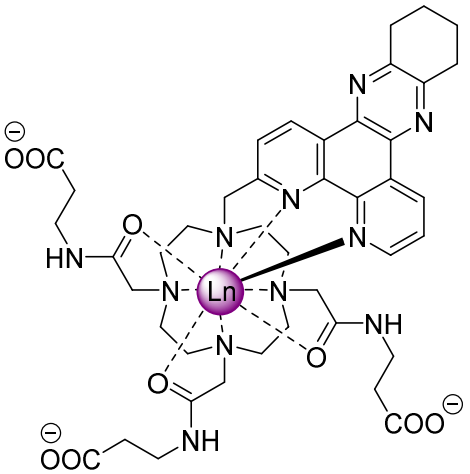
Figure 1.11. Anion binding approaches in Ln(III) complexes: (a) Chelation to the metal center causing 'turn-on' in luminescence and 'turn-off' in MRI relaxivity. (b) Modulating Ln luminescence through binding to the sensitiser (adapted from Refs 10b and 192).

electron rich anions are used in nature as low MW anti-oxidants, operating in tandem to scavenge reactive oxygen species in cells.[199]

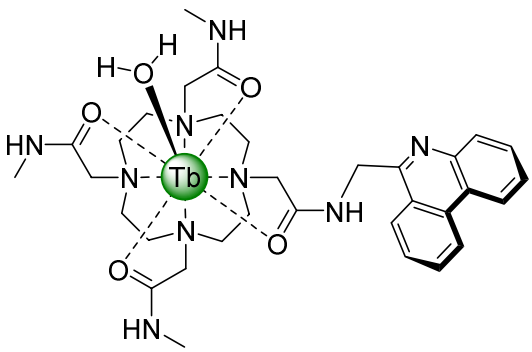
Alternatively, anion binding may involve a non-coordinative interaction with the antenna or other components of the ligand framework including π–π stacking between two aromatic components, hydrogen bonding, or electrostatic interactions with a cationic complex. In most of these cases, anion binding causes quenching of the singlet or triplet excited state of the antenna by an energy or charge transfer mechanism causing a decrease in Ln(III) emission intensity. This strategy is exemplified by the Tb(III) complex **20** developed by Pierre *et al.*[200] which is capable of binding ATP through a combination of electrostatic and π–π stacking interactions between the adenine group and phenanthridine antenna resulting in the quenching of Tb(III) luminescence.

1.6.4.3. Tuning Anion Affinity of Lanthanide-Based Receptors and Gaining Selectivity

By varying the charge density on the lanthanide ion and modifying the ligand architecture to change overall charge or modulate steric demand at the metal centre, the binding selectivity for an anion can be controlled. This allows the desired



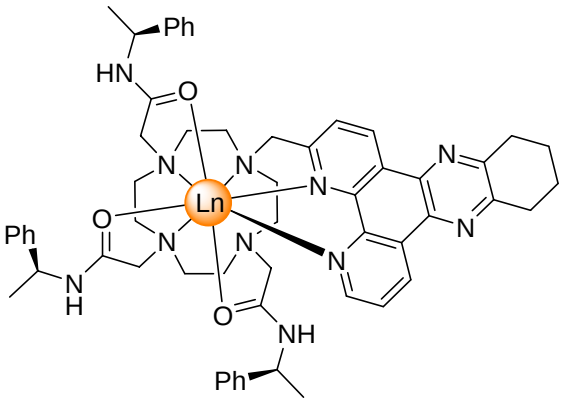
18 Ln = Eu
19 Ln = Tb



20

anion affinity to be tuned to the relevant concentration range in the background medium. The use of time-gated spectroscopy and microscopy allows variations in selected anion concentrations to be monitored with enhanced sensitivity. In certain cases (chloride, ATP, and hydroxide),[193a,198] a selective quenching strategy can be adopted based on reversible interactions of the anion with the ligand signalled by Ln(III) emission modulation. The ease of variation of the lanthanide ion in its complexes allows ratiometric analyses to be undertaken, e.g., by permuting the Ln(III) ion in complexes with a common ligand. Thus, anions such as citrate can be examined rapidly in serum, prostatic or seminal fluids, simply by diluting the sample and measuring the intensity ratio of two Eu(III) emission bands.[201]

The sensitivity of Eu(III) and Tb(III) macrocyclic complexes to dynamic quenching of their relatively long-lived excited state is a key factor in defining their utility as probes for intracellular imaging. The relative insensitivity of more sterically encumbered complexes **21** and **22** (Ln = Eu(III) and Tb(III)) to dynamic quenching by urate is exploited for *in cellulo* applications.[202] Noncovalent binding of the complexes by albumin through the heterocyclic pendant arm also shields the excited Ln(III) ion from collisional quenching. The development of Ln(III) complexes to signal the local concentration of anions including lactate and citrate in complex bio-fluids and bicarbonate inside the mitochondria of living cells is reviewed.[163] The recent study of Sørensen *et al*.[203] on the effect of a change in structure of the binding pocket on the binding event of a series of bidentate carboxylate anions by oxyanion responsive [Eu(**DO3A**)] complexes by altering the lipophilicity of the fourth appended arm of the DO3A scaffold demonstrates the feasibility of developing responsive luminescent lanthanide complexes for a specific analyte by tuning the lipophilicity of the host systems.



21 Ln = Eu
22 Ln = Tb

1.6.4.4. Constitution and Configuration of Anion Adducts Formed at Ln(III) Centres

The constitution and configuration of a variety of anion adducts have been defined using a combination of X-ray, NMR, and optical emission studies.[186c,d,e,187a,193b] A range of chelate ring sizes of differing stability has been confirmed, with the more stable systems involving four- to six-membered ring formation. Seven-ring chelate formation is far less common and both eight- and nine-ring chelate formation are very strongly disfavoured, both entropically and enthalpically.[48,163,192] Thus, succinate binds like acetate and does not chelate, while citrate and malate bind via the α-hydroxyl- and carboxylate groups forming a five-ring chelate, rather than exhibiting dual carboxylate ligation.[186a,b] Phosphate and its oxy-anion congeners prefer to act as monodentate ligands or to bridge between two Ln(III) centres.

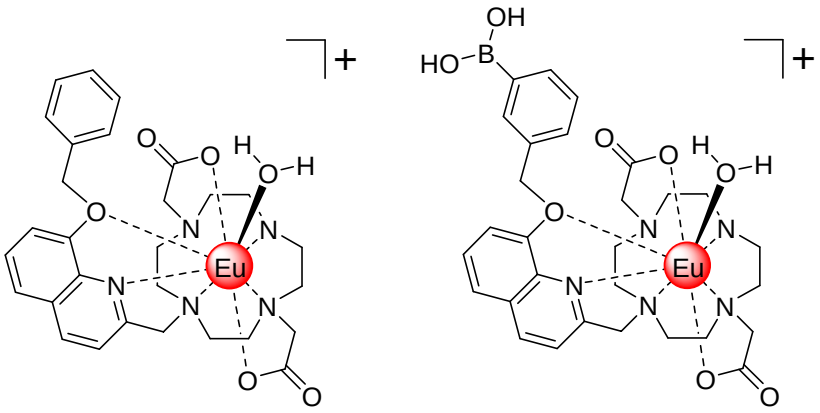
1.6.5. Luminescent Lanthanide(III)-Based Receptors for Anion Sensing: *Bioimaging Applications*

1.6.5.1. Selective Recognition of Phosphate in Water

The development of phosphate receptors that are both effective and selective in water is key to the treatment of medical conditions such as hyperphosphatemia[204] and ectopic mineralisation[205] and to address environmental problems such as the eutrophication of surface water.[206] The design of many synthetic supramolecular

receptors for phosphate rely on the interplay of electrostatic and hydrogen bonding interactions.[207] Ln(III)-based receptors are well suited for sensing phosphate species in water due to the inherent affinity of Ln(III) ions for hard oxyanions.[163,186a,192,208] The recognition of inorganic phosphate is particularly challenging because of its high hydration energy and pH dependent speciation. Developing Ln(III)-based receptors for phosphate or AMP is difficult because other oxyanions such as ATP, bicarbonate, and lactate can compete for coordination to the Ln(III) centre.[163,192,208] Pierre *et al.*[209] developed a series of acyclic tripodal Eu(III) complexes of hydroxypyridinone-based ligands containing a single charged group ($-NH_3^+$, $-CO_2^-$, or $-SO_3^-$) or neutral hydrogen-bonding moiety (−OH) on the periphery with an open coordination site that bind 2 or 3 molecules of phosphate with high affinity and very good selectivity. Using a series of related tripodal Gd(III) complexes, Pierre *et al.*[210] determined the affinity and selectivity for phosphate as a function of the stability of the Gd(III) complex and the basicity of the anion. Albrecht *et al.*[211] developed a double stranded Eu(III) helicate that exhibits a highly specific emission enhancement upon binding AMP and remarkable discrimination of AMP from ADP, ATP, PO_4^{3-}, HPO_4^{2-}, and $H_2PO_4^-$.

Butler *et al.*[212] have reported macrocyclic Eu(III) receptors **23** and **24** capable of selectively sensing inorganic phosphate and AMP in water. The receptors contain a sterically demanding 8-(benzyloxy)quinoline pendant arm that coordinates to the metal centre, blocking the axial site thereby creating a binding pocket suitable for monodentate binding of phosphate and AMP, while excluding potentially interfering chelating anions, in particular ATP, bicarbonate, and lactate. The sensing selectivity of the Eu(III) receptors follows the order: AMP > ADP > ATP. The excellent selectivity of **23** for phosphate was exploited for measuring phosphate

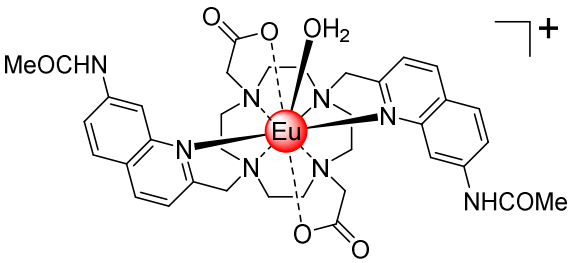


23 **24**

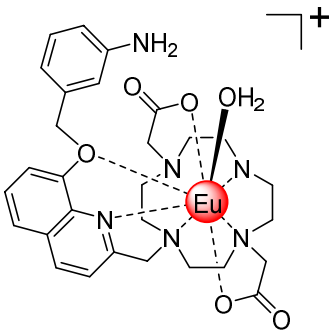
levels in human serum samples. A major advantage of these Eu(III) receptors is their high discriminatory ability toward AMP over ATP.

A Ln(III) receptor that binds ADP selectively could allow real-time analysis of kinase enzyme activity by monitoring the production of ADP, thereby providing a convenient luminescence assay for high throughput screening of potential kinase inhibitors for the treatment of cancer.[213] The phosphoanion binding and sensing properties of the cationic Eu(III) complex **25** is exploited by Butler *et al.*[214] to develop an assay platform for real-time monitoring of a range of pharmaceutically important nucleoside polyphosphate (NPP)-utilising enzyme reactions, including kinases, glycosyltransferases, and phosphodiesterases. The ability of **25** to discriminate between nucleoside tri-, di-, and mono-phosphate anions is used to monitor the enzymatic production of different NPP anions in a convenient luminescence-based increase-in-signal format. It binds reversibly to ATP and ADP in water at neutral pH in the presence of Mg(II) ions, providing distinctive luminescence responses that permits the change in ADP/ATP ratio to be dynamically monitored during kinase-catalysed conversion of ATP to ADP in real-time.[215] Butler *et al.*[216] have developed a Eu(III)-based probe **26** that binds reversibly to both adenosine-3′-phosphate-5′-phosphosulfate (PAPS) and

adenosine-3′,5′-diphosphate (PAP), producing a larger luminescence enhancement with the latter anion.

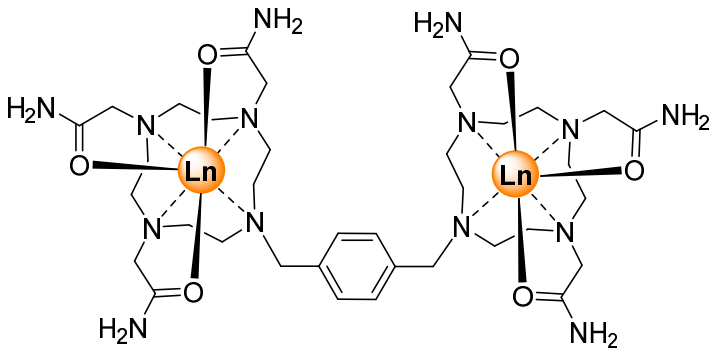


25



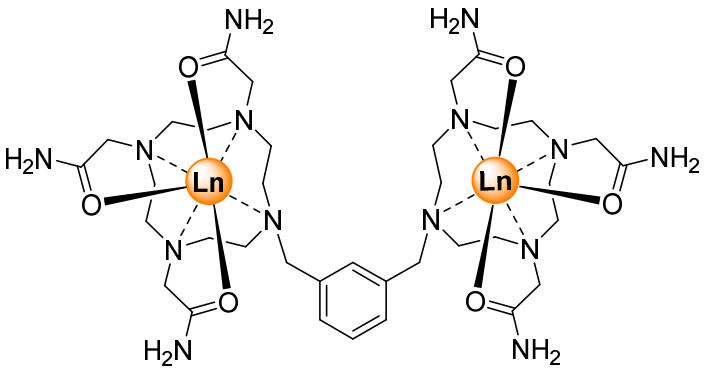
26

Morrow *et al.*[217] have accomplished sensing of biologically relevant anions by exploiting luminescence resonance energy transfer in heterodinuclear Ln(III) complexes of the macrocycles **27** and **28** (Ln(III) = Eu, Tb). The binding of phosphate, methylphosphate, double-stranded DNA, a DNA hairpin loop, and fluoride to both Eu(III) centers in [Eu_2(**27**)] (pH 7.0, 0.1 M $NaNO_3$) is studied by monitoring the $^7F_0 \rightarrow {}^5D_0$ excitation peak. The $^5D_0 \rightarrow {}^7F_0$ transition occurs between two electronic states that are non-degenerate and are thus not split by ligand fields; this gives rise to a single excitation peak for each Eu(III) complex species, barring the overlap of peaks. The recovered luminescence lifetime data indicates anion binding to the metal centers by the replacement of coordinated water molecules. There are distinct changes in the relative intensities of Eu(III) emission peaks for



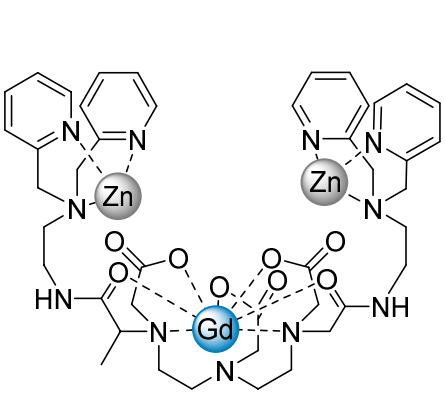
27

complexes of [Eu_2(**27**)] and [Eu_2(**28**)] with phosphate, fluoride, carbonate, and phosphate ester ligands. The Eu(III) luminescence lifetime data for the binuclear complexes bound to these anions can be fitted to a single exponential decay upon addition of saturating ligand concentrations.

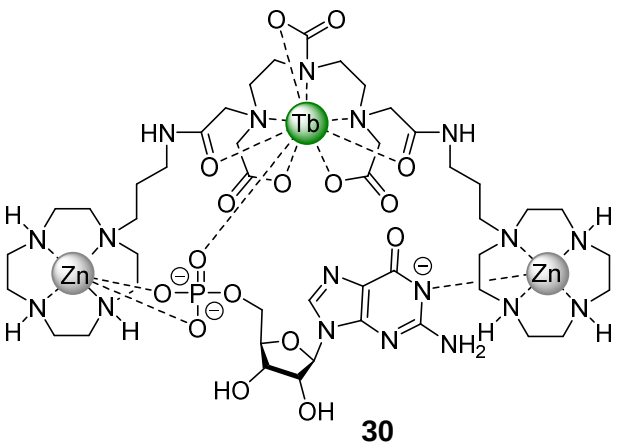


28

Vilar *et al.*[218] have developed a pyrophosphate-responsive MRI contrast agent **29** by coupling a Gd(III) complex of DTPA bisamide ligand with Zn(II)-dipicolylamine moieties. The binding of pyrophosphate anions in water at the physiological pH modulates the relaxivity of the Gd(III) complex. The 'switching on′ of Ln(III) emission upon binding an anion was employed for the selective recognition of GMP using a Tb-Zn_2 complex **30** which becomes emissive upon sensitisation of the Tb(III) centre by the proximal guanine unit.[219]



29

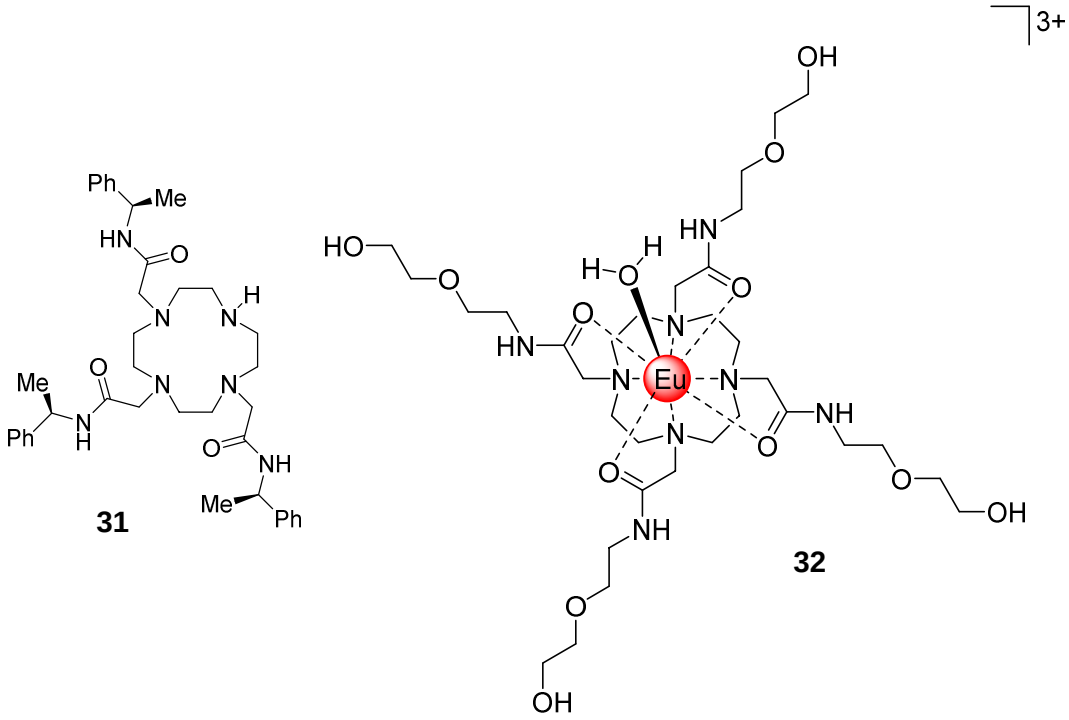


30

1.6.5.2. Lanthanide Complexes as Receptors for Hydroxy Acids (lactate, malate, and citrate)

The α-hydroxy acids such as lactate, malate, and citrate play an important role in the Krebs cycle and in glycolysis. Monitoring of lactate concentration is important for clinical diagnostics since this anion is a specific biomarker for prostate and breast cancer, and elevated lactate levels are found in patients with Parkinson's disease.[220] Parker *et al.*[186b] demonstrated reversible binding of lactate and citrate to cationic chiral diaqua Ln(III) complexes of **31** (Ln = Yb, Eu, and Gd) and **32** (achiral) using a combination of solution NMR studies and X-ray crystallography. A ratiometric probe for the citrate anion was devised using the cationic Eu(III) complex incorporating a pyridothioxanthone sensitiser that can be excited in the range 365 to 405 nm. An apparent binding constant of log K_a = 2.67 was estimated in diluted prostatic fluid in the presence of 0.1 M sodium lactate.

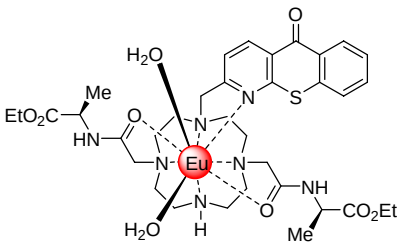
A family of nine luminescent Eu(III) complexes **33**-**41**, based on a common macrocyclic core which incorporates a heterocyclic azaxanthone or



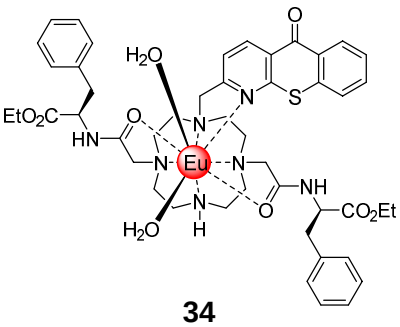
31 **32**

azathiaxanthone moiety for facilitating the sensitisation of lanthanide emission, was evaluated for their binding affinity for lactate, citrate, and bicarbonate in solution by observing the change in the intensity ratio of the Eu emission bands at 616/686 nm as a function of added anion.[194b] Pronounced selectivity for citrate or lactate was observed with the cationic complexes in which the ring NH group was retained. For example, the complex **35** exhibits citrate/lactate affinity constants ratio of 42:1. Lactate binding is preferred by the more sterically demanding ono-anionic complex **41**, in which the side chain glutarate is introduced to tune anion binding to the desired range and suppress citrate complexation, which exhibits the lactate/citrate binding ratio of 30:1, allowing lactate to be measured in the range 10 to 100 mM in the presence of up to 100 mM citrate. This methodology has been applied to the measurement of citrate in seminal fluid samples. The concentration of citrate in 0.5 μL seminal fluid samples was assessed using the ratiometric analysis of two well separated Eu(III) emission bands.[194b,c]

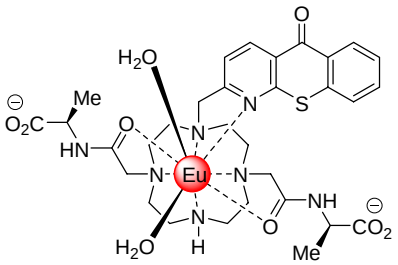
The high sensitivity of CPL spectroscopy to subtle changes in Ln(III) coordination environment is exploited for sensing chiral moieties using Ln(III) probes. Eu(III) complexes (q = 1) of achiral triazacyclononane-based ligands bearing arylalkynyl pyridyl antenna with phosphinate, amide, or carboxylate donors, reported by Parker *et al*.,[221] bind chiral carboxylic acids and α-hydroxy acids such as lactate and mandelate, forming 1:1 adducts. Anion binding was monitored by emission spectroscopy and signalled by the switching on of strong circularly polarised emission. The strongest binding to lactate was observed for the tricationic Eu(III) bis(amide) complex **42** with log K_a = 4.57, whereas the bis(phosphinate)



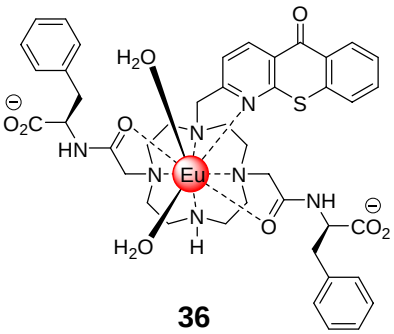
33



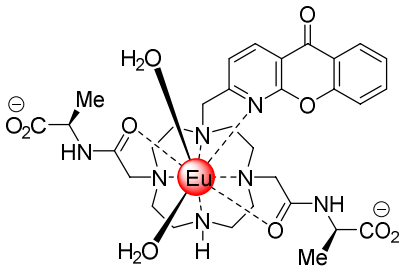
34



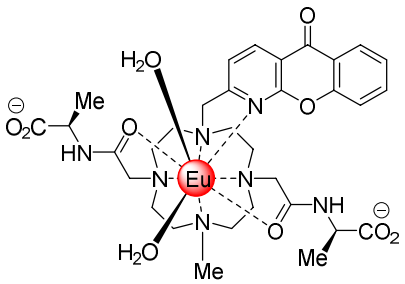
35



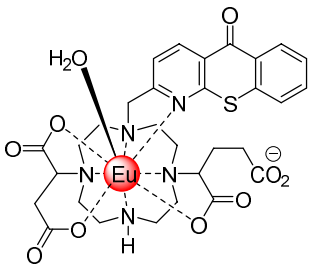
36



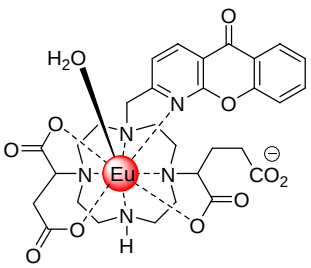
37



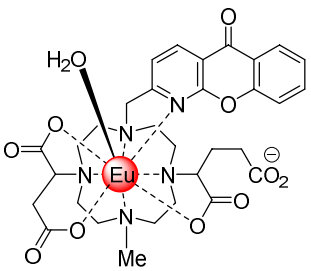
38



39



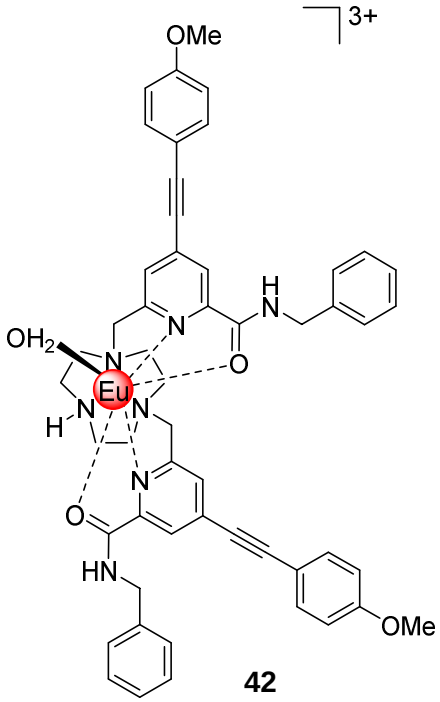
40



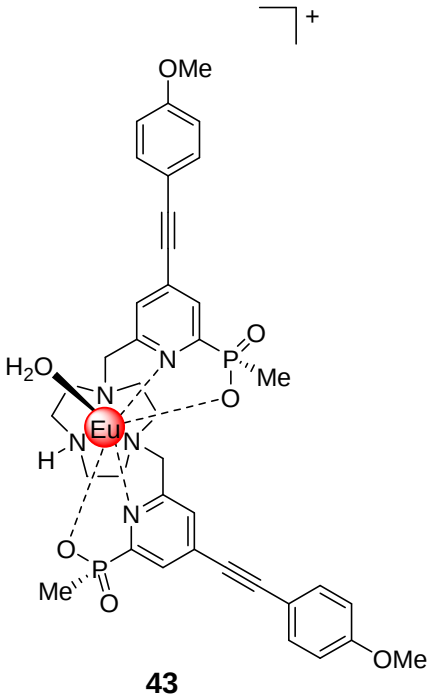
41

complex **43** showed the weakest affinity for lactate (log K_a = 2.76). Luminescence lifetimes of the lactate adducts in water and D_2O revealed q = 0 for **43** and q = 0.6 for **42**, respectively, indicating chelation of lactate to the latter complex via the OH

and CO_2^- oxygens, forming a 5-ring chelate, in which there is one O–H oscillator in the Eu(III) coordination environment.



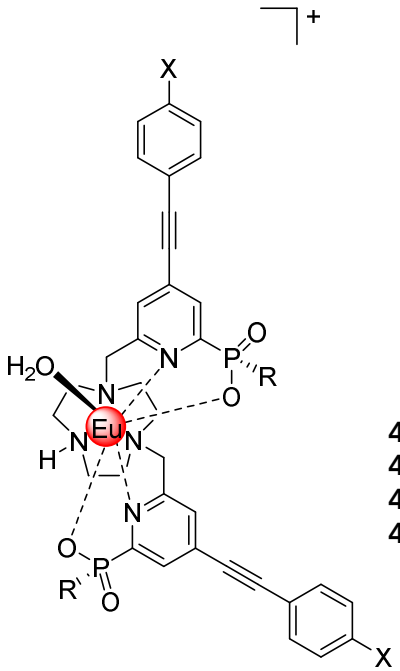
42



43

Parker *et al.*[222] have reported five Eu(III) complexes of triazacyclononane based ligand **43**-**47** with two strongly absorbing arylkynyl pyridyl chromophores, generating "bright" complexes. The binding of oxy anions such as carboxylates, lactate, and citrate at the metal centre by the displacement of coordinated water molecule has been studied by emission spectral titrimetry. Upon the binding of bicarbonate there is a pronounced change in emission spectral form, characterised by an increase in intensity of the $\Delta J = 2$ band and a 30% rise in the ratio of the intensities of the $\Delta J = 2/\Delta J = 1$ manifolds. Selectivity of **43** for bicarbonate allows its rapid determination in human serum with K_d = 37 mM by means of a ratiometric analysis of the bright Eu(III)-based luminescence. Parker *et al.*[195b] have developed Eu(III) and Tb(III) complexes **48**-**51** of four chiral ligands incorporating an

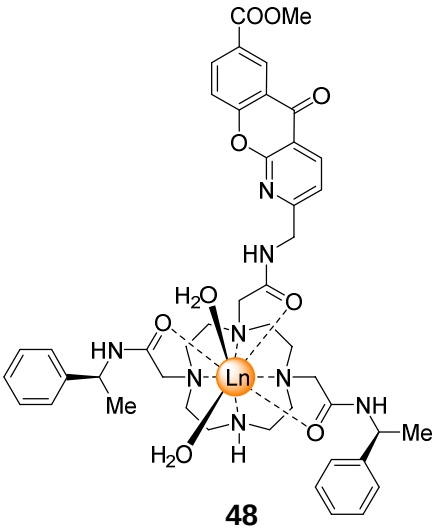
azaxanthone sensitiser and studied their binding affinities with bicarbonate, lactate, citrate, phosphate, and serum albumin. The anion binding event was signalled by modulation of circularly polarised luminescence and the affinity constants were measured by examining changes in emission intensity ratios.



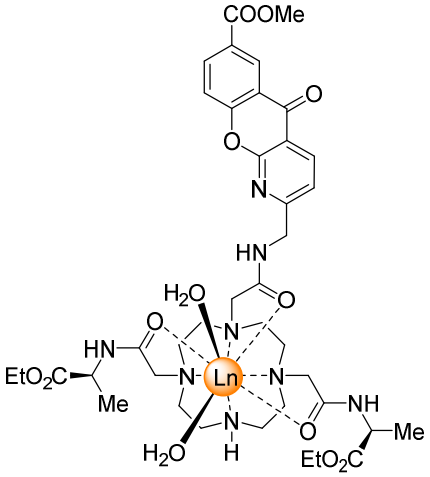
44, X = $O(CH_2CH_2O)_3Me$, R = Ph
45, X = CF_3, R = Ph
46, X = OCH_2COOH, R = Me
47, X = $OCH_2CONHCH_2[CH(OH)]_4CH_2OH$, R = Me

The ability of the Eu(III) complexes **44-47** and **52** to signal lactate binding by the switching on of CPL was demonstrated. Addition of *R*- and *S*-lactate to each complex in methanol gave rise to mirror image induced CPL spectra. The *N*-benzyl complex **52** produced the strongest CPL signal, ascribed to helical alignment of the benzyl and two pyridyl groups, creating a more rigidified chiral structure. The *R*-enantiomer gave rise to a common induced CPL signature across the series of Eu(III) complexes, identified by the $\Delta J = 4$ emission band around 700 nm.

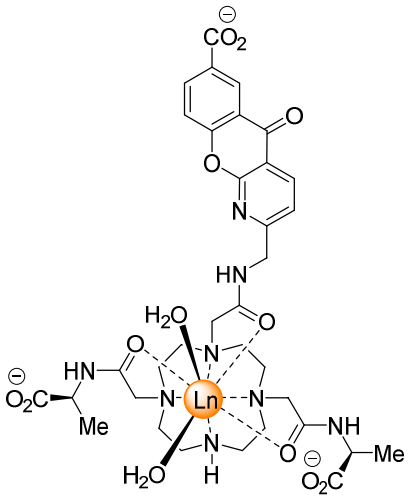
The chiral Tb(III) complex **53**, developed by Piccinelli *et al.*,[223] binds lactate weakly in water. The ligand is based on a *trans*-1,2-diaminocyclohexane scaffold



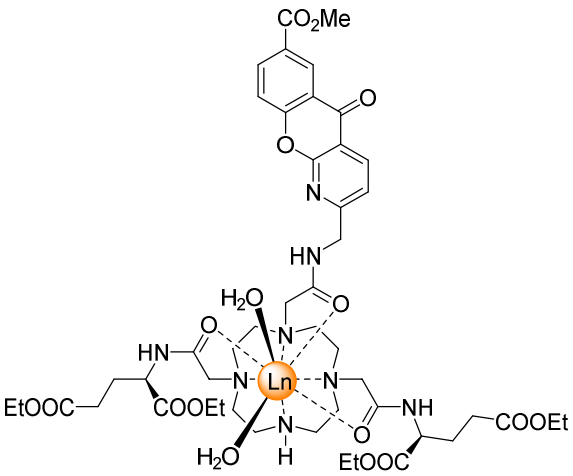
48



49

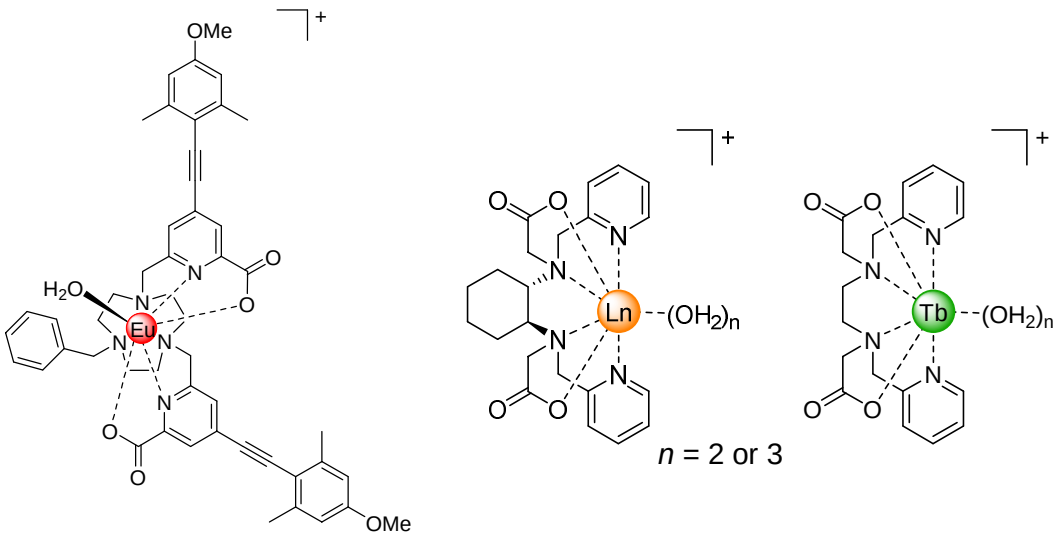


50



51

which upon binding a Ln(III) ion creates a dissymmetric environment with q = 2. Lactate displaces the two inner-sphere water molecules, signalled by an increase in Tb(III) emission intensity, particularly the band at 546 nm, which plateaued after the addition of 100 equiv of lactate. In contrast, the achiral complex **54** did not show CPL activity due to the flexible nature of the ethylenic group allowing the interconversion between the two isomers compared with the cyclohexane derivative. The potential biological utility of **53** was demonstrated by detecting lactate levels in a commercial aqueous Ringer′s solution, commonly used to treat metabolic acidosis.



52 **53 (**Ln = Eu or Tb) **54**

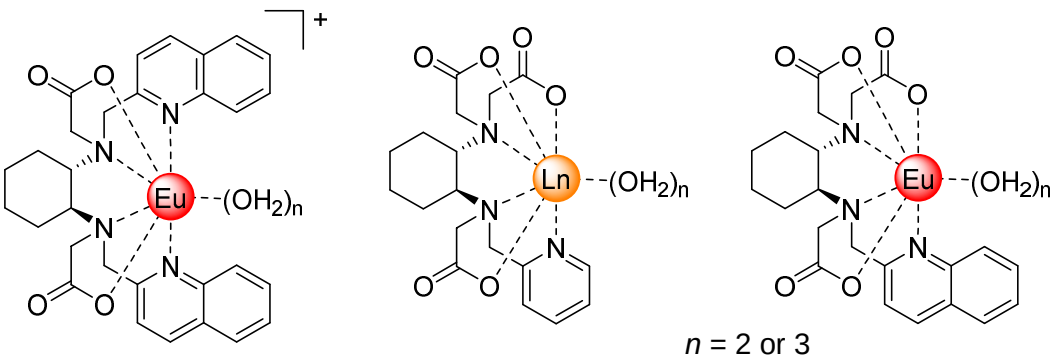
1.6.5.3. Luminescent Lanthanide Receptors for Bicarbonate

Bicarbonate plays important roles in the regulation of cellular pH, removal of metabolic waste, and kidney function.[224] Probes capable of monitoring spatio-temporal bicarbonate dynamics in living cells would provide a deeper understanding of the diverse biological processes this anion controls, potentially facilitating the development of new therapeutic agents (e.g. channel replacement therapies). Given that the concentration range of HCO_3^- in human serum is 24-27 mM, around 10-20 times higher than other oxyanions (including phosphate, lactate, and citrate),[163] it was proposed that selective sensing of HCO_3^- could be attained. Parker group[195] have reported reversible selective binding of bicarbonate by the Eu(III) and Tb(III) complexes **48**-**51**, bearing an amide-linked azaxanthone sensitiser, in the presence of endogenous anions such as phosphate, lactate, and citrate when present at their common biological concentrations. The Eu(III) complexes **48** and **49** bind reversibly to bicarbonate in water (log K_a = 3.85, 0.1 M NaCl, pH 7.4), causing displacement of the two inner-sphere water molecules and a large increase in emission intensity, particularly the ΔJ = 2 band. The concentration of bicarbonate was determined directly in cellular mitochondria and

in human serum by measuring the ratio of the intensity of a pair of emission bands within the Eu(III) emission spectrum or a red/green band intensity ratio when using mixtures of Eu(III)/Tb(III) complexes of a common ligand.[195b] Measurements of Eu(III)/Tb(III) emission intensity ratios report changes in the steady-state bicarbonate concentrations both *in vitro* and *in cellulo*. Furthermore, the Eu(III) complex **48** is able to selectively stain the mitochondrial region of HeLa cells and to increase the image intensity upon increasing percentage of CO_2. The Tb(III) complex **49** showed negligible changes in emission, thereby allowing ratiometric analysis of intracellular HCO_3^- levels by monitoring the red/green (600-720/450-570 nm) emission ratio.

Butler *et al*.[225] have exploited the luminescent Eu(III) complex **25** to study the transmembrane transport of bicarbonate. It binds reversibly to HCO_3^- in aqueous solution and shows an increase in Eu(III) emission intensity upon binding. Parker *et al*.[222] examined the binding of HCO_3^- to a series of highly emissive Eu(III) complexes, **43-47**, based on the TACN macrocycle, bearing two strongly absorbing pyridylalkynylaryl chromophores. Anion binding studies in 50% aqueous methanol reveal changes in emission spectra for HCO_3^-, citrate, lactate, and benzoate, indicative of a common chelation binding mode. Estimation of binding constants revealed similar affinities for HCO_3^-, citrate, lactate, and monophosphate anions in the range log K_a = 3-4. However, HCO_3^- binding could be distinguished readily from the other anions by the large enhancement in the $\Delta J = 2$ emission band, giving rise to a 30% increase in the $\Delta J = 2/\Delta J = 1$ emission ratio. The ability of receptor **43** to signal HCO_3^- in the presence of other biological anions is promising for the rapid quantification of HCO_3^- in blood serum samples.

The binding of a series of Eu(III) and Tb(III) complexes of chiral hexadentate ligands to bicarbonate was reported by Piccinelli *et al.*[226] The complexes differ in their overall charge (**53**-**55** are cationic, whereas **56** and **57** are neutral), steric hindrance at the metal ion, and lipophilicity of the heterocycles which impact on the stability of the host-guest complexes. Each complex possesses either two- or three inner-sphere water molecules (q = 2.5).[227] Addition of HCO_3^- to the Eu(III) complexes in water (pH 7.4) gave rise to an increase in intensity of the $\Delta J = 2$ band and a small decrease in the $\Delta J = 0$ band. The cationic complexes **53** and **55** were shown to bind two HCO_3^- ions with relatively high affinity, in the range log K_a = 4.62-5.94. In contrast, the neutral and less sterically hindered complexes **56** and **57** bind only one equiv of HCO_3^- with lower affinity in the range log K_a = 2.06-3.11 probably due to the negative charge of the 1:1 adducts which disfavours binding of a second HCO_3^- ion.



n = 2 or 3

55 **56 (**Ln = Eu or Tb) **57**

Sørensen *et al.*[228] have investigated the binding of HCO_3^- to Eu(III) complexes of classical DOTA and DO3A ligands. The study highlighted the influence of buffer type, ionic strength, and pH on anion affinity. [Eu(**DO3A**)$(OH_2)_2$] binds to HCO_3^- in aqueous buffer by displacing the two coordinated water molecules, but was not selective for HCO_3^- over other oxyanions, including

HPO_4^{2-}, lactate, and citrate. The luminescence response of [Eu(**DO3A**)$(OH_2)_2$] in the presence of 30 mM HCO_3^- was also shown to be pH dependent, with the emission signal significantly increasing at higher pH (from 6.8 to 8.0).

1.6.5.4. Interaction of anions with Lanthanides: innocent versus non-innocent anions

Sørensen *et al.*[229] have revisited the effect of anion binding with free lanthanide metals. The interaction of various anions such as acetate, nitrate, sulfate, hydrogen sulfate, fluoride, carbonate, chloride, perchlorate, and triflate were compared against EDTA which is known to chelate lanthanide metals. The interaction of these anions with lanthanides was classified under four types as illustrated in Figure 1.12.

Historically, anions in types I and II are classified as non-innocent counterions, while anions in types III and IV are classified as innocent counterions. While anions are influenced by pH, ionic strength, additional ligands, and electrolytes, these effects are accounted in assigning the anion types using Eu(III) luminescence, crystal-field, and excited state lifetime of the metal. Using EDTA as a reference to all anionic interactions, acetate and nitrate are classified as type-I. In the case of nitrate, a second coordination event of either type-I or type-II may be present. Hydrogensulfate and sulfate alter the emission intensity and excited-state lifetime, but the fine structure of the emission spectra of Eu(III) is negligibly altered except the hypersensitive band, therefore they are classified as type-II. Perchlorate, chloride, and triflate are classified as type-III anions as they do not cause any observable changes to the Eu(III) emission, and excited state lifetimes. Therefore, perchlorate, chloride, and triflate must be regarded as innocent counterions in Ln-based solution studies.

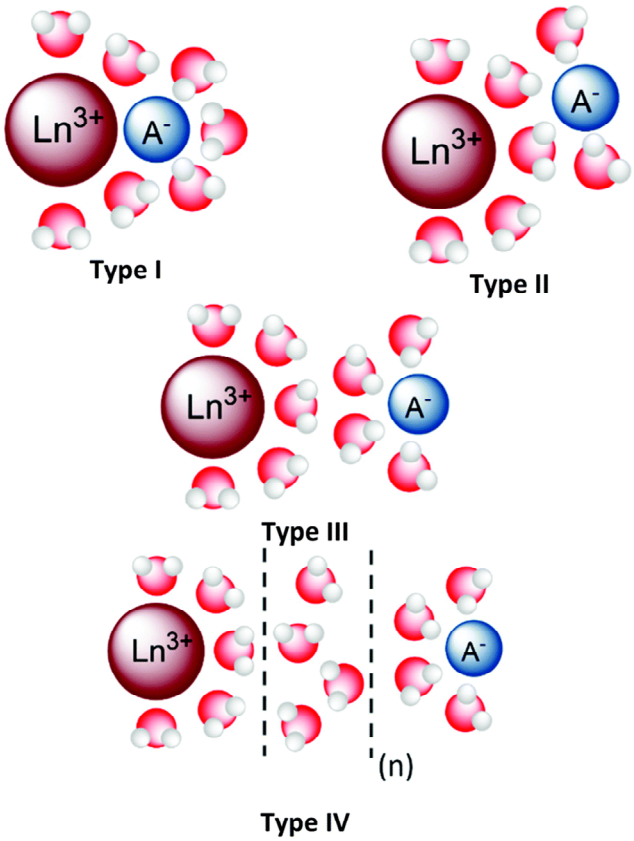


Figure 1.12. Illustration of the four different types of Ln^{3+}-anion (A^-) interactions. ***Type I:*** the anion directly coordinates to the metal ion, whereby it acts as a ligand in the inner-coordination sphere. ***Type II:*** the anion resides in the second coordination sphere of the metal ion, with the anion and metal ion sharing the solvent ligand from the inner-coordination sphere of the metal ion. ***Type III:*** both the metal ion and anion retain their own inner-coordination sphere-described as the first solvent shell by Marcus & Hefter, but with the coordination spheres in close contact. ***Type IV:*** represents the free ions, with neither restriction on ion mobility nor any appreciable interaction energy (reproduced from Ref 229 with permission).

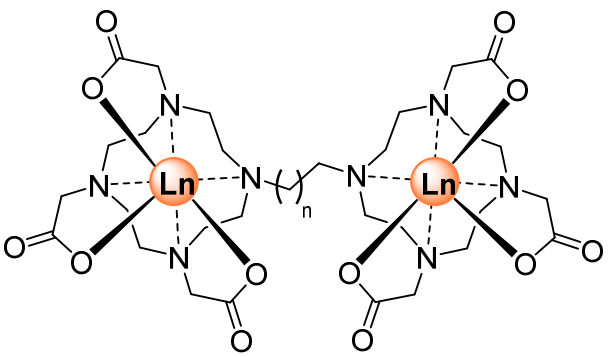
1.7. Aim and Scope of this Thesis

Lanthanide complexes are an attractive choice as host receptors to bind guest anions due to their ability to form isostructural complexes combining paramagnetism and luminescence, provided that the appropriate metal is chelated to generate the host coordination complex. In MRI, anion binding at the metal center generates a ‘turn-off’ effect since the functioning of MRI contrast agents

requires the presence of water molecules in the inner-coordination sphere which exchange with the bulk water. In the case of luminescent lanthanide complexes, the luminescence that is quenched by the inner-sphere water, is a 'turn-on' effect upon the displacement of water at the metal center by the anion. Kinetically inert lanthanide complexes are vital to achieve anion binding without dissociation of the metal complex which is achieved by employing macrocyclic ligands like DOTA, whose Gd(III) complex is a clinically approved MRI contrast agent. [Ln(**DO3A**)], containing two inner-sphere water, offers scope to chelate bidendate and larger anions than [Ln(**DOTA**)]$^-$ which contains one inner-sphere water. This thesis aims at developing binuclear lanthanide chelates based on the DO3A macrocyclic ligand for recognising two different biological anions, chloride and sialic acid (Neu5Ac), which are challenging to recognise selectively in physiological conditions.

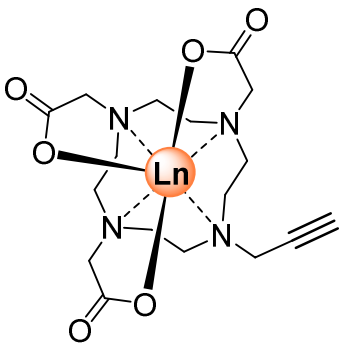
1.7.1. Aim of the Thesis

The principal objective in Chapter-II is to achieve chloride recognition in water. Mononuclear Ln(III) complexes have been explored for halide recognition, but they recognise fluoride strongly and do not respond to other halides. Learning from our previous work on neutral binuclear Ln(III) complexes that bind dicarboxylates, the same strategy is employed, but a flexible ethane or propane



[Ln_2(**DO3A**)$_2$**C-2**], *n* = 1

[Ln_2(**DO3A**)$_2$**C-3**], *n* = 2

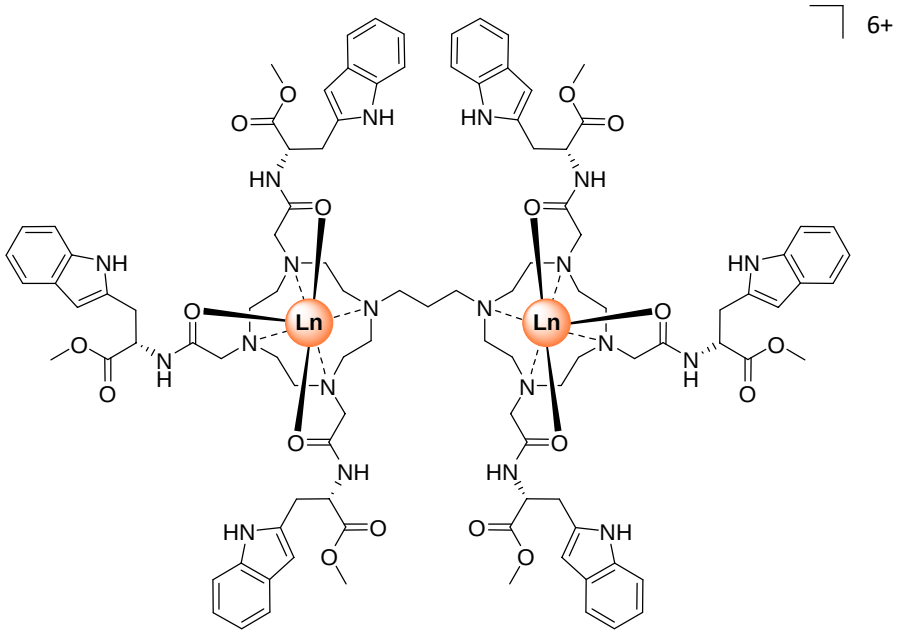


[Ln(**pDO3A**)]

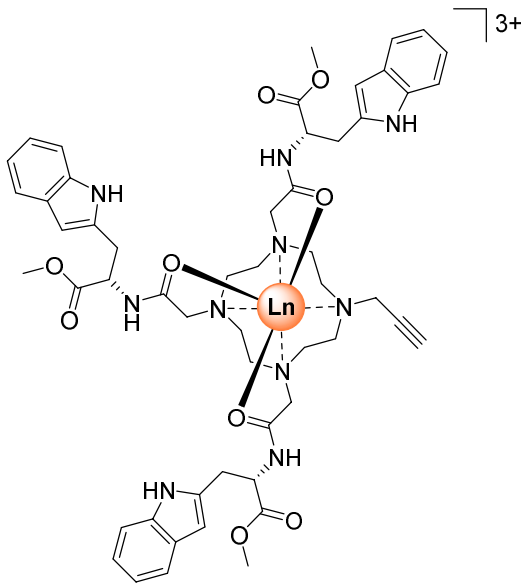
linker that connects the two [Ln(**DO3A**)] domains are utilised, forming [Ln_2(**DO3A**)$_2$**C-2**] and [Ln_2(**DO3A**)$_2$**C-3**] binuclear host complexes. This proof of concept contains a neutral receptor which will be evaluated for halide recognition. Based on its success, the receptor can be made cationic to suffice the law of coulombic attraction such that an anion is recognised by a cationic receptor to increase the host-guest affinity.[163] In order to understand the binding affinity, mode of binding (axial or equatorial to the metal centre), and selectivity over other halides, halide binding is monitored by: (1) steady-state luminescence and excited state lifetime with the binuclear Eu(III) complexes, (2) paramagnetic ^{1}H NMR studies with Eu(III) and Yb(III) analogues, (3) ^{19}F NMR with Eu(III) and Y(III) complexes, (4) ^{35}Cl NMR studies with Tb(III) complexes, (5) MRI T_1^{-1} relaxivity with Gd(III) complexes, and (6) solid-state structures determined by single crystal X-ray diffraction of Eu(III) and Yb(III) complexes. Studies involving chloride binding using the binuclear complexes are compared with the mononuclear complex [Ln(**pDO3A**)], to emphasise the need to have the binuclear binding pocket for chloride recognition in water.

Following the success of the binuclear Ln(III) complexes described in Chapter-II, Chapter-III describes the second-generation binuclear Ln(III) complexes for chloride recognition. The cyclen core contains tryptophan pendant arms to chelate the metal instead of carboxylate arms, forming [Ln_2(**DO3AM-L-TrpOMe**)$_2$**C-3**]$^{6+}$. This is designed to improve the sensitivity of the host where tryptophan is a good light harvesting antenna for Tb(III) sensitisation and to further strengthen chloride recognition using amide nitrogen and imidazole nitrogen forming hydrogen bonds with the halide guests. Halide binding is monitored through (1) steady-state luminescence and excited state lifetime with

Tb(III) complexes, (2) paramagnetic ^{1}H and ^{19}F NMR studies with Eu(III) complex, and ^{35}Cl NMR studies with Tb(III) complex, and (4) studies on the chirality of the receptor using CD and CPL.

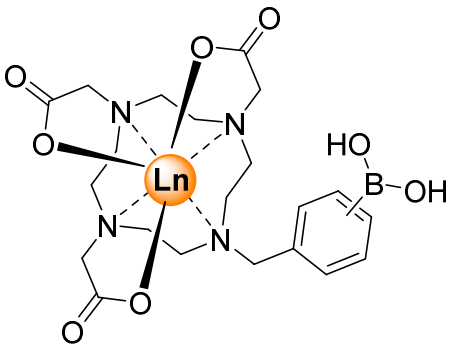


[Ln$_2$(DO3AM-L-TrpOMe)$_2$C-3]$^{6+}$



[Ln(pDO3AM-L-TrpOMe)]$^{3+}$

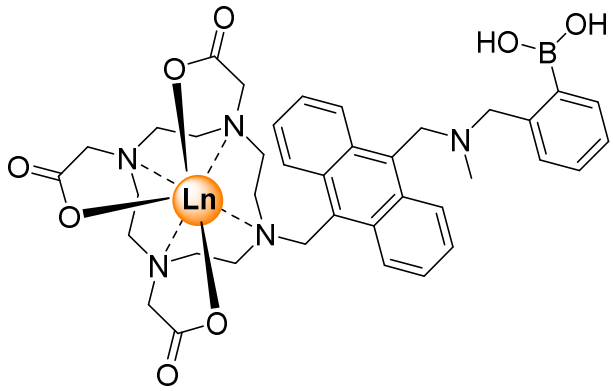
Chapter-IV is aimed at investigating sialic acid (Neu5Ac) recognition by revisiting the cooperative two coordinate approach by combining phenylboronic acid to the DO3A domain, such that the vicinal diol from the sugar binds to the boronic acid, while the carboxylate of the sugar chelates the lanthanide metal ion. The conformational space of binding is explored by altering the boronate substituent on the aryl ring, and synthesising the complexes, [Ln(**DO3A**)***o*-PBA**], [Ln(**DO3A**)***m*-PBA**], and [Ln(**DO3A**)***p*-PBA**]. The binding of sialic acid and other monosaccharides are investigated through (1) steady-state luminescence and excited state lifetime with Eu(III) complexes, (2) paramagnetic ^{1}H NMR studies with Eu(III) complexes, (3) CPL studies with Tb(III) complexes, (4) ^{11}B NMR studies with Eu(III) and Lu(III) complexes, and (5) solid-state structures determined by single crystal X-ray diffraction.



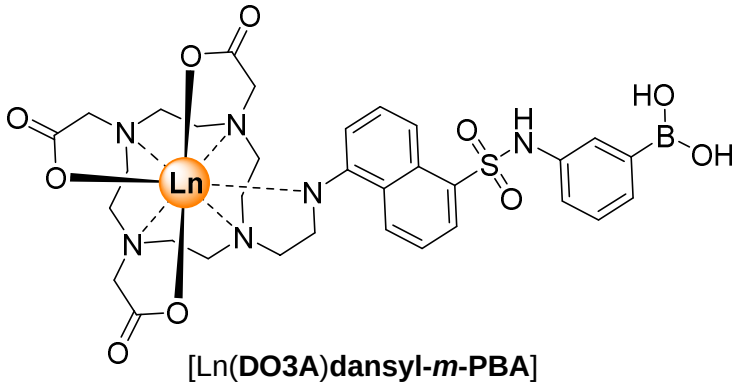
[Ln(**DO3A**)***o*-PBA**]
[Ln(**DO3A**)***m*-PBA**]
[Ln(**DO3A**)***p*-PBA**]

Chapter-V picks up on the drawbacks from Chapter-IV towards sialic acid binding. The distance between the arylboronate and the lewis acid (Ln(III) center) is increased by incorporating anthracene and dansyl chromophores, [Ln(**DO3A**)**anth-*o*-PBA**] and [Ln(**DO3A**)**dansyl-*m*-PBA**] complexes were synthesised. The design of [Ln(**DO3A**)**anth-*o*-PBA**] is inspired from a previous strategy, where sialic acid induces PeT to the metal centre upon binding of the vicinal diol of the sugar to the *ortho* arylboronate. This design is also known to increase the binding affinity of the sugar on the boronate centre. Dansyl is

investigated as an alternative to anthracene to explore the prospects of sialic acid binding in solution.



[Ln(**DO3A**)**anth-*o*-PBA**]



[Ln(**DO3A**)**dansyl-*m*-PBA**]

1.7.2.Scope of the Thesis

Chloride recognition in water is a long-standing challenge pursued by supramolecular and coordination chemists for decades. Apart from fundamental chemistry, chloride is the most abundant physiological anion and plays numerous roles in living systems, whose functions are yet to be understood fully due to the lack of a non-invasive probe for physiological chloride tracking. Therefore, chloride binding achieved by lanthanide complexes opens up new avenues for applications from biology to sensor development. The present bismacrocyclic ligand framework can be expanded further by incorporating light harvesting antenna for *in vitro*

imaging of chloride, MRI relaxivity, and saturation transfer experiments for *in vivo* imaging of chloride. Furthermore, this framework can be altered for targeted chloride binding in biology.

Phenylboronic acids are widely known for the selective recognition of sugars, but selective binding within sugars can be established by using a Lewis acid that can bind to the carboxylate in a sugar moiety. Furthermore, every sugar has its unique chiral signature which can be exploited for selective tracking of these sugars using CPL. The difference in the rate of interaction of these saccharides to the paramagnetic complexes can be exploited in the MRI saturation transfer experiments like paraCEST and paraSHIFT, thereby leading to the development of new generation receptors for *in vitro* and *in vivo* tracking of sialic acid.

1.8. References

1. (a) Cotton, S. A.; Raithby, P. R. *Coord. Chem. Rev*. **2017**, *340*, 220−231. (b) Bünzli, J.-C. G. *Acc. Chem. Res*. **2006**, *39*, 53−61.
2. Ketelaar, J. A. A. *Physica* **1937**, *4*, 619−630.
3. Helmholz, L. *J. Am. Chem. Soc.* **1939**, *61*, 6, 1544−1550.
4. Zalkin, A.; Forrester, J. D.; Templeton, D. H. *J. Chem. Phys*. **1963**, *39*, 2881−2891.
5. Lind, M. D.; Lee, B.; Hoard, J. L. *J. Am. Chem. Soc*. **1965**, *87*, 1611−1612.
6. Cotton, S. A.; Hart, F. A.; Hursthouse, M. B.; Welch, A. J. *J. Chem. Soc., Chem. Commun*. **1972**, 1225−1226.
7. Ghotra, J. S.; Hursthouse, M. B.; Welch, A. J. *J. Chem. Soc., Chem. Commun*. **1973**, 669−670.
8. Eaborn, C.; Hitchcock, P. B.; Izod, K.; Smith, J. D. *J. Am. Chem. Soc*. **1994**, *116*, 12071−12072.
9. Seitz, M.; Oliver, A. G.; Raymond, K. N. *J. Am. Chem. Soc*. **2007**, *129*, 11153−11160.
10. (a) Turro, N. J.; Ramamurthy, V.; Sciano J. C. *Modern Molecular Photochemistry of Organic Molecules*; University Science Books: Sausalito, 2010. (b) *Luminescence of Lanthanide Ions in Coordination Compounds and Nanomaterials*; de Bettencourt-Dias, A., Ed.; John Wiley & Sons, Incorporated: New York, United Kingdom, 2014.
11. (a) Bünzli, J.-C. G.; Piguet, C. *Chem. Soc. Rev*. **2005**, *34*, 1048–1077. (b) Hasegawa, Y.; Wada, Y.; Yanagida, S. *J. Photochem. Photobiol. C* **2004**, *5*, 183–202.

12. Görller-Walrand, C.; Binnemans K. In: *Handbook on the Physics and Chemistry of Rare Earths*; Gschneidner, Jr., K. A., Eyring, L., Eds.; 1988; Vol. 25; pp 101–264.
13. Wybourne, B. G. *Mol. Phys.* **2003**, *101*, 899–901.
14. Carnall, W. T.; Fields, P. R.; Wybourne, B. G. *J. Chem. Phys*. **1965**, *42*, 3797–3806.
15. Judd, B. R. *Phys. Rev.* **1962**, *127*, 750–761.
16. Ofelt, G. S. *J. Chem. Phys.* **1962**, *37*, 511–520.
17. Carnall, W. T.; Fields, P. R.; Rajnak, K. *J. Chem. Phys.* **1968**, *49*, 4424–4442.
18. Carnall, W. T.; Fields, P. R.; Rajnak, K. *J. Chem. Phys*. **1968**, *49*, 4412–4423.
19. Henrie, D. E.; Fellows, R. L.; Choppin, G. R. *Coord. Chem. Rev*. **1976**, *18*, 199–224.
20. Peacock, R. D. In: *Structure and Bonding*; Dunitz, J. D., Hemmerich, P., Holm, R. H., Ibers, J. A., Joergensen, K., Neilands, J. B., Reinen, D., Williams, R. J. P., Eds.; Springer: Heidelberg, 1975; Vol. 22.
21. (a) Mason, S. F.; Peacock, R. D.; Stewart, B. *Chem. Phys. Lett.* **1974**, *29*, 149–153. (b) Mason, S. F.; Peacock, R. D.; Stewart, B. *Molec. Phys*. **1975**, *30*, 1829–1841.
22. Richardson, F. S.; Saxe, J. D.; Davis, S. A.; Faulkner, T. R. *Mole. Phys*. **1981**, *42*, 1401–1429.
23. Weissman, S. I. *J. Chem. Phys.* **1942**, *10*, 214–217.
24. Moore, E. G.; Samuel, A. P. S.; Raymond, K. N. *Acc. Chem. Res.* **2009**, *42*, 542–552.
25. Crosby, G. A.; Kasha, M. *Spectrochim. Acta* **1958**, *10*, 377–382.
26. Sabbatini, N.; Guardigli, M.; Lehn, J.-L. *Coord. Chem. Rev.* **1993**, *123*, 201–228.
27. Rudzinski, C. M.; Engebretson D. S.; Hartmann, W. K.; Nocera, D. G. *J. Phys. Chem. A* **1998**, *102*, 7442–7446.
28. (a) Yang, C.; Fu, L. M.; Wang, Y.; Zhang, J. P.; Wong, W. T.; Ai, X. C.; Qiao, Y. F.; Zou, B. S.; Gui, L. L. *Angew. Chem., Int. Ed.* **2004**, *43*, 5010–5013. (b) Andres, J.; Chauvin, A.-S. *Phys. Chem. Chem. Phys.* **2013**, *15*, 15981–15994.
29. Botelho, M. B. S.; Galvez-Lopez, M. D.; De Cola, L.; Albuquerque, R. Q.; de Camargo, A. S. S. *Eur. J. Inorg. Chem*. **2013**, *2013*, 5064–5070.
30. (a) D′Aléo, A.; Pointillart, F.; Ouahab, L.; Andraud, C.; Maury, O. *Coord. Chem. Rev*. **2012**, *256*, 1604–1620. (b) Pointillart, F.; Bourdolle, A.; Cauchy, T.; Maury, O.; Gal, Y. L.; Golhen, S.; Cador, O.; Ouahab, L. *Inorg. Chem*. **2012**, *51*, 978–984. (c) Pointillart, F.; Cauchy, T.; Maury, O.; Gal, Y. L.; Golhen, S.; Cador, O.; Ouahab, L. *Chem. - Eur. J.* **2010**, *16*, 11926–11941.
31. (a) Ward, M. D. *Coord. Chem. Rev.* **2010**, *254*, 2634–2642. (b) Xu, L. J.; Xu, G. T.; Chen, Z. N. *Coord. Chem. Rev.* **2014**, *273–274*, 47–62. (c) Wei, Q.-H.; Lei, Y.-F.; Xu, W.-R.; Xie, J.-M.; Chen, G. N. *Dalton Trans.* **2012**, *41*, 11219–11225. (d) Li, L.; Zhang, S.; Xu, L.; Chen, Z. N.; Luo, J. *J. Mater. Chem. C* **2014**, *2*, 1698–1703.

(e) Sykes, D.; Cankut, A. J.; Ali, N. M.; Stephenson, A.; Spall, S. J. P.; Parker, S. C.; Weinstein, J. A.; Ward, M. D. *Dalton Trans.* **2014**, *43*, 6414–6428.

32. Crosby, G. A.; Alire, R. M.; Whan, R. E. *J. Chem. Phys*. **1961**, *34*, 743–748.
33. (a) Beeby, A.; Clarkson, I. M.; Dickins, R. S.; Faulkner, S.; Parker, D.; Royle, L.; de Sousa, A. S.; Williams, J. A. G.; Woods, M. *J. Chem. Soc., Perkin Trans. 2* **1999**, 493–504. (b) Haas, Y.; Stein, G. *J. Phys. Chem.* **1971**, *75*, 3677–3681. (c) Ning, Y.; Liu, Y.-W.; Meng, Y.-S.; Zhang, J.-L. *Inorg. Chem*. **2018**, *57*, 1332–1341. (d) Yang, Z.-R.; Lu, Z.-Y.; Lin, M.-L.; Feng, C.-C.; Zhou, H.-Y.; Zhang, K.; Lü, Y.-H.; Huang, W. *Polyhedron* **2018**, *145*, 108–113.
34. (a) Ahmed, Z.; Iftikhar, K. *J. Phys. Chem. A* **2013**, *117*, 11183–11201. (b) Daumann, L. J.; Tatum, D. S.; Snyder, B. E. R.; Ni, C.; Law, G.-L.; Solomon, E. I.; Raymond, K. N. *J. Am. Chem. Soc*. **2015**, *137*, 2816–2819.
35. Latva, M.; Takalo, H.; Mukkala, V.-M.; Matachescu, C.; Rodriguez-Ubis, J. C.; Kankare, J. *J. Lumin.* **1997**, *75*, 149–169.
36. Yuster, P.; Weissman, S. I. *J. Chem. Phys*. **1949**, *17*, 1182–1188.
37. Petoud, S.; Cohen, S. M.; Bünzli, J. C.-G.; Raymond, K. N. *J. Am. Chem. Soc.* **2003**, *125*, 13324–13325.
38. Walton, J. W.; Bourdolle, A.; Butler, S. J.; Soulie, M.; Delbianco, M.; McMahon, B. K.; Pal, R.; Puschmann, H.; Zwier, J. M.; Lamarque, L.; Maury, O.; Andraud, C.; Parker, D. *Chem. Commun.* **2013**, *49*, 1600–1602.
39. Kovacs, D.; Lu, X.; Mészáros, L. S.; Ott, M.; Andres, J.; Borbas, K. E. *J. Am. Chem. Soc.* **2017**, *139*, 5756–5767.
40. Dexter, D. L. *J. Chem. Phys.* **1953**, *21*, 836–850.
41. Förster, T. *Ann. Physik*. **1948**, *2*, 55–75.
42. (a) Reinhard, C.; Güdel, H. U. *Inorg. Chem.* **2002**, *41*, 1048–1055. (b) Pope, S. J. A.; Burton-Pye, B. P.; Berridge, R.; Khan, T.; Skabara, P. J.; Faulkner, S. *Dalton Trans*. **2006**, 2907–2912.
43. Lakowicz, J. R. *Principles of Fluorescence Spectroscopy;* Plenum: New York, 1999.
44. Lazarides, T.; Sykes, D.; Faulkner, S.; Barbieri, A.; Ward, M. D. *Chem. - Eur. J.* **2008**, *14*, 9389–9399.
45. Kovacs, D.; Borbas, K. E. *Coord. Chem. Rev.* **2018**, *364*, 1–9.
46. Horrocks, W. DeW., Jr.; Bolender, J. P.; Smith, W. D.; Supkowski, R. M. *J. Am. Chem. Soc.* **1997**, *119*, 5972–5973.
47. (a) Kovacs, D.; Mathieu, E.; Kiraev, S. R. Wells, J. A. L.; Demeyere, E.; Sipos, A.; Borbas, K. E. *J. Am. Chem. Soc.* **2020**, *142*, 13190–13200. (b) Kovacs, D.; Kiraev, S. R.; Phipps, D.; Orthaber, A.; Borbas, K. E. *Inorg. Chem.* **2020**, *59*, 106–117. (c)

Kovacs, D. *Photoinduced Electron Transfer in Luminescent Lanthanide Complexes*; PhD thesis, Uppsala University, Sweeden, 2019.

48. Parker, D.; Dickins, R. S.; Puschmann, H.; Crossland, C.; Howard, J. A. K. *Chem. Rev.* **2002**, *102*, 1977–2010.
49. Kropp, J. L.; Windsor, M. W. *J. Chem. Phys.* **1963**, *39*, 2769–2770.
50. (a) Horrocks, W. DeW., Jr.; Sudnick, D. R. *Acc. Chem. Res.* **1981**, *14*, 384–392. (b) Horrocks, W. DeW., Jr.; Sudnick, D. R. *J. Am. Chem. Soc.* **1979**, *101*, 334–340.
51. Sørensen, T. J.; Faulkner, S. *Acc. Chem. Res.* **2018**, *51*, 2493–2501.
52. (a) Sánchez-Carnerero, E. M.; Agarrabeitia, A. R.; Moreno, F.; Maroto, B. L.; Muller, G.; Ortiz, M. J.; de la Moya, S. *Chem. - Eur. J.* **2015**, *21*, 13488–13500. (b) Zinna, F.; Di Bari, L. *Chirality* **2015**, *27*, 1–15.
53. MacKenzie, L. E.; Pal, R. *Nat. Rev. Chem.* **2021**, *5*, 109–124.
54. (a) Bünzli, J.-C. G. *Chem. Rev.* **2010**, *110*, 2729–2755. (b) Richardson, F. S. *Chem. Rev.* **1982**, *82*, 541–552.
55. (a) Alexander, V. *Chem. Rev.* **1995**, *95*, 273–342. (b) Fenton, D.; Vigato, P. *Chem. Soc. Rev.* **1988**, *17*, 69–90.
56. Stasiuk, G. J.; Long, N. J. *Chem. Commun.* **2013**, *49*, 2732−2746.
57. Peters, J. A.; Djanashvili, K.; Geraldes, C. F. G. C.; Platas-Iglesias, C. *Coord. Chem. Rev.* **2020**, *406*, 213146.
58. (a) Martell, A. E.; Smith, R. M. *Critical Stability Constants*; Plenum Press: New York, 1974; Vol. 1. (b) Cacheris, W. P.; Nickle, S. K.; Sherry, A. D. *Inorg. Chem.* **1987**, *26*, 958−960. (c) Moeller, T.; Thompson, L. C. *J. Inorg. Nucl. Chem.* **1962**, *24*, 499−510. (d) Grimes, T. S.; Nash, K. L. *J. Solution Chem.* **2014**, *43*, 298−313.
59. (a) Baranyai, Z.; Botta, M.; Fekete, M.; Giovenzana, G. B.; Negri, R.; Tei, L.; Platas-Iglesias, C. *Chem. - Eur. J.* **2012**, *18*, 7680−7685. (b) Negri, R.; Baranyai, Z.; Tei, L.; Giovenzana, G. B.; Platas-Iglesias, C.; Bényei, A. C.; Bodnár, J.; Vágner, A.; Botta, M. *Inorg. Chem.* **2014**, *53*, 12499−12511.
60. Voss, D. A., Jr.; Farquhar, E. R.; Horrocks, W. DeW., Jr.; Morrow, J. R. *Inorg. Chim. Acta* **2004**, *357*, 859−863.
61. Roca-Sabio, A.; Mato-Iglesias, M.; Esteban-Gomez, D.; Tóth, É.; de Blas, A.; Platas-Iglesias, C.; Rodríguez-Blas, T. *J. Am. Chem. Soc.* **2009**, *131*, 3331−3341.
62. Chang, C. A.; Rowland, M. E. *Inorg. Chem.* **1983**, *22*, 3866−3869.
63. Hu, A.; MacMillan, S. N.; Wilson. J. J. *J. Am. Chem. Soc.* **2020**, *142*, 13500−1350.
64. Shannon, R. D. *Acta Crystallogr. Sect. A* **1976**, *32*, 751−767.
65. Chang, C. A. Lanthanide Macrocyclic Complexes: Structure, Thermodynamics, Kinetics, and Applications, In *Handbook on the Physics and Chemistry of Rare*

Earths: Including Actinides; Bünzli, J.-C. G., Pecharsky, V. K., Eds.; Elsevier Science B.V., 2017, Chapter 297; Vol. 51; pp 169-299.

66. Kumar, K.; Chang, C. A.; Tweedle, M. F. *Inorg. Chem*. **1993**, *32*, 587−593.
67. Sherry, A. D.; Caravan, P.; Lenkinski, R. E. *J. Magn. Reson. Imaging* **2009**, *30*, 1240−1248.
68. (a) Tóth, É.; Brücher, E.; Lázár, I.; Tóth, I. *Inorg. Chem*. **1994**, *33*, 4070–4076. (b) Balogh, E.; Tripier, R.; Ruloff, R.; Tóth, É. *Dalton Trans*. **2005**, 1058–1065. (c) Brücher, E.; Sherry, A. D. *Inorg. Chem*. **1990**, *29*, 1555–1559.
69. Stetter, H.; Frank, W. *Angew. Chem., Int. Ed*. **1976**, *15*, 686.
70. Bryden, C. C.; Reilley, C. N.; Desreux, J. F. *Anal. Chem*. **1981**, *53*, 1418–1425.
71. (a) Desreux, J. F. *Inorg. Chem*. **1980**, *19*, 1319–1324. (b) Loncin, M. F.; Desreux, J. F.; Merciny, E. *Inorg. Chem*. **1986**, *25*, 2646–2648. (c) Desreux, J. F.; Barthlemy, P. P. *Nucl. Med. Biol*. **1988**, *15*, 9−15.
72. Spirlet, M.; Rebizant, J.; Desreux, J. F.; Loncin, M. F. *Inorg. Chem*. **1984**, *23*, 359−363.
73. (a) Chang, C. A.; Francesconi, L. C.; Malley, M. F.; Kumar, K.; Gougoutas, J. Z.; Tweedle, M. F.; Lee, D. W.; Wilson, L. J. *Inorg. Chem*. **1993**, *32*, 3501–3508. (b) Dubost, J.-P.; Leger, M.; Langlois, M.-H.; Meyer, D.; Schaefer, M. *C. R. Acad. Sci. Paris, Ser. 2* **1991**, *312*, 349−354.
74. Aime, S.; Barge, A.; Botta, M.; Fasano, M.; Ayala, J. D.; Bombieri, G. *Inorg. Chim. Acta* **1996**, *246*, 423−429.
75. Frullano, L.; Caravan, P. *Curr. Org. Synth*. **2011**, *8*, 535−565.
76. (a) Kumar, K.; Chang, C. A.; Francesconi, L.; Dischino, D.; Malley, M.; Gougoutas, J.; Tweedle, M. F. *Inorg. Chem*. **1994**, *33*, 3567–3575. (b) Chang, C. A.; Wang, I-F.; Lee, H-Y.; Meng, C-N.; Liu, K-Y.; Chen, Y-F.; Yang, T-H.; Wang, Y-M.; Tsay, Y-G. *Dalton Trans.* **2012**, *41*, 14697–14706.
77. Aime, S.; Botta, M.; Ermondi, G. *Inorg. Chem*. **1992**, *31*, 4291–4299.
78. (a) Parker, D.; Pulukkody, K.; Smith, F. C.; Batsanov, A.; Howard, J. A. K. *J. Chem. Soc., Dalton Trans*. **1994**, 689−693. (b) Benetollo, F.; Bombieri, G.; Aime, S.; Botta, M. *Acta Crystallogr. Sect. C Cryst. Struct. Commun*. **1999**, *55*, 353−356.
79. Morrow, J. R.; Amin, S.; Lake, C. H.; Churchill, M. R. *Inorg. Chem*. **1993**, *32*, 4566−4572.
80. Chin, K. O. A.; Morrow, J. R.; Lake, C. H.; Churchill, M. R. *Inorg. Chem*. **1994**, *33*, 656−664.
81. Aime, S.; Batsanov, A. S.; Botta, M.; Howard, J. A. K.; Parker, D.; Senanayake, K.; Williams, G. *Inorg. Chem*. **1994**, *33*, 4696−4706.

82. Kang, S. I.; Ranganathan, R. S.; Emswiler, J. E.; Kumar, K.; Gougoutas, J. Z.; Malley, M. F.; Tweedle, M. F. *Inorg. Chem.* **1993**, *32*, 2912−2918.
83. Jacques, V.; Desreux, J. F. *Inorg. Chem.* **1994**, *33*, 4048–4053.
84. Aime, S.; Botta, M.; Fasano, M.; Marques, M. P. M.; Geraldes, C. F.; Pubanz, D.; Merbach, A. E. *Inorg. Chem.* **1997**, *36*, 2059–2068.
85. Ren, J.; Sherry, A. D. *J. Magn. Reson*. **1996**, *111*, 178−182.
86. Parker, D.; Suturina, E. A.; Kuprov, I.; Chilton, N. F. *Acc. Chem. Res.* **2020**, *53*, 1520–1534.
87. Duan, C-K.; Tanner, P. A. *J. Phys. Chem. A* **2010**, *114*, 6055–6062.
88. Peters, J. A.; Huskens, J.; Raber, D. J. *Prog. Nucl. Magn. Reson. Spectrosc*. **1996**, *28*, 283–350.
89. McConnell, H. M. *J. Chem. Phys.* **1957**, *27*, 226–229.
90. Suturina, E. A.; Mason, K.; Geraldes, C. F. G. C.; Kuprov, I.; Parker, D. *Angew. Chem., Int. Ed.* **2017**, *56*, 12215–12218.
91. Bleaney, B. *J. Magn. Reson.* **1969**, *8*, 91–100.
92. Bleaney, B.; Dobson, C. M.; Levine, B. A.; Martin, R. B.; Williams, R. P. J.; Xavier, A. V. *J. Chem. Soc., Chem. Commun*. **1972**, 791b–793.
93. Rinehart, J. D.; Long, J. R. *Chem. Sci.* **2011**, *2*, 2078–2085.
94. (a) Caravan, P.; Ellison, J. J.; McMurry, T. J.; Lauffer, R. B. *Chem. Rev*. **1999**, *99*, 2293−2352. (b) Wahsner, J.; Gale, E. M.; Rodríguez-Rodríguez, A.; Caravan, P. *Chem. Rev*. **2019**, *119*, 957−1057. (c) *The Chemistry of Contrast Agents in Medical Magnetic Resonance Imaging*, 2nd ed.; Merbach, A. E., Helm, L., Tóth, É., Eds.; Wiley: Chichester, U. K, 2013.
95. Caravan, P. *Chem. Soc. Rev*. **2006**, *35*, 512−523.
96. Mansfield, P.; Morris, P. G. *NMR Imaging in Biomedicine*; Advance in Magnetic Resonance. Supplement 2.; Academic Press: New York, 1982.
97. (a) *Magnetic Resonance Imaging*; Stark, D. D., Bradley, W. G. Jr., Eds.; The C. V. Mosby Company: St. Louis, Missouri, 1988. (b) Koeing, S. H. *Isr. J. Chem*. **1988**, *28*, 345−353.
98. (a) Liang, P.; Lauterbur, P. C. *IEEE Trans. Med. Imaging* **1994**, *13*, 677−686. (b) Bowtell, R. W.; Peters, A.; Sharp, J. C.; Mansfield, P.; Hsu, E. W.; Aiken, N.; Horsman, A.; Blackman, S. J. *Magn. Reson. Med*. **1995**, *33*, 790−794.
99. Shapiro, E. M.; Sharer, K.; Skrtic, S.; Koretsky, A. P. *Magn. Reson. Med*. **2006**, *55*, 242−249.
100. *Lanthanide Probes in Life Chemical and Earth Science*; Bünzli, J. C. G., Choppin, G. R. Eds.; Elsevier: Amsterdam, 1989.

101. Ranganathan, R.; Raju, N.; Fan, H.; Zhang, X.; Tweedle, M.; Desreux, J.; Jacques, V. *Inorg. Chem*. **2002**, *41*, 6856−6866.
102. Tweedle, M. F.; Gaughan, G. T.; Hagan, J.; Wedeking, P. W.; Sibley, P.; Wilson, L. J.; Lee, D. W. *Nucl. Med. Biol*. **1988**, *15*, 31−36.
103. Carr, D. H.; Brown, J.; Bydder, G. M.; Weinmann, H. J.; Speck, U.; Thomas, D. J.; Young, I. R. *Lancet* **1984**, *323*, 484−486.
104. (a) Tweedle, M. F.; Brittain, H. G.; Eckelman, W. C.; Gaughan, G. T.; Hagan, J. J.; Wedeking, P. W.; Runge, V. M. In *Magnetic Resonance Imaging*, 2nd ed.; Partain, C. L., Ed.; Philadelphia, 1988, Vol. 1; pp 793−809. (b) Bianchi, A.; Calabi, L.; Corana, F.; Fontana, S.; Losi, P.; Maiocchi, A.; Paleari, L.; Valtancoli, B. *Coord. Chem. Rev*. **2000**, *204*, 309−393. (c) Uzal-Varela, R.; Rodríguez-Rodríguez, A.; Wang, H.; Esteban-Gómez, D.; Brandariz, I.; Gale, E. M.; Caravan, P.; Platas-Iglesias, C. *Coord. Chem. Rev*. **2022**, *467*, 214606.
105. Chan, K. W. Y.; Wong, W. T. *Coord. Chem. Rev*. **2007**, *251*, 2428−2451.
106. Prince, M. R.; Zhang, H. L.; Zou, Z. T.; Staron, R. B.; Brill, P. W. *Am. J. Roentgenol*. **2011**, *196*, W138−W143.
107. Lohrke, J.; Frenzel, T.; Endrikat, J.; Alves, F. C.; Grist, T. M.; Law, M.; Lee, J. M.; Leiner, T.; Li, K. C.; Nikolaou, K.; Prince, M. R.; Schild, H. H.; Weinreb, J. C.; Yoshikawa, K.; Pietsch, H. *Adv. Ther*. **2016**, *33*, 1−28.
108. Villaraza, A. J. L.; Bumb, A.; Brechbiel, M. W. *Chem. Rev*. **2010**, *110*, 2921−2959.
109. (a) Weinmann, H. J.; Brasch, R. C.; Press, W. R.; Wesby, G. E. *Am. J. Roentgenol*. **1984**, *142*, 619−624. (b) Laniado, M.; Weinmann, H. J.; Schorner, W.; Felix, R.; Speck, U. *Physiol. Chem. Phys. Med. NMR* **1984**, *16*, 157−165. (c) Weinmann, H. J.; Linado, M.; Mutzel, W. *Physiol. Chem. Phys. Med. NMR* **1984**, *16*, 167−172. (d) Cacheris, W. P.; Quay, S. C.; Rocklage, S. M. *Magn. Reson. Imaging* **1990**, *8*, 467−481. (e) Konings, M. S.; Dow, W. C.; Love, D. B.; Raymond, K. N.; Quay, S. C.; Rocklage, S. M. *Inorg. Chem.* **1990**, *29*, 1488−1491. (f) Harpur, E. S.; Worah, D. I.; Hals, P.-A.; Holtz, E. C.; Furuhama, K.; Nomura, H. *Invest. Radiol*. **1993**, *28*, S21−S43. (g) Greco, A.; McNamara, M. T.; Lanthiez, P.; Quay, S. C.; Michelozzi, G. *Radiology* **1990**, *176*, 451−456.
110. (a) Geraldes, C. F. G. C.; Urbano, A. M.; Alpoim, M. C.; Sherry, A. D.; Kuan, K.-T.; Rajagopalan, R.; Maton, F.; Muller, R. N. *Magn. Reson. Imaging* **1995**, *13*, 401−420. (b) Periasamy, M.; White, D.; De Learie, L.; Moore, D.; Wallace, R.; Lin, W.; Dunn, J.; Hirth, W.; Cacheris, W.; Pilcher, G.; Galen, K.; Hynes, M.; Bosworth, M.; Lin, H.; Adams, M. *Invest. Radiol*. **1991**, *26*, S217−S220.
111. (a) Tweedle, M. F.; Runge, V. M. *Drugs Future* **1992**, *17*, 187−190. (b) Tweedle, M. F. *Invest Radiol*. **1992**, *27*, S2−S6.

112. (a) Vittadini, G.; Felder, E.; Tirone, P.; Lorusso, V. *Invest. Radiol*. **1988**, *23*, S246−S248. (b) Cavagna, F.; Dapra, M.; Maggioni, F.; de Haen, C.; Felder, E. *Magn. Reson. Med.* **1991**, *22*, 329−333. (c) Uggeri, F.; Aime, S.; Anelli, P. L.; Botta, M.; Brocchetta, M.; de Haen, C.; Ermondi, G.; Grandi, M.; Paoli, P. *Inorg. Chem.* **1995**, *34*, 633−643.

113. Pan, D. P. J.; Schmieder, A. H.; Wickline, S. A.; Lanza, G. M. *Tetrahedron* **2011**, *67*, 8431−8444.

114. (a) Brucher, E. *Top. Curr. Chem*. **2002**, *221*, 103−122. (b) Gries, H. *Top. Curr. Chem*. **2002**, *221*, 1−24.

115. (a) Solomon, I. *Phys. Rev*. **1955**, *99*, 559−565. (b) Bloembergen, N. *J. Chem. Phys*. **1957**, *27*, 572−573. (c) Bloembergen, N.; Morgan, L. O. *J. Chem. Phys*. **1961**, *34*, 842−850. (d) Bloembergen, N. *Phys. Rev*. **1956**, *104*, 1542−1547. (e) Bloembergen, N.; Purcell, E. M.; Pound, R. V. *Phys. Rev*. **1948**, *73*, 679−712. (f) Bernheim, R. A.; Brown, T. H.; Gutowsky, H. S.; Woessner, D. E. *J. Chem. Phys*. **1959**, *30*, 950−956. (g) Morgan, L. O.; Nolle, A. W. *J. Chem. Phys*. **1959**, *31*, 365−368. (h) Kowalewski, J. Paramagnetic Relaxation in Solution, In *Encyclopedia of NMR*; Grant, D., M., Harris, R. K., Eds.; Wiley: Chichester, 1996; pp 3456−3462.

116. (a) Bertini, I.; Kowalewski, J.; Luchinat, C.; Nilsson, T.; Parigi, G. *J. Chem. Phys*. **1999**, *111*, 5795−5807. (b) Bertini, I.; Luchinat, C.; Parigi, G. Solution NMR of Paramagnetic Molecules; Elsevier: Amsterdam, 2001. (c) Kowalewski, J.; Luchinat, C.; Nilsson, T.; Parigi, G. *J. Phys. Chem. A* **2002**, *106*, 7376−7382. (d) Kruk, D.; Nilsson, T.; Kowalewski, J. *Phys. Chem. Chem. Phys*. **2001**, *3*, 4907−4917.

117. (a) Pfeifer, H. *Ann. Phys*. **1961**, *463*, 1−8. (b) Hwang, L. P.; Freed, J. J. *J. Chem. Phys*. **1975**, *63*, 4017−4025. (c) Freed, J. J. *J. Chem. Phys*. **1978**, *68*, 4034−4037.

118. (a) Aime, S.; Barge, A.; Botta, M.; de Sousa, A. S.; Parker, D. *Angew. Chem., Int. Ed.* **1998**, *37*, 2673−2675. (b) Aime, S.; Barge, A.; Bruce, J. I.; Botta, M.; Howard, J. A. K.; Moloney, J. M.; Parker, D.; De Sousa, S.; Woods, M. *J. Am. Chem. Soc*. **1999**, *121*, 5762−5771. (c) Dunand, F. A.; Aime, S.; Merbach, A. E. *J. Am. Chem. Soc*. **2000**, *122*, 1506−1512.

119. Dumas, S.; Jacques, V.; Sun, W.-C.; Troughton, J. S.; Welch, J. T.; Chasse, J. M.; Schmitt-Willich, H.; Caravan, P. *Invest. Radiol*. **2010**, *45*, 600−612.

120. (a) Grobner, T. *Nephrol., Dial., Transplant*. **2006**, *21*, 1104−1108. (b) Marckmann, P.; Skov, L.; Rossen, K.; Dupont, A.; Damholt, M. B.; Heaf, J. G.; Thomsen, H. S. *J. Am. Soc. Nephrol*. **2006**, *17*, 2359−2362.

121. (a) Laurent, S.; Elst, L. V.; Copoix, F.; Muller, R. N. *Invest. Radiol*. **2001**, *36*, 115−122. (b) Laurent, S.; Botteman, F.; Elst, L. V.; Muller, R. N. *Helv. Chim. Acta* **2004**, *87*, 1077−1089. (c) Laurent, S.; Elst, L. V.; Henoumont, C.; Muller, R. N.

Contrast Media Mol. Imaging **2010**, *5*, 305−308. (d) Frenzel, T.; Lengsfeld, P.; Schirmer, H.; Hutter, J.; Weinmann, H.-J. *Radiol*. **2008**, *43*, 817−828. (e) Telgmann, L.; Wehe, C. A.; Künnemeyer, J.; Bülter, A. C.; Sperling, M.; Karst, U. *Anal. Bioanal. Chem.* **2012**, *404*, 2133−2141. (f) Laurent, S.; Elst, L. V.; Muller, R. N. *Contrast Media Mol. Imaging* **2006**, *1*, 128−137.

122. (a) Tweedle, M. F.; Wedeking, P.; Kumar, K. *Invest. Radiol*. **1995**, *30*, 372−380. (b) Sieber, M. A.; Lengsfeld, P.; Frenzel, T.; Golfier, S.; Schmitt-Willich, H.; Siegmund, F.; Walter, J.; Weinmann, H. J.; Pietsch, H. *Eur. Radiol*. **2008**, *18*, 2164−2173. (c) Sieber, M. A.; Lengsfeld, P.; Walter, J.; Schirmer, H.; Frenzel, T.; Siegmund, F.; Weinmann, H. J.; Pietsch, H. J. *Magn. Reson. Imaging* **2008**, *27*, 955−962. (d) Sieber, M. A.; Pietsch, H.; Walter, J.; Haider, W.; Frenzel, T.; Weinmann, H.-J. *Invest. Radiol*. **2008**, *43*, 65−75. (e) Pietsch, H.; Lengseld, P.; Steger-Hartmann, T.; Lowe, A.; Frenzel, T.; Huetter, J.; Sieber, M. A. *Invest. Radiol*. **2009**, *44*, 226−233. (f) Fretellier, N.; Idee, J. M.; Dencausse, A.; Karroum, O.; Guerret, S.; Poveda, N.; Jestin, G.; Factor, C.; Raynal, I.; Zamia, P.; Port, M.; Corot, C. *Invest. Radiol*. **2011**, *46*, 292−300.
123. White, G. W.; Gibby, W. A.; Tweedle, M. F. *Invest. Radiol*. **2006**, *41*, 272−278.
124. Dischino, D. D.; Delaney, E. J.; Emswiler, J. E.; Gaughan, G. T.; Prasad, J. S.; Srivastava, S. K. *Inorg. Chem*. **1991**, *30*, 1265−1269.
125. (a) Helm, L.; Merbach, A. E. *Chem. Rev*. **2005**, *105*, 1923−1960. (b) Jaszberenyi, Z.; Sour, A.; Tóth, É.; Benmelouka, M.; Merbach, A. E. *Dalton Trans*. **2005**, 2713−2719. (c) Laus, S.; Ruloff, R.; Tóth, É.; Merbach, A. E. *Chem. - Eur. J*. **2003**, *9*, 3555−3566. (d) Tóth, É.; Burai, L.; Brucher, E.; Merbach, A. E. *J. Chem. Soc. Dalton Trans*. **1997**, 1587−1594. (e) Powell, D. H.; Ni Dhubhghaill, O. M.; Pubanz, D.; Helm, L.; Lebedev, Y. S.; Schlaepfer, W.; Merbach, A. E. *J. Am. Chem. Soc.* **1996**, *118*, 9333−9346.
126. (a) Hallenga, K.; Koenig, S. H. *Biochemistry* **1976**, *15*, 4255−4264. (b) Koenig, S. H.; Schillinger, W. S. *J. Biol. Chem*. **1969**, *244*, 3283−3289.
127. Comblin, V.; Gilsoul, D.; Hermann, M.; Humblet, V.; Jacques, V.; Mesbahi, M.; Sauvage, C.; Desreux, J. F. *Coord. Chem. Rev*. **1999**, *185−186*, 451−470.
128. Werner, E. J.; Datta, A.; Jocher, C. J.; Raymond, K. N. *Angew. Chem., Int. Ed*. **2008**, *47*, 8568−8580.
129. Caravan, P. *Acc. Chem. Res*. **2009**, *42*, 851−862.
130. (a) Lauffer, R. B. *Magn. Reson. Med.* **1991**, *22*, 339−342. (b) Caravan, P.; Cloutier, N. J.; Greenfield, M. T.; McDermid, S. A.; Dunham, S. U.; Bulte, J. W.; Amedio, J. C.; Looby, R. J. Jr.; Supkowski, R. M.; Horrocks Jr., W. DeW.; McMurry, T. J.; Lauffer, R. B. *J. Am. Chem. Soc.* **2002**, *124*, 3152−3162. (c) Aime, S.; Botta, M.;

Crich, S. G.; Giovenzana, G. B.; Pagliarin, R.; Piccinini, M.; Sisti, M.; Terreno, E. *J. Biol. Inorg. Chem.* **1997**, *2*, 470−479. (d) Aime, S.; Gianolio, E.; Terreno, E.; Giovenzana, G. B.; Pagliarin, R.; Sisti, M.; Palmisano, G.; Botta, M.; Lowe, M. P.; Parker, D. *J. Biol. Inorg. Chem.* **2000**, *5*, 488−497.

131. Wallace, R. A.; Haar, J. P. Jr.; Miller, D. B.; Woulfe, S. R.; Polta, J. A.; Galen, K. P.; Hynes, M. R.; Adzamli, K. *Magn. Reson. Med.* **1998**, *40*, 733−739.
132. (a) Moats, R. A.; Fraser, S. E.; Meade, T. J. A. *Angew. Chem., Int. Ed. Engl.* **1997**, *36*, 726−728. (b) Que, E. L.; Chang, C. J. *Chem. Soc. Rev.* **2010**, *39*, 51−60. (c) Zhang, L.; Wang, Y.; Ye, Z.; Jin, D.; Yuan, J. *Bioconjugate Chem.* **2012**, *23*, 1244−1251. (d) Ma, H.; Song, B.; Wang, Y.; Cong, D.; Jiang, Y.; Yuan, J. *Chem. Sci.* **2017**, *8*, 150−159. (e) Hingorani, D. V.; Bernstein, A. S.; Pagel, M. D. *Contrast Media Mol. Imaging* **2015**, *10*, 245−265. (f) Lux, J.; Sherry, A. D. *Curr. Opin. Chem. Biol.* **2018**, *45*, 121−130. (g) Li, H.; Meade, T. J. *J. Am. Chem. Soc.* **2019**, *141*, 17025−17041.
133. Lowe, M. P. *Aust. J. Chem.* **2002**, *55*, 551−556.
134. Ward, K. M.; Aletras, A. H.; Balaban, R. S. *J. Magn. Reson.* **2000**, *143*, 79-87.
135. (a) Sherry, A. D.; Wu, Y. *Curr. Opin. Chem. Biol.* **2013**, *17*, 167−174. (b) Soesbe, T. C.; Wu, Y.; Sherry, A. D. *NMR Biomed.* **2013**, *26*, 829−838.
136. Guivel-Scharen, V.; Sinnwell, T.; Wolff, S. D.; Balaban, R. S. *J. Magn. Reson.* **1998**, *133*, 36−45.
137. (a) Vinogradov, E.; Sherry, A. D.; Lenkinski, R. E. *J. Magn. Reson.* **2013**, *229*, 155−172. (b) van Zijl, P. C. M.; Yadav, N. *Magn. Reson. Med.* **2011**, *65*, 927−948.
138. (a) Zhou, J.; van Zijl, P. C. M. *Prog. Nucl. Magn. Reson. Spectrosc.* **2006**, *48*, 109−136. (b) Hancu, I.; Dixon, W. T.; Woods, M.; Vinogradov, E.; Sherry, A. D.; Lenkinski, R. E. *Acta Radiol.* **2010**, *51*, 910−923.
139. Evbuomwan, O. M.; Terreno, E.; Aime, S.; Sherry, A. D. CEST and PARACEST Agents for Molecular Imaging, In *The Chemistry of Molecular Imaging*; Long, N., Wong, W.-T. Eds.; John Wiley & Sons, Inc., 2015, Chapter 10; pp 225–243.
140. (a) Stevens, T. K.; Palaniappan, K. K.; Ramirez, R. M.; Francis, M. B.; Wemmer, D. E.; Pines, A. *Magn. Reson. Med.* **2013**, *69*, 1245−1252. (b) Zaiss, M.; Schnurr, M.; Bachert, P. *J. Chem. Phys.* **2012**, *136*, 144106.
141. Castelli, D. D.; Longo, D.; Aime, S.; Terreno, E. *NMR Biomed.* **2013**, *26*, 839−849.
142. Walker, T. G.; Happer, W. *Rev. Mod. Phys.* **1997**, *69*, 629−642.
143. Zhang, S.; Winter, P.; Wu, K.; Sherry, A. D. *J. Am. Chem. Soc.* **2001**, *123*, 1517−1518.
144. Zhang, S.; Michaudet, L.; Burgess, S.; Sherry, A. D. *Angew. Chem., Int. Ed.* **2002**, *41*, 1919–1921.
145. Aime, S.; Carrera, C.; Castelli, D. D.; Crich, S. G.; Terreno, E. *Angew. Chem., Int. Ed.* **2005**, *44*, 1813−1815.

146. (a) Chauvin, T.; Durand, P.; Bernier, M.; Meudal, H.; Doan, B.-T.; Noury, F.; Badet, B.; Beloeil, J.-C.; Tóth, É. *Angew. Chem., Int. Ed.* **2008**, *47*, 4370−4372. (b) Yoo, B.; Pagel, M. D. *J. Am. Chem. Soc*. **2006**, *128*, 14032−14033. (c) Yoo, B.; Raam, M. S.; Rosenblum, R. M.; Pagel, M. D. *Contrast Media Mol. Imaging* **2007**, *2*, 189−198.
147. (a) Aime, S.; Barge, A.; Castelli, D. D.; Fedeli, F.; Mortillaro, A.; Nielsen, F. U.; Terreno, E. *Magn. Reson. Med.* **2002**, *47*, 639−648. (b) Aime, S.; Castelli, D. D.; Terreno, E. *Angew. Chem., Int. Ed.* **2002**, *41*, 4334−4336.
148. Zhang, S.; Malloy, C. R.; Sherry, A. D. *J. Am. Chem. Soc*. **2005**, *127*, 17572−17573.
149. (a) Zhang, S.; Trokowski, R.; Sherry, A. D. *J. Am. Chem. Soc*. **2003**, *125*, 15288−15289. (b) Trokowski, R.; Zhang, S.; Sherry, A. D. *Bioconjugate Chem*. **2004**, *15*, 1431−1440.
150. Aime, S.; Castelli, D. D.; Fedeli, F.; Terreno, E. *J. Am. Chem. Soc.* **2002**, *124*, 9364−9365.
151. Aime, S.; Castelli, D. D.; Terreno, E. *Angew. Chem., Int. Ed.* **2003**, *42*, 4527−4529.
152. Trokowski, R.; Ren, J.; Kalman, F. K.; Sherry, A. D. *Angew. Chem., Intl. Ed*. **2005**, *44*, 6920−6923.
153. Ratnakar, S. J.; Chirayil, S.; Funk, A. M.; Zhang, S.; Queiró, J. F.; Geraldes, C. F. G. C.; Kovacs, Z.; Sherry, A. D. *Angew. Chem., Int. Ed*. **2020**, *59*, 21671−21676.
154. Woods, M.; Woessner, D. E.; Sherry, A. D. *Chem. Soc. Rev*. **2006**, *35*, 500–511.
155. Moss, B. *Chem. Ind*. **1996**, *11*, 407–411.
156. Glidewell, C. *Chem. Brit*. **1990**, *26*, 137–140.
157. (a) Pflugrath, J. W.; Quiocho, F. A. *J. Mol. Biol*. **1988**, *200*, 163–180. (b) Kanyo, Z. F.; Christianson, D. W. *J. Biol. Chem*. **1991**, *266*, 4264–4268.
158. (a) Sessler, J. L.; Gale, P. A.; Cho, W.-S. In *Anion Receptor Chemistry*; Stoddart, J. F. Ed.; Monographs in Supramolecular Chemistry, Royal Society of Chemistry: Cambridge, 2006; Vol. 8, Chapter 2; pp 27–130. (b) Evans, N. H.; Beer, P. D. *Angew. Chem., Int. Ed*. **2014**, *53*, 11716–11754.
159. (a) Hribar, B.; Southall, N. T.; Vlachy, V.; Dill, K. A. *J. Am. Chem. Soc*. **2002**, *124*, 12302–12311. (b) Yang, L.; Fan, Y.; Gao, Y. Q. *J. Phys. Chem. B* **2011**, *115*, 12456–12465.
160. Morita, T.; Westh, P.; Nishikawa, K.; Koga, Y. *J. Phys. Chem. B* **2014**, *118*, 8744–8749.
161. Hofmeister, F. *Arch. Exp. Pathol. Pharmakol*. **1888**, *24*, 247–260.
162. Steed, J. W.; Atwood, J. L. *Supramolecular Chemistry*; John Wiley & Sons, 2013.
163. Butler, S. J.; Parker, D. *Chem. Soc. Rev*. **2013**, *42*, 1652–1666.
164. (a) Antonisse, M. M. G.; Reinhoudt, D. N. *Chem. Commun*. **1998**, 443–448. (b) Schmidtchen, F. P.; Berger, M. *Chem. Rev*. **1997**, *97*, 1609–1646. (c) Beer, P. D.; Gale, P. A. *Angew. Chem., Int. Ed. Engl*. **2001**, *40*, 486–516. (d) Kubik, S.;

Reyheller, C.; Stiwe, S. *J. Inclusion Phenom. Macrocyclic Chem*. **2005**, *52*, 137–187. (e) Kubik, S. *Chem. Soc. Rev*. **2010**, *39*, 3648–3663.

165. Matthew, J. L.; Christopher, J. S.; Beer, P. D. *Angew. Chem., Int. Ed*. **2016**, *55*, 1974–1987.
166. (a) Gale, P. A.; Tong, C. C.; Haynes, C. J. E.; Adeosun, O.; Gross, D. E.; Karnas, E.; Sedenberg, E. M.; Quesada, R.; Sessler, J. L. *J. Am. Chem. Soc*. **2010**, *132*, 3240–3241. (b) Fiehn, T.; Goddard, R.; Seidel, R. W.; Kubik, S. *Chem. - Eur. J*. **2010**, *16*, 7241–7255. (c) Schmuck, C.; Schwegmann, M. *J. Am. Chem. Soc*. **2005**, *127*, 3373–3379.
167. (a) Gale, P. A.; Caltagirone, C. *Chem. Soc. Rev*. **2015**, *44*, 4212–4227. (b) Chen, L.; Berry, S, N.; Wu, X.; Howe, E. N. W.; Gale, P. A. *Chem* **2020**, *6*, 61–141. (c) Macreadie, L. K.; Gilchrist, A. M.; McNaughton, D. A.; Ryder, W. G.; Fares, M.; Gale, P. A. *Chem* **2022**, *8*, 46–118.
168. (a) Beer, P. D. *Acc. Chem. Res*. **1998**, *31*, 71−80. (b) Beer, P. D. *Chem. Commun*. **1996**, 689−696.
169. (a) Dickins, R. S.; Gunnlaugsson, T.; Parker, D. Peacock, R. D. *Chem. Commun*. **1998**, 1643–1644. (b) de Silva, A. P.; Gunaratne, H. Q. N.; Gunnlaugsson, T.; Huxley, A. J. M.; McCoy, C. P.; Rademacher, J. T.; Rice, T. E. *Chem. Rev*. **1997**, *97*, 1515–1566. (c) *Chemosensors of Ion and Molecular Recognition*; Desverne, J.-P., Czarnik, A. W., Eds.; NATO ASI Series, Ser. C; Kluwer: Dordrecht, The Netherlands, Vol. 492, 1997. (d) Fabbrizzi, L.; Faravelli, I.; Francese, G.; Licchelli, M.; Perotti, A.; Tagletti, A. *Chem. Commun*. **1998**, 971–972. (e) Black, C. B.; Andrioletti, B.; Try, A. C.; Ruiperez, C.; Sessler, J. L. *J. Am. Chem. Soc*. **1999**, *121*, 10438–10439.
170. Czarnik, A. W. *Acc. Chem. Res*. **1994**, *27*, 302–308.
171. de Silva, A. P.; Guarantee, H. Q. N.; McVeigh, C.; Maguire, M. G. E.; Maxwell, P. R. S.; O'Hanlon, E. *Chem. Commun*. **1996**, 2191–2192.
172. Fabbrizzi, L.; Francese, G.; Licchelli, M.; Perotti, A.; Taglietti, *Chem. Commun*. **1997**, 581–582.
173. Miyaji, H.; Anzenbacher, Jr. P.; Sessler, J. L.; Bleasdale, E. R.; Gale, P. A. *Chem. Commun*. **1999**, 1723–1724.
174. (a) Martínez-Máñez, R.; Sancenón, F. *Chem. Rev*. **2003**, *103*, 4419–4476. (b) Martínez-Máñez, R.; Sancenón, F. *Coord. Chem. Rev*. **2006**, *250*, 3081–3093.
175. (a) Newcomb, M.; Horner, J. H.; Blanda, M. T. *J. Am. Chem. Soc*. **1987**, *109*, 7878–7879. (b) Newcomb, M.; Blanda, M. T. *Tetrahedron Lett*. **1988**, *29*, 4261–4264. (c) Katz, H. E. *Organometallics* **1987**, *6*, 1134–1136. (d) Wuest, J. D.; Zacharie, B. *J. Am. Chem. Soc*. **1987**, *109*, 4714–4715.

176. (a) Schmidtchen, F. P. *Angew. Chem., Int. Ed. Engl*. **1977**, *16*, 720–721. (b) Schmidtchen, F. P. *Chem. Ber*. **1981**, *114*, 597–607.

177. Park, C. H.; Simmons, H. E. *J. Am. Chem. Soc*. **1968**, *90*, 2431–2432.

178. (a) Dietrich, B.; Hosseini, M. W.; Lehn, J.-M.; Sessions, R. B. *J. Am. Chem. Soc*. **1981**, *103*, 1282–1283. (b) Dietrich, B.; Hosseini, M. W.; Lehn, J.-M.; Sessions, R. B. *Helv. Chim. Acta* **1983**, *66*, 1262–1278. (c) Hosseini, M. W.; Lehn, J.-M. *Helv. Chim. Acta* **1986**, *69*, 587–603.

179. (a) Lehn, J.-M.; Sonveaux, E.; Willard, A. K. *J. Am. Chem. Soc*. **1978**, *100*, 4914–4916. (b) Dietrich, B.; Guilhem, J.; Lehn, J.-M.; Pascard, C.; Sonveaux, E. *Helv. Chim. Acta* **1984**, *67*, 91–104. (c) Lehn, J.-M.; Pine, S. H.; Watanabe, E.; Willard, A. K. *J. Am. Chem. Soc*. **1977**, *99*, 6766–6768. (d) Dietrich, B.; Hosseini, M. W.; Lehn, J.-M.; Sessions, R. B. *Helv. Chim. Acta* **1985**, *68*, 289–299. (e) Hosseini, M. W.; Lehn, J.-M. *Helv. Chim. Acta* **1988**, *71*, 749–756. (f) Motekaitis, R. J.; Martell, A. E.; Murase, I.; Lehn, J.-M.; Hosseini, M. W. *Inorg. Chem*. **1988**, *27*, 3630–3636. (g) Heyer, D.; Lehn, J.-M. *Tetrehedron Lett*. **1986**, *27*, 5869–5872.

180. (a) Graf, E.; Lehn, J.-M. *J. Am. Chem. Soc*. **1976**, *98*, 6403–6405. (b) Fujita, T.; Lehn, J.-M. *Tetrahedron Lett*. **1988**, *29*, 1709–1712.

181. Lehn, J.-M. *Acc. Chem. Res*. **1978**, *11*, *2*, 49–57.

182. Dietrich, B.; Fyles, T. M.; Lehn, J.-M.; Pease, L. G.; Fyles, D. *J. Chem. Soc., Chem. Commun*. **1978**, 934–936.

183. García-España, E.; Diaz, P.; Llinares, J. M.; Bianchi, A. *Coord. Chem. Rev*. **2006**, *250*, 2952–2986.

184. (a) Bünzli, J.-C. G. *J. Lumin*. **2016**, *170*, 866–878. (b) Faulkner, S.; Pope, S. J. A.; Burton-Pye, B. P. *Appl. Spectrosc. Rev*. **2005**, *40*, 1–31. (c) Breen, C.; Pal, R.; Elsegood, M. R. J.; Teat, S. J.; Iza, F.; Wende, K.; Buckley, B. R.; Butler, S. J. *Chem. Sci*. **2020**, *11*, 3164–3170.

185. (a) New, E. J.; Parker, D.; Smith, D. G.; Walton, J. W. *Curr. Opin. Chem. Biol*. **2010**, *14*, 238–246. (b) Thibon, A.; Pierre, V. C. *Anal. Bioanal. Chem*. **2009**, *394*, 107−120. (c) Allain, C.; Faulkner, S. *Future Med. Chem*. **2010**, *2*, 339−350.

186. (a) Bruce, J. I.; Dickins, R. S.; Govenlock, L. J.; Gunnlaugsson, T.; Lopinski, S.; Lowe, M. P.; Parker, D.; Peacock, R. D.; Perry, J. J. B.; Aime, S.; Botta, M. *J. Am. Chem. Soc*. **2000**, *122*, 9674–9684. (b) Dickins, R. S.; Aime, S.; Batsanov, A. S.; Beeby, A.; Botta, M.; Bruce, J. I.; Howard, J. A. K.; Love, C. S.; Parker, D.; Peacock, R. D.; Puschmann, H. *J. Am. Chem. Soc*. **2002**, *124*, 12697–12705. (c) Lima, L. M. P.; Tripier, R. *Curr. Methods Inorg. Chem*. **2011**, *1*, 36–60. (d) dos Santos, C. M. G.; Harte, A. J. Gunnlaugsson, T. *Coord. Chem. Rev*. **2008**, *252*, 2512–2527. (e)

Dickins, R. S.; Batsanov, A. S.; Parker, D.; Puschmann, H.; Salamano, S.; Howard, J. A. K. *Dalton Trans*. **2004**, 70–80.

187. (a) Parker, D. *Coord. Chem. Rev*. **2000**, *205*, 109–130. (b) Bünzli, J.-C. G. *Coord. Chem. Rev*. **2015**, *293–294*, 19–47. (c) de Bettencourt-Dias, A.; Barber, P. S.; Viswanathan, S. *Coord. Chem. Rev*. **2014**, *273–274*, 165–200.
188. (a) Eliseeva, S. V.; Bünzli, J.-C. G. *Chem. Soc. Rev*. **2010**, *39*, 189–227. (b) Parker, D.; Shuvaev, S.; Starck, M. *Chem. - Eur. J*. **2017**, *23*, 9974–9989.
189. Carnall, W. T.; Fields, P. R.; Rajnak, K. *J. Chem. Phys*. **1968**, *49*, 4447–4449.
190. Mathieu, E.; Sipos, A.; Demeyere, E.; Phipps, D.; Sakaveli, D.; Borbas, K. E. *Chem. Commun*. **2018**, *54*, 10021–10035.
191. (a) Heffern, M. C.; Matosziuk, L. M.; Meade, T. J. *Chem. Rev*. **2014**, *114*, 4496–4539. (b) Aletti, A. B.; Gillen, D. M.; Gunnlaugsson, T. *Coord. Chem. Rev*. **2018**, *354*, 98–120. (c) Aulsebrook, M. L.; Graham, B.; Grace, M. R.; Tuck, K. L. *Coord. Chem. Rev*. **2018**, *375*, 191–220.
192. Bodman, S. E.; Butler, S. J. *Chem. Sci*. **2021**, *12*, 2716–2734.
193. (a) Parker, D.; Senanayake, P. K.; Williams, J. A. G. *J. Chem. Soc., Perkin Trans. 2* **1998**, 2129–2139. (b) Parker, D. *Chem. Soc. Rev*. **2004**, *33*, 156–165. (c) Pandya, S.; Parker, D.; Yu, J. *Dalton Trans*. **2006**, 2757–2766. (d) Carr, R.; Di Bari, L.; Lo Piano, S.; Parker, D.; Sanderson, J. M. *Dalton Trans*. **2012**, *41*, 13154–13158.
194. (a) Bretonniere, Y.; Cann, M. J.; Parker, D.; Slater, R. *Org. Biomol. Chem*. **2004**, *2*, 1624–1632. (b) Pal, R.; Parker, D.; Costello, L. C. *Org. Biomol. Chem*. **2009**, *7*, 1525–1528. (c) Pal, R.; Beeby, A.; Parker, D. *J. Pharm. Biomed. Anal*. **2011**, *56*, 352–358. (d) Parker, D. A.; Yu, J. *Chem. Commun*. **2005**, 3141–3143.
195. (a) Smith, D. G.; Law, G.-L.; Pal, R.; Parker, D.; Wong, K.-L. *Chem. Commun*. **2011**, *47*, 7347–7349. (b) Smith, D. G.; Pal, R.; Parker, D. *Chem. - Eur. J*. **2012**, *18*, 11604–11613.
196. Parker, D.; Senanayake, K.; Williams, J. A. G. *Chem. Commun*. **1997**, 1777–1778.
197. Hammell, J.; Buttarazzi, L.; Huang, C.-H.; Morrow, J. R. *Inorg. Chem*. **2011**, *50*, 4857–4867.
198. Schaferling, M.; Wolfbeis, O. S. *Chem. —Eur. J*. **2007**, *13*, 4342–4349.
199. Poole, R. A.; Kielar, F.; Parker, D.; Richardson, S. L.; Stenson, P. A. *Chem. Commun*. **2006**, 4084–4086.
200. Weitz, E. A.; Chang, J. Y.; Rosenfield, A. H.; Pierre, V. C. *J. Am. Chem. Soc*. **2012**, *134*, 16099–16102.
201. Gunnlaugsson, T.; Harte, A. J.; Leonard, J. P.; Nieuwenhuyzen, M. *Chem. Commun*. **2002**, 2134–2135.

202. Poole, R. A.; Montgomery, C. P.; New, E. J.; Congreve, A.; Parker, D.; Botta, M. *Org. Biomol. Chem*. **2007**, *5*, 2055–2062.
203. Grenier, L. L. A.; Nielsen, L. G.; Sørensen, T. J. *Anal. Sens.* **2022**, e202200033, 1-8.
204. (a) Rodriguez-Benot, A.; Martin-Malo, A.; Alvarez-Lara, M. A.; Rodriguez, M.; Aljama, P. *Am. J. Kidney Dis*. **2005**, *46*, 68−77. (b) Marco, M. P.; Craver, L.; Betriu, A.; Belart, M.; Fibla, J.; Fernandez, E. *Kidney Int.* **2003**, *63*, S111−S114. (c) Block, G. A.; Klassen, P. S.; Lazarus, J. M.; Ofsthun, N.; Lowrie, E. G.; Chertow, G. M. *J. Am. Soc. Nephrol*. **2004**, *15*, 2208−2218.
205. Persy, V. P.; Behets, G. J.; Bervoets, A. R.; De Broe, M. E.; D′Haese, P. C. *Semin. Dial*. **2006**, *19*, 195−199.
206. (a) Smith, V. H.; Tilman, G. D.; Nekola, J. C. *Environ. Pollut*. **1999**, *100*, 179−196. (b) Lürling, M.; Waajen, G.; van Oosterhout, F. *Water Res*. **2014**, *54*, 78−88. (c) Conley, D. J.; Paerl, H. W.; Howarth, R. W.; Boesch, D. F.; Seitzinger, S. P.; Havens, K. E.; Lancelot, C.; Likens, G. E. *Science* **2009**, *323*, 1014−1015. (d) Correll, D. L. *J. Environ. Qual*. **1998**, *27*, 261−266.
207. (a) Ju, J.; Park, M.; Suk, J.-M.; Lah, M. S.; Jeong, K.-S. *Chem. Commun*. **2008**, 3546−3548. (b) Sasaki, S.; Citterio, D.; Ozawa, S.; Suzuki, K. *J. Chem. Soc. Perkin Trans. 2* **2001**, 2309−2313. (c) Byrne, J. P.; Blasco, S.; Aletti, A. B.; Hessman, G.; Gunnlaugsson, T. *Angew. Chem., Int. Ed*. **2016**, *55*, 8938−8943. (d) Fan, E.; Van Arman, S. A.; Kincaid, S.; Hamilton, A. D. *J. Am. Chem. Soc*. **1993**, *115*, 369−370.
208. Raju, M. V. R.; Harris, S. M.; Pierre, V. C. *Chem. Soc. Rev*. **2020**, *49*, 1090–1108.
209. Huang, S.-Y.; Qian, M.; Pierre, V. C. *Inorg. Chem*. **2019**, *58*, 16087–16099.
210. Raju, M. V. R.; Wilharm, R. K.; Dresel, M. J.; McGreal, M. E.; Mansergh, J. P.; Marting, S. T.; Goodpaster, J. D.; Pierre, V. C. *Inorg. Chem*. **2019**, *58*, 15189–15201.
211. Sahoo, J.; Arunachalam, R.; Subramanian, P. S.; Suresh, E.; Valkonen, A.; Rissanen, K.; Albrecht, M. *Angew. Chem., Int. Ed*. **2016**, *55*, 9625–9629.
212. Bodman, S. E.; Breen, C.; Kirkland, S.; Wheeler, S.; Robertson, E.; Plasser, F.; Butler, S. J. *Chem. Sci*. **2022**, *13*, 3386–3394.
213. Müller, S.; Chaikuad, A.; Grey, N. S.; Knapp, S. *Nat. Chem. Biol*. **2015**, *11*, 818–821.
214. Hewitt, S. H.; Ali, R.; Mailhot, R.; Antonen, C. R.; Dodson, C. A.; Butler, S. J. *Chem. Sci*. **2019**, *10*, 5373–5381.
215. Hewitt, S. H.; Parris, J.; Mailhot, R.; Butler, S. J. *Chem. Commun*. **2017**, *53*, 12626–12629.
216. Wheeler, S.; Breen, C.; Li, Y.; Hewitt, S. H.; Robertson, E.; Yates, E. A.; Barsukov, I. L.; Fernig, D. G.; Butler, S. J. *Org. Biomol. Chem*. **2022**, *20*, 596–605.
217. Andolina, C. M.; Morrow, J. R. *Eur. J. Inorg. Chem*. **2011**, 154–164.

218. Surman, A. J.; Bonnet, C. S.; Lowe, M. P.; Kenny, G. D.; Bell, J. D.; Tóth, É.; Vilar, R. *Chem. —Eur. J*. **2011**, *17*, 223–230.
219. Aulsebrook, M. L.; Starck, M.; Grace, M. R.; Graham, B.; Thordarson, P.; Pal, R.; Tuck, K. L. *Inorg. Chem.* **2019**, *58*, 495–505.
220. (a) Lupo, J. M.; Chen, A. P.; Zierhut, M. L.; Bok, R. A.; Cunningham, C. H.; Kurhanewicz, J.; Vigneron, D. B.; Nelson, S. J. *Magn. Reson. Imaging* **2010**, *28*, 153–162. (b) Beal, M. F. *Ann. Neurol*. **2003**, *53*, S39–S48.
221. Neil, E. R.; Fox, M. A.; Pal, R.; Palsson, L.-O.; O′Sullivan, B. A.; Parker, D. *Dalton Trans*. **2015**, *44*, 14937–14951.
222. Butler, S. J.; McMahon, B. K.; Pal, R.; Parker, D.; Walton, J. W. *Chem. —Eur. J*. **2013**, *19*, 9511–9517.
223. Leonzio, M.; Melchior, A.; Faura, G.; Tolazzi, M.; Bettinelli, M.; Zinna, F.; Arrico, L.; Di Bari, L.; Piccinelli, F. *New J. Chem.* **2018**, *42*, 7931–7939.
224. Tresguerres, M.; Buck, J.; Levin, L. R. *Pflügers Arch – Eur. J. Physiol*. **2010**, *460*, 953–964.
225. Martínez-Crespo, L.; Hewitt, S. H.; De Simone, N. A.; Šindelář, V.; Davis, A. P.; Butler, S.; Valkenier, H. *Chem. —Eur. J*. **2021**, *27*, 7367–7375.
226. Piccinelli, F.; De Rosa, C.; Melchior, A.; Faura, G.; Tolazzi, M.; Bettinelli, M. *Dalton Trans*. **2019**, *48*, 1202–1216.
227. Leonzio, M.; Melchior, A.; Faura, G.; Tolazzi, M.; Zinna, F.; Di Bari, L.; Piccinelli, F. *Inorg. Chem.* **2017**, *56*, 4413–4421.
228. Bridou, L.; Nielsen, L. G.; Sørensen, T. J. *J. Rare Earths* **2020**, *38*, 498–505.
229. Kofod, N.; Thomsen, M. S.; Nawrocki, P.; Sørensen, T. J. *Dalton Trans.* **2022**, *51*, 7936–7949.
230. Lunkley, J. L.; Shirotani, D.; Yamanari, K.; Kaizaki, S.; Muller, G. *J. Am. Chem. Soc*. **2008**, *130*, 13814–13815.

CHAPTER-II

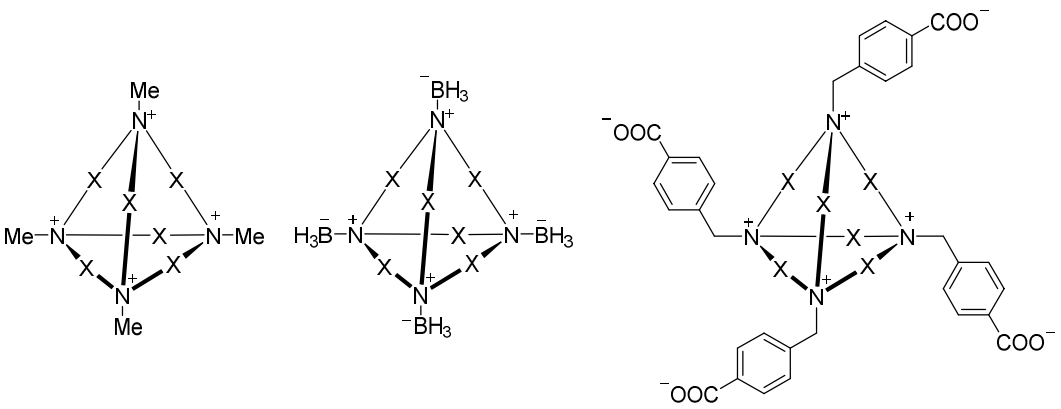
Chapter-II: Binuclear Lanthanide Complexes for Halide Chelation in Water

In the world of anion recognition, halide recognition in water has been pursued for decades, owing to their importance in physiology and the environment.[1] Fluoride is an essential mineral in maintaining oral hygiene, therefore it is used in a wide range of dental products and has led to the artificial fluoridation of drinking water in certain countries.[2] Fluoride is also present as an effluent in industrial waste from manufacturing phosphate containing fertilisers and aluminium processing.[3] In 2006, the U.S. National Research Council (NRC) evaluated the fluoride standards of the Environmental Protection Agency (EPA) and concluded that fluoride can adversely affect the brain through both direct and indirect means, that elevated fluoride concentrations in drinking-water may be of concern for neurotoxic effects.[4] Approximately 75–90% of ingested fluoride is absorbed and readily distributed throughout the body with ~ 99% of retained fluoride being bound in calcium rich tissues such as bone and teeth (leading to skeletal and dental fluorosis)[3d,5] and the calcified parts of the pineal gland.[6] The epidemiological studies of fluoride neurotoxicity associated with elevated fluoride exposure, especially during early development has been reviewed and supported the earlier reports on cognitive deficits in children with elevated fluoride content.[7] Therefore, controlling the level of fluoride consumption is a global governmental concern; the World Health Organisation (WHO) recommends 20 to 210 μM of fluoride in drinking water,[3c] while up to 70 μM is found in sea water.[3d] Consequently, the development of convenient analytical methods for the rapid, quantitative detection of fluoride in water samples and the monitoring of fluoride activity in biology has become an active area of research.[1]

Chloride is the most abundant transportable anion in all cells of the body and it performs fundamental biological functions in all tissues. It is the main physiological anion, serving as the principal compensatory ion for the movement of major cations such as Na^+, K^+, and Ca^{2+} across cell membranes.[8] Anion channels are proteinaceous pores in biological membranes that allow the passive diffusion of anions along their electrochemical gradient. Cl^- channels reside both in the plasma membrane and in intracellular organelles. Their functions include controlling membrane potential and cell volume homeostasis, regulation of cell proliferation and apoptosis,[9] transepithelial transport, and regulation of electrical excitability. The extracellular Cl^- concentration ($[Cl^-]_e$) is ~104 – 115 mM, while the intracellular Cl^- concentration ($[Cl^-]_i$) is variable (up to 70 mM found in eukaryotic cells) and determined by various regulatory mechanisms.[10] Chloride ion plays important roles in the central nervous system (CNS) through the functions of chloride channels. In the CNS, the Cl^- channels and transporters play key roles in neuronal growth and development, neurotransmitter uptake, intracellular pH modulation, cell volume regulation and setting $[Cl^-]_i$ either above or below its equilibrium potential.[11] The intraneuronal ionic composition is an important determinant of brain function. $[Cl^-]_i$ plays a crucial role in moderating neuronal excitability and neurotransmission by determining the postsynaptic responses to the neurotransmitters GABA and glycine.[12] Tracking chloride in living systems is vital if we are to understand diseases related to chloride transport defects such as cystic fibrosis and epilepsy.[8a,13] However, there are very few direct handles to recognise chloride in water, which are summarised below.

2.1. Supramolecular Assemblies for Chloride Recognition in Water

The macrotricyclic quaternary ammonium hosts **58** and **59**, reported by Schmidtchen, form complexes with a variety of anionic guests in water.[14] The cavity in receptor **58** has an internal diameter of 4.6 Å and forms a strong complex with iodide (diameter: 4.12 Å). The crystal structure of the iodide complex reveals that the anion is encapsulated within the macrotricycle.[15] The larger receptor **59** is able to form complexes with anions such as *p*-nitrophenolate. These receptors are positively charged and are therefore associated with counterions that may compete for the anion binding site. To overcome this, Schmidtchen *et al.*[16] developed neutral zwitterionic receptors **60** and **61**.[16] NMR studies showed that receptor **61** forms stronger complexes with chloride, bromide, and iodide ions than receptor **58** in water.

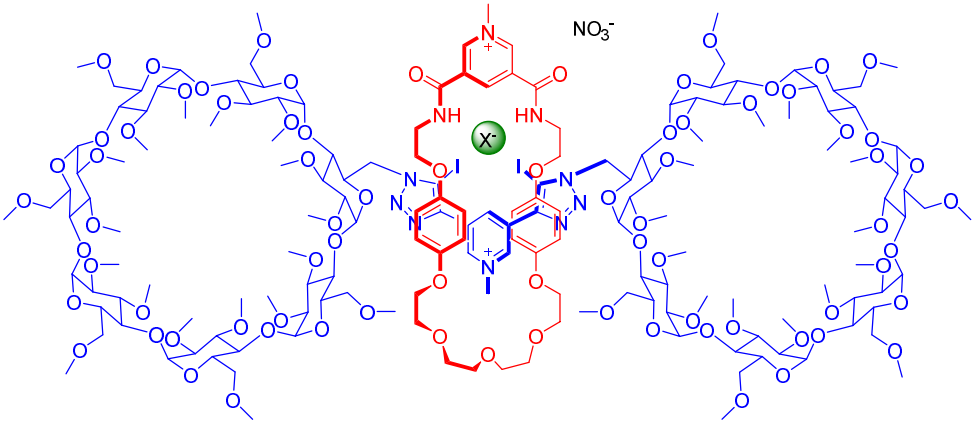


58, X = -$(CH_2)_6$-
59, X = -$(CH_2)_8$-

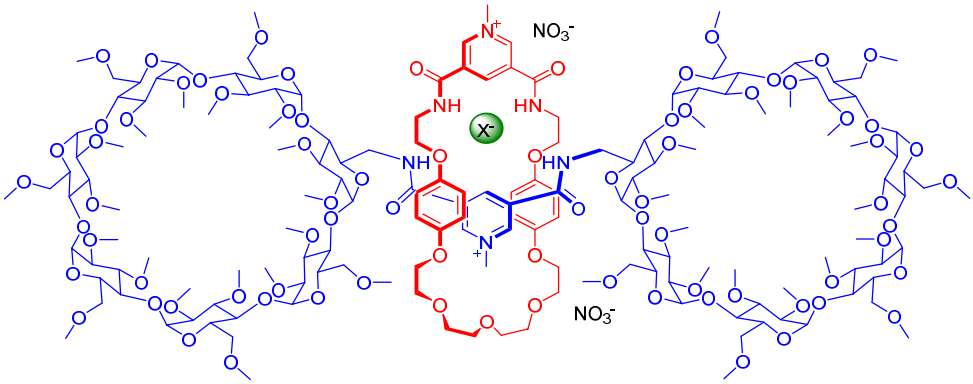
60, X = -$(CH_2)_6$-

61, X = -$(CH_2)_6$-

Beer *et al.*[17] have designed the rotaxane hosts **62** and **63** stoppered by permethylated *β*-cyclodextrin. **62** is based on iodotriazole halogen bonding and amide hydrogen bonding with the halogens, but it recognises iodide (K_a = 2,200 M^{-1}) better than chloride (K_a = 55 M^{-1}) and bromide in water; **63** recognises iodide (K_a = 50 M^{-1}) better than chloride (K_a = 15 M^{-1}) and bromide in water.

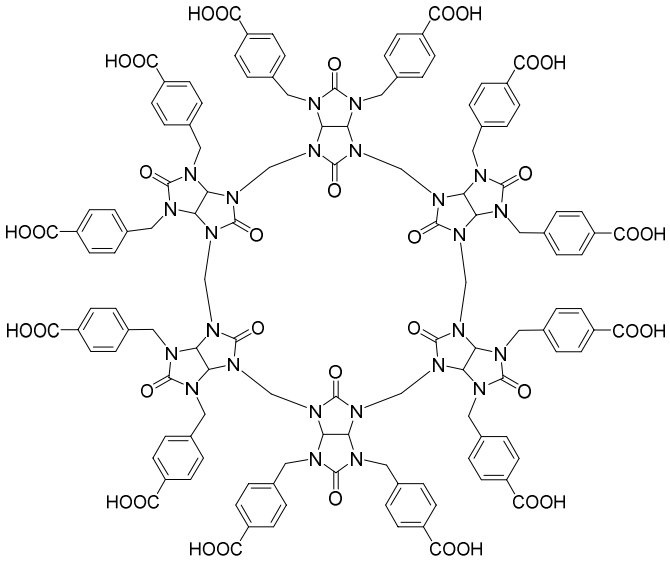


62, X = Cl, Br, I



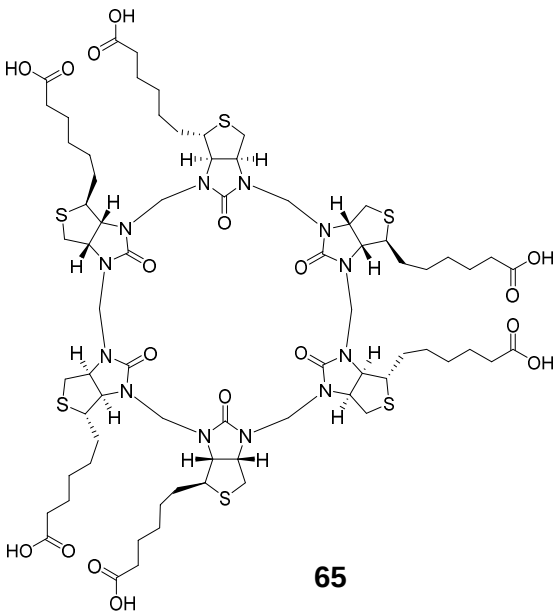
63, X = Cl, Br,

Sindelar *et al.*[18] have reported a water-soluble variant of the bambusuril macrocycle **64** and accomplished high anion-recognition strength in water using this hydrophobic neutral host molecule. It binds various inorganic anions in water within the hydrophobic cavity in an enthalpy-driven process, while additional stabilisation of the complex arises from multiple CH-anion hydrogen bonding interactions. It binds the anion guests with high affinity in phosphate buffer, with the affinity ranging from *ca.* 10^3 M^{-1} for Cl^- to *ca.* 10^5 M^{-1} for Br^- and NO_3^-, with the strongest binding being observed for I^- and ClO_4^- (K~10^7 M^{-1}). These remarkable affinities are ascribed to the total isolation of the bound anion from water molecules by inclusion within the hydrophobic bambusuril cavity.

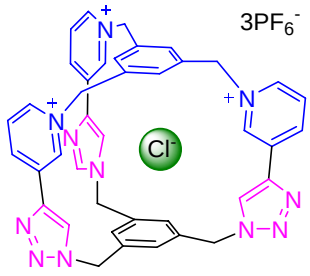


64

Pittelkow *et al.*[19] have developed the macrocyclic 6 + 6 hexamer **65** of D-biotin and formaldehyde by the halide-anion-templated synthesis and demonstrated the binding of a range of monovalent anions in water at pH 7.5 in 100 mM phosphate buffer. The binding of softer anions such as NCS^-, I^-, and $SeCN^-$ is favoured with association constants ranging from log K = 4.5 for SCN^- down to log K = 1.8 for Cl^-. Furthermore, the X-ray crystal structure of **65** with iodide provided evidence for C–H hydrogen bonding interactions between the host and anion.



65

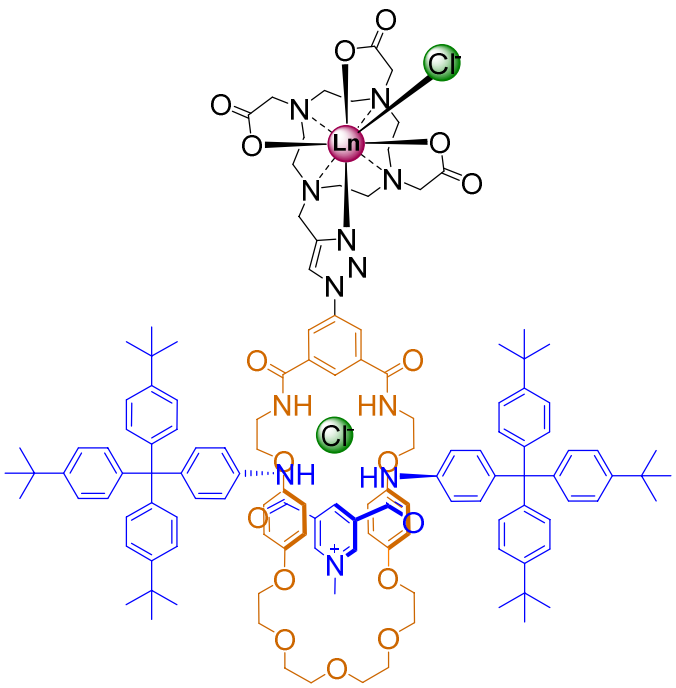


66

Li *et al.*[20] have reported a tricationic cage **66** made via a Cu catalysed click reaction, forming a triangular cage containing three pyridinium units. This cage contains six C–H acidic bonds on 5 positions of the triazole unit pointing inwards and takes advantage of a combination of electrostatic attractions, hydrogen bonding interactions, and anion-π interactions, to recognise a variety of anions. Cl^- exhibits the strongest binding affinity of up to $10^4\ M^{-1}$ in DMSO, but in water, it binds Cl^- with binding affinity of $26\ M^{-1}$. No other anions tested are bound inside the cage in water. Single crystal X-ray structure ascertains the encapsulation of Cl^- in the cage. Other chloride binding supramolecular assemblies have been extensively reviewed elsewhere.[21]

2.2. Lanthanide Complexes as Hosts for Halide Recognition

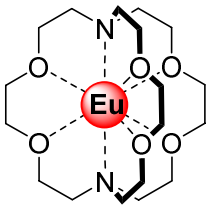
In the world of lanthanide-based coordination complexes, chloride binding is achieved only through collisional quenching of the excited state upon interaction



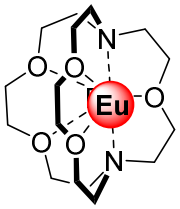
67

of halides to the sensitiser (vide Chapter-I), but it is indistiguishable between one quencher and the other.

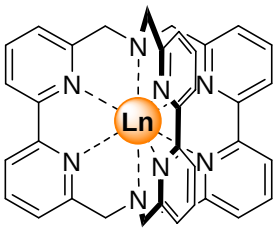
Faulkner, Beer *et al.*[22] reported a lanthanide tethered rotaxane **67** that binds to chloride only in apolar media (wet DCM and wet DCM:MeOH). In this, the first binding of chloride involves chelation to the metal, a second binding event occurs by encapsulation within the rotaxane.[22] However, in regard to halides, lanthanide complexes are only known to strongly chelate fluoride in water. Lanthanide-halide bonds have been characterised in the solid state, but are solvolysed in water readily.[23] Some of the fluoride chelating lanthanide complexes are highlighted below.



68

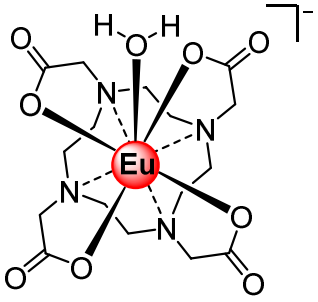


69



70, Ln(III) = Eu and Tb

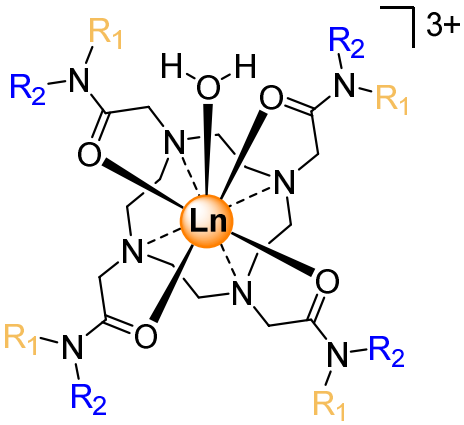
The first lanthanide complex that binds to fluoride was reported in 1977 by Scarborough and Smith,[24] where a cryptand host containing lanthanide centre **68** chelates to fluoride. Cryptands from Weaver *et al.*[25] (**69**) and Sammes *et al.*[26] (**70**) also chelate fluoride at the metal centre in water. Binding strengths of these systems were around log $K \approx 2–4$.[24-26]



71, [Eu(**DOTA**)(H_2O)]$^-$

Aime *et al.*[27] studied the prospects of fluoride binding on [Eu(**DOTA**)]$^-$ (**71**) where fluoride is reported to bind axially to the metal centre by replacing the axially bound water to form [Eu(**DOTA**)F]$^-$. This bound fluoride was found to exchange with the bulk water in NMR timescale, suggesting its reversible interaction at the metal centre. No evidence of chloride binding was observed in this study.

Faulkner *et al.*[28] synthesised a series of C_4 symmetric tricationic Ln(III) complexes based on the tetraamide ligands **72-78** and investigated the displacement of the axially bound water molecule by F^- using a combination of NMR and emission spectroscopy. ^{19}F and 2D NMR EXchange SpectroscopY (EXSY) studies revealed dramatic changes in crystal field splitting upon F^- binding, which plays a significant role in determining the observed spectral properties of paramagnetic host–guest complexes. The ^{19}F NMR spectra of Ln(III) complexes of **73** with bound F^- revealed peaks with large shifts (e.g. -479 ppm for [Eu(**73**)]$^{3+}$), consistent with slow exchange of F^- on the NMR timescale. Titration experiments revealed relatively weak binding of F^- to the Eu(III), Yb(III), and Lu(III) complexes with 1:1 binding constants in the range log K_a = 1.0–1.9.

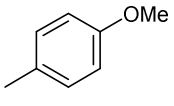


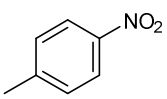
72, [Ln(**DOTAM**)]$^{3+}$ R^1 = H R^2 = H

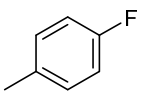
73, [Ln(**DTMA**)]$^{3+}$ R^1 = H R^2 = Me

74, [Ln(**DOTTA**)]$^{3+}$ R^1 = Me R^2 = Me

75, R^1 = Bn R^2 = Bn

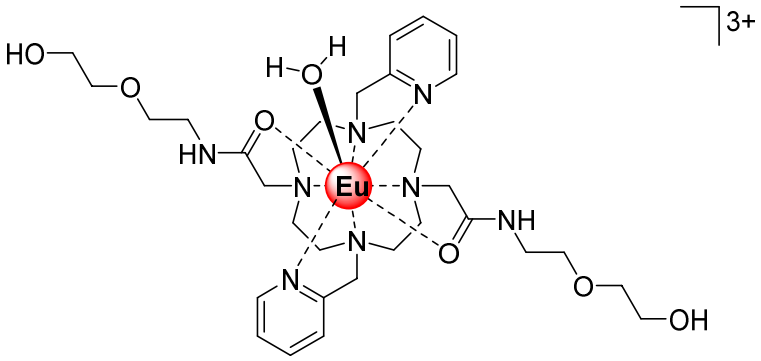
76, R^1 = H R^2 = 

77, R^1 = H R^2 

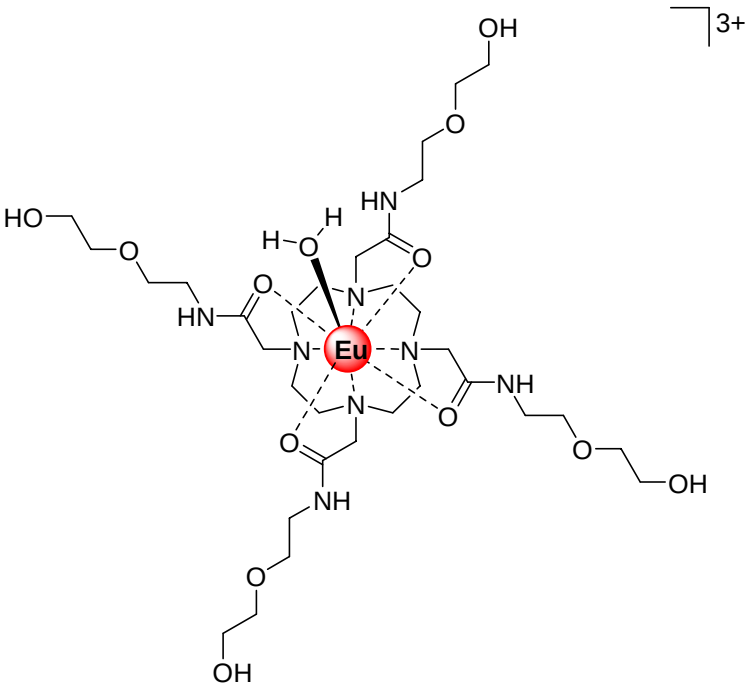
78, R^1 = H R^2 = 

In a subsequent work, the Ln(III) complexes of tetraamide-based ligands **74-78** were studied to explore the effect of variations in amide structure and peripheral hydrophobicity on F^- binding.[28b] Binding constants, determined by ^1H and ^{19}F NMR and emission titration experiments, were in the range log K_a = 1.3–2.0. The incorporation of methyl groups into the ligand amides (**72**, **73**, and **74**) causes the fluoride affinity to decrease. Moreover, as the electron withdrawing nature of the benzyl substituent is increased (from OMe (**76**) to F (**78**) to NO_2 (**77**)), the binding constant increases, indicating that the residual charge on the Ln(III) centre strongly impacts on the binding constant. These studies highlight how upon F^- binding to axially symmetric Ln(III) complexes, the sign and magnitude of the crystal field coefficient was altered upon increased electron withdrawing substituents, resulting in change of the sign and magnitude of the crystal field coefficient, observed in dramatic changes in NMR and luminescence spectra. Platas-Iglesias *et al.*[29] investigated theoretically the nature of axial ligands coordinating to [Yb(**DOTAM**)]$^{3+}$ in order to account for the crystal field calculations associated with the observed pseudocontact shifts in NMR and optical spectroscopy.

Ln(III) complexes of C_2 symmetric DO2A ligands with two inner-sphere water molecules readily form Ln−F bond reversibly. The Eu(III) tetraamide complexes **79** and **80** bind fluoride and form ternary adducts with affinity constants of log K_a = 1.4 and 2.9, respectively (298 K, pH 7.0, 0.01 M Tris-HCl). Eu(III) emission spectral changes signalled this change and were consistent with replacement of the bound water molecule, albeit with rather slow exchange kinetics.[30]



79

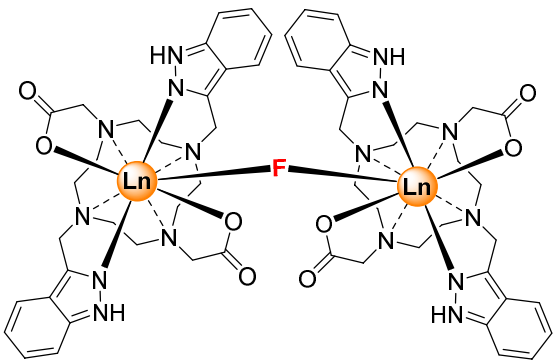


80

One of the earlier examples of fluoride recognition involved a cationic Eu(III) complex reported by Charbonnière *et al.*,[31] wherein F^- is sequestered in a supramolecular lanthanide dimer. Upon the addition of F^-, a sandwich-like structure **81** is formed involving a linear Eu–F–Eu bonding array, stabilised by π–π stacking of the imidazole heterocycles. Luminescence titrations revealed strong cooperative binding in aqueous solution (log β = 13.0 ± 0.3) with a 22-fold enhancement in emission intensity (Φ = 4.9%) upon addition of F^-, providing a highly sensitive response with a detection limit of 24 nM. The X-ray crystal

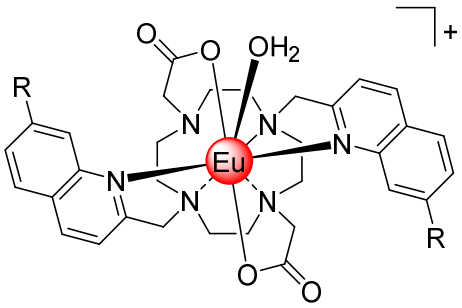
structure of the europium dimer revealed that the architecture of the scaffold is stabilised by synergistic effects of the Eu-F-Eu bridging motive, π-stacking interactions, and a four-component hydrogen-bonding network, which control the assembly of the two Eu(III) complexes entities around the fluoride ion. The strong fluoride binding in water leads to very sensitive detection of the anion to a limit of 0.46 ppb. The complex showed high selectivity for F^- over a range of anions including Cl^-, Br^-, HPO_4^{2-}, CH_3CO^{2-}, and HCO_3^-.

Using the Er(III) complex of the same ligand the same authors reported the first evidence of molecular up-conversion in D_2O at room temperature.[32] Low energy excitation of the Er complex at 980 nm in D_2O resulted in weak emission at 525, 550, and 650 nm, ascribed to Er(III) centred transitions via a two-step excitation. The up-conversion signal was significantly increased by 7.7-fold upon the addition of 0.5 equiv of F^-, owing to the formation of the supramolecular Er-F-Er assembly. In subsequent work, heterodimer formation was achieved using equimolar mixtures of Eu(III) and Tb(III) complexes. In the presence of fluoride, selective excitation of the Tb(III) metal (λ_{ex} = 488 nm) of the heterodimer resulted in Tb-to-Eu down-shifting energy transfer with 34% efficiency.[33] Utilising this dual Eu/Tb emission (700/545 nm), ratiometric sensing of fluoride in water (pH 7.4) was achieved with a detection limit of 17.7 nM.



81

Butler[34] has developed two water-soluble luminescent probes **82** and **83** capable of binding and sensing fluoride in water with high selectivity over other anions including Cl^-, Br^-, I^-, HPO_4^{2-}, $CH_3CO_2^-$, HSO_4^-, and NO_3^-. Fluoride binds reversibly to each probe, displacing the coordinated water, resulting in a 9-fold enhancement in Eu(III) emission intensity and dramatic changes in emission spectral form, particularly within the $\Delta J = 1$ band around 595 nm, which enabled quantification of fluoride in drinking water samples, within the environmentally relevant concentration range of 20–210 μM.



82, R = H
83, R = NHCOMe

2.3. Design Inspiration for Halide Recognition

In Chapter-I, the effectiveness of mononuclear and binuclear heptadendate [Ln(**DO3A**)] derivatives for chelating bidendate anions have been reviewed. Allen *et al.*[35] reported a pH sensor comprising an isopropanol linker between two [Ln(**DO3A**)] units. The luminescence decay rate is found to be slow owing to the absence of inner-sphere water. However, a steady increase in luminescence decay rate is observed at increasing pH due to protonation of the bridging alkoxide at low pH. This suggests the effectiveness of the metal centres in responding to the change in chemical environment of the bridging alkoxide. This work gave inspiration to design a similar receptor, but without the alkoxide and attempt to host chloride between the metal centres.

The ionic radius of hydroxide is compared with halides in Table 2.1. The high hydration enthalpy, free energy of hydration, and ionic radii of hydroxide and halides makes halide recognition in water very challenging.[36]

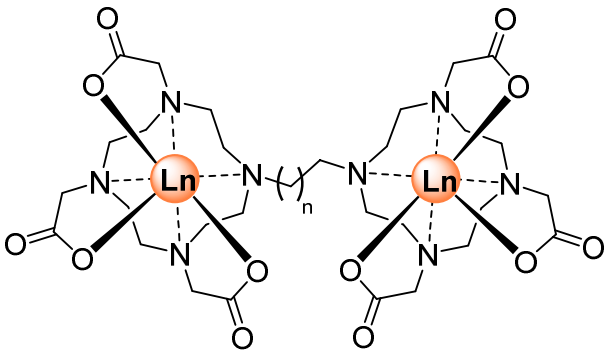
Table 2.1. Table of anions size, radius, hydration sphere, free energy of hydration, and enthalpy of hydration for hydroxide and halides taken from ref 36

Anion	**Radius** (Å)	n_{hyd}	$-\Delta G^{\circ}_{hyd}$ (kJ mol^{-1})	$-\Delta H^{\circ}_{hyd}$ (kJ mol^{-1})
HO^-	1.33	2.7	430	520
F^-	1.33	2.7	465	510
Cl^-	1.81	2	340	367
Br^-	1.96	1.8	315	336
I^-	2.2	1.6	275	291

Halide anions exhibit different levels of hydration in different solvents as reflected by the Hofmeister series of anion hydrophobicity.[37] Across the series,[1] the decrease in charge density results in increasing lipophilicity and weaker hydration. Supramolecular architectures contain receptors to bind halides accounting for its size, but fail to account for the hydration sphere surrounding the halides.

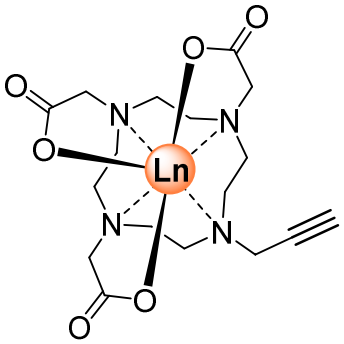
The extent of solvation of the host, guest, and supramolecular assemblies depends on the solvent. Polar protic solvents such as water and methanol strongly solvate charged species, forming hydrogen bonds with both the anion and the host molecule.[38] By contrast, in less polar aprotic solvents such as dichloromethane, the anion is weakly solvated and neutral receptors are able to function.[37,38] Strong

[1] *Hofmeister series of anion hydrophobicity (taken from ref 33):* $CO_3^{2-} > SO_4^{2-} > S_2O_3^{2-} > H_2PO_4^- > HO^- > F^- > HCO_2^- > CH_3CO_2^- > Cl^- > Br^- > NO_3^- > I^- > ClO_4^- > SCN^-$



[Ln_2(**DO3A**)$_2$**C-2**], *n* = 1

[Ln_2(**DO3A**)$_2$**C-3**], *n* = 2



[Ln(**pDO3A**)]

electrostatic or metal–ligand interactions offer the potential to overcome the anion hydration energy, thereby allowing binding in biological media.[39]

2.4. Aim of Chapter-II

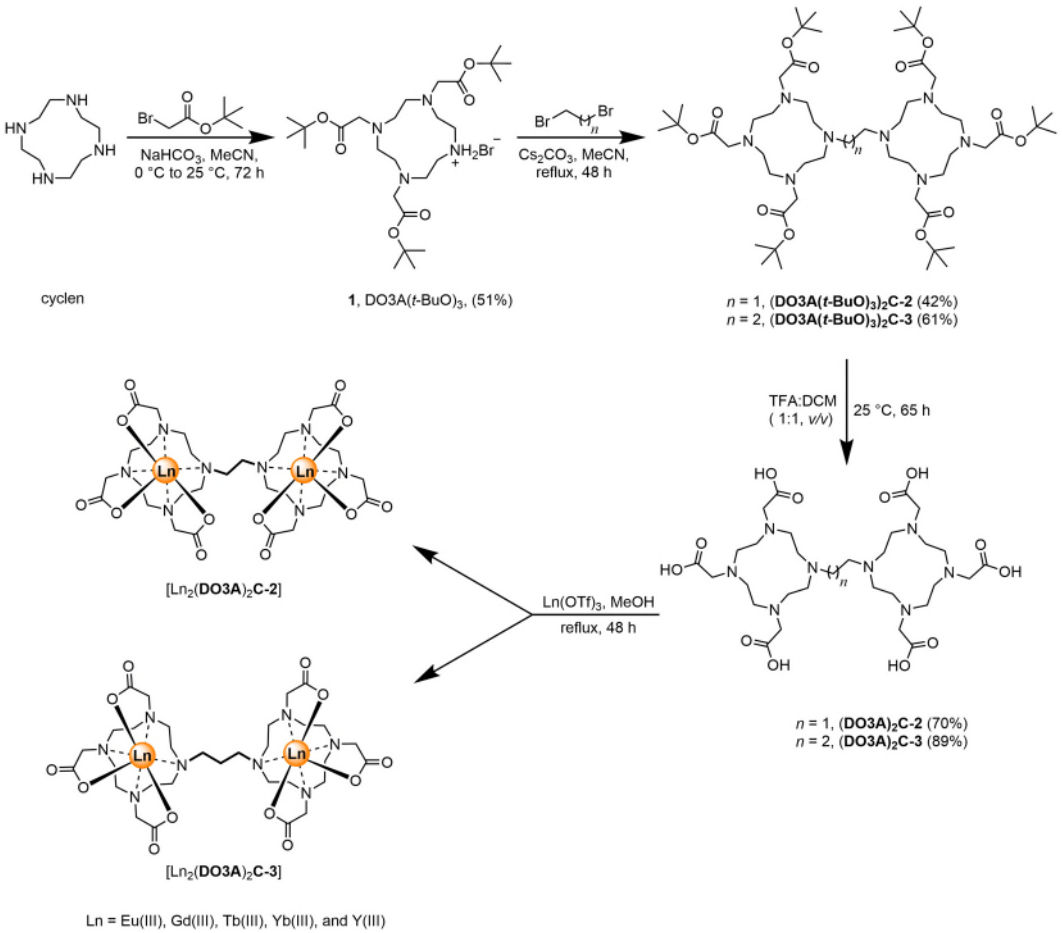
In this chapter, the effective chelation of chloride ions in water using binuclear complexes is pursued under conditions where mononuclear complexes[23-34,39b,c] and free lanthanide ions[40] do not interact with chloride. It is hypothesised that coordinatively unsaturated neutral binuclear Ln(III) complexes of DO3A ligands bridged by ethane and propane linkers ([Ln_2(**DO3A**)$_2$**C-2**] and [Ln_2(**DO3A**)$_2$**C-3**]) would create a pre-organised binding pocket between the metal centres capable of hosting halides coordinated to the lanthanide metal centres. Furthermore, having a short and flexible spacer would increase the steric strain thereby limiting the conformational freedom of the DO3A cores,[41] where subsequent halide binding would lead to a smaller entropy loss in the host. In order to ascertain the effectiveness of the binuclear lanthanide complexes towards chloride binding, kinetically inert neutral mononuclear lanthanide propargyl DO3A complex [Ln(**pDO3A**)], was used as model compound.[42] From the reported literature on fluoride chelation by several mononuclear complexes which are

highlighted above,[23-34] fluoride chelation is expected to happen in these binuclear complexes as fluoride is a harder Lewis base than other halides.[36] However, this work will also explore the chelation of halides in competing and non-competing media to investigate the effectiveness of halide chelation in challenging conditions.

2.5. Results and Discussion

2.5.1. Synthesis of the Proposed Binuclear Complexes

Synthetic scheme is present below (Scheme 2.1). Commercially procured cyclen was tri-*N*-alkylated using *tert*-butyl bromoacetate in a S_N2 type reaction to form DO3A(*t*-BuO)$_3$ using a slightly modified procedure.[43] Cyclen was dissolved in acetonitrile in the presence of sodium carbonate as a proton scavenger. The reaction



Scheme 2.1. Synthesis of binuclear lanthanide complexes under study.

was carried out in acetonitrile at 0 °C with dropwise addition of *tert*-butyl bromo ester in order to facilitate trialkylation over tetraalkylated product. After stirring the reaction in 25 °C for 3 days, the undesirable di- and tetraalkylated products formed as side products were washed off by stirring with toluene for 24 h, followed by filtration to afford an off-white solid. Recrystallisation of the product in toluene afforded colourless crystals which was characterised by single crystal X-ray diffraction. pDO3A(*t*-BuO)$_3$ and pDO3A were prepared as reported.[44] Single crystals of pDO3A(*t*-BuO)$_3$, suitable for X-ray diffraction, were obtained upon recrystallisation in toluene. All precursors and ligands were characterised by spectroscopic techniques (Chapter-VII, Section 7.6.1). The crystal structures of DO3A(*t*-BuO)$_3$ and pDO3A(*t*-BuO)$_3$ are depicted in Figure 2.1.

DO3A(*t*-BuO)$_3$ has a vacant secondary amine on the macrocycle which was treated with caesium carbonate to deprotonate the nitrogen followed by dropwise addition of 1,2-dibromoethane or 1,3-dibromopropane to afford the bismacrocycles, (DO3A(*t*-BuO)$_3$)$_2$C-2 or (DO3A(*t*-BuO)$_3$)$_2$C-3 (Scheme 2.1). The insoluble base was removed upon filtration and the residue evaporated under reduced pressure.

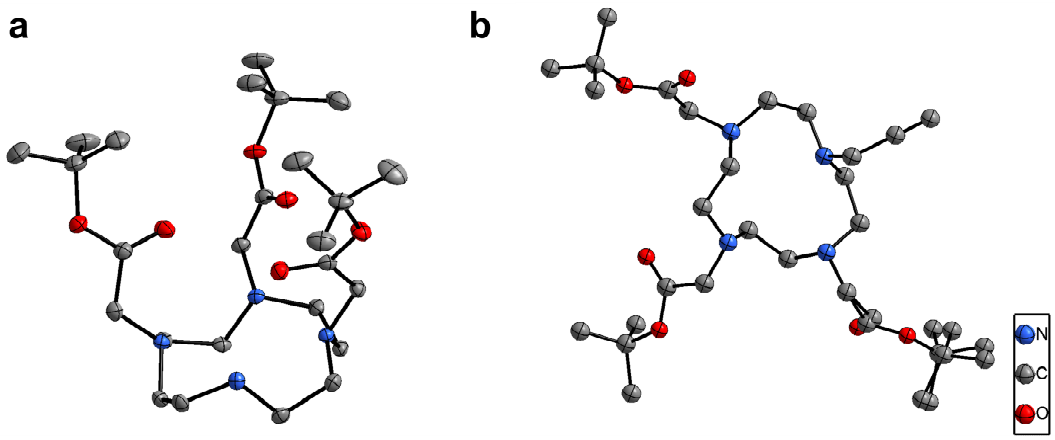


Figure 2.1. (a) Single crystal X-ray structure of (a) DO3A(*t*-BuO)$_3$ (*left*). (b) pDO3A(*t*-BuO)$_3$ (*right*). DCM, Br, and H atoms omitted for clarity. In both the structures, thermal ellipsoid drawn at 30% probability level. X-ray crystal structure was solved by Dr. Kirsten Christensen, Chemical Crystallography, University of Oxford.

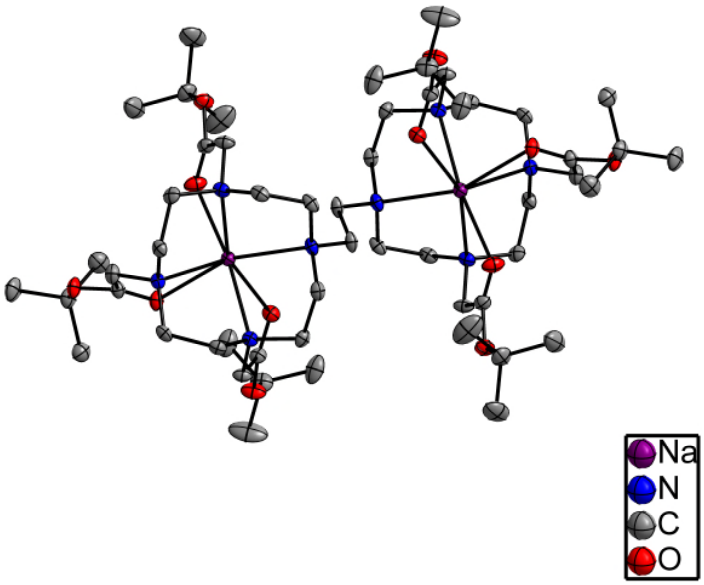


Figure 2.2. Single crystal X-ray structure of (DO3A(*t*-BuO)$_3$)$_2$C-2; $CHCl_3$ and H atoms omitted for clarity. X-ray crystal structure was solved by Dr. Kirsten Christensen, Chemical Crystallography, University of Oxford.

The resulting ethane bridged crude was purified by column chromatography under gradient elution using DCM/MeOH solvent system on silica to afford the product, while the propane bridged product was purified under gradient elution in MeCN/H_2O solvent system over neutral alumina to afford the product. Single crystals of (DO3A(*t*-BuO)$_3$)$_2$C-2 suitable for X-ray diffraction grown upon slow diffusion of pentane over concentrated solution of compound in $CDCl_3$ (Figure 2.2).

(DO3A(*t*-BuO)$_3$)$_2$C-2 and (DO3A(*t*-BuO)$_3$)$_2$C-3 are hydrophobic scaffolds. These compounds were dissolved individually in DCM and trifluoroacetic acid (TFA) added dropwise under stirring and left to stir for 3 days to deprotect the *t*-Bu esters. Following product formation using LRMS, the reaction was evaporated in vacuum to remove the solvent and the acid, and this residue further treated with methanol to create an azeotrope and evaporated to remove TFA as much as possible. This leaves the products as a brown oil which were dissolved in minimum methanol followed by trituration with excess diethyl ether to precipitate the products as a solid. This mixture was centrifuged and solution decanted. This process was

repeated thrice to remove residual TFA as much as possible from the hydrophilic ligands, $(DO3A)_2C$-2 and $(DO3A)_2C$-3. In spite of repeated trituration, the product still contains TFA salt and it was difficult to remove it completely.

Finally, the ligands were subjected to complexation with the appropriate lanthanide metals. From Chapter-I Section 1.6.5.4, it is clear that lanthanide metals have a very weak interaction with chloride, triflate, and perchlorate (type-III anions);[40] therefore, they appear as potential choices of salt to be used for complexation. Since this chapter is exploring chloride binding, $LnCl_3$ salts are avoided to introduce any residual chloride into the system. Triflate is a weak anion which does not have any profound effect on the lanthanide coordination,[40] therefore $[Ln(OTf)_3.xH_2O]$ salts were used throughout the thesis.

The ligands (1 equiv) were dissolved individually in minimum MeOH and the appropriate lanthanide triflate salt (2.05 equiv) added and sonicated until complete dissolution. This mixture was refluxed for 1 h following which, the pH of this reaction adjusted between 5 and 6 using 1 M NaOH and left to reflux for 2 days. After confirming the completion of the reaction using LRMS, the reaction was evaporated under reduced pressure. This residue contains free Ln(III) metal which was removed as reported.[45] The residue was dissolved in deionised water and basified to pH 10 using 1 M NaOH, whereupon free lanthanide ions precipitated at pH 10, while the lanthanide complex remains in solution. This precipitate was removed by centrifugation and the complex in solution decanted and neutralised using 1 M HCl. This pH adjustments during complexation and workup forms NaCl which must be removed. Therefore, the complexes were dialysed in deionised water for 48 h to remove salts and afford the complexes, $[Ln_2(\mathbf{DO3A})_2\mathbf{C\text{-}2}]$ and $[Ln_2(\mathbf{DO3A})_2\mathbf{C\text{-}3}]$. The mononuclear model complexes [Ln(**pDO3A**)] [Ln = Eu(III),

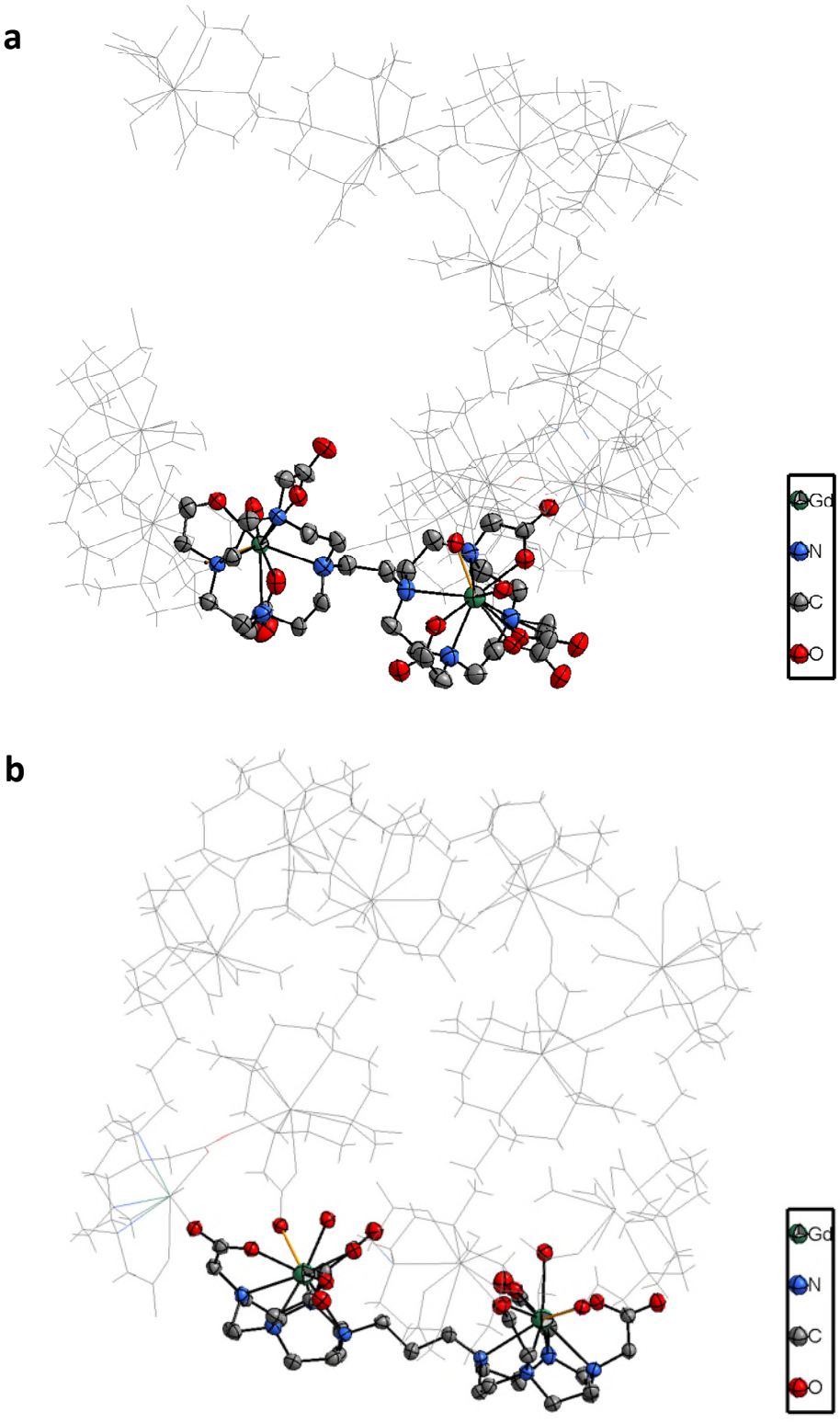


Figure 2.3. X-ray crystal structures of (a) [Gd_2(**DO3A**)$_2$**C-2**] (*top*) and (b) [Gd_2(**DO3A**)$_2$**C-3**] (*bottom*). H atoms and water omitted for clarity. Except selected structure, the rest are shown in wireframe format, H atoms and water are omitted for clarity. Thermal ellipsoid drawn at 30% probability level. μ-oxo bridging bond is shown in orange. X-ray crystal structure was solved by Dr. Kirsten Christensen, Chemical Crystallography, University of Oxford.

Gd(III), Tb(III), Yb(III), and Y(III)] were synthesised as reported.[44,46] All the ligands and complexes obtained were characterised using multiple spectroscopic techniques such as NMR, HRMS, and single crystal X-ray structures which are reported in detail in Chapter-VII Section 7.6.1, and Appendix-C.

Single crystals of [Ln_2(**DO3A**)$_2$**C-3**] (Ln = Eu, Gd, and Yb) and [Gd_2(**DO3A**)$_2$**C-2**] suitable for X-ray diffraction were obtained by slow diffusion of glyme over concentrated solution of the binuclear complexes in D_2O. In these structures, the complexes crystallised as a cluster. In the C-3 complex, the crystal contained 12 metal centres (Eu, Gd, and Yb complexes crystallised with the same unit cell dimensions), while [Gd_2(**DO3A**)$_2$**C-2**] contained 24 metal centres. The coordination complexes in these clusters were bridged by μ-oxo bridges from a carbonyl oxygen coordinating to the neighbouring complex metal centre (Figure 2.3). However, the covalent connectivity and neutral charge of the complex was maintained (structure and data presented in Appendix-C). However, it must be noted that this supramolecular self-assembly is merely a kinetic trap imposed in solution state equilibrium of the complexes which does not reflect the true structure in solution. This is verified using MRI T_1^{-1} relaxivity measurements with the Gd(III) complexes (Section 2.5.6).

[Lu(**pDO3A**)] has previously been reported as a dimer, linked by a carbonate anion between two Lu centres.[22] However, single crystal X-ray diffraction of [Ln(**pDO3A**)] (Ln = Eu and Yb, having same unit cell dimensions) showed no influence of any anion. Crystals were obtained by slow diffusion of acetone over concentrated solution of the complex in deionised H_2O[47] (structure and data located in Appendix-C).

^{1}H NMR spectra of the binuclear Eu(III) and Yb(III) complexes were recorded. The NMR signals in these complexes were found to be broad which is typically observed in [Ln(**DO3A**)] and its derivatives. This is due to the rapid fluctional isomerism that exists between the SAP and TSAP isomeric forms which does not lock on the NMR timescale.[48] However, [Ln(**DOTA**)]$^{-}$ consists of sharp ^{1}H NMR signals with Eu-, Tb-, and Yb(III)complexes as the SAP and TSAP interconversion is locked on the NMR timescale due to slow exchange in comparison with the heptadentate analogue.[47,48] The ^{1}H NMR spectrum of [Yb_2(**DO3A**)$_2$**C-2**] contains sharp spectral lines, probably due to a hydroxide bridging between the metal centres, which slows down the rate of interconversion between the two isomeric forms of the complex, leading to sharp spectral lines. As Yb is a smaller metal and correspondingly a better Lewis acid than Eu,[36a] it is more likely to polarise a bound water molecule to the point where it could possibly deprotonate thereby favouring bridging the metal centres by hydroxide (NMR spectra located in Section 2.5.3).

2.5.2. Photophysics of the Binuclear and Mononuclear Eu(III) Complexes

2.5.2.1. Electronic, excitation, and emission spectra of binuclear Eu(III) complexes

Steady state luminescence spectra of the complexes were obtained by direct excitation on the Eu(III) centre at 393 nm, determined through the absorption (Figure 2.4) and excitation spectra (Figure 2.5). From Chapter-I Section 1.2.5, it is evident that a light harvesting antenna would sensitise lanthanide emission very effectively. However, in this work, only the change in emission upon the interaction of the anion to host is desired; therefore, no sensitiser was incorporated in order to understand the anion interaction in detail. Therefore, high concentration of the host is required to record emission spectra. Thus, 1 mM of complex was used throughout

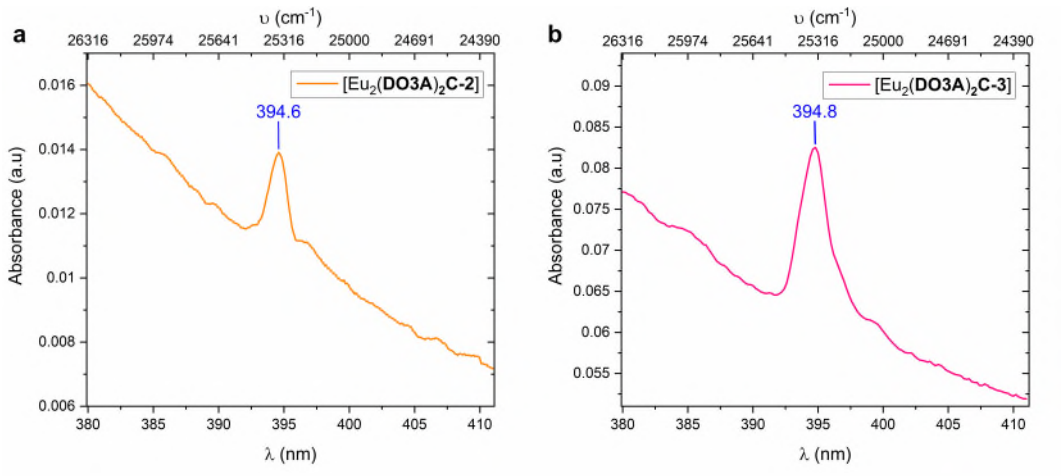


Figure 2.4. Electronic absorption spectra of 5 mM solution of (a) [Eu_2(**DO3A**)$_2$**C-2**] and (b) [Eu_2(**DO3A**)$_2$**C-3**] in deionised H_2O at 298 K.

the luminescence studies. Emission is achieved by direct excitation of the higher energy (emissive) manifold of the Eu(III) ion which decays to the ground state in the form of luminescence emission. The excitation spectra in both water and methanol for [Eu_2(**DO3A**)$_2$**C-2**] and [Eu_2(**DO3A**)$_2$**C-3**] (Figure 2.5) contain an emission maxima at 393 nm which arises from the Eu(III) centre. Therefore, the

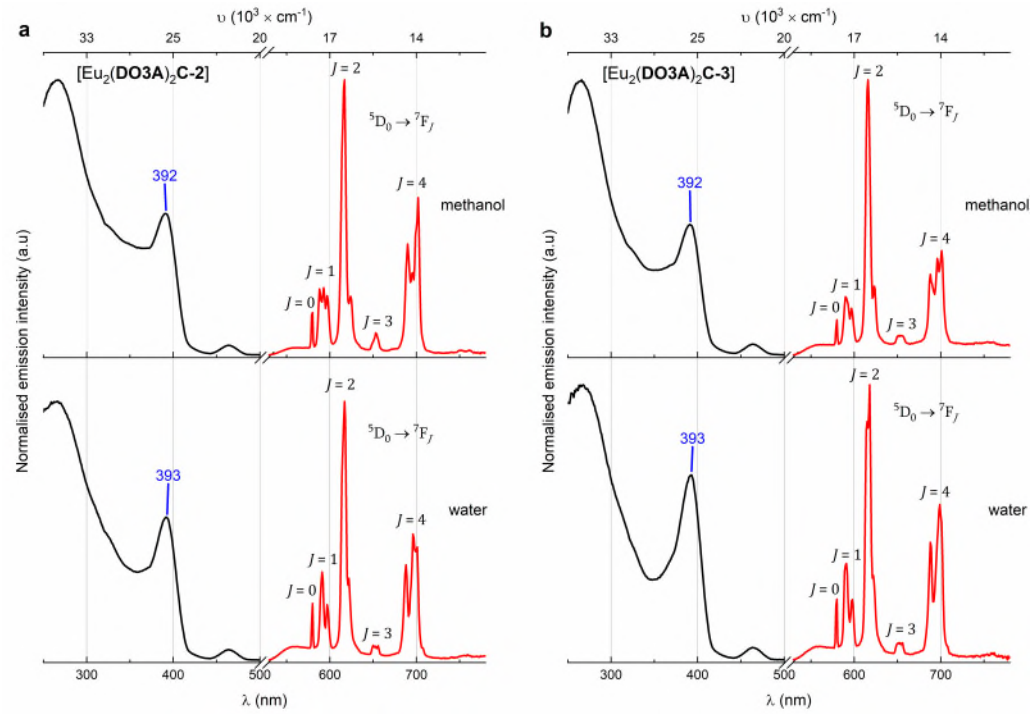


Figure 2.5. Excitation and emission spectra of 1 mM solution of (a) [Eu_2(**DO3A**)$_2$**C-2**] and (b) [Eu_2(**DO3A**)$_2$**C-3**] in H_2O and MeOH.

emission spectra for the binuclear complexes were obtained by exciting the complexes at 393 nm. Characteristic fingerprint Eu(III) emission spectra was observed which was assignable to the $^5D_0 \rightarrow {}^7F_J$ transitions, where J = 0-4 (Figure 2.5). The hypersensitive J = 2 transition is higher in intensity than the other transitions which is characteristic for the Eu(III) complexes of heptadendate DO3A and its derivatives.[48] A broad signal at around 550 nm is observed. It is difficult to rationalise its presence, but it is absent under time-resolved phosphorescence mode, implying that it is a short-lived species. Based on the steady-state spectra obtained in Chapter-5, it can be assumed that this broad signal is absent in complexes that contain light-harvesting antenna and the low intense direct excitation leads to the emergence of artefacts owing to the wide slit widts used in recording a spectrum here.

2.5.2.2. Effect of pH on binuclear Eu(III) complexes

[Ln(**DO3A**)] complexes are known to bind to hydroxide at basic pH.[42,46] This was put to test in the binuclear complexes. At pH 4 and 7, there was no significant change in the emission spectra of [Eu_2(**DO3A**)$_2$**C-2**] and [Eu_2(**DO3A**)$_2$**C-3**]. At pH 9.9, there was a sharp increase in the intensity of the

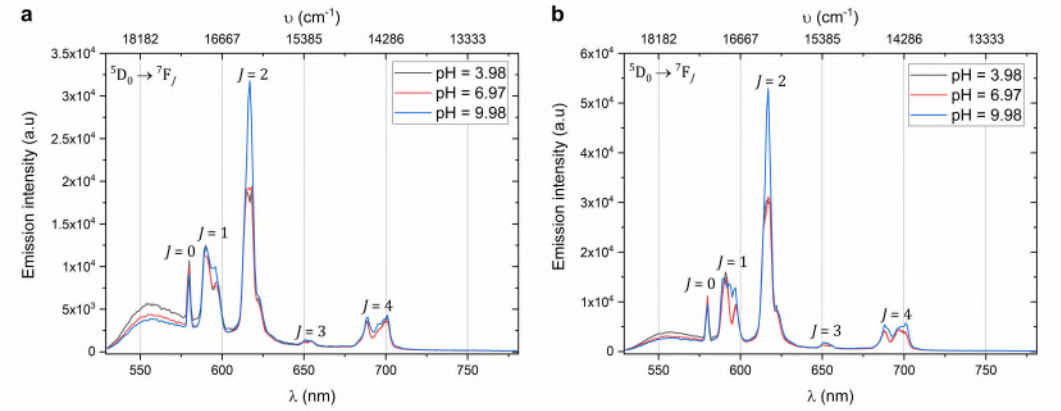


Figure 2.6. Steady state luminescence spectra of [Eu_2(**DO3A**)$_2$**C-2**] (*a*) and [Eu_2(**DO3A**)$_2$**C-3**] (*b*) at varying pH.

hypersensitive $^5D_0 \rightarrow {}^7F_2$ transition and the shape of the magnetically sensitive $^5D_0 \rightarrow {}^7F_1$ transition altered which accounts for the chelation of hydroxide to the metal centre (Figure 2.6). The steady-state luminescence spectra of the binuclear Eu complexes at different pD is presented in Appendix-A.

Time resolved luminescence lifetimes of the complexes at basic pH had longer lifetimes than the complexes at acidic and neutral pH which further proves the involvement of hydroxide chelation to the metal centres (Table 2.2). The lifetime curve was best fitted to a monoexponential decay to obtain the luminescence lifetimes. The hydration number was calculated using the modified Horrocks′ equation (vide Chapter-I, Section 1.2.8.2). Although the hydration number provides limited information due to the presence of two identical lanthanide metals which act as quenchers,[42] it can still be used to understand the difference in coordination environment upon the chelation of an incoming anion. The reduction in hydration number at basic pH again reflects the hydroxide anion binding to the metal center (Table 2.2).

Table 2.2. Luminescence lifetime of [Eu_2(**DO3A**)$_2$**C-2**] and [Eu_2(**DO3A**)$_2$**C-3**] at varying pH and pD

Complex	pH/pD	Lifetime in H_2O (ms)*	Lifetime in D_2O (ms)*	Hydration number (*q*)
[Eu_2(**DO3A**)$_2$**C-2**]	3.98/4.01	0.42	1.62	1.8
[Eu_2(**DO3A**)$_2$**C-3**]	3.98/4.01	0.48	1.63	1.5
[Eu_2(**DO3A**)$_2$**C-2**]	6.97/7.05	0.38	1.69	2.1
[Eu_2(**DO3A**)$_2$**C-3**]	6.97/7.05	0.47	1.72	1.5
[Eu_2(**DO3A**)$_2$**C-2**]	9.98/10.12	0.54	1.59	1.2
[Eu_2(**DO3A**)$_2$**C-3**]	9.98/10.12	0.67	1.77	0.8

* All lifetime values are subjected to an error of ±10%.

2.5.2.3. Chloride chelation on the binuclear Eu(III) complexes

The binding of chloride to the host molecules were investigated using steady-state luminescence titrations. The ratiometric change in binding was observed by comparing the integral of the hypersensitive $^5D_0 \rightarrow {}^7F_2$ transition against the integral of the magnetically sensitive $^5D_0 \rightarrow {}^7F_1$ transition.[39b,c] The theory and method of this ratiometric measurement are discussed in detail in Chapter-I, Section 1.6.4.2. The details for the protocol followed in performing the anion binding titrations through luminescence and data processing are located in Chapter-VII, Section 7.4.8.

Titration of the binuclear complexes [Eu_2(**DO3A**)$_2$**C-2**] and [Eu_2(**DO3A**)$_2$**C-3**] against chloride was carried out using KCl salt in deionised water (Figure 2.7). The changes in steady-state luminescence upon the incremental addition of KCl was monitored and the spectra stacked to understand the mode of binding and its speciation. The emission intensity was found to decrease upon increasing addition of KCl. In Chapter-I, Section 1.6.4.2, the increase in lanthanide centered emission intensity upon the chelation of guest to the metal centre by replacing the inner-sphere water was discussed. Therefore, the decreased emission intensity was not expected. However, it is noteworthy that chloride is a PeT quencher which can decrease the observed lanthanide centered intensity.[49]

In addition, the metal centres are identical, implying that a Dexter quenching[41,42,48,49] is possible throughout the luminescence study, which could also account for the drop in the emission intensity during the course of the titration. No change in the fine structure of the emission spectra is observed during the course of the titration. Corresponding binding isotherm was generated using DYNAFIT®.[50]

The binding strength was K_1 = 2,800 M^{-1} (±7%) for the C-2 complex and K_1 = 4,550 M^{-1} (±3.9%) for the C-3 complex.

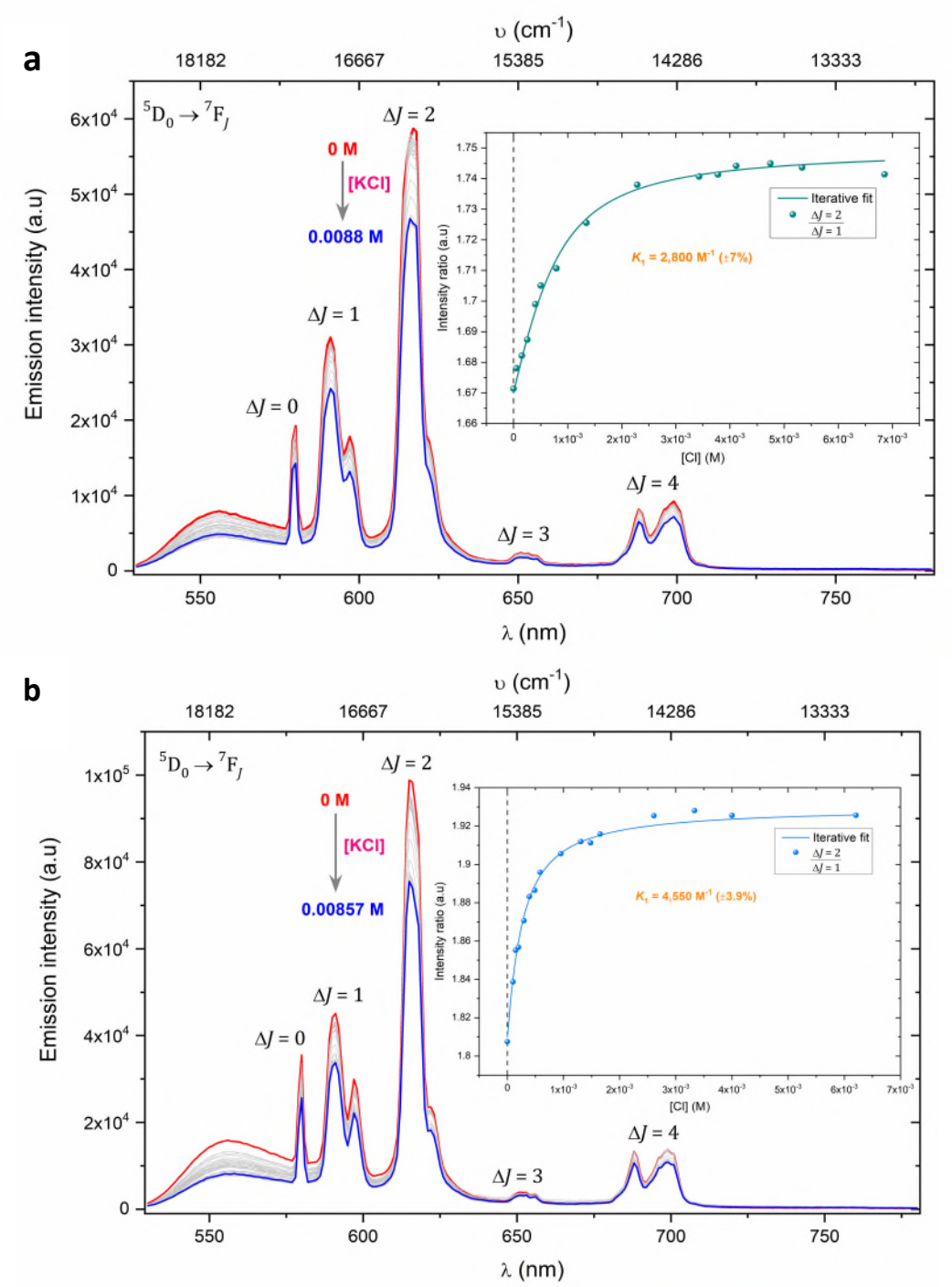


Figure 2.7. Steady-state luminescence titration spectra of [Eu_2(**DO3A**)$_2$**C-2**] (*a*) and [Eu_2(**DO3A**)$_2$**C-3**] (*b)* with KCl in deionised water; spectrum of neat complex solution (***red in bold***), spectra upon the additions of KCl (*grey*), spectrum upon the final addition of KCl (***blue in bold***). *Inset*: binding isotherm generated from the corresponding titrations.

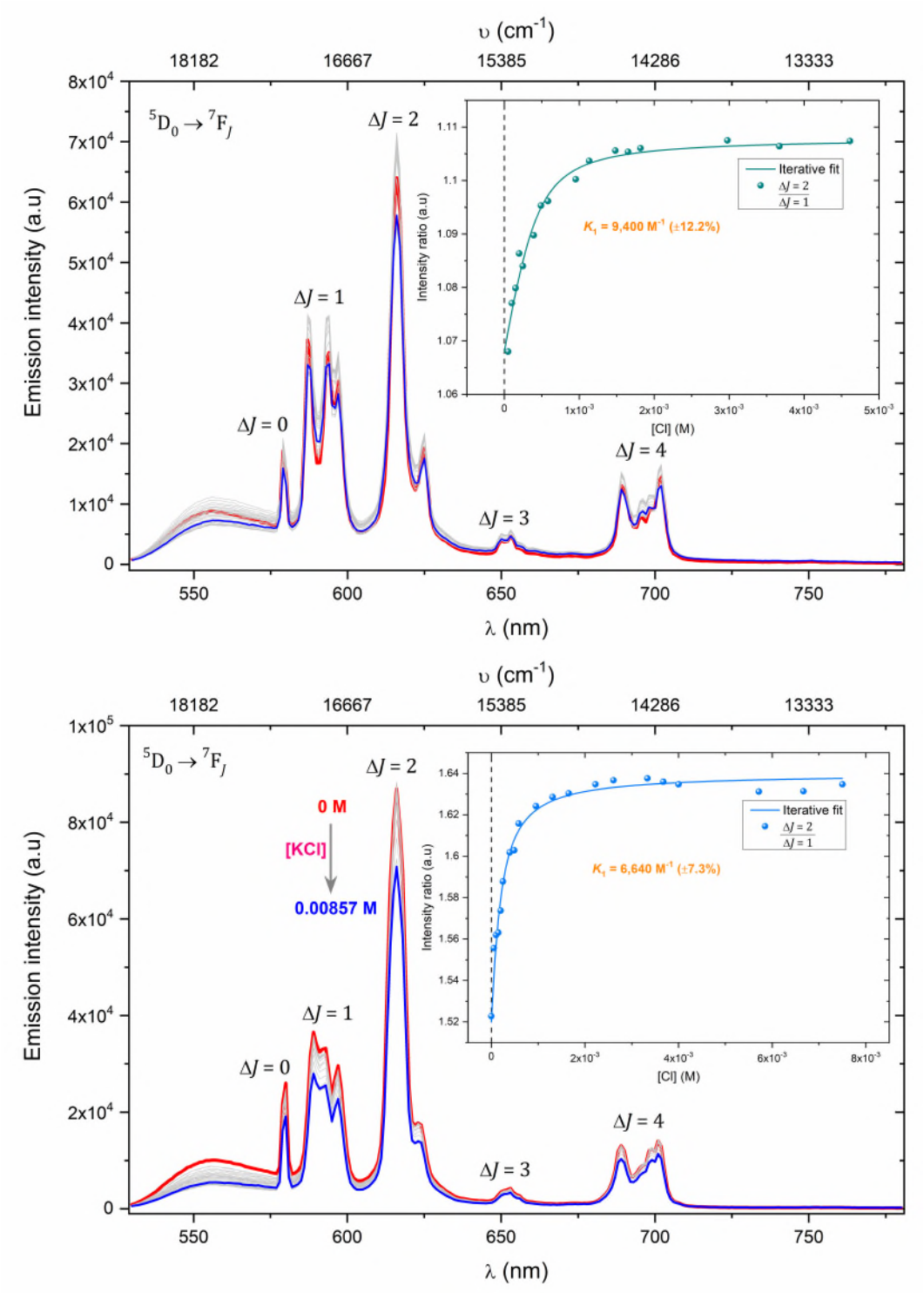


Figure 2.8. Steady-state luminescence titration spectra of [Eu_2(**DO3A**)$_2$**C-2**] (*top*) and [Eu_2(**DO3A**)$_2$**C-3**] (*bottom*) with KCl in 0.01 M phosphate buffer at pH 7.4; spectrum of neat complex solution (***red in bold***), spectra upon the additions of KCl (*grey*), spectrum upon the final addition of KF (***blue in bold***). *Inset*: binding isotherm generated from the corresponding titrations.

Next, the titration was performed in competing binding media. Titration of the binuclear complexes [Eu_2(**DO3A**)$_2$**C-2**] and [Eu_2(**DO3A**)$_2$**C-3**] was carried out using KCl in phosphate buffer at pH 7.4 (Figure 2.8). Upon the increasing addition of KCl, a decrease in emission intensity was observed similar to the titration in water. However, the fine structure at the start is different to that observed in water, possibly due to phosphate interaction with the metal as reported in the case of [Ln(**pDO3A**)].[51]

But, no change in the fine structure of the emission spectra during the course of the titration was observed. The binding isotherm was found to be greater than that observed in water (K_1 = 9,400 M^{-1} (±12.2%) for C-2 complex and K_1 = 6,640 M^{-1} (±7.3%) for C-3 complex), implying that the binuclear complexes can compete very effectively against phosphate in solution. This observation of a guest binding strongly to a binuclear lanthanide host in phosphate buffer was reported for [Ln_2(**DO3A**)$_2$] bridged by 3,5-lutidine spacer, where the host was found to bind strongly to dinicotinate, amidst phosphate competition in solution.[52]

From the pH studies (Section 2.5.2.2), hydroxide was found to bind to the metal centre at basic pH. In order to test the potency of the binuclear complexes to bind chloride by competing against hydroxide, titrations with KCl against the binuclear Eu(III) complexes were performed at basic pH. Steady-state luminescence titration of [Eu_2(**DO3A**)$_2$**C-2**] with KCl in CHES buffer at pH 9.9 showed an increase in emission intensity upon the addition of chloride (Figure 2.9). Changes in the fine structure of the emission spectra was observed in both J = 2 and J = 1 transitions. However, the luminescence intensity change was inconsistent throughout the course of the titration. This did not affect the binding isotherm as it was generated from the ratiometric analysis. Time-resolved luminescence titration was performed in the case of [Eu_2(**DO3A**)$_2$**C-3**] as the steady-state luminescence

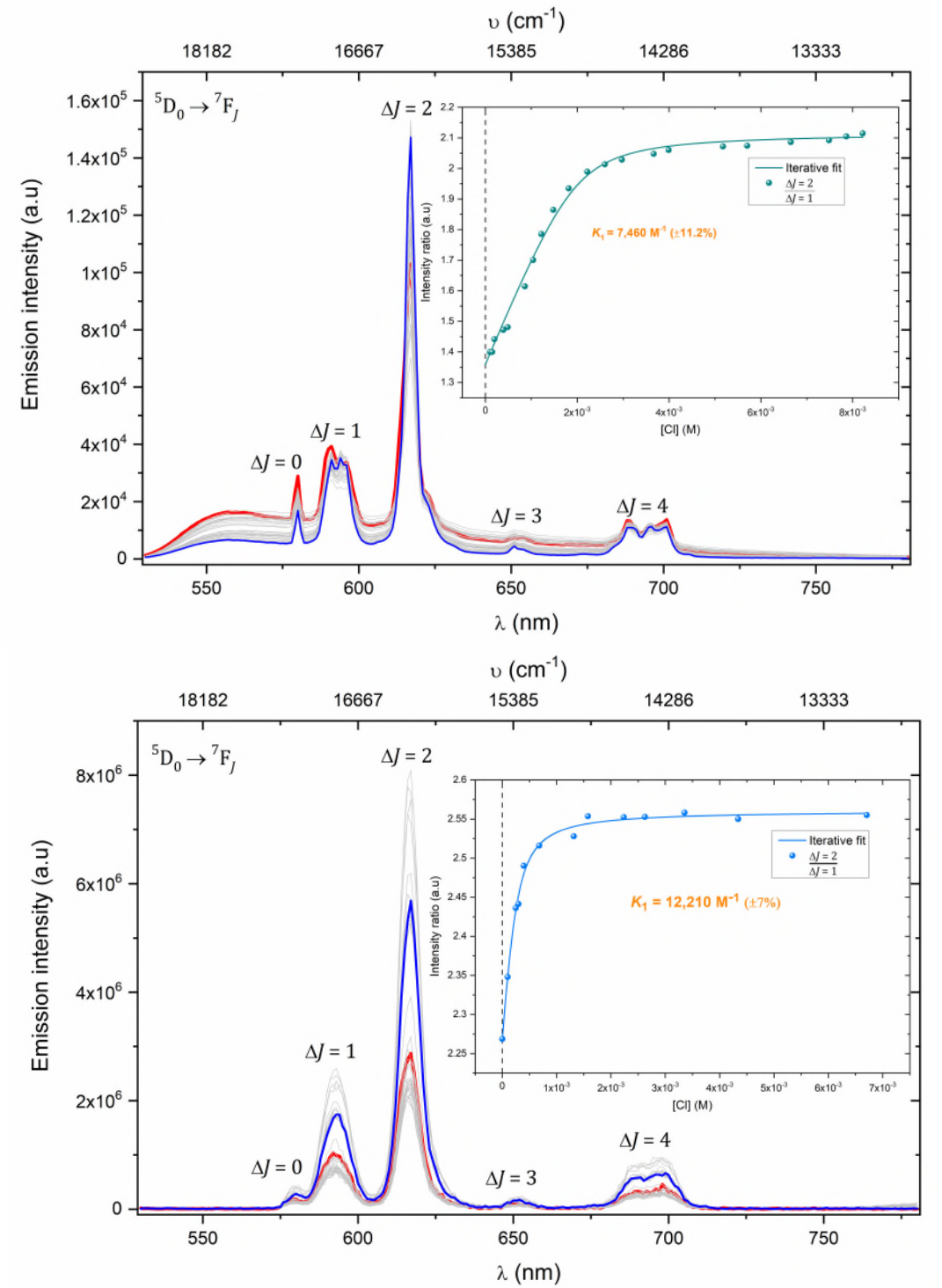


Figure 2.9. Steady-state luminescence titration spectra of [Eu_2(**DO3A**)$_2$**C-2**] (*top*) and [Eu_2(**DO3A**)$_2$**C-3**] (*bottom*) with KCl in 0.01 M CHES buffer at pH 9.98; spectrum of neat complex solution (***red in bold***), spectra upon the additions of KCl (***grey***), spectrum upon the final addition of KF (***blue in bold***). *Inset*: binding isotherm generated from the corresponding titrations.

titration generated a spectra whose baseline was uneven for unknown reasons. However, the inconsistency in emission intensity change was observed similarly to the C-2 system. The broad spectra proved difficult to observe the fine structure changes in the emission bands. The binding isotherm reveals that the C-3 complex chelates chloride strongly at basic pH (K_1 = 12,210 M^{-1} (±7%)) to that of the C-2 analogue (K_1 = 7,460 M^{-1} (±11.2%)).

The binding strength of chloride in buffers are much stronger than the ones in water. Although there is no evidence as such to explain this trend, it is plausible that the ions in the buffers (phosphate and CHES) can interact strongly with [Eu_2(**DO3A**)$_2$**C-3**] containing larger cavity between the metal centres which makes it prone for interference with the competing ions more than [Eu_2(**DO3A**)$_2$**C-2**], thereby accounting for the strong binding of chloride in C-2 complex. From the above titrations, it was hypothesised that the chelation of chloride involves bridging between the metal centres (Figure 2.10) as mononuclear lanthanide complexes do not bind to chloride in water.[23-34] DFT and other modelling studies would shed light on the binding affinities for the C-2 and C-3 complexes towards halides.

In all the titrations involving halides (which is present later), there is an initial broad hump which alters upon the increasing addition of the guest halides. Plotting them against halide addition did not result in any meaningful observations. However, this is absent in time-gated phosphorescence emission, implying that it is a short-lived species (Titrations were done in steady-state mode because it was crucial for monitoring fluoride chelation and following a uniform method to monitor anion binding titrations is important to obtain meaningful binding constant which can be rationalised and compared throughout).

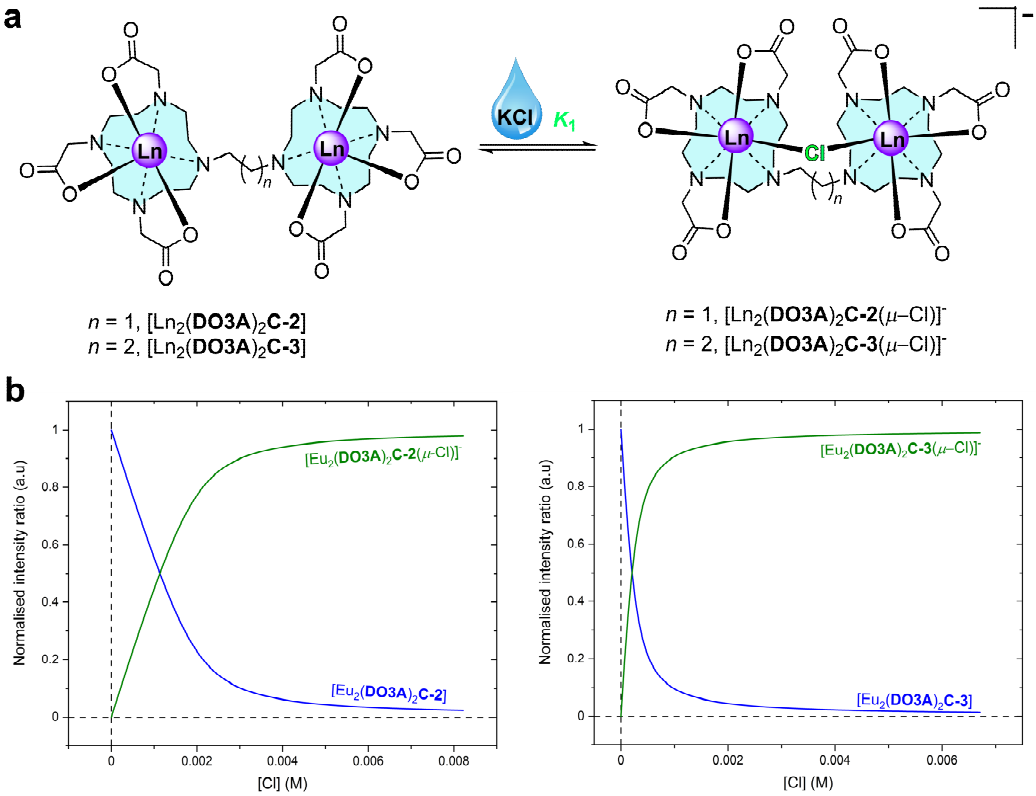


Figure 2.10. (a) Proposed speciation for chloride chelation by the binuclear complexes in water. (b) Normalised model of speciation obtained from $\Delta J = 2/\Delta J = 1$ bands from steady state emission titration spectra of [Eu_2(**DO3A**)$_2$**C-2**] (*left*) and [Eu_2(**DO3A**)$_2$**C-3**] (*right*) with KCl in CHES buffer at pH 9.9. (Binding isotherm and speciation best fitted to a 1:1 stoichiometry)

2.5.2.4. Fluoride chelation on the binuclear Eu(III) complexes

In order to investigate the influence of other anions that can bind to the binuclear receptor, titrations with fluoride was pursued. Although fluoride chelation was observed in the binuclear complexes, it can be neglected as a potential interferent due to its low concentration in biology and the environment (vide section 2). However, its mode of binding to the binuclear complexes can be utilised to understand the mode of chelation for chloride.

Titration of the binuclear [Eu_2(**DO3A**)$_2$**C-2**] and [Eu_2(**DO3A**)$_2$**C-3**] complexes were carried out using KF salt in deionised water (Figures 2.11 and 2.12). The emission intensity was found to decrease upon increasing KF addition, until a

certain point where a rise in emission intensity in the last few additions were observed. The generation of binding constants from ratiometric analysis could not be used in this case as fluoride chelation involved a dramatic change in intensity, form and shape of the emission spectra. Therefore, selected individual emission wavelengths in $^5D_0 \rightarrow {}^7F_0$ and $^5D_0 \rightarrow {}^7F_1$ transitions were used to generate the binding isotherm and to probe the speciation (Figures 2.11 and 2.12). From this analysis, up to three consecutive binding events occurred and utilised to generate a meaningful binding isotherm using DYNAFIT®.[50] The first binding event (K_1 = 10,480 M^{-1} (±5.9%) for C-2 complex and K_1 = 600,000 M^{-1} (±39.7%) for C-3 complex) was stronger than the other two (K_2 = 10,950 M^{-1} (±4%), K_3 = 6,570 M^{-1} (±3.6%) for C-2 complex; K_2 = 144,000 M^{-1} (±33.5%), K_3 = 394.9 M^{-1} (±2.3%) for C-3 complex) which suggested chelation of fluoride for K_1 occurred by fluoride bridging between the metal centres. This can be verified by comparing the binding constants of fluoride to mononuclear lanthanide complexes reported in the literature[23-34] whose binding strengths were profoundly lower than what was observed here. However, there is ambiguity on how the second and third binding event would appear as it is possible for the second fluoride also to bridge between the metal centres. In order to address this problem, titration was carried out in wet MeOH.

From Chapter-I, Section 1.2.8.2, it is evident that lanthanide luminescence is quenched by O–H oscillators. Although the incoming anion would replace the inner-sphere water, the solvent O–H oscillators would quench the weak emission coming from direct excitation of the binuclear complexes. Also, wet MeOH has less O–H oscillators than water, implying there is less competition between fluoride and hydroxide in MeOH. Therefore, it was hypothesised that titration in MeOH would

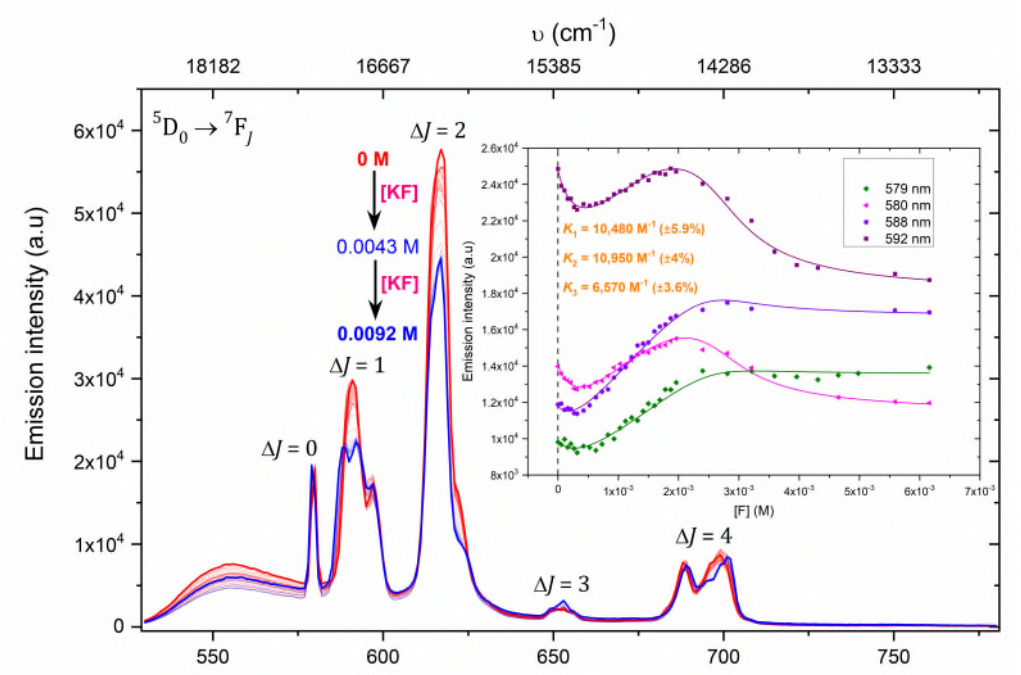


Figure 2.11. Steady-state emission titration spectra of [Eu_2(**DO3A**)$_2$**C-2**] with KF in deionised water. Spectrum of neat complex solution (***red in bold***), spectra upon the additions of KF (*red to blue*), spectrum upon the final addition of KF (***blue in bold***). *Inset:* binding isotherm generated from the titration spectra.

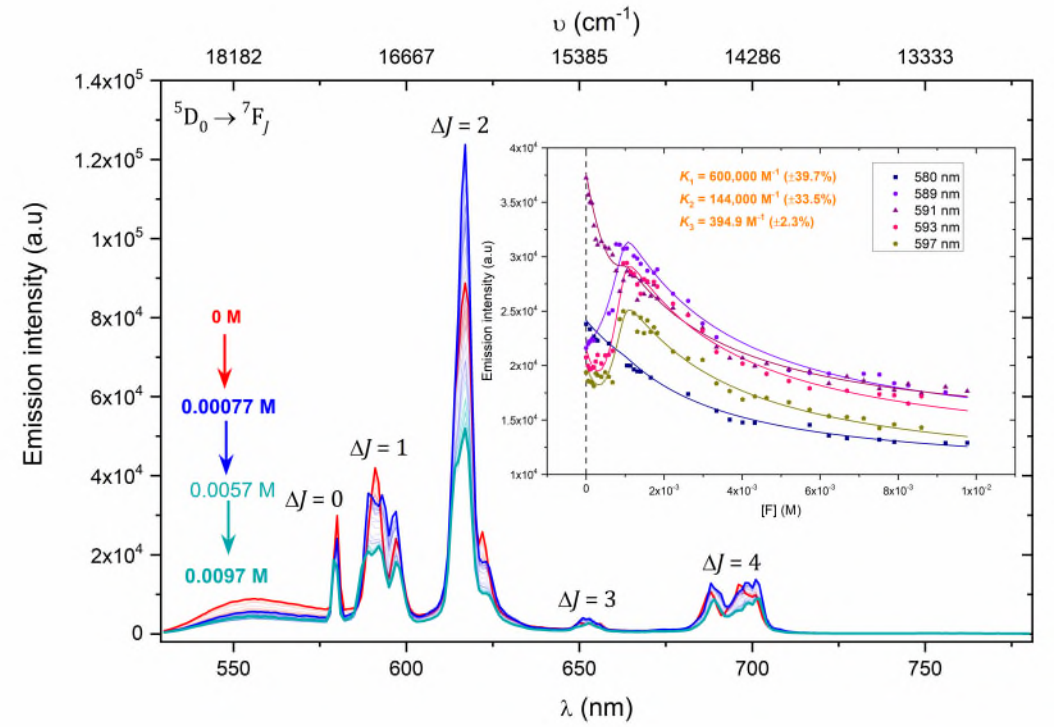


Figure 2.12. Steady-state luminescence titration spectra of [Eu_2(**DO3A**)$_2$**C-3**] with KF in deionised water; spectrum of neat complex solution (***red in bold***), spectra upon the additions of KF (*red*, ***blue in bold***, *blue to cyan*), spectrum upon the final addition of KF (***cyan in bold***). *Inset:* binding isotherm generated from the titrations.

provide a better emission spectrum with more information on the speciation of fluoride chelation. Solvation of KF is slightly better in MeOH[53] which gives an added advantage to do the titration in MeOH.

Titration of the binuclear complexes [Eu_2(**DO3A**)$_2$**C-2**] and [Eu_2(**DO3A**)$_2$**C-3**] were carried out using KF in MeOH (Figure 2.13). As expected, the spectra were well-resolved with dramatic changes in form, shape and intensity of the emission bands. Selected individual emission wavelengths in $^5D_0 \rightarrow {}^7F_0$ and $^5D_0 \rightarrow {}^7F_1$ transitions were used to generate the binding isotherm and to probe the speciation (similar to the titration of the binuclear Eu(III) complexes with KF in deionised H_2O). Three successive binding events were observed where the first fluoride bound stronger than the other two.

From the emission titration spectra (Figure 2.13), it was evident that there is a decrease in intensity upon the addition of KF initially, which suggests that fluoride was chelated between the metal centres in the first binding event (K_1 = 54,800 M^{-1} (±11.8%) for C-2 complex and K_1 = 179,000 M^{-1} (±13.2%) for C-3 complex, Figure 2.14). When the second binding event of fluoride occurs (the shape of $^5D_0 \rightarrow {}^7F_1$ band was altered which suggests the start of the second binding event), the emission intensity was still decreasing, suggesting that the second binding event (K_2) involves binding of fluoride to each metal centre individually, implying the existence of intermetallic repulsion in K_2 binding event (K_2 = 20,200 M^{-1} (±10.6%) for C-2 complex and K_2 = 32,000 M^{-1} (±13%) for C-3 complex, Figure 2.14). However, when the third binding event (K_3) begins (the shape of the $^5D_0 \rightarrow {}^7F_1$ band is again altered), the emission intensity begins to rise (Figure 2.13) (K_3 = 0.002843 M^{-1} (±0.6%) for C-2 complex and K_3 = 728 M^{-1} (±7.5%) for C-3 complex, Figure 2.14). This is hypothesised to be the chelation of the third fluoride by bridging

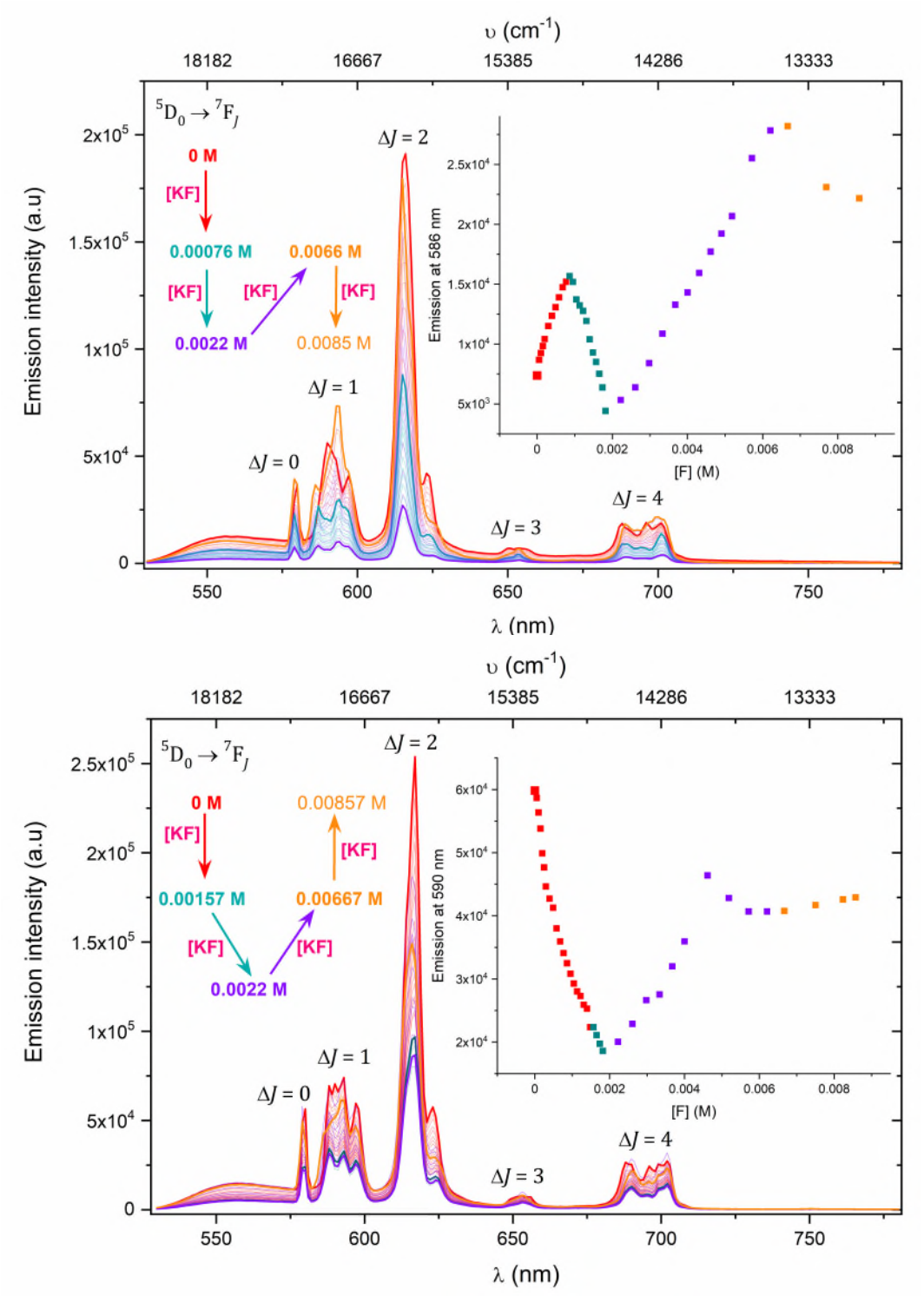


Figure 2.13. Steady-state luminescence titration spectra of [Eu_2(**DO3A**)$_2$**C-2**] (*top*) and [Eu_2(**DO3A**)$_2$**C-3**] (*bottom*) with KF in methanol; spectrum of neat complex solution (***red in bold***), spectra upon the additions of KF (*red*, ***cyan in bold***, *cyan*, ***violet in bold***, *violet*, ***orange in bold***, *and orange*), spectrum upon the final addition of KF (*orange*). *Inset:* the course of the titration at 586 nm emission (*top*) and 590 nm emission (*bottom*). The color coding on the inset is identical to that of the titration spectra.

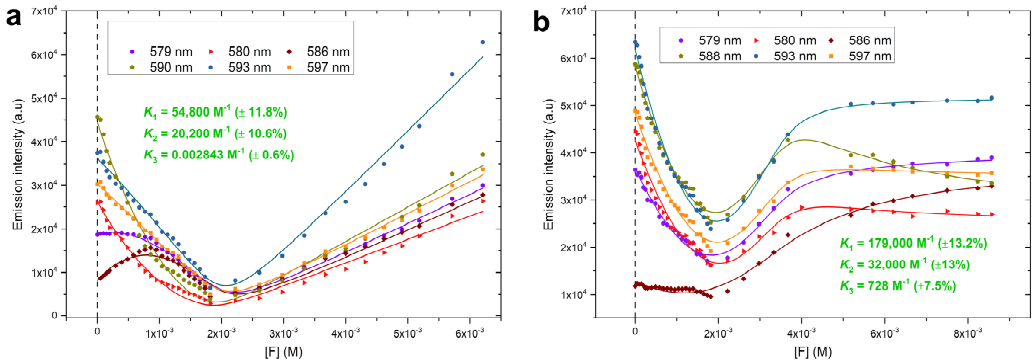


Figure 2.14. Binding isotherm for the binding of fluoride to [Eu_2(**DO3A**)$_2$**C-2**] (*a*) and [Eu_2(**DO3A**)$_2$**C-3**] (*b*), obtained by plotting the intensity of the emission maxima of the $\Delta J = 0$ and $\Delta J = 1$ emission bands as a function of the concentration of KF in methanol.

between the metal centres (in addition to two fluorides chelated at each metal centre), where the intermetallic quenching of lanthanide luminescence is blocked by the third fluoride, because the metal sites begin to coordinatively saturate (Figure 2.15). Towards the end of the titration (~0.006M of KF addition), the emission intensity starts to drop due to quenching of the Eu(III) luminescence by free fluoride in solution. When the binding isotherm was generated with all aliquots of KF added, the decrease in emission intensity from 0.006M of KF addition suggested the presence of a weaker fourth binding event, but the error associated with this fit was very high. Therefore, the last three points were masked to generate a meaningful three binding event fit using DYNAFIT® (Figure 2.14).

After studying the binding of fluoride in neat solvents, the speciation of fluoride binding was explored in buffers. This was planned in order to account for the chelation of fluoride to the binuclear complexes in challenging environments. Three buffers: PBS (pH 7.4), Tris HCl (pH 7.4), and CHES (pH 9.9) were selected. PBS is a commonly used biological buffer and is interesting to compare anion binding in this media, as phosphate is a competing anion. By carrying out the titration in PBS, fluoride chelation in competing media will be discerned. This will be compared against fluoride chelation in non-competing binding media, for which titration was

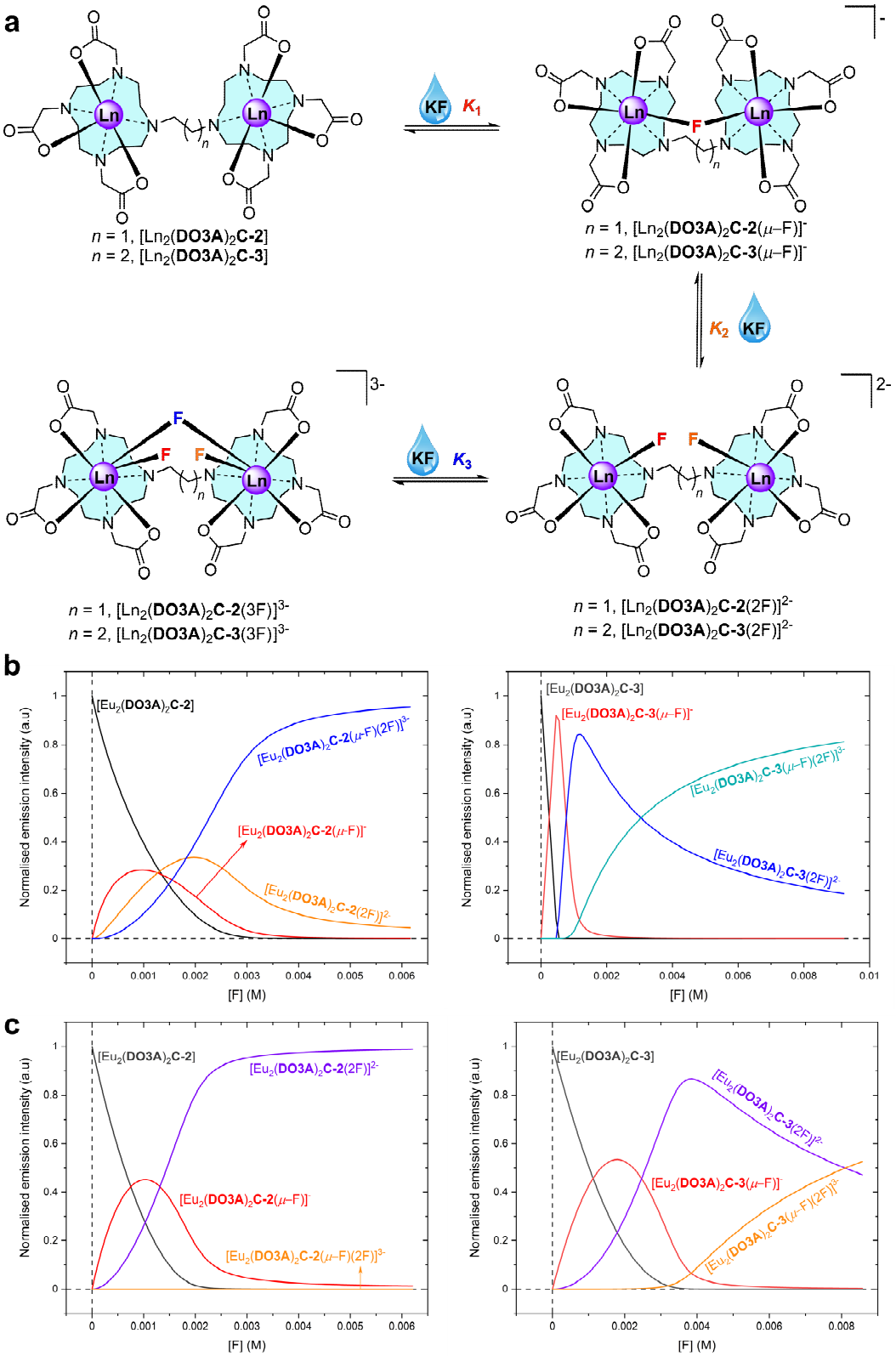


Figure 2.15. (a) Proposed speciation of fluoride chelation to the binuclear complexes in aqueous media. (b) Normalised model of speciation obtained from 580 nm emission in steady-state emission titration spectra of [Eu_2(**DO3A**)$_2$**C-2**] (left) and [Eu_2(**DO3A**)$_2$**C-3**] (right) with KF in deionised water. (c) Normalised model of speciation obtained from 586 nm emission in steady-state emission titration spectra of [Eu_2(**DO3A**)$_2$**C-2**] with KF in MeOH (left). Normalised model of speciation obtained from 588 nm emission in steady-state emission titration spectra of [Eu_2(**DO3A**)$_2$**C-3**] with KF in MeOH (*right*).

done in Tris HCl. Since fluoride is isoelectronic to hydroxides (vide Table 2.1) and hydroxide binds to the binuclear complex (vide Section 2.5.2.2), titration in CHES buffer will account for the fluoride binding amidst hydroxide competition from the buffer.

Titration of the binuclear complexes [Eu_2(**DO3A**)$_2$**C-2**] and [Eu_2(**DO3A**)$_2$**C-3**] were carried out using KF in PBS (Figures 2.16 and 2.17). The emission intensity decreased upon increasing fluoride concentration. The form and shape of the emission bands did not change during the course of the titration, which was observed otherwise in the C-3 complex. Binding isotherm was generated ratiometrically which showed a single binding event with the C-2 complex (K_1 = 4,030 M^{-1} (±2.9%)) and a weaker second binding event with the C-3 complex (K_1 = 5,350 (±6.9%), K_2 = 18.57 M^{-1} (±1%)). The emission spectra of both the

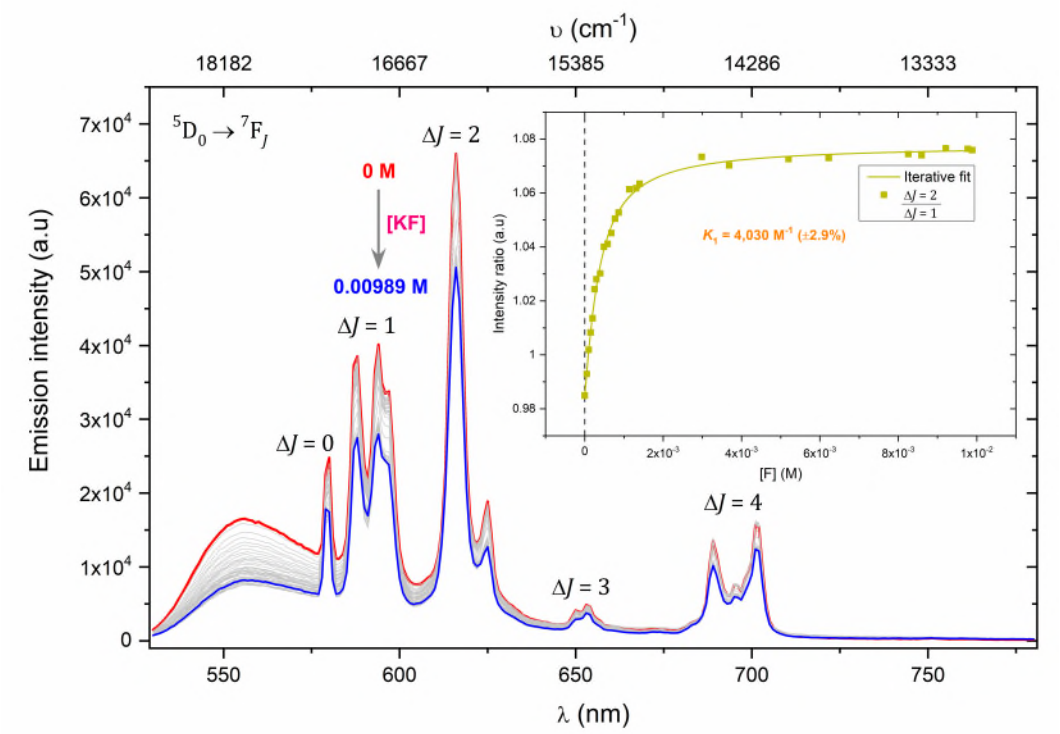


Figure 2.16. Steady-state emission titration spectra of [Eu_2(**DO3A**)$_2$**C-2**] with KF in 0.01M PBS at pH 7.4. Spectrum of neat complex solution (***red in bold***), spectra upon the additions of KF (*grey*), spectrum upon the final addition of KF (***blue in bold***). *Inset*: binding isotherm generated from the titration spectra.

complexes at the start of titration look different to the one recorded in deionised H_2O, suggesting phosphate chelation from the buffer.

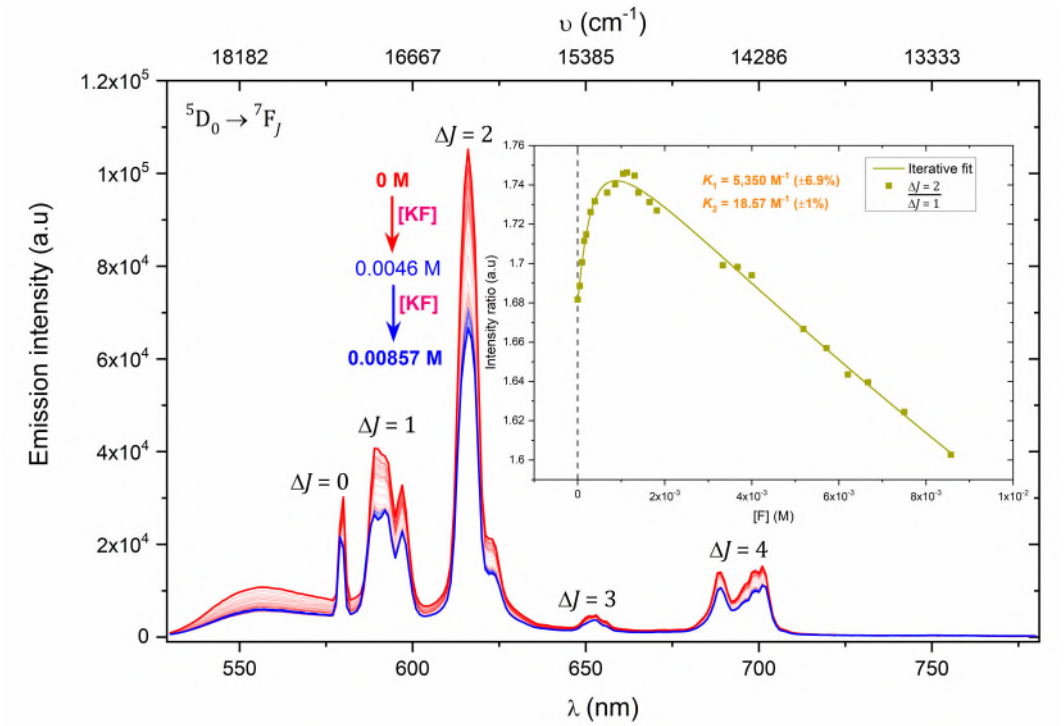


Figure 2.17. Steady-state emission titration spectra of [Eu_2(**DO3A**)$_2$**C-3**] with KF in 0.01M PBS at pH 7.4. Spectrum of neat complex solution (***red in bold***), spectra upon the additions of KF (*red to blue*), spectrum upon the final addition of KF (***blue in bold***). *Inset:* binding isotherm generated from the titration spectra.

Titration of the binuclear [Eu_2(**DO3A**)$_2$**C-2**] and [Eu_2(**DO3A**)$_2$**C-3**] complexes were carried out using KF in Tris-HCl buffer (Figures 2.18 and 2.19). Emission intensity was observed to decrease upon incremental fluoride addition. The form and shape of the emission bands did not change during the titration initially, but they were altered towards the end of the titration, probably due to the binding of second fluoride to the binuclear complexes. Ratiometric analysis of the binding isotherm revealed up to two binding events where the first binding event was stronger than the second (K_1 = 1,670 M^{-1} (±14.7%), K_2 = 116.4 M^{-1} (±1.7%) for C-2 complex; K_1 = 106,000 M^{-1} (±38.9%), K_2 = 219.1 M^{-1} (±0.8%) for C-3 complex). Since the form and shape of the emission spectra was altered during the

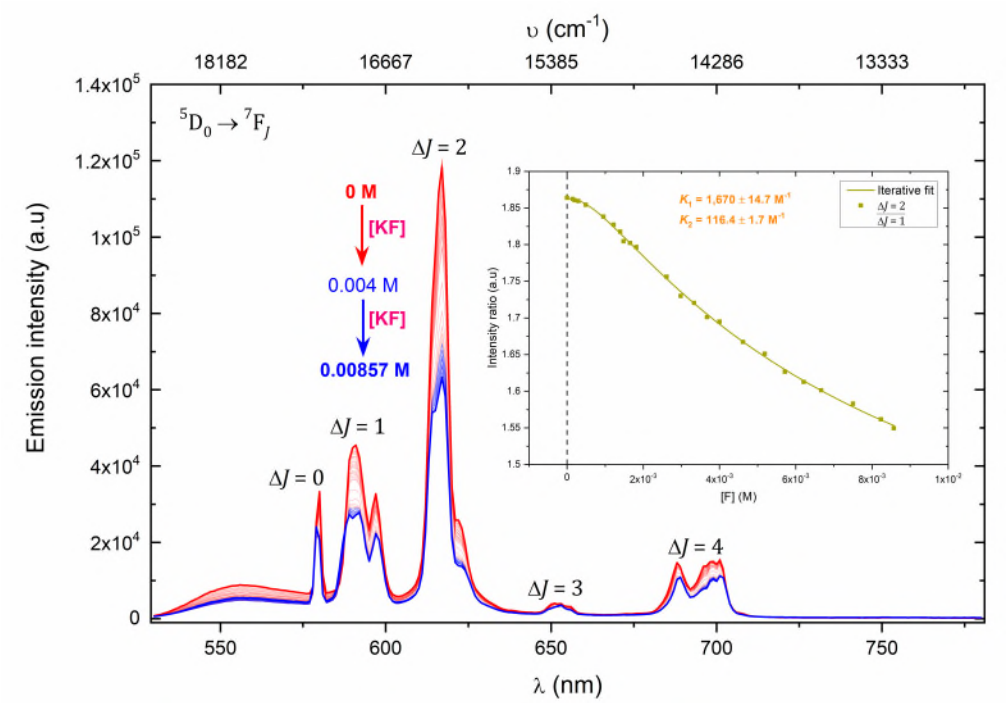


Figure 2.18. Steady-state luminescence titration spectra of [Eu_2(**DO3A**)$_2$**C-3**] with KF in 0.01 M Tris-HCl buffer at pH 7.4; spectrum of neat complex solution (***red in bold***), spectra upon the additions of KF (*red to blue*), spectrum upon the final addition of KF (***blue in bold***). *Inset*: binding isotherm generated from the corresponding titrations.

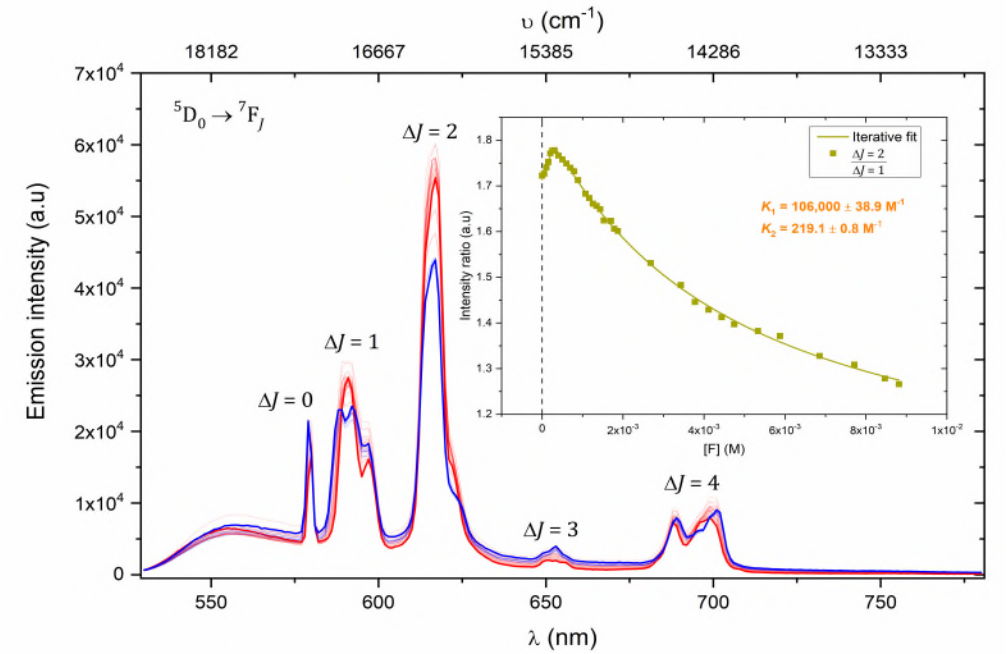


Figure 2.19. Steady-state luminescence titration spectra of [Eu_2(**DO3A**)$_2$**C-2**] with KF in 0.01 M Tris-HCl buffer at pH 7.4; spectrum of neat complex solution (***red in bold***), spectra upon the additions of KF (*red to blue*), spectrum upon the final addition of KF (***blue in bold***). *Inset*: binding isotherm generated from the corresponding titrations.

course of the titration, binding isotherms were generated using selected individual emission wavelengths in $J = 0$ and $J = 1$ transitions were done, but it did not make any difference from the ratiometric analysis.

Fluoride being isoelectronic with hydroxide, can compete against each other in water for the same receptor. This was also studied with the binuclear Eu(III) complexes by titrating them against KF in CHES buffer at pH 9.9. A decrease in the emission intensity was observed during the course of the titration with subtle changes in the shape of the emission bands. A binding isotherm determined ratiometrically from $\Delta J = 1$ and $\Delta J = 2$ from these titrations showed that the C-2 complex had a single binding event (K_1 = 13,600 M^{-1} (±9.9%)) while C-3 complex had up to two binding events (K_1 = 3,840 M^{-1} (±9.6%), K_2 = 3,494 M^{-1} (±2.8%)) with comparable binding strengths (Figure 2.20).

Therefore, from the titrations involving fluoride in neat solvents, up to three binding events were observed (Figure 2.15). In the case of competing (PBS) and non-competing (Tris-HCl) buffering media, no more than two binding events were observed. (Table 2.3) This suggests that fluoride binding suffers from competing ions in buffers which was not the case for chloride binding (Figure 2.21).

Steric factors come into play for the binuclear complexes to accommodate more than one fluoride, but only one for chloride. Fluoride is a smaller ion than other halides (vide Table 2.1) that two or three of them can fit well into the cavity created between the metal centres as the DO3A scaffolds are separated by flexible two or three carbon tether. Furthermore, the stronger affinity for fluoride over chloride with the binuclear complexes in water and methanol can rationalised by the electrostatic interactions between the metal and halide, alongside the thermodynamics of desolvation of the halide ion upon binding with the complexes.

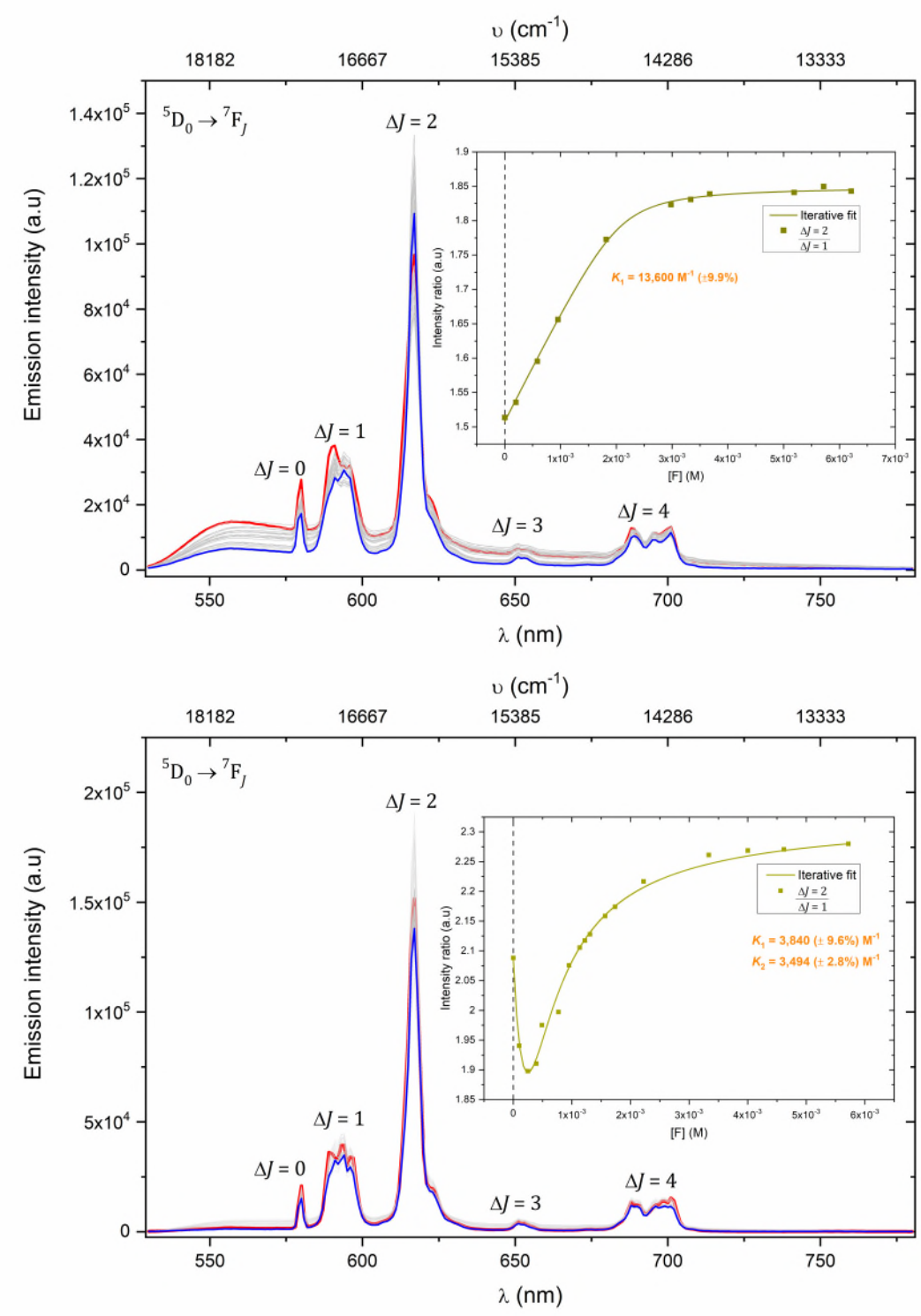


Figure 2.20. Steady-state emission titration spectra of [Eu_2(**DO3A**)$_2$**C-2**] (*top*) and [Eu_2(**DO3A**)$_2$**C-3**] (*bottom*) with KF in 0.01M CHES buffer at pH 9.9. Spectrum of neat complex solution (***red in bold***), spectra upon the additions of KF (*grey*), spectrum upon the final addition of KF (***blue in bold***). *Inset*: binding isotherm generated from the titration spectra.

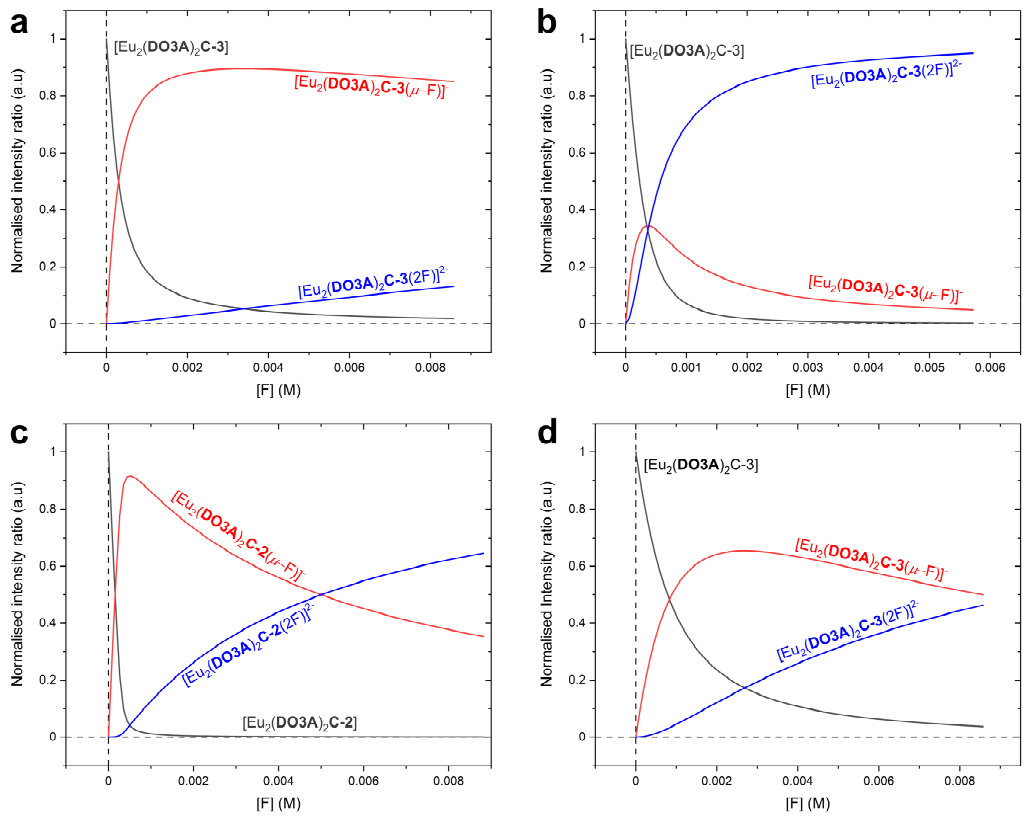


Figure 2.21. Normalised model of speciation for the binding of fluoride to (a) [Eu_2(**DO3A**)$_2$**C-3**] in PBS, (b) [Eu_2(**DO3A**)$_2$**C-3**] in CHES buffer, (c) [Eu_2(**DO3A**)$_2$**C-2**] in Tris-HCl buffer, and (d) [Eu_2(**DO3A**)$_2$**C-3**] in Tris-HCl buffer, obtained by plotting the ratiometric change as a function of the concentration of KF added.

Descending group XVII in the periodic table, the halide ions get larger, decreasing in charge density which has a significant effect on their hydration enthalpy (ΔH_{hyd}), with a less negative ΔG_{hyd} values when descending the group due to contributions from both the enthalpic and entropic terms (vide Table 2.1). Strong electrostatic interaction of fluoride with the solvent results in a greater (more favourable) enthalpic gain upon solvation. Additionally, the entropic term becomes less negative down the group. Chloride has a larger ionic radius and more polarising, implies that there is much less order imposed on the surrounding solvent molecules, hence a more positive (less negative) entropic term is achieved. However, desolvation of the anion must also be considered: descending group XVII in the periodic table, the number of water molecules in the hydration shell decreases (vide

Table 2.1) and upon binding with the lanthanide metal centres, these water molecules are released into the bulk solvent, contributing to a more disordered system. Hence, the entropy of desolvation is greater for fluoride than chloride and thus fluoride binding is more favourable in water and methanol to the proposed binuclear complexes, leading to stronger binding strengths.

2.5.2.5. Chelation of heavier halides to the binuclear Eu(III) complexes

Significant interference from the heavier halides to the binuclear complexes was expected. Therefore, the binuclear Eu(III) complexes were titrated against KBr and KI in deionised water (Figure 2.22). The emission intensity consistently decreased throughout the course of the titration with both the salts. This could be due to the increasing ionic strength upon KBr and KI addition to the charge neutral

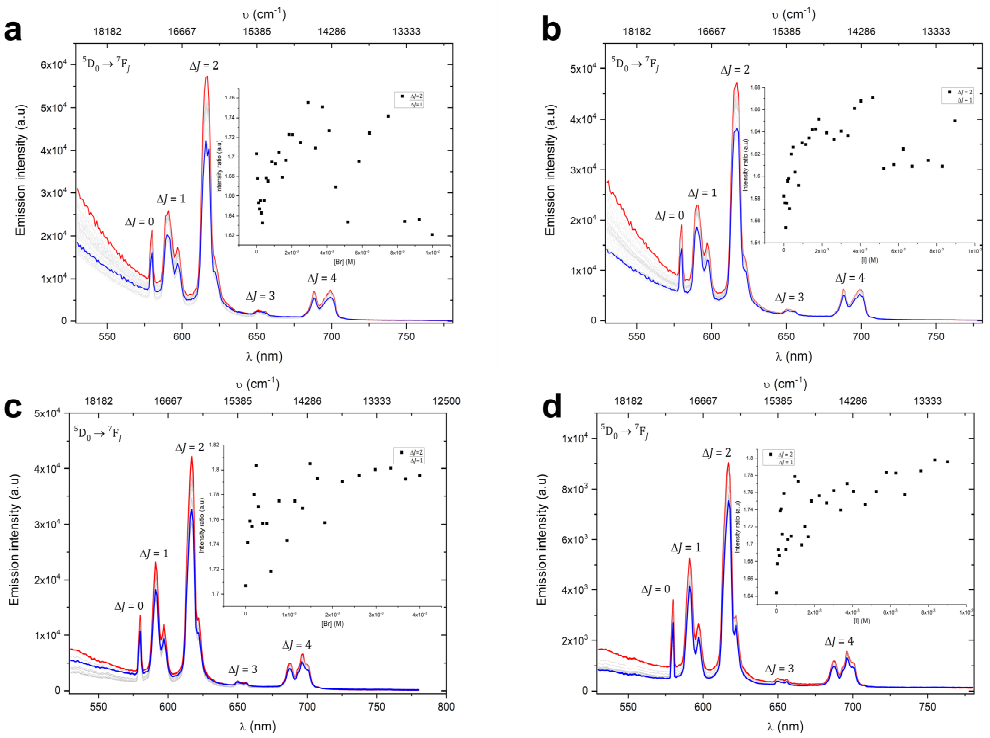


Figure 2.22. Steady-state emission titration spectra of (a) [Eu_2(**DO3A**)$_2$**C-2**] with KBr, (b) [Eu_2(**DO3A**)$_2$**C-2**] with KI, (c) [Eu_2(**DO3A**)$_2$**C-3**] with KBr, and [Eu_2(**DO3A**)$_2$**C-3**] with KI in deionised water. Spectrum of neat complex solution (***red in bold***), spectra upon the additions of halide (*grey*), spectrum upon the final addition of halide (***blue in bold***). *Inset*: ratiometric analysis generated from the corresponding titration spectra.

binuclear complexes. The binding isotherm was difficult to generate, which suggests weak binding of these halides. This data, along with the competing buffer experiments with fluoride, show that the binuclear complexes are highly selective towards chloride.

2.5.2.6. Halide chelation on [Eu(pDO3A)]

The effect of halide association was studied using the mononuclear neutral complex in order to compare the effect of chelation to the binuclear complexes. Kinetically inert [Eu(**pDO3A**)] was used as a model compound. Steady state luminescence titration of this complex with KCl did not result in any observable binding event through ratiometric analysis of $\Delta J = 1$ and $\Delta J = 2$ bands and through analysis of the emission wavelengths in the $\Delta J = 0$ and $\Delta J = 1$ bands (Figure 2.23). No change in the form and shape of the emission spectra was observed. The only observable change was the decrease in emission intensity upon incremental KCl addition, which could probably be due to the increase in ionic strength upon KCl addition to the charge neutral complex. This verifies the hypothesis on chloride chelation in the binuclear complexes (Figure 2.23), where both the metal centres are required to accommodate the chloride in the pre-organised binding pocket.

Although no binding of chloride was observed, the emission intensity was decreasing during the titration which was similar to the titration in the binuclear Eu(III) complexes with bromide and iodide. In order to confirm this change as a consequence of increasing ionic strength and not binding, titration of KBF_4 against [Eu(**pDO3A**)] was performed (KBF_4 does not bind to the complex as verified by NMR analysis). Similar decrease in emission intensity with no change in the fine structure of the emission spectra and no evidence of binding through ratiometric analysis ($\Delta J = 2/\Delta J = 1$) or by analysis of $\Delta J = 0$ and $\Delta J = 1$ emission bands was

observed which confirms the decrease in emission intensity was due to change in ionic strength and not by binding (Titration spectra located in Appendix-A).

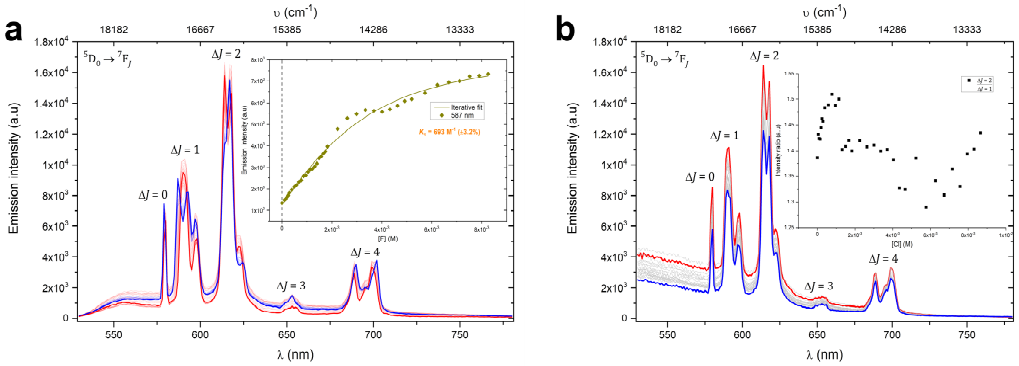


Figure 2.23. (*a*) Steady-state emission titration spectra of [Eu(**pDO3A**)] with KF in deionised water. Spectrum of neat complex solution (***red in bold***), spectra upon the additions of KF (*red* to *blue*), spectrum upon the final addition of KF (***blue in bold***). *Inset*: binding isotherm obtained from plotting the 587 nm emission as a function of KF added. (*b*) Steady-state emission titration spectra of [Eu(**pDO3A**)] with KCl in deionised water. Spectrum of neat complex solution (***red in bold***), spectra upon the additions of KCl (*grey*), spectrum upon the final addition of KCl (***blue in bold***). *Inset*: $\Delta J = 2$ / $\Delta J = 1$ ratiometric analysis as a function of KCl added generated from the titration spectra.

Steady-state luminescence titration of [Eu(**pDO3A**)] with KF was performed in deionised water (Figure 2.23) and MeOH (Figure 2.24). In both cases, the form and shape of the emission spectra was dramatically altered upon the increasing addition of KF. In water, the emission intensity was decreasing at the start followed by an increase during the course of the titration. The binding isotherm generated using 587 nm emission demonstrated a single binding event (Figure 2.23). It is noteworthy that this binding strength (K_1 = 693 M^{-1} (±3.2%)) is exceptionally lower than that of the K_1 binding event in the binuclear complexes with fluoride chelation (Figures 2.11 and 2.12, Table 2.3), further confirming that in the binuclear complexes, the K_1 binding mode involves both the metal sites for fluoride chelation (Figure 2.23). The titration of [Eu(**pDO3A**)] with KF in methanol was much difficult to follow due to the dramatic changes in the emission spectra upon fluoride

chelation (Figure 2.24) which made the binding isotherm, harder to generate. Despite this, a weaker second binding event was observed (K_1 = 5,720 M^{-1} (±6.4%), K_2 = 0.0068 M^{-1} (±1.2%)).

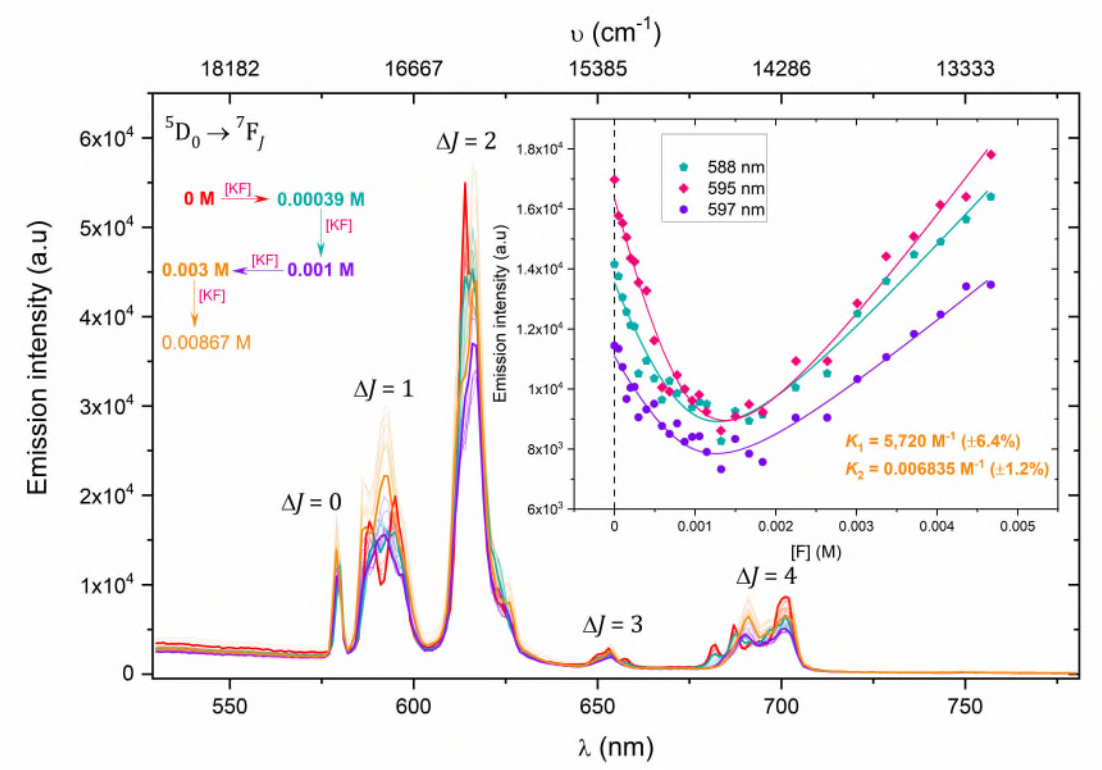


Figure 2.24. Steady-state luminescence titration spectra of [Eu(**pDO3A**)] with KF in methanol; spectrum of neat complex solution (***red in bold***), spectra upon the additions of KF (*red*, ***cyan in bold***, *cyan*, ***violet in bold***, *violet*, ***orange in bold***, *and orange*), spectrum upon the final addition of KF (orange). *Inset*: the binding isotherm for the binding of fluoride to [Eu(**pDO3A**)], obtained by plotting few intensities in the Δ*J* = 1 transition as a function of the concentration of KF in methanol.

From the titrations with the binuclear and mononuclear Eu(III) charge neutral complexes, it is clear that chloride binds to the binuclear cavity which does not occur in the mononuclear model complex. Fluoride chelation was observed in both the C-2 and C-3 complexes. However, it does not need the binuclear binding pocket which chloride demands. Table 2.3 summarises the binding affinities of halides to the mononuclear and binuclear Eu(III) complexes studied in this Chapter.

Table 2.3. Apparent binding constants for the binuclear and mononuclear lanthanide complexes in aqueous media[§]

Halide	Media[‡]	Binding constant (K in M^{-1})[#]	
		[Eu_2(**DO3A**)$_2$**C-2**]	[Eu_2(**DO3A**)$_2$**C-3**]
Cl^-	Water	K_1 = 2,800 ± 200	K_1 = 4,550 ± 180
	PB	K_1 = 9,400 ± 1,100	K_1 = 6,640 ± 490
	CHES	K_1 = 7,460 ± 830	K_1 = 12,210 ± 860[†]
F^-	Water	K_1 = 10,480 ± 620 K_2 = 10,950 ± 440 K_3 = 6,570 ± 240	K_1 = 600,000 ± 240,000 K_2 = 144,000 ± 48,000 K_3 = 394.9 ± 9.1
	Methanol	K_1 = 54,800 ± 6,400 K_2 = 20,200 ± 2,100 K_3 = 0.002843 ± 1.8 × 10^{-5}	K_1 = 179,000 ± 24,000 K_2 = 32,000 ± 4,100 K_3 = 728 ± 55
	PBS	K_1 = 4,030 ± 120	K_1 = 5,350 ± 370 K_2 = 18.57 ± 0.18
	Tris-HCl	K_1 = 106,000 ± 41,000 K_2 = 219.1 ± 1.7	K_1 = 1,670 ± 250 K_2 = 116.4 ± 1.9
	CHES	K_1 = 13,600 ± 1,300	K_1 = 3,840 ± 370 K_2 = 3,494 ± 97
Halide	Media	Binding constant (K in M^{-1})[#] for [Eu(**pDO3A**)]	
F^-	Water	K_1 = 693 ± 22	
	Methanol	K_1 = 5,720 ± 370; K_2 = 0.00068 ± 8.2 × 10^{-5}	

[§] The binding of halides with the complexes were studied by steady-state luminescence titrations with varying concentration of potassium halides and binding isotherm generated using DYNAFIT®.

[†] Titration performed in time-resolved phosphorescence mode.

[‡] All buffers were maintained at 0.01 M in deionised water: PBS = phosphate buffer saline at pH 7.4; PB = phosphate buffer at pH 7.4; CHES = *N*-cyclohexyl-2-aminoethane- sulfonic acid at pH 9.98; Tris-HCl = *tris*(hydroxymethyl)aminomethane hydrochloride at pH 7.4.

[#] K_1 = first binding event; K_2 = second binding event; K_3 = third binding event-deduced from binding isotherm generated using DYNAFIT®.

± is the standard error for each binding event obtained from the best-fitted binding isotherm plotted in DYNAFIT® by employing trust-region algorithm in confidence interval at 95% probability level.

2.5.2.7. Luminescence lifetime of binuclear and mononuclear complexes with halides

Time resolved luminescence lifetime with the mono- and binuclear Eu(III) complexes were determined in water, MeOH, and their deuterated counterparts upon increasing addition of KF (Tables 2.4 to 2.6). The increase in luminescence lifetime and the corresponding decrease in hydration number accounted for the replacement of the inner-sphere water by fluoride. The hydration number was calculated using the modified Horrocks′ equation (in Chapter-I eq 1.8). Table of luminescence lifetime in MeOH and all lifetime spectra are presented in Appendix-A.

Table 2.4. Luminescence lifetime of [Eu_2(**DO3A**)$_2$**C-2**] with increasing addition of KF in H_2O and D_2O* (Stock conc of host is 1 mM, KF in stock is 0.02 M)

Complex and amount of KF added	Lifetime in H_2O (ms)	Lifetime in D_2O (ms)	Hydration number (q)
Complex	0.31	1.55	2.8
Complex + 50 μL KF	0.57	1.7	1.1
Complex + 200 μL KF	0.6	1.71	1
Complex + 1000 μL KF	0.66	1.63	0.8

* All lifetime values are subject to an error of ±10%.

Table 2.5. Luminescence lifetime of [Eu_2(**DO3A**)$_2$**C-3**] with increasing addition of KF in H_2O and D_2O* (Stock conc of host is 1 mM, KF in stock is 0.02 M)

Complex and amount of KF added	Lifetime in H_2O (ms)	Lifetime in D_2O (ms)	Hydration number (q)
Complex	0.48	1.68	1.5
Complex + 50 μL KF	0.48	1.7	1.5
Complex + 250 μL KF	0.51	1.8	1.4
Complex + 1500 μL KF	0.54	1.88	1.3

* All lifetime values are subject to an error of ±10%.

However, when the luminescence lifetime was recorded for the binuclear Eu(III) and Tb(III) complexes with increasing addition of KCl in H_2O and D_2O, no change in the luminescence lifetime observed. While it is unknown on the reason behind it, this effect could be possibly due to a counteracting influence between PeT effect from chloride and intermetallic luminescence quenching.[49]

Table 2.6. Luminescence lifetime of [Eu(**pDO3A**)] with increasing addition of KF in H_2O and D_2O* (Stock conc of host is 1 mM, KF in stock is 0.02 M)

Complex and amount of KF added	Lifetime in H_2O (ms)	Lifetime in D_2O (ms)	Hydration number (q)
[Eu(**pDO3A**)]	0.38	1.98	2.2
[Eu(**pDO3A**)] + 50 μL KF	0.35	2.01	2.5
[Eu(**pDO3A**)] + 200 μL KF	0.45	1.98	1.7
[Eu(**pDO3A**)] + 1500 μL KF	0.59	2.11	1.2

* All lifetime values are subject to an error of ±10%.

2.5.3. NMR Studies on Lanthanide Complexes

2.5.3.1. NMR studies at basic pD

[Ln(**DO3A**)] complexes are known to bind hydroxide at basic pH.[42,46] Therefore, hydroxide binding in the binuclear complexes were examined by ^{1}H NMR spectroscopy at varying pD. At neutral pD, the NMR spectra of the Yb(III) binuclear complexes consist of broad lines; however, at pD 10.12, the lines are sharp and well-defined (Figure 2.25), which could be ascribed to the slow rate of interconversion between the diastereomeric forms of the complexes (Figures 2.25). Similar results were observed in the ^{1}H NMR spectra with the binuclear Eu(III) complexes which is located in Appendix-A.

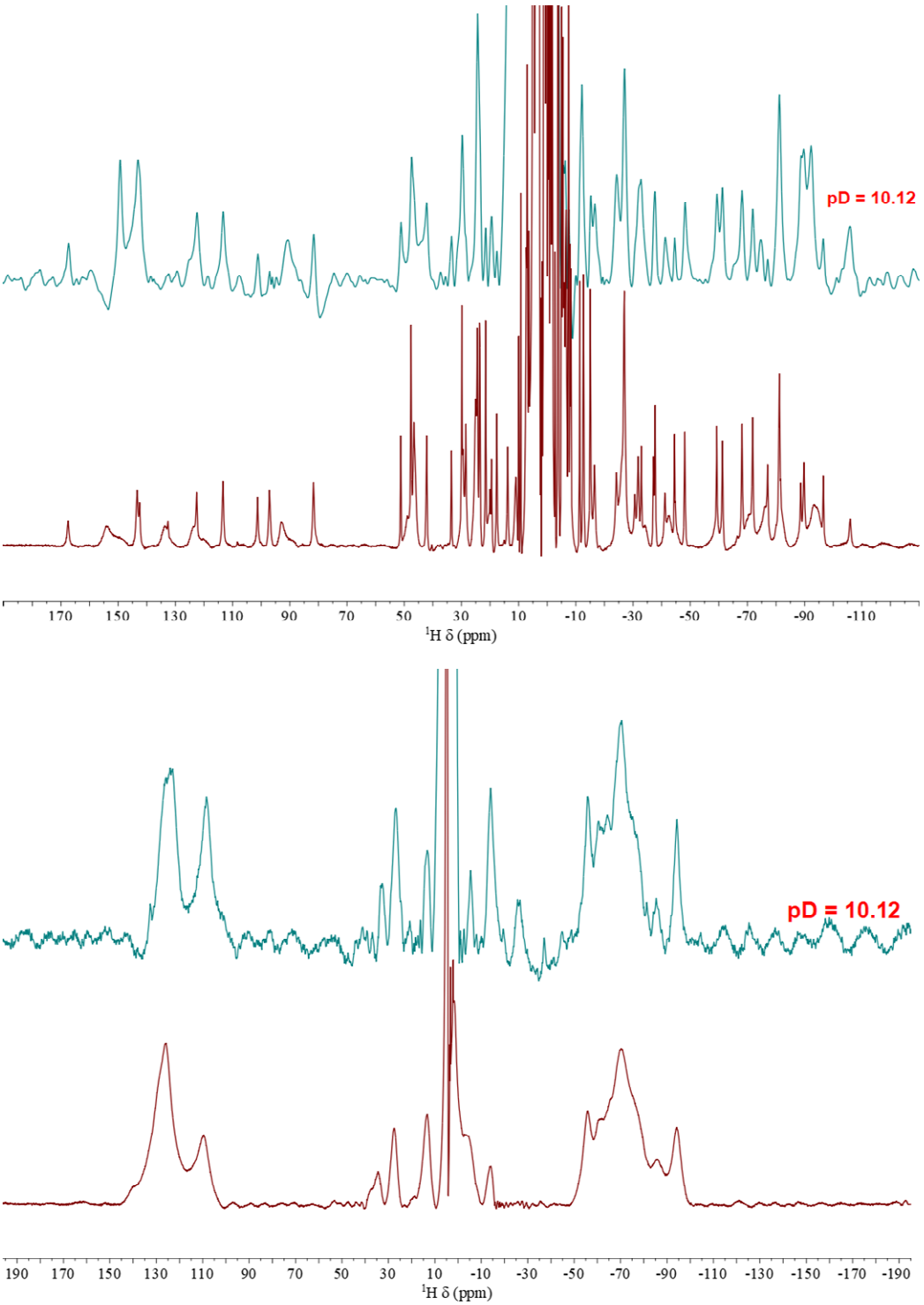


Figure 2.25. ^{1}H NMR spectra of [Yb_2(**DO3A**)$_2$**C-2**] (*top*) and [Yb_2(**DO3A**)$_2$**C-3**] (*bottom*) in D_2O and at pD 10.12.

^{1}H NMR spectra of the Eu(III) and Yb(III) complexes were recorded in D_2O with increasing addition of fluoride. The broad spectra of the complexes sharpen upon increasing addition of fluoride. For example, the ^{1}H NMR spectra of [Yb_2(**DO3A**)$_2$**C-2**] and [Yb_2(**DO3A**)$_2$**C-3**] with increasing KF addition are shown in Figures 2.26 and 2.27. The NMR spectral window had to be increased to accommodate new signals arising upon the addition of fluoride; this was observed more in Yb(III) complexes in both mononuclear and binuclear complexes. This expansion of the NMR window upon fluoride chelation suggests equatorial fluoride binding with respect to the metal centre; axial binding of fluoride commonly results in a decrease or inversion of the local crystal field by destabilising axially oriented m_J states, while equatorial binding destabilises other m_J states.[28-33] The ^{1}H NMR spectra of [Yb_2(**DO3A**)$_2$**C-2**] and [Yb_2(**DO3A**)$_2$**C-3**] with increasing KF in D_2O are depicted in Figures 2.26 and 2.27. The ^{1}H NMR spectra of Eu(III) complexes upon fluoride addition and at pD 10.12 with added fluoride are presented in Appendix-A.

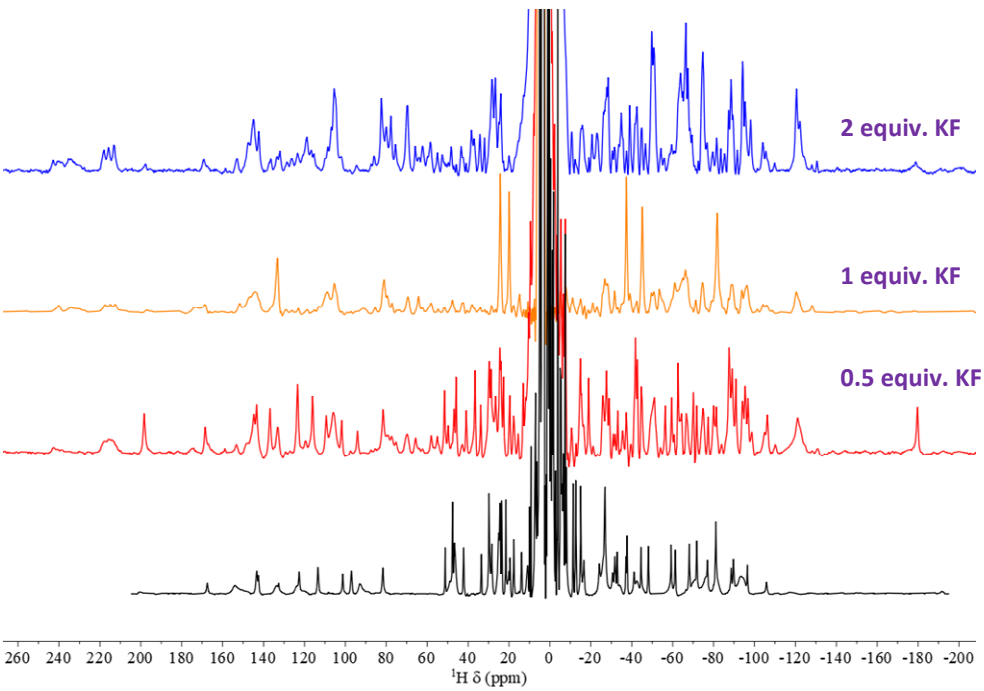


Figure 2.26. ^{1}H NMR spectra of [Yb_2(**DO3A**)$_2$**C-2**] with increasing KF in D_2O.

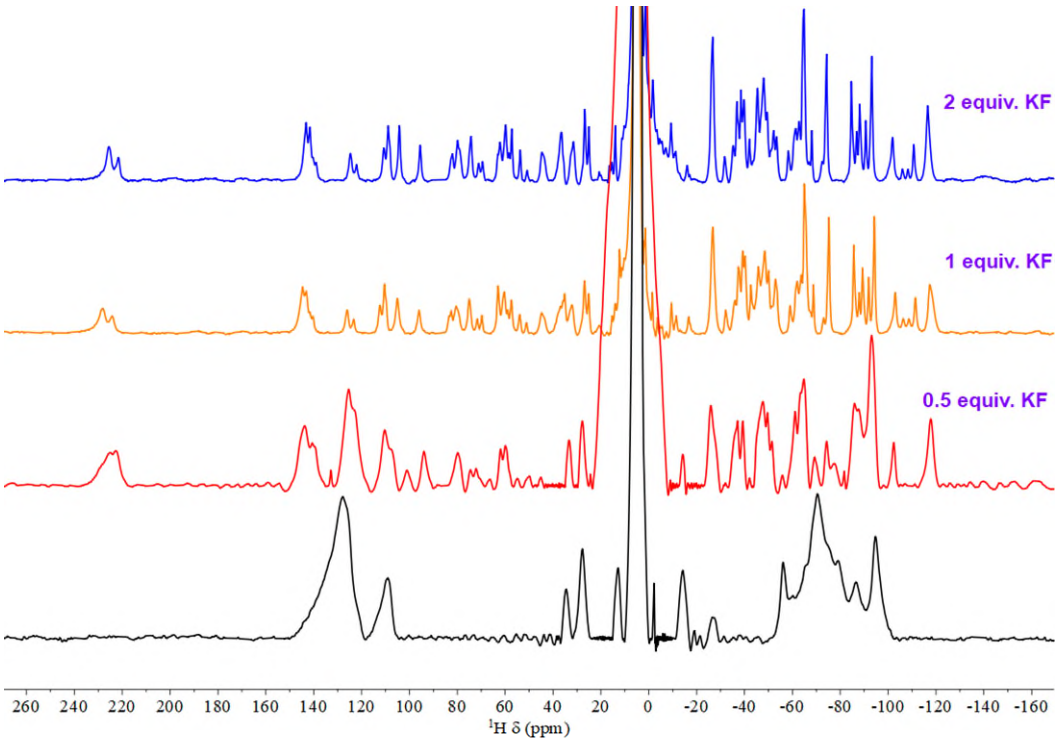


Figure 2.27. ^{1}H NMR spectra of [Yb_2(**DO3A**)$_2$**C-3**] with increasing KF in D_2O.

Since fluoride is isoelectronic to hydroxide (Table 2.1), the ^{1}H NMR spectra of the binuclear Eu(III) and Yb(III) complexes with added KF were recorded at pD 10.12. The signals are distinctively sharper from the hydroxide and are well resolved to observe fluoride chelation at basic pD (spectra located in Appendix-A). In the case of [Yb(**pDO3A**)], the NMR signals are well-resolved and the NMR window expands similar to the binuclear Yb(III) complexes (Figure 2.28). However, some signals were found to be inverted at 2 equiv of fluoride addition which was not observed in the binuclear complexes. This suggests the axial binding of fluoride (in addition to the existing equatorially bound fluoride) at higher concentration of KF. Paramagnetic ^{1}H NMR spectra of [Eu(**pDO3A**)] with added KF in H_2O, and [Yb(**pDO3A**)] complexes with added KF in MeOH are presented in Appendix-A.

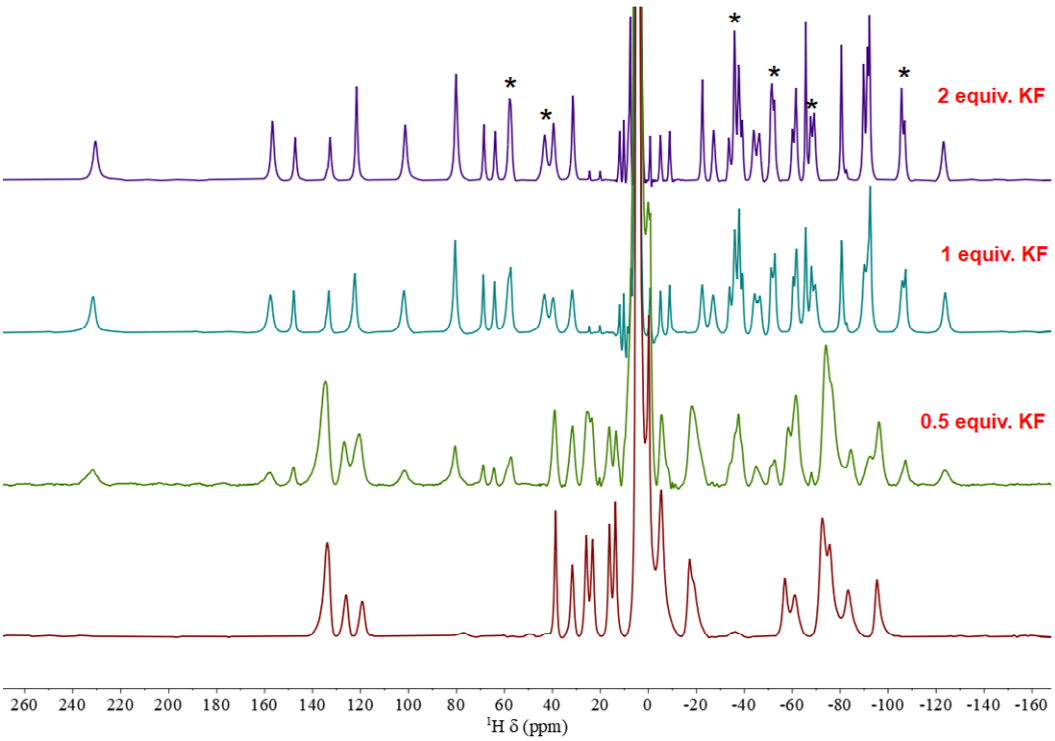


Figure 2.28. ^{1}H NMR spectra of [Yb(**pDO3A**)] with increasing KF in D_2O. Signals which invert during the course of the titration are highlighted with asterisk (*) on the spectrum recorded with 2 equiv of KF added to the complex.

2.5.3.2. Fluorine NMR studies to explore fluoride binding

Chelation of fluoride to the complexes were further studied using ^{19}F NMR. Fluoride bound signals in mononuclear Eu(III) complexes have been reported to be around −450 ppm.[28-34] Here, the Eu(III) bound fluoride both in the mono- and binuclear complexes displays a signal around −450 ppm and no other bound fluoride signals were observed in all the three systems (Figure 2.29). Mononuclear Yb(III) complexes are reported to have a bound fluoride signal at around −900 ppm,[28] but it was not observed in any of the Yb(III) complexes reported in this work (for reasons unknown), probably due to lack of skill in recording one in high sweep-width range.

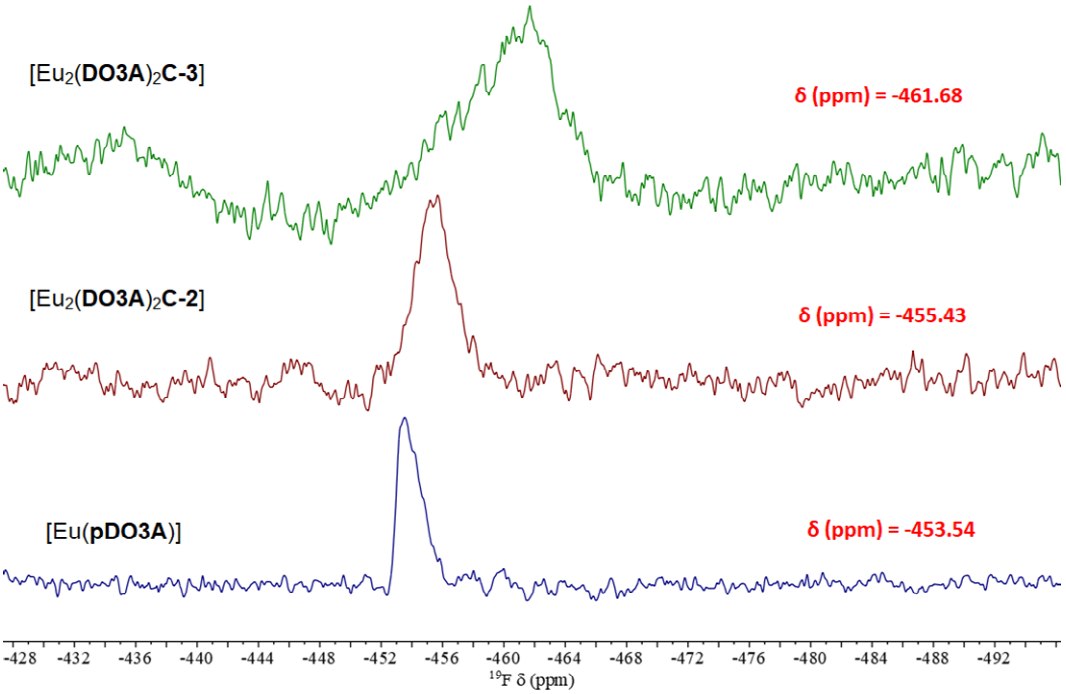


Figure 2.29. Stacked ^{19}F NMR spectra of binuclear and mononuclear Eu(III) complexes with 5 equiv KF in D_2O. Chemical shift of the bound fluoride is shown in red. Spectral window is adjusted only to see the bound fluoride shift.

Yttrium is a transition metal. However, it has similar properties to lanthanides than those of *d*-block metals. Therefore, it is regarded as a lanthanide metal. ^{89}Y is a naturally occurring isotope with 100% natural abundance and a nuclear spin quantum number (I) of ½.[54] The ^{19}F NMR and ^{89}Y-^{19}F HMBC 2D NMR spectra of fluoride bound [Y(**DTMA**)]$^{3+}$ complex was recorded to study the cross peaks associated with fluoride bound to the yttrium centre.[28b] This is due to the splitting of the bound fluoride resonance into a doublet. For the binuclear complexes described herein, it was expected that multiple bound fluoride resonances would be present due to multiple fluoride interaction inferred from the steady-state luminescence titrations, and cross peak examination using ^{89}Y-^{19}F HMBC NMR would shed light on the coordination mode of fluoride in detail.

The ^{19}F NMR spectrum of [Y_2(**DO3A**)$_2$**C-3**] in D_2O in the presence of 0.5 equiv of KF contains two weak fluoride bound resonances at −38.2 and −52.1 ppm. Lowering the temperature to 282 K and increasing the concentration of KF to 5 equiv resulted in intense signals, but no splitting of those signals was observed (Figure 2.30).

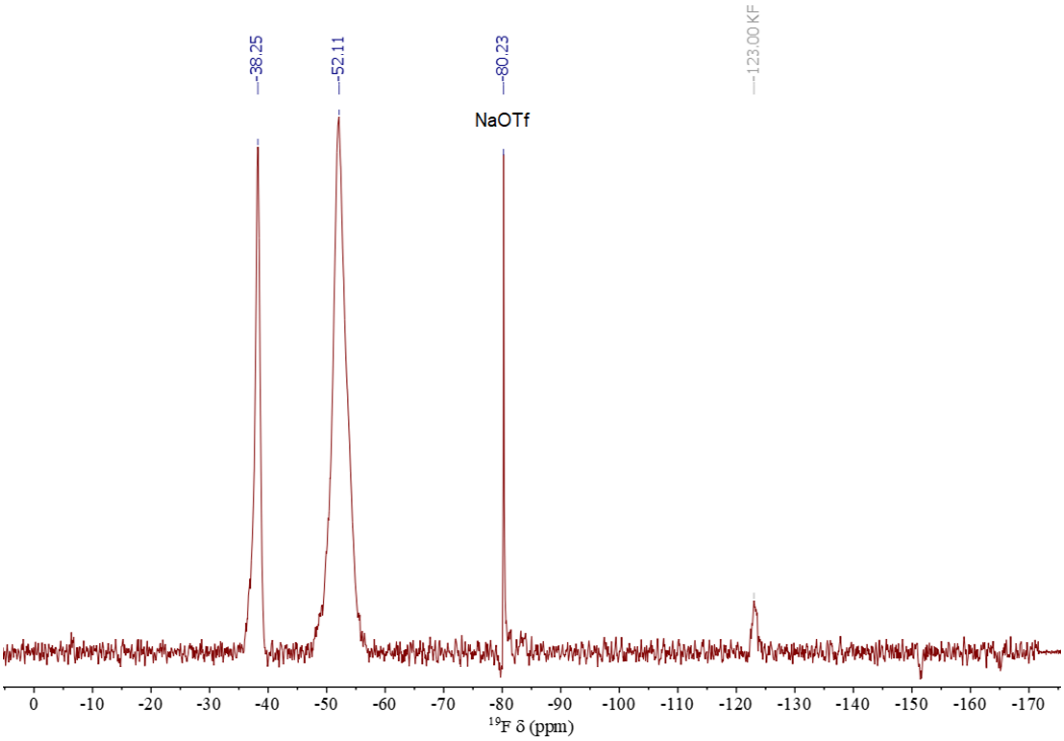


Figure 2.30. ^{19}F NMR spectrum of [Y_2(**DO3A**)$_2$**C-3**] with 5 equiv KF in D_2O at 282 K.

The ^{19}F NMR spectra of [Y_2(**DO3A**)$_2$**C-3**] in MeOD at 298 and 282 K in the presence of KF (0.5 equiv) showed signals which were too weak to interpret. The ^{19}F NMR spectra were recorded up to 231 K in MeOD with KF (2 equiv) added, but no splitting observed, and therefore the 2D NMR was not recorded. However, a weak splitting of the signal at −59.9 ppm was observed (Figure 2.31). Due to the rapid exchange between the isomeric forms of the complex, the energy barrier to overcome the exchange is too low and therefore, a sharp ^{19}F signal of fluoride bound

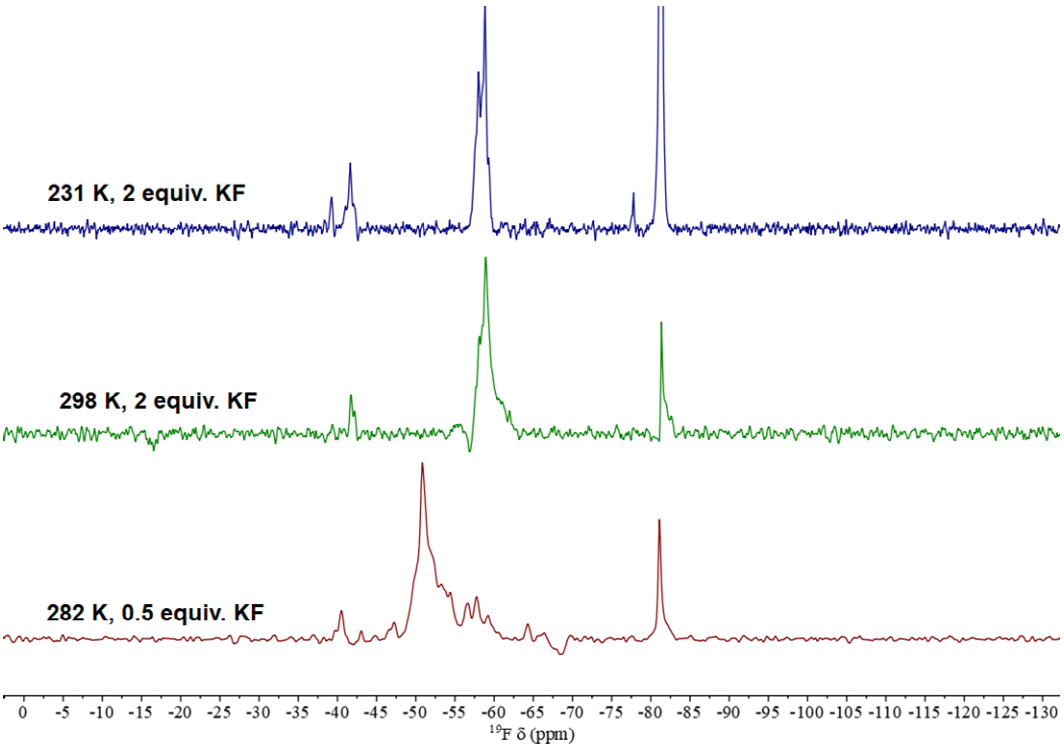


Figure 2.31. Stacked ^{19}F NMR spectra of [Y_2(**DO3A**)$_2$**C-3**] with KF in MeOD at varying temperature and concentration of KF.

to Y(III) centre with splitting could not be observed. This is complemented by the ^{19}F NMR spectra of [Y(**pDO3A**)] in D_2O and MeOD at 298 K, where the splitting of the fluoride resonance bound to the Y(III) centre could not be observed due to

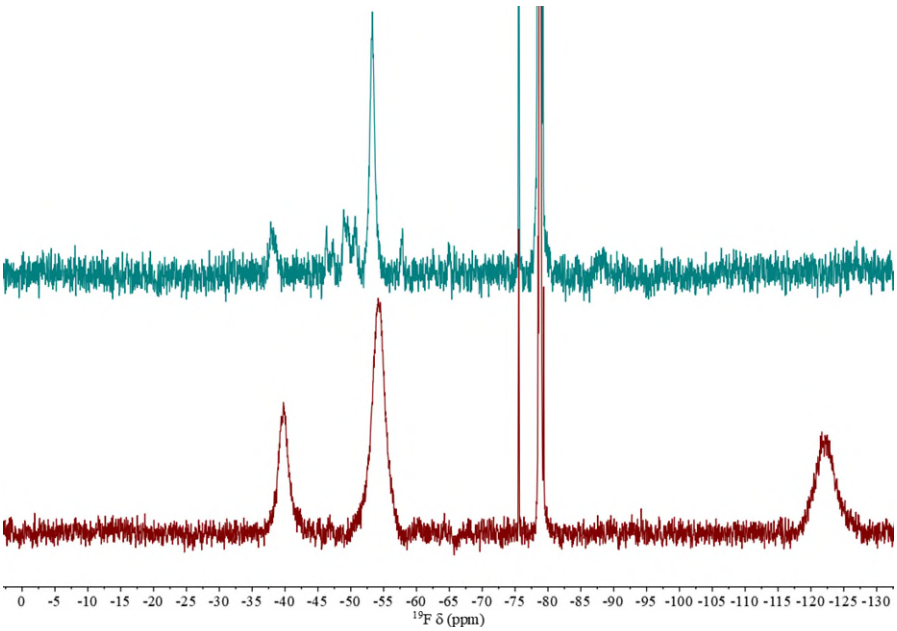


Figure 2.32. Stacked ^{19}F NMR spectra of [Y(**pDO3A**)] with 5 equiv KF in D_2O (*bottom*) and MeOD (*top*).

rapid exchange between the isomeric forms, which is characteristic of the complexes of this heptadendate ligand (Figure 2.32). However, these experiments must be repeated in future by recording the NMR at 193 K in a hope to sharpen the signals in order to pull out more information from the splitting of the ^{19}F signals.

2.5.3.3. Chlorine NMR studies to explore chloride binding

The NMR studies of chloride binding at the paramagnetic lanthanide centre present difficulties due to the interference of the quadrupolar relaxation from the low symmetry ^{35}Cl nucleus with the paramagnetic metal centre resulting in broad ^{1}H and ^{35}Cl NMR signals. However, dipolar ^{35}Cl NMR chemical shifts induced by the Tb(III) complexes give fairly well-resolved ^{35}Cl NMR spectra; the axially symmetric [Ln(**DOTA**)]$^{-}$ complexes [Ln = Tb(III) and Dy(III)] were reported to be good dipolar ^{35}Cl NMR shift reagents (Figure 2.33).[55] This can be interpreted as evidence of interaction with chloride. While the ^{1}H NMR spectra are too broad to

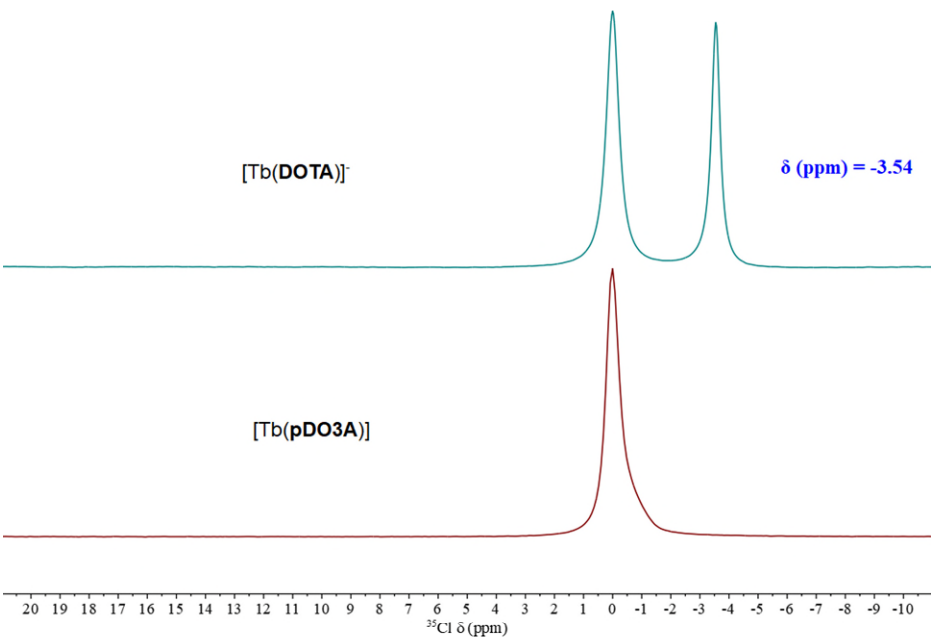


Figure 2.33. ^{35}Cl NMR spectra of [Tb(**pDO3A**)] and [Tb(**DOTA**)]$^{-}$ with 5 equiv KCl in D_2O. Spectra were recorded with a capillary tube insert containing saturated KCl in D_2O. [Tb(**DOTA**)]$^{-}$ made by Dr. Grace McMullon.

draw any conclusions, the ^{35}Cl NMR spectrum of [Tb(**pDO3A**)] with KCl in D_2O did not contain any resonance for bound chloride, but the free chloride shift (at 0 ppm) (Figure 2.33). Thus, it is concluded that no chloride binding was observed for the charge neutral, mononuclear lanthanide complex.

The ^{35}Cl NMR spectra of binuclear [Tb_2(**DO3A**)$_2$**C-2**] and [Tb_2(**DO3A**)$_2$**C-3**] complexes were recorded with increasing addition of KCl in D_2O (Figures 2.34 and 2.35). Chloride bound signals were observed at 6.8 and 11.19 ppm for the C-2 and C-3 complexes, respectively. These signals were downshifted with increasing KCl addition, which is ascribed to fast exchange between the bound and free chloride. Binding of chloride is equatorial with respect to the metal centre as the bound signal is on the positive region of the NMR timescale, while [Tb(**DOTA**)]$^-$ has axial chloride bound shift in the negative region of the NMR timescale.[55] This reported

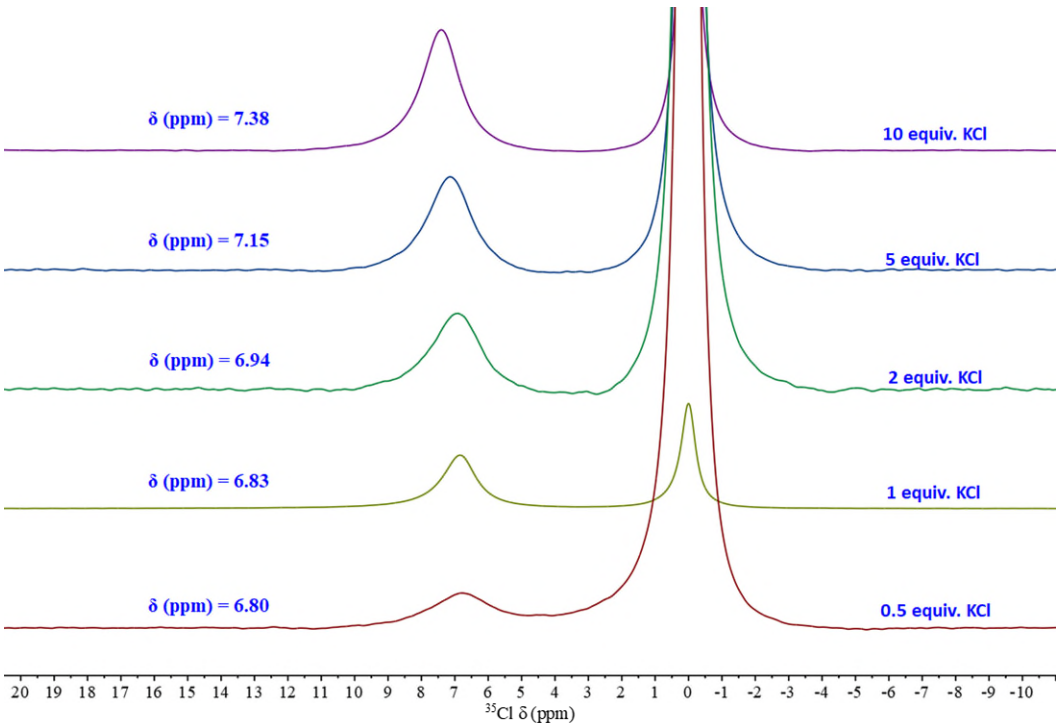


Figure 2.34. Stacked ^{35}Cl NMR spectra of [Tb_2(**DO3A**)$_2$**C-2**] with increasing KCl in D_2O. The highlighted chemical shift values correspond to the bound chloride shift which is in exchange with the bulk chloride at 0 ppm. Spectra were recorded with a capillary tube insert containing saturated KCl in D_2O.

data was verified by ^{35}Cl NMR of [Tb(**DOTA**)]$^{-}$ with 5 equiv of KCl added, where the axial bound chloride resonance, which exchanges with bulk chloride, was found at -3.5 ppm (Figure 2.33).

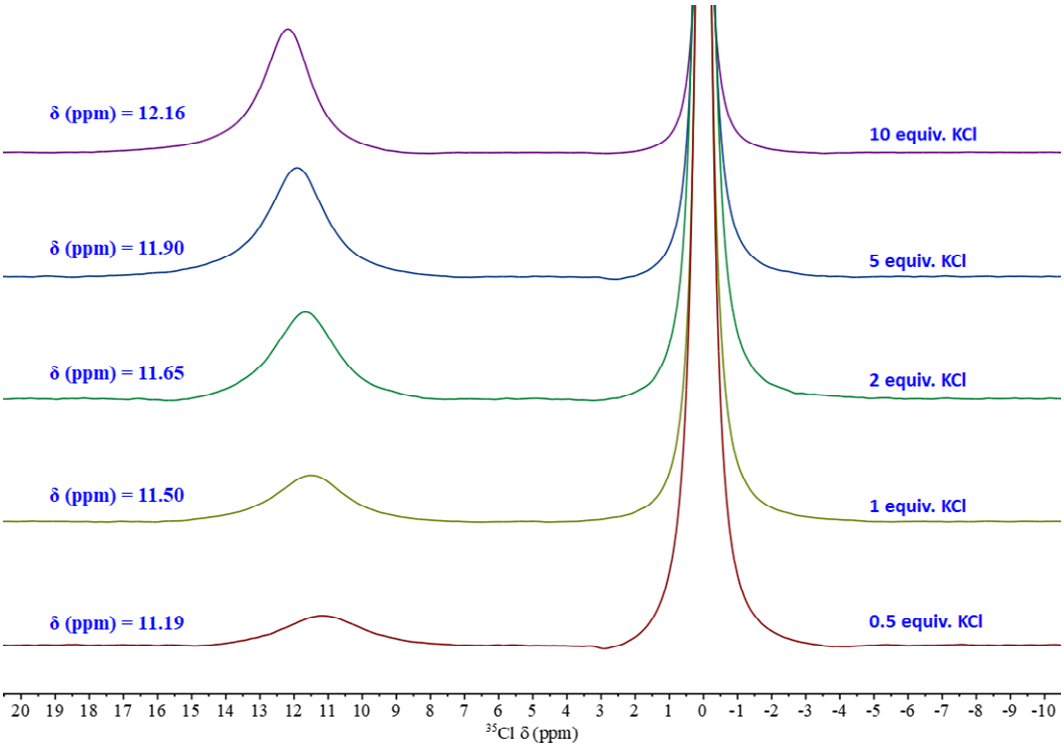


Figure 2.35. Stacked ^{35}Cl NMR spectra of [Tb$_2$(**DO3A**)$_2$**C-3**] with increasing KCl in D_2O. The highlighted chemical shift values correspond to the bound chloride shift which is in exchange with the bulk chloride at 0 ppm. Spectra were recorded with a capillary tube insert containing saturated KCl in D_2O.

2.5.4. Mass Spectral Studies of Halide Binding with Lanthanide Complexes

Association of the halides to the complexes were pursued by HRMS. ESI-MS of chloride-bound C-2 and C-3 binuclear Eu(III) complexes show peaks at *m/z* 1051.1486 and *m/z* 1065.1640, respectively. The calculated isotopic distribution pattern of the mass spectral peaks further supports the formation of the ternary complexes [Ln$_2$(**DO3A**)$_2$**C-2**(μ-Cl)]$^{-}$ and [Ln$_2$(**DO3A**)$_2$**C-3**(μ-Cl)]$^{-}$. The observed

and simulated ESI-mass spectra of the chloride bound ternary complexes are depicted in Figure 2.36.

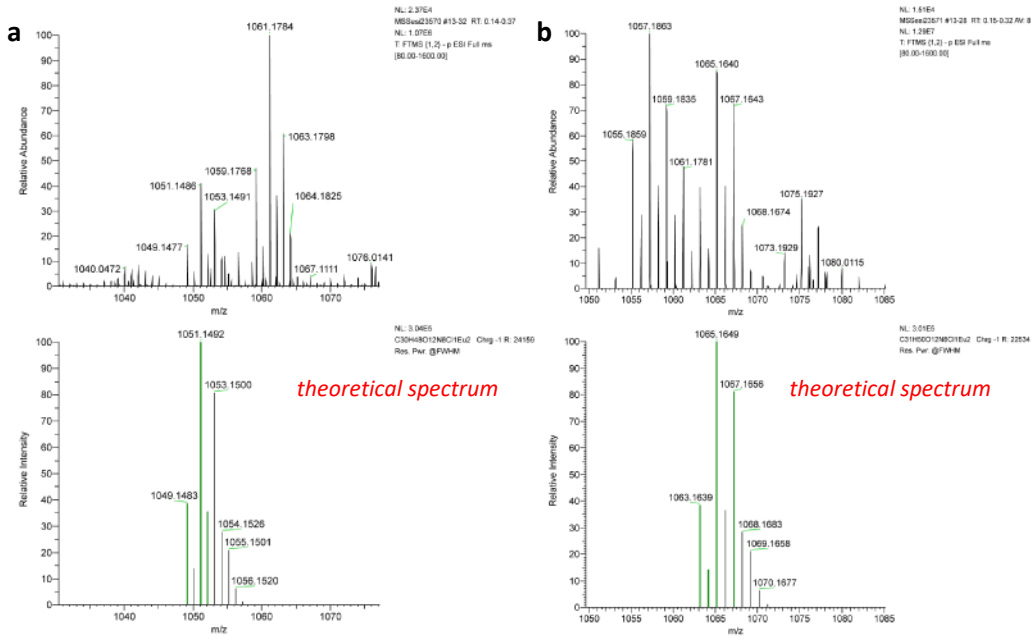


Figure 2.36. Observed and simulated ESI-Mass spectra of (a) $[Eu_2(\mathbf{DO3A})_2\mathbf{C\text{-}2}(\mu\text{-Cl})]^-$ and (b) $[Eu_2(\mathbf{DO3A})_2\mathbf{C\text{-}3}(\mu\text{-Cl})]^-$ in deionised H_2O.

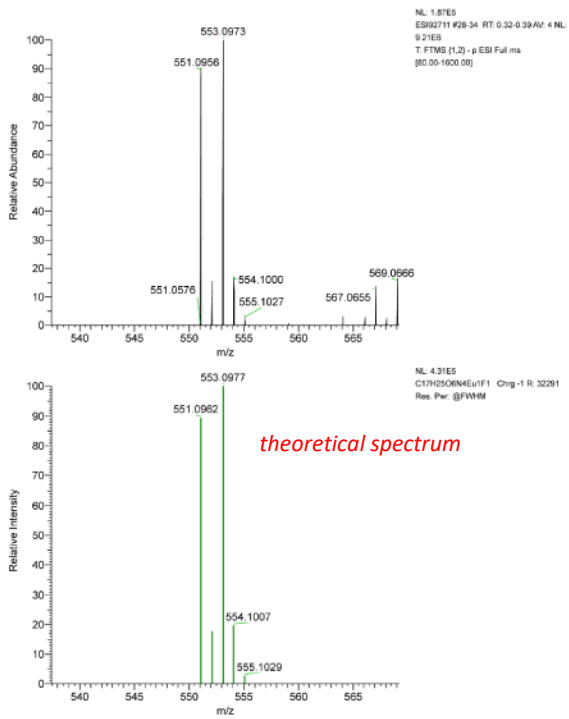


Figure 2.37. Observed and simulated ESI-Mass spectra of $[Eu(\mathbf{pDO3A})F]^-$ in deionised H_2O.

Association of fluoride to the binuclear Eu(III) complexes were studied by ESI-MS and MALDI-MS, but no fluoride bound species was observed. The concentration of fluoride added to the host binuclear complexes was gradually increased to capture the mass of any bound species as inferred from steady-state emission titration and speciation models, but in vain. However, ESI-MS peak for the mononuclear [Eu(**pDO3A**)] bound to fluoride was observed at *m/z* 553.0973 and consistent with the calculated isotopic distribution pattern. This supports the formation of the ternary fluoro complex [Eu(**pDO3A**)F]$^{-}$ (Figure 2.37).

2.5.5. X-Ray Crystal Structures of Anions-Bound Lanthanide Complexes

Single crystals of [Yb_2(**DO3A**)$_2$**C-3**(2F)]$^{2-}$ for X-ray diffraction was obtained by slow diffusion of glyme over concentrated solution of [Yb_2(**DO3A**)$_2$**C-3**] with added KF in D_2O (Figure 2.38). The crystal structure is identical to the K_2 binding mode determined through steady-state titrations and the corresponding speciation

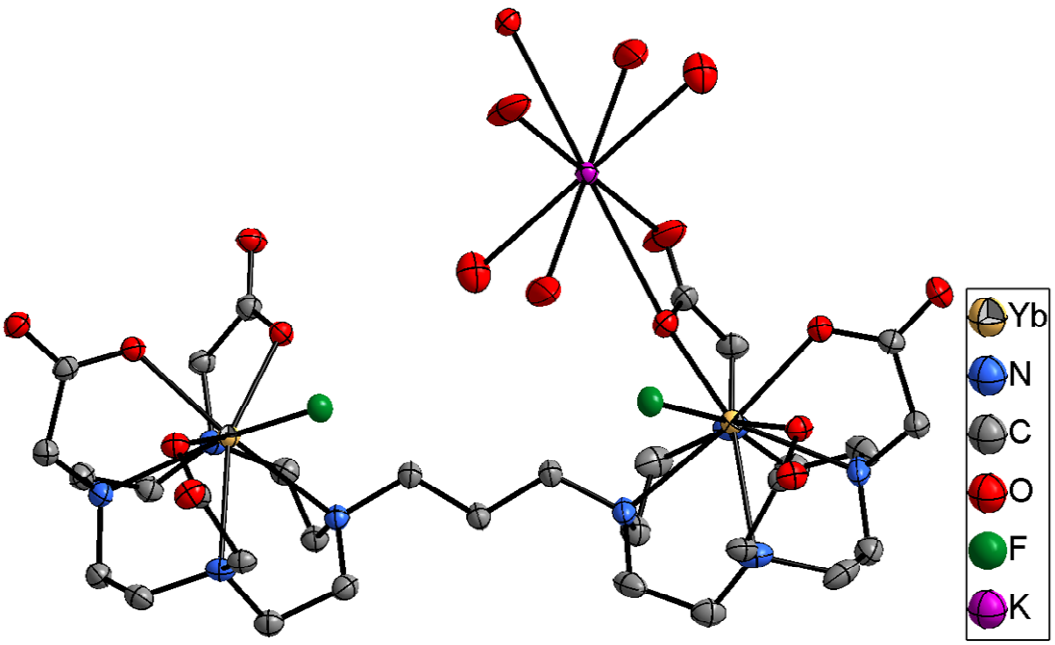


Figure 2.38. Single crystal X-ray structure of [Yb_2(**DO3A**)$_2$**C-3**(2F)]$^{2-}$. H atoms and water are omitted for clarity. Thermal ellipsoid drawn at 30% probability level. X-ray crystal structure was solved by Dr. Kirsten Christensen, Chemical Crystallography, University of Oxford.

models. However, only one potassium is available to balance the charge of the fluoride bound structure which was difficult to rationalise (Figure 2.38).

The concentration of KF added to the binuclear complexes were altered in an attempt to crystallise the complexes in other binding modes of fluoride, but in one such attempt, [Eu_2(**DO3A**)$_2$**C-2**] crystallised with a carbonate bound to one of the metal centres (Figure 2.39). It was obtained under the same solvent system as mentioned above. The source of carbonate is likely from an old open bottle of D_2O which was used to setup this crystallisation. Two potassium cations were found to neutralise the charge of the carbonate bound complex.

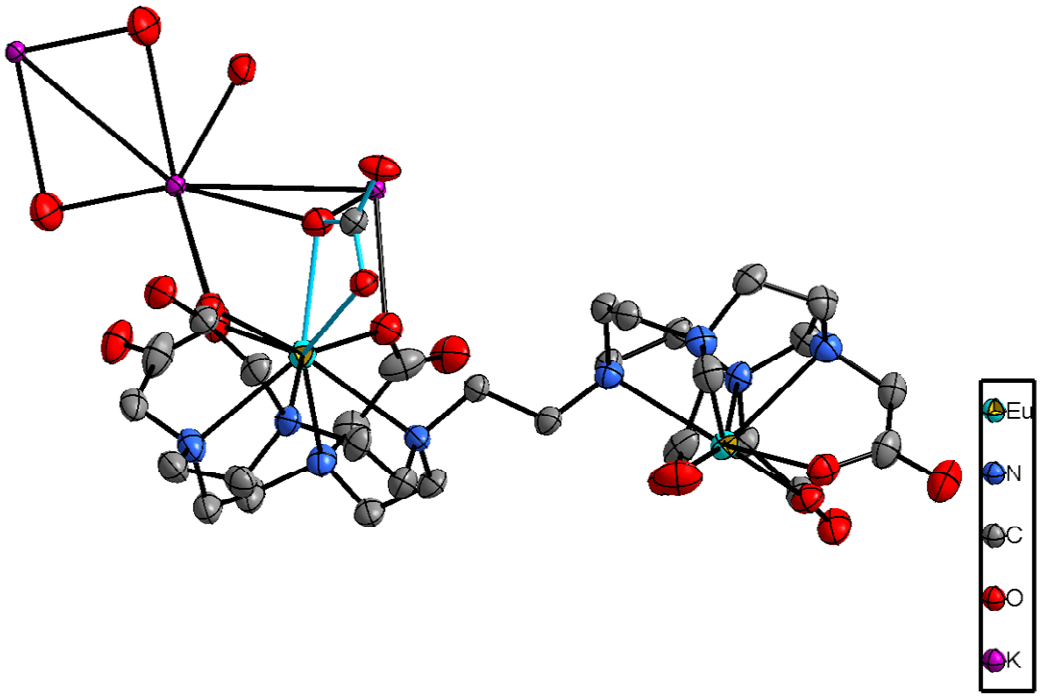


Figure 2.39. Single crystal X-ray of [Eu_2(**DO3A**)$_2$**C-2(**CO_3)]$^{2-}$. Thermal ellipsoid drawn at 30% probability level. Carbonate chelation to the metal shown in **sky-blue** coloured bond. X-ray crystal structure was solved by Dr. Kirsten Christensen, Chemical Crystallography, University of Oxford.

The equatorial chelation of carbonate to the metal centre is not surprising. In fact, this type of interaction was reported (this system was discussed for phosphate binding in Chapter-I, Section 1.6.5.1), where the binuclear

[Ln_2(**DO3AM**)$_2$] complex, bridged by *p*-xylene binds to a carbonate in a consecutive two binding event, however weakly (K_1 = 0.1 μM, K_2 = 95 μM).[51] A similar binding mode is expected in the binuclear complexes reported here because of the presence of two heptadentate acceptors, similar to the reported variant. Moreover, the presence of amides strengthens carbonate binding through H-bonding which is not possible in the binuclear systems explored in this chapter: it is not possible for the carbonate to chelate by bridging the metal centres because of the smaller binding pocket between the metal centres. Even for [Ln_2(**DO3AM**)$_2$] based binuclear complex, carbonate did not bind between the metal centres whose complex has a bigger pocket than the binuclear complex under study in this chapter.

Therefore, for strong carbonate binding, large intermetallic distance is required to host the carbonate between the acceptors which is clearly not offered by the binuclear complexes under study. This applies to phosphate coordination too, as the *p*- and *m*-xylene spacers offers the space to accommodate a phosphate strongly between the DO3A based domains and not by the ethane and propane spacers used in this study. Also, carbonate binding is stronger at basic pH (mentioned in Chapter-1, Section 1.6.5.1) when coordinating to [Ln(**DO3A**)] based systems. It is noteworthy that anions possess geometries and receptors that are designed to bind to these anions by maintaining their geometry is a criterion for strong binding. [Gd(**DO3A**)] binds to carbonate, where three complexes bind to three oxygen atoms on the carbonate which exist in a trigonal planar geometry.[56] Therefore, the interference of carbonate binding can be neglected for the binuclear systems under study in this chapter. The C-2 and C-3 binuclear complexes with other binding modes of fluoride could not be crystallised. Several attempts were made to crystallise binuclear complexes bound to chloride, but all in vain.

[Eu(**pDO3A**)] was attempted for crystallisation with added KF. At low concentrations of added KF (0.5 to 1.5 equiv), the complex crystallised as such without any potassium or fluoride ions in the crystal structure (quality of the data was also poor). However, at excess amount of added KF, the complex crystallised with two fluorides bound to the metal centre (Figure 2.40). This structure was neutralised by two potassium atoms found in the crystal structure. Single crystals of [Eu(**pDO3A**)(2F)]$^{2-}$ for X-ray diffraction was obtained by slow diffusion of dioxane over concentrated solution of [Eu(**pDO3A**)] with excess KF in D_2O (Figure 2.40).

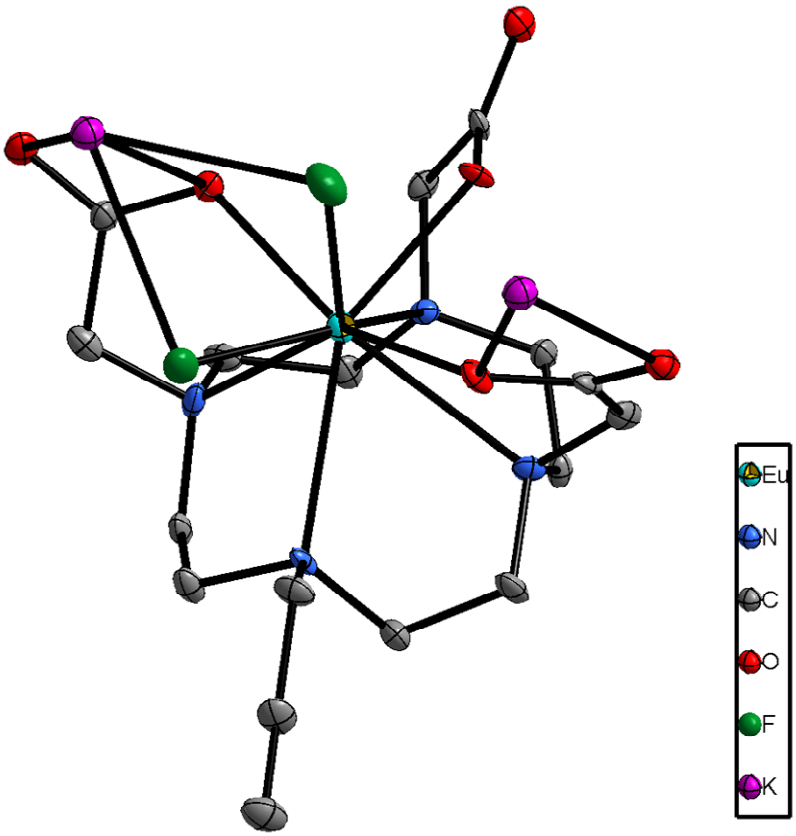


Figure 2.40. Single crystal X-ray structure of [Eu(**pDO3A**)2F]$^{2-}$. H atoms and water are omitted for clarity. Thermal ellipsoid drawn at 30% probability level. X-ray crystal structure was solved by Dr. Kirsten Christensen, Chemical Crystallography, University of Oxford.

This verifies the hypothesis made in Section 2.5.3.2 (from the ^{1}H NMR spectra of [Yb(**pDO3A**)] with added KF, Figure 2.28 and Figure A10, Appendix-A), that there is a second binding event of fluoride which occurs at the axial position to the metal (though the luminescence titration in Figure 2.23(*a*) and mass spectrum in Figure 2.37 showed only a single binding event). Therefore, the second binding of fluoride to the metal centre occurs at excess addition of KF.

2.5.6. MRI Longitudinal Relaxivity Studies on Halide Binding to Binuclear Gd(III) Complexes

The prospects of MRI detection of halides were studied by measuring the longitudinal relaxivity of the binuclear Gd(III) complexes in water, phosphate buffer (pH 7.4), and PBS (pH 7.4) (Figure 2.41). The relaxivity of the complexes suggest that they suffer from competing ions in buffer, which is characteristic to [Gd(**DO3A**)] and its analogues.[51,57] Nonetheless, the "per Gd" relaxivity of the binuclear Gd(III) complexes was found to be higher than the mononuclear [Gd(**DO3A**)][51] due to the presence to two metal centres that accelerate T_1 relaxation.

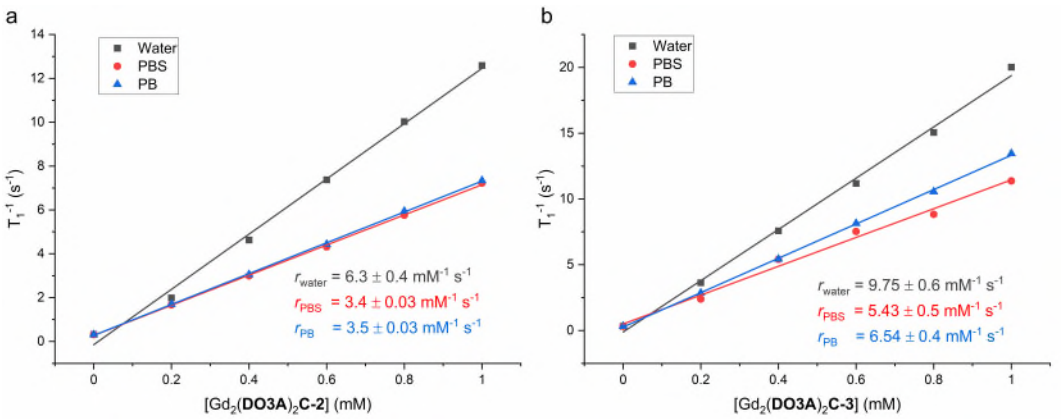


Figure 2.41. Plot of $1/T_1$ versus concentration of [Gd$_2$(**DO3A**)$_2$**C-2**] (a) and [Gd$_2$(**DO3A**)$_2$**C-3**] (b) in deionised water, 0.01 M PBS at pH 7.4 and 0.01 M PB at pH 7.4 at 298 K. Relaxation rate reported 'per Gd' of the complex. These measurements were made on a 60 MHz benchtop NMR instrument.

Single crystal X-ray structure of the binuclear Gd(III) complexes was obtained as a supramolecular assembly with 12 to 24 metal centres (Figure 2.3). The relaxivity value obtained for these complexes is in the expected range and if the solution structure contained more than 2 metal centres, the relaxivity would be higher than the observed values, which implies that the supramolecular assembly observed in the crystal structure does not wholly reflect the solution state structure.

As a preliminary test, KF and KCl were added to the binuclear Gd complex (1 mM) and the relaxivity measured in deionised water (for KF and KCl), PBS (for KF), and PB (for KCl) (Table 2.7). 1 mM of KF was added to 1 mM of complex, but 100 mM of KCl was added to 1 mM of complex. This is to compare the effect of guest added in its biological concentration (although fluoride is present in micromolar range, 1 mM was added to observe the changes in relaxivity, under constant concentration of the binuclear Gd complex (1 mM)).

In buffers, the relaxivity of chloride added to the binuclear complex was recorded in PB as the buffer does not contain chloride in it to pre-saturate the complex before the addition of chloride as KCl to measure relaxivity. This was the reason behind performing titrations with KCl in phosphate buffer throughout the study. A decrease in relaxivity was observed upon the addition of halides due to the replacement of the inner-sphere water by fluoride and chloride (Table 2.7), which corroborates the luminescence, NMR, and X-ray crystal structures, thus confirming the binding of these halide guests to the lanthanide metal centres in the binuclear complexes studied. This experiment must be repeated in future with incremental addition of fluoride and chloride to study the variation of relaxivity upon the addition of these anions up to the concentration range found in biology and in sea water. It is noteworthy that no change in relaxivity was observed upon the addition

of KCl to [Gd(**pDO3A**)] in deionised water and phosphate buffer at pH 7.4 which suggests the absence of chloride binding in this model compound which corroborates to the luminescence and NMR studies.

Table 2.7. Longitudinal relaxation rate of binuclear Gd(III) complexes (1mM) with KF and KCl added[†]. Relaxation rate reported 'per Gd' of the complex.

Complex and amount of guest added	Relaxivity (mM^{-1} s^{-1})[*]		
	H_2O	PBS[‡]	PB[‡]
[Gd_2(**DO3A**)$_2$**C-2**]	**6.4**	**3.4**	**3.5**
[Gd_2(**DO3A**)$_2$**C-2**] with 1 mM KF	5.2	2.9	
[Gd_2(**DO3A**)$_2$**C-2**] with 100 mM KCl	4.1		2.8
[Gd_2(**DO3A**)$_2$**C-3**]	**9.7**	**5.4**	**6.5**
[Gd_2(**DO3A**)$_2$**C-3**] with 1 mM KF	8.7	4.9	
[Gd_2(**DO3A**)$_2$**C-3**] with 100 mM KCl	3.9		3.1

[†] Relaxivity measurements were made on a 60 MHz benchtop NMR instrument at 298 K.

[*] All relaxivity values are subject to ±0.05% error.

[‡] All buffers are maintained at 0.01 M, pH 7.4. PBS = phosphate buffered saline; PB = phosphate buffer.

2.6. Conclusion

The binuclear complexes [Ln_2(**DO3A**)$_2$**C-2**] and [Ln_2(**DO3A**)$_2$**C-3**], reported in this Chapter, chelate chloride strongly in water and even more strongly under physiological conditions. Although fluoride chelation is observed, fluoride is not predominant in physiological conditions, unlike chloride. However, fluoride's association to the binuclear complexes helped in understanding the mode of chloride chelation in detail. Chloride binding strength reported in this Chapter in

water and in buffers is the strongest to report to date. Much remains to be done in understanding the solution behaviour of these complexes in detail, such as determining the exchange rates of chloride and fluoride chelation, confirming speciation models by EPR and NMR spectroscopy, DFT studies to look at the mode of binding and rationalising the binding affinities of chloride to the binuclear systems, evaluating the change in thermodynamics upon chelation of different halides, and application of these binuclear complexes towards *in vitro* and *in vivo* mapping of chloride. In future, the reported binuclear complexes can be modified by incorporating light-harvesting antenna and other functionalities onto the cyclen framework (either by attaching an antenna to the pendant carboxylate or amide arm(s) or direct covalent attachment to the macrocycle) to develop new-generation Ln-receptors to improve the association and selectivity of chloride in water and biological media. Furthermore, this work has the potential to expand towards the direction of developing biorthogonal probes by attaching small molecular handles to tag biomolecules of interest for monitoring chloride ion concentration in physiology and to develop fluorescent sensors for environmental, biological and medical applications.

2.7. References

1. Zhou, Y.; Zhang, Z. F.; Yoon, J. *Chem. Rev*. **2014**, *114*, 5511−5571.
2. (a) Kirk, L. K. *Biochemistry of the Halogens and Inorganic Halides*; Plenum Press: New York, 1991. (b) Kleerekoper, M. *Endocrinol. Metab. Clin. North Am*. **1998**, *27*, 441–452. (c) Briançon, D. *Rev. Rhum., Eng. Ed*. **1997**, *64*, 78–81. (d) Michigami, Y.; Kuroda, Y.; Ueda, K.; Yamamoto, Y. *Anal. Chim. Acta* **1993**, *274*, 299–302.
3. (a) Pflugrath, J. W.; Quiocho, F. A. *J. Mol. Biol*. **1988**, *200*, 163–180. (b) Kanyo, Z. F.; Christianson, D. W. *J. Biol. Chem*. **1991**, *266*, 4264–4268. (c) *Fluoride in Drinking-Water*; Fawell, J., Bailey, K., Chilton, E., Dahi, E., Fewtrell, L., Magara, Y., Eds.; World Health Organisation, IWA Publishing: London, 2006. (d) *Fluoride in Drinking Water: A Scientific Review of EPA's Standards*; National Research Council, National Academy Press: Washington, D.C., 2006.

4. O'Mullane, D. M.; Baez, R. J.; Jones, S.; Lennon, M. A.; Petersen, P. E.; Rugg-Gunn, A. J.; Whelton, H.; Whitford, G. M. *Community Dent. Health* **2016**, *33*, 69–99.
5. Luke, J. *Caries Res*. **2001**, *35*, 125–128.
6. Ron, M.; Singer, L.; Menczel, J.; Kidroni, G. *Eur J. Obstet. Gynecol. Reprod. Biol*. **1986**, *21*, 213–218.
7. Grandjean, P. *Environ. Health* **2019**, *18*, 110.
8. (a) Jentsch, T. J.; Stein, V.; Weinreich, F.; Zdebik, A. A. *Physiol. Rev*. **2002**, *82*, 503–568. (b) Nilius, B.; Droogmans, G. *Acta Physiol. Scand*. **2003**, *177*, 119–147.
9. Wilson, C. S.; Mongin, A. A. *Neurosci. Lett*. **2018**, *689*, 33–44.
10. (a) Rivera, C.; Voipio, J.; Payne, J. A.; Ruusuvuori, E. *Nature* **1999**, *397*, 251–255. (b) Glykys, J.; Dzhala, V.; Egawa, K.; Balena, T.; Saponjian, Y.; Kuchibhotla, K.; Bacskai, B. J.; Kahle, K. T.; Zeuthen, T.; Staley, K. J. *Science* **2014**, *343*, 670–675.
11. (a) Sangan, P.; Rajendran, V. M.; Geibel, J. P.; Binder, H. J. *J. Biol. Chem*. **2002**, *277*, 9668–9675. (b) Deidda, G.; Bozarth, I. F.; Cancedda, L. *Front. Cell. Neurosci*. **2014**, *8*, 119. (c) Ruffin, V. A.; Salameh, A. I.; Boron, W. F.; Parker, M. D. *Front. Physiol*. **2014**, *5*, 43. (d) Jentsch, T. J. *Nat. Rev. Mol. Cell Biol*. **2016**, *17*, 293–307. (e) Glykys, J.; Dzhala, V.; Egawa, K.; Kahle, K. T.; Delpire, E.; Staley, K. *Trends Neurosci*. **2017**, *40*, 276–294.
12. (a) Ben-Ari, Y.; Gaiarsa, J.-L.; Tyzio, R.; Khazipov, R. *Physiol. Rev*. **2007**, *87*, 1215–1284. (b) Branchereau, P.; Cattaert, D.; Delpy, A.; Allain, A.-E.; Martin, E.; Meyrand, P. *Sci. Rep*. **2016**, *6*, 21753. (c) Doyon, N.; Vinay, L.; Prescott, S. A.; Koninck, Y. D. *Neuron* **2016**, *89*, 1157–1172.
13. (a) Reuter, D.; Zierold, K.; Schröder, W. H.; Frings, S. *J. Neurosci*. **1998**, *18*, 6623−6630. (b) Bregestovski, P.; Waseem, T.; Mukhtarov, M. *Front. Mol. Neurosci*. **2009**, *2*, 1−15. (c) Arosio, D.; Ratto, G. M. *Front. Cell. Neurosci*. **2014**, *8*, 258.
14. (a) Schmidtchen, F. P. *Angew. Chem., Int. Ed.* **1977**, *16*, 720–721. (b) Schmidtchen, F. P. *Chem. Ber*. **1981**, *114*, 597–607.
15. Schmidtchen, F. P.; Müller, G. *J. Chem. Soc., Chem. Commun*. **1984**, 1115–1116.
16. (a) Worm, K.; Schmidtchen, F. P.; Schier, A.; Schäfer, A.; Hesse, M. *Angew. Chem., Int. Ed*. **1994**, *33*, 327–329. (b) Worm, K.; Schmidtchen, F. P. *Angew. Chem., Int. Ed*. **1995**, *34*, 65–66.
17. (a) Langton, M. J.; Robinson, S. W.; Marques, I.; Félix, V.; Beer, P. D. *Nat. Chem*. **2014**, *6*, 1039–1043. (b) Langton, M. J. *Interlocked Host Structures for Anion Recognition and Sensing in Aqueous Solutions*; DPhil thesis, University of Oxford, Oxford, UK, 2014.
18. Yawer, M. A.; Havel, V.; Sindelar, V. *Angew. Chem., Int. Ed*. **2015**, *54*, 276–279.

19. (a) Lisbjerg, M.; Jessen, B. M.; Rasmussen, B.; Nielsen, B. E.; Madsen, A. O.; Pittelkow, M. *Chem. Sci*. **2014**, *5*, 2647–2650. (b) Lisbjerg, M.; Nielsen, B. E.; Milhøj, B. O.; Sauer, S. P. A.; Pittelkow, M. *Org. Biomol. Chem*. **2014**, *13*, 369–373.
20. Chen, Y.; Wu, G.; Chen, L.; Tong, L.; Lei, Y.; Shen, L.; Jiao, T.; Li, H. *Org. Lett*. **2020**, *22*, 4878–4882.
21. (a) Schmidtchen, F. P. *Chem. Soc. Rev*. **2010**, *39*, 3916–3935. (b) Kubik, S. *Chem. Soc. Rev*. **2010**, *39*, 3648–3663. (c) Langton, M. J.; Serpell, C. J.; Beer, P. D. *Angew. Chem., Int. Ed*. **2015**, *55*, 1974–1987. (d) Cremer, P. S.; Flood, A. H.; Gibb, B. C.; Mobley, D. L. *Nat. Chem*. **2018**, *10*, 8–16. (e) Kubik, S. *Chemistry Open* **2022**, *11*, e202200028. (f). Gilday, L. C.; Robinson, S. W.; Barendt, T. A.; Langton, M. J.; Mullaney, B. R.; Beer, P. D. *Chem. Rev*. **2015**, *115*, 7118–7195. (g) Wu, X.; Gilchrist, A. M.; Gale, P. A. *Chem* **2020**, *6*, 1296–1309. (h) Macreadie, L. K.; Gilchrist, A. M.; McNaughton, D. A.; Ryder, W. G.; Fares, M.; Gale, P. A. *Chem* **2022**, *8*, 46–118.
22. Allain, C.; Beer, P. D.; Faulkner, S.; Jones, M. W.; Kenwright, A. M.; Kilah, N. L.; Knighton, R. C.; Sørensen, T. J.; Tropiano, M. *Chem. Sci*. **2013**, *4*, 489–493.
23. Natrajan, L. S.; Khoabane, N. M.; Dodds, B. L.; Muryn, C. A.; Pritchard, R. G.; Heath, S. L.; Kenwright, A. M.; Kuprov, I.; Faulkner, S. *Inorg. Chem*. **2010**, *49*, 7700–7709.
24. Scarborough Jr, R. M.; Smith III, A. B. *J. Am. Chem. Soc*. **1977**, *99*, 7087–7089.
25. Yee, E. L.; Gansow, O. A.; Weaver, M. J. *J. Am. Chem. Soc*. **1980**, *102*, 2278–2285.
26. Cross, J. P.; Dadabhoy, A.; Sammes, P. G. *J. Lumin*. **2004**, *110*, 113–124.
27. Aime, S.; Botta, M.; Fasano, M.; Marques, M. P. M.; Geraldes, C. F. G. C.; Pubanz, D.; Merbach, A. E. *Inorg. Chem*. **1997**, *36*, 2059–2068.
28. (a) Blackburn, O. A.; Chilton, N. F.; Keller, K.; Tait, C. E.; Myers, W. K.; McInnes, E. J. L.; Kenwright, A. M.; Beer, P. D.; Timmel, C. R.; Faulkner, S. *Angew. Chem., Int. Ed*. **2015**, *54*, 10783–10786. (b) Blackburn, O. A.; Routledge, J. D.; Jennings, L. B.; Rees, N. H.; Kenwright, A. M.; Beer, P. D.; Faulkner, S. *Dalton Trans*. **2016**, *45*, 3070–3077. (c) Blackburn, O. A.; Kenwright, A. M.; Beer, P. D.; Faulkner, S. *Dalton Trans*. **2015**, *44*, 19509–19517.
29. Rodríguez-Rodríguez, A.; Arnosa-Priesto, Á.; Brandariz, I.; Esteban-Gómez, D.; Platas-Iglesias, C. *J. Phys. Chem. A* **2020**, *124*, 1362–1371.
30. (a) Tripier, R.; Platas-Iglesias, C.; Boos, A.; Morfin, J.-F.; Charbonnière, L. *Eur. J. Inorg. Chem*. **2010**, *18*, 2735–2745. (b) Lima, L. M. P.; Lecointre, A.; Morfin, J.-F.; de Blas, A.; Visvikis, D.; Charbonnière, L. J.; Platas-Iglesias, C.; Tripier, R. *Inorg. Chem*. **2011**, *50*, 12508–12521.

31. Liu, T.; Nonat, A.; Beyler, M.; Regueiro-Figueroa, M.; Nchimi Nono, K.; Jeannin, O.; Camerel, F.; Debaene, F.; Cianférani-Sanglier, S.; Tripier, R.; Platas-Iglesias, C.; Charbonnière, L. J. *Angew. Chem., Int. Ed*. **2014**, *53*, 7259–7263.
32. Nonat, A.; Chan, C. F.; Liu, T.; Platas-Iglesias, C.; Liu, Z.; Wong, W.-T.; Wong, W.-K.; Wong, K.-L.; Charbonnière, L. J. *Nat. Commun.* **2016**, *7*, 1–8.
33. Nonat, A.; Liu, T.; Jeannin, O.; Camerel, F.; Charbonnière, L. J. *Chem. —Eur. J.* **2018**, *24*, 3784–3792.
34. Butler, S. J. *Chem. Commun*. **2015**, *51*, 10879–10882.
35. Moore, J. D.; Lord, R. L.; Cisneros, G. A.; Allen, M. J. *J. Am. Chem. Soc*. **2012**, *134*, 17372–17375.
36. (a) Shannon, R. D. *Acta Crystallogr. Sect. A* **1976**, *32*, 751–767 (b) Marcus, Y. *J. Chem. Soc., Faraday Trans*. **1991**, *87*, 2995–2999. (c) Marcus, Y. *J. Chem. Soc., Faraday Trans. 1* **1987**, *83*, 339–349.
37. Hofmeister, F. *Arch. Exp. Pathol. Pharmakol*. **1888**, *24*, 247–260.
38. (a) Beer, P. D.; Gale, P. A. *Angew. Chem., Int. Ed*. **2001**, *40*, 486–516. (b) Steed, J. W.; Atwood, J. L. *Supramolecular Chemistry*; 3rd ed.; John Wiley and Sons: New York, 2022.
39. (a) Steed, J. W. *Chem. Soc. Rev*. **2009**, *38*, 506–519. (b) Butler, S. J.; Parker, D. *Chem. Soc. Rev*. **2013**, *42*, 1652–1666. (c) Bodman, S. E.; Butler, S. J. *Chem. Sci.* **2021**, *12*, 2716–2734.
40. Kofod, N.; Thomsen, M. S.; Nawrocki, P.; Sørensen, T. J. *Dalton Trans*. **2022**, *51*, 7936–7949.
41. Tropiano, M.; Blackburn, O. A.; Tilney, J. A.; Hill, L. R.; Placidi, M. P.; Aarons, R. J.; Sykes, D.; Jones, M. W.; Kenwright, A. M.; Snaith, J. S.; Sørensen, T. J.; Faulkner, S. *Chem. - Eur. J.*, **2013**, *19*, 16566–16571.
42. Sørensen, T. J.; Faulkner, S. *Acc. Chem. Res*. **2018**, *51*, 2493–2501.
43. Dadabhoy, A.; Faulkner, S.; Sammes, P. G. *J. Chem. Soc., Perkin Trans. 2* **2002**, 348–357.
44. McMullon, G. T. *A Molecular Toolkit for Immunological Imaging*; DPhil thesis, University of Oxford, Oxford, UK, 2022.
45. Aime, S.; Botta, M.; Crich, S. G.; Giovenzana, G. B.; Pagliarin, R.; Piccinini, M.; Sisti, M.; Terreno, E. *J. Biol. Inorg. Chem*. **1997**, *2*, 470–479.
46. Junker, A. K. R.; Tropiano, M.; Faulkner, S.; Sørensen, T. J. *Inorg. Chem*. **2016**, *55*, 12299–12308.
47. Tropiano, M. *Lanthanide Architectures, Rotaxanes, and Responsive d-f Assemblies*; DPhil thesis, University of Oxford, Oxford, UK, 2013.
48. Nielsen, L. G.; Sørensen, T. J. *Inorg. Chem*. **2020**, *59*, 94–105.

49. (a) Parker, D.; Senanyake, K.; Williams, J. A. G. *J. Chem. Soc., Perkin Trans. 2*, **1998**, 2129–2139. (b) Parker, D.; Dickins, R. S.; Puschmann, H.; Crossland, C.; Howard, J. A. K. *Chem. Rev*. **2002**, *102*, 1977–2010.
50. (a) Kuzmič, P. *Anal. Biochem*. **1996**, *237*, 260–273. (b) Kuzmič, P. *Methods Enzymol*. **2009**, *467*, 247–280.
51. (a) Tear, L. R.; Maguire, M. L.; Tropiano, M.; Yao, K.; Farrer, N. J.; Faulkner, S.; Schneider, J. E. *Dalton Trans.* **2020**, *49*, 2989–2993. (b) Tear, L. R. *Molecular Imaging Probes for ^{31}P Contrast*; DPhil thesis, University of Oxford, Oxford, UK, 2018.
52. (a) Hill, L. R.; Sørensen, T. J.; Blackburn, O. A.; Brown, A.; Beer, P. D.; Faulkner, S. *Dalton Trans*. **2013**, *42*, 67–70. (b) Hill, L. R. *Binuclear Complexes as Quantitative Imaging Agents*; DPhil thesis, University of Oxford, Oxford, UK, 2018.
53. Hefter, G. T. *Rev. Inorg. Chem*. **1989**, *10*, 185–224.
54. Tickner, B. J.; Stasiuk, G. J.; Duckett, S. B.; Angelovski, G. *Chem. Soc. Rev*. **2020**, *49*, 6169–6185.
55. Bryden, C. C.; Reilley, C. N.; Desreux, J. F. *Anal. Chem*. **1981**, *53*, 1418–1425.
56. Chang, C. A.; Francesconi, L. C.; Malley, M. F.; Kumar, K.; Gougoutas, J. Z.; Tweedle, M. F.; Lee, D. W.; Wilson, L. J. *Inorg. Chem.* **1993**, *32*, 3501–3508.
57. Wahsner, J.; Gale, E. M.; Rodríguez- Rodríguez, A.; Caravan, P. *Chem. Rev*. **2019**, *119*, 957–1057.

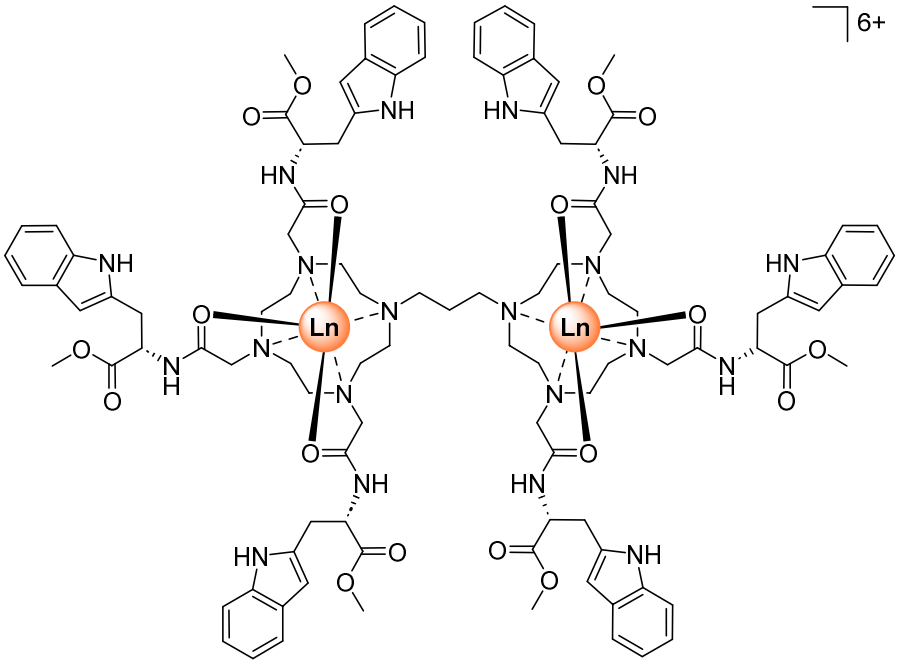
CHAPTER-III

Chapter-III: Binuclear Lanthanide Complex Bearing Tryptophan Pendant Arm for Halide Chelation in Water

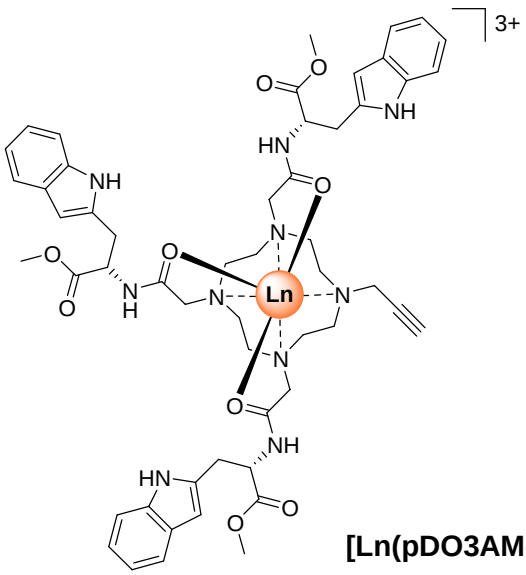
In the previous Chapter, the importance of developing chloride sensors was introduced and binuclear lanthanide complexes of two DO3A-based ligands, $(DO3A)_2C$-2 and $(DO3A)_2C$-3, that chelate chloride in water and in buffers were discussed. This successful approach had a drawback of lacking a sensitiser to effectively monitor chloride in real-world applications through luminescence. Furthermore, improving the binding affinity is vital for *in vitro* and *in vivo* mapping of chloride. Strong metal chelation is indispensable while developing Ln(III)-based receptors for halide recognition and sensing in order to avoid the precipitation of lanthanides as halide salts, LnX_3, upon halide addition.[1] According to the coulombic modulation of affinity, cationic receptors have better anion-host interaction than neutral and anionic receptors.[1a] Therefore, in order to improve the binding affinity of chloride, it was proposed to develop cationic binuclear Ln(III) complexes built on a DO3A platform by modifying the pendant arms.

L-Tryptophan (Trp), an essential amino acid, was identified as the suitable functionality to be conjugated onto the pendent arm of DO3A framework. This is a bulky arm which will impart rigidity on the fluctional isomerism of the DO3A core, as the ring inversion and arm rotation is increased with bulky pendant arms.[2] Therefore, this design was utilised to develop binuclear Ln(III) complexes $[Ln_2(\mathbf{DO3AM\text{-}L\text{-}TrpOMe})_2\mathbf{C\text{-}3}]^{3+}$ (Chart 3.1) in addition to the $[Ln_2(\mathbf{DO3A})_2\mathbf{C\text{-}2}]$ and $[Ln_2(\mathbf{DO3A})_2\mathbf{C\text{-}3}]$ binuclear host complexes studied in Chapter-II. A mononuclear complex $[Ln(\mathbf{pDO3AM\text{-}L\text{-}TrpOMe})]^{3+}$ was also designed to be used as a model compound to compare the effective interaction of halides to the binuclear complexes proposed here. Tryptophan (Trp) is a good sensitiser for Tb(III) as its

triplet energy level lies above the Tb(III) emissive levels [Trp (T_1) = ~23,697 cm^{-1}; first Tb(III) excited state ($^5D_4$) = 20,500 cm^{-1}].[3] Moreover, the incorporation of the amido functionality in the pendant arm would enable N-H interaction to the chelated halide leading to enhanced binding affinity.[4]



[Ln_2(DO3AM-L-TrpOMe)$_2$C-3]$^{6+}$



[Ln(pDO3AM-L-TrpOMe)]$^{3+}$

Chart 3.1. Proposed mono- and binuclear complexes for this Chapter.

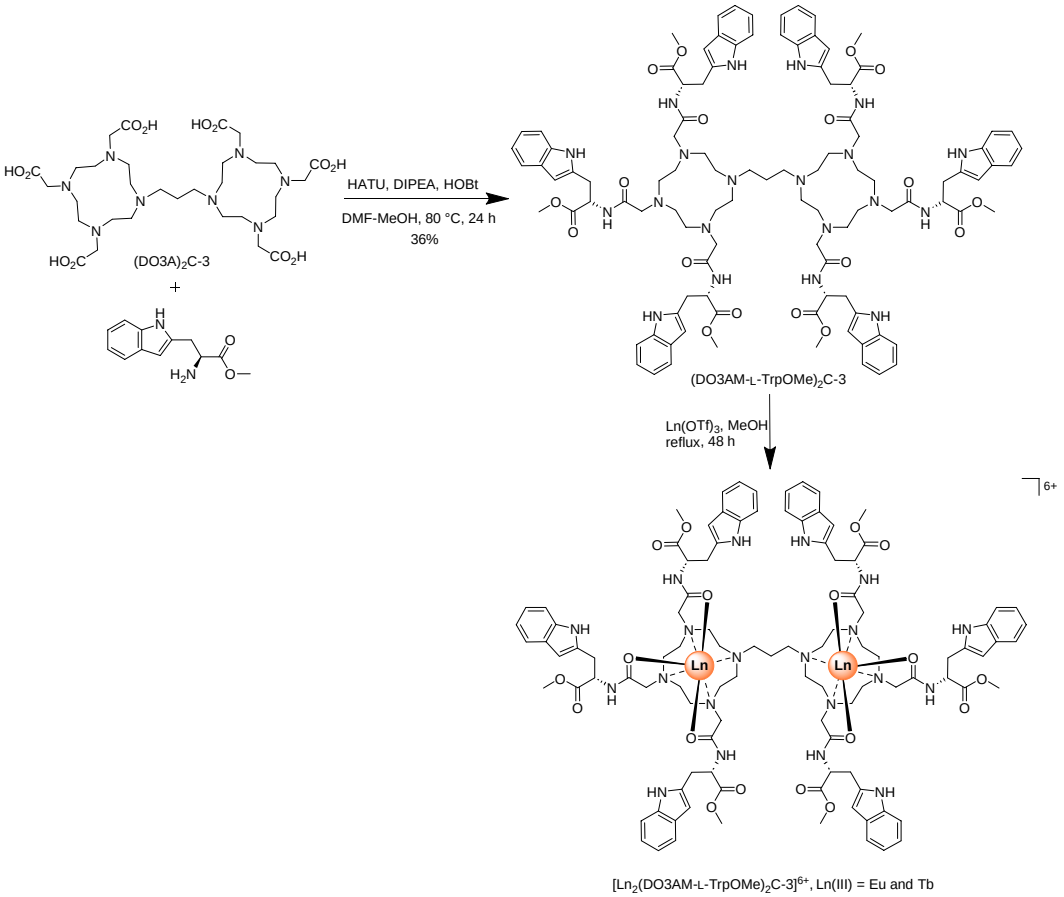
3.1. Results and Discussion

3.1.1. Synthesis of the Proposed Complexes

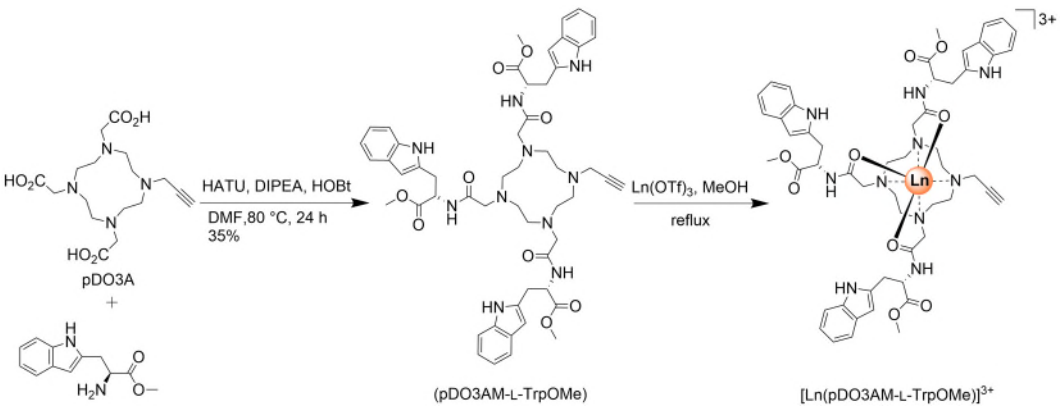
Detailed synthetic procedure including column chromatography conditions are described in Chapter-VII, Section 7.6.2. The proposed tryptophan-conjugated ligand (DO3AM-L-TrpOMe)$_2$C-3 was synthesised via acid-amine coupling (Scheme 3.1). (DO3A)$_2$C-3 (synthesised as reported in Chapter-II) was added to DMF-MeOH mixture and stirred, followed by the addition of DIPEA. After stirring for few min, the coupling agent HATU was added and the mixture stirred for 30 min at 50 ℃ to form an active ester. Tryptophan methyl ester (L-TrpOMe) in DMF was added slowly to the reaction mixture followed by the addition of promoter HOBt to facilitate the coupling of the tryptophan ester to the bis-macrocycle. The reaction was heated to 80 ℃ for 16 h, cooled to 25 ℃, toluene added to form an azeotrope with DMF, and evaporated under reduced pressure to dryness. This process of removing DMF by azeotrope formation with toluene was repeated until the formation of the crude product as a thick slurry. This was column purified on neutral alumina under gradient MeCN/H_2O solvent system.

Initial purification by column chromatography on neutral alumina (MeCN/H_2O) resulted in only partial purification, and a second column purification on silica (DCM/EtOH) was required for the product to be isolated. However, the ligand remained impure despite further purification by recrystallisation and multiple column purifications. The impurity was mainly free tryptophan, the starting material, along with partially coupled products. The reaction was carried out under the same conditions for longer time for its completion (to get hexa coupling), but the product formed as mixture of other coupled products. pDO3AM-L-TrpOMe was

synthesised by following the same protocol from **pDO3A** (Scheme 3.2), and encountered similar purification issues like its bismacrocyclic tryptophan analogue.



Scheme 3.1. Proposed synthetic scheme for the tryptophan-based binuclear complexes.



Scheme 3.2. Proposed synthetic scheme for the tryptophan-based mononuclear complexes.

Among the wide array of coupling agents, HATU was specifically chosen because of its ability to facilitate acid-amine coupling without altering the chirality of the amino acids in peptide coupling.[5] Moreover, HATU is considered to be the standard for hindered coupling, which is ideal in this case as the hexa-coupling of the L-TrpOMe to the bismacrocycle is quite sterically hindered on the acid groups near the flexible spacer which connects the macrocycles. Owing to the bulkiness of both the DO3A (acid) and L-TrpOMe (amine), the promoter (HOBt) was deemed necessary to facilitate the coupling. It also suppresses racemisation during the coupling reaction. The reaction was performed in DMF which is the ideal condition for HATU coupling.[5]

The binuclear Ln(III) complexes of tryptophan-conjugated binuclear ligand (DO3AM-L-TrpOMe)$_2$C-3 was prepared by reacting the preformed ligand with the lanthanide salt in MeOH under reflux for 48 h. The solvent was reduced under pressure and the crude product dissolved in minimum MeOH and triturated with diethyl ether to afford the lanthanide complexes [Ln$_2$(**DO3AM-L-TrpOMe**)$_2$**C-3**]$^{6+}$ [Ln = Eu(III) and Tb(III)].

^{1}H NMR spectroscopy with the binuclear Tb complexes was attempted in D_2O and MeOD with no avail. Solubility of the complex in D_2O was poor to get observable NMR resonances. Although the complex dissolves well in MeOD, no NMR signal was observed here as well. Therefore, the binuclear Eu complex in MeOD was used to record a NMR spectrum, shown in Figure 3.1. The NMR signals observed are identical to that of a [Ln(**DO3A**)] based system with a broad signal at 24 ppm, assignable to the TSAP isomer of this binuclear complex. This NMR was recorded with 8 mg of sample, which ideally would have been recorded with a higher concentration of the complex.

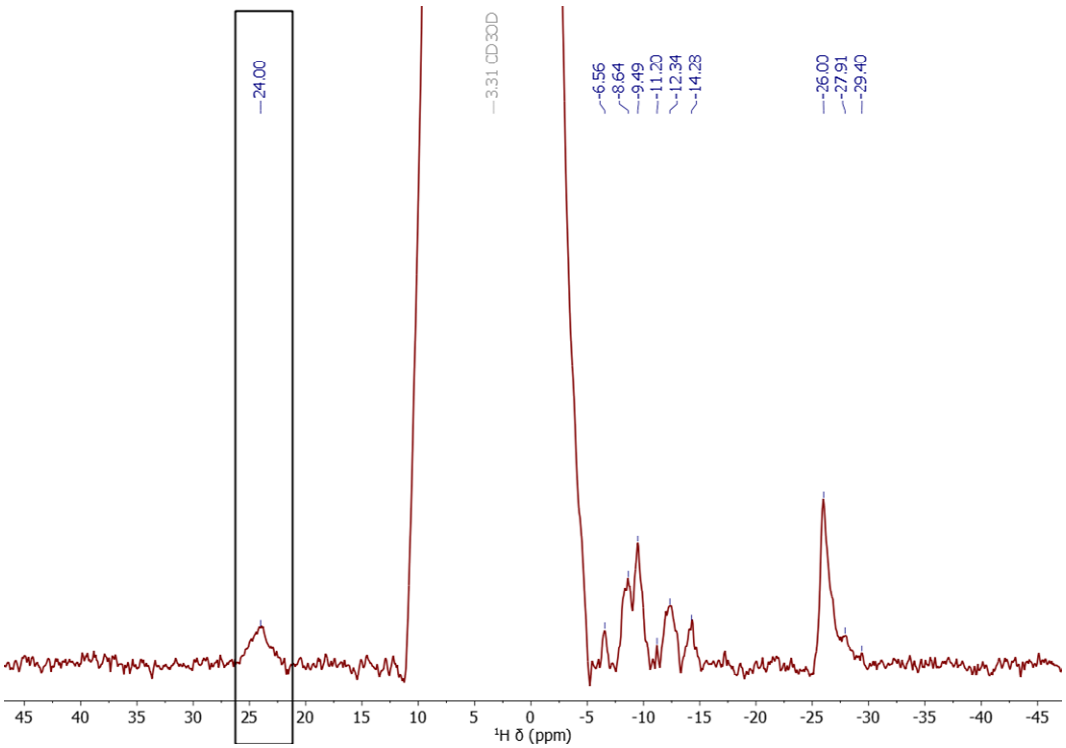
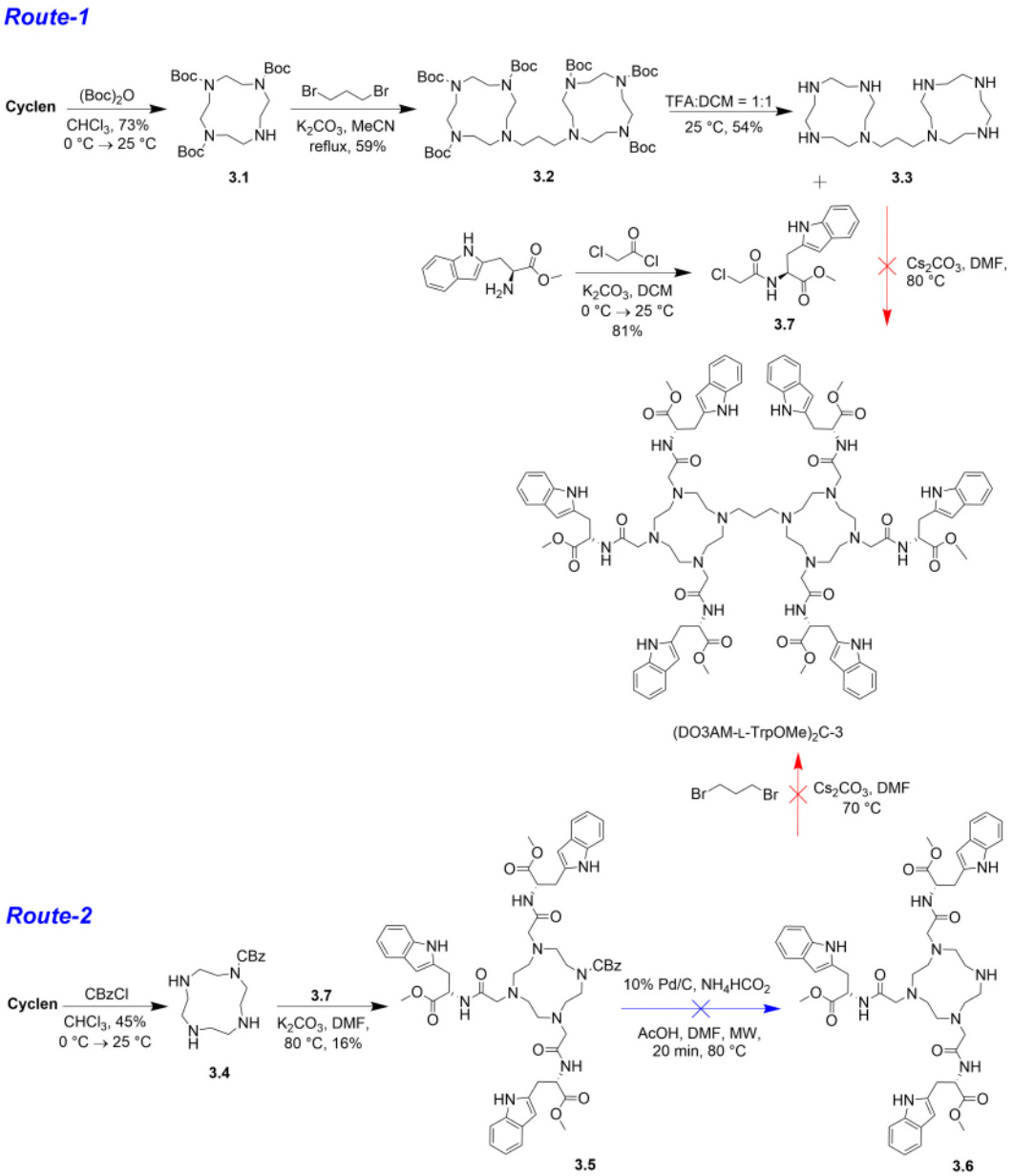


Figure 3.1. 500 MHz paramagnetic ^{1}H NMR spectrum of [Eu_2(**DO3AM-L-TrpOMe**)$_2$**C-3**]$^{6+}$ in MeOD at 298 K. The signal due to the SAP isomer is highlighted in the black box.

3.1.1.1. Alternative Approaches Attempted to Make the Proposed Binuclear Complexes

The alternative approaches to synthesise the binuclear complex was explored through a series of *N*-alkylation as shown in Scheme 3.3. In *route-1*, cyclen was protected with Boc group to form tri-boc cyclen (**3.1**) by following the literature procedure.[6] After column purification through isocratic elution in diethyl ether on silica gel, **3.1** was obtained as a white solid which on alkylation using 1,3-dibromopropane yielded the *bis*(tri-boc cyclen) **3.2** after column purification through gradient elution in chloroform/*iso*-propanol on silica gel. The boc groups were removed using TFA in DCM within 4 h to obtain *bis*(cyclen) **3.3**. When it was hexa *N*-alkylated using **3.7** (**3.7** was prepared according to the literature[7]), the reaction did not proceed towards hexa *N*-alkylation. The base and solvent were changed to improve the reaction, shown in Table 3.1, but the reaction would not reach to hexa *N*-alkylation.



Scheme 3.3. Synthetic routes attempted to make (DO3AM-L-TrpOMe)$_2$C-3. Red arrow indicates unsuccessful reaction, blue arrow indicates product with very poor yield which needs optimisation.

Subsequently, *route-2* was explored as shown in Scheme 3.3. Cyclen was mono protected using CBzCl by a modified literature procedure.[8] CBzCl was added slowly for 30 min to a solution of cyclen in $CHCl_3$ at 0 °C. After the addition, the reaction was gradually warmed to 25 °C under stirring for 12 h. The insoluble salts were filtered off through a celite pad and the filtrate evaporated to dryness. The

Table 3.1. Conditions used towards (DO3AM-L-TrpOMe)$_2$C-3 from compound **3.3**

Base	Solvent
K_2CO_3*	MeCN/DMF
Na_2CO_3*	MeCN
Cs_2CO_3	MeCN/DMF
Et_3N	MeCN/DMF
DIPEA*	MeCN/DMF

* Reaction attempted with and without KI as a catalyst (10 mol%).
Equivalents of base added was altered between 7 to 10.

resulting crude product was column purified in gradient DCM/MeOH/aq.NH_3 on silica gel to afford **3.4**. Slow evaporation in MeOH afforded crystals of **3.4** which was characterised by single crystal X-ray diffraction (Figure 3.2).

Compound **3.4** was then tri *N*-alkylated using compound **3.7** in the presence of potassium carbonate in DMF (Scheme 3.3). This resulted in the formation of the product along with impurities such as di- and mono-alkylated products and unreacted **3.7**. DMF was removed under reduced pressure by azeotrope mixture with toluene. The resulting thick slurry was purified by column chromatography on neutral alumina under a gradient MeCN/H_2O solvent system to afford the product with impurities. Further column purification was performed on silica gel under gradient DCM/EtOH solvent system to afford the product **3.5**. However, the next step of removing CBz proved challenging. Table 3.2 summarises the conditions explored towards CBz removal.

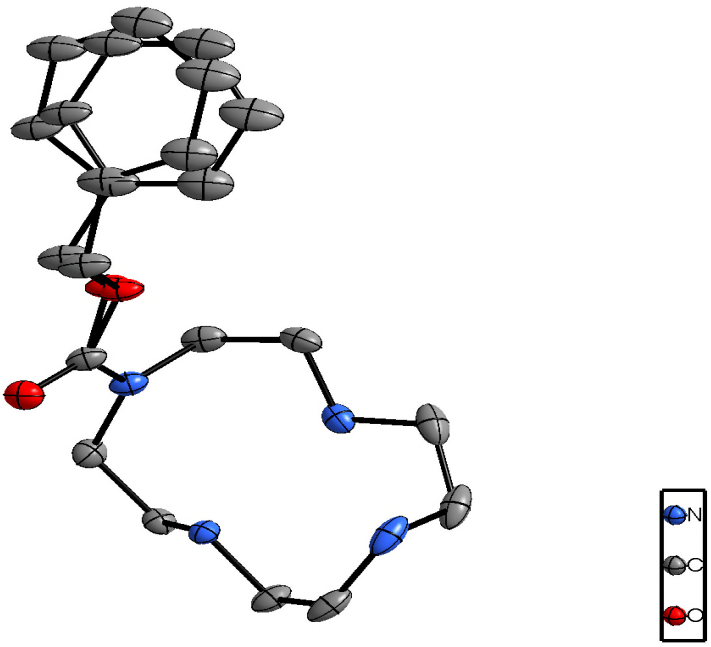


Figure 3.2. X-ray crystal structure of mono-CBz cyclen, **3.4**. H, Cl, and solvent omitted for clarity. Thermal ellipsoid drawn at 30% probability level. Structure disordered on the CBz arm. Structure solved by Dr. Kirsten Christensen at Chemical Crystallography, University of Oxford.

Table 3.2. Attempts made to deprotect CBz from compound **3.5**

Catalyst‡	Solvent
$NaBH_4$	MeOH[9]
Ammonium formate*	DMF/MeCN/IPA[10]
H_2 balloon	MeOH

‡ All reactions were carried out using 10% wet Pd/C.

* Reaction was attempted with and without microwave use.

It is likely that the deprotection of CBz was difficult to accomplish due to the steric effect where H_2 could not access the site of CBz reduction, as a result of the bulkiness from the macrocycle. Therefore, reduction was attempted using ammonium formate in DMF in the presence of acetic acid using 10% wet Pd/C in

a microwave reactor for 20 min at 80 °C. CBz was successfully deprotected from the macrocycle. The reaction mixture was filtered on a celite pad to remove Pd/C and solvent removed under pressure by forming azeotropic mixture with toluene. However, during the workup of the crude product by the addition of water followed by basification using 2 M NaOH to remove ammonium formate,[10] the amide bonds underwent partial hydrolysis. After basification, the attempt to extract the product from the basic layer using $CHCl_3$ did not work out, as the expected product was soluble in water. After acidifying the aqueous layer, the product was partially extracted into chloroform, dried over sodium sulfate, filtered and evaporated to dryness. However, the yield was very low (< 10%) but, there is scope to optimise this procedure. A test reaction of alkylating **3.5** to 1,3-dibromopropane was attempted in DMF at 70 °C in the presence of K_2CO_3, but no product formation observed by TLC and MS. Therefore, this approach was terminated. Attaching tryptophan side chains to the cyclen through *N*-alkylation via acetyl chloride was found to be difficult,[11] while acid-amine coupling is suggested as the best approach which is proved successful here.

3.1.2. Photophysics of $[Tb_2(DO3AM\text{-}L\text{-}TrpOMe)_2C\text{-}3]^{6+}$

3.1.2.1. Electronic, excitation, and emission spectra

The electronic absorption spectrum of the binuclear Tb complex (Figure 3.3a) in deionised water displayed 3 shoulders (sh) at 269.5, 278, and 326 nm which correspond to the $\pi \rightarrow \pi^*$ transition from the conjugated groups within the tryptophan moiety. The metal centred excitation spectrum, recorded with the emission set at 547 nm, contains two prominent maxima at 278 and 351 nm (Figure 3.3b). Emission spectrum was recorded by exciting at 278 which is the reported excitation maxima to achieve Tb emission through the tryptophan moiety.[3] Visualising Tb emission

through direct excitation of the Tb metal at 366 nm did not afford an emission spectrum. Steady-state emission for the binuclear Tb complex in deionised water was achieved upon sensitising the tryptophan arms at 278 nm, with emission bands assignable to the $^5D_4 \rightarrow {}^7F_J$ (J = 6 – 3) transitions (Figure 3.3c). The baseline at the start of the steady-state emission spectrum begins with a hump due to ligand fluorescence. However, in time-resolved phosphorescence mode, this hump was absent due to the short-lived ligand fluorescence. This gave a well-resolved emission spectrum with a flat baseline (Figure 3.3d).

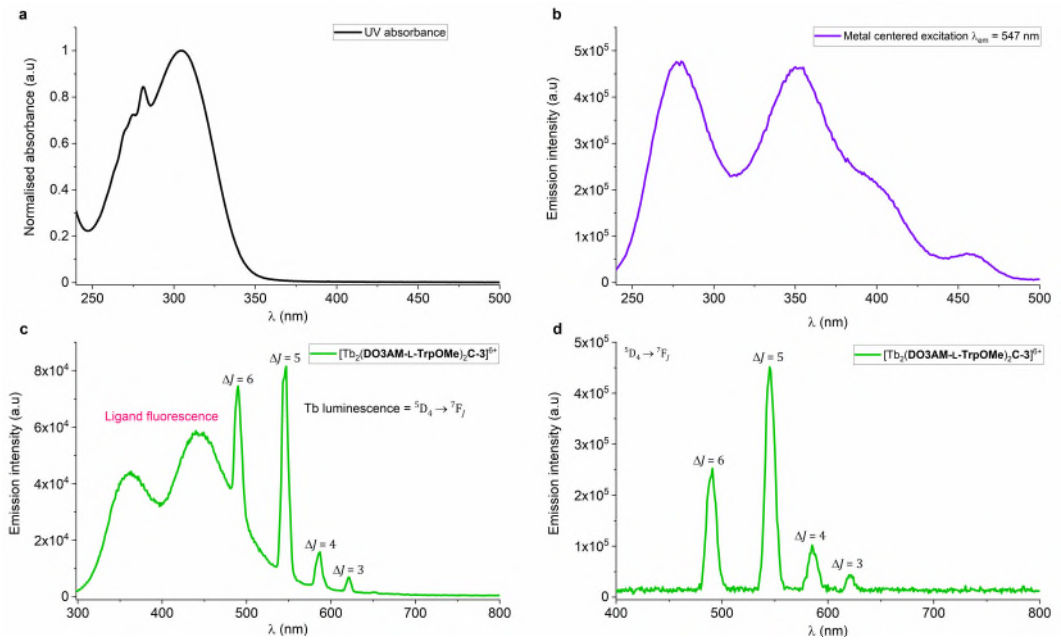


Figure 3.3. Photophysics of [Tb_2**(DO3AM-L-TrpOMe)$_2$C-3**]$^{6+}$: (a) Normalised electronic absorption spectrum, (b) excitation spectrum, (c) steady-state emission spectrum (λ_{exc} = 278 nm), and (d) time-resolved phosphorescence emission spectrum. All measurements were made in deionised water at 298 K (concentration of the complex, 10^{-5} M).

Absorption spectra were recorded upon the addition of fluoride and chloride (Figure 3.4). Apart from the change in intensity, no change in the absorption bands was observed.

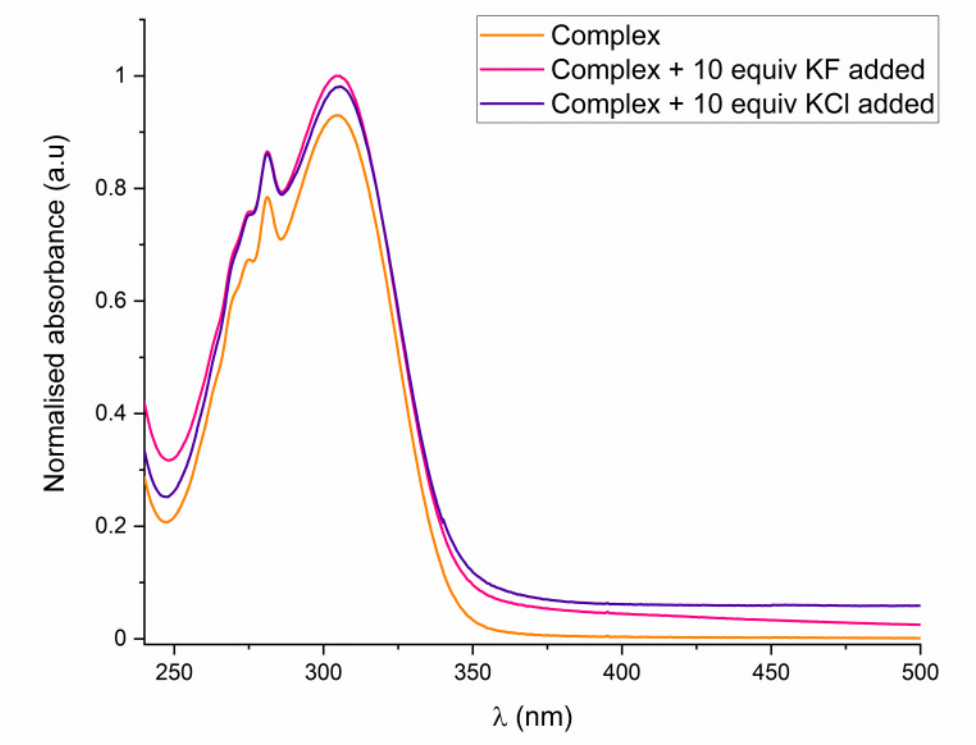


Figure 3.4. Electronic absorption spectra of $[Tb_2(\mathbf{DO3AM\text{-}L\text{-}TrpOMe})_2C\text{-}3]^{6+}$ with fluoride and chloride added at 298 K in deionised water (concentration of the complex, 10^{-5} M; stock KF and KCl concentration, 2×10^{-4} M).

3.1.2.2. Luminescence of the Binuclear Tb Complex upon Halide Addition

Due to the ligand fluorescence at the start of the steady-state emission spectrum, emission intensity change upon the addition of fluoride and chloride to the Tb centre was hard to follow as the baseline was found to be compromised throughout the spectra (Figure 3.5). Therefore, luminescence spectra were recorded on time-resolved phosphorescence mode, whereupon increasing fluoride addition (Figure 3.6) a consistent decrease in the luminescence intensity along with the change in form and shape of the emission bands was observed which accounts for fluoride binding to the metal centre. Analysis of $\Delta J = 5$ band reveals a consistent decay pattern upon fluoride addition. Upon increasing chloride equivalents (Figure 3.7), a decrease in luminescence intensity at the Tb centre was initially observed, but the intensity changes wobble with increasing addition of chloride rather than

being consistent. Analysis of ΔJ = 5 band reveals a decay pattern with an outlier which was unexpected. This decay pattern confirms chloride binding to the binuclear Tb(III) complex, but fluoride binding is stronger as the change in fine structure of the Tb(III) emission spectra is well resolved. Upon replacement of the inner-sphere water by the incoming anion, an increase in the Tb(III) emission intensity is expected (discussed in Chapter-I, Section 1.6.4.2). Here, a decrease in Tb(III) emission intensity was observed due to the combined effects of Dexter quenching between the identical metal centres[12] and PeT from the halides[13] which offsets the gain in luminescence intensity obtained by replacing the inner-sphere water (which is a similar observation in the binuclear Eu(III) complexes, discussed in Chapter-II). Due to lack of time, titrations of the mononuclear and binuclear Tb(III) complexes with fluoride and chloride were not performed.

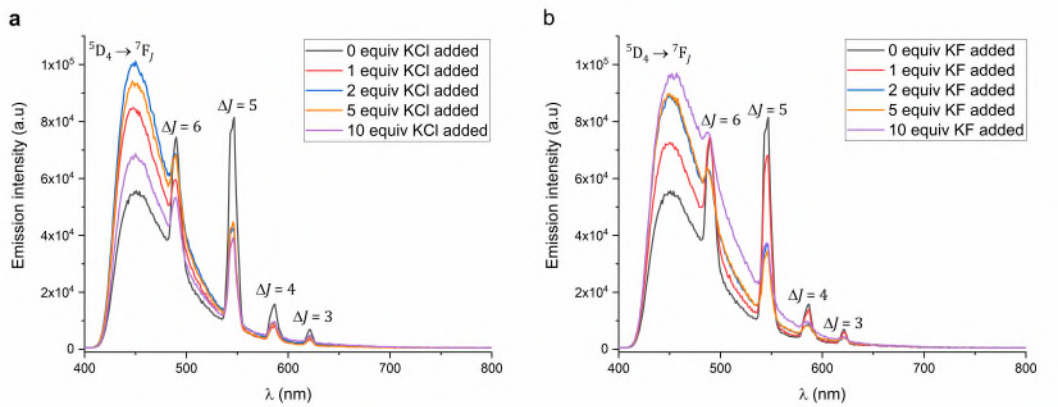


Figure 3.5. Steady-state emission spectra of [Tb_2(**DO3AM-L-TrpOMe**)$_2$**C-3**]$^{6+}$ with (a) increasing KCl and (b) increasing KF in deionised water at 298 K (concentration of the complex, 10^{-5} M; stock KF and KCl concentration, 2×10^{-4} M; λ_{ex} = 278 nm).

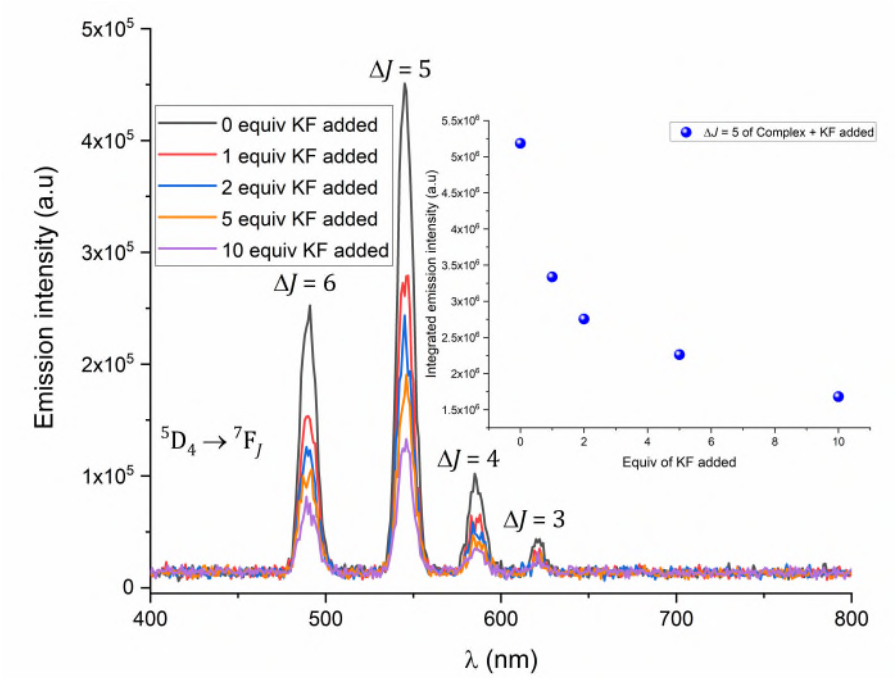


Figure 3.6. Time-resolved phosphorescence spectra of [Tb_2(**DO3AM-L-TrpOMe**)$_2$**C-3**]$^{6+}$ with increasing KF in deionised water at 298 K. *Inset*: ΔJ = 5 transition changes upon fluoride addition to the complex (concentration of the complex, 10^{-5} M; stock KF concentration, 2×10^{-4} M; λ_{ex} = 278 nm).

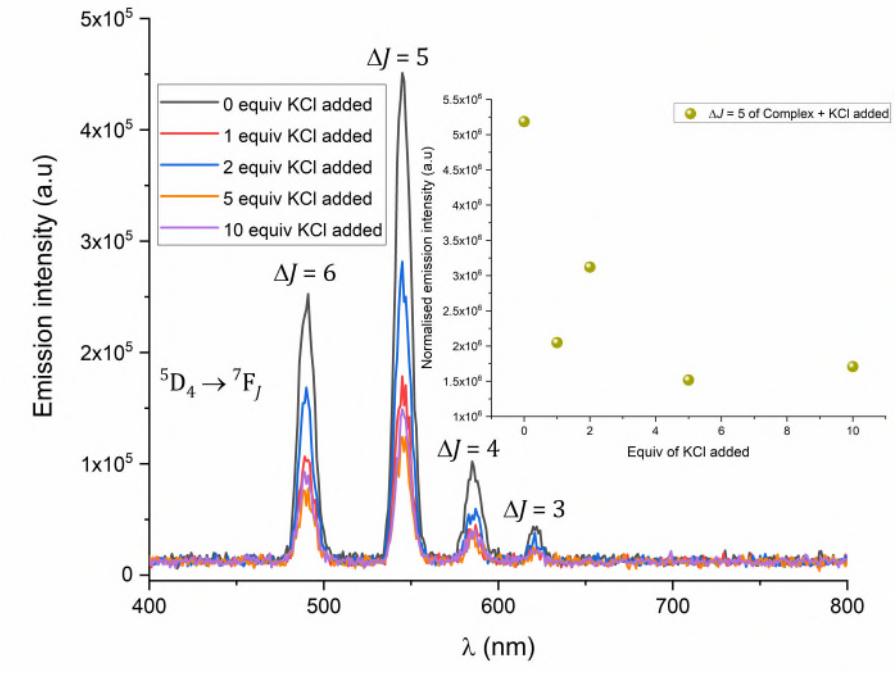


Figure 3.7. Time-resolved phosphorescence spectra of [Tb_2(**DO3AM-L-TrpOMe**)$_2$**C-3**]$^{6+}$ with increasing KCl in deionised water at 298 K. *Inset*: the ΔJ = 5 transition change upon fluoride addition to the complex (concentration of the complex, 10^{-5} M; stock KCl concentration, 2×10^{-4} M; λ_{ex} = 278 nm).

3.1.2.3. Luminescence Lifetime of the Binuclear Complex

Luminescence lifetime for $[Tb_2(\textbf{DO3AM-L-TrpOMe})_2\textbf{C-3}]^{6+}$ upon fluoride and chloride addition was determined in deionised water. The lifetime curve was best fitted to a monoexponential decay. Lifetime of the complex was found to be 1.4 ms. A decrease in the luminescence lifetime upon fluoride and chloride addition was observed (τ = 1.1 ms for 10 equiv fluoride added to the Tb(III) complex and τ = 1.2 ms for 10 equiv chloride added to the Tb(III) complex) which accounts for the replacement of inner-sphere water by these anions in the binuclear cationic complex reported here (Figure 3.8). The log values of the lifetimes upon the addition of fluoride and chloride, suggest a decreasing trend. In Chapter-II, no

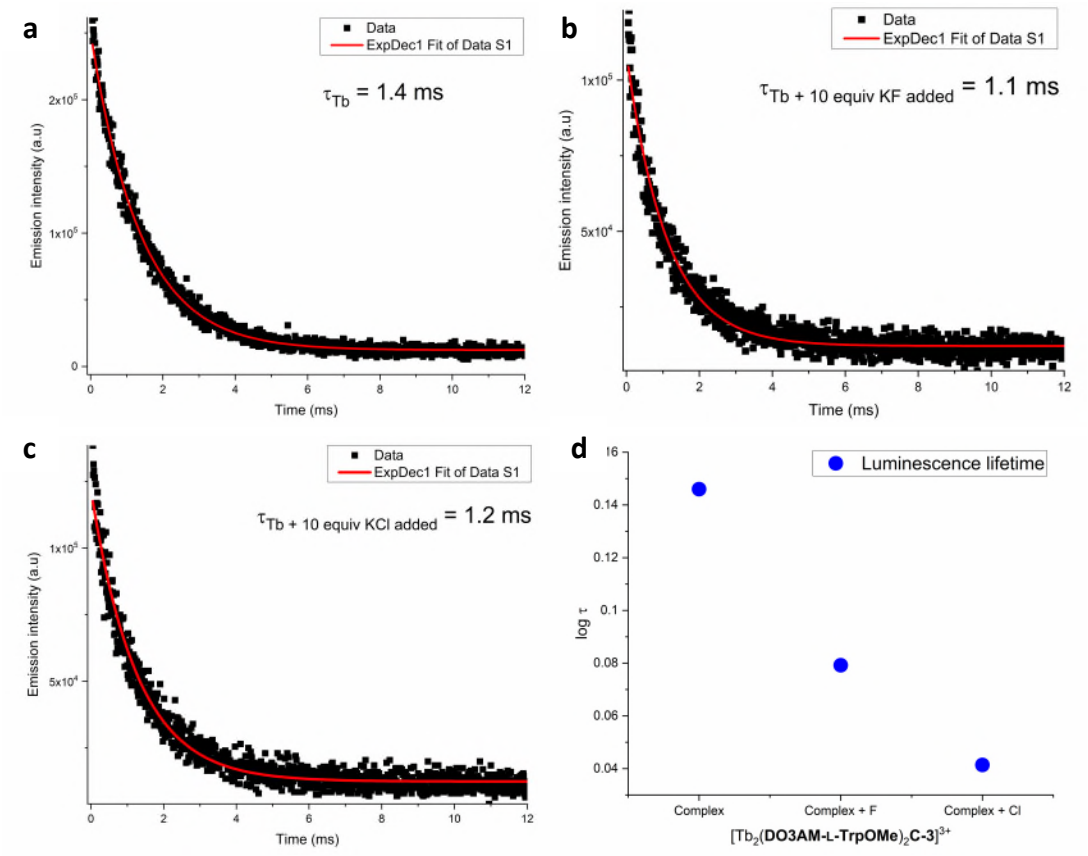


Figure 3.8. (a) Luminescence lifetime of $[Tb_2(\textbf{DO3AM-L-TrpOMe})_2\textbf{C-3}]^{6+}$, (b) with 10 equiv of KF added, (c) with 10 equiv of KCl added. (d) A plot of log values from luminescence lifetime of the Tb complex and upon the addition of 10 equiv KF and KCl. All measurements were made in deionised water at 298 K (concentration of the complex, 10^{-5} M; stock concentration of KF and KCl, 2×10^{-4} M).

change in the luminescence lifetime was observed on the [Ln_2(**DO3A**)$_2$**C-2**] and [Ln_2(**DO3A**)$_2$**C-3**] (Ln = Eu(III) and Tb(III)) complexes upon chloride addition. However, this observation was found to be otherwise in [Tb_2(**DO3AM-L-TrpOMe**)$_2$**C-3**]$^{6+}$. Due to lack of time, luminescence lifetime of the mononuclear and binuclear Tb(III) complexes with added fluoride and chloride in D_2O were not performed.

3.2. Conclusion

The binuclear tryptophan complex [Ln_2(**DO3AM-L-TrpOMe**)$_2$**C-3**]$^{6+}$ was successfully synthesised. However, there is scope to improve the yield of the ligand and purification of the complex through size-exclusion chromatography. Preliminary studies with this binuclear Tb(III) complex show promising results towards chloride chelation which can be explored in detail via luminescence titrations, luminescence lifetime, NMR, and X-ray crystal structure studies with a range of lanthanides. [Ln(**pDO3AM-L-TrpOMe**)]$^{3+}$ must be investigated further to ascertain its effectiveness towards halide binding. Furthermore, [Ln_2(**DO3AM-L-TrpOMe**)$_2$**C-2**]$^{6+}$ can be studied to explore the effect of shorter spacer towards halide chelation. Much remains to be done, but there is scope for detailed investigation towards chloride recognition.

3.3. References

1. (a) Butler, S. J.; Parker, D. *Chem. Soc. Rev*. **2013**, *42*, 1652–1666. (b) Blackburn, O. A.; Chilton, N. F.; Keller, K.; Tait, C. E.; Myers, W. K.; McInnes, E. J. L.; Kenwright, A. M.; Beer, P. D.; Timmel, C. R.; Faulkner, S. *Angew. Chem., Int. Ed*. **2015**, *54*, 10783–10786.
2. (a) Sørensen, T. J.; Faulkner, S. *Acc. Chem. Res*. **2018**, *51*, 2493–2501. (b) Montgomery, C. P.; Murray, B. S.; New, E. J.; Pal, R.; Parker, D. *Acc. Chem. Res*. **2009**, *42*, 925–937.
3. (a) Lincheneau, C.; Leonard, J. P.; McCabe, T.; Gunnlaugsson, T. *Chem. Commun.* **2011**, *47*, 7119–7121. (b) di Gennaro, A. K.; Gurevich, L.; Skovsen, E.; Overgaard,

M. T.; Fojan, P. *Phys. Chem. Chem. Phys.* **2013**, *15*, 8838–8844. (c) Cosby, A. G.; Quevedo, G.; Boros, E. *Inorg. Chem.* **2019**, *58*, 10611−10615. (d) Featherstone, E. R.; Issertell, E. J.; Cotruvo, J. A. *J. Am. Chem. Soc.* **2021**, *143*, 14287–14299.

4. (a) Liu, T.; Nonat, A.; Beyler, M.; Regueiro-Figueroa, M.; Nchimi Nono, K.; Jeannin, O.; Camerel, F.; Debaene, F.; Cianférani-Sanglier, S.; Tripier, R.; Platas-Iglesias, C.; Charbonnière, L. J. *Angew. Chem., Int. Ed.* **2014**, *53*, 7259–7263. (b) Chifotides, H. T.; Dunbar, K. R. *Acc. Chem. Res.* **2013**, *46*, 894–906.
5. (a) Carpino, L. A. *J. Am. Chem. Soc.* **1993**, *115*, 4397–4398. (b) Carpino, L. A.; Imazumi, H.; El-Faham, A.; Ferrer, F. J.; Zhang, C.; Lee, Y.; Foxman, B. M.; Henklein, P.; Hanay, C.; Mügge, C.; Wenschuh, H.; Klose, J.; Beyerman, M.; Bienert, M. *Angew. Chem., Int. Ed.* **2002**, *41*, 441–445. (c) El-Faham, A.; Albericio, F. *Chem. Rev.* **2011**, *111*, 6557–6602.
6. Woods, M.; Kiefer, G. E.; Bott, S.; Castillo-Muzquiz, A.; Eshelbrenner, C.; Michaudet, L.; McMillan, K.; Mudigunda, S. D. K.; Ogrin, D.; Tircsó, G.; Zhang, S.; Zhao, P.; Sherry, A. D. *J. Am. Chem. Soc.* **2004**, *126*, 9248–9256.
7. Adhikari, A.; Kumari, N.; Adhikari, M.; Kumar, N.; Tiwari, A. K.; Shukla, A.; Mishra, A. K.; Datta, A. *Bioorg. Med. Chem.* **2017**, *25*, 3483–3490.
8. Bruce, J. I.; O'Connell, P. J.; Taylor, P. G.; Smith, D. P. T.; Adkin, R. C.; Pearson, V. K. *Molecules* **2020**, *25*, 4253.
9. Sultane, P. R.; Mete, T. B.; Bhat, R. G. *Tetrahedron Lett.* **2015**, *56*, 2067–2070.
10. Hopper, L. E.; Allen, M. J. *Tetrahedron Lett.* **2014**, *55*, 5560–5561.
11. De León Rodríguez, L. M.; Viswanathan, S.; Sherry, A. D. *Contrast Media Mol. Imaging* **2010**, *5*, 121–125.
12. Tropiano, M.; Blackburn, O. A.; Tilney, J. A.; Hill, L. R.; Placidi, M. P.; Aarons, R. J.; Sykes, D.; Jones, M. W.; Kenwright, A. M.; Snaith, J. S.; Sørensen, T. J.; Faulkner, S. *Chem. —Eur. J.* **2013**, *19*, 16566–16571.
13. (a) Parker, D.; Senanyake, K.; Williams, J. A. G. *J. Chem. Soc., Perkin Trans. 2* **1998**, 2129–2139. (b) Parker, D.; Dickins, R. S.; Puschmann, H.; Crossland, C.; Howard, J. A. K. *Chem. Rev.* **2002**, *102*, 1977–2010.

CHAPTER-IV

Chapter-IV: Revisiting Lanthanide Complexes of PBA-Conjugated DO3A Towards Sialic Acid Recognition

4.1. The Biology of Glycans

Each type of human cell displays on its surface an array of glycans attached to proteins or lipids to form glycoconjugates. Glycosylation is an essential cellular process which involves the synthesis and attachment to cell surface proteins (glycoproteins) and lipids (glycolipids) of a structurally diverse group of oligosaccharides chains, known as glycans, that are synthesised in the endoplasmic reticulum and Golgi apparatus of all human cells. Glycosylation of cell surface proteins is involved in cell-cell communication, migration, and cell differentiation, and is frequently altered in disease, particularly in cancer.[1] The type and degree of expression of glycans is determined by the type and activities of the proteins involved in their synthesis that can be different from one cell type to another and even differ to some extent between the same types of cell. This dynamic temporospatial characteristic of glycosylation and the intrinsic information it can carry as a "glycan code" have been evolutionarily selected as an important mechanism for cells to communicate and enhance distinct physiologic and pathologic states, including malignant transformation.[2] Different types of monosaccharides and linkage combinations can be found on glycans code for biological information that translates into structural or functional properties of the glycoconjugate. Sialic acids (*Sia*) are typically found attached to the outermost ends of glycan chains of glycoproteins and glycolipids present on the cell surface.[3]

Given their location and ubiquitous distribution, *Sia* can mediate or modulate a wide variety of physiological and pathological processes. By virtue of their negative charge and hydrophilicity, *Sia* play many structural and modulatory

roles. *Sia* also serve as components of binding sites for various pathogens and toxins.[3a,b,4] In most such interactions, a pathogen binding protein recognises certain forms of *Sia* presented in a defined sugar chain. Several *Sia* binding proteins have been discovered over the last few decades.[3,4] A final class of function is 'molecular mimicry', in which successful microbial pathogens decorate themselves with sialic acids, assisting in evasion of host immunity.[5] The established and emerging roles of sialic acids in human physiology and disease is reviewed.[6]

4.1.1. Sialic Acids (*Sias*)

Sia are a diverse family of nine-carbon naturally occurring 2-keto-deoxy-nononic acids, which consists of one of nine major monosaccharide building blocks of mammalian glycans, with a carboxy group at the anomeric carbon atom that gives the molecule a negative charge at physiological pH (pK_a = 2.2). *Sia* are ubiquitous in vertebrates and highly expressed on vertebrate cell surfaces (up to 10 million molecules per human erythrocyte and 100 mM is the estimated local concentration in cell surface glycocalyx). The three major *Sia* found in nature are *N*-acetylneuraminic acid (Neu5Ac, **84**), *N*-glycolylneuraminic acid (Neu5Gc, **85**), and 2-keto-3-deoxy-D-glycero-D-galacto-nononic acid (KDN, **86**). The most abundant *Sia* in humans by far is Neu5Ac.[7] *Sia* generally occupies the terminal positions of carbohydrate chains of glycoproteins, glycolipids, glycophospholipid anchors, and proteoglycans (glycoconjugates) on the cell surface, and they appear to play important roles in cellular recognition processes.[6]

Neu5Ac is present in serum as a mixture of α- (5-8%) and β-pyranose (92-95%) forms, while the absence of the furanose form can be attributed to the acetamide group at the C-5 position.[8] In addition to these cyclic forms, three acyclic forms have been detected at low levels (0.5-1.9% at pH 2).[9] All known glycosides

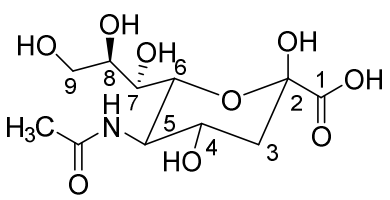
of Neu5Ac are α-linked, often to a galactose or a *N*-galactosamine residue through a R(2→3) or R(2→6) linkage.[3b,c,10]

4.1.2. *Sia* Modifications

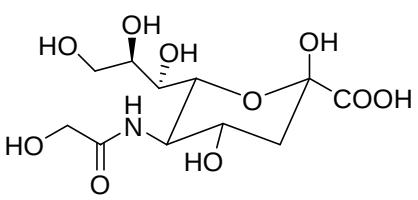
The *Sia* family is further diversified by modifications based on the three core structures (Neu5Ac, Neu5Gc, and KDN). *Sia* structure differs from the hexoses in having only two hydroxyl residues attached directly to the hexose ring. The amine at position C-5 is modified predominately as *N*-acetyl and *N*-glycoyl, but can also be a hydroxyl or amine. The 4-OH can also be acetylated. So far, more than 50 distinct *Sia* structures have been identified in nature, arising from acetylation, methylation, lactylation, and sulfation of the aliphatic side chain of three hydroxyl residues at C-6.[11] Such modifications can determine or modify their recognition by glycan-binding proteins (GBPs) and modulate *Sia* functions. Overall, the structural flexibility innate within the *Sia* backbone increases the potential chemical information that can be stored within these molecules when compared with the hexoses and pentoses. The amount of information in the form of chemical complexity that each glycan monomer contains has led them being described as a sugar code.[12] *Sia* are therefore the versatile structures on the glycan platforms.

4.1.3. *Sia* as a Tumour Marker

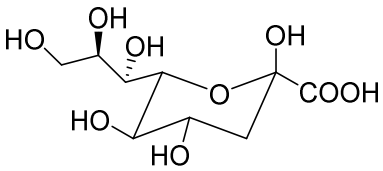
Glycans can be used as biomarkers of many diseases,[13] including cancer.[14] Changes in sialic acid expression are seen in many pathological states. Sialic acid is considered to be a tumour marker because it is known to be overexpressed on the



84, Neu5Ac (β-anomer)



85, Neu5Gc



86, KDN

surface of tumour cells.[3a,15] Many tumour-associated carbohydrate antigens possess sialic acid,[16] and its overexpression has been correlated with the malignant and metastatic phenotypes in epithelial-derived cancers and can result in the presentation of up to 10^9 sialic acid residues per tumour cell,[17] compared to 20×10^6 for a normal human erythrocyte. In clinical pathology, serum levels of sialic acid can predict the risk of various diseases[18] and can be used as a biological marker of a cancerous state.[19]

4.2. Changes in Glycosylation During Cancer Progression

Changes in glycosylation are a classic hallmark of malignant transformation.[20] Altered glycosylation of cell surface proteins and lipids is frequently associated with tumourigenic and metastatic processes.[21] These changes in glycosylation are mainly caused by an increased expression of sialyltransferases, which glycosylate exposed glycans at their terminal positions with anionic monosaccharide sialic acid residues. Tumour cells overexpressing *Sia* appear protected against the immune defense system, and as a result, malignancy is increased.[7,22] It has been demonstrated that *Sia* are relevant biomarkers of metastatic activity of tumours, and that the amount of *Sia* expression on cancer cells correlates with the prognosis of patients.[23] During malignant transformation, glycosylation is heavily altered compared with healthy tissue due to differential expression of glycosyltransferases, glycosidases, and monosaccharide transporters within the cancer microenvironment. One key change of malignant tissue glycosylation is the alteration of sialic acid processing that leads to a general upregulation of sialylated glycans (hypersialylation) on cell surfaces and an

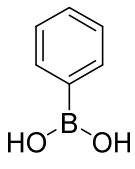
increased introduction of the non-human sialic acid *N*-glycolylneuraminic acid (Neu5Gc) instead of Neu5Ac into cell surface glycans. These changes have been shown to be the result of altered sialyltransferase and sialidase expression. Functionally, cancer-associated hypersialylation appears to directly impact tumour cell interaction with the microenvironment, in particular the modulation of sialic acid-binding lectins on immune cells. Moreover, Neu5Gc expression in human tissues enhances inflammation due to an anti Neu5Gc immune response, which can potentially influence inflammation-induced cancer and cancer-associated inflammation. The role of *Sia* in cancer biology and immunity is reviewed.[24]

4.3. Boronic Acid-Based Molecular Receptors for Monosaccharides

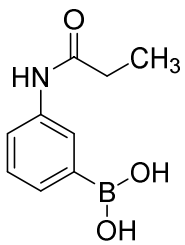
Molecular recognition of *Sia* is important for developing assays that could enable the detection of malignancies and other diseases involving high *Sia* levels. Boronic acids are a promising class of recognition moieties for the development of artificial receptors and sensors for saccharides.[25] Boronic acids interact with 1,2- and 1,3-diol units in saccharides selectively and form reversible and covalent five- and six-membered cyclic boronate esters in aqueous solution, and has been exploited in the design of various saccharide sensors.[25a,d,26] They are weak Lewis acids (pK_a ~ 8.67 for phenylboronic acid (PBA)), and the boron has sp^2 hybridisation. Upon increase in pH, boronates are formed in which the boron hybridisation is sp^3.[27] The association constant of a boronate complex with a carbohydrate is higher than that of the corresponding boronic acid complex, because the cyclic esters with a sp^3 boron atom are less strained than those with a sp^2 boron atom.[28] Consequently, the binding ability of boronic acid is optimal under basic conditions (pH > 9) where the concentration of the boronate anion is maximal. Wulff *et al.*[29] have shown that the conversion of a trigonal boronic acid to a

tetragonal boronate function is established at much lower pH when an aminomethyl group is introduced at the *ortho*-position.[29] Mulla *et al*.[30] have demonstrated that functionalisation of PBA (**87**) with electron-withdrawing substituents can decrease its pK_a substantially and, consequently, lead to an improved carbohydrate recognition at physiological pH. PBA derivatives have been explored as saccharide sensors by Shinkai group.[25a]

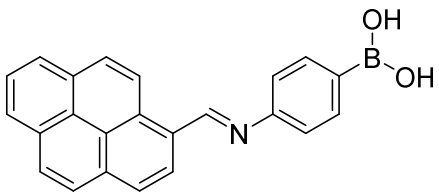
PBA was first synthesised by Michaelis and Becker in 1880,[31] but 74 years passed before the first binding studies of diols (or saccharides) with boronic acid were published in 1954 by Kuivila *et al*.[32] The first quantitative evaluation of interactions between saccharides and PBA was reported by Lorand and Edwards in 1959.[33] Detailed investigations on the interaction of Neu5Ac with PBA[34] and 3-(propionamido)phenylboronic acid (PAPBA, **88**)[35] have been accounted. A potentiometric detection of free- and cell membrane surface *Sia* using a PBA-modified gold electrode without any enzymatic and labeling procedures has been reported.[36] Binding of diboronate receptors with free *Sia* through both the glycerol side chain and the α-hydroxy acid function at the anomeric position is also reported.[37] The sensing and other applications of boronic acids,[38] development of saccharide sensors based on boronic acid,[26] boronic acid interactions with *cis*-diols and sensing applications,[39] and an account of boronic acid sensor molecules are reviewed.[40]



87

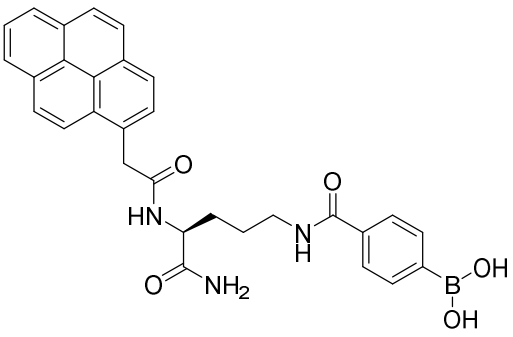


88

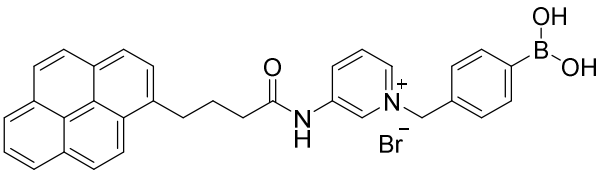


89

The pyrene-iminemonoboronic acid probe **89**[41] and ornithine amino acid-based pyrene-boronic acid sensor **90**[42] for monosaccharides based on PET mechanism were reported. The well-known Alizarin Red S (ARS)-phenylboronic acid displacement assay, developed by Springsteen and Wang,[43] was adapted using a fluorescent dye and a quencher-boronic acid appended viologen. The quenched fluorescence of the dye was recovered upon boronic acid-glucose interaction.[44] Aggregates of an amphiphilic monoboronic acid bearing hydrophobic pyrene fluorophore **91** was employed for highly modulating, sensitive, and selective ratiometric fluorescent sensing of glucose in aqueous solution by Huang *et al.*[45] The selectivity for glucose was improved by "knock-out" binding of fructose by PBA. Boronic acid-carbohydrate interactions were also employed for the fluorescence visualisation of tumours. Sensor system prepared using a peptide connected with two boronic acid groups (anthracene-based sensors) exhibits high specificity towards over-expressed carbohydrate-based carcinoma biomarker, sialyl Lewis X (sLex) and used for the selective labeling of cell-surface glycans of human hepatic cancer cells.[46] Sialyl Lewis X was selectively labeled in the mouse xenograft tumour *via* the boronolectin-fluorophore conjugate.[47]



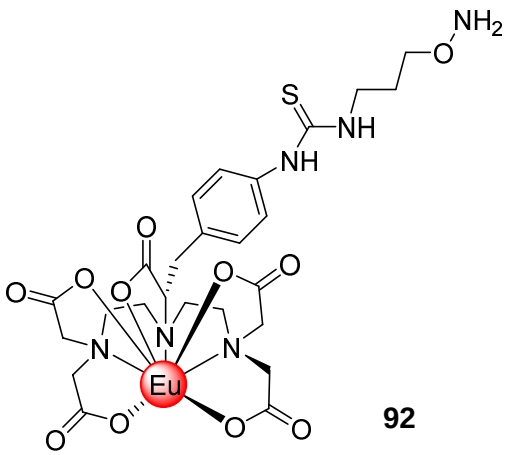
90



91

4.4. *Sia* Sensing and Imaging by Lanthanide(III) Complexes

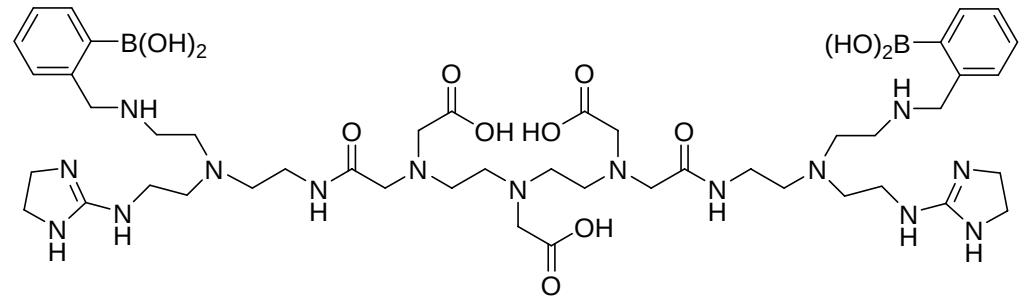
Altered cell surface glycosylation is a hallmark of disease, particularly cancer, and MRI is a widely used imaging technique for the rapid assessment of disease related changes on glycosylation *in vivo*. The high expression of *Sia* on the cell surface permits their MRI visualisation both *in vitro* and *in vivo* by using low molecular weight Gd complexes. Several lanthanide probes have been reported to target *Sia* and signal its detection using MRI[48] and emission-based techniques.[49] The incorporation of a PBA moiety into the ligand framework of a lanthanide complex has demonstrated the utility of this moiety, in the putative dynamic covalent binding to the 1,2-diol group of sialic acid.[48b,c] The intrinsic differences in *Sia* expression by cancer cells has been exploited by Bertozzi *et al*.[48b] for the selective targeting by Eu(III) complex **92** of aminooxy-terminated DTPA-based ligand. The selective targeting of **92** to cells on the basis of differential *Sia* is investigated by treating the complex with cultured Jurkat cells, a heavily sialylated human T-cell lymphoma cell line. The heavily sialylated normal Jurkat cells accumulated over twice the number of **92** ions than the mutant Jurkat cells with lower sialic acid levels.



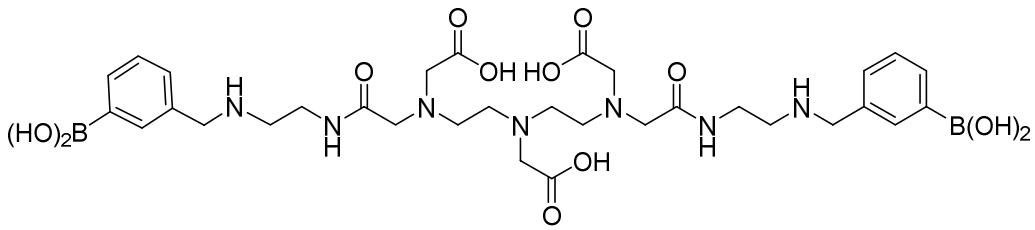
92

Gd(III) and ^{153}Sm(III) complexes of DTPA-bisamide ligands **93** and **94** which contain phenylboronate function for the molecular recognition of *Sia* were

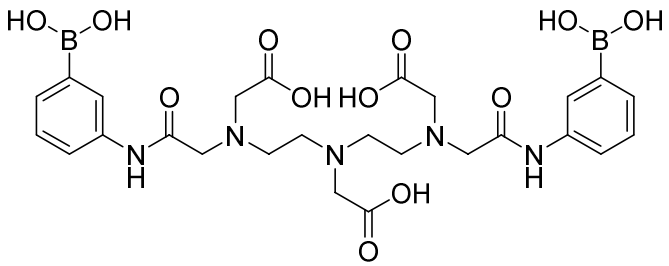
reported by Peters *et al.*[48c] The Gd(III) complexes recognise *Sia* with good selectivity in the presence of other sugars-the conditional formation constant of the adduct formed by [Gd(**94**)] with *Sia* is 50.43 ± 4.61 M^{-1} at pH 7.4. Gd(III) complex of 3-aminophenylboronate-functionalised DTPA (**95**) for the determination of glycated proteins by water proton NMR relaxation was reported by Aime *et al.*[50]



93

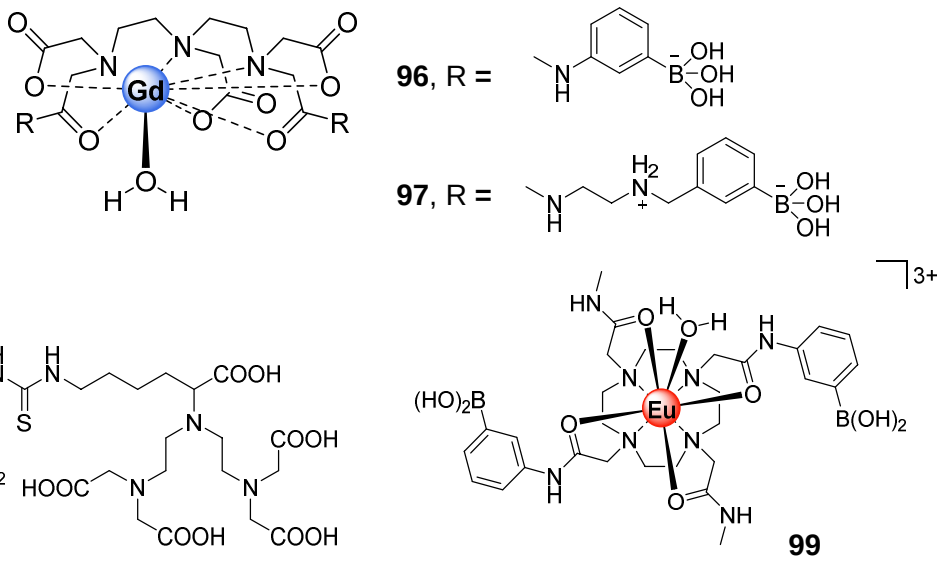


94

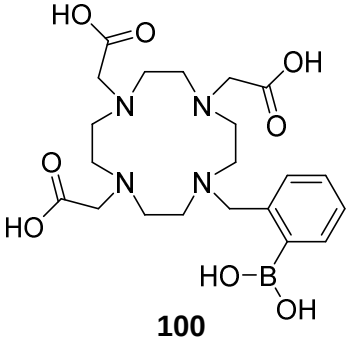


95

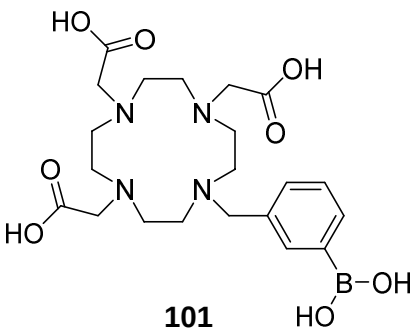
Molecular recognition of *Sia* on the surface of human glioma cells by ^{160}Tb complexes of PBA-conjugated DTPA ligands **96** and **97** was studied by Peters *et al*.[51] The complex [Tb(**97**)] was found to be an efficient targeting agent due to the electrostatic interaction between its two positively charged ammonium groups and the negatively charged cell surface which provides an additional stabilisation of the covalent binding through the PBA moieties and the *Sia* diol functions. Up to 5.5 nmol Tb/mg protein is taken up by the cells. Molecular recognition study of sugars by Gd(III) complex of phenylboronate-conjugated DTPA indicates that the DTPA derivative **98** is suitable for the molecular recognition of saccharides. The interactions of [Gd(**98**)] with carbohydrates are stronger than those of the parent compound PBA. In particular, strong interactions occur with saccharides in a furanose form that contains a *cis*-diol function in their structure.[52] The Eu(III) complex **99** of DOTA tetraamide derivative with two phenylboronate arms has been shown to bind reversibly with glucose with K_a = 383 M^{-1}. Such binding alters the water exchange between the Eu(III)-bound water molecule and bulk water, and is easily detected by CEST imaging. This prototype CEST agent is sensitive to changes in glucose over the physiological concentration range of 5-10 mM.[53]



Platas-Iglesias *et al.*[49a] have reported Ln(III) complexes (Ln(III) = La, Eu, Gd, and Tb) of PBA-appended DO3A ligand **100** and **101** for *Sia* recognition in aqueous medium. Interaction of the Ln(III) complexes with Neu5Ac and other competing monosaccharides was investigated by spectrophotometric titrations, ^{1}H, ^{13}C, and ^{11}B NMR spectroscopy, and by DFT calculations. The binding of these receptors with competing monosaccharides such as D-(+)-glucose, D-fructose, D-mannose, D-galactose, methyl *α*-D-galactoside, and methyl *α*-D-mannoside were studied. The binding constants indicate selectivity of [Gd(**101**)] for Neu5Ac (K_{eq} = 151 M^{-1}) over D-(+)-glucose (K_{eq} = 12.3 M^{-1}), D-mannose (K_{eq} = 21.9 M^{-1}), and D-galactose (K_{eq} = 24.5 M^{-1}). Furthermore, a very weak binding affinity was observed in the case of methyl *α*-D-galactoside and methyl *α*-D-mannoside. Compared with simple PBA, it exhibits an 8-fold increase in affinity and about 3.4-fold in selectivity for Neu5Ac over glucose *in vivo*, due to a cooperative two-site binding of Neu5Ac through ester formation by interaction with the PBA function of the receptor and coordination of the carboxylate group of Neu5Ac to the Ln(III) ion. Furthermore, [Gd(**101**)] also shows good selectivity for Neu5Ac over lactate and citrate. On the contrary, PBA forms stronger complexes with both lactate and citrate than with Neu5Ac. The emission lifetime of the $^{5}D_4$ level of Tb(III) in [Tb(**101**)] increases upon Neu5Ac binding, concomitant with the displacement of inner-sphere water molecules due to coordination of Neu5Ac to the metal ion.



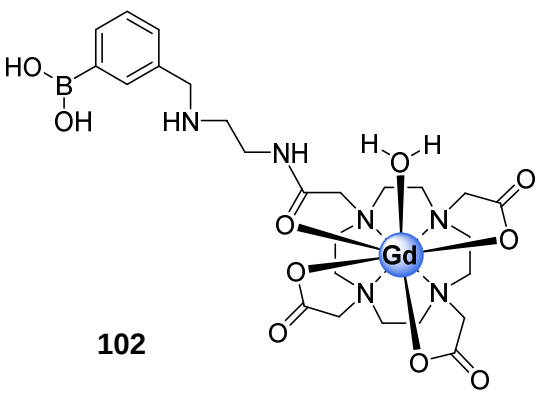
100



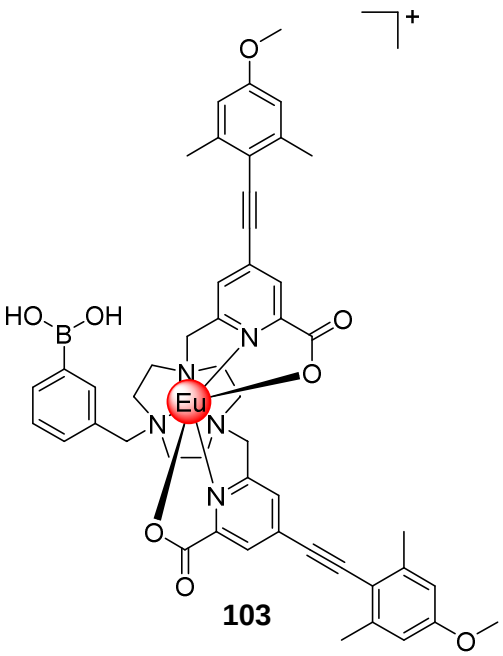
101

Crich, Aime *et al.*[48a] demonstrated *in vivo* visualisation of tumours by a highly selective dynamic covalent binding between the diol function of overexpressed *Sia* and a PBA-targeting vector conjugated with the MRI reporter **102**. The PBA group is attached to the macrocycle via an ethylenediamine (en) spacer. As the amino group of DOTA-en-PBA is positively charged at physiological pH, it facilitates the recognition mechanism through the electrostatic affinity to the negatively charged carboxylate of *Sia* residue. The role of this auxiliary interaction has been supported computationally.[51] There is a marked accumulation of the complex at the melanogenic cells that yields high relaxation rates, as a result of a higher Gd content, confirmed by ICP-MS measurements.

Parker *et al.*[54] reported the europium complex **103** bearing a PBA group that binds reversibly to *Sia* and lactic acid, as signalled by changes in the Eu(III) total emission spectrum and the induction of strong 'finger-print' CPL response. The CPL signature is distinctive for *Sia*, and differs from that observed with methyl sialate and *N*-acetyl glucosamine.



102



103

4.5. Bioorthogonal Chemistry-*An Introduction*

Bioorthogonal chemistry has become an indispensible tool for modern chemical biology research. Bioorthogonal reactions enable biomolecules to be studied in real time and in their native environments. They are chemical reactions that neither interact nor interfere with biological systems.[55] The participating functional groups must be stable in aqueous environments, inert to biological moieties, selectively reactive with each other, form a stable covalent linkage between the two functional groups under biocompatible conditions, and must be nontoxic to cells and organisms. Further, the reaction must proceed in water at physiological ranges of pH and temperatures. The reaction should have fast kinetics so that product is formed at a reasonable rate even when reactant concentrations are very low, as is required in many biological labeling experiments. The reagents must tolerate aqueous environments and large concentrations of cellular nucleophiles.[56] Bioorthogonal reagents and transformations must be orthogonal to biology, i.e., non-interacting (orthogonal) to the functionalities presented in biological systems.

Historically, the concept of bioorthogonality has strong roots in the much older field of bioconjugation, wherein bioorthogonal reaction development focused on methods to covalently target amino acids with small molecule probes.[57] In 1990, Rideout *et al*.[58] demonstrated that the selective condensation of hydrazine and aldehyde groups could be harnessed to assemble toxins from inactive prodrugs within live cells. In 1998, Tsien *et al*.[59] reported the first example of live cell protein labeling using bisarsenical dyes. These early examples foreshadowed the power of bioorthogonal chemistry as an instrument for chemical biology and biotechnology. While the use of a unique reactive group as ‘‘chemical handle’’ to direct selective reaction in a complex biological environment was reported long ago.[60] The first

published use of the term "bioorthogonal" by Bertozzi in 2003[61] and formalisation of "bioorthogonal chemistry" shortly afterwards[56b,62] unleashed a flurry of activities by many research groups in searching for new bioorthogonal reactions and their biological applications. Since then, bioorthogonal chemistry has become a mainstay of chemical biology and several biorthogonal reactions have been developed to tag proteins and other biomolecules,[63] profile active enzymes,[64] identify drug targets,[65] study glycans, lipids, and to target individual biomolecules with imaging agents or other probes, even in live cells and organisms. Advances in bioorthogonal reactions are enabling new pursuits in drug delivery,[66] genetic code expansion,[67] and protein activation.[68] Bioorthogonal reactions are click reactions starting from Cu(I) catalysed click reactions, and followed by modified Saudinger ligation, strain promoted click reactions, other transition metal catalysed click reactions, bioorthogonal cycloadditions, and tetrazine ligations.[61-67] For this seminal work that defined the synthetic world on all realms, Carolyn Ruth Bertozzi, Karl Barry Sharpless, and Morten Peter Meldal won the Chemistry Nobel Prize in 2022.[69]

4.6. Aim of Chapter-IV

Boronic acids have been recently introduced in the tool-kit of bioorthogonal reagents owing to its propensity to form esters *in vivo* via vicinal diols of saccharides in living systems.[38,70] Ln complexes with heptadentate ligands like DO3A and its derivatives are diaqua systems, known to bind various oxyanions replacing the inner-sphere water (reviewed in Chapter-1). By combining a phenylboronic acid (PBA) and a coordinatively unsaturated [Gd(**DO3A**)] chelate, a fundamental relationship was studied between various sugars and this probe as reported by Platas-Iglesias *et al*.[49a] Binding interactions has been studied by UV-Vis spectroscopy and longitudinal relaxivity. However, this probe recognises

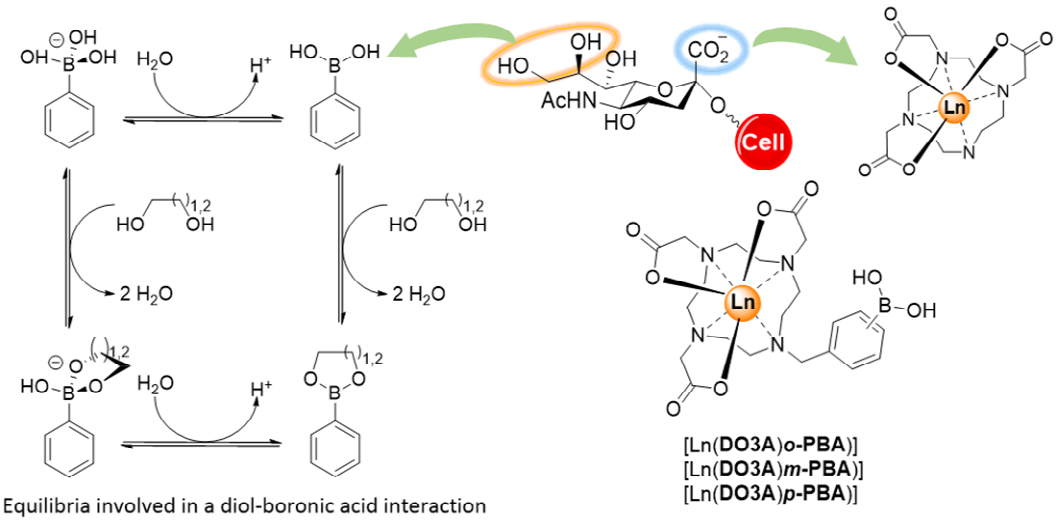


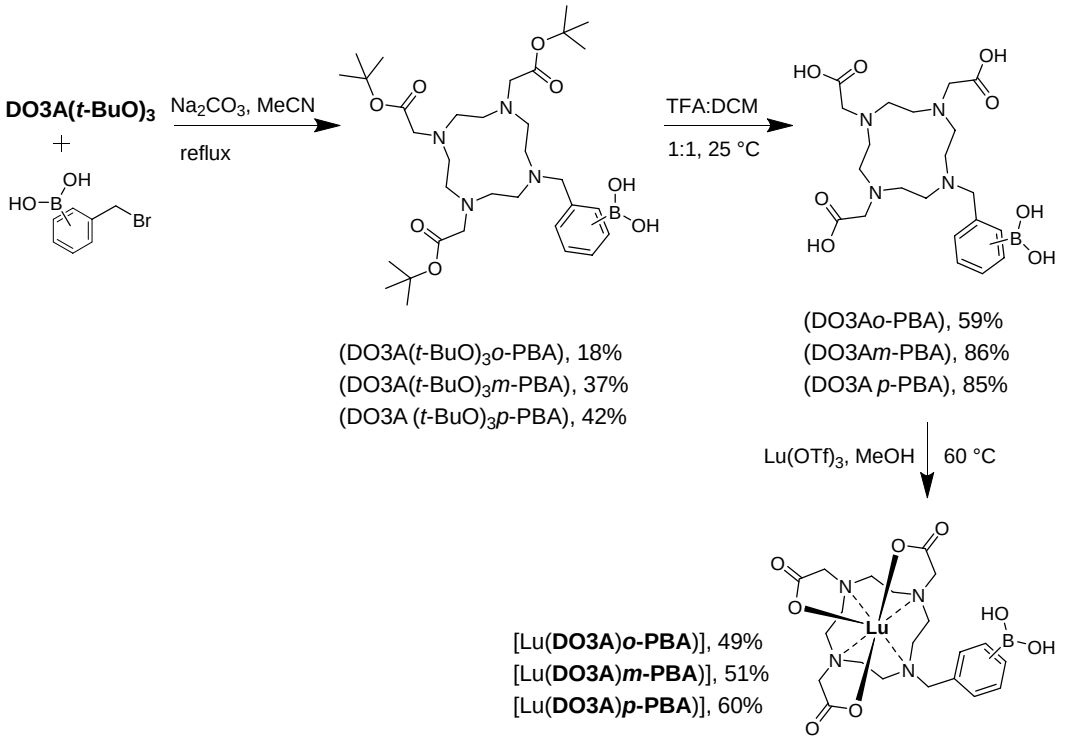
Figure 4.1. Proposed sialic acid (Neu5Ac) binding to the [Ln(**DO3A**)] and PBA groups, leading to the target [Ln(**DO3A**)**PBA**] complexes.

fructose better than *Sia*. Given that their systems rely exclusively on binding, the aim was to revisit this work and explore methods of understanding and exploiting interactions between species: luminescence titrations in buffers to understand the ditopic chelation of sugars to this complex (as luminescence is sensitive than UV-Vis spectroscopy and longitudinal relaxivity), kinetic study to understand the order to chelation of sugars (i.e., binding to boronate followed by chelation to the metal or vice versa), paraSHIFT or paraCEST measurements which are inherently less dependent on selectivity (since they exploit itself as part of the process). Furthermore, varying the substitution pattern on the aryl ring will help to explore the effects of conformational space on binding with sugars (Figure 4.1).

4.7. Results and Discussion

4.7.1. Synthesis of the Ditopic Complexes

Detailed synthetic protocol, purification, and characterisation are located in Chapter-VII, Section 7.6.3. Synthesis of the ditopic complexes were achieved as



Scheme 4.1. Synthesis of Lu(III) chelated DO3A-PBA with *ortho*-, *meta*-, and *para* boronates.

follows (Scheme 4.1). DO3A(*t*-BuO)$_3$ was alkylated with the appropriate (bromomethyl)phenylboronic acid in the presence of sodium carbonate in acetonitrile at reflux. After 12 h, the reaction mixture was filtered to remove the inorganic solids and the filtrate evaporated to dryness. The resulting crude product was column purified on silica under DCM/*iso*-propanol system to afford DO3A(*t*-BuO)$_3$*o*-PBA, DO3A(*t*-BuO)$_3$*m*-PBA, or DO3A(*t*-BuO)$_3$*p*-PBA as a white solid. Column purification was very challenging as the product was eluted in different gradients due to the different protonation states of the boronate which moves at different R_f values in a silica column.

The *t*-Bu esters in the macrocycle are removed by dissolving DO3A(*t*-BuO)$_3$*o*-PBA, DO3A(*t*-BuO)$_3$*m*-PBA, or DO3A(*t*-BuO)$_3$*p*-PBA in DCM followed by dropwise addition of TFA and stirring for 12 h. The solvent was evaporated to dryness, MeOH added (to create an azeotrope with TFA) and

evaporated to dryness to remove TFA as much as possible. The resulting residue was dissolved in minimum MeOH and triturated with excess diethyl ether to precipitate the ligand DO3A*o*-PBA, DO3A*m*-PBA, or DO3A*p*-PBA as a white solid and isolated by centrifugation. Upon injecting DO3A*m*-PBA or DO3A*p*-PBA on a prep HPLC, the product moved in at *m/z* 479.180 and 481.195 corresponding to the species $[M - H]^-$ and $[M + H]^+$, respectively, due to the two different protonation states of the boronate, that caused the product to elute at 2 different times, as shown by the HPLC traces in Appendix-B.

The ligands are complexed with $Lu(OTf)_3$ by mixing both the ligand and the metal in methanol and refluxing for 48 h. The solvent was removed under reduced pressure, the resulting crude redissolved in water and pH adjusted to 10 to

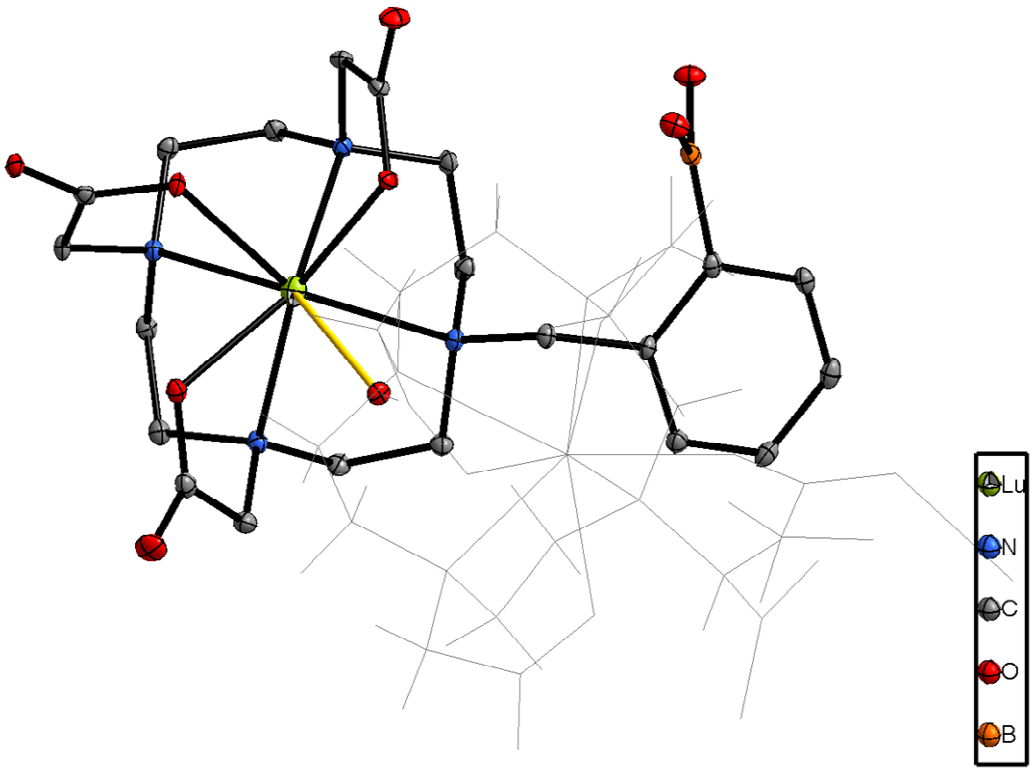
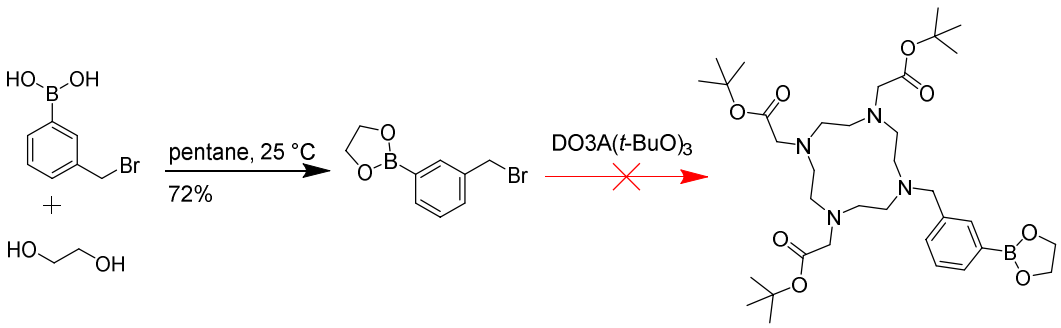


Figure 4.2. Single crystal X-ray structure of [Lu(**DO3A**)***o*-PBA**)]. Except selected structure, the rest are shown in wireframe format, H atoms and water are omitted for clarity. Thermal ellipsoid drawn at 20% probability level. μ-oxo bridging bond is shown in yellow. Structure solved by Dr. Kirsten Christensen at Chemical Crystallography, University of Oxford.

precipitate free metals as $Lu(OH)_3$ and removed by centrifugation. The centrifugate was neutralised followed by dialysis for 48 h to afford the complexes [Lu(**DO3A**)***o*-PBA**], [Lu(**DO3A**)***m*-PBA**], or [Lu(**DO3A**)***p*-PBA**] as a white solid. Complex formation was verified using ^{1}H and ^{11}B NMR spectroscopy, and HRMS. Crystals of [Lu(**DO3A**)***o*-PBA**] were obtained by slow diffusion of glyme over concentrated solution of the complex in deionised water and characterised by X-ray crystal structure (Figure 4.2). This Lu(III) complex crystallised as a cluster containing four complex molecules which are connected to each other via μ-oxo bridge from a carbonyl oxygen coordinated to the metal centre of another complex. The covalent connectivity was observed as expected. This cluster formation is a kinetic trap imposed during crystallisation and does not reflect its solution state behaviour.

4.7.1.1. Attempts to make the DO3A-PBA ligands

The procedure reported for the synthesis of DO3A*o*-PBA and DO3A*m*-PBA involves alkylating 2-(2-(bromomethyl)phenyl)-1,3,2-dioxaborolane or 2-(3-(bromomethyl)phenyl)-1,3,2-dioxaborolane to DO3A(*t*-BuO)$_3$ to get the respective pro-ligands.[49a] When this was attempted with 2-(3-(bromomethyl)phenyl)-1,3,2-dioxaborolane to DO3A(*t*-BuO)$_3$ (Scheme 4.2), it was unsuccessful under the reported conditions and also by modifying those conditions as presented in Table 4.1.



Scheme 4.2. Attempted monoalkylation with **DO3A(*t*-BuO)$_3$ (**ref 49a).

Table 4.1. Reaction conditions used in alkylating 2-(3-(bromomethyl)phenyl)-1,3,2-dioxaborolane to DO3A(*t*-BuO)$_3$

Base[I]	Solvent[‡]	Time (h)	Temperature (°C)
K_2CO_3	MeCN	72	reflux
K_2CO_3	DMF	72	50
Cs_2CO_3[†]	MeCN	72	reflux
Cs_2CO_3[†]	DMF	72	50
Na_2CO_3	MeCN	24	reflux
$NaHCO_3$[†]	MeCN	24	reflux
Et_3N	MeCN	72	reflux

[‡] Dry solvents used.

[†] KI (10 mol%); [I] 2-3 equiv of base used in all the attempts.

The alkylation did not proceed and no product formation observed. When reattempted using the same reaction conditions, the aryl ring attached to DO3A did not have the boronate on it, as confirmed by ^{11}B NMR spectroscopy and LRMS, but this observation was not reproducible. This led to the new synthetic strategy for the synthesis of DO3A*o*-PBA and DO3A*m*-PBA by alkylating DO3A(*t*-BuO)$_3$ with the respective arylbromomethyl boronate without any protecting group over it. However, the column purification was much harder due to the different protonation states of the boronic acid (as mentioned in Section 4.7.1). It has been reported that alkylation in the presence of other protecting groups on the boronate did not proceed due to steric effects from the protecting groups onto the macrocycle.[49a]

4.7.1.2. Protodeboronation of PBA-conjugated ligands by Eu(III) and Tb(III)

Complexation of DO3A*o*-PBA, DO3A*m*-PBA, and DO3A*p*-PBA was achieved with Lu(III) (vide Section 4.7.1). However, upon complexation of these ligands

with Eu(III) and Tb(III) using the same procedure as done with Lu(III), the desired complexes were not formed. LRMS analysis revealed the mass of the complex with the aryl ring and not with the boronate on it, but it was initially assumed that this could be a fragmentation pattern. ^{11}B NMR spectroscopy did not reveal any well-resolved boron signals, but it was assumed that the boron signals were obscured by the paramagnetic metal. ^{1}H NMR spectroscopy was not useful in elucidating the presence of boronate on the aryl ring. Therefore, X-ray crystal structure was sought. When the crude obtained upon reacting $Eu(OTf)_3$ with DO3A*m*-PBA was crystallised by slow diffusion of glyme over a concentrated solution of the complex in deionised water, it crystallised as the complex with the aryl ring containing a boron atom without the OH groups

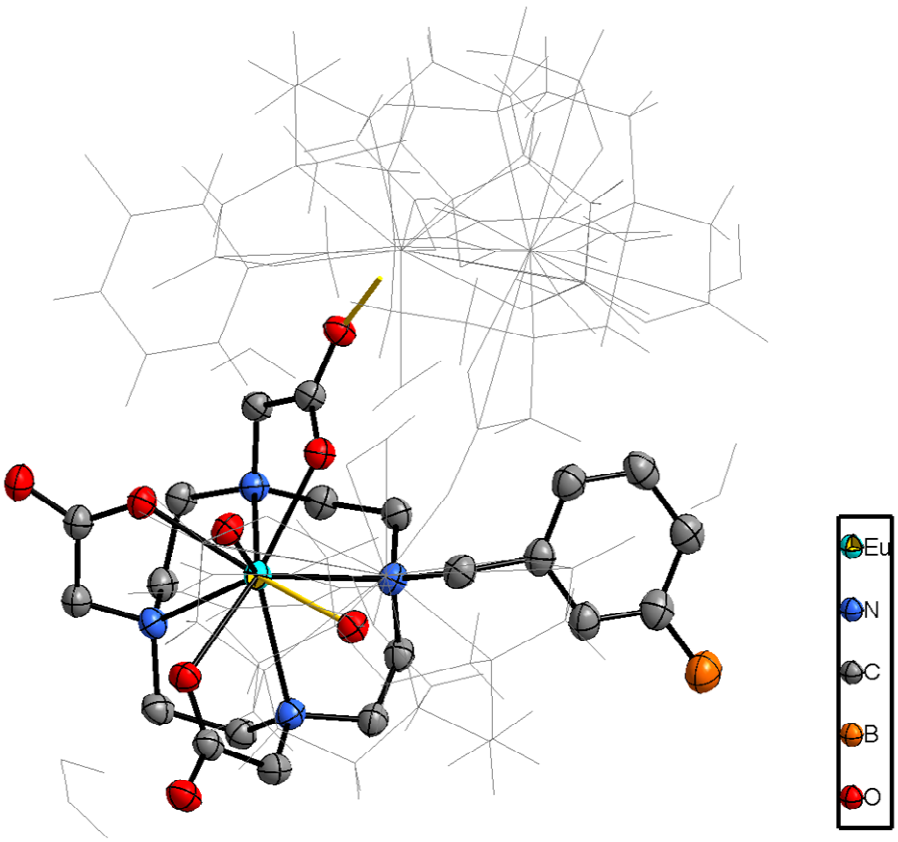


Figure 4.3. Single crystal X-ray structure of [Eu(**DO3A**)**benzyl-*m*-B**]. Except selected structure, the rest are shown in wireframe format, H and water are omitted for clarity. Thermal ellipsoid drawn at 30% probability level. μ-oxo bridging bond is shown in yellow. Structure solved by Dr. Kirsten Christensen at Chemical Crystallography, University of Oxford.

on it (Figure 4.3). Upon crystallisation the crude obtained upon reacting $Eu(OTf)_3$ with **DO3A*o*-PBA**, it crystallised with the aryl ring and no boronic acid group was present (Figure 4.4). This showed that the boronate group is cleaved off during complexation of the DO3A-PBA ligands with paramagnetic metals like Eu(III) and Tb(III), but it stays intact as expected when chelated to a diamagnetic metal like Lu(III) (although the Eu(III) complex crystallised as a cluster containing 4 metal centres, similar to the Lu(III) complexes). This effect of boronic acid cleavage on the aryl ring, catalysed by metals is called "protodeboronation". Crystal structure from the crude obtained upon reacting $Eu(OTf)_3$ with DO3A*p*-PBA is located in Appendix-C (Crystallisation conditions same as $Eu(OTf)_3$ with DO3A*m*-PBA).

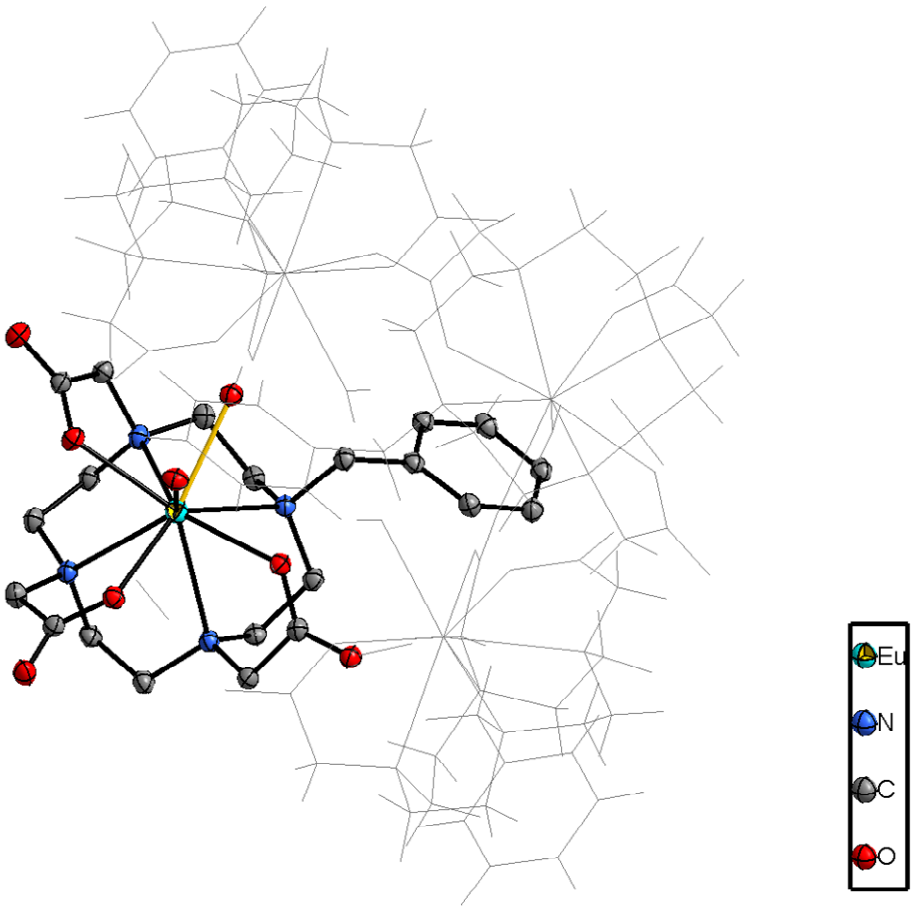
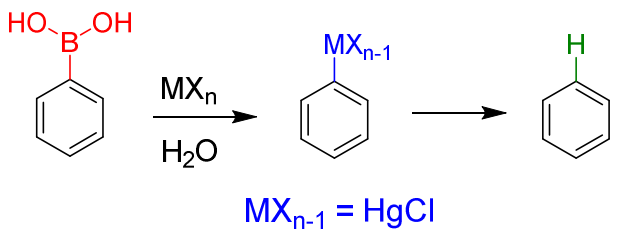


Figure 4.4. Single crystal X-ray structure of [Eu(**DO3A**)**benzyl**]. Except selected structure, the rest are shown in wireframe format, H and water are omitted for clarity. Thermal ellipsoid drawn at 30% probability level. μ-oxo bridging bond is shown in yellow. Structure solved by Dr. Kirsten Christensen at Chemical Crystallography, University of Oxford.

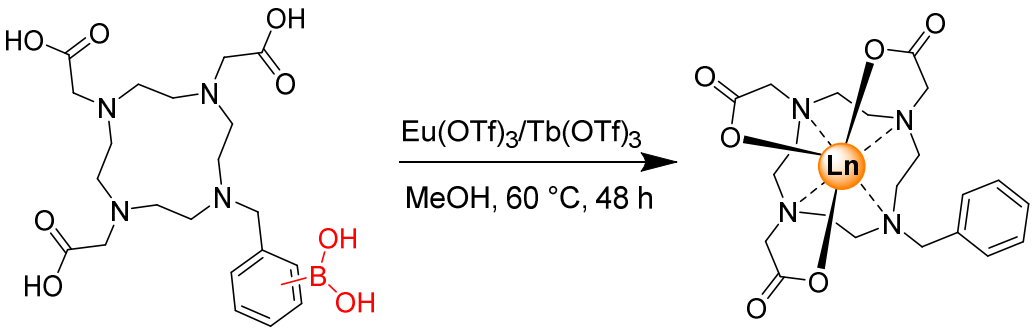
Zn(II) assisted protodeboronation on cyclen-PBA has been reported.[71] For the first time, Eu(III) and Tb(III) assisted protodeboronation is observed with structural evidence in this work.

Protodeboronation was first observed by Michaelis and Becker in 1882 during the preparation of phenylmercuric chloride from PBA and aqueous mercuric chloride. PBA was transformed into benzylmercuric chloride which resists hydrolysis during its preparation (Scheme 4.3).[31,72] Later, mechanistic studies reveal this reaction proceeds through the hydroxyboronate ion.[73] One of the early realisations concerning the reactivity of aryl boronates is that several metal ions can induce protodeboronation in water, presumably via the intermediary arylmetal species. This was explored over the years and found that the effective protodeboronation in PBA, assisted by metal ions, follow the order: Cu(II) > Pb(II) > Ag(I) > Cd(II) > Zn(II) > Co(II) > Mg(II) > Ni(II).[74] Protodeboronation, assisted by lanthanides is reported here, though it is puzzling that this effect was not observed with a stronger Lewis acid like Lu(III), but with a weaker Lewis acid like Eu(III) and Tb(III). The presence of a boron atom with no oxygens in [Eu(**DO3A**)**benzyl-*m*-B**] (Figure 4.3), suggests that this could be an intermediary stage during the Eu(III) assisted protodeboronation, but further mechanistic studies are required to understand this behavior in detail. Therefore, the product formed during the chelation of Eu(III) and Tb(III) to DO3A*o*-PBA, DO3A*m*-PBA, or DO3A*p*-PBA



Scheme 4.3. Protodeboronation of boronic acid by mercuric chloride. Redrawn from ref 31,72.

is [Ln(**DO3A**)**benzyl**] (Ln = Eu(III), Tb(III)) (Scheme 4.4). The effect of protodeboronation with other lanthanide metals was not pursued due to time constraints, though the lack of an obvious pattern suggests that deboronation may be capricious. While the binding of *Sia* and other monosaccharides with the Eu(III) and Tb(III) complexes of DO3A-PBA ligands will exclude covalent attachment to the sugar molecules by the boronic acid group, the coordination of *Sia* and other guests on the metal centre was studied by steady-state luminescence and CPL titrations.



(DO3A*o*-PBA)
(DO3A*m*-PBA)
(DO3A *p*-PBA)

[Ln(**DO3A**)**benzyl**]

Scheme 4.4. Eu(III) and Tb(III) assisted protodeboronation to form [Ln(**DO3A**)**benzyl**].

4.7.2. Electronic, Excitation, and Emission Spectra

The electronic absorption spectrum of [Eu(**DO3A**)**benzyl**] in water shows absorption bands at 263, 270 (sh), and 310 nm assignable to the $\pi \rightarrow \pi^*$ transition of benzene[75] and the ligand (Figure 4.5a). Upon excitation at 270 nm, the complex exhibits five emission bands assignable to the $^5D_0 \rightarrow {}^7F_J$ (J = 0-4) transitions, characteristic of Eu(III), clearly illustrating that the chromophore is an effective sensitiser for europium emission (Figure 4.5b). The emission intensity of the ΔJ = 2 transition is hypertensive, characterised by its higher intensity than that of other

bands (similar to [Ln(**DO3A**)] and its derivatives). The emission lifetimes of the Eu(III) excited state ($^5D_0$) was determined in H_2O (τ = 0.51 ms) and D_2O (τ = 1.18 ms) in order to establish the hydration number (q = 1.0) of the metal using modified Horrocks′ equation (mentioned in detail in Chapter-I).

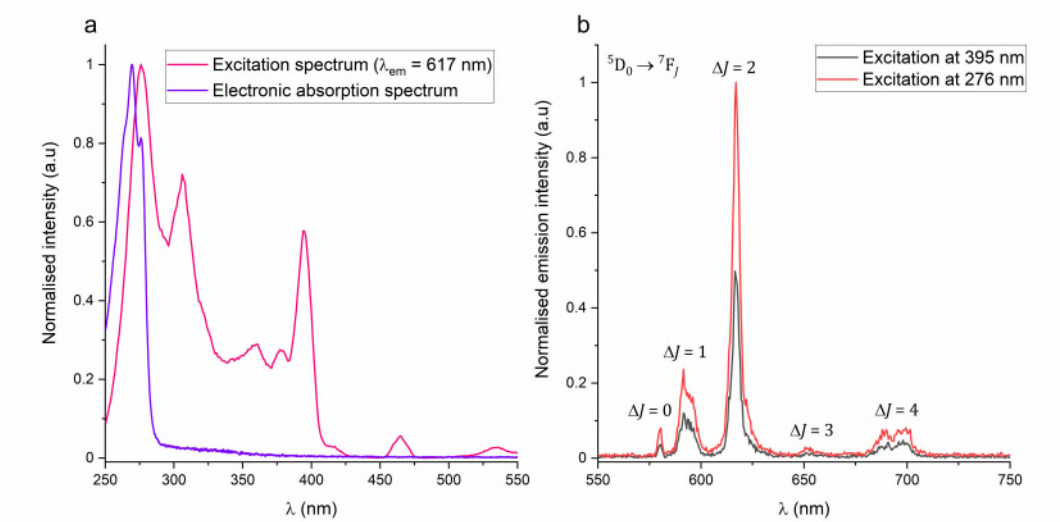


Figure 4.5. Photophysics of [Eu(**DO3A**)**benzyl**] in deionised water (10^{-5} M). (a) Normalised electronic absorption spectrum (*purple*) and excitation spectrum (*magenta*). (b) Normalised steady-state luminescence spectrum by direct excitation (λ_{ex} = 394 nm) via the metal (black) and indirect excitation (λ_{ex} = 270 nm) via benzene (*red*).

4.7.3. Luminescence Titrations of [Eu(DO3A)benzyl] with Monosaccharides

The Eu(III) complex was subjected to steady-state luminescence titration with a range of chiral guests which are highlighted in Figure 4.6. These are selected chiral guests, found in biology. The aim was to look at the binding of Neu5Ac with [Eu(**DO3A**)**benzyl**] and compare its binding with other guests. Steady-state luminescence titrations were carried out in 0.01 M PBS and 0.01 M Tris-HCl buffer at pH 7.4 to look at the binding affinities in competing and non-competing media. However, the complex bound to L-lactate and D-gluconate, and no binding was observed with other guests (Figures 4.7 to 4.9).

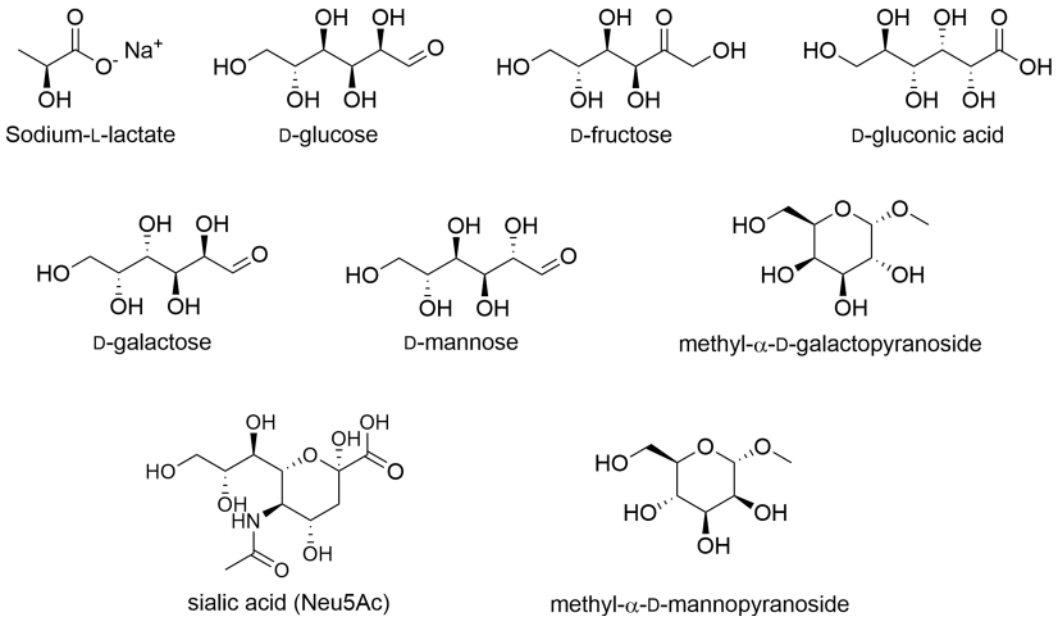


Figure 4.6. Chiral guests used to study binding with Ln(III) complexes in this chapter.

L-Lactate and D-gluconate bind to the metal centre through coordination of their carboxylate group. The emission intensity increases with incremental addition of L-lactate and D-gluconate to [Eu(**DO3A**)**benzyl**] due to the binding of the carboxylates of these guests by the replacement of inner-sphere water (expected luminescence response, Chapter-I, Section 1.6.4.2). The binding of L-lactate and D-gluconate is stronger in the non-competing Tris-HCl buffer (K_1 = 2,384 M^{-1} (±86) and 871 M^{-1} (±33), respectively), than that in the competing PBS buffer (K_1 = 558 M^{-1} (±24) and 803 M^{-1} (±33), respectively), due to strong interference of phosphate which competes for chelation at the metal centre, in addition to the guest that was added. The binding of these guests to lanthanide based DO3A complexes have been reported (vide Section 1.6.5.2). Regarding other guests, they contain hydroxy groups which do not coordinate to the metal due to its nature of being a weak Lewis base. As a result, no binding was achieved (binding would have been achieved if boronate had remained intact on the aryl ring, wherein the *cis*-diols of sugar would coordinate to the boronic acid to form a cyclic boronic ester and this binding is

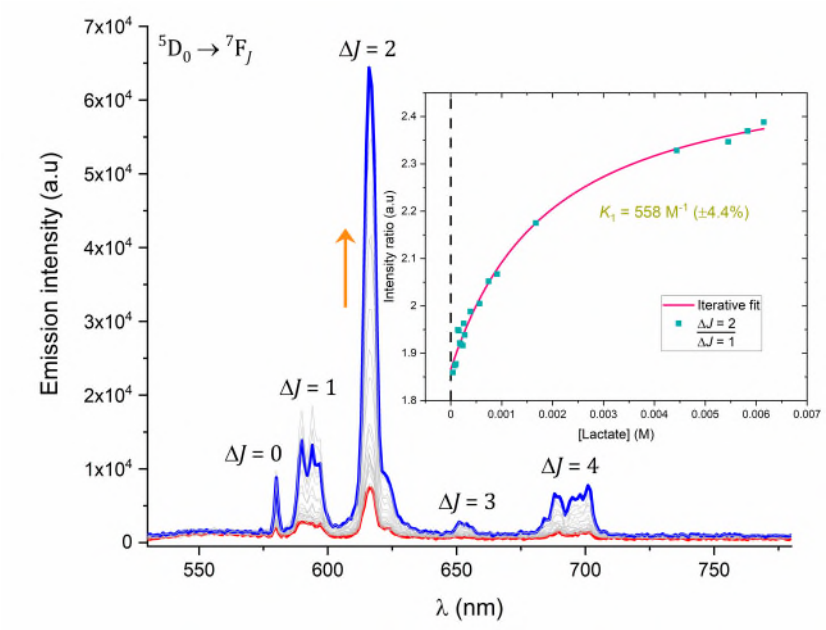


Figure 4.7. Steady-state Luminescence titration of [Eu(**DO3A**)**benzyl**)] (λ_{ex} = 270 nm) with increasing addition of L-lactate in 0.01 M PBS at pH 7.4; spectrum of neat complex solution (***red in bold***), spectra upon the additions of L-lactate (***grey***), spectrum upon the final addition of L-lactate (***blue in bold***). *Inset*: binding isotherm from the ratiometric analysis $\Delta J = 2/\Delta J = 1$, generated from the corresponding titration. Concentration of the complex was 2×10^{-4} M; stock concentration of the guest was 0.01 M.

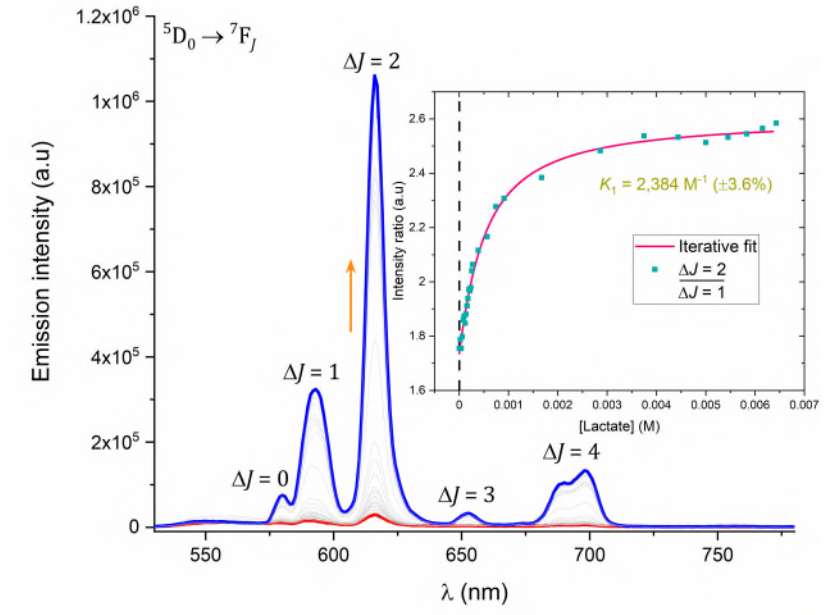


Figure 4.8. Steady-state luminescence titration of [Eu(**DO3A**)**benzyl**)] (λ_{ex} = 270 nm) with increasing addition of L-lactate in 0.01 M Tris-HCl at pH 7.4; spectrum of neat complex solution (***red in bold***), spectra upon the additions of L-lactate (***grey***), spectrum upon the final addition of L-lactate (***blue in bold***). *Inset*: binding isotherm from the ratiometric analysis $\Delta J = 2/\Delta J = 1$, generated from the corresponding titration. Concentration of the complex was 2×10^{-4} M; stock concentration of the guest was 0.01 M.

observed in the luminescence titration). Although Neu5Ac contains a carboxylic acid, its chelation to the metal centre was not observed at all. In titrations with organic guests involving carboxylic acid, it has been reported by Faulkner *et al.*[76] that guests would require base like LiOH to deprotonate the carboxylate to facilitate its binding at the metal site. Although L-lactate and D-gluconate did not require base for binding at the metal site, it was plausible that Neu5Ac required a base. However, due to time constraints, this was not attempted.

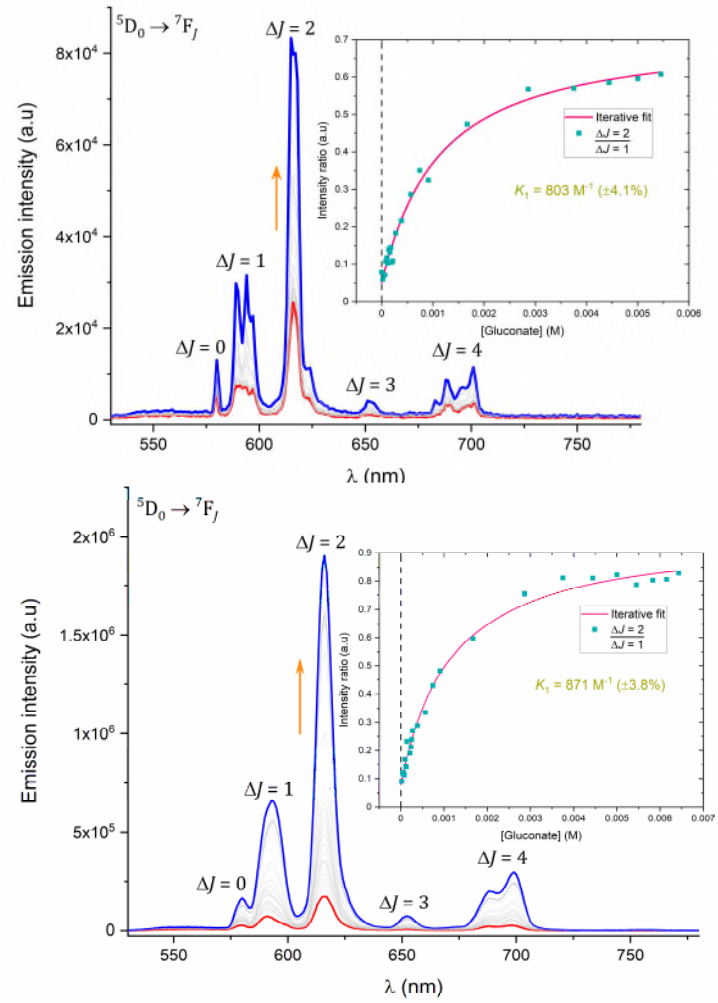


Figure 4.9. Steady-state luminescence titration spectra of [Eu(**DO3A**)**benzyl**] (λ_{ex} = 270 nm) with D-gluconate in (a) 0.01 M PBS at pH 7.4 (*top*) and (b) 0.01 M Tris-HCl at pH 7.4 (*bottom*); spectrum of neat complex solution (***red in bold***), spectra upon the additions of D-gluconate (*grey*), spectrum upon the final addition of D-gluconate (***blue in bold***). *Inset*: binding isotherm from the ratiometric analysis $\Delta J = 2/\Delta J = 1$, generated from the corresponding titration. Concentration of the complex was 2×10^{-4} M; stock concentration of the guest was 0.01 M.

Time resolved luminescence lifetime was measured with the Eu(III) complex upon the addition of guests (Table 4.2). With the exception of L-lactate and D-gluconate, which both exhibit strong binding to the metal, other guests did not replace the inner-sphere water in the complex (Lifetime best fitted to monoexponential decay).

Table 4.2. Luminescence lifetime of [Eu(**DO3A**)**benzyl**] with chiral guests*

[Eu(**DO3A**)**benzyl**] + 10 equiv chiral guests	Lifetime in PBS (ms)	Lifetime in Tris-HCl (ms)
[Eu(**DO3A**)**benzyl**]	0.50	0.34
D-Gluconic acid	0.75	0.76
Sodium-L-Lactate	0.69	0.7
D-Glucose	0.51	0.35
D-Galactose	0.5	0.5
D-Mannose	0.54	0.4
D-Fructose	0.52	0.41
Methyl-α-D-galactopyrannoside	0.52	0.41
Methyl-α-D-mannopyrannoside	0.52	0.41
Neu5Ac	0.51	0.42

* Lifetimes are subject to ±10% error. All buffers are maintained at 0.01 M at pH 7.4.

4.7.4. Circularly Polarised Luminescence Study for the Detection of Monosaccharides

In order to ascertain the chelation of guests to [Tb**(DO3A)benzyl**], the complex was subjected to CPL studies. This was pursued under the assumption that [Tb**(DO3A)benzyl**] is a racemic complex which is CPL silent. When a chiral guest chelates to the metal centre, a chiral induction occurs wherein the guest induces

chirality to the host upon binding. This host-guest adduct is now chiral and must be CPL-active. [Eu**(DO3A)benzyl**] was subjected for CPL studies with L-lactate, D-gluconate, and Neu5Ac with no avail due to poor quantum yield of the complex. CPL works best for lanthanide complexes with strong chromophores whose molar absorption coefficient must be at least 10,000 L mol^{-1} cm^{-1} or the complex must have a quantum yield of at least 10%.[77] Benzene is not a strong chromophore to sensitise Eu(III) and Tb(III) emission, but the strongly emissive nature of Tb(III) (mentioned in Section 1.3) might help to observe CPL signals. CPL was attempted for [Tb**(DO3A)benzyl**] with increasing addition of L-lactate, D-gluconate, and Neu5Ac in 0.01 M PBS buffer at pH 7.4 (Figures 4.10 to 4.12). Except for Neu5Ac, CPL signals were observed for the rest.

The g_{lum} for lactate bound species was 0.04 (at 543 nm, 10 equiv L-lactate added) and for the gluconate bound species, -0.101 (at 543 nm, 10 equiv D-gluconate added) (***Note:*** *for the above-mentioned* g_{lum} *values, error was not determined due to these values being lower than the error with which the instrument operates*). From the CPL spectra, it was evident that D-gluconate induces chirality

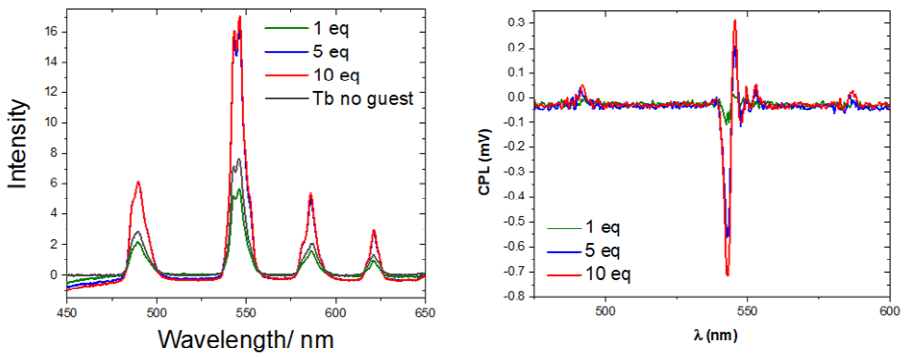


Figure 4.10. Steady-state luminescence (*left*) and CPL (*right*) spectra of [Tb(**DO3A**)**benzyl**] (λ_{ex} = 269 nm) with increasing addition of D-gluconate in 0.01M PBS buffer at pH 7.4. Recorded with Dr. Lewis E. Mackenzie and Robert Pal group, Durham University. Concentration of the complex was 2 × 10^{-4} M; stock concentration of the guest was 0.01 M. (eq = equivalents)

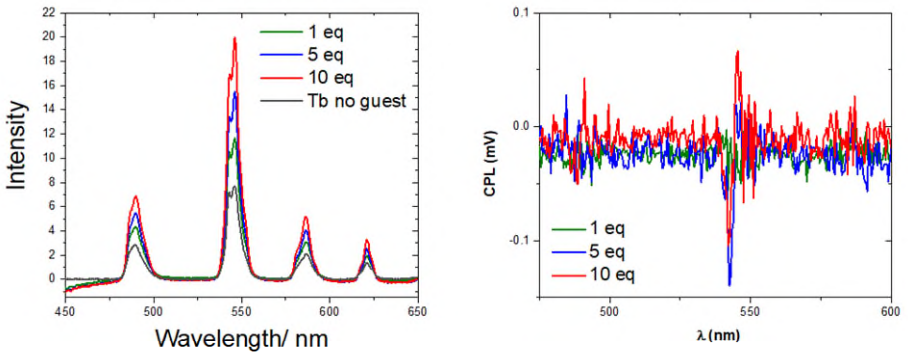


Figure 4.11. Steady-state luminescence (*left)* and CPL (*right*) spectra of [Tb(**DO3A**)**benzyl**] (λ_{ex} = 269 nm) with increasing addition of L-lactate in 0.01M PBS buffer at pH 7.4. Recorded with Dr. Lewis E. Mackenzie and Robert Pal group, Durham University. Concentration of the complex was 2 × 10^{-4} M; stock concentration of the guest was 0.01 M. (eq = equivalents)

to the metal centre better than L-lactate, as the former CPL signal was well-resolved than the latter. This can be attributed to the higher binding affinity of D-gluconate to [Tb**(DO3A)benzyl**] than L-lactate in PBS which was observed in the binding strengths from the luminescence titrations with [Eu**(DO3A)benzyl**]. The addition of base to Neu5Ac might have led to CPL signals due to deprotonation of the carboxylic acid leading to binding, but this was not attempted due to time restraints.

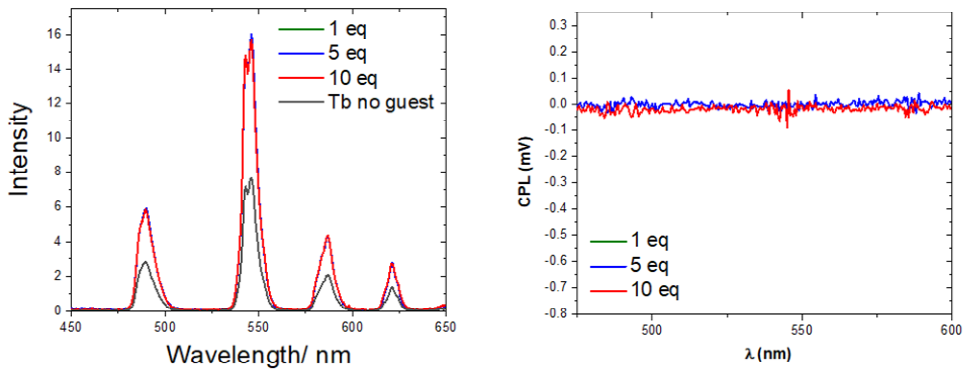


Figure 4.12. Steady-state luminescence (*left)* and CPL (*right*) spectra of [Tb(**DO3A**)**benzyl**] (λ_{ex} = 269 nm) with increasing addition of Neu5Ac in 0.01M PBS buffer at pH 7.4. Recorded with Dr. Lewis E. Mackenzie and Robert Pal group, Durham University. Concentration of the complex was 2 × 10^{-4} M; stock concentration of the guest was 0.01 M. (eq = equivalents.)

4.7.5. NMR Binding Studies of Monosaccharides with [Eu(DO3A)benzyl]

Paramagnetic ^{1}H NMR spectra were recorded with [Eu**(DO3A)benzyl**] containing 1 equiv of L-lactate, D-gluconate, and Neu5Ac in D_2O (Figure 4.13). The ^{1}H NMR signals expand in both the positive and negative chemical shift regions upon the addition of these guests due to its influence in the crystal field of the metal upon binding. The binding of these guests was found to be equatorial with respect to the metal centre as no signal is found to be inverted upon the addition of guest (inversion in ^{1}H NMR signals upon the addition of guest signifies axial binding, described in Chapter-II, Section 2.3). Upon the addition of Neu5Ac to the complex in D_2O, aggregation was observed. The broad signal at 25 ppm which was not observed in the spectrum of neat complex suggested this aggregation (formation of a white precipitate was found in the NMR tube). No visible aggregation was observed upon the addition of Neu5Ac to the complex during luminescence and CPL studies due to low concentration range used in these experiments. However,

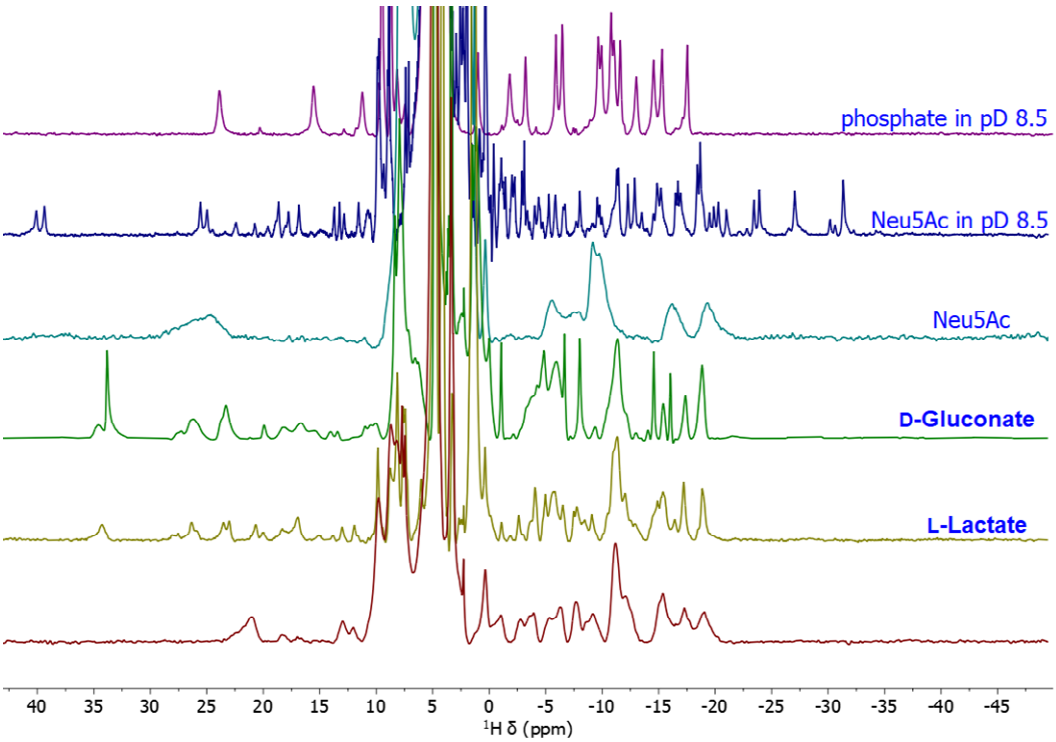


Figure 4.13. Paramagnetic ^{1}H NMR spectra of [Eu(**DO3A**)**benzyl**] with 1 equiv of different guests in D_2O at 298 K. pD = 8.5 was achieved from 0.01 M phosphate buffer.

when the ^{1}H NMR spectra of the complex with 1 equiv of added Neu5Ac were recorded at pD 8.5 in 0.01 M phosphate buffer, the aggregation disappeared, leading to a clear yellow solution in the NMR tube and well-resolved ^{1}H NMR signals which suggest equatorial binding to the complex (Figure 4.13). However, the phosphate from the buffer can compete with Neu5Ac, and the observed paramagnetic NMR resonances could be a consequence of phosphate binding rather than Neu5Ac binding. [Ln(**DO3A**)] and its derivatives bind to phosphates (vide Chapter-I, Section 1.6.5.1). Therefore, the NMR spectra were recorded with the complex in phosphate buffer at pD 8.5. Although phosphate binding was equatorial on the complex, the NMR signals are distinctly different from the complex with added Neu5Ac in phosphate buffer at pD 8.5 which suggests Neu5Ac binding on the complex. However, LiOH was not added to deprotonate the carboxylic acid of Neu5Ac which must be explored to determine the potency of the complex to chelate Neu5Ac at physiological pH.

4.8. Conclusion

The proposed DO3A-PBA complexes were prepared successfully with Lu(III). During complexation of the DO3A-PBA ligands with the paramagnetic Eu(III) and Tb(III) metal ions, the boronate moiety was cleaved off from benzene ring due to protodeboronation, leading to the formation of benzyl appended DO3A complexes. This result reported here, contradicts the literature report of the formation of [Ln(**DO3A**)**PBA**] complexes with boronate on *ortho*- and *meta*-substituted benzene. [Ln(**DO3A**)**benzyl**] [Ln = Eu(III) and Tb(III)] were investigated for the recognition of chiral guests, in which, binding of L-lactate, D-gluconate, and Neu5Ac observed. The addition of base to Neu5Ac (to deprotonate the acid group) before adding it to the complex must be pursued to

ascertain its binding to the benzyl complex, especially in CPL as it confirms the formation of the host-guest adduct through chiral induction. The protodeboronation observed in this study needs to be mechanistically studied in detail to look into the possibility of discovering an alternative to transition metal catalysed coupling reactions that can open a new door in boronic acid chemistry towards synthetic applications.

4.9. References

1. Fuster, M. M.; Esko, J. D. *Nat. Rev. Cancer* **2005**, *5*, 526−542.
2. *Essentials of Glycobiology*; 2nd ed.; Varki, A., Cummings, R. D., Esko, J. D., Freeze, H. H., Stanley, P., Bertozzi, C. R., Hart, G. W., Etzler, M. E., Eds.; Cold Spring Harbor Laboratory Press: New York; 2009.
3. (a) Schauer, R. *Glycoconj. J*. **2000**, *17*, 485–499. (b) Angata, T.; Varki, A. *Chem. Rev*. **2002**, *102*, 439–469. (c) Varki, A. *Nature* **2007**, *446*, 1023–1029.
4. (a) Ilver, D.; Johansson, P.; Miller-Podraza, H.; Nyholm, P.-G.; Teneberg, S.; Karlsson, K.-A. *Methods Enzymol*. **2003**, *363*, 134–157. (b) Lehmann, F.; Tiralongo, E.; Tiralongo, J. *Cell. Mol. Life Sci*. **2006**, *63*, 1331–1354.
5. Vimr, E. R.; Kalivoda, K. A.; Deszo, E. L.; Steenbergen, S. M. *Microbiol. Mol. Biol. Rev*. **2004**, *68*, 132–153.
6. Varki, A. *Trends Mol. Med.* **2008**, *14*, 351–360.
7. Schauer, R. *Zoology* **2004**, *107*, 49–64.
8. Friebolin, H.; Kunzelmann, P.; Supp, M.; Brossmer, R.; Keilich, G.; Ziegler, D. *Tetrahedron Lett*. **1981**, *22*, 1383–1386.
9. Klepach, T.; Carmichael, I.; Serianni, A. S. *J. Am. Chem. Soc*. **2008**, *130*, 11892–11900.
10. Murrey, H. E.; Hsieh-Wilson, C. *Chem. Rev*. **2008**, *108*, 1708–1731.
11. (a) Schauer, R. *Hoppe-Seyler's Z. Physiol Chem*. **1970**, *351*, 595–602. (b) Schauer, R. *Hoppe-Seyler's Z. Physiol. Chem*. **1970**, *351*, 749–758.
12. Gabius, H. J. *Trends Biochem. Sci*. **2015**, *40*, 341.
13. Lebrilla, C. B.; An, H. J. *Mol. Biosyst*. **2009**, *5*, 17–20.
14. (a) Kufe, D. W. *Nat. Rev. Cancer* **2009**, *9*, 874–885. (b) An, H. J.; Kronewitter, S. R.; de Leoz, M. L.; Lebrilla, C. B. *Curr. Opin. Chem. Biol*. **2009**, *13*, 601–607.
15. (a) Yogeeswaran, G.; Stein, B. S.; Sebastian, H. *Cancer Res*. **1978**, *38*, 1336–1344. (b) Roth, J.; Zuber, C.; Wagner, P.; Taatjes, D. J.; Weisgerber, C.; Heitz, P. U.; Goridis, C.; Bitter-Suermann, D. *Proc. Natl. Acad. Sci. U. S. A*. **1988**, *85*, 2999–3003.

16. Varki, N. M.; Varki, A. *Lab. Invest.* **2007**, *87*, 851–857.
17. Jourdian, G. W.; Dean, L.; Roseman, S. *J. Biol. Chem.* **1971**, *246*, 430–435.
18. (a) Pickup, J. C.; Mattock, M. B.; Crook, M. A.; Chusney, G. D.; Burt, D.; Fitzgerald, A. P. *Diabetes Care* **1995**, *18*, 1100–1103. (b) Crook, M. A.; Earle, K.; Morocutti, A.; Yip, J.; Viberti, G.; Pickup, J. C. *Diabetes Care* **1994**, *17*, 305–310. (c) Pönniö, M.; Alho, H.; Nikkari, S. T.; Olsson, U.; Rydberg, U.; Sillanaukee, P. *Clin. Chem.* **1999**, *45*, 1842–1849. (d) Afzali, B.; Bakri, R. S.; Bharma-Ariza, P.; Lumb, P. J.; Dalton, N.; Turner, N. C.; Wierzbicki, A. S.; Crook, M. A.; Goldsmith, D. J. *J. Nephrol.* **2003**, *16*, 540–545.
19. Krolikowski, F. J.; Reuter, K.; Waalkes, T. P.; Sieber, S. M.; Adamson, R. H. *Pharmacology* **1976**, *14*, 47–51.
20. (a) Boligan, K. F.; Mesa, C.; Fernandez, L. E.; von Gunten, S. *Cell Mol. Life Sci.* **2015**, *72*,1231–1248. (b) Pinho, S. S.; Reis, C. A. *Nat. Rev. Cancer* **2015**, *15*, 540–555.
21. (a) Wang, P.-H. J. *Cancer Mol.* **2005**, *1*, 73–81. (b) Cui, H.; Lin, Y.; Yue, L.; Zhao, X.; Liu, J. *Oncol. Rep.* **2011**, *25*, 1365–1371.
22. Kannagi, R.; Izawa, M.; Koike, T.; Miyazaki, K.; Kimura, N. *Cancer Sci.* **2004**, *95*, 377–384.
23. (a) Duncker, I. M.; Salinas-Marin, R.; Martinez-Duncker, C. *Int. J. Mol. Imaging* **2011**, 283497. (b) Cazet, A.; Julien, S.; Bobowski, M.; Krzewinski-Recchi, M.-A.; Harduin-Lepers, A.; Groux-Degroote, S.; Delannoy, P.; *Carbohydr. Res.* **2010**, *345*, 1377–1383. (c) Fernndez-Briera, A.; Garzia-Parcerio, I.; Cuevas, E.; Gili-Martin, E. *Oncology* **2010**, *78*, 196–204.
24. Pearce, O. M. T.; Läubli, H. *Glycobiology* **2016**, *26*, 111–128.
25. (a) James, T. D.; Shinkai, S. *Top. Curr. Chem.* **2002**, *218*, 159–200. (b) Mader, H. S.; Wolfbeis, O. S. *Microchim. Acta* **2008**, *162*, 1–34. (c) James, T. D. *Top. Curr. Chem.* **2007**, *277*, 107–152. (d) James, T. D.; Tony, D.; Sandanayake, K. R. A. S.; Shinkai, S. *Angew. Chem., Int. Ed.* **1996**, *35*, 1910–1922.
26. Striegler, S. *Curr. Org. Chem.* **2003**, *7*, 81–102.
27. Duin, M. V.; Peters, J. A.; Kieboom, A. P. G.; Bekkum, H. V. *Tetrahedron* **1984**, *40*, 2901–2911.
28. Edwards, J. O.; Sederstrom, R. *J. Phys. Chem.* **1961**, *65*, 862–863.
29. Burgemeister, T.; Grobe-Einsler, R.; Grotstollen, R.; Mannschreck, A.; Wulff, G. *Chem. Ber.* **1981**, *114*, 3403–3411.
30. Mulla, H. R.; Agard, R. J.; Basu, A. *Bioorg. Med. Chem. Lett.* **2004**, *14*, 25–27.
31. Michaelis, A.; Becker, P. *Ber. Dtsch. Chem. Ges.* **1880**, *13*, 58–61.
32. Kuivila, H. G.; Keough, A. H.; Soboczenski, E. J. *J. Org. Chem.* **1954**, *19*, 780–783.
33. Lorand, J. P.; Edwards, J. O. *J. Org. Chem.* **1959**, *24*, 769–774.

34. Djanashvili, K.; Frullano, L.; Peters, J. A. *Chem. —Eur. J*. **2005**, *11*, 4010–4018.
35. Otsuka, H.; Uchimura, E.; Koshino, H.; Okano, T.; Kataoka, K. *J. Am. Chem. Soc*. **2003**, *125*, 3493–3502.
36. Matsumoto, A.; Sato, N.; Kataoka, K.; Miyahara, Y. *J. Am. Chem. Soc*. **2009**, *131*, 12022–12023.
37. Levonis, S. M.; Kiefel, M. J.; Houston, T. A. *Chem. Commun*. **2009**, 2278–2280.
38. Lacina, K.; Skládal, P.; James, T. D. *Chem. Cent. J*. **2014**, *8*, 60.
39. Bull, S. D.; Davidson, M. G.; van den Elsen, J. M. H.; Fossey, J. S.; Jenkins, A. T. A.; Jiang, Y.-B.; Kubo, Y.; Marken, F.; Sakurai, K.; Zhao, J.; James, T. D. *Acc. Chem. Res*. **2013**, *46*, 312–326.
40. Wu, X.; Li, Z.; Chen, X.-X.; Fossey, J. S.; James, T. D.; Jiang, Y.-B. *Chem. Soc. Rev*. **2013**, *42*, 8032–8048.
41. Tharmaraj, V.; Pitchumani, K. *RSC Adv*. **2013**, *3*, 11566–11570.
42. Neupane, L. N.; Lohani, C. R.; Kim, J.; Lee, K.-H. *Tetrahedron* **2013**, *69*, 11057–11063.
43. Springsteen, G.; Wang, B. *Chem. Commun*. **2001**, *17*, 1608–1609.
44. Wang, Z. J.; Lei, H. Y.; Feng, L. H. *Spectrochim. Acta A* **2013**, *114*, 293–297.
45. Huang, Y. J.; Ouyang, W. J.; Wu, X.; Li, Z.; Fossey, J. S.; James, T. D.; Jiang, Y. B. *J. Am. Chem. Soc*. **2013**, *135*, 1700–1703.
46. Xu, X.-D.; Cheng, H.; Chen, W.-H.; Cheng, S.-X.; Zhuo, R.-X.; Zhang, X.-Z. *Sci. Rep*. **2013**, *3*, 2679.
47. Chu, Y.; Wang, D. Z.; Wang, K.; Liu, Z.-R.; Weston, B.; Wang, B. H. *Bioorg. Med. Chem. Lett*. **2013**, *23*, 6307–6309.
48. (a) Crich, S. G.; Alberti, D.; Szabo, I.; Aime, S.; Djanashvili, K. *Angew. Chem., Int. Ed*. **2013**, *52*, 1161–1164. (b) Lemieux, G. A.; Yarema, K. J.; Jacobs, C. L.; Bertozzi, C. R. *J. Am. Chem. Soc*. **1999**, *121*, 4278–4279. (c) Frullano, L.; Rohovec, J.; Aime, S.; Maschmeyer, T.; Prata, M. I.; de Lima, J. J. P.; Geraldes, C. F. G. C.; Peters, J. A. *Chem. —Eur. J*. **2004**, *10*, 5205–5217.
49. (a) Regueiro-Figueroa, M.; Djanashvili, K.; Esteban-Gómez, D.; Chauvin, T.; Tóth, É.; de Blas, A.; Rodríguez-Blas, T.; Platas-Iglesias, C. *Inorg. Chem*. **2010**, *49*, 4212–4223. (b) Ouchi, K.; Saito, S.; Shibukawa, M. *Inorg. Chem*. **2013**, *52*, 6239–6241.
50. Aime, S.; Botta, M.; Dastrú, W.; Fasano, M.; Panero, M. *Inorg. Chem*. **1993**, 32, 2068–2071.
51. Djanashvili, K.; Koning, G. A.; van der Meer, A. J. G. M.; Wolterbeek, H. T.; Peters, J. A. *Contrast Media Mol. Imaging* **2007**, *2*, 35–41.
52. Battistini, E.; Mortillaro, A.; Aime, S.; Peters, J. A. *Contrast Media Mol. Imaging* **2007**, *2*, 163–171.
53. Zhang, S.; Trokowski, R.; Sherry, A. D. *J. Am. Chem. Soc*. **2003**, *125*, 15288–15289.

54. Neil, E. R.; Parker, D. *RSC Adv*. **2017**, *7*, 4531–4540.
55. Sletten, E. M.; Bertozzi, C. R. *Angew. Chem., Int. Ed*. **2009**, *48*, 6974–6998.
56. (a) Patterson, D. M.; Nazarova, L. A.; Prescher, J. A. *ACS Chem. Biol*. **2014**, *9*, 592−605. (b) Prescher, J. A.; Bertozzi, C. R. *Nat. Chem. Biol*. **2005**, *1*, 13−21.
57. (a) Giepmans, B. N.; Adams, S. R.; Ellisman, M. H.; Tsien, R. Y. *Science* **2006**, *312*, 217−224. (b) Scheck, R. A.; Schepartz, A. *Acc. Chem. Res*. **2011**, *44*, 654−665.
58. Rideout, D.; Calogeropoulou, T.; Jaworski, J.; McCarthy, M. *Biopolymers* **1990**, *29*, 247–262.
59. Griffin, B. A.; Adams, S. R.; Tsien, R. Y. *Science* **1998**, *281*, 269–272.
60. (a) Rideout, D. *Science* **1986**, *233*, 561–563. (b) Cornish, V. W.; Hahn, K. M.; Schultz, P. G. *J. Am. Chem. Soc*. **1996**, *118*, 8150–8151.
61. Hang, H. C.; Yu, C.; Kato, D. L.; Bertozzi, C. R. *Proc. Natl. Acad. Sci. U.S.A*. **2003**, *100*, 14846–14851.
62. van Swieten, P. F.; Leeuwenburgh, M. A.; Kessler, B. M.; Overkleeft, H. S. *Org. Biomol. Chem*. **2005**, *3*, 20–27.
63. Lang, K.; Chin, J. W. *Chem. Rev*. **2014**, *114*, 4764−4806.
64. (a) Willems, L. I.; van der Linden, W. A.; Li, N.; Li, K.-Y.; Liu, N.; Hoogendoorn, S.; van der Marel, G. A.; Florea, B. I.; Overkleeft, H. S. *Acc. Chem. Res*. **2011**, *44*, 718−729. (b) Nomura, D. K.; Dix, M. M.; Cravatt, B. F. *Nat. Rev. Cancer* **2010**, *10*, 630−638.
65. (a) Yang, K. S.; Budin, G.; Tassa, C.; Kister, O.; Weissleder, R. *Angew. Chem., Int. Ed*. **2013**, *52*, 10593−10597. (b) Rutkowska, A.; Thomson, D. W.; Vappiani, J.; Werner, T.; Mueller, K. M.; Dittus, L.; Krause, J.; Muelbaier, M.; Bergamini, G.; Bantscheff, M. *ACS Chem. Biol*. **2016**, *11*, 2541−2550.
66. (a) Versteegen, R. M.; Rossin, R.; ten Hoeve, W.; Janssen, H. M.; Robillard, M. S. *Angew. Chem., Int. Ed*. **2013**, *52*, 14112−14116. (b) Mejia Oneto, J. M.; Khan, I.; Seebald, L.; Royzen, M. *ACS Cent. Sci*. **2016**, *2*, 476−482.
67. (a) Stone, S. E.; Glenn, W. S.; Hamblin, G. D.; Tirrell, D. A. *Curr. Opin. Chem. Biol*. **2017**, *36*, 50−57. (b) Alvarez-Castelao, B.; Schanzenbächer, C. T.; Hanus, C.; Glock, C.; tom Dieck, S.; Dörrbaum, A. R.; Bartnik, I.; Nassim-Assir, B.; Ciirdaeva, E.; Mueller, A.; Dieterich, D. C.; Tirrell, D. A.; Langer, J. D.; Schuman, E. M. *Nat. Biotechnol*. **2017**, *35*, 1196−1201.
68. (a) Li, J.; Chen, P. R. *Nat. Chem. Biol*. **2016**, *12*, 129−137. (b) Fan, X.; Ge, Y.; Yang, Y.; Zhang, G.; Ngai, W. S. C.; Lin, Z.; Wang, J.; Zhao, J.; Li, J.; Chen, P. R.; Lin, F.; Zheng, S. *Angew. Chem., Int. Ed*. **2016**, *55*, 14046−14050. (c) Zhang, G.; Li, J.; Xie, R.; Fan, X.; Liu, Y.; Zheng, S.; Ge, Y.; Chen, P. R. *ACS Cent. Sci*. **2016**, *2*, 325−331. (d) Völker, T.; Meggers, E. *Curr. Opin. Chem. Biol*. **2015**, *25*, 48−54. (e)

Li, J.; Yu, J.; Zhao, J.; Wang, J.; Zheng, S.; Lin, S.; Chen, L.; Yang, M.; Jia, S.; Zhang, X.; Chen, P. R. *Nat. Chem*. **2014**, *6*, 352−361.

69. https://www.nobelprize.org/prizes/chemistry/2022/summary/
70. Akgun, B.; Hall, D. G. *Angew. Chem., Int. Ed.* **2018**, *57*, 13028-13044.
71. (a) Peters, J. A. *Coord. Chem. Rev.* **2014**, *268*, 1–22. (b) Kitamura, M.; Suzuki, T.; Abe, R.; Ueno, T.; Aoki, S. *Inorg. Chem.* **2011**, *50*, 11568–11580.
72. Michaelis, A.; Becker, P. *Ber. Dtsch. Chem. Ges.* **1882**, *15*, 180–185.
73. Matteson, D. A.; Krämer, E. *J. Am. Chem. Soc.* **1968**, *90*, 7261–7267.
74. *Boronic Acids: Preparation and Applications in Organic Synthesis and Medicine*; 1st ed.; Hall, D. G., Ed.; Wiley-VCH Verlag GmbH & Co. KGaA: Weinheim; 2005.
75. Ramsey, B. G. *J. Phys. Chem.* **1970**, *74*, 2464–2469.
76. Sørensen, T. J.; Hill, L. R.; Faulkner, S. *ChemistryOpen* **2015**, *4*, 509–515.
77. MacKenzie, L. E.; Pal, R. *Nat. Rev. Chem*. **2021**, *5*, 109–124.

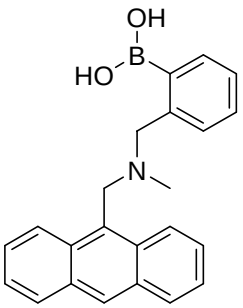
CHAPTER-V

Chapter-V: Towards Molecular Recognition of Sialic Acid by [Ln(DO3A)] Tethered to Anthracene and Dansyl-Conjugated Phenylboronic Acid

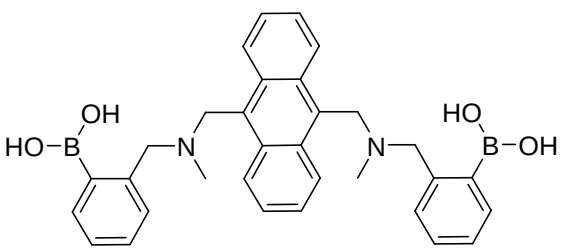
In Chapter-IV, the stability of phenylboronate during complexation with the lanthanides was found to be different among the metals. The use of cyclen-based phenylboronic acid (PBA) conjugates for sialic acid (*Sia*) recognition was reviewed in Chapter-IV, Section 4.4. In all of those examples, PBA was not directly attached to the macrocycle. In order to explore that approach, this Chapter extends from the previous Chapter on *Sia* recognition by [Ln(**DO3A**)] chelate tethered to PBA unit, but here, these are separated by anthracene and dansyl spacers to improve the stability of PBA unit from protodeboronation during complexation of the lanthanide. Also, this approach can increase selectivity towards *Sia* from other chiral guests, and improved sensitisation of lanthanide luminescence.

5.1. Design Inspiration

James *et al.*[1] have reported two saccharide PeT sensors **104** and **105**, based on the interaction of boronic acid and amine. When saccharides form cyclic boronate ester with PBA, the Lewis acid-base interaction between the tertiary amine and PBA is strengthened as the acidity of PBA is enhanced.[1] While **104** exhibits typical selectivity of PBA towards sugars, the sensor **105**, which has a cleft-like structure,



104



105

is selective and sensitive to glucose owing to the formation of an intramolecular 1:1 complex between two PBA units and the 1,2- and 4,6-hydroxyls of glucose. However, PeT from the boronate anion was not efficient even though it is directly bound to the chromophore (Figure 5.1).[1] Using slight modifications on this approach, a variety of anthracence-based PBA sensors were developed for sugar recognition because of their selectivity for saccharides.[2] However, it was reported by the same authors recently that the functioning of the anthracene based PeT sensor (Figure 5.1) is incorrect and the modulation of the -$B(OH)_2$ based internal conversion on a loose-bolt effect explains the potential working of these sensors to interact with sugars.[3]

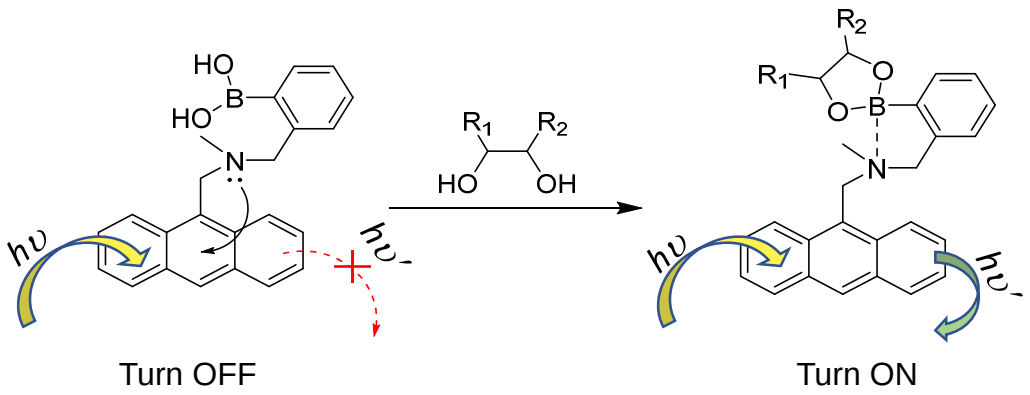
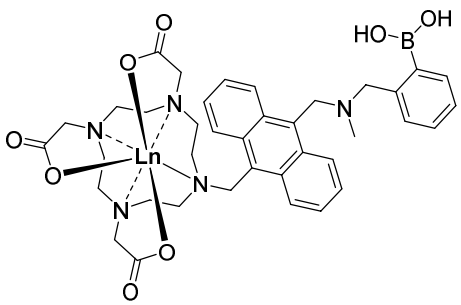


Figure 5.1. Saccharide PeT sensor concept reported by James *et al*. (adapted from ref 1).

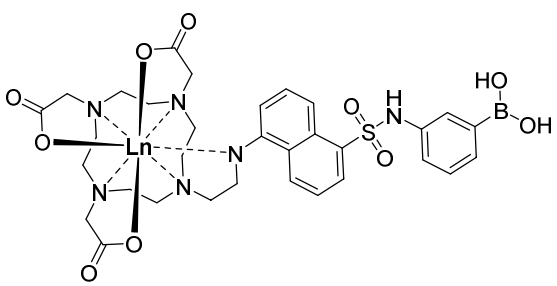
It was hypothesised that by conjugating **104** with [Ln(**DO3A**)] chelate, its affinity to *Sia* can be enhanced via a cooperative two coordinate recognition involving the coordination of the carboxylate in *Sia* to the metal centre and the formation of cyclic boronate ester by the *cis*-diol of *Sia* with PBA. The increase in fluorescence by the anthracene moiety upon saccharide recognition can be used to sensitise Tb(III) centre. This is in addition to the gain in luminescence intensity obtained from replacing the inner-sphere water by the carboxylate of *Sia*. Other saccharides which contain *cis*-diol or carboxylate groups will bind to this receptor,

but *Sia* can be identified amidst different sugars by exploiting the unique chiral signature of these saccharides using CPL and the different mobility of these chiral guests in solution using paraCEST MRI.

In another effort towards selective recognition of *Sia*, the prospects of 3-dansylamino-PBA is proposed. This molecule, coated on gold nanoparticles, has been used for fluorescence imaging of *Sia* in cell-surface glycans.[4] (3-(5-(Dimethylamino)naphthalene-1-sulfonamido)phenyl)boronic acid (DNSBA) is known to bind saccharides which produces an enhancement in fluorescence intensity. Sugars bind well to this moiety at pH 8.2 and the pH responsiveness of DNSBA is also reported.[5] On the basis of these observations, development of 3-dansylamino-*m*-PBA tethered [Ln(**DO3A**)] chelate is proposed for sensing *Sia*. Similar to the anthracene approach, this molecule is expected to recognise *Sia* in a cooperative two coordinate approach where the carboxylate chelates the metal centre, while the *cis*-diol chelates the PBA unit. However, this complex must be studied for its pH behavior due to the secondary amine which is closer to the macrocycle and can coordinate to the metal in the absence of *Sia*.[6] This secondary amine which bridges the dansyl and PBA could form H-bonding interaction with the hydroxyls of *Sia* thereby improving the binding strength. The prospects of CPL and paraCEST MRI would also be interesting to explore *Sia* sensing by this system.



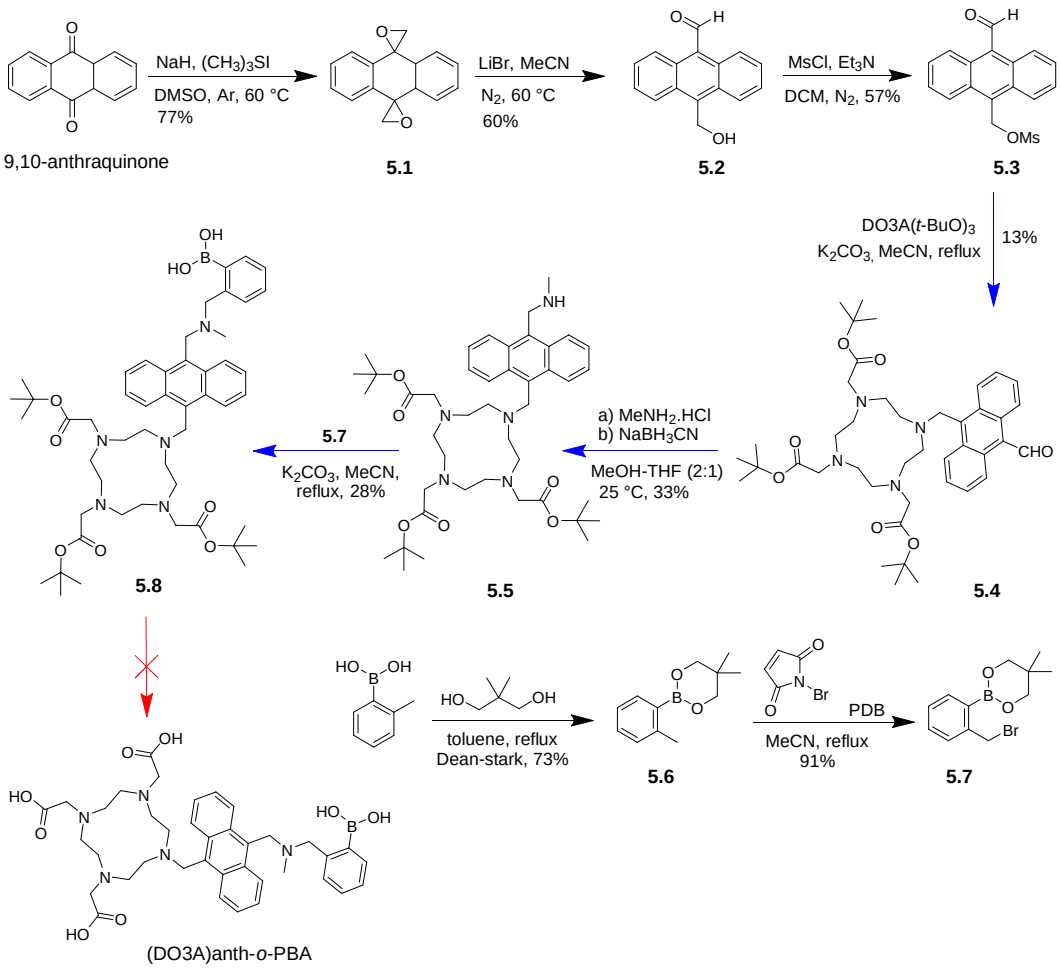
[Ln(**DO3A**)**anth-*o*-PBA**]



[Ln(**DO3A**)**dansyl-*m*-PBA**]

Thus, in the light of the above hypothesis, it was proposed to develop two new Ln(III) chelates, [Ln(**DO3A**)anth-*o*-PBA] and [Ln(**DO3A**)dansyl-*m*-PBA], bearing a PBA moiety for *Sia* recognition.

5.2. Towards the Synthesis of [Ln(DO3A)anth-*o*-PBA]



Scheme 5.1. Synthetic route towards [Ln(**DO3A**)**anth-*o*-PBA**]. Blue arrow indicates difficulty in purification of the subsequent steps. Red arrow indicates that the expected product was not obtained. *Inset*: Synthesis of dioxaborinane (**5.7**) from *o*-tolylboronic acid.

Detailed attempted synthetic procedure for (DO3A)anth-*o*-PBA is described in Chapter-VII, Section 7.6.4. The synthesis of the DO3A-anthracene-PBA system (Scheme 5.1) proved challenging from the start. The synthetic protocol was taken from the literature.[1,2a,2c,2e] 9,10-Anthraquinone was

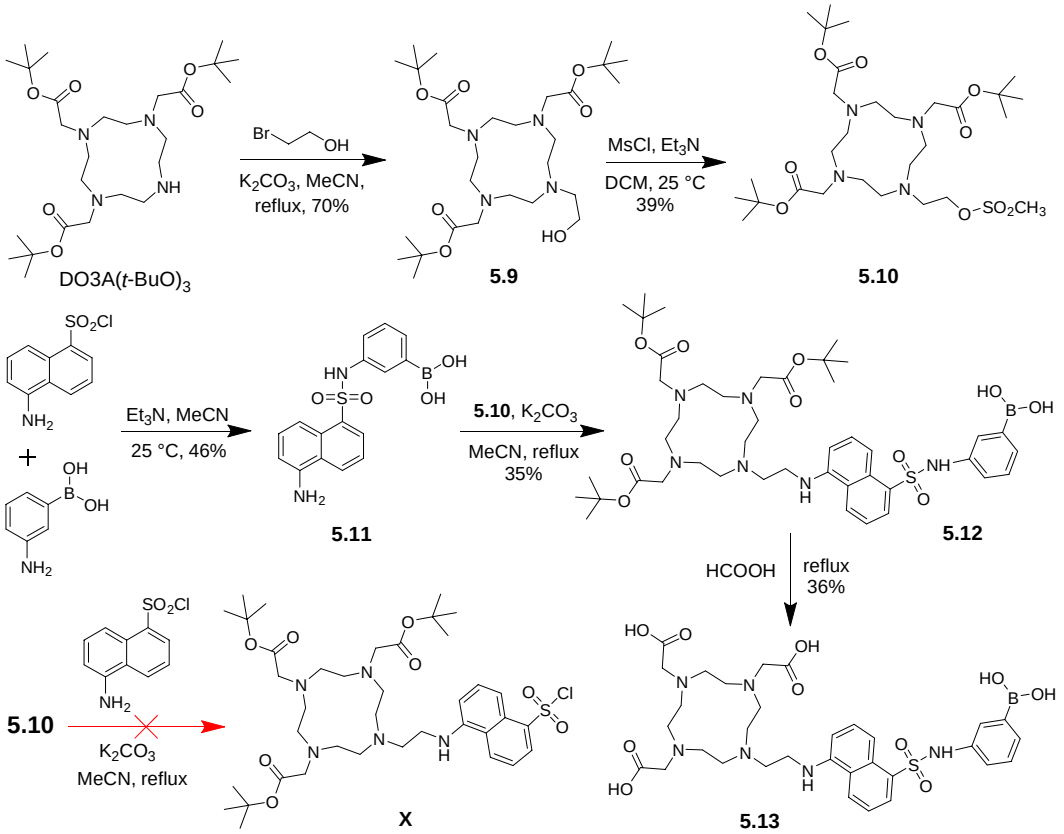
transformed to **5.1** via Corey-Chaykovsky reaction.[7] These epoxides were opened using lithium bromide, where one epoxide opened into an aldehyde while the other, into a secondary alcohol **5.2**. Although these compounds were synthesised according to the literature procedure, column purification involved separating a lot of impurities, rendering the purification difficult. Compound **5.2** was reacted with mesyl chloride in DCM in the presence of triethylamine in an inert atmosphere to get the mesylated product **5.3**. Compound **5.3** was alkylated to DO3A(*t*-BuO)$_3$ in MeCN in the presence of potassium carbonate as proton scavenger under reflux conditions to yield **5.4**, but the subsequent column purification was highly challenging and clear separation was unachievable, even in different solvent systems. However, it was used to react further with the aim of purification in the consecutive steps. In the next stage, the aldehyde in **5.4** underwent Schiff-base condensation[8] with methylamine to form an imine which was reduced using sodium cyanoborohydride to form **5.5**. After column purification under gradient elution using DCM/*iso*-propanol in silica gel (all gradient conditions are found in Chapter-VII, Section 7.6.4), **5.5** was *N*-alkylated with the protected *o*-phenylboronic acid[9] (**5.7**) to obtain a dark-brown crude product which was column purified under gradient elution using DCM/MeOH on silica gel to afford **5.8**. Column purification of products **5.4**, **5.5**, and **5.8** was challenging due to an additional constraint as the products eluted in different gradients containing sodium and potassium cations (from the silica column) included in the macrocycle. This resulted in the product eluting at different R_f values and the formation of these products was confirmed using LRMS.

In the final stage, when the ester **5.8** was subjected to hydrolysis using TFA to get the target molecule ((DO3A)anth-*o*-PBA), the DO3A moiety cleaved off

from the anthracene-PBA moiety. The deprotection conditions were altered by dropwise addition of TFA into an ice-cooled mixture and by using milder acids such as formic acid[10] and aqueous phosphoric acid[11] for hydrolysis, but all resulted in cleaving off the macrocycle from the anthracene-PBA unit. Therefore, the synthesis of the target compound could not be accomplished. Other protecting groups on PBA were explored to avoid this cleavage such as pinacol and ethylene glycol, but they had similar outcomes with no improvement. However, there is still scope for improving this synthesis by attaching the anthracene arm with PBA[2e] and purifying products of every stage by multiple column purifications/recrystallisation, followed by appending the anthracene-appended PBA to the DO3A moiety. Further, DO3A could be protected using different protecting group like methyl ester or ethyl ester which on hydrolysis at basic conditions might result in the production of the desired ligand, (DO3A)anth-*o*-PBA.

5.3. Towards the Synthesis of [Ln(DO3A)dansyl-*m*-PBA]

Detailed synthetic procedure for (DO3A)dansyl-*m*-PBA is described in Chapter-VII, Section 7.6.4. The synthesis of the dansyl probe consisted of multistage synthetic protocol involving the synthesis of the protected macrocycle and attaching it to the dansyl-*m*-PBA unit via an amine linker (Scheme 5.2). The macrocyclic unit was prepared by *N*-alkylation of DO3A(*t*-BuO)$_3$ with 2-bromoethanol in the presence of potassium carbonate in acetonitrile at reflux.[12] Subsequent filtration to remove the inorganic base followed by column purification using gradient DCM/MeOH under silica gel afforded **5.9**. This was crystallised by slow evaporation in MeCN and characterised by single crystal X-ray diffraction (Figure 5.2). The alcohol-functionalised DO3A(*t*-BuO)$_3$ (**5.9**) was reacted with mesyl chloride to form the mesylated macrocycle **5.10**.



Scheme 5.2. Synthetic route towards (DO3A)dansyl-*m*-PBA.

The PBA-conjugated dansyl derivative **5.11** was prepared by the addition-elimination reaction. The sulfonyl of 5-amino-naphthalene-1-sulfonyl chloride, was attacked by the primary amine of 3-aminophenylboronic acid, followed by the elimination of chloride to afford **5.11**. To achieve this, 3-aminophenylboronic acid was dissolved in acetonitrile and stirred with triethylamine for 30 min. A solution of dansyl chloride in acetonitrile was added dropwise over 15 min followed by vigorous stirring at 25 °C overnight. This reaction produced the desired product **5.11** along with side products, formed by the dimerisation of 5-amino-naphthalene-1-sulfonyl chloride and by the addition-elimination of **5.11** with another molecule of 5-amino-naphthalene-1-sulfonyl chloride. The desired product was separated from these side products through column purification by isocratic elution on silica gel using acetonitrile (100%)

followed by gradient elution in DCM/isopropanol to afford **5.11**. This was crystallised by slow evaporation of the solution in MeOD and characterised by single crystal X-ray diffraction (Figure 5.3). Initially, compound **5.10** was attempted for functionalising with 5-aminonaphthalene-1-sulfonyl chloride to get compound **X** (shown in red arrow, Scheme 5.2) *en route* to the target ligand, but that protocol was found to be nonviable.

Compound **5.12** was synthesised by the amination of the mesylated macrocycle **5.10** by the dansyl unit **5.11** in the presence of potassium carbonate in acetonitrile at reflux. The mesylate ester of **5.10** acts as a better leaving group during amination with the primary amine of **5.11** thereby facilitating the formation of **5.12**. The inorganic base was removed by filtration and column purification of the fitrate

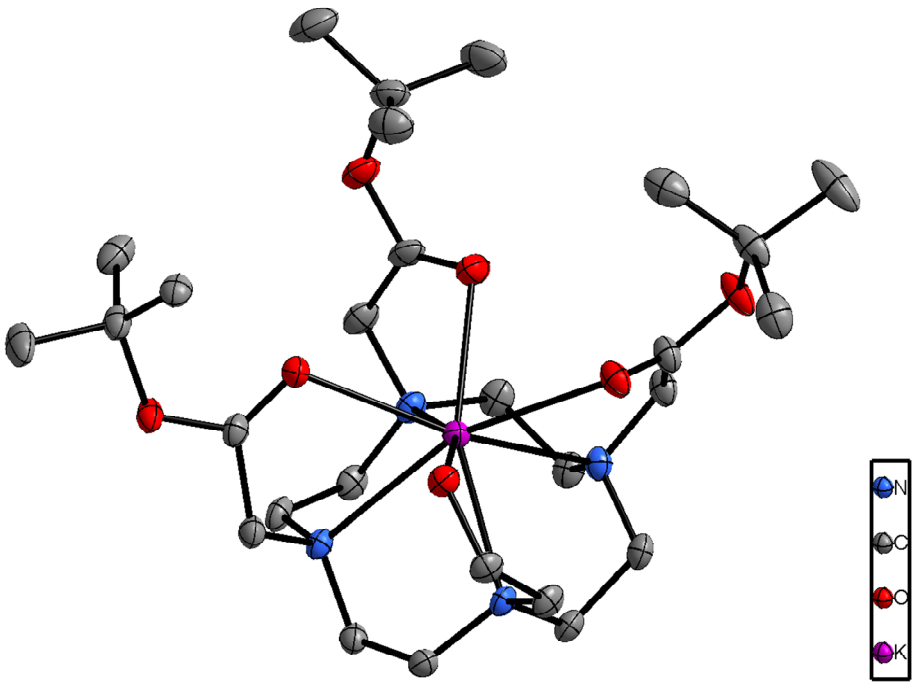


Figure 5.2. X-ray crystal structure of **5.9**. Br and H atoms omitted for clarity. Thermal ellipsoid drawn at 30% probability level. Structure solved by Dr. Kirsten Christensen, Chemical Crystallography, University of Oxford.

in gradient conditions using DCM/EtOH solvent system on silica gel afforded **5.12**. The esters in **5.12** were subsequently hydrolysed using formic acid at reflux[9] followed by evaporation under reduced pressure to yield **5.13**. Deprotection was first attempted using TFA, but product formation was not observed by NMR and LCMS. Formic acid proved successful in deprotection of the esters. Synthesis of Ln(III) complexes of **5.13** was not attempted due to time restraints. This dansyl-PBA-appended DO3A can be complexed with the lanthanide metal of interest to study the recognition of *Sia* and other sugars. All the compounds synthesised and discussed in this Chapter were characterised using NMR and MS techniques (reported in Chapter-VII, Section 7.6.4).

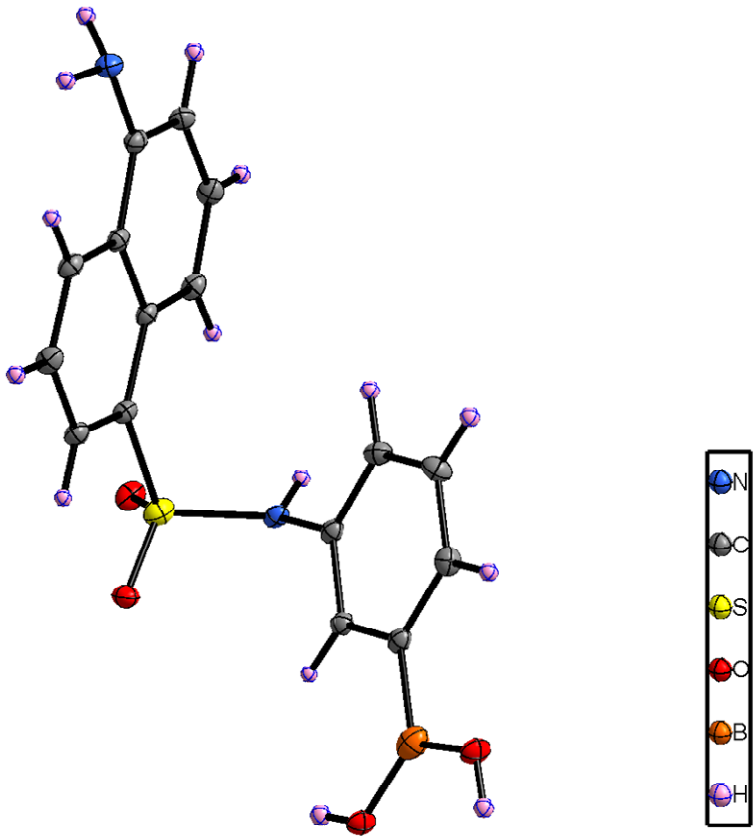


Figure 5.3. X-ray crystal structure of **5.11**. Thermal ellipsoid drawn at 30% probability level. Structure solved by Dr. Kirsten Christensen, Chemical Crystallography, University of Oxford.

5.4. Conclusion

Anthracene- and dansyl-conjugated phenylboronic acid appended DO3A derivatives for *Sia* recognition were investigated. The synthesis of the anthracene-conjugated phenylboronic acid tethered DO3A ((DO3A)anth-*o*-PBA) was not successful due to the fragility of the ligand which did not survive ester hydrolysis, but by altering the synthetic protocol by using alternative ester protecting groups (other than *tert*-butyl) to protect the carboxylates on DO3A, it may be possible to synthesise the desired anthracene bridged ligand. Also, by synthesising anthracene attached to *o*-PBA, followed by tethering it to the DO3A core is a potential route to be explored. Dansyl bridged DO3A ligand was synthesised using the current synthetic protocol and this system can be investigated in detail for *Sia* recognition and sensing using its Ln(III) complexes. Further, compound **5.10** can act as an effective building block to functionalise organic architectures containing primary amine with the DO3A core.

5.5. *References*

1. James, T. D.; Sandanayake, K. R. A. S.; Iguchi, R.; Shinkai, S. *J. Am. Chem. Soc*. **1995**, *117*, 8982–8987.
2. (a) Deng, G.; James, T. D.; Shinkai, S. *J. Am. Chem. Soc*. **1994**, *116*, 4567–4572. (b) Yoon, J.; Czamik, A. W. *J. Am. Chem. Soc.* **1992**, *114*, 5874–5875. (c) Ludwig, R.; Harada, T.; Ueda, K.; James, T. D.; Shinkai, S. *J. Chem. Soc. Perkin Trans. 2*, **1994**, *4*, 697–702. (d) Czamik, A. W. *Fluorescent Chemosensors for Ion and Molecule Recognition*; American Chemical Society: Washington, D.C., 1993. (e) James, T. D.; Shinmori, H.; Shinkai, S. *Chem. Commun.* **1997**, 71–72. Wang, W.; Gao, S.; Wang, B. *Org. Lett.* **1999**, *1* 1209–1212. (f) Cooper, C. R.; James, T. D. *J. Chem. Soc., Pekin Trans. 1* **2000**, 963–969. (g) Yang, W.; Yan, J.; Fang, H.; Wang, B. *Chem. Comun.* **2003**, 792–793. (h) Yang, W.; Fan, H.; Gao, X.; Gao, S.; Karnati, V. V. R.; Ni, W.; Hooks, W. B.; Carson, J.; Weston, B.; Wang, B. *Chem. Biol.* **2004**, *11*, 439–448. (i) *Boronic acids: Preparation, Applications in Organic Synthesis and Medicine*; Hall, D. G. Ed.; Wiley-VCH Verlag GmbH & Co. KGaA: Weinheim; 2005. (j) Larkin, J. D.; Frimat, K. A.; Fyles, T. M.; Flower, S. E.; James, T. D. *New J. Chem.* **2010**, *34*,

2922–2931. (k) Sun, X.; Zhai, W.; Fossey, J. S.; James, T. D. *Chem. Commun.* **2016**, *52*, 3456–3469.

3. Sun, X.; James, T. D.; Anslyn, E. V. *J. Am. Chem. Soc.* **2018**, *140*, 2348–2354.
4. Qian, R.; Ding, L.; Yan, L.; Ju, H. *Anal. Chim. Acta* **2015**, *894*, 85–90.
5. Elfeky, S. *Curr. Org. Synth.* **2011**, *8*, 872–880.
6. Lowe, M. P.; Parker, D. *Inorg. Chim. Acta* **2001**, *317*, 163–173.
7. (a) Corey, E. J.; Chaykovsky, M. *J. Am. Chem. Soc.* **1962**, *84*, 867–868. (b) Corey, E. J.; Chaykovsky, M. *J. Am. Chem. Soc.* **1962**, *84*, 3782–3783. (c) Corey, E. J.; Chaykovsky, M. *J. Am. Chem. Soc.* **1962**, *86*, 1639–1640. (d) Corey, E. J.; Chaykovsky, M. *J. Am. Chem. Soc.* **1964**, *86*, 867–868. (e) Li, A.-H.; Dai, L.-X.; Agarwal, V. K. *Chem. Rev.* **1997**, *97*, 2341–2372.
8. (a) Schiff, H. *Justus Liebigs Ann. Chem.* **1864,** *131*, 118–119. (b) Fabrizzi, L. *J. Org. Chem.* **2020**, *85*, 12212–12226.
9. Stones, D.; Manku, S.; Lu, X.; Hall, D. G. *Chem. —Eur. J.* **2004**, *10*, 92–100.
10. Günduz, S.; Vibhute, S.; Botár, R.; Kálmán, F. K.; Tóth, I.; Tircsó, G.; Regueiro-Figueroa, M.; Esteban-Gómez, D.; Platas-Iglesias, C.; Angelovski, G. *Inorg. Chem.* **2018**, *57*, 5973–5986.
11. Li, B.; Berliner, M.; Buzon, R.; Chiu, C. K.-F.; Colgan, S. T.; Kaneko, T.; Keene, N.; Kissel, W.; Le, T.; Leeman, K. R.; Marquez, B.; Morris, R.; Newell, L.; Wunderwald, S.; Witt, M.; Weaver, J.; Zhang, Z.; Zhang, Z. *J. Org. Chem.* **2006**, *71*, 9045–9050.
12. Dissanayake, P.; Allen, M. J. *J. Am. Chem. Soc.* **2009**, *131*, 6342–6343.

CHAPTER-VI

Chapter-VI: Summary and Conclusion

Realising the importance of anions in biology and for the need to track them in their natural setting, this thesis accounts for the work performed on lanthanide complexes of DO3A-based ligands for chloride and saccharide recognition in solution. The versatility of lanthanide complexes in the world of imaging is well known as they are characterised by their long-lived luminescence and paramagnetism in MRI. Isostructural chelators, combining the best of both worlds in imaging can be explored, as long as the appropriate metal is utilised. Since lanthanide complexes can be designed as coordinatively unsaturated systems, anion chelation is possible through coordination at the metal centre, exemplified by the dramatic effects in the crystal field of the metal, thereby leading to changes in their luminescence and paramagnetic properties.

The long-standing challenge of chloride recognition in water was addressed in Chapter-II. Mononuclear lanthanide complexes do not bind to chloride. Therefore, a binuclear approach was undertaken in hope of accommodating chloride in a binding pocket between the metal centres, bridged by short and flexible spacers. Two DO3A-based chelators separated by ethane or propane spacer, $(DO3A)_2C$-2 and $(DO3A)_2C$-3, respectively, were synthesised and structurally characterised. Binuclear Ln(III) complexes [Ln_2(**DO3A**)$_2$**C-2**] and [Ln_2(**DO3A**)$_2$**C-3**] [Ln = Eu(III), Tb(III), Gd(III), Yb(III) and Y(III)] were synthesised and representative complexes characterised by X-ray crystallography. Using these neutral binuclear Ln(III) complexes, strong binding of chloride in water was observed, which holds promise towards chloride recognition in water. Fluoride was the potential interferent which can be neglected owing to its low concentration in biology and sea-water in comparison with chloride. But its interaction with the complexes was

used to understand chloride chelation better. A comprehensive study on chloride and fluoride chelation to these binuclear complexes was explored using luminescence, ^{1}H-, ^{19}F-, and ^{35}Cl NMR spectroscopy, mass spectrometry, and single crystal X-ray diffraction. From the above-mentioned studies with the Eu(III) mono- and binuclear complexes, it was hypothesised that the chelation of chloride involves bridging between the metal centres (Figure 6.1). However, fluoride chelation involves consecutive three binding events: first involves chelation of fluoride between the metal centres, the second binding event involves fluoride binding to both the metal sites individually, while the third binding event involves an additional fluoride bridging between the metal centres. However, fluoride binding suffers from competition which chloride binding overcomes. This Chapter identifies the simplest possible coordination complexes for chloride binding in water, which opens a new arena in anion coordination chemistry to explore further in tracking chloride for physiology and medicine.

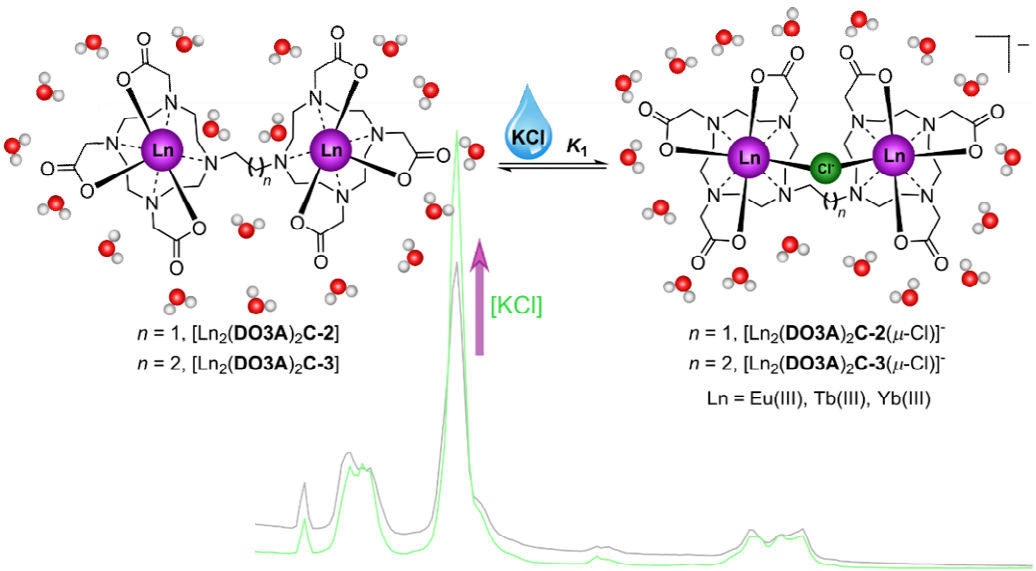
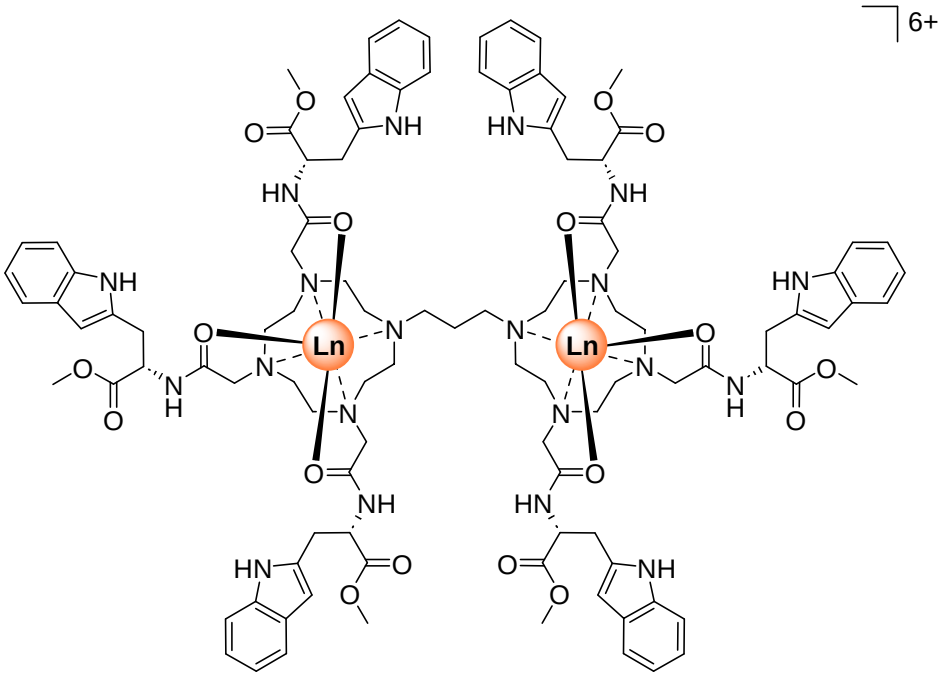


Figure 6.1. Key observation of chloride binding with binuclear Ln(III) complexes in Chapter-II.

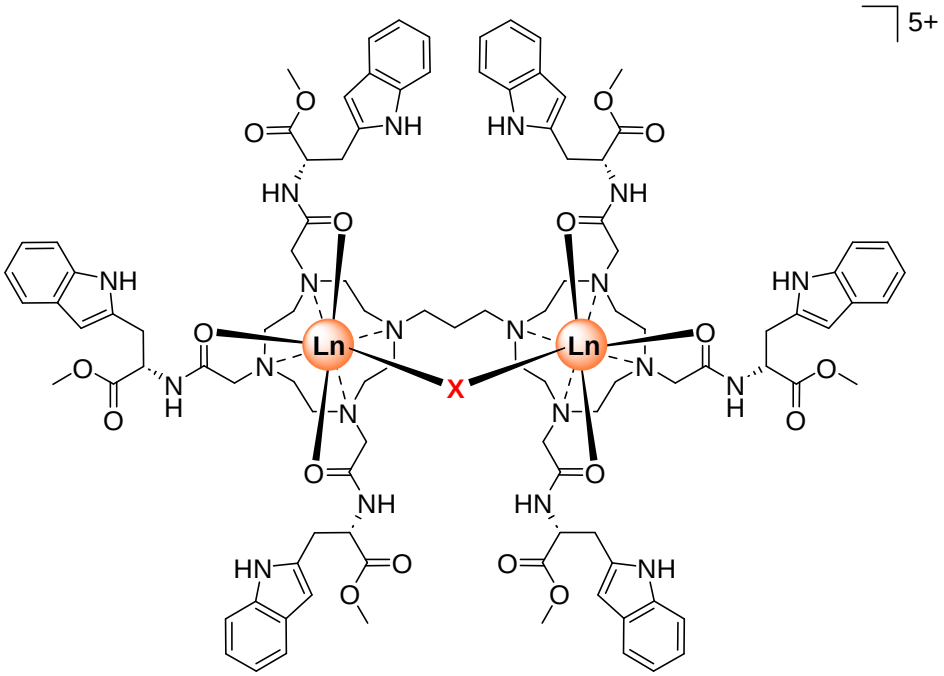
The binuclear complexes reported in Chapter-II had a drawback of lacking a sensitiser for lanthanide luminescence in real-world applications. Extending from this, binuclear cationic complex bearing tryptophan pendant arms was pursued in Chapter-III. Tryptophan, being a good sensitiser for Tb(III), was used to conjugate on the carboxylate arm of the DO3A-framework in the C-3 binuclear ligand. Tryptophan also imparts rigidity on the fluxional DO3A moiety which is coordinated to the metal. Chloride and fluoride binding with the binuclear complex $[Tb_2(\mathbf{DO3AM\text{-}L\text{-}TrpOMe})_2\mathbf{C\text{-}3}]^{6+}$, performed by luminescence titrations on time-resolved phosphorescence mode, and analysis of $\Delta J = 5$ band upon the addition of the halides account for their binding with the metal centres. A decrease in the luminescence lifetime upon fluoride and chloride addition accounts for the replacement of inner-sphere water by these anions in the binuclear cationic complex reported here. Further studies are needed to ascertain the binding of halides to this complex and to confirm the kinetic inertness of the complex in physiological conditions (Figure 6.2).

In Chapter-IV, the importance of sialic acid (*Sia*) as a tumour biomarker for cancer imaging was highlighted. Binding and sensing of this sugar, by a cooperative two coordinate approach by employing a neutral arylboronate-conjugated [Ln(**DO3A**)] chelate was revisited along with altering the boronate position on the aryl ring to explore the effect of conformational space upon binding. While the synthesis of Lu(III) complexes were achieved, synthesis of Eu(III) and Tb(III) complexes led to the paramagnetic metal assisted protodeboronation on the arylboronate, reported for the first time with structural characterisation in this Chapter (Figure 6.3a). This effect must be explored in detail to understand its



$[Ln_2(DO3AM\text{-}L\text{-}TrpOMe)_2C\text{-}3]^{6+}$





$[Ln_2(DO3AM\text{-}L\text{-}TrpOMe)_2C\text{-}3(\mu\text{-}X)]^{5+}$

Figure 6.2. Future prospects to explore in detail from Chapter-III.

mechanism and to look for suitable applications in synthesis and sensing. Although protodeboronation by Eu(III) and Tb(III) led to the cleavage of the boronic acid moiety leading to the formation of benzyl appended lanthanide complex, an unexpected event, the resulting complexes were still used to explore the binding of *Sia* and other sugars. The potential of these monosaccharides to act as chiral auxiliaries for lanthanide complexes were also studied using CPL, which showed the binding of L-lactate and D-gluconate concomitant with chiral induction to the

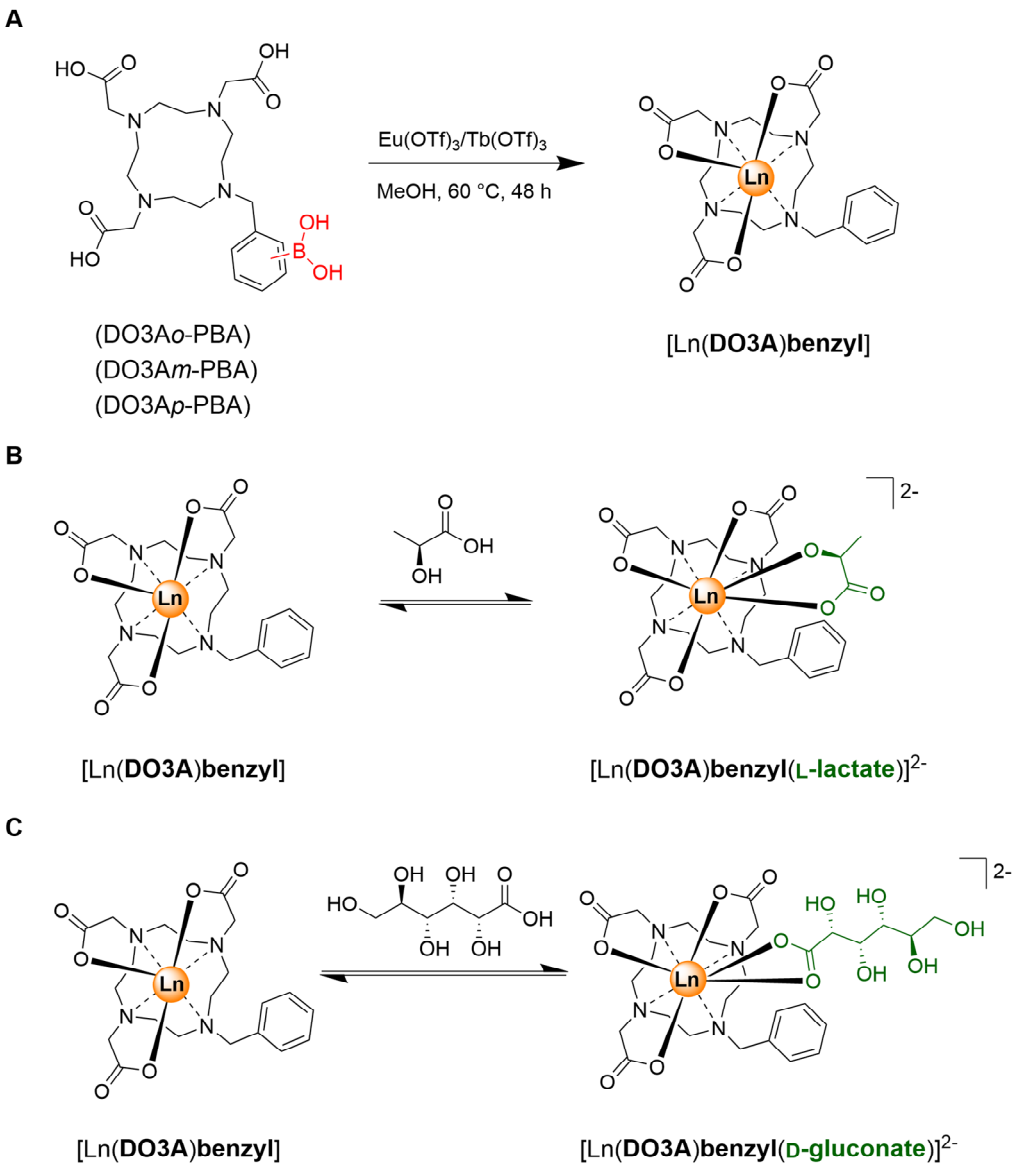
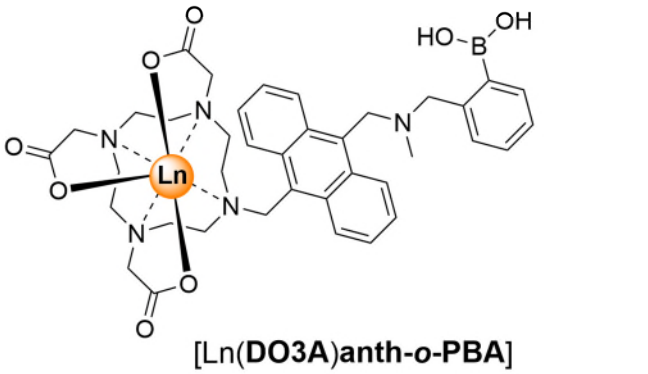


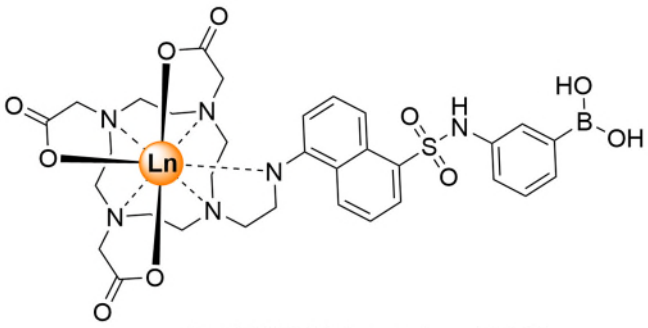
Figure 6.3. Key observations in Chapter-IV: Ln(III) assisted protodeboronation (A), and Ln(**DO3A**)**benzyl**] coordinating to L-lactate (B) and D-gluconate (C).

racemic complex (Figure 6.3b and c). While *Sia* binding was not observed in the luminescence and CPL studies, ^{1}H NMR spectroscopy showed binding, provided base was added to deprotonate the carboxylic acid of *Sia* to facilitate its chelation to the lanthanide centre. The addition of base to facilitate chelation must be validated in luminescence and CPL studies to confirm the binding of *Sia* to the benzyl appended lanthanide complex.

In Chapter-IV, it was observed that boronate in close proximity to the lanthanide centre in the arylboronate-conjugated [Ln(**DO3A**)] chelates underwent paramagnetic Ln(III) metal-assisted protodeboronation. In Chapter-V Ln(III) complexes of two arylboronate-conjugated ligands, (DO3A)anth-PBA and (DO3A)dansyl-PBA, wherein the boronate and the lanthanide centre was separated by a rigid anthracene or dansyl spacer to improve the stability of the boronate, were



[Ln(**DO3A**)**anth-*o*-PBA**]



[Ln(**DO3A**)**dansyl-*m*-PBA**]

Figure 6.4. Target complexes pursued in Chapter-V.

identified to study the binding of *Sia* and other monosaccharides (Figure 6.4). Further, these ligands with the boronate functionality at the *ortho*- and *meta*-position on the phenyl ring were also considered to look into the effect of conformational space upon saccharide binding. However, during synthesis of (DO3A)anth-*o*-PBA, in the final stage of deprotection of the esters to afford the target ligand, the macrocyclic moiety was cleaved off from the anthracene-PBA unit. Other synthetic alternatives can be pursued to achieve the anthracene-based target ligand. While the dansyl appended ligand was successfully synthesised, complexation with the Ln metal, spectroscopic studies with sugars and pH were not pursued due to time constraints, but there is scope in exploring this in detail.

In summary, the versatility of lanthanide complexes as hosts for anion recognition was explored. Chloride binding in water by practically useful binuclear lanthanide complexes is exemplified in this thesis which can be tailored for various applications. Protodeboronation is a key observation which must be considered while developing phenylboronate-appended lanthanide complexes. Furthermore, the kinetics of cyclic boronate ester formation and the interaction of boronate to haemoglobin and human serum albumin makes them problematic for use *in vivo*. Therefore, a suitable alternative which uses a new biorthogonal tag or a metal complex design that can bind selectively to *Sia* needs to be explored for its recognition in biology towards tumour targeting.

CHAPTER-VII

Chapter-VII: Experimental Procedures

7.1. Reagents and Solvents

1,2-dibromoethane (99%), 1,3-dibromopropane (99%), sodium bicarbonate (99.7%), sodium hydroxide (98%), trimethylsulfonium iodide, methylamine hydrochloride (≥ 98%), propargyl bromide solution (80 wt. % in toluene, 0.3% MgO stabiliser), dibenzoyl peroxide (PDB) (70% remainder water), sodium dihydrogenphosphate (anhydrous, 99%), sodium hydrogenphosphate (anhydrous, 99%), sodium hydride (60% dispersion in mineral oil), acetone, acetonitrile, chloroform, methanol, ethanol, tetrahydrofuran, diethyl ether, pentane, ethyl acetate, toluene, *N*,*N*-dimethyl formamide, dimethyl sulfoxide (anhydrous, ≥99.9%), Tris-HCl (Trizma® hydrochloride) (99%), HEPES sodium salt (≥99.5%, titration), PBS tablet, CHES sodium salt, europium(III) trifluoromethanesulfonate hydrate (98%), ytterbium(III) trifluoromethanesulfonate (98%), yttrium trifluoromethanesulfonate (98%), lutetium trifluoromethanesulfonate (98%), magnesium sulfate (anhydrous, ReagentPlus®, ≥99.5%), sodium chloride (puriss. p.a., ACS reagent, ISO, ≥99.5%), potassium carbonate (ACS reagent, ≥99%), ammonium formate (granular, 97%), ethylene glycol (99%), D-(+)-glucose (≥99.5%), *N*-bromosuccinimide (ReagentPlus®, 99%), chloroacetyl chloride (98%), 9,10-anthraquinone, 2-bromoethanol (95%), D-gluconic acid (97%), and methanesulfonyl chloride (97%), triethylamine, acetone (ACS, ISO, Reag. Ph Eur-used to wash glasswares), CD_3OD ≥99.8 atom % D, CD_2Cl_2 99.8 atom % D, DMSO-d_6 99.9 atom % D, D_2O 99.9 atom % D, trifluoroacetic acid-*d* (99.5 atom % D), and NaOD (40 wt. % solution in D_2O, 99+ atom % D) were from Sigma Aldrich and used as received.

Cyclen (CheMatech, Dijon, France); gadolinium trifluoromethane sulfonate (Chem Cruz®); caesium carbonate, L-tryptophan methyl ester hydrochloride, *o*-tolylboronic acid (contains varying amounts of aldehyde), 3-tolylboronic acid (97%), 2-bromomethylphenylboronic acid (95%), 3-bromomethylphenylboronic acid (95%), 4-bromomethylphenylboronic acid (95%, contains varying amounts of aldehyde), 3-aminophenylboronic acid (95%), 5-amino-naphthalene-1-sulfonyl chloride, di-*tert*-butyl-dicarbonate, *N*,*N*-diisopropylethylamine (99%), HATU (98%), and 10% palladium on carbon (wet, 55-65%) (Fluorochem); trifluoroacetic acid (99%), molecular sieves (3 Å, 8-12 mesh), and 1-hydroxybenzotriazole (98%) (Acros Organics); dichloromethane and 1,4-dioxane (reagent grade, ≥99%) (Honeywell); hydrochloric acid (~37%, analytical reagent grade), nitric acid (70%), glacial acetic acid (laboratory reagent grade), and potassium iodide (Fisher Scientific); anhydrous sodium acetate (99%), anhydrous sodium sulfate (99.99%), neutral alumina (activated, Brockmann grade II), *tert*-butylbromoacetate (98%), terbium(III) trifluoromethanesulfonate (98%), ethylene glycol dimethyl ether (glyme, 99%, stabilised with BHT), sodium cyanoborohydride (95%), sodium L-lactate (97%), D-(+)-galactose (98%), D-fructose (99%), D-mannose (99%), lithium bromide (anhydrous, 99% min), 2,2-dimethyl-1,3-propanediol (99%), and pinacol (99%) (Alfa Aesar); potassium fluoride (Riedel-de Haën®); potassium chloride and potassium bromide (BDH®); *N*-acetyl neuraminic acid (Neu5Ac), methyl α-D-galactopyrannoside, and methyl α-D-mannopyrannoside (Carbosynth) were used as received.

Melting point tubes (100 mm, soda glass sealed ends) were from Sigma Aldrich. Anhydrous solvents were obtained from an MBraun SPS800 and used without further purification (solvents purchased from commercial suppliers as

stated above). Deionised water was used throughout the study which was obtained from Elga PURELAB® Chorus 1 complete with conductivity of 18.2 MΩ.cm.

7.2. Vacuum Processing, Dialysis, Centrifugation, Filtration, TLC, and Column Chromatography

Buchi Rotavapor® R-200 and Heidolph Laborota 4000-efficient Rotary Evaporator were used to evaporate solvents under reduced pressure. Compounds were dried in high-vac Schlenk line with an Edwards RV3 Vacuum Pump. Dialysis of the complexes were performed using Spectra-Por® Float-A-Lyzer® G2 dialysis membrane tubing made from cellulose ester (Spectrum Labs) with a molecular weight cut-off of either 100-500 Da or 500-1000 Da. Centrifugations were performed using Beckman Coulter® Allegra® X-12R Benchtop Centrifuge. All centrifugations were performed at 3750 RPM for 6 min at 4 ℃. Filtrations during reaction workup were performed under gravity using a Whatman filter paper (grade 1 circles) on a glass funnel or using celite (Filter aid, Celite Hyflo Super-cel® from Alfa-Aesar) under vacuum. Column chromatography was performed using Geduran silica gel 60 (0.040-0.063 mm mesh, Sigma Aldrich) and neutral alumina (activated, Brockmann grade II). Analytical thin layer chromatography (TLC) was performed on aluminium sheet supported silica gel plates coated with silica gel 60 F_{254} (0.2 mm, Merck) or aluminium sheet supported plates coated with neutral alumina 60 F_{254} (0.2 mm, Merck) using different solvent systems as mobile phase. The compounds were visualised in TLC by potassium permanganate stain prepared as per literature protocol,[1] and using a UV TLC chamber in short wavelength (254 nm) and long wavelength (365 nm) as appropriate.

7.3. Preparation of Buffers and Standard Solutions

7.3.1 Buffers prepared in water

PBS buffer (0.01 M, pH 7.4) was prepared by dissolving one PBS tablet in 200 mL deionised water.

Tris-HCl buffer (0.01 M, pH 7.4) was prepared by dissolving 242.28 mg of Trizma base in 100 mL deionised water followed by the dropwise addition of 138 μL of concentrated HCl (37%, 12.1 M), and made up to 200 mL using deionised water.

Phosphate buffer (0.01 M, pH 7.4) was prepared by dissolving sodium hydrogenphosphate (505 mg) and sodium dihydrogenphosphate (85 mg) in 250 mL deionised water. The pH was adjusted using 0.01M aqueous NaOH.

Acetate buffer (0.01 M, pH 3.98) was prepared by dissolving 7 mg of sodium acetate in 20 mL deionised water followed by the addition of 18.12 μL of glacial acetic acid under stirring and adjusting the pH to 3.98 using 0.01 M aqueous CF_3COOH. The final volume was adjusted to 40 mL using deionised water.

HEPES buffer (0.01 M, pH 6.97) was prepared by dissolving 100 mg of *N*-(2-Hydroxyethyl)piperazine-*N*′-(2-ethanesulfonic acid) sodium salt in 20 mL deionised water and adjusting the pH using 0.01 M aqueous NaOH. The final volume was adjusted to 40 mL using deionised water.

CHES buffer (0.01 M, pH 9.98) was prepared by dissolving 80 mg of 2-(Cyclohexylamino)ethanesulfonic acid sodium salt in 20 mL deionised water and adjusting the pH using 0.01 M aqueous NaOH. The final volume was adjusted to 40 mL using deionised water.

Aqueous NaOH (0.01 M) was prepared by dissolving 40 mg of NaOH in 50 mL deionised water and making up to 100 mL in a standard flask. Aqueous CF_3COOH (0.01 M) was prepared by the dropwise addition of 76.58 μL CF_3COOH in 50 mL deionised water and making up to 100 mL in a standard flask.

7.3.2 Buffers prepared in deuterium oxide

Acetate buffer (0.01 M, pD 4.1) was prepared by dissolving 3 mg of sodium acetate in 4 mL D_2O followed by the addition of 3.8 μL glacial acetic acid under stirring and adjusting the pH using 0.01 M aqueous CF_3COOD. The final volume was adjusted to 10 mL using D_2O.

HEPES buffer (0.01 M, pD 7.05) was prepared by dissolving 20 mg of HEPES sodium salt in 4 mL D_2O and adjusting the pH using 0.01 M aqueous NaOD. The final volume was adjusted to 10 mL using D_2O.

Phosphate buffer (0.01 M, pD 8.5) was prepared by dissolving sodium hydrogenphosphate (110 mg) and sodium dihydrogenphosphate (10 mg) in 7 mL D_2O. The pH was adjusted using 0.01M NaOD.

CHES buffer (0.01 M, pD 10.12) was prepared by dissolving 20 mg of CHES sodium salt in 4 mL D_2O and adjusting the pH using 0.01 M aqueous NaOD. The final volume was adjusted to 10 mL using D_2O.

NaOD (0.1 M) was prepared by dissolving 102.4 μL NaOD in 5 mL D_2O and diluted to 10 mL. NaOD (0.01 M) was prepared by dissolving 10.2 μL of NaOD in 5 mL D_2O and diluted to 10 mL. CF_3COOD (0.01 M) was prepared by dissolving 7.8 μL of CF_3COOD in 5 mL D_2O and diluted to 10 mL.

7.4. Physical Methods

7.4.1 NMR Spectra

NMR spectra were recorded on a Bruker Biospin AG Avance III HD Nanobay 400 MHz NMR Spectrometer equipped with a 9.4 T magnet (^{1}H 400.2 MHz, ^{11}B 128.4 MHz, ^{13}C 100.6 MHz, ^{19}F 376.5 MHz) or Bruker Avance III NMR equipped with a 11.75 T magnet (^{1}H 500 MHz, ^{11}B 160.4 MHz, ^{13}C 125.7 MHz,

^{19}F 470.4 MHz, ^{35}Cl 49 MHz) or Bruker Avance Ultrashield Neo 600 MHz NMR Spectrometer equipped with a 14.1 T magnet (^{1}H 600.4 MHz, ^{13}C 151 MHz). All NMR spectra were recorded in deuterated solvents (Sigma Aldrich). Chemical shifts were assigned by comparison with the residual proton and carbon resonances of the solvents.[2] The NMR spectrometers were set with $(CH_3)_4Si$ in $CDCl_3$ as the internal reference for ^{1}H and ^{13}C; $BF_3.OEt_2$ in $CDCl_3$ for ^{11}B; $CFCl_3$ in $CDCl_3$ for ^{19}F; and NaCl in D_2O for ^{35}Cl NMR, (δ = 0 ppm). NMR samples were placed in Norrell® standard series™ 5 mm NMR tubes (600 MHz frequency, Sigma Aldrich) and the spectra recorded. NMR spectra of samples involving boronates were recorded using a Wilmad® quartz 5 mm NMR tube (600 MHz frequency with boron content up to 0.1 ppm, Fluorochem). NMR spectra of samples containing anthracence and dansyl moieties, except for ^{11}B NMR, were recorded in an amberised Norrell® 5 mm NMR tube (600 MHz frequency, Sigma Aldrich).

7.4.2 Mass Spectrometry

ESI mass spectra were recorded on the Thermofisher Exactive™ Plus mass spectrometer with a Waters Acuity UPLC system and Waters Bioaccord 2 Loop injection MS (HIGH MASS, + ion, and data processed using spectral works remote analyzer®). LRMS was recorded on a Waters LCT Premier XE bench-top orthogonal acceleration time-of-flight ESI mass spectrometer and data processed in Mestrenova. MALDI-TOF mass spectra were recorded on a Bruker AutoFlex Mass Spectrometer. All MALDI-TOF MS were run in a DCTB matrix.

7.4.3 Elemental Analysis

CHN microanalyses were carried out on Thermo Scientific™ FLASH 2000 CHNS/O Analyzer at London Metropolitan University, London. All samples were

submitted in pre-scored long stem Vacule® cryogenic glass ampules (Sigma Aldrich) sealed using a blow torch.

7.4.4 X-ray Crystallography

Low temperature single crystal X-ray diffraction data were collected using a (Rigaku) Oxford Diffraction SuperNova A diffractometer. Raw frame data were reduced using CrysAlisPro and the structure solved from the integrated intensities with charge-flipping using `Superflip'.[3] The structure was refined using full-matrix least squares on F^2 using the CRYSTALS suite.[4]

7.4.5 pH Meter

Hanna Instruments pH 210 Microprocessor pH Meter with a HI 1131B electrode was used for the pH measurements of complexes in water and D_2O. The pH meter was calibrated using pH 4.01 and 7.01 buffer solutions (Hannah Instruments). The electrodes were stored in inorganic cleaning solution (Hanna Instruments) for 20 min and washed with deionised water before use. In D_2O, the pD of the solution was determined using the equation pD = pH + 0.45 (pH is the "pH meter reading" obtained from the pH meter standardised to read pH in water).[5]

7.4.6 Optical Rotation Determination

Specific rotation [α] of chiral compounds was determined by recording the observed rotation (α) using Schmidt-Haensch Unipol digital polarimeter. All samples were dissolved in MeOH (1 mg/1 mL) and recorded as an average of 10 readings. The instrument was programmed to method 1, wavelength at 589.44 nm (using sodium D-line), absorbance of 0.1, and the temperature (T) of 25 °C, maintained using an external water bath connected to the cell holder. Cell of path length (l) 100 mm was used. Specific rotation was calculated using the formula:[6]

$$[\alpha]_{\lambda}^{T} = \frac{\alpha}{l \times c}$$

7.4.7 Microwave reactor

Reaction on a microwave was performed using CEM Discover® microwave synthesiser, running discover V2.15. Vial caps (20 mm, HS AL Crimp), PTFE/S from Agilent® were used to seal the thick microwave vial containing the reaction mixture.

7.4.8 Electronic Absorption Spectra

Electronic absorption spectra were recorded on a Jasco V-770 UV-Visible/ NIR spectrophotometer operated under Spectra Manager™ suite. Points were recorded at 0.2 nm interval with a UV/Vis bandwidth of 1 nm, UV/Vis response of 0.06 sec in continuous scan mode at the rate of 400 nm/min. All measurements were auto-zeroed before use. Baseline correction was performed for every measurement by the instrument by measuring the solvent absorption (blank) in which the measurements were taken. The electronic absorption spectra were recorded for solution of compounds using 1 mL Hellma Analytics precision quartz cell (SUPRASIL®, type: 114F-QS).

7.4.9 Luminescence Spectra

Steady-state excitation and emission spectra were recorded on a Horiba Jobin Yvon Fluorolog® 3-12 Fluorometer equipped with a Hamamatsu R928 detector and a double-grating emission monochromator. A 2″ square unmounted longpass 550 nm filter (FGL 550S) or 400 nm filter (FGL 400S) fabricated using a 2 mm thick Schott® coloured glass (Thor Labs) was used while recording the steady-state emission spectra of Eu(III) and Tb(III) complexes. For [Eu_2(**DO3A**)$_2$**C-2**] and [Eu_2(**DO3A**)$_2$**C-3**], slits of 20 nm with a band pass of 1 nm

for excitation at 393 nm was used; for **[Tb$_2$(DO3AM-L-TrpOMe)$_2$C-3]$^{6+}$**, slits of 10 nm with a band pass of 1 nm for excitation at 278 nm was used; for [Ln(**DO3A**)**benzyl**] (Ln = Eu(III) and Tb(III)), slits of 10 nm with a band pass of 1 nm for excitation at 270 nm was used. Points were recorded at 1 nm intervals with a 0.1 s to 0.5 s integration time. S1/R1 response was used throughout to obtain the steady-state luminescence output.

Time-resolved phosphorescence emission spectra were recorded with time per flash of 41 ms, flash count as 10 ms, delay after flash as 0.05 ms, and sample window as 0.2 ms for Eu and 2 ms for Tb complexes. Slit width in phosphorescence: for [Eu$_2$(**DO3A**)$_2$**C-2**] and [Eu$_2$(**DO3A**)$_2$**C-3**] slits of 15 nm with a band pass of 5 nm for excitation at 393 nm was used; for **[Tb$_2$(DO3AM-L-TrpOMe)$_2$C-3]$^{6+}$,** slits of 15 nm with a band pass of 5 nm for excitation at 278 nm was used; for [Ln(**DO3A**)**benzyl**] (Ln = Eu(III) and Tb(III))**,** slits of 15 nm with a band pass of 1 nm for excitation at 270 nm was used. Lifetime measurements were made on the same instrument for the Eu(III) complexes with a max delay of 2 or 8 or 12 ms. Luminescence lifetimes were obtained by tail fit for Eu(III) and Tb(III) complexes using exponential decay function in Origin 8 operated with the FluorEssence™ software for Windows®. All lifetimes gave satisfactory fitting using a mono exponential decay function; fitting to a double exponential decay did not improve the fit. S1 response was used throughout for obtaining the time-resolved, and steady-state excitation output. Luminescence lifetimes were calculated for Eu(III) complexes using the modified Horrocks′ equation as mentioned in Chapter-I. The steady-state and time resolved measurements were carried out for solution of samples taken in a 3500 μL quartz macro fluorescence cuvette with screw cap (Starna

Scientific, type: 3/GL14/Q/10). All measurements were performed at ambient temperature and averaged to three measurements.

7.4.9.1 Luminescence titration protocol

The binding of halides to the complexes was quantified to compute the binding constants (*K*) by steady-state luminescence titration, employing the non-dilution method,[7] by fixing the concentration of the host complex and varying the concentration of the guest (halides). This was accomplished by carrying out the luminescence titrations by adding aliquots of halide (guest), pre-dissolved in a solution containing the host complex, to a solution of a fixed concentration of the host complex to maintain the concentration of the complex uniform, while increasing the concentration of the guest. Stock solution of the host complex (2 mL) was taken in a cuvette and the solution of the guest added in aliquots using Gilson® micropipettes. After each aliquot addition (30-40 μL total), the solution was mixed by agitation using 1000 μL micropipette inside the cuvette. After complete addition, the sample was left to stand for 2 min prior to the measurement was taken. For titrations, the concentration of the stock solution of [Eu_2(**DO3A**)$_2$**C-2**] and [Eu_2(**DO3A**)$_2$**C-3**] was 1 mM and the stock concentration of the guest was 0.02 M; for **[Tb_2(DO3AM-L-TrpOMe)$_2$C-3]$^{6+}$** stock concentration was 10^{-5} M and the stock guest concentration was 2×10^{-4} M; and for [Ln(**DO3A**)**benzyl**] (Ln = Eu(III) and Tb(III)), stock concentration was 2×10^{-4} M and the stock guest concentration was 0.01 M. In titrations and luminescence experiments involving [Ln(**DO3A**)**benzyl**] with sugars and other chiral guests, all addition of the guest anions to the host were individually made 24 h in advance in order to attain anomeric equilibrium of such guests in solution.

Luminescent lanthanide complexes have been used as probes for the detection of anions. Eu(III) complexes have sharp line-like emission spectra, which allows ratiometric analysis by measuring the change in intensity of one emission band relative to the intensity of an almost stationary band.[8] Anion binding occurs directly at the Ln(III) metal centre by the displacement of one or more inner-sphere water molecules with concomitant variations in the Ln(III) coordination environment and the local ligand field, resulting in changes in the emission intensity, spectral form, and lifetime of the complex. Notably, for Eu(III) complexes the changes in emission spectral form induced by anion binding is typically characterised by a large change in the intensity of the electric-dipole allowed, hypersensitive $^5D_0 \rightarrow {}^7F_2$ ($\Delta J = 2$) emission band relative to the intensity of the magnetic-dipole allowed $^5D_0 \rightarrow {}^7F_1$ ($\Delta J = 1$) emission band whose splitting and intensity is relative to the local symmetry at the metal centre and to the magnetic anisotropy factor, δ' (eq 1.19.1).[8] Therefore, ratiometric change in binding was monitored upon the addition of each aliquot portion of the guest by comparing the integral of the hypersensitive $\Delta J = 2$ band against the integral of the magnetically sensitive $\Delta J = 1$ band. This ratiometric change is then plotted as a function of the concentration of the guest added to the host (equivalent guests) and the concentration of the halides is determined alongside a known concentration curve.[8] The resulting titration curve, known as the binding isotherm, is then best fitted to a mathematical model corresponding to the postulated chemical equilibria (eq 1 to 3 mentioned below) to obtain the association constants for one- (K_1) or two- (K_2) or three binding events (K_3) in M^{-1} via an iterative least square fitting process using DYNAFIT® software[9] with uncertainty (±) expressed as coefficient of variation in percentage and standard error.

$$[Host] + [Guest] \underset{K_1}{\Leftrightarrow} [Host - Guest] \qquad K_1 = \frac{[Host-Guest]}{[Host][Guest]} \qquad (1)$$

$$[Host-Guest]+[Guest] \underset{K_2}{\Leftrightarrow} [Host-Guest_2]\ K_2 = \frac{[Host-Guest_2]}{[Host-Guest][Guest]} \quad (2)$$

$$[Host-Guest_2]+[Guest] \underset{K_3}{\Leftrightarrow} [Host-Guest_3]\ K_3 = \frac{[Host-Guest_3]}{[Host-Guest_2][Guest]} \quad (3)$$

However, in luminescence titrations involving fluoride binding in neat solvents, the form and shape of the emission bands change dramatically over the increasing addition of fluoride, such that integrating the area under the emissive bands does not account for the changes in the crystal-field splitting.[8] Therefore, selected emission maxima of the $\Delta J = 0$ and $\Delta J = 1$ bands are used to quantify binding by plotting their intensity via an iterative least square fitting process,[7,8] similar to the ratiometric method mentioned above. Luminescence titrations have been performed at least twice or more and the best was chosen based on the titration spectra which afforded the strongest binding constant (regardless of the anion under study).

7.4.9.2 Generation of binding isotherms and speciation plots using DYNAFIT

Data on all luminescence titrations of the host Eu(III) and Tb(III) complexes with the guest ions were processed and plotted using Origin software. For the ratiometric study of binding interactions, the area under the emission bands were integrated by summing over the wavelength range under each band (585 – 603 nm for $\Delta J = 1$ and 610 – 628 nm for $\Delta J = 2$ transitions for Eu complexes) and the ratio was performed in Origin. For luminescence titrations involving fluoride binding in neat solvents (i.e., deionised water and methanol), binding isotherms were generated after baseline subtraction from an emission wavelength. Baseline corrections were carried out for the $\Delta J = 0$ and $\Delta J = 1$ transitions by subtracting the intensity of the emission at 582 nm and 604 nm which has no characteristic Eu emission (only for binuclear Eu complexes), respectively. Baseline subtractions for other titrations did not show any difference. All binding isotherms are generated from DYNAFIT® version 4.08 using its default setting (Trust region algorithm in

confidence intervals at 95% probability level) which is transported to replot in Origin. Few outliers from the dataset were masked to improve the quality of the iterative fit for binding isotherms. Masking outliers only improved the fit but did not affect the overall result. Speciation models were generated using DYNAFIT® by employing the data used to produce the binding isotherm. A modification of the EQUIL algorithm[10] has been implemented in DYNAFIT® as reported by Stoddart *et al.*[11a] and Sørensen *et al.*[11b] to generate speciation models. DYNAFIT® scripts used to generate binding isotherm and speciation plot are presented in Appendix-D.

7.4.10 Circularly Polarised Luminescence

CPL measurements were recorded on a home built modular spectrometer by Prof. Robert Pal and his group at Durham University, UK. The design and operation of this CPL spectrometer is reported.[12] Tb samples were dissolved in 0.01 M PBS (pH 7.4) and appropriate guest was added at ambient temperature (non-dilution method used) and CPL recorded in a 3500 μL quartz macro fluorescence cuvette with screw cap (Starna Scientific, type: 3/GL14/Q/10).

7.4.11 Longitudinal Relaxivity Measurements

Longitudinal relaxivity measurements were performed on a 60 MHz (1.41 T) benchtop NMR instrument from Magritek Spinsolve™ at 298 K. Measurements were performed using the following parameters: number of scans, 2; acquisition time, 1.6 s; number of steps, 11; repetition time and maximum inversion time were altered depending on the fit of the exponential growth curve from the sample recorded. The data were processed using Mestrenova. After the experiment, the water proton relaxation rate is integrated from the water signal in 4 to 5 ppm chemical shift range for a given concentration of the Gd complex, and the resulting 11 points were plotted using three parameter exponential fit to obtain an exponential

growth curve (Figure 7.1, insert). The G value of this fit generates the longitudinal relaxation rate constant (T_1, s) for a given sample. All measurements were made thrice and the resulting values averaged to obtain the T_1^{-1} value for each concentration of the Gd complex. For each complex, measurements were carried out using five different concentrations and the plot of T_1^{-1} versus concentration of the complex generated the longitudinal relaxivity. The sample solutions of different concentrations were taken in capillary tubes and sealed using a Bunsen burner.

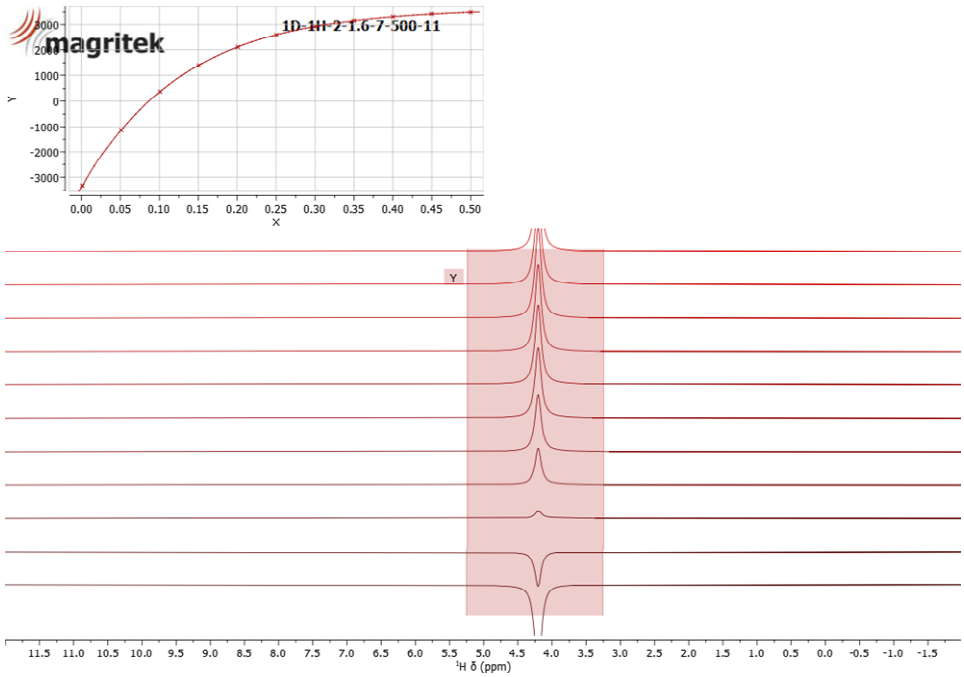


Figure 7.1. Mestrenova view of a Gd complex (for a given concentration) whose longitudinal relaxation data appears along the fit. *Inset*: Magritek generated exponential growth curve showing time (s) verses relaxation time (T_1 (s)).

7.5. Software details

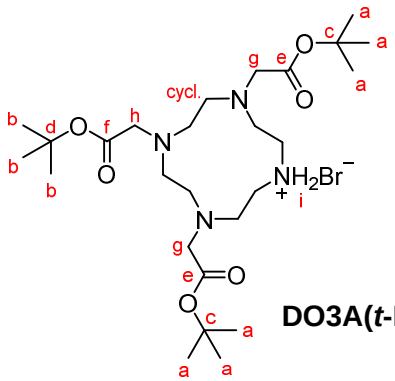
Structures were drawn using Chem Draw 20 and IUPAC names predicted using the same and MarvinView. NMR and mass spectrometry data were processed using Mestrenova software version 14.2. All electronic absorption, luminescence, binding isotherms, speciation plots, and fitted data were plotted using Origin

software version 2020b. Pictures were generated using Inkscape. Single crystal X-ray structures were rendered using Diamond software version 3.7.[13]

7.6. Synthesis of Ligands and Complexes

7.6.1. Synthesis and characterisation of compounds in Chapter-II

7.6.1.1 Synthesis of tri-*tert*-butyl 2,2′,2″-(1,4,7,10-tetraazacyclododecane-1,4,7-triyl)triacetate DO3A(*t*-BuO)$_3$



DO3A(*t*-BuO)$_3$

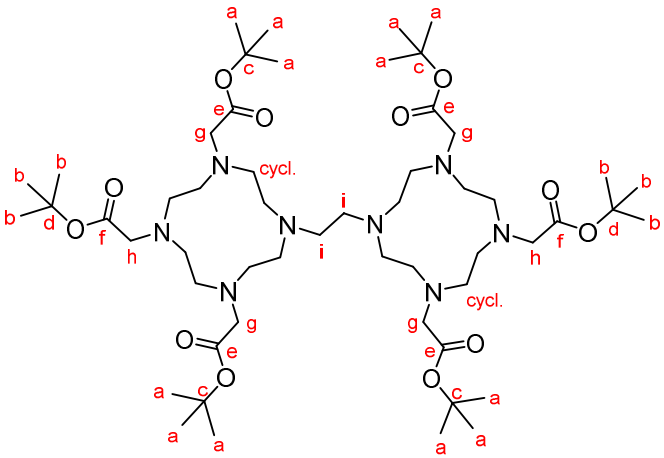
DO3A(*t*-BuO)$_3$ was synthesised by modifying the reported procedure.[14] To a suspension of cyclen (5.00 g, 28.4 mmol, 1.00 equiv) in acetonitrile (250 mL) was added sodium bicarbonate (7.36 g, 87.0 mmol, 3.05 equiv) and stirred at 25 ℃ for 30 min. *tert*-butylbromoacetate (13 mL, 87.0 mmol, 3.05 equiv) in acetonitrile (50 mL) was added dropwise over 2 h at 0 ℃ to this mixture and stirred at 25 ℃ for 72 h. This reaction mixture was filtered to remove the inorganic solids and the resulting filtrate reduced under low pressure to produce an off-white solid, washed with toluene (500 mL) for 24 h under stirring, and filtered to afford the crude product. This process was repeated to afford the title compound as a white powder (7.50 g, 14.6 mmol, 51%); mp 164–168 ℃ (lit.[12] 178–180 ℃); R_f = 0.42 (silica, CH_2Cl_2/CH_3OH, 95:5); ^{1}H NMR (400 MHz, DMSO-d_6, 298 K) δ (ppm): 9.47 – 8.49 (br s, 2H, H^i + N*H*.*H*Br), 3.74 – 2.36 (br m, 22H, $H^{g,h,cycl}$), 1.82 – 1.00 (br s, 27H, $H^{a,b}$); ^{13}C NMR (101 MHz, DMSO-d_6, 298 K) δ (ppm): 170.5 (C^e), 169.9 (C^f),

80.5 (C^{d}), 80.4 (C^{c}), 56.1 (C^{g}), 51.7 (C^{cycl}), 50.4 (C^{h}), 49.7 – 45.6 (C^{cycl}), 27.81 (C^{a}), 27.79 (C^{b}); HRMS (ESI in CH_3OH) *m/z* (% relative intensity): $[M + H]^+$ calcd for $C_{26}H_{51}N_4O_6$, M_r = 515.3803; found, 515.3796 (100%).

7.6.1.2. General procedure 1 for the synthesis of *tert*-butyl 2-{4,7-bis[2-(*tert*-butoxy)-2-oxoethyl]-10-(2-{4,7,10-tris[2-(*tert*-butoxy)-2-oxoethyl]-1,4,7,10-tetraazacyclo- dodecan-1-yl}ethyl)-1,4,7,10-tetraazacyclododecan-1-yl}acetate ((DO3A(*t*-BuO)$_3$)$_2$C-2) and *tert*-butyl 2-{4,7-bis[2-(*tert*-butoxy)-2-oxoethyl]-10-(3-{4,7,10-tris[2-(*tert*-butoxy)-2-oxoethyl]-1,4,7,10-tetraazacyclododecan-1-yl}propyl)-1,4,7,10-tetraazacyclododecan-1-yl}acetate ((DO3A(*t*-BuO)$_3$)$_2$C-3)

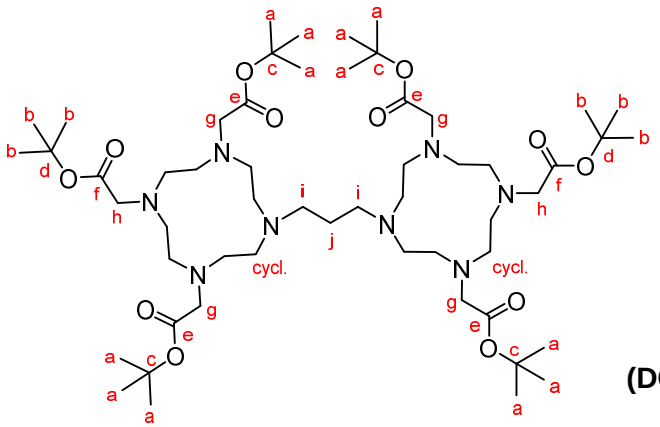
DO3A(*t*-BuO)$_3$ (2.00 equiv) was dissolved in 100 mL acetonitrile and stirred with caesium carbonate (3.00 equiv) for 30 min at 25 °C. To this, the appropriate dibromoalkane (1.05 equiv) was added dropwise for 1 h and stirred under reflux for 48 h. The reaction mixture was cooled to 25 °C and filtered. The filtrate was evaporated under reduced pressure and the resulting yellow oily residue suspended in 10 mL water and extracted with chloroform (3 × 20 mL). The organic layers were combined, dried over anhydrous sodium sulfate, filtered, and evaporated to dryness under reduced pressure. The crude orange product was purified by flash column chromatography to afford the title compound.

(DO3A(*t*-BuO)$_3$)$_2$C-2: Prepared from **DO3A(*t*-BuO)$_3$** (3.80 g, 6.38 mmol, 2.00 equiv) and 1,2-dibromoethane (289 μL, 3.35 mmol, 1.05 equiv) following general procedure **1**. Purification by flash column chromatography over silica gel by gradient elution with CH_2Cl_2/CH_3CH_2OH (100:0→99:1→98:2→97:3→96:4→94:6→90:10, *v*/*v*) afforded the desired product as a yellow solid (1.50 g, 1.42 mmol, 42%); R_f = 0.67 (silica, CH_2Cl_2/CH_3OH, 9:1); mp 175–180 °C; ^{1}H NMR (500 MHz, CD_2Cl_2, 203 K) δ (ppm): 3.55 – 1.76 (br m, 50H, $H^{g,h,i,cycl}$ + 2 *H*Br), 1.73 – 1.18 (br m, 54H, $H^{a,b}$); ^{13}C NMR (126 MHz, CD_2Cl_2, 203 K) δ (ppm): 173.5 – 172.2 ($C^{e,f}$),



(DO3A(*t*-BuO)$_3$)$_2$C-2

83.1 (C^{d}), 82.2 (C^{c}), 55.5 – 47.0 ($C^{g,h,i,cycl}$), 27.4 – 27.0 ($C^{a,b}$); HRMS (ESI in CH_3OH) *m/z* (% relative intensity): $[M + H]^+$ calcd for $C_{54}H_{103}N_8O_{12}$, M_r = 1055.7690; found, 1055.7672 (100%); Anal. Calcd for $C_{54}H_{102}N_8O_{12}$•2HBr•3.9H_2O: C, 50.37; H, 8.75; N, 8.70. Found: C, 50.38; H, 8.53; N, 8.76.



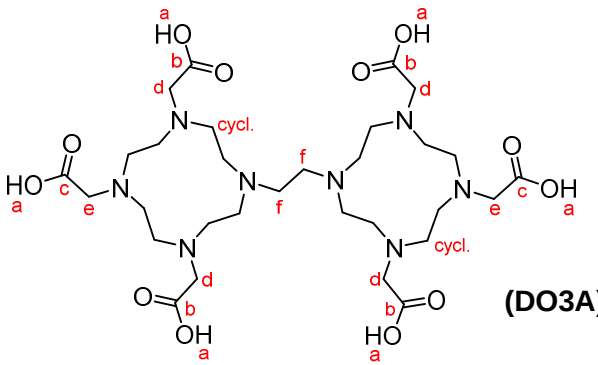
(DO3A(*t*-BuO)$_3$)$_2$C-3

(DO3A(*t*-BuO)$_3$)$_2$C-3: Prepared from **DO3A(*t*-BuO)$_3$** (3.50 g, 5.94 mmol, 2.00 equiv) and 1,3-dibromopropane (316 μL, 3.11 mmol, 1.05 equiv) following general procedure **1**. Purified by flash column chromatography over neutral Al_2O_3 by gradient elution with CH_3CN/H_2O (100:0→99:1→98:2→97:3→96:4→ 95:5→ 93:7→90:10→80:20, *v/v*) to afford the desired product as an orange solid (1.42 g,

1.32 mmol, 61%); R_f = 0.62 (neutral alumina, CH_3CN/H_2O, 95:5); mp 160–165 °C; ^{1}H NMR (500 MHz, CD_2Cl_2, 193 K) δ (ppm): 3.72 – 1.86 (br m, 52H, $H^{g,h,i,cycl}$ + 2*H*Br), 1.74–1.18 (br m, 56H, $H^{a,b,j}$); ^{13}C NMR (126 MHz, CD_2Cl_2, 203 K) δ (ppm): 173.9 – 172.1 ($C^{e,f}$), 82.9 – 81.1 ($C^{c,d}$), 56.5 – 46.9 ($C^{g,h,i,cycl}$), 27.3 – 27.0 ($C^{a,b}$), 19.7 (C^{j}); HRMS (ESI in CH_3OH) *m/z* (% relative intensity): $[M + H]^+$ calcd for $C_{55}H_{105}N_8O_{12}$, M_r = 1069.7846; found, 1069.7831 (100%); Anal. Calcd for $C_{55}H_{104}N_8O_{12}$•2HBr•1.7H_2O: C, 52.35; H, 8.74; N, 8.88. Found: C, 52.34; H, 8.99; N, 8.97.

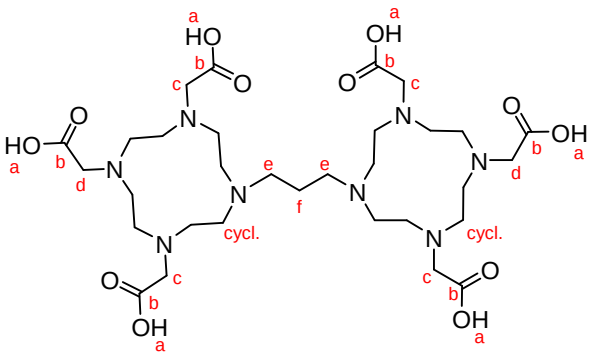
7.6.1.3. General procedure 2 for the synthesis of 2-[4,7-bis(carboxymethyl)-10-{2-[4,7,10-tris(carboxymethyl)-1,4,7,10-tetraazacyclododecan-1-yl]ethyl}-1,4,7,10-tetraazacyclododecan-1-yl]acetic acid ((DO3A)$_2$C-2) and 2-[4,7-bis-(carboxymethyl)-10-{3-[4,7,10-tris(carboxymethyl)-1,4,7,10-tetraazacyclodo-decan-1-yl]propyl}-1,4,7,10-tetraazacyclododecan-1-yl]acetic acid ((DO3A)$_2$C-3)

The ligands **(DO3A)$_2$C-2** and **(DO3A)$_2$C-3** were synthesised by adapting a procedure from the literature.[15] The appropriate bismacrocyclic ester was dissolved in 10 mL dichloromethane and trifluoroacetic acid (10 mL) was added dropwise over 1 h and the mixture stirred at 25 °C for 72 h. The reaction mixture was diluted with equal volume of methanol and concentrated to dryness. The resulting oil was dissolved in methanol (~ 4 mL) and triturated with diethyl ether (~ 160 mL) to afford a precipitate that was isolated by centrifugation. This trituration protocol was repeated twice and the desired product dried under vacuum.



(DO3A)$_2$C-2

(DO3A)$_2$C-2: Prepared from **(DO3A(*t*-BuO)$_3$)$_2$C-2** (400 mg, 0.379 mmol) following general procedure **2**. Yellow powder (240 mg, 0.33 mmol, 70%); mp 212–216 °C; ^{1}H NMR (500 MHz, DMSO-d_6, 403 K) δ (ppm): 9.32 – 7.52 (br s, 6H, –COO*H*^{a}), 4.33 – 2.48 (br m, 48H, *H*^{d,e,f,cycl}); ^{13}C NMR (126 MHz, DMSO-d_6, 403 K) δ (ppm): 170.7 – 170.6 (*C*^{b,c}), 55.1 (*C*^{d}), 54.9 (*C*^{e}), 51.1 – 47.9 (*C*^{f,cycl}); ^{19}F NMR (565 MHz, DMSO-d_6, 298 K) δ (ppm): -73.36 (C*F*$_3$COOH); HRMS (ESI in CH$_3$OH) *m/z* (% relative intensity): [M – H]$^-$ calcd for $C_{30}H_{53}N_8O_{12}$, M_r = 717.3788; found, 717.3776 (100%); Anal. Calcd for $C_{30}H_{54}N_8O_{12}$•1.8CF_3COOH•4H_2O: C, 40.51; H, 6.46; N, 11.25. Found: C, 40.43; H, 6.35; N, 11.25.



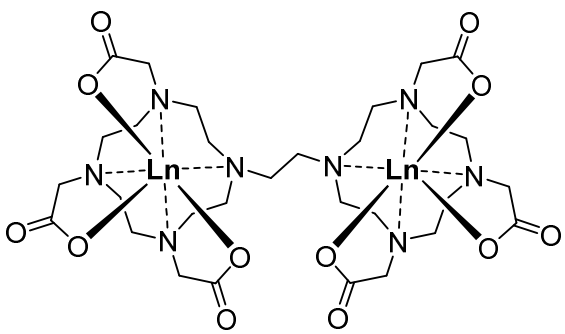
(DO3A)$_2$C-3

(DO3A)$_2$C-3: Prepared from **(DO3A(*t*-BuO)$_3$)$_2$C-3** (1.00 g, 0.935 mmol) following general procedure **2**. Orange powder (yield 478 mg, 0.65 mmol, 89%); mp 214–219 °C; ^{1}H NMR (500 MHz, DMSO-d_6, 403 K) δ (ppm): 9.62 – 9.14 (br s, 6H, –COO*H*^{a}), 4.61 – 2.13 (br m, 48H, *H*^{c,d,cycl}), 2.12 – 1.70 (br s, 2H, *H*^{f}); ^{13}C NMR (126 MHz, DMSO-d_6, 403 K) δ (ppm): 170.9 (*C*^{b}), 55.4 (*C*^{c}), 54.8 (*C*^{d}), 51.4 – 47.9 (*C*^{e,cycl}), 19.9 (*C*^{f}); ^{19}F NMR (565 MHz, DMSO-d_6, 298 K) δ (ppm): –73.53 (C*F*$_3$COOH); HRMS (ESI in CH$_3$OH) *m/z* (% relative intensity): [M – H]$^-$ calcd for $C_{31}H_{55}N_8O_{12}$, M_r = 731.3945; found, 731.3932 (100%); Anal. Calcd for

$C_{31}H_{56}N_8O_{12}$•1.5 CF_3COOH•1.6H_2O: C, 43.78; H, 6.56; N, 12.01. Found: C, 43.80; H, 6.58; N 12.09.

7.6.1.4. General Procedure 3 for the Synthesis of Binuclear Lanthanide(III) Complexes [Ln$_2$(DO3A)$_2$C-2] and [Ln$_2$(DO3A)$_2$C-3]

The complexes were synthesised by adapting the procedure from the literature.[15,16] The ligands **(DO3A)$_2$C-2** or **(DO3A)$_2$C-3** (100 mg, 1.00 equiv) was combined with the respective lanthanide triflate [Ln(OTf)$_3$.*x*H_2O] (2.05 equiv), methanol (2 mL) added, and the mixture sonicated until complete dissolution. The resulting solution was stirred under reflux for 1 h, aqueous NaOH (1 M) added dropwise to pH 5 - 6 and the resulting mixture heated under reflux for 48 h. The solvent was evaporated under reduced pressure to afford a crude residue, dissolved in 10 mL of water and basified to pH 10 using 1 M aqueous NaOH. The precipitate was removed by centrifugation and the resulting solution neutralised using 1 M HCl, an equal volume of ethanol added, and the solvent was evaporated to dryness. The crude product was redissolved in 3 mL of deionised water and purified by dialysis (5 mL dialysis tube, molecular weight cut-off: 500 – 1000 Da). After 48 h and 6 water changes (4 L), the solvent was removed under reduced pressure to afford the desired complex.



[Ln$_2$(**DO3A**)$_2$**C-2**]
Ln(III) = Eu, Gd, Tb, Yb, and Y

[Eu_2(DO3A)$_2$C-2]: Prepared from (DO3A)$_2$C-2 and [Eu(OTf)$_3$.*x*H_2O] by following general procedure **3**. Yellow hygroscopic crystalline powder (70 mg, 0.067 mmol, 48%); ^{1}H NMR (400 MHz, D_2O, 298 K) δ (ppm): 30.54, 25.62, 22.29, 19.36, 17.95, 14.20, 11.38, -0.44, -1.96, -2.71, -4.99, -6.76, -8.46, -10.26, -12.71, -14.14, -17.76, -18.23, -19.29, -20.28, -21.61 (only resolved peaks outside 0 – 10 ppm reported); ^{19}F NMR (377 MHz, D_2O, 298 K): -75.58 (C*F*$_3$COOH), -78.82 (C*F*$_3$$SO_3$Na); HRMS (MALDI in H_2O) *m/z*: $[M + Na]^+$ calcd for $Eu_2C_{30}H_{48}N_8O_{12}Na$, M_r = 1039.170; found, 1039.170; Anal. Calcd for $Eu_2C_{30}H_{48}N_8O_{12}$•0.7$CF_3COOH$•0.7$CF_3SO_3Na$•0.5$H_2O$: C, 31.45; H, 4.09; N, 9.14. Found: C, 31.44; H, 4.99; N, 9.36.

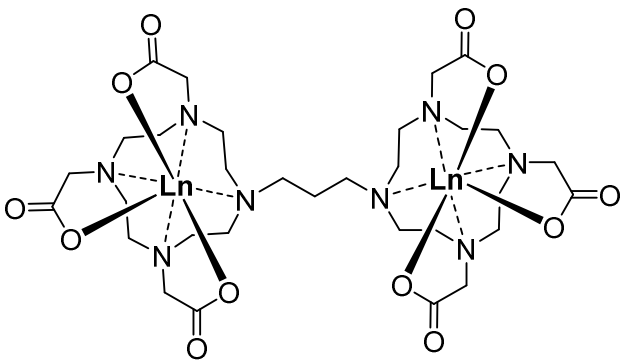
[Gd_2(DO3A)$_2$C-2]: Prepared from (DO3A)$_2$C-2 and [Gd(OTf)$_3$.*x*H_2O] by following general procedure **3**. Brown hygroscopic crystalline powder (34 mg, 0.033 mmol, 24%); HRMS (ESI in CH_3OH) *m/z* (% relative intensity): $[M – H]^-$ calcd for $Gd_2C_{30}H_{46}N_8O_{12}$, M_r = 1026.1723; found, 1026.1701 (45%); Anal. Calcd for $Gd_2C_{30}H_{48}N_8O_{12}$•0.6 H_2O): C, 34.71; H, 4.78; N, 10.79. Found: C, 35.98; H, 6.02; N, 10.78.

[Tb_2(DO3A)$_2$C-2]: Prepared from (DO3A)$_2$C-2 and [Tb(OTf)$_3$.*x*H_2O] by following general procedure **3**. Brown hygroscopic crystalline powder (57 mg, 0.054 mmol, 39%); HRMS (MALDI in H_2O) *m/z*: $[M + Na]^+$ calcd for $Tb_2C_{30}H_{48}N_8O_{12}Na$, M_r = 1053.179; found, 1053.035; Anal. Calcd for $Tb_2C_{30}H_{48}N_8O_{12}$•0.8$CF_3COOH$•1.5$CF_3SO_3Na$•10$H_2O$: C, 25.48; H, 4.45; N, 7.18. Found: C, 24.32; H, 4.40; N, 7.18.

[Yb_2(DO3A)$_2$C-2]: Prepared from (DO3A)$_2$C-2 and [Yb(OTf)$_3$.*x*H_2O] by following general procedure **3**. Yellow hygroscopic crystalline powder (60 mg, 0.059 mmol, 42%); ^{1}H NMR (500 MHz, D_2O, 298 K) δ (ppm): 167.38, 154.00, 143.25, 142.39, 132.48, 122.45, 113.25, 101.15, 96.98, 92.79, 81.60, 51.11, 47.50, 46.52, 42.06, 33.38, 29.38, 28.34, 24.92, 24.34, 24.33, 23.60, 23.43, 21.44, 19.40,

17.54, 13.73, 10.86, -11.44, -12.74, -15.12, -16.65, -24.27, -27.07, -30.72, -31.85, -32.97, -37.24, -37.77, -41.24, -44.58, -48.18, -59.36, -61.34, -68.19, -71.89, -77.12, -81.23, -88.69, -89.83, -96.59, -105.96 (only the resolved peaks outside -10 – 10 ppm reported); ^{19}F NMR (470 MHz, D_2O, 298 K) δ (ppm): -75.52 (C*F*$_3$COOH), -78.2 (C*F*$_3$SO$_3$Na).

[Y$_2$(DO3A)$_2$C-2]: Prepared from (DO3A)$_2$C-2 and [Y(OTf)$_3$.*x*H_2O] by following general procedure **3**. Purified by dialysis using 5 mL dialysis tube, molecular weight cut-off: 100 – 500 Da; yellow hygroscopic crystalline powder (42 mg, 0.046 mmol, 33%); ^{1}H NMR (500 MHz, D_2O, 298 K) δ (ppm): 4.52 – 1.96 (br m, 48H); HRMS (MALDI in H_2O) *m/z*: $[M + Na]^+$ calcd for $Y_2C_{30}H_{48}N_8O_{12}Na$, M_r = 913.140; found, 913.980; Anal. Calcd for $Y_2C_{30}H_{48}N_8O_{12}$•1.2H_2O: C, 39.50; H, 6.18; N, 12.03. Found: C, 39.47; H, 6.24; N, 12.00.



[Ln$_2$(**DO3A**)$_2$**C-3**]
Ln(III) = Eu, Gd, Tb, Yb, and Y

[Eu$_2$(DO3A)$_2$C-3]: Prepared from (DO3A)$_2$C-3 and [Eu(OTf)$_3$.*x*H_2O] by following general procedure **3**. Orange hygroscopic crystalline powder (60 mg, 0.057 mmol, 42%); ^{1}H NMR (500 MHz, D_2O, 298 K) δ (ppm): 33.59, 31.66, 23.45, 21.01, 20.02, 18.93, 17.11, 16.24, 14.52, 12.88, 11.79, 10.99, 0.16, -1.07, -1.43, -1.76, -4.11, -5.35, -5.68, -6.65, -7.12, -7.90, -8.95, -9.64, -10.67, -11.48, -12.21, -13.73, -14.46, -15.86, -16.93, -17.78, -19.14, -20.22, -20.81, -21.93, -23.24, -24.40, -25.77, -27.18 (only the resolved peaks outside 0 – 10 ppm reported); ^{19}F NMR (377 MHz, 298 K,

D_2O) δ (ppm): -78.48 (C*F*$_3$SO$_3$Na); HRMS (MALDI in H_2O) *m/z*: $[M + Na]^+$ calcd for $Eu_2C_{31}H_{50}N_8O_{12}Na$, M_r = 1053.185; found, 1053.029; Anal. Calcd for $Eu_2C_{31}H_{50}N_8O_{12}$•1.1$CF_3SO_3Na$•1.5$H_2O$): C, 31.25; H, 4.34; N, 9.11. Found: C, 31.24; H, 4.88; N, 9.08.

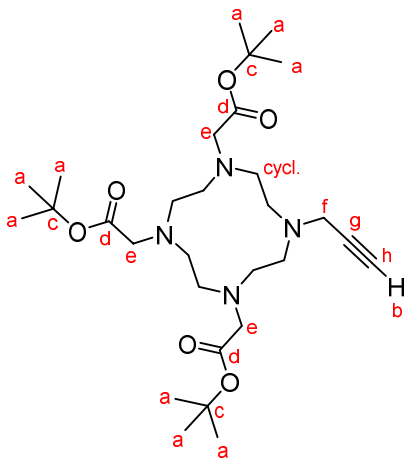
[Gd$_2$(DO3A)$_2$C-3]: Prepared from (DO3A)$_2$C-3 and [Gd(OTf)$_3$.*x*H_2O] by following general procedure **3**. Yellow hygroscopic powder (30 mg, 0.028 mmol, 21%); HRMS (MALDI-MS in H_2O): *m/z* $[M + Na]^+$ calcd. for $Gd_2C_{31}H_{50}N_8O_{12}Na$ 1065.194, found 1065.099; Anal. Calcd for $Gd_2C_{30}H_{48}N_8O_{12}$•3$CF_3SO_3Na$•8.1 H_2O): C, 23.97; H, 3.92; N, 6.58. Found: C, 23.98; H, 4.14; N, 6.63.

[Tb$_2$(DO3A)$_2$C-3]: Prepared from (DO3A)$_2$C-3 and [Tb(OTf)$_3$.*x*H_2O] by following general procedure **3**. Orange hygroscopic crystalline powder (45 mg, 0.043 mmol, 31%); HRMS (ESI in CH_3OH) *m/z* (% relative intensity): $[M + H]^+$ calcd for $Tb_2C_{31}H_{51}N_8O_{12}$, M_r = 1045.2128; found, 1045.2130 (100%); Anal. Calcd for $Tb_2C_{31}H_{50}N_8O_{12}$•1.6$CF_3SO_3Na$•3$H_2O$): C, 28.50; H, 4.11; N, 8.16. Found: C, 27.91; H, 5.03; N, 8.15.

[Yb$_2$(DO3A)$_2$C-3]: Prepared from (DO3A)$_2$C-3 and [Yb(OTf)$_3$.*x*H_2O] by following general procedure **3**. Yellow hygroscopic crystalline powder (50 mg, 0.046 mmol, 33%); ^{1}H NMR (500 MHz, D_2O, 298 K) δ (ppm): 125.83, 109.61, 34.41, 27.48, 13.35, -2.69, -14.15, -55.78, -70.33, -85.56, -94.16 (only resolved peaks outside -10 – 10 ppm reported); ^{19}F NMR (377 MHz, D_2O, 298 K) δ (ppm): -75.84 (C*F*$_3$COOH), -78.75 (C*F*$_3$SO$_3$Na); HRMS (MALDI in H_2O) *m/z*: $[M + Na]^+$ calcd for $Yb_2C_{31}H_{50}N_8O_{12}Na$, M_r = 1095.220; found, 1095.124; Anal. Calcd for $Yb_2C_{31}H_{50}N_8O_{12}$•0.3$CF_3COOH$•0.2$CF_3SO_3Na$•$H_2O$: C, 32.94; H, 4.55; N, 9.66. Found: C, 32.93; H, 4.99; N, 9.39.

[Y_2(DO3A)$_2$C-3]: Prepared from (DO3A)$_2$C-3 and [Y(OTf)$_3$.*x*H_2O] by following general procedure **3**. Purified by dialysis using 5 mL dialysis tube, molecular weight cut-off: 100 – 500 Da; yellow hygroscopic crystalline powder (45 mg, 0.048 mmol, 36%); ^{1}H NMR (500 MHz, D_2O, 298 K) δ (ppm): 4.44 – 2.17 (br m, 48H), 2.11 – 1.54 (br m, 2H, CH_2 bridge); HRMS (MALDI in H_2O) *m/z*: $[M + Na]^+$ calcd for $Y_2C_{31}H_{50}N_8O_{12}Na$, M_r = 927.156; found, 926.993; Anal. Calcd for $Y_2C_{30}H_{48}N_8O_{12}$•1.7CF_3SO_3Na•1.3H_2O: C, 32.18; H, 5.44; N, 9.28. Found: C, 32.17; H, 5.45; N, 9.28.

7.6.1.5. Synthesis of tri-*tert*-butyl 2,2′,2′′-(10-(prop-2-yn-1-yl)-1,4,7,10-tetraaza- cyclododecane-1,4,7-triyl)triacetate (pDO3A(*t*-BuO)$_3$)

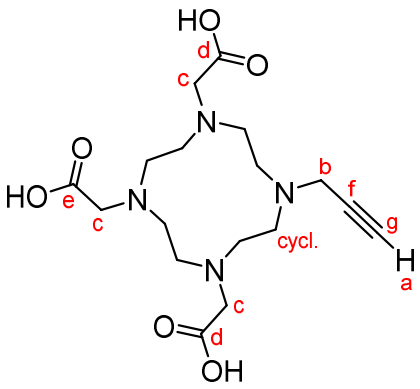


pDO3A(*t*-BuO)$_3$

pDO3A(*t*-BuO)$_3$ was synthesised by following a previous procedure.[17] **DO3A(*t*-BuO)$_3$** (4.00 g, 6.72 mmol, 1.00 equiv) was added to dry MeCN (60 mL) with potassium carbonate (2.32g, 16.8 mmol, 2.50 equiv) and stirred for 20 min. At 0 °C, propargyl bromide (0.75 mL, 5.83 mmol, 1.00 equiv) was added dropwise and the reaction left to gradually warm to 25 °C under stirring in nitrogen for 18 h. Inorganic solids were removed by filtration and the solvent removed under reduced

pressure. The resulting oil was dissolved in toluene (75 mL) and washed with water (60 mL × 3). The organic layers were combined and dried over $MgSO_4$, filtered, and the filtrate evaporated *in vacuo* to obtain a clear golden oil (2.61 g, 4.72 mmol, 70%); ^{1}H NMR (500 MHz, $CDCl_3$, 298 K) δ (ppm): 3.42 (s, 2H, H^f), 3.27 (s, 6H, H^e), 2.82 (s, 12H, H^{cycl}), 2.68 (m, 4H, H^{cycl}), 2.14 (s, 1H, H^b), 1.45 (s, 27H, H^a); ^{13}C NMR (126 MHz, D_2O, 298 K) δ (ppm): 171.3 (C^d), 80.9 (C^c), 79.4 (C^g) 72.6 (C^h), 56.9 (C^e), 52.3 – 51.2 (C^{cycl}), 43.2 (C^f), 28.4 (C^a); HRMS (ESI in CH_3OH) *m/z* (% relative intensity): $[M + H]^+$ calcd for $C_{29}H_{53}N_4O_6$, M_r = 553.3960; found, 553.3944 (100%).

7.6.1.6. Synthesis of 2,2′,2′′-(10-(prop-2-yn-1-yl)-1,4,7,10-tetraazacyclodo-decane-1,4,7-triyl)triacetic acid (pDO3A)

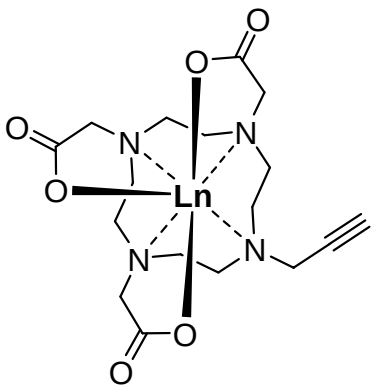


pDO3A

pDO3A was synthesised by following the literature procedure.[17b] **pDO3A(*t*-BuO)$_3$** (500 mg, 0.90 mmol) was dissolved in dichloromethane (7 mL) and trifluoroacetic acid (7 mL) added dropwise over 1 h and stirred at 25 °C for 12 h. The reaction mixture was diluted with equal volume of methanol and concentrated to dryness. The resulting oil was dissolved in methanol (~ 4 mL) and triturated with diethyl ether (~ 180 mL) to afford a colourless precipitate and isolated by centrifugation. This trituration protocol was repeated thrice to afford the

title compound as a white solid; (0.178 g, 0.462 mmol, 64%); mp 173–178 °C; ^{1}H NMR (500 MHz, D_2O, 298 K) δ (ppm): 3.94 – 3.71 (m, 6H, H^{c}), 3.62 (s, 2H, H^{b}), 3.51 – 3.25 (m, 8H, H^{cycl}), 3.25 – 3.05 (m, 8H, H^{cycl}), 2.78 (br. s, 1H, H^{a}); ^{13}C NMR (126 MHz, D_2O, 298 K) δ (ppm): 173.1 (C^{d}), 171.0 (C^{e}), 76.4 (C^{f}) 72.7 (C^{g}), 55.5 (C^{c}), 53.8 – 48.0 (C^{cycl}), 43.0 (C^{b}); ^{19}F NMR (565 MHz, D_2O, 298 K) δ (ppm): -73.24 (CF_3COOH); HRMS (ESI in CH_3OH) *m/z* (% relative intensity): $[M + H]^+$ calcd for $C_{17}H_{29}N_4O_6$, M_r = 385.2082; found, 385.2080 (100%).

7.6.1.7. General procedure 4 for the synthesis of mononuclear lanthanide(III) complex [Ln(pDO3A)]



[Ln(**pDO3A**)]
Ln(III) = Eu, Gd, Tb, Yb, and Y

The Ln(III) complexes of **pDO3A** were synthesised by the literature procedure.[16,17] The ligand **pDO3A** (200 mg, 0.4 mmol, 1.00 equiv) was added to the respective lanthanide triflate [$Ln(OTf)_3.xH_2O$] (1.05 equiv), methanol (2 mL) added, and the mixture sonicated until complete dissolution. The resulting solution was stirred under reflux for 1 h, before aqueous NaOH (1 M) was added dropwise to pH 5 - 6 and heated under reflux for 48 h. The solvent was evaporated under reduced pressure to afford a crude residue, dissolved in 10 mL of water and basified to pH 10 using 1 M aqueous NaOH. The precipitate was removed by centrifugation and the resulting solution neutralised using 1 M HCl, an equal volume of ethanol added, and the solvent flash evaporated to dryness. The crude product was

redissolved in 3 mL of deionised water and purified by dialysis (5 mL dialysis tube, molecular weight cut-off: 100 – 500 Da). After 48 h and 6 water changes (4 L), the solvent was removed under reduced pressure to afford the complex.

[Eu(pDO3A)]: Prepared from [$Eu(OTf)_3.xH_2O$] following general procedure **4**. Colourless hygroscopic powder (130 mg, 0.243 mmol, 60%); ^{1}H NMR (400 MHz, D_2O, 298 K) δ (ppm): 25.37, 18.86, 17.21, 15.36, 13.55, 12.06, 10.28, 0.84, -0.39, -1.34, -1.67, -5.76, -6.81, -8.96, -10.15, -11.16, -11.97, -13.91, -15.32, -19.11, -21.20 (only resolved peaks outside 0 – 10 ppm reported); ^{19}F NMR (376 MHz, D_2O, 298 K) δ (ppm): -75.55 (CF_3COOH), -78.80 (CF_3SO_3Na); HRMS (ESI in MeOH) *m/z* (% relative intensity): $[M + H]^+$ calcd for $EuC_{17}H_{26}N_4O_6$, M_r = 535.1060; found, 535.1058 (100%).

[Gd(pDO3A)]: Prepared from [$Gd(OTf)_3.xH_2O$] following general procedure **4**. Colourless hygroscopic powder (102 mg, 0.188 mmol, 47%); HRMS (ESI in MeOH) *m/z* (% relative intensity): $[M + H]^+$ calcd for $GdC_{17}H_{26}N_4O_6$, M_r = 540.1088; found, 540.1084 (20%).

[Tb(pDO3A)]: Prepared from [$Tb(OTf)_3.xH_2O$] following general procedure **4**. Off-white hygroscopic powder (101 mg, 0.186 mmol, 46%); ^{1}H NMR (500 MHz, D_2O, 298 K) δ (ppm): 405.28, 246.19, 222.90, 184.93, 121.09, 104.87, 82.82, 72.07, -78.48, -100.44, -122.03, -133.83, -139.73, -145.27, -167.22, -179.79, -203.59, -217.77, -225.23, -244.86, -286.33, -304.43, -333.16, -365.33, -380.66, -405.41 (only the resolved peaks outside -50 – 50 ppm reported); HRMS (ESI in MeOH) *m/z* (% relative intensity): $[M + H]^+$ calcd for $TbC_{17}H_{26}N_4O_6$, M_r = 541.1100; found, 541.1092 (100%).

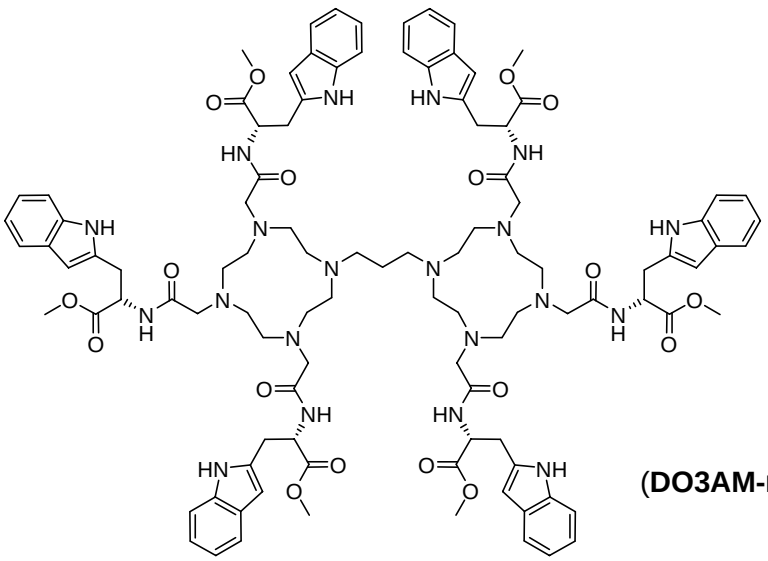
[Yb(pDO3A)]: Prepared from [$Yb(OTf)_3.xH_2O$] following general procedure **4**. Colourless hygroscopic powder (120 mg, 0.216 mmol, 54%); ^{1}H NMR (400 MHz,

D_2O, 298 K) δ (ppm): 133.93, 126.02, 119.29, 38.68, 31.71, 25.89, 23.25, 16.22, 13.73, -17.27, -56.95, -61.09, -72.58, -75.59, -83.27, -95.34. (only the resolved peaks outside -10 to 10 ppm reported); ^{19}F NMR (376 MHz, D_2O, 298 K) δ (ppm): -78.28 (CF_3SO_3Na); HRMS (ESI in MeOH) *m/z* (% relative intensity): $[M + H]^+$ calcd. for $YbC_{17}H_{26}N_4O_6$, M_r = 556.1235; found 556.1241 (100%).

[Y(pDO3A)]: Prepared from $[Y(OTf)_3.xH_2O]$ following general procedure **4**. Colourless hygroscopic powder (98 mg, 0.208 mmol, 52%); ^{1}H NMR (400 MHz, D_2O, 298 K) δ (ppm): 4.09 – 2.15 (br m, 25H); ^{19}F NMR (376 MHz, D_2O, 298 K) δ (ppm): -75.57 (CF_3COOH), -78.81 (CF_3SO_3Na); HRMS (ESI in MeOH) *m/z* (% relative intensity): $[M + H]^+$ calcd. for $YC_{17}H_{26}N_4O_6$, M_r = 470.0863; found 470.0859 (40%).

7.6.2. Synthesis and characterisation of compounds in Chapter-III

7.6.2.1. Synthesis of trimethyl 2,2′,2′′-((2,2′,2′′-(10-(3-(4,7,10-*tris*(2-(((*R*)-3-(1*H*-indol-2-yl)-1-methoxy-1-oxopropan-2-yl)amino)-2-oxoethyl)-1,4,7,10-tetraazacyclododecan-1-yl)propyl)-1,4,7,10-tetraazacyclododecane-1,4,7-triyl)*tris*(acetyl))*tris*(azanediyl))(2S,2'S,2''S)-*tris*(3-(1*H*-indol-2-yl)propanoate) (DO3AM-L-TrpOMe)$_2$C-3

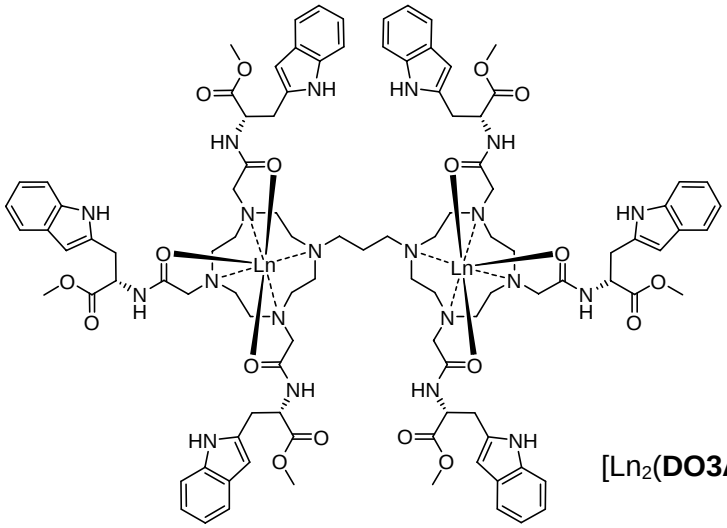


(DO3AM-L-TrpOMe)$_2$C-3

(DO3A)$_2$C-3 (100 mg, 0.14 mmol, 1.00 equiv) was added to a mixture of DMF (2 mL) and MeOH (1 mL) followed by DIPEA (190 μL, 1.09 mmol, 8 equiv) and stirred for 15 min at 25 °C. HATU (363 mg, 0.954 mmol, 7.00 equiv) was added to this mixture and stirred for 30 min at 25 °C. Upon heating to 50 °C, HOBt (129 mg, 0.954 mmol, 7.00 equiv) and L-tryptophan methyl ester (243.18 mg, 0.954 mmol, 7.00 equiv) were added in portions at the same time for 30 min. After complete addition, the reaction mixture was heated to 80 °C for 24 h, cooled to 25 °C, toluene added to form an azeotrope with DMF, and evaporated to dryness. This process of removing DMF by azeotrope formation with toluene was repeated thrice to obtain the crude product as a dark brown slurry and purified by flash column chromatography in gradient MeCN/H_2O/aq.NH_3 (100:0→98:2→96:4→94:6→92:8→90:10→89:10:1→79:20:1→59:38:3, *v*/*v*) using neutral alumina. The resulting product with impurities was further column purified in gradient DCM/EtOH/aq.NH_3 (100:0:→99:1→98:2→97:3→94:5:1→89:10:1→59:48:2, *v*/*v*) under silica gel to afford the desired product as a brown solid (95 mg, 0.049 mmol, 36%); $[\alpha]_D^{25}$ – 4 (*c* 1.00, MeOH); ^{1}H NMR (400 MHz, MeOD, 298 K) δ (ppm): 10.41 (-CON*H*-), 8.46 – 8.37 (dd, *J* = 1.4, 4.3 Hz, 6H, Ar*H*), 8.14 – 8.04 (dd, *J* = 1.4, 8.4 Hz, 6H, Ar*H*), 7.61 – 7.55 (dt, *J* = 4.3, 8.4 Hz, 12H, Ar*H*), 7.15 – 7.10 (s, 6H, imidazole C*H*), 4.09 – 3.94 (br m, 6H, C*H*), 3.92 – 3.78 (br m, 12H, arm-CH_2), 3.49 – 3.28 (br m, 12H, imidazole CH_2), 3.27 – 3.23 (s, 18H, CO_2CH_3), 3.22 – 2.97 (br m, 32H, H^{cycl}), 2.14 – 2.01 (br m, 4H, CH_2), 1.28 – 1.13 (br s, 2H, CH_2); ^{13}C NMR (101 MHz, MeOD, 298 K) δ (ppm): 174.6 (CH_3O-*C*=O-), 171.7 (-NH*C*=O-), 149 (Ar$C^{quaternary}$), 138.3 (Ar*C*H), 136.3 (Ar*C*H), 128.4 ($C^{quaternary}$), 125.3 (Ar*C*H), 122.6 (Ar*C*H), 121.3 (Ar$C^{quaternary}$), 112.2 (*C*H), 109.4 (imidazole *C*H), 58.7 (*C*H), 56.5 (arm-*C*H_2), 53.2 (*C*H_3), 31.2 (imidazole *C*H_2), 45.5 – 52.8

(C^{cycl}), 28.4 (CH_2), 25.7 (CH_2); HRMS (ESI in MeOH) *m/z* (% relative intensity): $[M + H]^+$ calcd for $C_{103}H_{129}N_{20}O_{18}$, M_r = 1934.2850; found, 1934.2847 (100%).

7.6.2.2. General procedure 5 for the synthesis of $[Ln_2$(DO3AM-L-TrpOMe)$_2$C-3$]^{6+}$



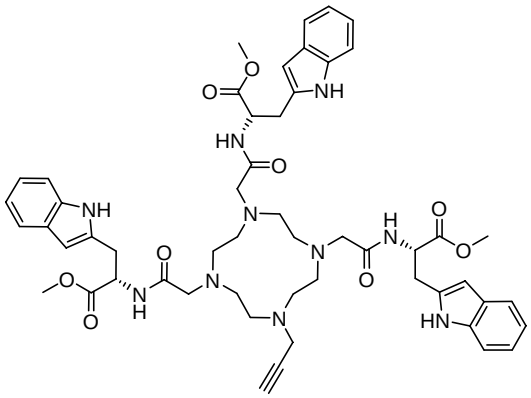
$[Ln_2$(**DO3AM-L-TrpOMe**)$_2$**C-3**$]^{6+}$

(DO3AM-L-TrpOMe)$_2$C-3 (40 mg, 0.0206 mmol, 1.00 equiv) and the appropriate $Ln(OTf)_3.xH_2O$ (2.05 equiv) was added to MeOH (2 mL) and refluxed for 48 h. The resulting solution was triturated with diethyl ether (~ 50 mL) to precipitate the complex and collected by centrifugation. This process was repeated thrice to afford the desired binuclear Ln(III) complex. The resulting complexes were used without further purification.

$[Eu_2$(DO3AM-L-TrpOMe)$_2$C-3$]^{6+}$: Prepared from $[Eu(OTf)_3.xH_2O]$ following general procedure **5**. Yellow hygroscopic powder (10 mg, 0.0045 mmol, 22%); ^{1}H NMR (400 MHz, MeOD, 298 K) δ (ppm): 24.00, -6.56, -8.64, -9.49, -11.20, -12.34, -14.28, -26.00, -27.91, -29.40 (only resolved peaks outside 0 – 10 ppm reported); ^{19}F NMR (377 MHz, MeOD, 298 K) δ (ppm): -80.04 (CF_3SO_3Na); HRMS (MALDI in MeOH) *m/z*: $[M + Na]^+$ calcd. for $Eu_2C_{103}H_{128}N_{20}O_{18}Na$, M_r = 2261.207; found, 2261.190.

[Tb$_2$(DO3AM-L-TrpOMe)$_2$C-3]$^{6+}$: Prepared from [Tb(OTf)$_3$.xH$_2$O] following general procedure **5**. Brown hygroscopic powder (17 mg, 0.0075 mmol, 37%); $[\alpha]_D^{25}$ – 1 (*c* 1.00, MeOH); HRMS (MALDI in MeOH) *m/z*: [M + Na]$^+$ calcd. for $Tb_2C_{103}H_{128}N_{20}O_{18}Na$, M_r = 2272.820; found, 2272.795.

7.6.2.3. Synthesis of trimethyl 2,2′,2′′-((2,2′,2′′-(10-(prop-2-yn-1-yl)-1,4,7,10-tetraazacyclododecane-1,4,7-triyl)tris(acetyl))tris(azanediyl))(2S,2'S,2''S)-*tris*-(3-(1*H*-indol-2-yl)propanoate) (pDO3AM-L-TrpOMe)

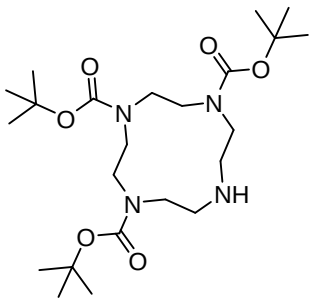


(pDO3AM-L-TrpOMe)

pDO3A (100 mg, 0.26 mmol, 1.00 equiv) was added to DMF (2 mL) followed by DIPEA (227 μL, 1.30 mmol, 5.00 equiv) and stirred for 15 min at 25 ℃. HATU (346.38 mg, 0.91 mmol, 3.50 equiv) was added to this mixture and stirred for 30 min at 25 ℃. Upon heating this mixture to 50 ℃, HOBt (175.84 mg, 1.30 mmol, 5.00 equiv) and L-tryptophan methyl ester (212.15 mg, 0.83 mmol, 3.2 equiv) were added in portions at the same time for 30 min and heated to 80 ℃ for 24 h. The resulting solution was cooled to 25 ℃, toluene added to form an azeotrope with DMF, and evaporated to dryness. This process of removing DMF by azeotrope formation with toluene was repeated thrice to obtain the crude product as a dark brown slurry and purified using flash column chromatography in gradient MeCN/H$_2$O/aq.NH$_3$ (100:0→98:2→96:4→95:5→94:6→92:8→90:10→87:10:3→

79:20:1, *v*/*v*) under neutral alumina and further column purified in gradient DCM/EtOH/aq.NH_3 (100:0→99:1→98:2→97:3→94:5:1→91:8:2 →79:19:2, *v*/*v*) under silica gel to afford the desired product as a brown solid (89 mg, 0.0903 mmol, 35%); $[\alpha]_D^{25}$ – 2 (*c* 1.00, MeOH); ^{1}H NMR (400 MHz, MeOD, 298 K) δ (ppm): 10.51 (-CON*H*-), 8.74 – 8.69 (dd, *J* = 1.4, 4.3 Hz, 3H, Ar*H*), 8.68 – 8.63 (dd, *J* = 1.5, 4.5 Hz, 3H, Ar*H*), 8.40 – 8.33 (ddd, *J* = 1.4, 6.5, 8.3 Hz, 6H, Ar*H*), 7.24 – 7.22 (s, 3H, imidazole C*H*), 4.25 – 4.06 (br m, 3H, C*H*), 4.04 – 3.78 (br m, 8H, arm-CH_2), 3.73 – 3.41 (br m, 6H, imidazole CH_2), 3.38 – 3.34 (s, 9H, CO_2CH_3), 3.28 – 2.54 (br m, 17H, H^{cycl} + alkyne CH); ^{13}C NMR (101 MHz, MeOD, 298 K) δ (ppm): 177.9 (CH_3O-*C*=O-), 174.8 (-NH*C*=O-), 163.4 (Ar$C^{quaternary}$), 138.3 (Ar*C*H), 137.8 (Ar*C*H), 129.2 ($C^{quaternary}$), 125.4 (Ar*C*H), 124.5 (Ar*C*H), 122.6 (Ar$C^{quaternary}$), 112.5 (*C*H), 109.5 (imidazole *C*H), 75.6 (alkyne *C*), 69.9 (alkyne *C*H), 57.2 (alkyne CH_2) 56.5 (arm-*C*H_2), 55.3 (CO_2CH_3), 53.2 – 46.5 (C^{cycl}), 28.4 (imidazole CH_2); HRMS (ESI in MeOH) *m*/*z* (% relative intensity): $[M + H]^+$ calcd for $C_{53}H_{65}N_{10}O_9$, M_r = 985.1650; found, 985.1643 (100%).

7.6.2.4. Synthesis of tri-*tert*-butyl-1,4,7,10-tetraazacyclododecane-1,4,7-tricarboxylate (3.1)

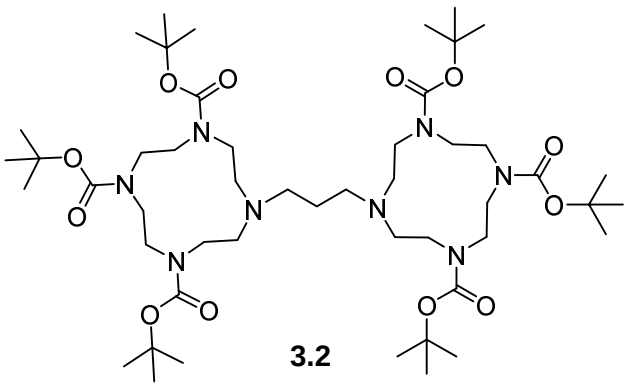


3.1

This compound was synthesised as reported.[18] At 0 °C, di-*tert*-butyl dicarbonate (12.10 mL, 52.70 mmol, 3.03 equiv) in chloroform (65 mL) was added

dropwise over 2 h to a solution of cyclen (3.0 g, 17.41 mmol, 1.00 equiv) and triethylamine (7.5 mL, 52.70 mmol, 3.03 equiv) in chloroform (85 mL). The solution was allowed to gradually warm to 25 ℃ under stirring for 18 h. The reaction mixture was transferred to a separatory funnel and washed with water (4 × 50 mL). The organic layers were combined, dried over sodium sulfate, filtered, and the filtrate evaporated *in vacuo* to afford a residue which was purified using flash column chromatography using isocratic diethyl ether (100%, *v/v*) over silica gel to afford the tri-boc cyclen (**3.1**) as a colourless solid (5.98 g, 12.64 mmol, 73%); ^{1}H NMR (400 MHz, DMSO-d_6, 298 K) δ (ppm): 3.62 – 3.47 (dd, J = 6.5, 11.8 Hz, 4H, H^{cycl}), 3.30 – 3.10 (m, 8H, H^{cycl}), 2.71 – 2.55 (d, J = 9.4 Hz, 4H, H^{cycl}), 2.02 – 1.84 (d, J = 8.3 Hz, 1H, NH^{cycl}), 1.47– 1.28 (br m, 27H, CH_3); HRMS (ESI in MeOH) *m/z* (% relative intensity): $[M + H]^+$ calcd for $C_{23}H_{44}N_4O_6$, M_r = 472.6348; found, 472.6336 (100%).

7.6.2.5. Synthesis of hexa-*tert*-butyl 10,10′-(propane-1,3-diyl)*bis*(1,4,7,10-tetraazacyclododecane-1,4,7-tricarboxylate) (3.2)

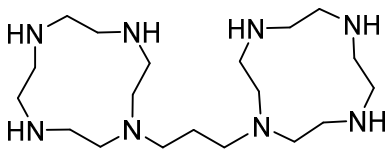


3.2

Tri-boc cyclen (200 mg, 0.423 mmol, 2.00 equiv) was dissolved in MeCN (25 mL) followed by the addition of caesium carbonate (189.50 mg, 0.582 mmol, 2.75 equiv) and stirred for 15 min. 1,3-dibromopropane (42.80 μL, 0.211 mmol,

1.00 equiv) was added to this mixture and refluxed for 12 h. The inorganic base was filtered off, the filtrate evaporated to dryness to afford the crude product, and purified by flash column chromatography using gradient chlorofrom/*iso*-propanol (100:0→99:1→98:2→95:5→90:10→50:50, *v*/*v*) over silica gel to afford the product as a yellow solid (123 mg, 0.125 mmol, 59%); ^{1}H NMR (400 MHz, $CDCl_3$, 298 K) δ (ppm): 3.61 – 3.43 (s, 8H, $H^{cycl.}$), 3.37 – 3.05 (m, 20H, H^{cycl}), 2.81 – 2.66 (m, 8H, $H^{cycl.}$ + CH_2), 2.06 – 2.04 (s, 2H, CH_2), 1.39 – 1.30 (d, J = 8.2 Hz, 54H); HRMS (ESI in MeOH) *m/z* (% relative intensity): $[M + H]^+$ calcd for $C_{49}H_{93}N_8O_{12}$, M_r = 985.6848; found, 985.6842 (100%).

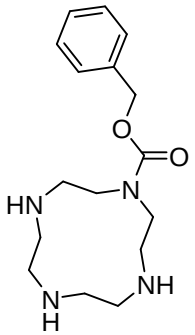
7.6.2.6. Synthesis of 1,3-di(1,4,7,10-tetraazacyclododecan-1-yl)propane (3.3)



3.3

This compound was prepared by the literature protocol.[18] Compound **3.2** (100 mg, 0.101 mmol) was dissolved in DCM (2 mL), TFA (2 mL) added, and stirred for 4 h at 25 °C. After confirming product formation by LRMS, the solvent was evaporated *in vacuo* and TFA removed by adding MeOH to create an azeotrope. This process of removing TFA by azeotrope formation with MeOH was repeated twice to afford **3.3** as a yellow solid (21 mg, 0.0546 mmol, 54%); ^{1}H NMR (400 MHz, MeOD, 298 K) δ (ppm): 3.73 – 2.85 (br m, 32H, H^{cycl}), 1.98 – 1.96 (s, 4H, CH_2), 1.36 – 1.24 (br s, 2H, CH_2); HRMS (ESI in MeOH) *m/z* (% relative intensity): $[M + H]^+$ calcd for $C_{19}H_{44}N_8$, M_r = 384.3698; found, 384.3689 (100%).

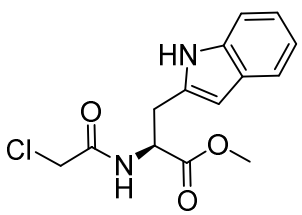
7.6.2.7. Synthesis of benzyl 1,4,7,10-tetraazacyclododecane-1-carboxylate (mono-CBz cyclen, 3.4)



3.4

This compound was synthesised by modifying the reported procedure.[19] Cyclen (2.5 g, 14.5 mmol, 1.00 equiv) was dissolved in $CHCl_3$ (50 mL) and cooled to 0 °C. CBzCl (2.25 mL, 15.90 mmol, 1.05 equiv) added dropwise for 10 min under stirring. The resulting solution was allowed to gradually warm to 25 °C, stirred for 12 h, and quenched by adding aqueous NaOH (5%, 25 mL). The resulting mixture was transferred to a separatory funnel, the organic layer separated, followed by washing the aqueous layer using chloroform (3 × 25 mL). The combined organic layer was dried over $MgSO_4$ and evaporated to dryness. The resulting oil was purified by flash column chromatography using DCM/MeOH/aq.NH_3 (100:0:0→98:2:0→90:10:0→89:10:1→48:50:2, *v/v*) on silica gel to afford mono-CBz cyclen (**3.4**) as a colourless oil (2 g, 6.53 mmol, 45%); ^{1}H NMR (400 MHz, $CDCl_3$, 298 K) δ (ppm): 7.37 – 7.11 (m, 5H, Ar*H*), 5.05 – 5.00 (s, 2H, -CO_2CH_2Ar), 3.87 – 3.13 (br m, 12H, H^{cycl}), 2.93 – 2.59 (br m, 4H, H^{cycl}); ^{13}C NMR (101 MHz, $CDCl_3$, 298 K) δ (ppm): 156.0 (*C*=O), 136.3 (Ar$C^{quaternary}$), 128.0 (Ar*C*), 127.7 (Ar*C*), 127.2 (Ar*C*), 66.4 (-CO_2CH_2Ar), 50.8 – 45.2 (C^{cycl}); HRMS (ESI in MeOH) *m/z* (% relative intensity): $[M + H]^+$ calcd for $C_{16}H_{27}N_4O_2$, M_r = 307.2134; found, 307.2126 (100%).

7.6.2.8. Synthesis of methyl(2-chloroacetyl)-L-tryptophanate (3.7)



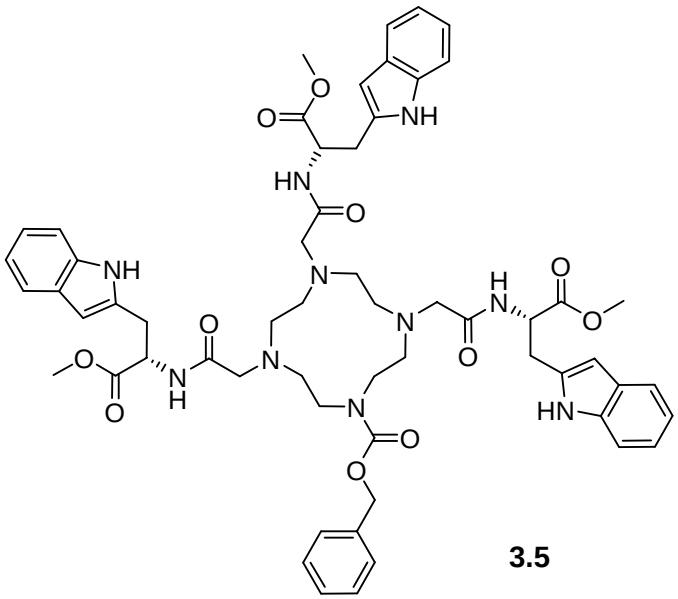
3.7

This compound was synthesised from a reported procedure.[20] L-Tryptophan methyl ester (1.00 g, 4.58 mmol, 1.00 equiv) was dissolved in DCM (30 mL). Chloroacetyl chloride (474 μL, 5.96 mmol, 1.3 equiv) in DCM (10 mL) and potassium carbonate (2.22 g, 16.03 mmol, 3.50 equiv) in H_2O (25 mL) were added simultaneously over a period of 30 min at 0 °C. The reaction mixture was gradually warmed to 25 °C under stirring for 18 h, transferred into a separatory funnel, and the organic layer separated. The aqueous layer was extracted with DCM (3 × 50 mL) and the combined organic layer dried over sodium sulfate, filtered, and evaporated to dryness to afford **3.7** as a yellow solid, which turned into a yellow oil over time. This was used without further purification (1.10 g, 3.73 mmol, 81%); $[\alpha]_D^{25}$ + 44 (*c* 1.00, MeOH); ^{1}H NMR (400 MHz, $CDCl_3$, 298 K) δ (ppm): 8.85 – 8.67 (s, 1H, -CON*H*-), 7.86 – 7.79 (d, *J* = 7.8 Hz, 1H, Ar*H*), 7.65 – 7.58 (d, *J* = 8.1 Hz, 1H, Ar*H*), 7.52 – 7.32 (t, *J* = 9.3 Hz, 2H, Ar*H*), 6.57 (s, 1H, imidazole C*H*), 5.25 – 5.16 (dt, *J* = 5.5, 8.1 Hz, 1H, -NHC*H*-), 4.28 – 4.24 (s, 2H, -NHCOCH_2Cl), 4.00 – 3.94 (s, 3H, CO_2CH_3), 3.69 – 3.61 (d, *J* = 5.5 Hz, 2H, CH_2); ^{13}C NMR (101 MHz, $CDCl_3$, 298 K) δ (ppm): 171.8 (CH_3O-*C*=O-), 166 (O=*C*-NH), 136.2 (Ar*C*^{quaternary}), 127.4 (*C*^{quaternary}), 123 (Ar*C*^{quaternary}), 122.3 (Ar*C*), 119.7 (Ar*C*), 118.5 (Ar*C*), 111.5 (Ar*C*), 109.3 (Ar*C*), 53.3 (-NH*C*H-), 52.6 (CO_2CH_3), 42.5 (-NHCO*C*H_2Cl), 27.5 (imidazole *C*H_2); HRMS (ESI in MeOH) *m/z* (% relative intensity): $[M + H]^+$ calcd for $C_{14}H_{15}ClN_2O_3$, M_r = 294.7428; found, 294.7420 (100%).

7.6.2.9. Synthesis of trimethyl 2,2′,2′′-((2,2′,2′′-(10-((benzyloxy)carbonyl)-1,4,7,10-tetraazacyclododecane-1,4,7-triyl)tris(acetyl))tris(azanediyl)) (2*S*,2′*S*,2′′*S*)-*tris*(3-(1*H*-indol-2-yl)propanoate) (3.5)

Mono-CBz cyclen (195 mg, 0.634 mmol, 1.00 equiv) was dissolved in DMF (2 mL), potassium carbonate (526 mg, 3.81 mmol, 6.00 equiv) added, and stirred for 15 min. A solution of compound **3.7** (750 mg, 2.54 mmol, 4.00 equiv) in DMF

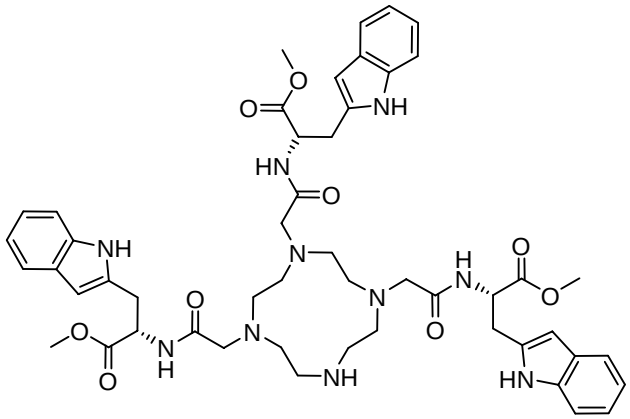
(1 mL) was added dropwise for 10 min followed by a pinch of KI (10 mol%) and heated to 80 ℃ for 16 h. The reaction mixture was filtered, toluene added to the filtrate to form an azeotrope with DMF and evaporated under reduced pressure.



3.5

This process of removing DMF by azeotrope formation with toluene was repeated thrice to afford a brown slurry and purified via flash column chromatography in gradient MeCN/H_2O (100:0→99:1→98:2→97:3→96:4, *v/v*) over neutral alumina. The resulting product was purified again by flash column chromatography in gradient DCM/EtOH/aq.NH_3 (100:0:→99:1→98:2→97:3→ 94:5:1, *v/v*) over silica gel to afford the product as a brown solid (110 mg, 0.1017 mmol, 16%); $[\alpha]_D^{25}$ – 4 (*c* 1.00, MeOH); ^{1}H NMR (400 MHz, MeOD, 298 K) δ (ppm): 10.22 (-CON*H*-), 7.95 – 7.89 (s, 5H, Ar*H*), 7.57 -7.02 (br m, 12 H, Ar*H*), 7.00 – 6.94 (s, 3H, imidazole C*H*), 5.03 – 4.87 (br s, 2H, CH_2), 4.77 – 4.69 (s, 3H, C*H*), 3.8 – 3.5 (s, 9H, CO_2CH_3), 3.45 – 2.02 (br m, 28H, CH_2 + H^{cycl}); HRMS (ESI in MeOH) *m/z* (% relative intensity): $[M + H]^+$ calcd for $C_{58}H_{69}N_{10}O_{11}$, M_r = 1081.5126; found, 1081.5122 (100%).

7.6.2.10. Synthesis of trimethyl 2,2′,2′′-((2,2′,2′′-(1,4,7,10-tetraazacyclododecane-1,4,7-triyl)*tris*(acetyl))tris(azanediyl))(2S,2′S,2′′S)-*tris*(3-(1*H*-indol-2-yl)propanoate) (3.6)



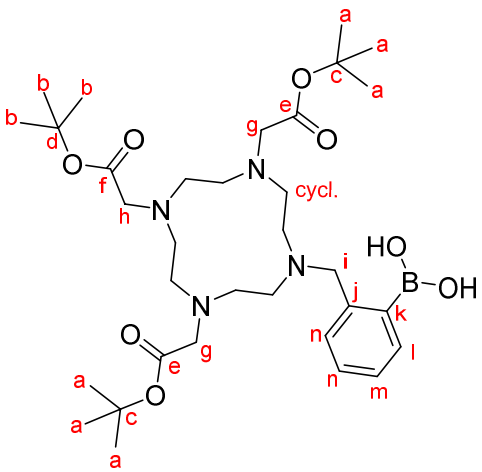
3.6

This compound was prepared by modifying the literature protocol.[21] Compound **3.5** (150 mg, 0138 mmol, 1.00 equiv) was dissolved in DMF (2 mL) in a microwave vial and added ammonium formate (402.32 mg, 6.38 mmol, 46.00 equiv) followed by wet 10% Pd/C (20 wt%) and glacial acetic acid (100 μL). The reaction mixture was heated at 80 °C under stirring in a microwave reactor for 15 min and filtered using a celite pad. The filtrate was evaporated to dryness by adding toluene to create an azeotrope for the removal of DMF. This process of removing DMF by azeotrope formation and evaporation was repeated thrice to afford a brown residue. The residue was dissolved in water (10 mL), basified to pH 9 using 2M aqueous NaOH and the white residue discarded by centrifugation. The resulting solution was acidified using 1 M HCl to pH 5 and extracted with $CHCl_3$ (3 × 15 mL). The organic layers were combined, dried over Na_2SO_4, filtered, and the filtrate evaporated to dryness to afford the compound **3.6** as a dark-yellow solid (10 mg, 0.0105 mmol, 7%); ^{1}H NMR (400 MHz, MeOD, 298 K) δ (ppm): *NMR signals were too weak to be observed for characterisation*; HRMS (ESI in MeOH) *m/z* (% relative intensity): $[M + H]^+$ calcd for $C_{50}H_{63}N_{10}O_9$, M_r = 947.4730; found, 947.4724 (100%).

7.6.3. Synthesis and characterisation of compounds in Chapter-IV

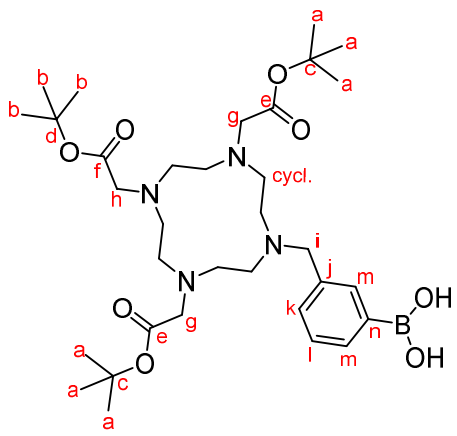
7.6.3.1. General procedure 6 for the synthesis of (2-((4,7,10-tris(2-(*tert*-butoxy)-2-oxoethyl)-1,4,7,10-tetraazacyclododecan-1-yl)methyl)phenyl)boronic acid DO3A(*t*-BuO)$_3$*o*-PBA, (3-((4,7,10-tris(2-(*tert*-butoxy)-2-oxoethyl)-1,4,7,10-tetraazacyclododecan-1-yl)methyl)phenyl)boronic acid DO3A(*t*-BuO)$_3$*m*-PBA, and (4-((4,7,10-tris(2-(*tert*-butoxy)-2-oxoethyl)-1,4,7,10-tetraazacyclododecan-1-yl)methyl)phenyl)boronic acid DO3A(*t*-BuO)$_3$*p*-PBA

DO3A(*t*-BuO)$_3$ (2.00 g, 3.35 mmol, 1.00 equiv) was dissolved in acetonitrile (75 mL) and stirred with sodium carbonate (1.42 g, 13.4 mmol, 4.00 equiv) for 10 min at 25 ℃. To this, the appropriate (bromomethyl)phenylboronic acid (0.94 g, 214.85 mmol, 1.30 equiv) was added in portions over 1 h and the mixture stirred under reflux for 12 h. The reaction mixture was cooled to 25 ℃ and filtered. The filtrate was evaporated under reduced pressure and the resulting residue suspended in water (40 mL) and extracted with chloroform (3 × 25 mL). The organic layers were combined, dried over anhydrous sodium sulfate, filtered, and evaporated to dryness *in vacuo*. The crude product was purified by flash column chromatography to afford the title compound.



DO3A(*t*-BuO)$_3$*o*-PBA

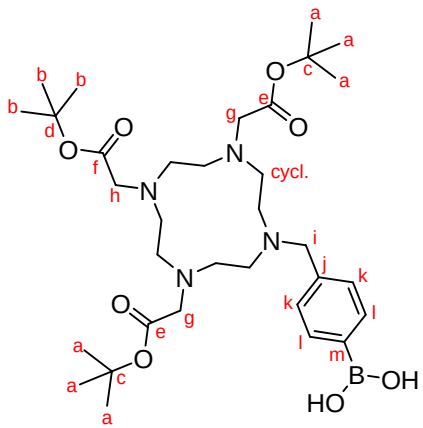
DO3A(*t*-BuO)$_3$*o*-PBA: Prepared from 2-(bromomethyl)phenylboronic acid following general procedure **6**. Purification by flash column chromatography over silica gel by gradient elution with DCM/*iso*-propanol (100:0→99:1→98:2→ 97:3→96:4→95:5→93:7, *v/v*) to DCM/MeOH/aq.NH_3 (90:10→85:15→ 80:20→ 59:40:1, *v/v*) afforded the desired product as a white solid (400 mg, 0.616 mmol, 18%); mp = 90 – 95 °C; R_f = 0.26 (neutral Al_2O_3, $CHCl_3$/CH_3OH, 95:5); ^{1}H NMR (400 MHz, DMSO-d_6, 298 K) δ (ppm): 7.85 – 7.78 (m, 1H, H^l), 7.56 – 7.41 (dd, J = 7.2, 14.6 Hz, 2H, H^n), 7.34 – 7.28 (t, J = 7.3 Hz, 1H, H^m), 4.85 – 4.45 (s, 2H, Ar-*o*-B(O***H***)$_2$), 3.73 – 3.67 (br s, 2H, H^i), 3.56 – 1.94 (br m, 22H, H^{cycl} + $H^{g,h}$), 1.69 – 1.15 (m, 27H, $H^{a,b}$); ^{11}B NMR (193 MHz, DMSO-d_6, 298 K) δ (ppm): 27.6 (Ar-*o*-***B***(OH)$_2$); ^{13}C NMR (151 MHz, DMSO-d_6, 298 K) δ (ppm): 172.3 (C^f), 169.8 (C^e), 130.7 (C^j), 130.3 (C^k), 128.3 (C^l), 126.6 (C^m), 121.2 (C^n), 81.6 (C^d), 80.5 (C^c), 69.8 (C^i), 55.3 ($C^{g,h}$), 50.7 – 44.7 (C^{cycl}), 27.7 (C^a), 27.5 (C^b); HRMS (ESI in MeOH) *m/z* (% relative intensity): $[M + H]^+$ calcd for $C_{33}H_{58}N_4O_8B$, M_r = 649.4347; found, 649.4331 (100%).



DO3A(*t*-BuO)$_3$*m*-PBA

DO3A(*t*-BuO)$_3$*m*-PBA: Prepared from 3-(bromomethyl)phenylboronic acid following general procedure **6**. Purified by flash column chromatography over silica

gel by gradient elution with DCM/*iso*-propanol (100:0→99:1→98:2→96:4→92:8→ 90:10→90:10→85:15→80:20, *v/v*) to afford the desired product as a white solid (810 mg, 1.25 mmol, 37%); mp = 110 – 115 °C; R_f = 0.36 (neutral Al_2O_3, $CHCl_3$/ CH_3OH, 95:5); ^{1}H NMR (400 MHz, CD_2Cl_2, 298 K) δ (ppm): 7.83 – 7.73 (m, 2H, H^m), 7.63 – 7.58 (dt, *J* = 1.6, 7.6 Hz, 1H, H^l), 7.34 – 7.23 (td, *J* = 4.7, 7.5 Hz, 1H, H^k), 3.81 – 1.91 (br m, 24H, H^{cycl} + $H^{g,h,i}$), 1.54 – 1.33 (d, *J* = 4.3 Hz, 27H, $H^{a,b}$); ^{11}B NMR (193 MHz, DMSO-d_6, 298 K) δ (ppm): 27.74 (Ar-*m*-***B***$(OH)_2$); ^{13}C NMR (151 MHz, CD_2Cl_2, 298 K) δ (ppm): 173.7 (C^f), 172.7 (C^e), 137.4 (C^j), 136.1 (C^n), 134.0 (C^k), 131.2 (C^l), 128.3 (C^m), 83.3 (C^c), 82.9 (C^d), 65.2 (C^i), 64.3 ($C^{g,h}$), 59.7 – 49.9 (C^{cycl}), 28.1 (C^a), 28.0 (C^b); HRMS (ESI in MeOH) *m/z* (% relative intensity): $[M + H]^+$ calcd for $C_{33}H_{58}N_4O_8B$, M_r = 649.4347; found, 649.4331 (100%).



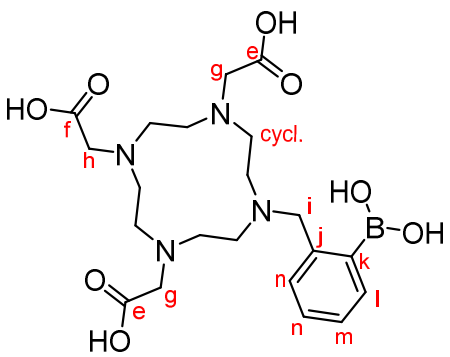
DO3A(*t*-BuO)$_3$*p*-PBA

DO3A(*t*-BuO)$_3$*p*-PBA: Prepared from 4-(bromomethyl)phenylboronic acid following general procedure **6**. Purification by flash column chromatography over silica gel by gradient elution with DCM/EtOH (100:0→99:1→98:2→97:3→ 96:4→95:5→93:7→90:10, *v/v*) to DCM/MeOH/aq.NH_3 (90:10→80:20→49:50:1, *v/v*) afforded the desired product as a white solid (921 mg, 1.418 mmol, 42%); mp = 120 – 125 °C; R_f = 0.4 (neutral Al_2O_3, $CHCl_3$/CH_3OH, 95:5); ^{1}H NMR (400 MHz,

CD_2Cl_2, 298 K) δ (ppm): 7.80 – 7.72 (d, J = 7.5 Hz, 2H, H^{l}), 7.43 – 7.38 (d, J = 7.5 Hz, 2H, H^{k}), 3.76 – 1.94 (br m, 24H, H^{cycl} + $H^{g,h,i}$), 1.54 – 1.32 (m, 27H, $H^{a,b}$); ^{11}B NMR (193 MHz, DMSO-d_6, 298 K) δ (ppm): 27.74 (Ar-*p*-***B***$(OH)_2$); ^{13}C NMR (151 MHz, CD_2Cl_2, 298 K) δ (ppm): 173.5 (C^{f}), 172.6 (C^{e}), 139.5 (C^{j}), 134.9 (C^{l}), 129.2 (C^{k}), 116.1 (C^{m}), 83.2 (C^{c}), 82.6 (C^{d}), 64.8 (C^{i}), 63.7 ($C^{g,h}$), 59.7 – 49.9 (C^{cycl}), 27.9 (C^{a}), 27.8 (C^{b}); HRMS (ESI in MeOH) *m/z* (% relative intensity): $[M + H]^+$ calcd for $C_{33}H_{58}N_4O_8B$, M_r = 649.4347; found, 649.4331 (100%).

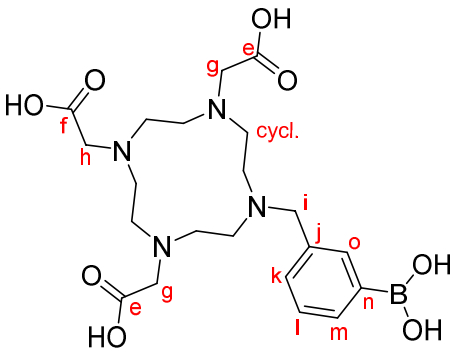
7.6.3.2. General procedure 7 for the synthesis of 2,2′,2″-(10-(2-boronobenzyl)-1,4,7,10-tetraazacyclododecane-1,4,7-triyl)triacetic acid (DO3A)*o*-PBA, 2,2′,2″-(10-(3-boronobenzyl)-1,4,7,10-tetraazacyclododecane-1,4,7-triyl)triacetic acid (DO3A)*m*-PBA, 2,2′,2″-(10-(4-boronobenzyl)-1,4,7,10-tetraazacyclo- dodecane-1,4,7-triyl)triacetic acid (DO3A)*p*-PBA

The ligands were synthesised by adapting a literature procedure.[15] The appropriate DO3A(*t*-BuO)$_3$PBA (310 mg, 0.369 mmol) was dissolved in dichloromethane (5 mL), trifluoroacetic acid (5 mL) added dropwise over 1 h, and stirred at 25 °C for 12 h. The reaction mixture was diluted with equal volume of methanol and concentrated to dryness. The resulting oil was dissolved in methanol (~ 4 mL), triturated with diethyl ether (~160 mL) to afford a colourless precipitate, and isolated by centrifugation. This trituration protocol was repeated twice and the desired product dried under vacuum.



(DO3A)*o*-PBA

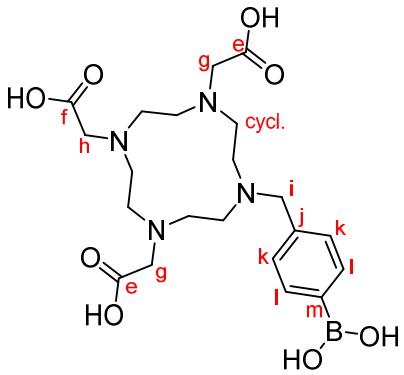
(DO3A)*o*-PBA: Prepared from **DO3A(*t*-BuO)$_3$*o*-PBA** following general procedure **7**. Brown powder (105 mg, 0.218 mmol, 59%); mp = 220 – 225 °C; ^{1}H NMR (600 MHz, DMSO-d_6, 298 K) δ (ppm): 7.83 – 7.79 (m, 1H, H^l), 7.59 – 7.44 (dd, J = 7.2, 14.6 Hz, 2H, H^n), 7.38 – 7.32 (t, J = 7.3 Hz, 1H, H^m), 4.88 – 4.46 (s, 2H, Ar-*o*-B(O***H***)$_2$), 3.95 – 2.66 (br m, 24H, H^{cycl} + $H^{g,h,i}$); ^{11}B NMR (193 MHz, DMSO-d_6, 298 K) δ (ppm): 29.59 (Ar-*o*-***B***(OH)$_2$); ^{13}C NMR (151 MHz, DMSO-d_6, 298 K) δ (ppm): 173.4 (C^f), 172.7 (C^e), 131.5 (C^j), 130.7 (C^k), 128.5 (C^l), 127.1 (C^m), 124.5 (C^n), 59.3 (C^i), 57.9 ($C^{g,h}$), 56.2 – 46.2 (C^{cycl}); ^{19}F NMR (565 MHz, DMSO-d_6, 298 K) δ (ppm): -73.53 (CF_3COOH); HRMS (ESI in MeOH) *m/z* (% relative intensity): [M – 2H]$^-$ calcd for $C_{21}H_{32}N_4O_8B$, M_r = 479.2310; found, 479.2304 (30%); [M + 2H]$^+$ calcd for $C_{21}H_{36}N_4O_8B$, M_r = 483.2019; found, 483.2021 (100%).



(DO3A)*m*-PBA

(DO3A)*m*-PBA: Prepared from **DO3A(*t*-BuO)$_3$*m*-PBA** following general procedure **7**. HPLC purification protocol is described in Appendix-B. Colourless powder (153 mg, 0.318 mmol, 86%); mp = 200 – 205 °C; ^{1}H NMR (400 MHz, MeOD, 298 K) δ (ppm): 7.67 – 7.62 (s, 1H, H^o), 7.58 – 7.52 (d, J = 7.4 Hz, 1H, H^k), 7.45 – 7.39 (d, J = 7.6 Hz, 1H, H^l), 7.25 – 7.17 (t, J = 7.5 Hz, 1H, H^m), 4.08 – 3.94 (s, 2H, Ar-*m*-B(O***H***)$_2$), 3.58 – 3.48 (s, 2H, H^i), 3.44 – 2.81 (br m, 22H, H^{cycl} + $H^{g,h}$); ^{11}B NMR (128 MHz, MeOD, 298 K) δ (ppm): 28.45 (Ar-*m*-***B***(OH)$_2$);

^{13}C NMR (101 MHz, MeOD, 298 K) δ (ppm): 174.0 (C^{f}), 173.8 (C^{e}), 138.3 (C^{j}), 136.5 (C^{n}), 136.1 ($C^{k,o}$), 133.6 (C^{l}), 130.0 (C^{m}), 59.5 (C^{i}), 55.7 ($C^{g,h}$), 53.8 – 49.8 (C^{cycl}); ^{19}F NMR (376 MHz, DMSO-d_6, 298 K) δ (ppm): -72.54 (CF_3COOH); HRMS (ESI in MeOH) *m/z* (% relative intensity): $[M + H]^+$ calcd for $C_{21}H_{34}N_4O_8B$, M_r = 481.2466; found, 481.2462 (100%).

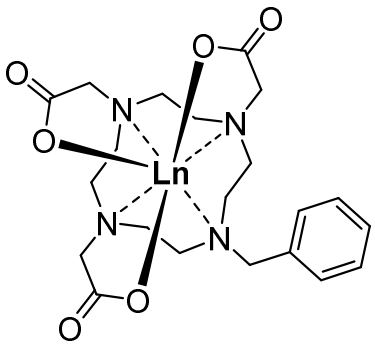


(DO3A) *p*-PBA

(DO3A)*p*-PBA: Prepared from **DO3A(*t*-BuO)$_3$*p*-PBA** following general procedure **7**. HPLC purification protocol is described in Appendix-B. Colourless powder (151 mg, 0.314 mmol, 85%); mp = 225 – 230 °C; ^{1}H NMR (400 MHz, MeOD, 298 K) δ (ppm): 7.86 – 7.72 (d, *J* = 7.5 Hz, 2H, H^{l}), 7.68 – 7.54 (d, *J* = 7.6 Hz, 2H, H^{k}), 4.78 – 4.31 (s, 2H, Ar-*p*-B(O***H***)$_2$), 4.29 – 3.89 (s, 2H, H^{i}), 3.85 – 2.79 (br m, 22H, H^{cycl} + $H^{g,h}$); ^{11}B NMR (193 MHz, MeOD, 298 K) δ (ppm): 30.58 (Ar-*p*-***B***(OH)$_2$); ^{13}C NMR (101 MHz, MeOD, 298 K) δ (ppm): 174.0 ($C^{e,f}$), 136.8 (C^{j}), 135.9 (C^{l}), 133.6 (C^{k}), 116.3 (C^{m}), 59.3 (C^{i}), 55.5 ($C^{g,h}$), 53.7 – 49.8 (C^{cycl}); ^{19}F NMR (565 MHz, DMSO-d_6, 298 K) δ (ppm): -73.57 (CF_3COOH); HRMS (ESI in MeOH) *m/z* (% relative intensity): $[M + H]^+$ calcd for $C_{21}H_{34}N_4O_8B$, M_r = 481.2466; found, 481.2462 (100%).

7.6.3.3. General procedure 8 for the synthesis of lanthanide(III) complexes [Ln(DO3A)benzyl], [Lu(DO3A)*o*-PBA], [Lu(DO3A)*m*-PBA], and [Lu(DO3A)*p*-PBA]

The complexes were synthesised by adapting the procedure from the literature.[15,16] The appropriate ligands of **(DO3A)PBA** (100 mg, 0.122 mmol, 1.00 equiv) was combined with the respective lanthanide triflate [Ln(OTf)$_3$.*x*H$_2$O] (1.05 equiv), methanol (2 mL) added, and the mixture sonicated until complete dissolution. The resulting solution was stirred under reflux for 1 h. Aqueous NaOH (1 M) added dropwise to pH 5 - 6 and the resulting mixture was heated under reflux for 48 h. The solvent was evaporated under reduced pressure to afford a crude residue, dissolved in 10 mL of water and basified to pH 10 using 1 M aqueous NaOH. The precipitate was removed by centrifugation and the resulting solution neutralised using 1 M HCl, an equal volume of ethanol added (to create an azeotrope), and the solvent was evaporated to dryness. The crude product was redissolved in 3 mL of deionised water and purified by dialysis (5 mL dialysis tube, molecular weight cut-off: 100 – 500 Da). After 48 h and 6 water changes (4 L), the solvent was removed under reduced pressure to afford the complex.

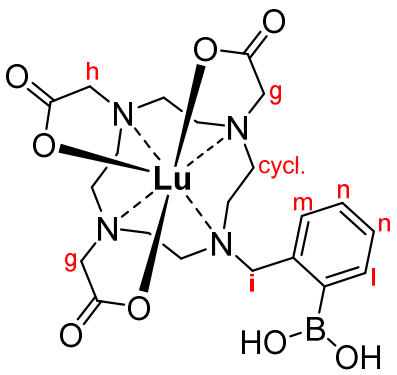


[Ln(**DO3A**)**benzyl**]
Ln(III) = Eu and Tb

[Eu(DO3A)benzyl]: Prepared from **DO3A*o*-PBA, DO3A*m*-PBA,** or **DO3A*p*-PBA** and [Eu(OTf)$_3$.*x*H$_2$O] by following general procedure **8**. White hygroscopic powder (45 mg, 0.076 mmol, 63%); ^{1}H NMR (400 MHz, D$_2$O, 298 K)

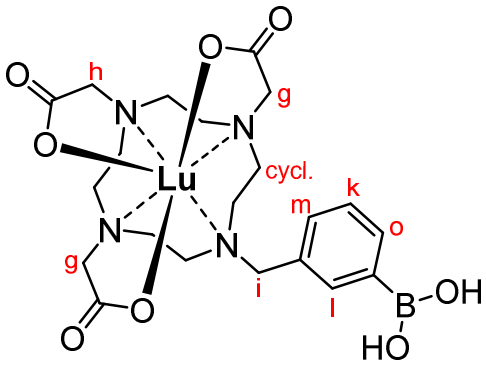
δ (ppm): 24.9, 23.5, -0.8, -1.5, -2.1, -3.2, -5.8, -9.4, -12.2, -12.5, -13.4, -14.8, -16.2, -17.1, -18.7, -23.4, -24.7 (only resolved peaks outside 0 – 10 ppm reported); ^{19}F NMR (377 MHz, D_2O, 298 K) δ (ppm): -75.58 (CF_3COOH), -78.82 (CF_3SO_3Na); HRMS (ESI in MeOH) *m/z* (% relative intensity): $[M + H]^+$ calcd for $EuC_{21}H_{30}N_4O_6$, M_r = 587.1372; found, 587.1367 (100%).

[Tb(DO3A)benzyl]: Prepared from **DO3A*o*-PBA, DO3A*m*-PBA,** or **DO3A*p*-PBA** and $[Tb(OTf)_3.xH_2O]$ by following general procedure **8**. White hygroscopic powder (38 mg, 0.064 mmol, 53%); HRMS (ESI in MeOH) *m/z* (% relative intensity): $[M + H]^+$ calcd for $TbC_{21}H_{30}N_4O_6$, M_r = 593.1363; found, 593.1360 (100%).



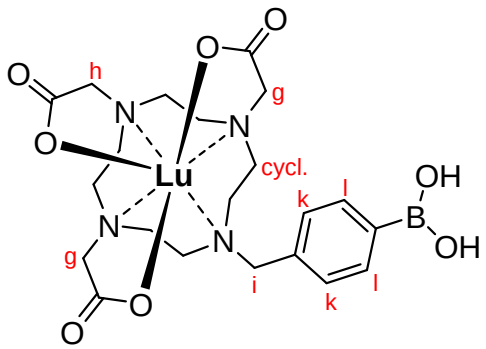
[Lu(**DO3A**)***o*-PBA**]

[Lu(DO3A)*o*-PBA]: Prepared from **DO3A*o*-PBA** following general procedure **8**. White hygroscopic powder (39 mg, 0.059 mmol, 49%); ^{1}H NMR (400 MHz, D_2O, 298 K) δ (ppm): 7.95 – 7.91 (m, 1H, H^l), 7.69 – 7.54 (dd, J = 7.2, 14.6 Hz, 2H, H^n), 7.49 – 7.41 (t, J = 7.3 Hz, 1H, H^m), 4.52 – 2.2 (br m, 22H, H^{cycl} + $H^{g,h,i}$ + Ar-*o*-B(O***H***)$_2$); ^{11}B NMR (128 MHz, D_2O, 298 K) δ (ppm): 28.8 (Ar-*o*-***B***$(OH)_2$); ^{19}F NMR (377 MHz, D_2O, 298 K) δ (ppm): -75.58 (CF_3COOH), -78.82 (CF_3SO_3Na); HRMS (ESI in MeOH) *m/z* (% relative intensity): $[M + H]^+$ calcd for $LuC_{21}H_{31}N_4O_8B$, M_r = 653.1637; found, 653.1631 (100%).



[Lu(**DO3A**)***m*-PBA**]

[Lu(DO3A)*m*-PBA]: Prepared from **DO3A*m*-PBA** following general procedure **8**. White hygroscopic powder (41 mg, 0.063 mmol, 51%); ^{1}H NMR (400 MHz, D_2O, 298 K) δ (ppm): 7.93 – 7.69 (s, 1H, H^{o}), 7.68 – 7.53 (s, 1H, H^{k}), 7.53 – 7.25 (d, J = 24.4 Hz, 2H, $H^{m,l}$), 4.53 – 2.03 (br m, 26H, H^{cycl} + $H^{g,h,i}$ + Ar-*m*-B(O***H***)$_2$); ^{11}B NMR (128 MHz, D_2O, 298 K) δ (ppm): 30.61 (Ar-*m*-***B***(OH)$_2$); ^{19}F NMR (377 MHz, D_2O, 298 K) δ (ppm): -75.49 (C***F***$_3$COOH), -78.76 (C***F***$_3$SO$_3$Na); HRMS (ESI in MeOH) *m/z* (% relative intensity): $[M + H]^+$ calcd for $LuC_{21}H_{31}N_4O_8B$, M_r = 653.1637; found, 653.1631 (100%).

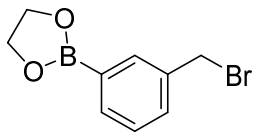


[Lu(**DO3A**)***p*-PBA**]

[Lu(DO3A)*p*-PBA]: Prepared from **DO3A*p*-PBA** following general procedure **8**. White hygroscopic powder (48 mg, 0.735 mmol, 60%); ^{1}H NMR (400 MHz, D_2O, 298 K) δ (ppm): 7.76 – 7.66 (d, J = 7.2 Hz, 2H, H^{l}), 7.37 – 7.25 (d, J = 7.5 Hz, 2H, H^{k}), 4.38 – 2.21 (br m, 26H, H^{cycl} + $H^{g,h,i}$ + Ar-*m*-B(O***H***)$_2$); ^{11}B NMR (128 MHz,

D_2O, 298 K) δ (ppm): 28.68 (Ar-*m*-***B***$(OH)_2$); ^{19}F NMR (377 MHz, D_2O, 298 K) δ (ppm): -75.49 (CF_3COOH), -78.76 (CF_3SO_3Na); HRMS (ESI in MeOH) *m/z* (% relative intensity): $[M + H]^+$ calcd for $LuC_{21}H_{31}N_4O_8B$, M_r = 653.1637; found, 653.1631 (100%).

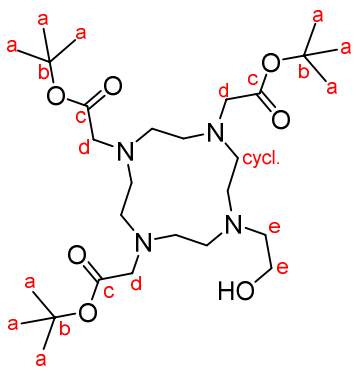
7.6.3.4. Synthesis of 2-(3-(bromomethyl)phenyl)-1,3,2-dioxaborolane



This compound was synthesised from the literature.[22] In a flame-dried RB flask under N_2, 3-(bromomethyl)phenylboronic acid (100 mg, 0.465 mmol, 1.00 equiv) was suspended in anhydrous pentane (15 mL) over molecular sieves. Ethylene glycol (30 μL, 0.512 mmol, 1.1 equiv) was added and the resulting white suspension was stirred at 25 ℃ for 2 h under N_2 atmosphere. 15 mL of DCM added to quench the reaction and filtered through a celite pad to remove molecular sieves. The filtrate was concentrated *in vacuo* to afford the title compound as a pale-yellow powder (81.4 mg, 0.378 mmol, 72%); ^1H NMR (400 MHz, $CDCl_3$, 298 K) δ (ppm): 7.87 – 7.81 (t, *J* = 1.5 Hz, 1H, Ar*H*), 7.78 – 7.70 (dt, *J* = 1.3, 7.3 Hz, 1H, Ar*H*), 7.54 – 7.45 (dt, *J* = 1.5, 7.2 Hz, 1H, Ar*H*), 7.41 – 7.33 (t, *J* = 7.5 Hz, 1H, Ar*H*), 4.53 – 4.47 (s, 2H, CH_2Br), 4.40 – 4.34 (d, *J* = 2.0 Hz, 4H, CH_2); ^{11}B NMR (128 MHz, $CDCl_3$, 298 K) δ (ppm): 30.9 (Ar-*m*-***B***$(OH)_2$); HRMS (ESI in MeOH) *m/z* (% relative intensity): $[M + H]^+$ calcd for $C_9H_{11}BBrO_2$, M_r = 241.9059; found, 241.9051 (100%).

7.6.4. Synthesis and characterisation of compounds in Chapter-V

7.6.4.1. Synthesis of tri-*tert*-butyl 2,2′,2′′-(10-(2-hydroxyethyl)-1,4,7,10-tetra azacyclododecane-1,4,7-triyl)triacetate (5.9)

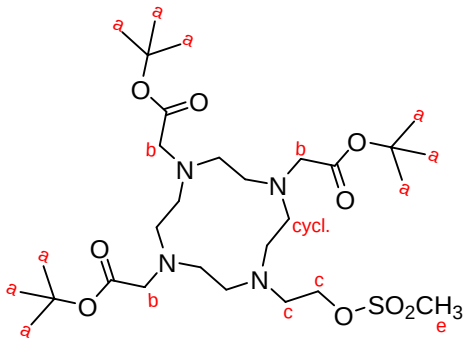


5.9

This compound was synthesised by modifying the literature protocol.[23] **DO3A(*t*-BuO)$_3$** (1.00 g, 1.68 mmol, 1.00 equiv) was dissolved in acetonitrile (70 mL) and stirred with potassium carbonate (1.16 g, 8.40 mmol, 5.00 equiv) for 5 min at 25 °C. 2-bromoethanol (596 μL, 8.40 mmol, 5.00 equiv) was added slowly to the reaction mixture and refluxed under stirring for 12 h. The reaction mixture was cooled to 25 °C and filtered. The filtrate was evaporated under reduced pressure and the resulting yellow oily residue suspended in 10 mL water and extracted with chloroform (3 × 20 mL). The organic layer was combined, dried over anhydrous sodium sulfate, filtered, and evaporated to dryness *in vacuo*. The resulting crude yellow oil was purified by flash column chromatography over silica gel by gradient elution with CH_2Cl_2/CH_3OH (100:0→99:1→98:2→97:3→96:4→94:6→90:10→80:20, *v*/*v*) to afford the title compound **5.9** as a yellow solid (657 mg, 14.6 mmol, 70%); ^{1}H NMR (400 MHz, $CDCl_3$, 298 K) δ (ppm): 3.33 – 3.02 (br s, 6H, H^d), 2.85 – 2.79 (br m, 4H, H^e), 2.78 – 2.70 (br m, 12H, H^{cycl}), 2.58 – 2.53 (br m, 4H, H^{cycl}), 1.37 – 1.41 (br s, 27H, H^a); ^{13}C NMR (101 MHz, $CDCl_3$, 298 K) δ (ppm): 172.4 (C^c),

82.4 (C^{b}), 58.6 – 48.1 ($C^{d,e,cycl}$), 28.01 (C^{a}); HRMS (ESI in MeOH) *m/z* (% relative intensity): $[M + H]^+$ calcd for $C_{28}H_{55}N_4O_7$, M_r = 559.4065; found, 559.4055 (100%).

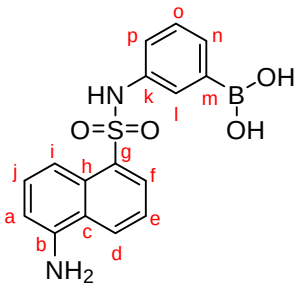
7.6.4.2. Synthesis of tri-*tert*-butyl 2,2′,2′′-(10-(2-((methylsulfonyl)oxy)ethyl)-1,4,7,10-tetraazacyclododecane-1,4,7-triyl)triacetate (5.10)



5.10

A solution of the compound **5.09** (1.00 g, 1.79 mmol, 1.00 equiv) in dry DCM (40 mL), taken in a flame dried RB flask under argon balloon, was stirred with triethylamine (1.18 mL, 8.42 mmol, 4.70 equiv) for 30 min. Methanesulfonyl chloride (278 μL, 3.58 mmol, 2.00 equiv) in dry DCM (10 mL) was added in portions to the mixture for 30 min. The reaction flask was foiled and the reaction mixture stirred for 50 h at 25 °C. The reaction was quenched by the addition of water (150 mL), transferred to a separatory funnel, and extracted with DCM (5 × 50 mL). The organic extracts were combined, dried over magnesium sulfate, and evaporated to dryness to afford **5.10** as a brown oil and used without further purification (450 mg, 0.705 mmol, 39%); ^{1}H NMR (400 MHz, $CDCl_3$, 298 K) δ (ppm): 3.8 – 3.02 (br m, 9H, $H^{b,e}$), 2.85 – 2.79 (br m, 4H, H^{c}), 2.78 – 2.53 (br m, 16H, H^{cycl}), 1.28 – 1.21 (br s, 27H, H^{a}); HRMS (ESI in MeOH) *m/z* (% relative intensity): $[M + H]^+$ calcd for $C_{29}H_{57}N_4O_9S$, M_r = 638.3821; found, 638.3794 (100%).

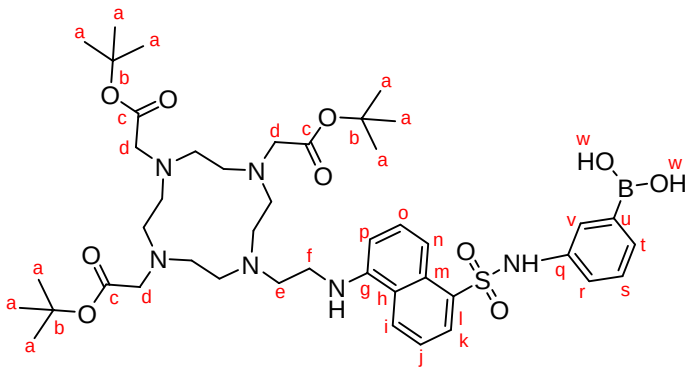
7.6.4.3. Synthesis of (3-((5-aminonaphthalene)-1-sulfonamido)phenyl)boronic acid (5.11)



5.11

Dry MeCN (150 mL) was taken in a flame dried, foiled RB flask under argon balloon. 3-aminophenylboronic acid (500 mg, 3.80 mmol, 2.00 equiv) was added followed by the addition of triethylamine (1.30 mL, 9.52 mmol, 5.00 equiv), and stirred for 15 min. 5-Aminonaphthalene-1-sulfonyl chloride (460 mg, 1.90 mmol, 1.00 equiv) was added in portions for 30 min and stirred for 16 h. The solvent was evaporated *in vacuo* to afford a dark-yellow crude and purified using flash column chromatography over silica gel by isocratic elution in MeCN (100%, *v*/*v*), followed by gradient elution in DCM/*iso*-propanol (100:0→95:5→90:10, *v*/*v*) to DCM/MeOH (90:10→80:20, *v*/*v*) to afford the desired product **5.11** as a yellow solid (300 mg, 0.874 mmol, 46%); ^{1}H NMR (400 MHz, $CDCl_3$, 298 K) δ (ppm): 8.19 – 8.25 (dt, *J* = 1.1, 8.5 Hz, 1H, H^{e}), 8.14 – 8.05 (m, 2H, $H^{f,i}$), 7.47 – 7.40 (dd, *J* = 7.6, 8.6 Hz, 1H, H^{d}), 7.38 – 7.30 (dd, *J* = 7.3, 8.5 Hz, 1H, H^{j}), 7.28 – 7.17 (m, 2H, $H^{o,n}$), 6.80 – 6.76 (ddd, *J* = 1.1, 2.4, 7.7 Hz, 3H, $H^{p,l,a}$); ^{11}B NMR (128 MHz, CD_3OD, 298 K) δ (ppm): 28.2 (-NHAr-*m*-***B***$(OH)_2$); ^{13}C NMR (101 MHz, $CDCl_3$, 298 K) δ (ppm): 147.6 (C^{b}), 146.2 (C^{g}), 138.0 (C^{k}), 131.3 (C^{m}), 130.8 (C^{h}), 129.3 (C^{o}), 127.2 (C^{j}), 124.7 ($C^{c,e}$), 123.7 (C^{d}), 123.0 (C^{f}), 121.8 (C^{n}), 118.3 ($C^{p,j}$), 115.0 (C^{l}), 111.2 (C^{a}); HRMS (ESI in MeOH) *m/z* (% relative intensity): $[M + H]^+$ calcd for $C_{16}H_{15}BN_2O_4S$, M_r = 343.0805; found, 343.0536 (100%).

7.6.4.4 Synthesis of (3-((5-((2-(4,7,10-tris(2-(*tert*-butoxy)-2-oxoethyl)-1,4,7,10-tetraazacyclododecan-1-yl)ethyl)amino)naphthalene)-1-sulfonamido)phenyl)-boronic acid (5.12)

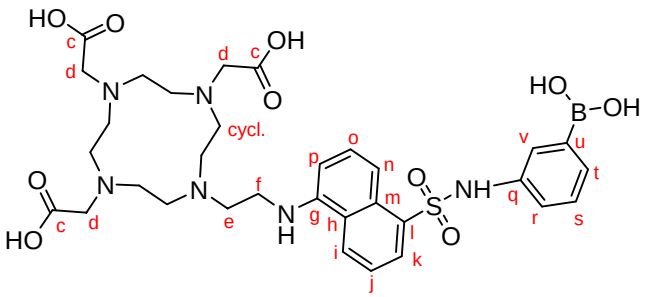


5.12

Compound **5.11** (81 mg, 0.235 mmol, 1.00 equiv) was mixed with sodium carbonate (125 mg, 1.178 mmol, 5.00 equiv) in MeCN (50 mL) and stirred at 45 °C for 30 min in a foil-covered RB flask. Compound **5.10** (150 mg, 0.235 mmol, 1.00 equiv) was added in parts to the reaction mixture for 1 h and refluxed for 14 h. The reaction mixture was cooled to 25 °C, filtered to remove the inorganic base, and the solvent reduced under vacuum to obtain a crude product and purified by flash column chromatography over silica gel by gradient elution with DCM/*iso*-propanol (100:0→99:1→98:2→97:3→96:4→94:6→90:10, *v*/*v*) to DCM/MeOH/ aq.NH_3 (79:20:1→59:40:1, *v*/*v*) to afford the title compound **5.12** as a dark-yellow solid (72 mg, 0.0815 mmol, 35%); ^{1}H NMR (400 MHz, CD_3CN, 298 K) δ (ppm): 8.46 – 8.19 (dd, *J* = 6.5, 10.0 Hz, 1H, H^{j}), 8.18 – 7.98 (m, 1H, H^{i}), 7.97 – 7.78 (s, 1H, H^{k}), 7.77 – 7.62 (m, 1H, H^{o}), 7.61 – 7.47 (d, *J* = 3.4 Hz, 1H, H^{n}), 7.46 – 7.34 (m, 1H, H^{p}), 7.32 – 7.17 (m, 1H, H^{t}), 7.10 – 7.01 (d, *J* = 2.6 Hz, 1H, H^{r}), 6.9 – 6.81 (t, *J* = 7.0 Hz, 1H, H^{s}), 6.8 – 6.37 (m, 1H, H^{v}), 5.41 – 4.94 (br s, 2H, H^{w}), 4.08 – 1.99 (br m, 26H, $H^{f,e,b,d,cycl}$), 1.48 – 1.27 (br m, 27H, H^{a}); ^{11}B NMR (128 MHz, CD_3OD, 298 K) δ (ppm): 28.84 (-NHAr-*m*-***B***$(OH)_2$); ^{13}C NMR (101 MHz, CD_3CN, 298 K) δ

(ppm): 174.3 – 174 (C^{c}), 146 (C^{g}), 139.2 (C^{l}), 138.7 (C^{q}), 135.1 (C^{u}), 134.5 (C^{m}), 131.6 (C^{h}), 131.5 (C^{o}), 130.6 (C^{k}), 129.7 (C^{i}), 129.0 (C^{t}), 125.0 (C^{r}), 123.0 (C^{n}), 114.9 (C^{v}), 110.5 (C^{p}), 83.3 – 83.0 (C^{b}), 57.3 – 47.8 ($C^{d,e,f,cycl}$), 28.4 – 28.1 (C^{a}); HRMS (ESI in MeOH) *m/z* (% relative intensity): $[M + H]^+$ calcd for $C_{44}H_{68}O_{10}N_6BS$, M_r = 883.4812; found, 883.4797 (100%).

7.6.4.5. Synthesis of 2,2′,2″-(10-(2-((5-(*N*-(3-boronophenyl)sulfamoyl)-naphthalen-1-yl)amino)ethyl)-1,4,7,10-tetraazacyclododecane-1,4,7-triyl)-triacetic acid (5.13)

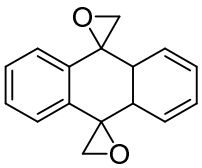


5.13

Compound **5.13** was synthesised by the literature procedure.[24] Compound **5.12** (50 mg) was taken in a foil-covered RB flask, formic acid added (5 mL), and refluxed under stirring for 14 h. The solvent was evaporated under reduced pressure and dried under high-vacuum to afford the title compound as a dark-yellow solid (15 mg, 0.002 mmol, 36%); ^{1}H NMR (400 MHz, D_2O, 298 K) δ (ppm): 8.55 – 8.42 (s, 1H, H^{i}), 8.22 – 8.06 (dd, *J* = 7.7, 17.3 Hz, 2H, $H^{j,k}$), 7.96 – 7.84 (d, *J* = 8.7 Hz, 1H, H^{n}), 7.79 – 7.60 (m, 1H, H^{p}), 7.58 – 7.46 (dd, *J* = 7.5, 14.2 Hz, 1H, H^{o}), 7.44 – 7.37 (s, 1H, H^{v}), 7.36 – 7.08 (m, 3H, $H^{r,s,t}$), 4.36 – 2.49 (m, 26H); ^{11}B NMR (128 MHz, CD_3OD, 298 K) δ (ppm): 28.17 (-NHAr-*m*-***B***$(OH)_2$); ^{13}C NMR (101 MHz, CD_3OD, 298 K) δ (ppm): 167.2 (C^{c}), 140.3 (C^{g}), 138.3 (C^{l}), 136.4 (C^{q}), 135.0 (C^{u}), 133.4 (C^{m}), 132.6 (C^{h}), 131.2 (C^{o}), 130.2 (C^{k}), 128.7 (C^{i}), 126.1 (C^{t}), 124.5 (C^{r}),

121.8 (C^{n}), 112.43 (C^{v}), 107.5 (C^{p}), 56.7 – 46.8 ($C^{d,e,f,cycl}$); HRMS (ESI in MeOH) *m/z* (% relative intensity): $[M + Na]^+$ calcd for $C_{32}H_{45}O_{10}N_6BSNa$, M_r = 739.2908; found, 739.2924 (100%).

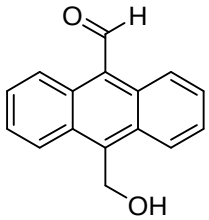
7.6.4.6. Synthesis of 4a,9a′-dihydrodispiro[oxirane-2,9′-anthracene-10′,2′′-oxirane] (5.1)



5.1

Compound was synthesised by the reported procedure.[25] Trimethylsulfonium iodide (12.76 g, 62.48 mmol, 2.60 equiv) was taken in anhydrous DMSO (20 mL) in a foil-covered, flame dried Schlenk flask. Sodium hydride (1.73 g, 72.09 mmol, 3.00 equiv) was added to this mixture followed by the addition of 9,10-anthraquinone (5 g, 24.03 mmol, 1.00 equiv) in anhydrous DMSO (20 mL). The reaction mixture was heated to 60 ℃ for 3.5 h (in argon atmosphere), quenched with 200 mL ice and warmed to 25 °C, whereupon a yellow precipitate separated out. The product was extracted with DCM (4 × 50 mL), the organic layers were combined, dried over sodium sulfate, and the solvent removed under reduced pressure. The resulting crude product was recrystallised in diethyl ether to afford **5.1** as a yellow powder (4.36 g, 18.47 mmol, 77%); ^{1}H NMR (400 MHz, $CDCl_3$, 298 K) δ (ppm): 7.43 – 7.34 (m, 8H, Ar*H*), 3.26 – 3.22 (s, 4H, CH_2); HRMS (ESI in $CHCl_3$) *m/z* (% relative intensity): $[M]^+$ calcd for $C_{16}H_{12}O_2$, M_r = 236.0824; found, 236.0793 (100%).

7.6.4.7. Synthesis of 10-(hydroxymethyl)anthracene-9-carbaldehyde (5.2)

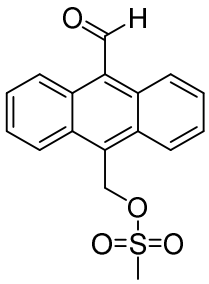


5.2

The compound **5.2** was synthesised as reported.[25] Compound **5.1** (2.00 g, 8.47 mmol, 1.00 equiv) in dry MeCN (100 mL) was taken in a foil-covered, flame dried flask. Lithium bromide (1.69 g, 19.48 mmol, 2.30 equiv) was added to it, and refluxed under inert atmosphere (N_2) for 18 h. The resulting solution was cooled to 25 °C, filtered using celite pad, and the filtrate was concentrated under reduced pressure to afford an orange residue. This was dissolved in MeOH (50 mL) and triturated with excess diethyl ether (~ 300 mL) to afford a yellow residue which was isolated by centrifugation. This trituration protocol was repeated thrice to yield the desired product **5.2** as a yellow powder and dried under vacuum (1.20 g, 5.08 mmol, 60%); ^{1}H NMR (400 MHz, $CDCl_3$, 298 K) δ (ppm): 11.47 (s, 1H, C*H*=O), 8.97 – 8.89 (d, *J* = 2.4 Hz, 2H, Ar*H*), 8.63 – 8.58 (d, *J* = 2.2 Hz, 2H, Ar*H*), 7.73 – 7.61 (dddd, *J* = 1.3, 6.5, 8.7, 22.0 Hz, 4H, Ar*H*), 5.65 – 5.56 (br s, 1H, CH_2O*H*), 5.50 – 5.40 (d, *J* = 3.8 Hz, 2H, CH_2); HRMS (ESI in MeOH) *m/z* (% relative intensity): $[M + H]^+$ calcd for $C_{16}H_{13}O_2$, M_r = 237.0904; found, 237.0781 (100%).

7.6.4.8. Synthesis of (10-formylanthracen-9-yl)methylmethanesulfonate (5.3)

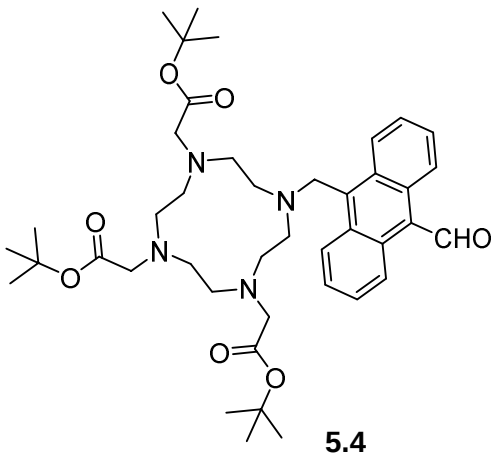
This compound was synthesised as reported.[26] Compound **5.2** (900 mg, 3.81 mmol, 1.00 equiv) and triethylamine (2.5 mL, 17.9 mmol, 4.70 equiv) in dry DCM (50 mL) was taken in a foil-covered, flame dried flask under argon balloon. A solution of methanesulfonyl chloride (410 μL, 7.618 mmol, 2.00 equiv) in dry DCM (20 mL) added dropwise over 30 min under stirring. The reaction was left under



5.3

stirring at 25 ℃ for 50 h. This reaction was quenched by the addition of water (150 mL), transferred to a separating funnel, and extracted with DCM (5 × 50 mL). The organic extracts were combined, dried over magnesium sulfate, and evaporated to dryness to afford the mesyl ester of **5.3** as a yellow solid and used without further purification (680 mg, 2.165 mmol, 57%); ^{1}H NMR (400 MHz, $CDCl_3$, 298 K) δ (ppm): 11.5 (s, 1H, C*H*=O), 8.93 – 8.84 (dt, *J* = 2.6, 7.5 Hz, 2H, Ar*H*), 8.46 – 8.37 (dt, *J* = 2.6, 7.8 Hz, 2H, Ar*H*), 7.73 – 7.64 (m, 4H, Ar*H*), 5.62 – 5.57 (s, 2H, CH_2), 1.33 – 1.16 (m, 3H, -SO_3CH_3); HRMS (ESI in MeOH) *m/z* (% relative intensity): $[M + H]^+$ calcd for $C_{17}H_{14}O_4S$, M_r = 314.0608; found, 314.0574 (100%).

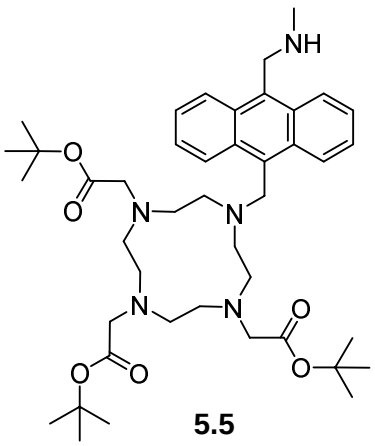
7.6.4.9. Synthesis of tri-*tert*-butyl 2,2′,2′′-(10-((10-formylanthracen-9-yl)methyl)-1,4,7,10-tetraazacyclododecane-1,4,7-triyl)triacetate (5.4)



5.4

DO3A(*t*-BuO)$_3$ (200 mg, 0.336 mmol, 1.00 equiv) and potassium carbonate (139.25 mg, 1.008 mmol, 3.00 equiv) were added to MeCN (30 mL) in a foil-covered RB flask. Compound **5.3** (158.7 mg, 0.504 mmol, 1.5 equiv) was added in portions for 15 min followed by potassium iodide (10 mol%). The reaction mixture was refluxed for 14 h. The inorganic solids were removed by filtration, and the filtrate evaporated in vacuum to afford a crude. This was purified by flash column chromatography over silica gel by gradient elution with DCM/EtOH/aq.NH_3(100:0→99:1→98:2→97:3→96:4→95:5→94:6→92:8→90:10 →80:20→60:39:1, *v*/*v*). The column purification was repeated under the same conditions to afford the title compound **5.4** as a brown solid (324 mg, 0.4437 mmol, 13%); ^{1}H NMR (400 MHz, $CDCl_3$, 298 K) δ (ppm): 11.49 (s, 1H, C*H*=O), 8.89 - 8.79 (m, 2H, Ar*H*), 8.78 – 8.62 (m, 2H, Ar*H*), 7.66 – 7.56 (m, 4H, Ar*H*), 4.20 (br d, 2H, CH_2), 3.9 – 1.95 (br m, 22H, arm-CH_2 + H^{cycl}), 1.49 – 1.39 (br m, 27H, arm-CH_3); HRMS (ESI in MeOH) *m/z* (% relative intensity): $[M + H]^+$ calcd for $C_{47}H_{61}N_4O_7$, M_r = 733.4540; found, 733.4268 (100%).

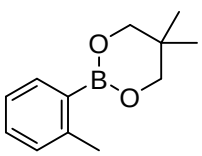
7.6.4.10. Synthesis of tri-*tert*-butyl 2,2′,2′′-(10-((10-((methylamino)methyl)-anthracen-9-yl)methyl)-1,4,7,10-tetraazacyclododecane-1,4,7-triyl)triacetate (5.5)



5.5

This compound was prepared by the literature procedure.[27] Compound **5.4** (450 mg, 0.614 mmol, 1.00 equiv) in a mixture of dry MeOH (20 mL) and dry THF (10 ml) was taken in a flame dried, foil-covered RB flask under argon balloon. Methylamine hydrochloride (62.2 mg, 0.92 mmol, 1.50 equiv) was added in portions for 10 minutes to the reaction mixture and stirred at 25 ℃ for 12 h. After confirming the formation of imine by TLC and MS, (Ar balloon was removed) sodium cyanoborohydride (116 mg, 1,842 mmol, 3.00 equiv) was added in portions for 15 min and stirred for 2 h at 25 ℃. The solvent was reduced under vacuum and the residue was dissolved in ethyl acetate (75 mL) and washed with water (3 × 30 mL). The organic layers were combined, dried over magnesium sulfate, filtered, and evaporated under reduced pressure to afford the crude and purified under flash column chromatography over silica gel by gradient elution with DCM/*iso*-propanol(100:0→99:1→98:2→97:3→96:4→95:5→94:6→92:8→90:10 →80:20→60:39:1 (aq.NH_3), *v*/*v*). The column purification was repeated to afford the title compound **5.5** as a brown solid (150 mg, 0.200 mmol, 33%); ^{1}H NMR (400 MHz, $CDCl_3$, 298 K) δ (ppm): 8.94 – 7.28 (m, 8H, Ar*H*), 5.06 – 4.77 (m, 2H, CH_2), 4.27 – 3.57 (m, 2H, CH_2), 3.38 – 1.79 (m, 22H, arm-CH_2 + H^{cycl}), 1.71 – 1.15 (m, 30H, arm-CH_3 + -NH-CH_3); HRMS (ESI in MeOH) *m/z* (% relative intensity): [M + H]$^+$ calcd for $C_{43}H_{65}N_5O_6$, M_r = 748.4925; found, 748.4268 (100%).

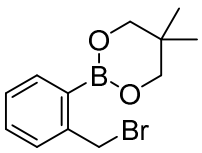
7.6.4.11. Synthesis of 5,5-dimethyl-2-(*o*-tolyl)-1,3,2-dioxaborinane (5.6)



5.6

This compound was synthesised by the literature procedure.[28] *o*-Tolylboronic acid (9.90 g, 72.80 mmol, 1.00 equiv) and 2,2-dimethyl-1,3-propanediol (9.89 g, 94.70 mmol, 94.70 mmol, 1.30 equiv) were taken in a round-bottom flask containing anhydrous toluene (250 mL) and refluxed under Dean – Stark conditions for 20 h. The solvent was removed under reduced pressure and the resulting crude was purified by flash column chromatography over silica gel by isocratic elution with DCM (100, *v*/*v*) to give the desired compound **5.6** as a clear oil (10.8 g, 52.92 mmol, 73%); ^{1}H NMR (400 MHz, $CDCl_3$, 298 K) δ (ppm): 7.67 – 7.61 (dd, *J* = 1.7, 7.3 Hz, 1H, Ar*H*), 7.20 – 7.12 (td, *J* = 1.6, 7.5 Hz, 1H, Ar*H*), 7.08 – 6.99 (t, *J* = 7.5 Hz, 2H, Ar*H*), 3.82 – 3.46 (s, 4H, CH_2), 2.56 – 2.32 (s, 3H, ArCH_3), 0.92 – 0.86 (s, 6H, CH_3); ^{11}B NMR (128 MHz, $CDCl_3$, 298 K) δ (ppm): 27.6 (Ar-*o*-***B***$(OH)_2$); HRMS (ESI in MeOH) *m/z* (% relative intensity): $[M + H]^+$ calcd for $C_{12}H_{18}BO_2$, M_r = 205.1379; found, 205.1328 (100%).

7.6.4.12. Synthesis of 2-(2-(bromomethyl)phenyl)-5,5-dimethyl-1,3,2-dioxaborinane (5.7)

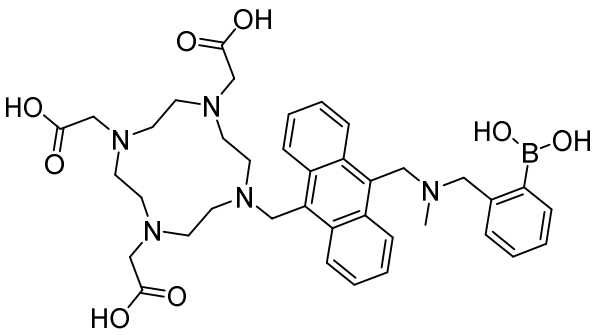


5.7

This compound was synthesised by following the reported protocol.[29] Compound **5.6** (5 g, 24.50 mmol, 1.00 equiv), *N*-bromosuccinimide (5.70 g, 31.85 mmol, 1.30 equiv), and benzoyl peroxide (178 mg, 3 mol%) were added to acetonitrile (150 mL) and refluxed for 6 h. The mixture was cooled to 25 °C and the solvent removed under reduced pressure. Pentane was added to dissolve the product and the remaining solid removed by filtration. The filtrate was concentrated

in vacuo, and the crude was purified by flash column chromatography over silica gel by isocratic elution with pentane/diethyl ether (90:10, *v*/*v*) to afford **5.7** as a light brown solid (6.32 g, 22.33 mmol, 91%); ^{1}H NMR (400 MHz, $CDCl_3$, 298 K) δ (ppm): 7.76 – 7.69 (dt, *J* = 1.1, 7.5 Hz, 1H, Ar*H*), 7.31 – 7.24 (m, 2H, Ar*H*), 7.14 – 7.22 (m, 1H, Ar*H*), 4.86 – 4.82 (s, 2H, Br-CH_2), 3.73 – 3.69 (s, 4H, CH_2), 0.99 – 0.95 (s, 6H, CH_3) ; ^{11}B NMR (128 MHz, $CDCl_3$, 298 K) δ (ppm): 27.6 (Ar-*o*-***B***$(OH)_2$); HRMS (ESI in MeOH) *m/z* (% relative intensity): $[M + H]^+$ calcd for $C_{12}H_{18}BO_2$, M_r = 205.1379; found, 205.1328 (100%).

7.6.4.13. Synthesis of (2-((methyl((10-((4,7,10-*tris*(2-(tert-butoxy)-2-oxoethyl)-1,4,7,10-tetraazacyclododecan-1-yl)methyl)anthracen-9-yl)methyl)amino)-methyl)phenyl)boronic acid (5.8)



5.8

Potassium carbonate (140.8 mg, 1.0109 mmol, 2.00 equiv) was added to a solution of **5.5** (381 mg, 0.509 mmol, 1.00 equiv) in MeCN (30 mL), and stirred for 15 min. Compound **5.7** (216.2 mg, 0.764 mmol, 1.50 equiv) was added and refluxed for 12 h. The inorganic base was removed by filtration and the solvent evaporated under reduced pressure. The resulting crude was purified by flash column chromatography over silica gel by gradient elution with DCM/MeOH (100:0→99:1→98:2→97:3→96:4→95:5→94:6→92:8→90:10, *v*/*v*) to afford **5.8** as a brown solid (127 mg, 0.200 mmol, 28%); ^{1}H NMR (400 MHz, $CDCl_3$, 298 K)

δ (ppm): 8.25 – 7.28 (m, 12H, Ar*H*), 5.26 – 4.25 (m, 6H, CH_2), 3.45 – 1.79 (m, 22H, arm-CH_2 + H^{cycl}), 1.71 – 1.18 (m, 30H, arm-CH_3 + -$(CH_2)_2$-N-CH_3); ^{11}B NMR (128 MHz, $CDCl_3$, 298 K) δ (ppm): 26.9 (-Ar-*o*-***B***$(OH)_2$); HRMS (ESI in MeOH) *m/z* (% relative intensity): $[M + H]^+$ calcd for $C_{50}H_{73}BN_5O_8$, M_r = 882.5548; found, 882.5150 (100%).

7.7. References

1. Leonard, J.; Lygo, B.; Procter, G. *Advanced Practical Organic Chemistry*; 3rd ed.; CRC Press: Boca Raton, 2013; Chapter 9, pp 137–189.
2. Fulmer, G. R.; Miller, A. J. M.; Sherden, N. H.; Gottlieb, H. E.; Nudelman, A.; Stoltz, B. M.; Bercaw, J. E.; Goldberg, K. I. *Organometallics* **2010**, *29*, 2176–2179.
3. Palatinus, L.; Chapius, G. *J. Appl. Cryst.* **2007**, *40*, 786–790.
4. (a) Parois, P.; Cooper, R. I.; Thompson, A. L. *Chem. Cent. J.* **2015**, *9*, 30. (b) Cooper, R. I.; Thompson, A. L.; Watkin, D. J. *J. Appl. Cryst.* **2010**, *43*, 1100–1107.
5. (a) Glasoe, P. K.; Long, F. A. *J. Phys. Chem.* **1960**, *64*, 188–190. (b) Krężel, A.; Bal, W. *J. Inorg. Biochem.* **2004**, *98*, 161–166.
6. Bruice, P. Y. *Organic Chemistry*; 8th ed.; Pearson Education Limited: Essex, England, **2017**.
7. Blackburn, O. A.; Kenwright, A. M.; Beer, P. D.; Faulkner, S. *Dalton Trans.* **2015**, *44*, 19509–19517.
8. (a) Bruce, J. I.; Dickins, R. S.; Govenlock, L. J.; Gunnlaugsson, T.; Lopinski, S.; Lowe, M. P.; Parker, D.; Peacock, R. D.; Perry, J. J. B.; Aime, S.; Botta, M. *J. Am. Chem. Soc.* **2000**, *122*, 9674–9684. (b) Butler, S. J.; Parker, D. *Chem. Soc. Rev.* **2013**, *42*, 1652–1666.
9. (a) Kuzmič, P. *Anal. Biochem.* **1996**, *237*, 260–273. (b) Kuzmič, P. *Methods Enzymol.* **2009**, *467*, 247–280.
10. Ting-Po, I.; Nancollas, G. H. *Anal. Chem.* **1972**, *44*, 1940–1950.
11. (a) Gasa, T. B.; Spruell, J. M.; Dichtel, W. R.; Sørensen, T. J.; Philip, D.; Stoddart, J. F.; Kuzmič, P. *Chem. —Eur. J.* **2009**, *15*, 106–116. (b) Nawrocki, P. R.; Kofod, N.; Juelsholt, M.; Jensen, K. M. Ø.; Sørensen, T. J. *Phys. Chem. Chem. Phys.* **2020**, *22*, 12794–12805.
12. MacKenzie, L. E.; Pålsson, L.-O.; Parker, D.; Beeby, A.; Pal, R. *Nat. Commun.* **2020**, *11*, 1676.
13. Putz, H.; Brandenburg GbR, K. *Diamond-Crystal and Molecular Structure Visualisation*, version 4.6.6; Crystal Impact: Bonn, Germany, 2021.

14. Dadabhoy, A.; Faulkner, S.; Sammes, P. G. *J. Chem. Soc., Perkin Trans. 2* **2002**, 348–357.
15. Moore, J. D.; Lord, R. L.; Cisneros, G. A.; Allen, M. J. *J. Am. Chem. Soc.* **2012**, *134*, 17372–17375.
16. Aime, S.; Botta, M.; Crich, S. G.; Giovenzana, G. B.; Pagliarin, R.; Piccinini, M.; Sisti, M.; Terreno, E. *J. Biol. Inorg. Chem.* **1997**, *2*, 470–479.
17. (a) Junker, A. K. R.; Tropiano, M.; Faulkner, S.; Sørensen, T. J. *Inorg. Chem.* **2016**, *55*, 12299–12308. (b) McMullon, G. T. A molecular toolkit for immunological imaging; DPhil thesis, University of Oxford, 2022.
18. Woods, M.; Kiefer, G. E.; Bott, S.; Castillo-Muzquiz, A.; Eshelbrenner, C.; Michaudet, L.; McMillan, K.; Mudigunda, S. D. K.; Ogrin, D.; Tircsó, G.; Zhang, S.; Zhao, P.; Sherry, A. D. *J. Am. Chem. Soc.* **2004**, *126*, 9248–9256.
19. Bruce, J. I.; O'Connell, P. J.; Taylor, P. G.; Smith, D. P. T.; Adkin, R. C.; Pearson, V. K. *Molecules* **2020**, *25*, 4253.
20. Adhikari, A.; Kumari, N.; Adhikari, M.; Kumar, N.; Tiwari, A. K.; Shukla, A.; Mishra, A. K.; Datta, A. *Bioorg. Med. Chem*. **2017**, *25*, 3483–3490.
21. Hopper, L. E.; Allen, M. J. *Tetrahedron Lett*. **2014**, *55*, 5560–5561.
22. Neil, E. R.; Parker, D. *RSC Adv.* **2017**, *7*, 4531–4540.
23. Dissanayake, P.; Allen, M. J. *J. Am. Chem. Soc.* **2009**, *131*, 6342–6343.
24. Günduz, S.; Vibhute, S.; Botár, R.; Kálmán, F. K.; Tóth, I.; Tircsó, G.; Regueiro-Figueroa, M.; Esteban-Gómez, D.; Platas-Iglesias, C.; Angelovski, G. *Inorg. Chem.* **2018**, *57*, 5973–5986.
25. (a) Lin, Y.; Lang Jr, S. A.; Seifert, C. M.; Child, R. G.; Morton, G. O.; Fabio, P. F. *J. Org. Chem.* **1979**, *44*, 4701–4703. (b) Chávez, D.; Ochoa, A.; Madrigal, D.; Castillo, M.; Espinoza, K.; González, T.; Vélez, E.; Meléndez, J.; García, J. D.; Rivero, I. A. *J. Comb. Chem.* **2003**, *5*, 149–154.
26. Cooper, C. R.; James, T. D. *J. Chem. Soc., Pekin Trans. 1*, **2000**, 963–969.
27. Yang, W.; Fan, H.; Gao, X.; Gao, S.; Karnati, V. V. R.; Ni, W.; Hooks, W. B.; Carson, J.; Weston, B.; Wang, B. *Chem. Biol.* **2004**, *11*, 439–448.
28. Stones, D.; Manku, S.; Lu, X.; Hall, D. G. *Chem. —Eur. J.* **2004**, *10*, 92–100.
29. Zhai, W.; Male, L.; Fossey, J. S. *Chem. Commun*. **2017**, *53*, 2218–2221.

APPENDIX-A

Appendix A: Additional information for Chapter-II

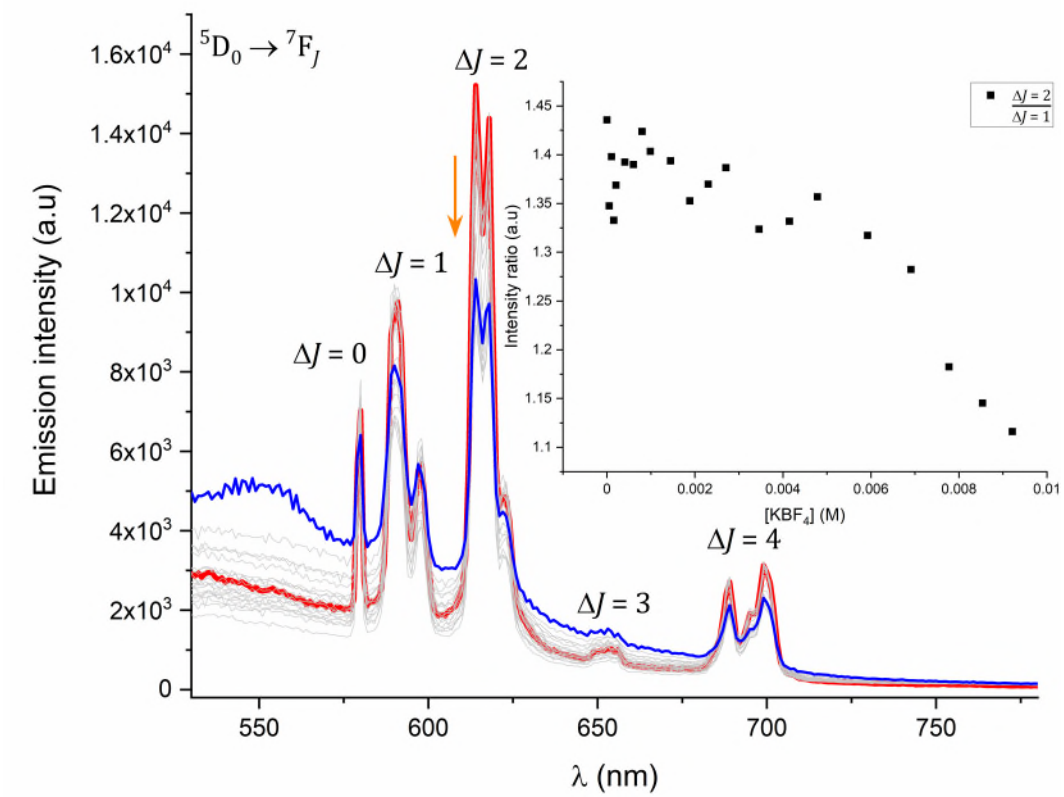


Figure A1. Steady-state emission titration spectra of [Eu(**pDO3A**)] against KBF_4 in deionised water. Spectrum of neat complex solution (***red in bold***), spectra upon the additions of KBF_4 (*grey*), spectrum upon the final addition of KBF_4 (***blue in bold***). *Inset*: $\Delta J = 2$ / $\Delta J = 1$ ratiometric analysis as a function of KBF_4 added generated from the titration spectra.

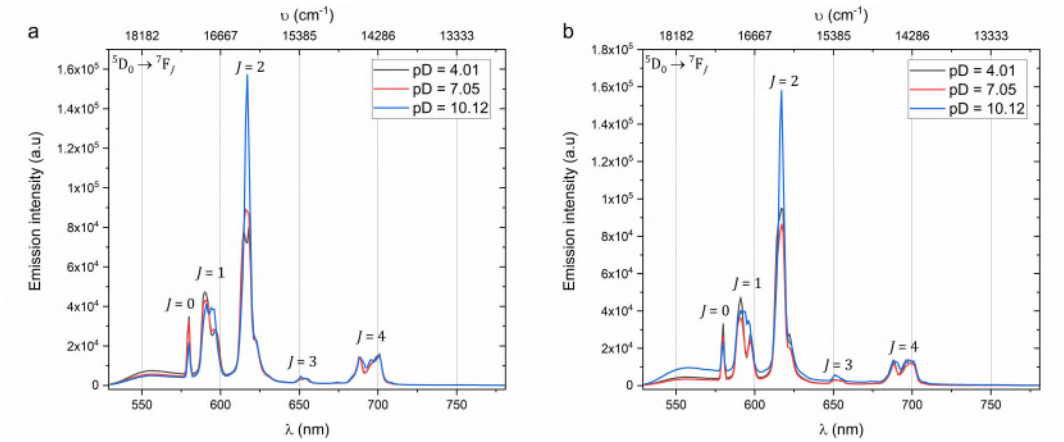


Figure A2. Steady-state luminescence spectra of [Eu_2(**DO3A**)$_2$**C-2**] (*a*) and [Eu_2(**DO3A**)$_2$**C-3**] (*b*) at varying pD.

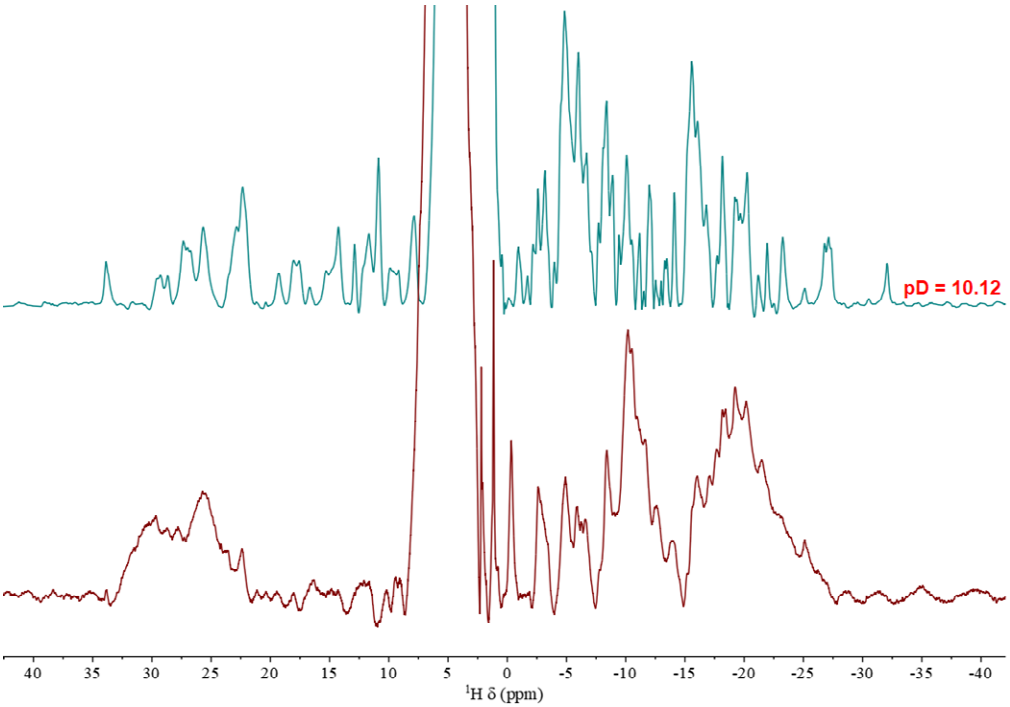


Figure A3. ^{1}H NMR spectra of [Eu_2(**DO3A**)$_2$**C-2**] at different pD in D_2O at 298 K.

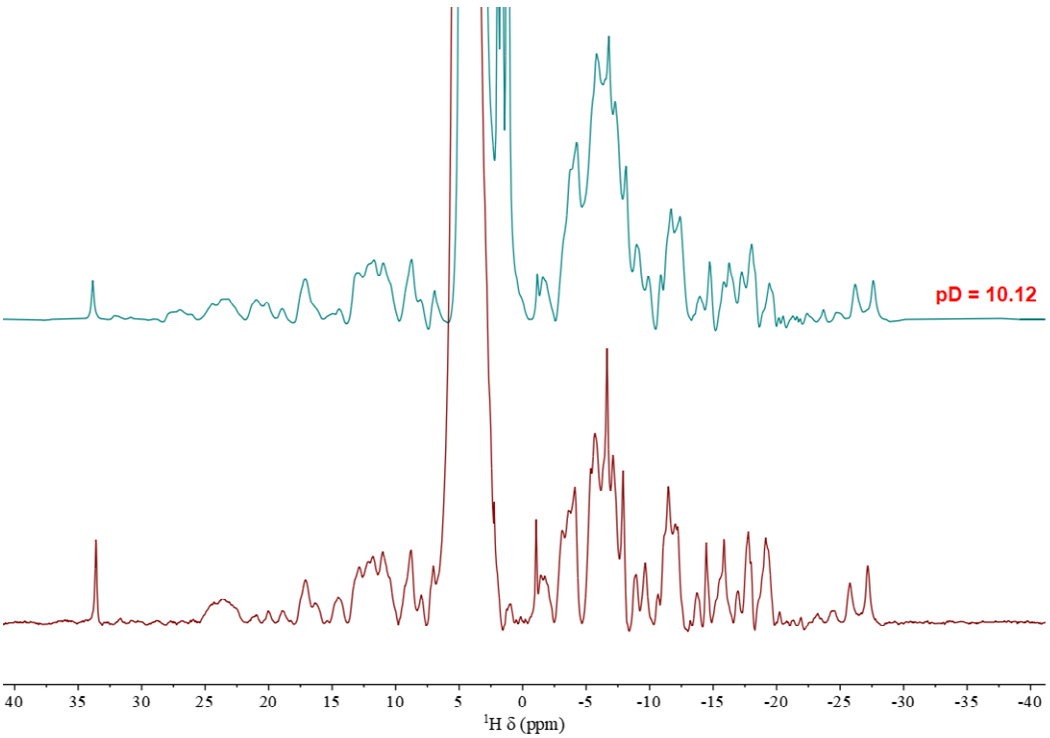


Figure A4. ^{1}H NMR spectra of [Eu_2(**DO3A**)$_2$**C-3**] at different pD in D_2O at 298 K.

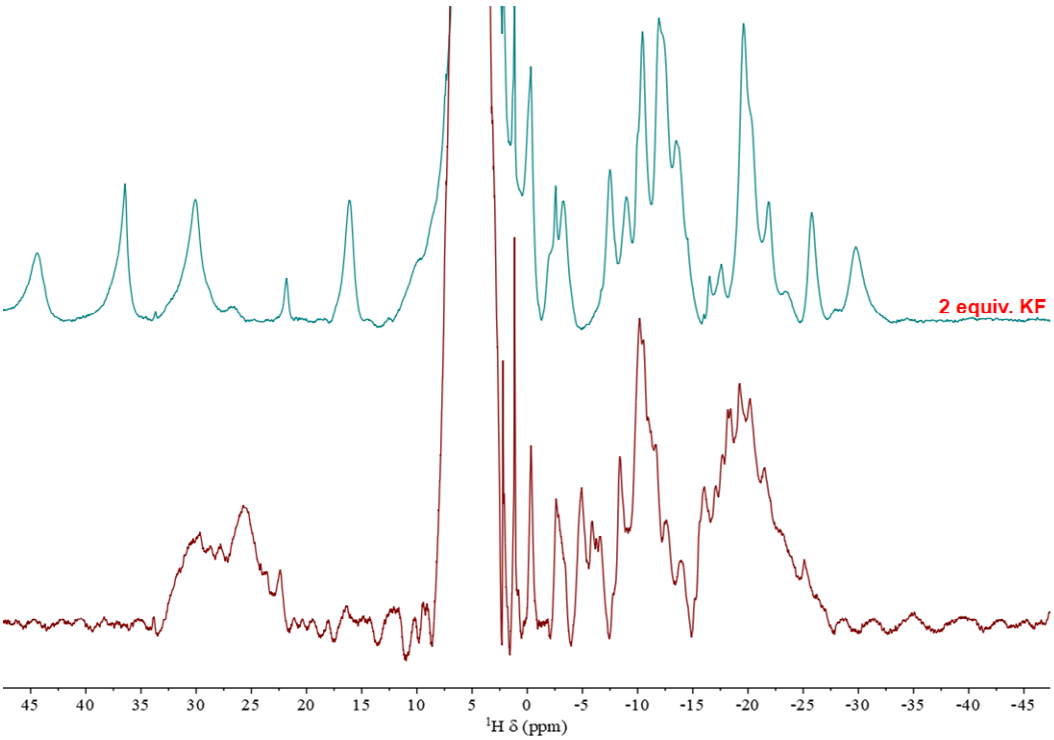


Figure A5. ^{1}H NMR spectra of [Eu_2(**DO3A**)$_2$**C-2**] with and without KF in D_2O.

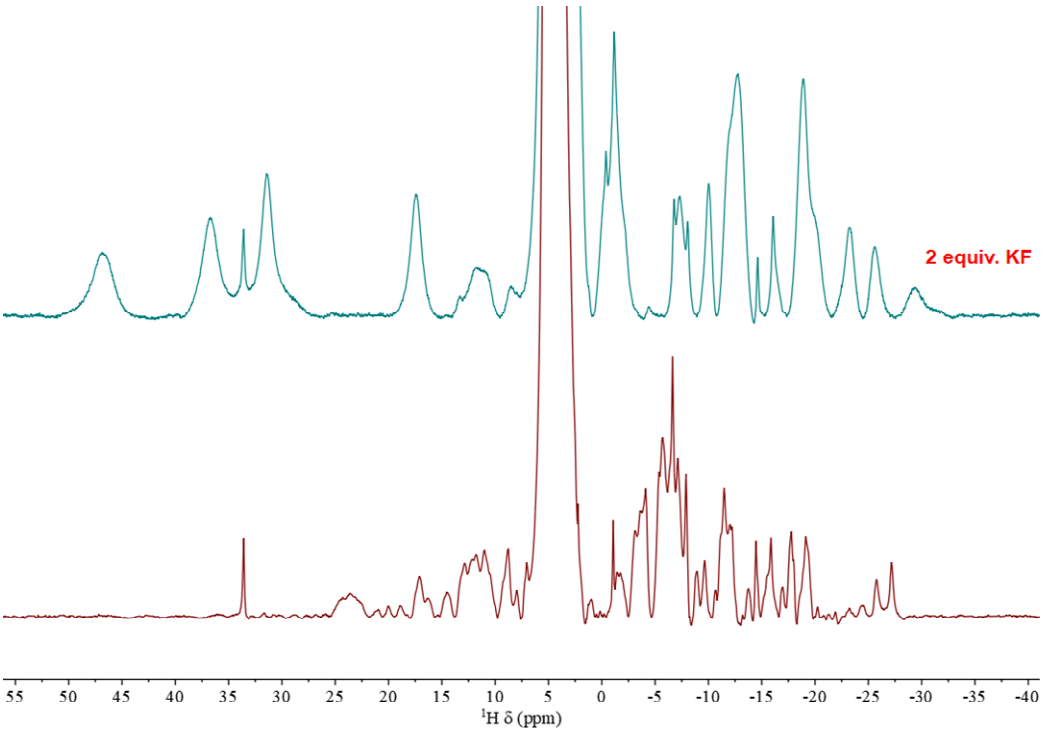


Figure A6. ^{1}H NMR spectra of [Eu_2(**DO3A**)$_2$**C-3**] with and without KF in D_2O.

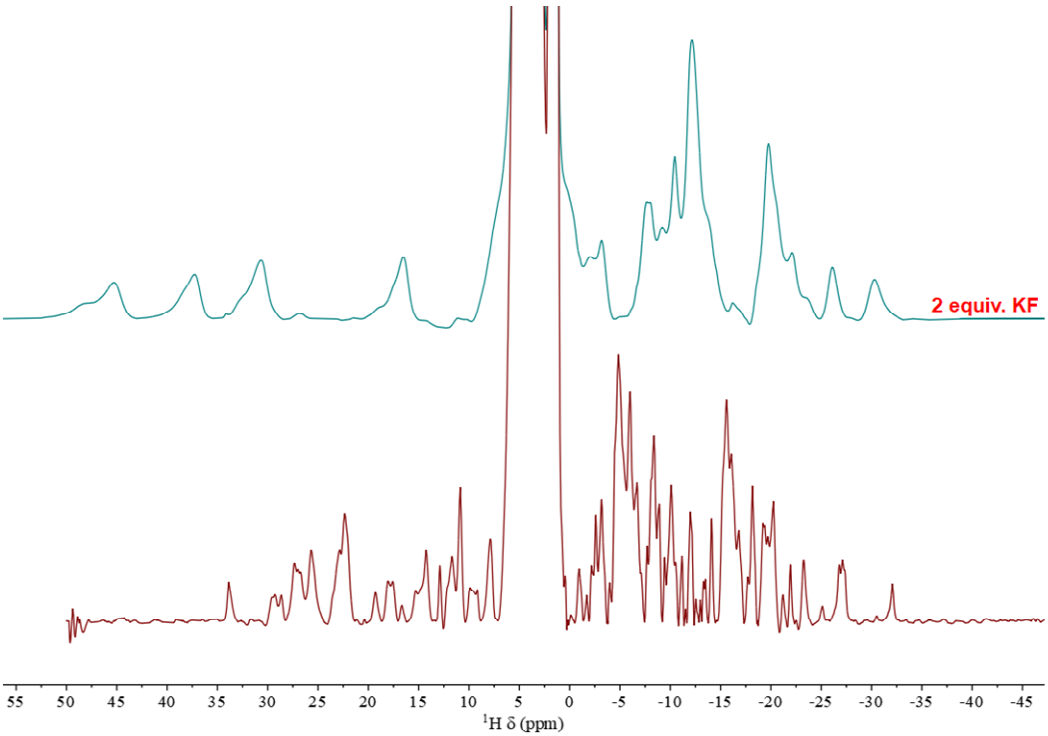


Figure A7. ^{1}H NMR spectra of [Eu_2(**DO3A**)$_2$**C-2**] with and without KF in pD 10 in D_2O.

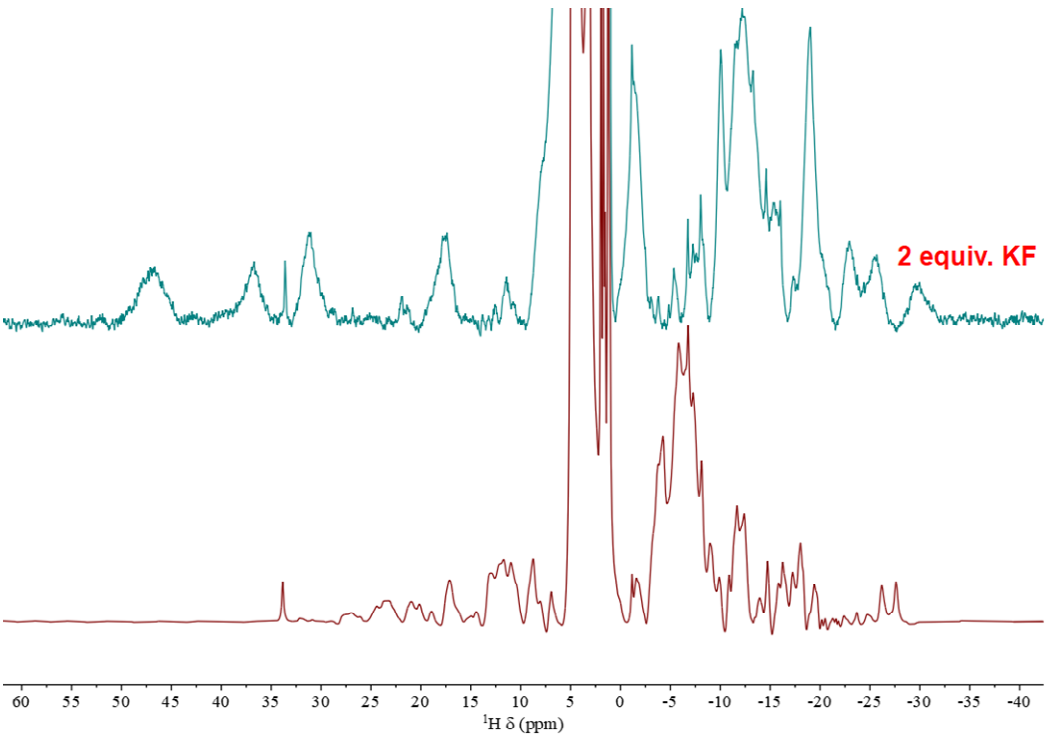


Figure A8. ^{1}H NMR spectra of [Eu_2(**DO3A**)$_2$**C-3**] with and without KF in pD 10 in D_2O.

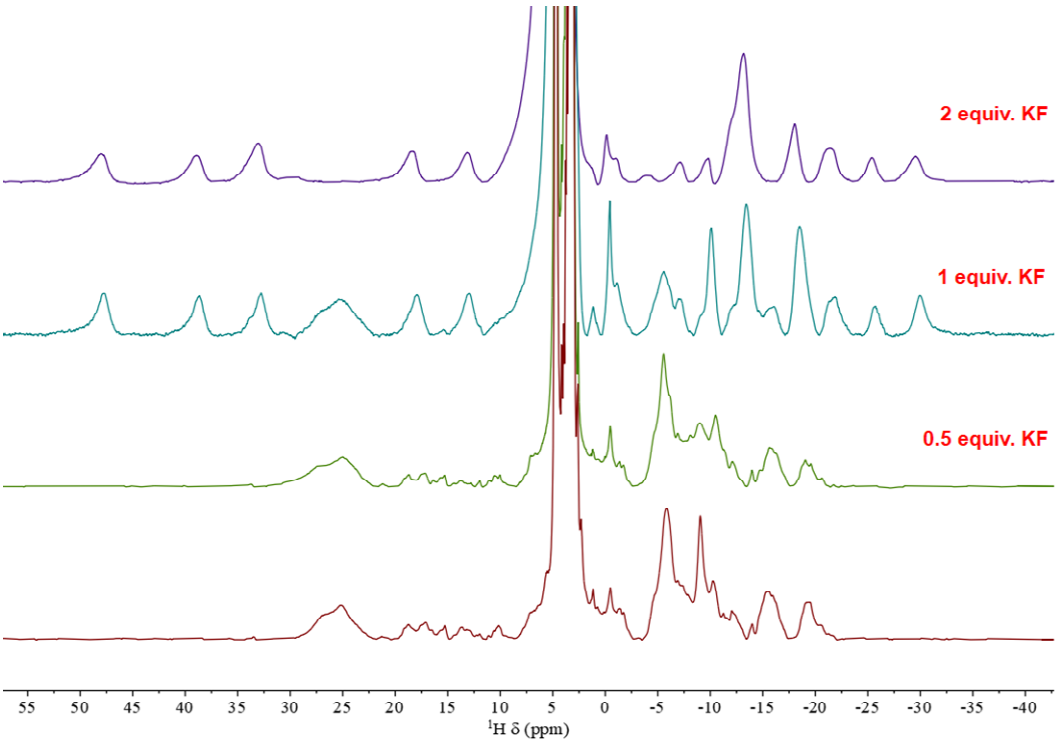


Figure A9. ^{1}H NMR spectra of [Eu(**pDO3A**)] with increasing KF in D_2O.

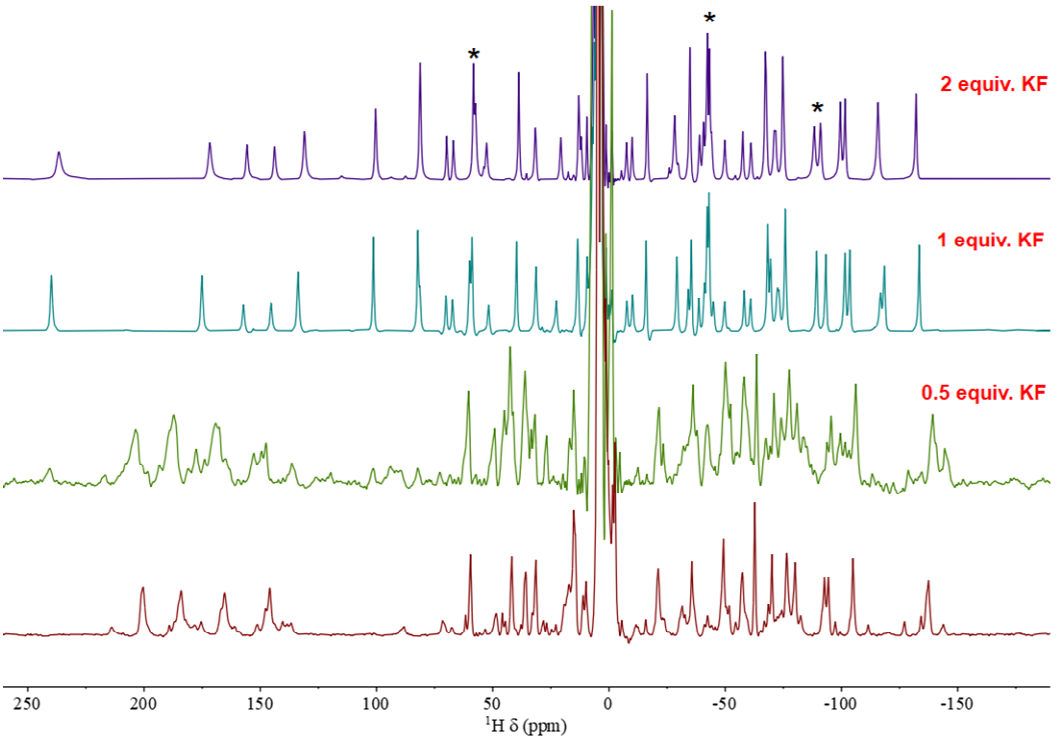


Figure A10. ^{1}H NMR spectra of [Yb(**pDO3A**)] with increasing KF in MeOD. Signals which invert during the course of the titration are highlighted with asterisk(*) on the spectrum recorded with 2 equiv of KF added to the complex.

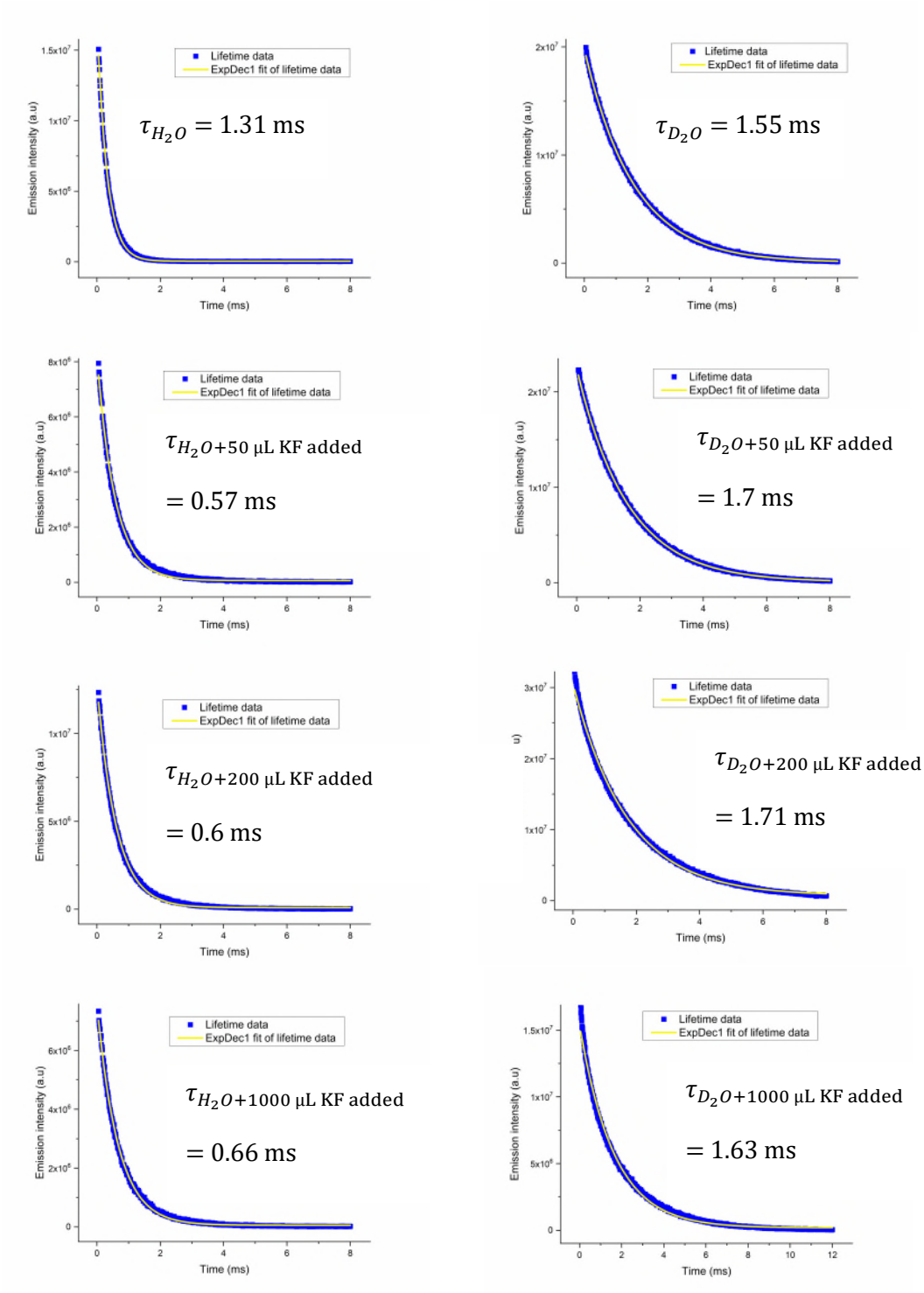


Figure A11. Luminescence lifetime spectra of [Eu_2(**DO3A**)$_2$**C-2**] with increasing concentration of KF in water (*left*) and deuterium oxide (*right*); concentration of [Eu_2(**DO3A**)$_2$**C-2**] is 10^{-3} M, concentration of stock solution of KF in [Eu_2(**DO3A**)$_2$**C-2**] is 0.02 M (non-dilution method used).

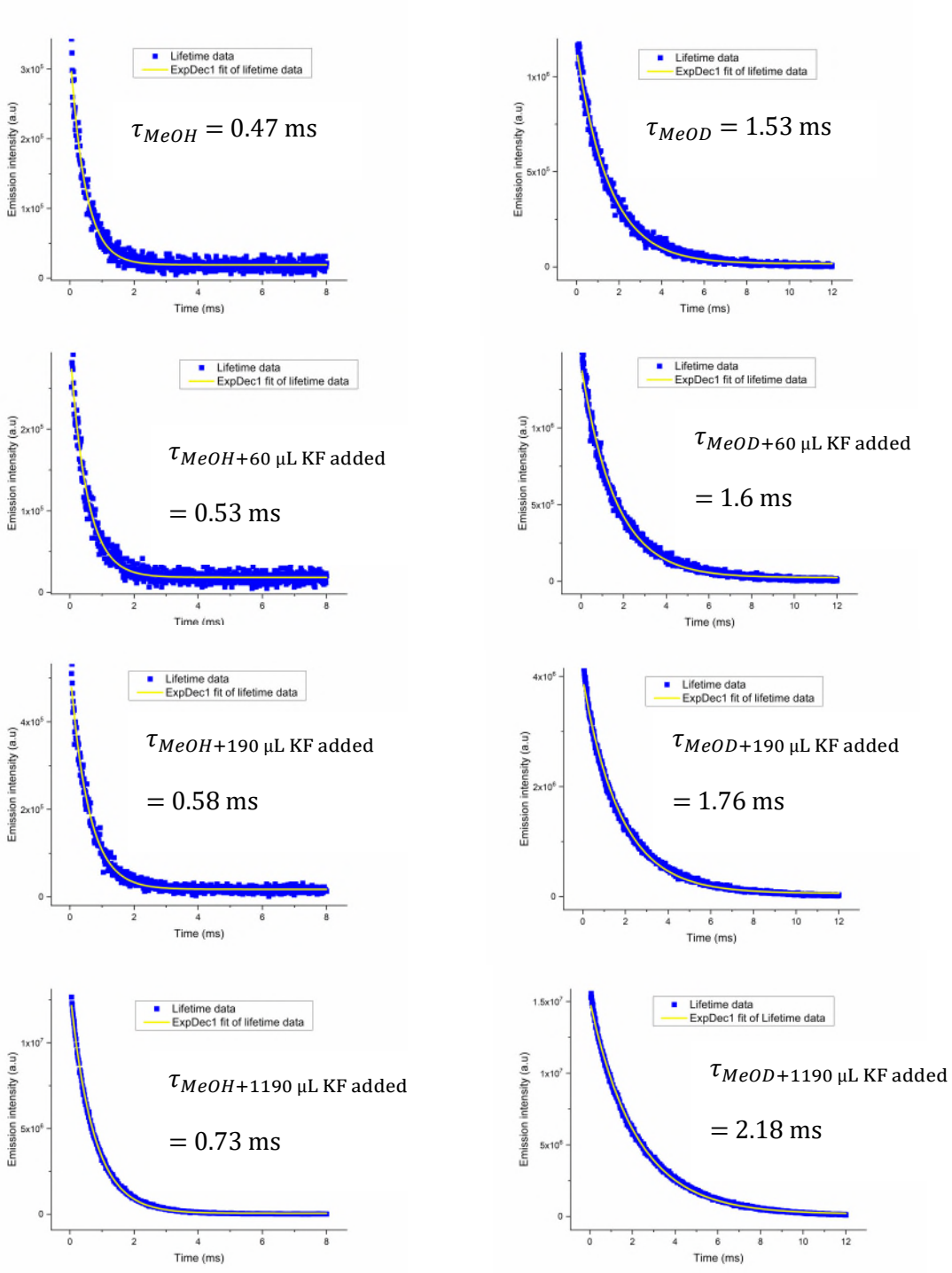


Figure A12. Luminescence lifetime spectra of [Eu_2(**DO3A**)$_2$**C-2**] with increasing concentration of KF in methanol (*left*) and deuterated methanol (*right*); concentration of [Eu_2(**DO3A**)$_2$**C-2**] is 10^{-3} M, concentration of stock solution of KF in [Eu_2(**DO3A**)$_2$**C-2**] is 0.02 M (non-dilution method used).

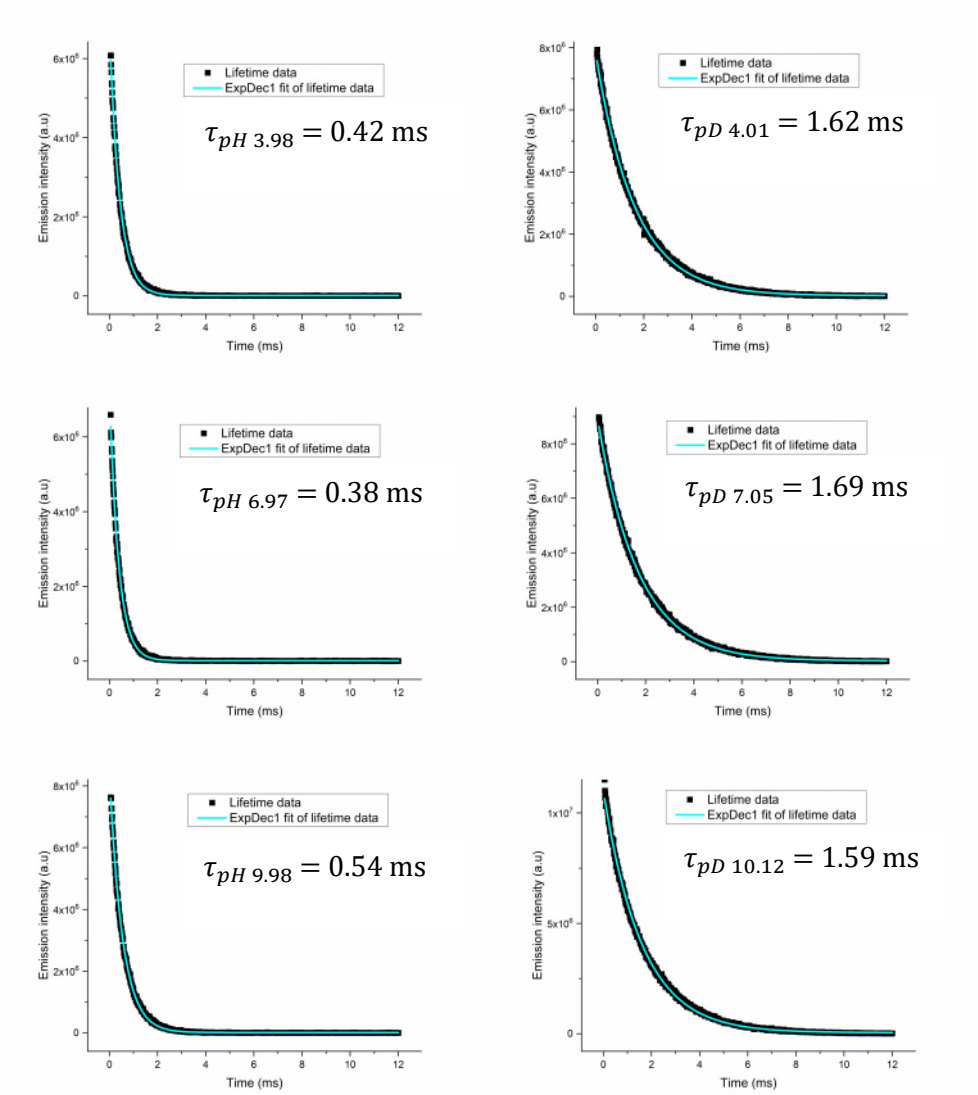


Figure A13. Luminescence lifetime spectra of [Eu_2(**DO3A**)$_2$**C-2**] at different pH (*left*) and pD (*right*); concentration of [Eu_2(**DO3A**)$_2$**C-2**] is 10^{-3} M.

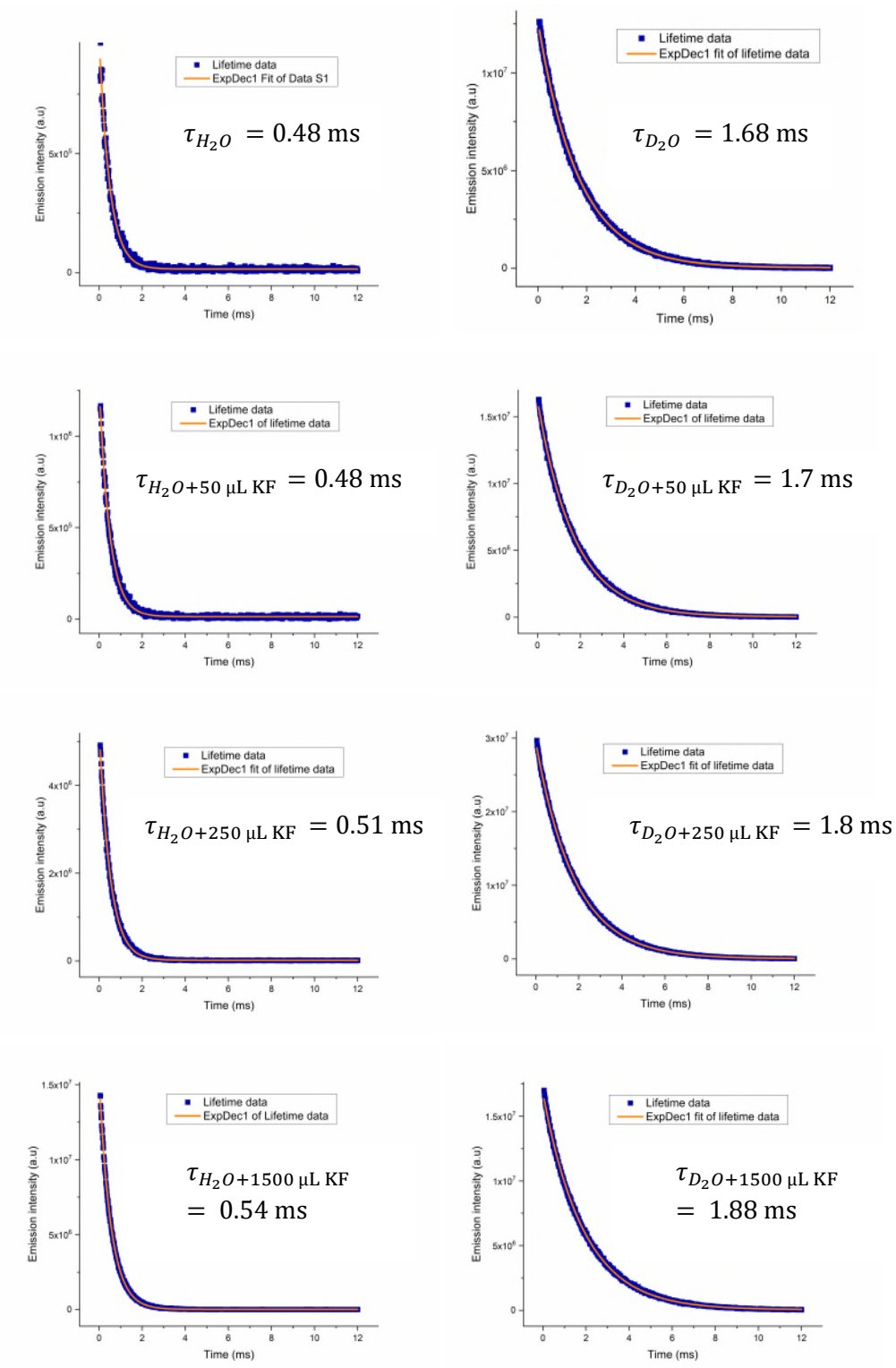


Figure A14. Luminescence lifetime spectra of [Eu_2(**DO3A**)$_2$**C-3**] with increasing concentration of KF in water (*left*) and deuterium oxide (*right*); concentration of [Eu_2(**DO3A**)$_2$**C-3**] is 10^{-3} M, concentration of stock solution of KF in [Eu_2(**DO3A**)$_2$**C-3**] is 0.02 M (non-dilution method used).

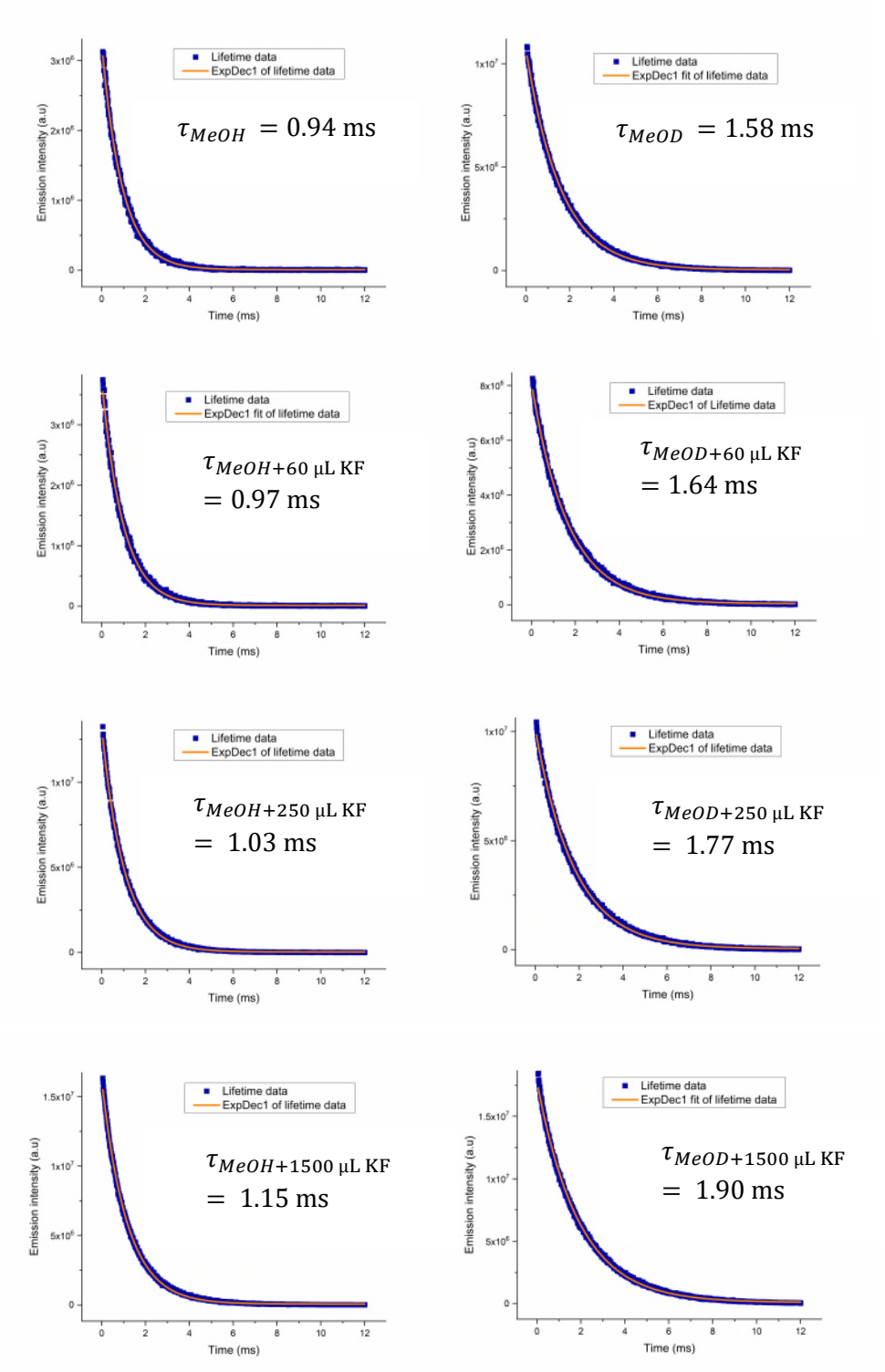


Figure A15. Luminescence lifetime spectra of [Eu_2(**DO3A**)$_2$**C-3**] with increasing concentration of KF in methanol (*left*) and deuterated methanol (*right*); concentration of [Eu_2(**DO3A**)$_2$**C-3**] is 10^{-3} M, concentration of stock solution of KF in [Eu_2(**DO3A**)$_2$**C-3**] is 0.02 M (non-dilution method used).

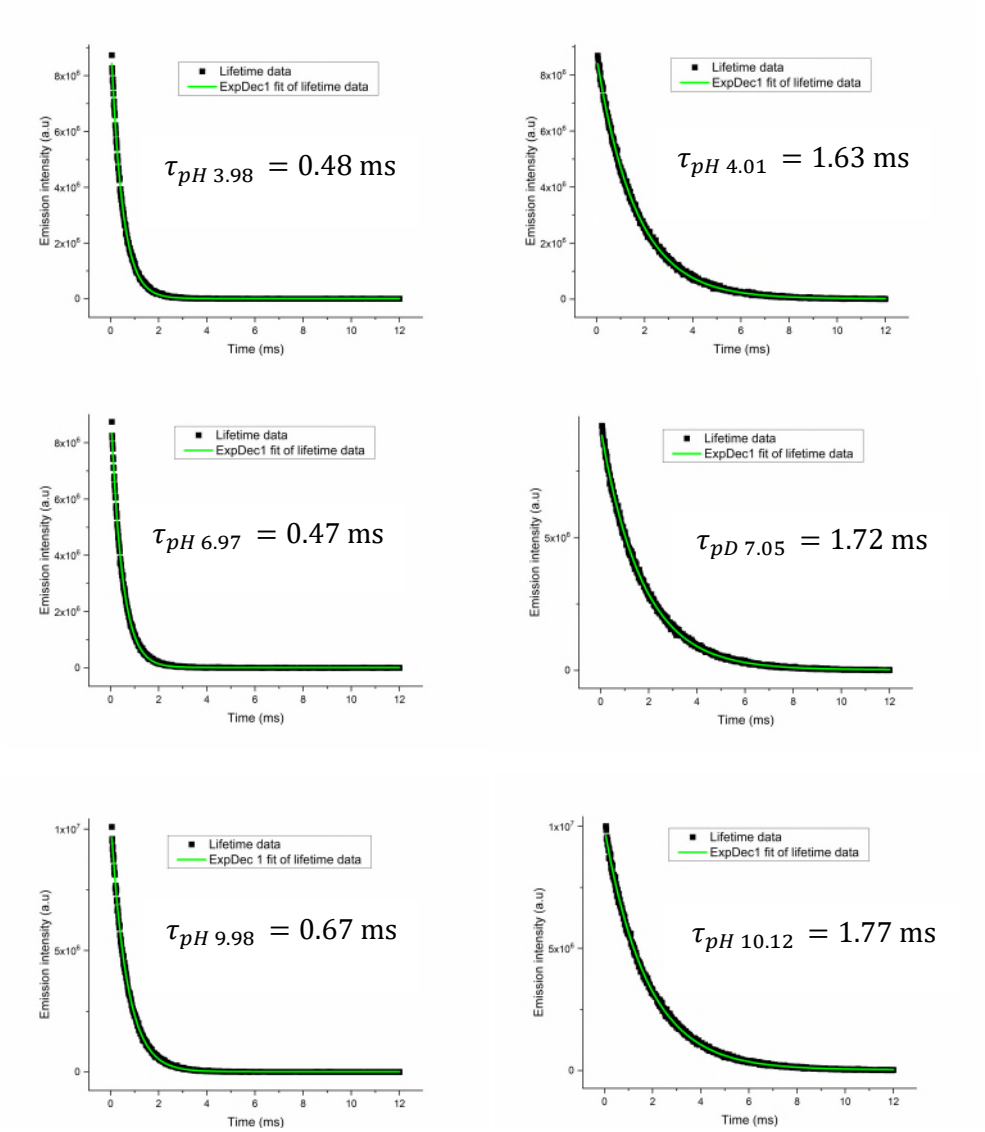


Figure A16. Luminescence lifetime spectra of [Eu_2(**DO3A**)$_2$**C-3**] at different pH (*left*) and pD (*right*); concentration of [Eu_2(**DO3A**)$_2$**C-3**] is 10^{-3} M.

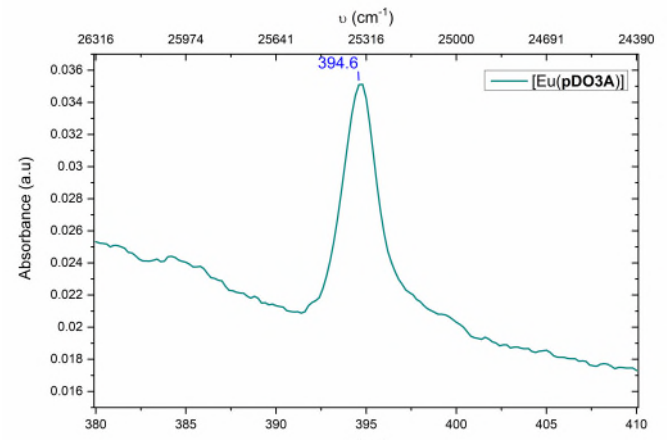


Figure A17. Electronic absorption spectra of 5 mM solution of [Eu(**pDO3A**)] in deionised water at 298 K.

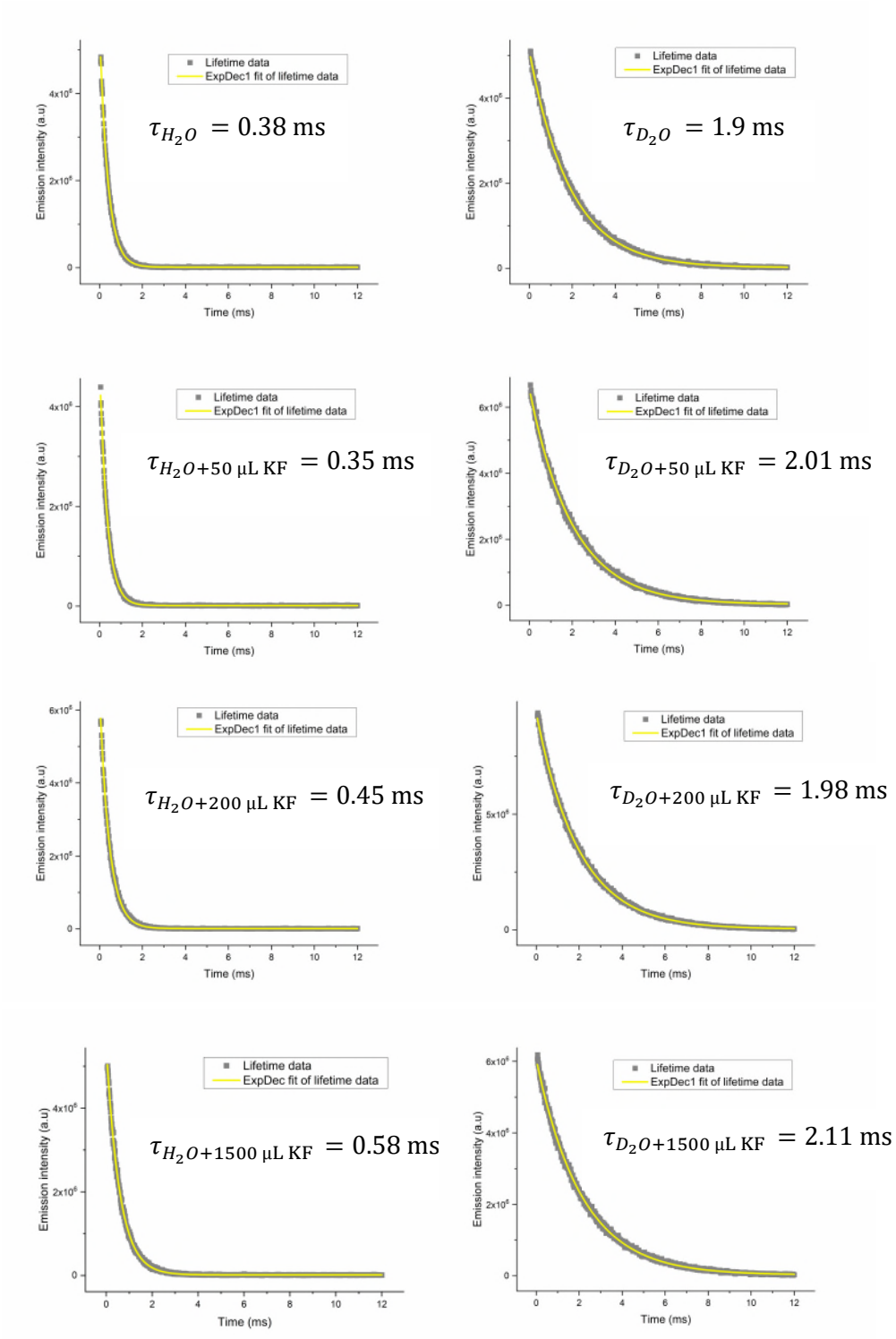


Figure A18. Luminescence lifetime spectra of [Eu(**pDO3A**)] with increasing concentration of KF in water (*left*) and deuterium oxide (*right*); concentration of [Eu(**pDO3A**)] is 10^{-3} M, concentration of stock solution of KF in [Eu(**pDO3A**)] is 0.02 M (non-dilution method used).

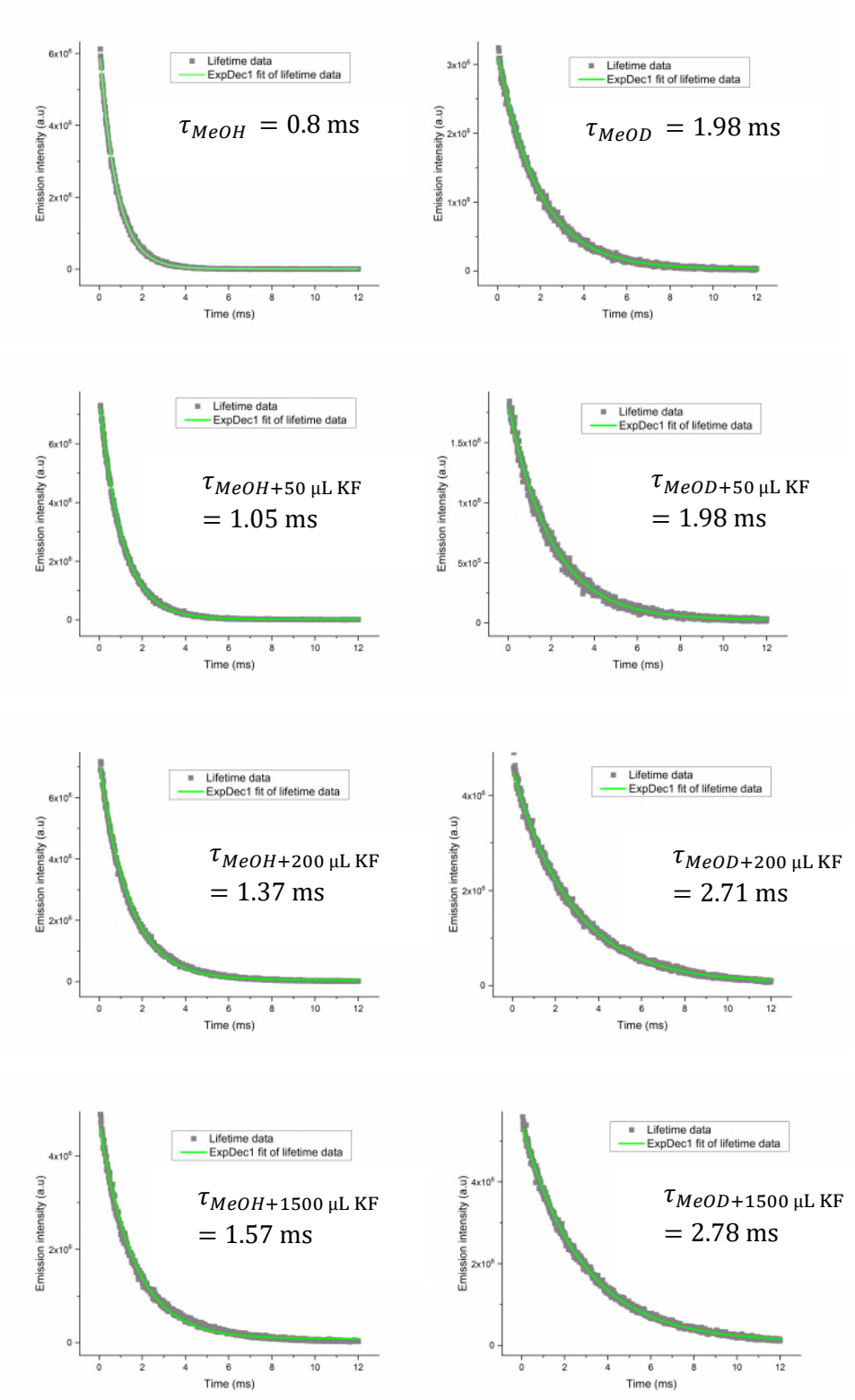


Figure A19. Luminescence lifetime spectra of [Eu(**pDO3A**)] with increasing concentration of KF in water (*left*) and deuterium oxide (*right*); concentration of [Eu(**pDO3A**)] is 10^{-3} M, concentration of stock solution of KF in [Eu(**pDO3A**)] is 0.02 M (non-dilution method used).

Table A1. Luminescence lifetimes for [Eu_2(**DO3A**)$_2$**C-2**] with increasing concentration of KF in CH_3OH and CD_3OD*

Complex and amount of KF added	Lifetime in MeOH (ms)	Lifetime in MeOD (ms)	Hydration number (*q*)
Complex	0.47	1.53	3.2
Complex + 60 μL KF	0.53	1.6	2.8
Complex + 190 μL KF	0.58	1.76	2.5
Complex + 1190 μL KF	0.73	2.18	1.9

* All lifetime values are subjected to an error of ±10%.

Table A2. Luminescence lifetimes for [Eu_2(**DO3A**)$_2$**C-3**] with increasing concentration of KF in CH_3OH and CD_3OD*

Complex and amount of KF added	Lifetime in MeOH (ms)	Lifetime in MeOD (ms)	Hydration number (*q*)
Complex	0.94	1.58	0.73
Complex + 60 μL KF	0.97	1.64	0.7
Complex + 200 μL KF	1.03	1.77	0.6
Complex + 1500 μL KF	1.15	1.90	0.5

* All lifetime values are subjected to an error of ±10%.

Table A3. Luminescence lifetimes for [Eu(**pDO3A**)] with increasing concentration of KF in CH_3OH and CD_3OD*

Complex and amount of KF added	Lifetime in MeOH (ms)	Lifetime in MeOD (ms)	Hydration number (*q*)
[Eu(**pDO3A**)]	0.8	1.9	1.4
[Eu(**pDO3A**)] + 50 μL KF	1.05	2	0.8
[Eu(**pDO3A**)] + 200 μL KF	1.37	2.71	0.6
[Eu(**pDO3A**)] + 1500 μL KF	1.57	2.8	0.4

* All lifetime values are subjected to an error of ±10%.

APPENDIX-B

Appendix-B: HPLC conditions used in Chapter-IV

HPLC was performed using deionised water and HPLC-grade solvent (MeCN from Sigma Aldrich). All aqueous solvents were degassed for 15 min before use. The column temperature used for HPLC was ambient. Sample diluent was H_2O/MeCN (95:5) at a concentration of 50-100 mg/mL. Samples were filtered through a nylon syringe filter (13mm, 0.45 μm) from Gilson Scientific Ltd prior to injection.

Instrument used for preparative HPLC was Agilent 1260 Infinity II system fitted with a G7157A autosampler, G1364 E 1260 FC-PS (fraction collector), G7114A 1260 VWD with an injection loop of 5 mL.

Table B1. Preparative HPLC conditions for DO3A*m*-PBA

Flow	: 25.00 mL/min
Low Pressure Limit	: 0.00 bar
High Pressure Limit	: 420.00 bar
Max. Flow Ramp Up	: 600.0 mL/min²
Max. Flow Ramp Down	: 600.0 mL/min²
Mobile Phase A	: water + 0.1% TFA (*v*/*v*)
Mobile Phase B	: MeCN + 0.1% TFA (*v*/*v*)
Auxiliary	
Draw Speed	: 900 μL/min
Eject Speed	: 3000 μL/min
High throughput	
Sample Flush-Out Factor	: 5.0
Injection Mode	: Injection with needle wash
Injection Volume	: 300 μL
Collection mode	: UV (DAD, λ = 269 nm)
Peak detection mode	: threshold

Table B1.1. Timetable of compound elution in preparative HPLC

Time (min)	Mobile phase A (%, *v*/*v*)	Mobile phase B (%, *v*/*v*)
0	95	5
1	90	10
10	90	10

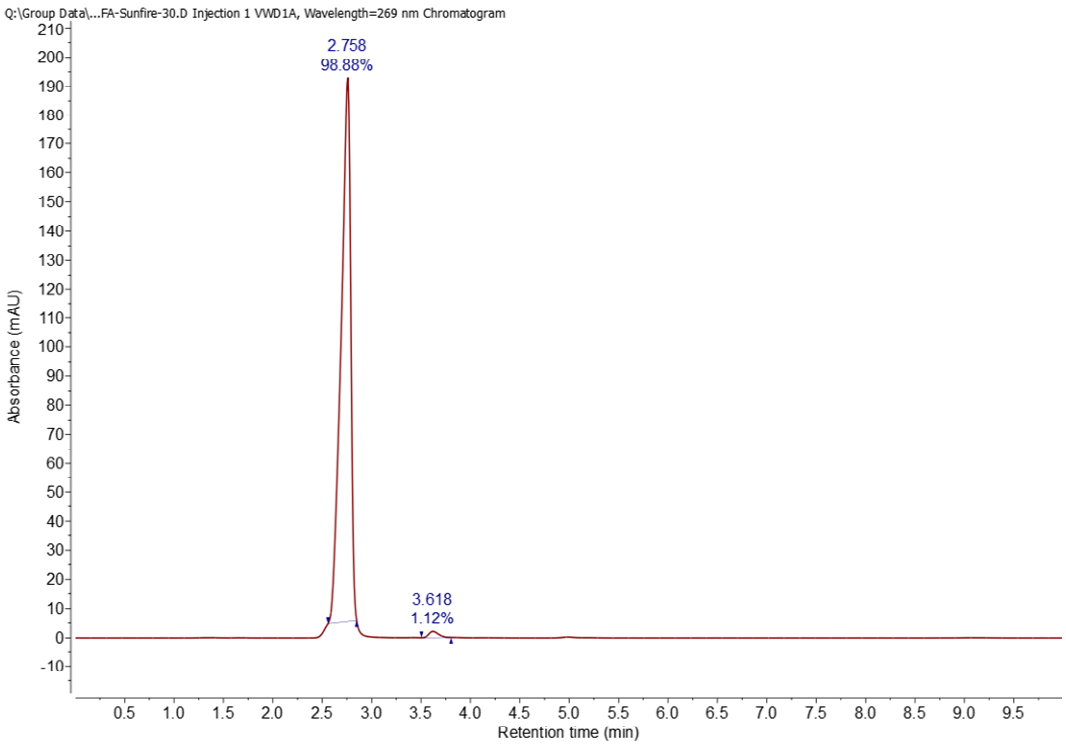


Figure B1. Preparative HPLC trace of **DO3A-*m*-PBA**, t_R = 2.8 min $[M + H]^+$

Table B2. Preparative HPLC conditions for DO3A*p*-PBA

Flow	: 25.00 mL/min
Low Pressure Limit	: 0.00 bar
High Pressure Limit	: 420.00 bar
Max. Flow Ramp Up	: 600.0 mL/min²
Max. Flow Ramp Down	: 600.0 mL/min²
Mobile Phase A	: water + 0.1% TFA (*v*/*v*)
Mobile Phase B	: MeCN + 0.1% TFA (*v*/*v*)
Auxiliary	
Draw Speed	: 900 μL/min
Eject Speed	: 3000 μL/min
High throughput	
Sample Flush-Out Factor	: 5.0
Injection Mode	: Injection with needle wash
Injection Volume	: 300 μL
Collection mode	: UV (DAD, λ = 269 nm)
Peak detection mode	: Threshold

Table B2.1. Timetable of compound elution in preparative HPLC

Time (min)	Mobile phase A (%, *v*/*v*)	Mobile phase B (%, *v*/*v*)
0	95	5
10	90	10
11	5	95
13.5	5	95
14	95	5
10	95	5

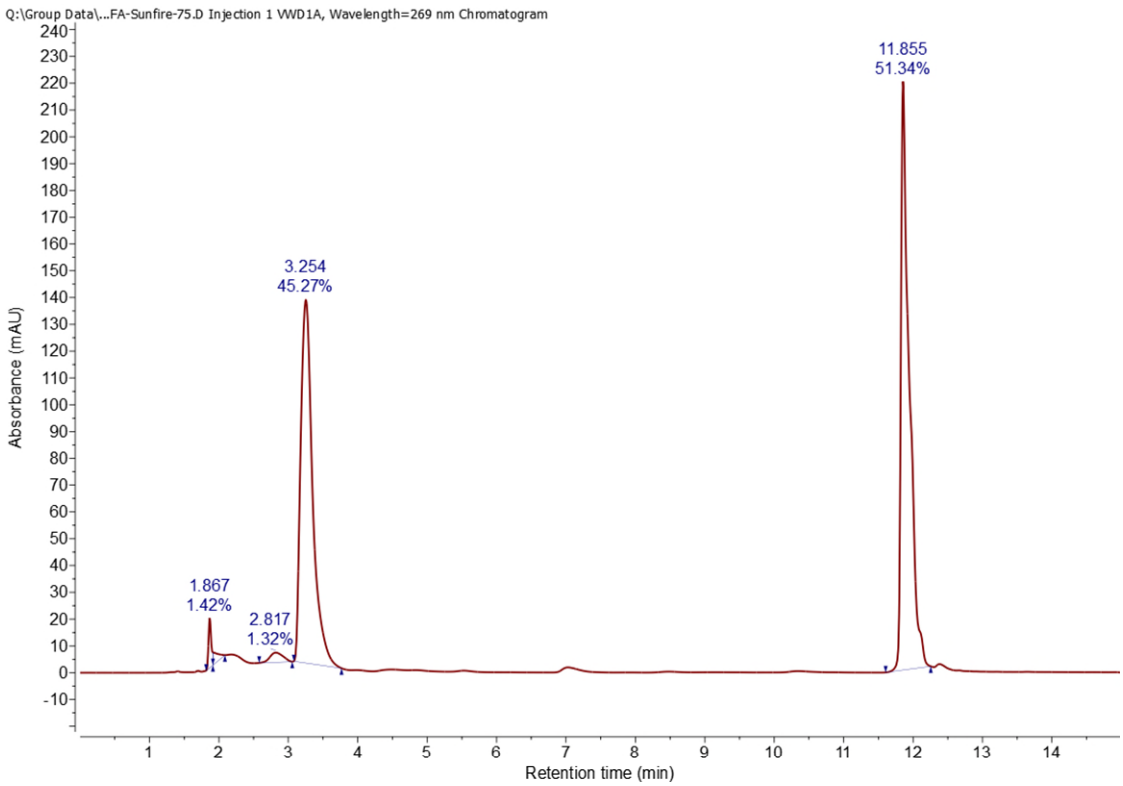


Figure B2. Preparative HPLC trace of **DO3A*p*-PBA**, t_R = 3.3 min $[M + H]^+$, 11.9 min $[M - H]^-$.

APPENDIX-C

Appendix C: X-ray Crystal Data

Table C1. Crystal data and structure refinement for DO3A(*t*-BuO)$_3$

Structure located in Chapter-II, Figure 2.1(*a*)

Identification code	7337	
Empirical formula	$C_{27}H_{55}Br_2Cl_2N_4O_7$	
Formula weight	778.47	
Temperature	150 K	
Wavelength	0.71073 Å	
Crystal system	Orthorhombic	
Space group	*Pbca*	
Unit cell dimensions	a = 10.9482(2) Å	α = 90°
	b = 19.5471(2) Å	β = 90°
	c = 35.5397(7) Å	γ = 90°
Volume	7605.7(2) Å^3	
Z	8	
Density (calculated)	1.360 mg/cm^3	
Absorption coefficient	2.315 mm^{-1}	
F(000)	3240	
Crystal size	0.28 × 0.25 × 0.03 mm^3	
Theta range for data collection	2.084 to 29.767°	
Index ranges	$-15 \le h \le 14$, $-26 \le k \le 26$, $-48 \le l \le 49$	
Reflections collected	127108	
Independent reflections	10470 [R(int) = .095]	
Completeness to theta = 27.684°	99.6 %	
Absorption correction	Semi-empirical from equivalents	
Max. and min. transmission	0.93 and 0.66	
Refinement method	Full-matrix least-squares on F^2	
Data/restraints/parameters	7464/36/395	
Goodness-of-fit on F^2	0.9977	
Final R indices [$I > 2\sigma(I)$]	R_1 = 0.0414, wR_2 = 0.0903	
R indices (all data)	R_1 = 0.0683, wR_2 = 0.1050	
Largest diff. peak and hole	1.15 and -1.17 e.Å^{-3}	

Table C2. Crystal data and structure refinement for (DO3A(*t*-BuO)$_3$)$_2$C-2

Structure located in Chapter-II, Figure 2.2

CCDC number	2201928	
Empirical formula	$C_{60}H_{108}Br_2C_{l18}N_8Na_2O_{12}$	
Formula weight	1977.49	
Temperature	150 K	
Wavelength	1.54180 Å	
Crystal system	Triclinic	
Space group	*P*-1	
Unit cell dimensions	a = 12.4765(3) Å	α = 71.979(2)°
	b = 13.7256(3) Å	β = 88.7149(18)°
	c = 15.0782(3) Å	γ = 78.9608(19)°
Volume	2408.12(10) Å^3	
Z	1	
Density (calculated)	1.364 mg/cm^3	
Absorption coefficient	6.175 mm^{-1}	
F(000)	1017.993	
Crystal size	0.20 × 0.14 × 0.10 mm^3	
Theta range for data collection	3.612 to 75.987°	
Index ranges	$-15 \leq h \leq 15$, $-17 \leq k \leq 17$, $-18 \leq l \leq 18$	
Reflections collected	50946	
Independent reflections	9968 [R(int) = 0.044]	
Completeness to theta = 73.257°	99.9 %	
Absorption correction	Semi-empirical from equivalents	
Max. and min. transmission	0.54 and 0.35	
Refinement method	Full-matrix least-squares on F^2	
Data/restraints/parameters	9966/12/473	
Goodness-of-fit on F^2	0.9928	
Final R indices [$I > 2\sigma(I)$]	R_1 = 0.0474, wR_2 = 0.1308	
R indices (all data)	R_1 = 0.0529, wR_2 = 0.1363	
Largest diff. peak and hole	1.79 and -0.81 e.Å^{-3}	

Table C3. Crystal data and structure refinement for compound pDO3A(*t*-BuO)$_3$

Structure located in Chapter-II, Figure 2.1(*b*)

CCDC number	2201929	
Empirical formula	$C_{29}H_{52}N_4O_6$	
Formula weight	552.75	
Temperature	150 K	
Wavelength	1.54184 Å	
Crystal system	Monoclinic	
Space group	*I*2/a	
Unit cell dimensions	a = 25.8831(10) Å	α = 90°
	b = 5.6524(4) Å	β = 94.085(4)°
	c = 43.780(2) Å	γ = 90°
Volume	6388.8(6) Å^3	
Z	8	
Density (calculated)	1.149 mg/cm^3	
Absorption coefficient	0.646 mm^{-1}	
F(000)	2416	
Crystal size	0.15 × 0.05 × 0.02 mm^3	
Theta range for data collection	3.424 to 77.581°	
Index ranges	$-32 \le h \le 29$, $-6 \le k \le 6$, $-54 \le l \le 55$	
Reflections collected	36069	
Independent reflections	6615 [R(int) = 0.079]	
Completeness to theta = 73.702°	99.6 %	
Absorption correction	Semi-empirical from equivalents	
Max. and min. transmission	0.99 and 0.96	
Refinement method	Full-matrix least-squares on F^2	
Data/restraints/parameters	6615/396/374	
Goodness-of-fit on F^2	0.9888	
Final R indices [$I > 2\sigma(I)$]	R_1 = 0.0553, wR_2 = 0.1266	
R indices (all data)	R_1 = 0.0867, wR_2 = 0.1556	
Largest diff. peak and hole	0.48 and -0.58 e.Å^{-3}	

Table C4. Crystal data and structure refinement for [Gd_2(DO3A)$_2$C-2]

Structure located in Chapter-II, Figure 2.3(*a*)

Identification code	7484
Empirical formula	$C_{360}H_{776}Gd_{24}N_{96}O_{244}$
Formula weight	14128.72
Temperature	150 K
Wavelength	1.54184 Å
Crystal system	Orthorhombic
Space group	Ccca
Unit cell dimensions	a = 39.4954(15) Å α = 90°
	b = 47.0650(15) Å β = 90°
	c = 43.4587(17) Å γ = 90°
Volume	80783(5) Å^3
Z	4
Density (calculated)	1.162 mg/cm^{-3}
Absorption coefficient	13.090 mm^{-1}
F(000)	28384
Crystal size	0.10 × 0.05 × 0.03 mm^3
Theta range for data collection	3.560 to 54.673°
Index ranges	$-43 \leq h \leq 49$, $-58 \leq k \leq 56$, $-54 \leq l \leq 40$
Reflections collected	145567
Independent reflections	42004 [R(int) = 0.1466]
Completeness to theta = 72.091°	99.1%
Absorption correction	Semi-empirical from equivalents
Max. and min. transmission	0.68 and 0.12
Refinement method	Full-matrix least-squares on F^2
Data/restraints/parameters	24798/224/1661
Goodness-of-fit on F^2	0.9964
Final R indices [$I > 2\sigma(I)$]	R_1 = 0.0658, wR_2 = 0.1586
R indices (all data)	R_1 = 0.1158, wR_2 = 0.1999
Largest diff. peak and hole	2.08 and -1.17 e.Å^{-3}

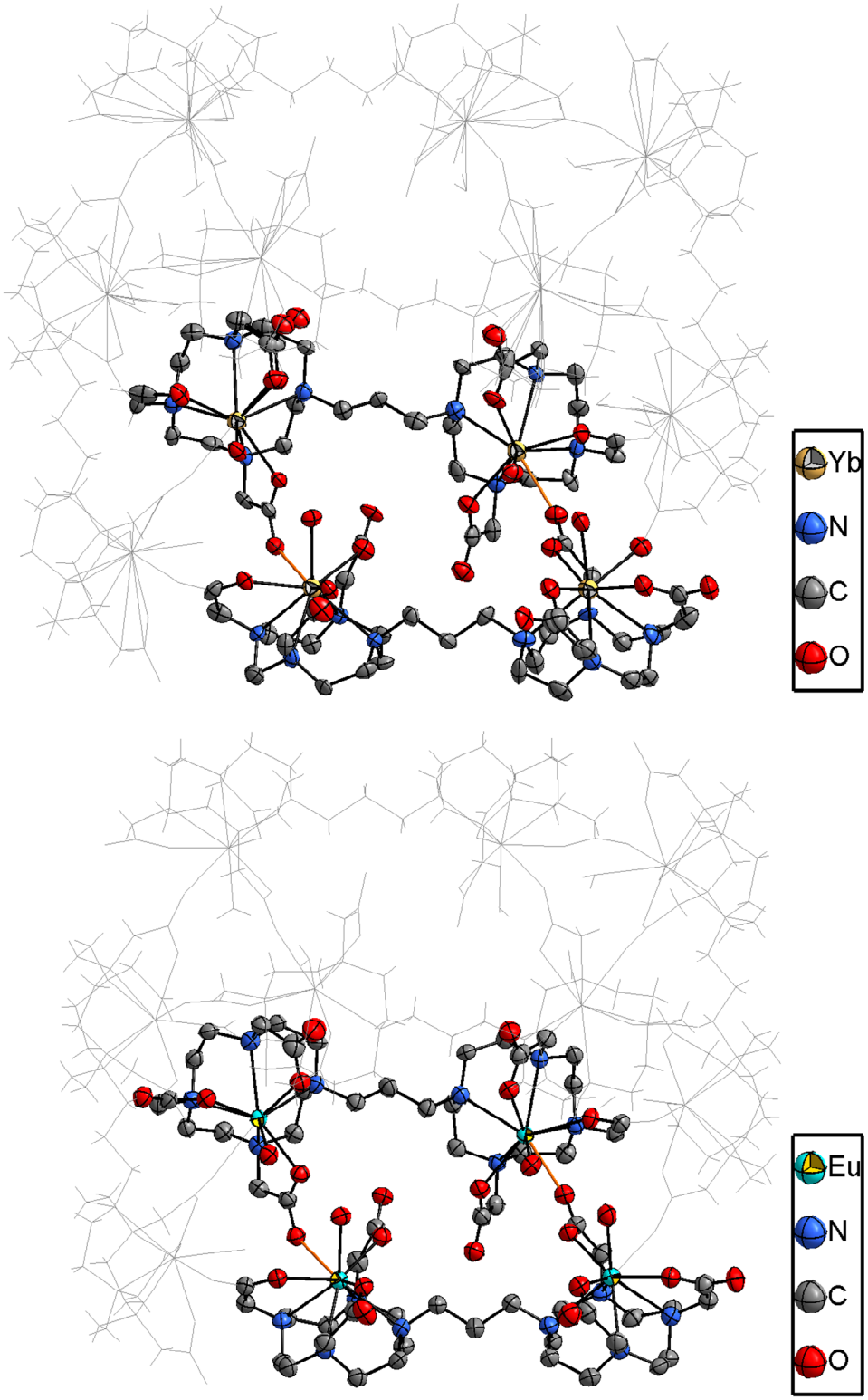


Figure C1. Single crystal X-ray structure of [Yb_2(**DO3A**)$_2$**C-3**] (top) and [Eu_2(**DO3A**)$_2$**C-3**] (bottom). Except selected structure, the rest are shown in wireframe format, H atoms and water are omitted for clarity. Thermal ellipsoid drawn at 30% probability level. μ-oxo bridging bond is shown in orange. Structure solved by Dr. Kirsten Christensen at Chemical Crystallography, University of Oxford.

Table C5. Crystal data and structure refinement for [Ln_2(DO3A)$_2$C-3] (Ln = Eu(III), Gd(III), and Yb(III))

Identification code	7548 (CCDC number: 2201930)	7532	7526 (CCDC number: 2201931)
Empirical formula	$C_{186}H_{324}Eu_{12}N_{48}O_{84}$	$C_{186}H_{324}Gd_{12}N_{48}O_{84}$	$C_{186}H_{316}N_{48}O_{84}Yb_{12}$
Formula weight	6400.45	6463.93	6645.35
Temperature	150 K	150 K	150 K
Wavelength	1.54180 Å	1.54184 Å	1.54180 Å
Crystal system	Monoclinic	Monoclinic	Monoclinic
Space group	*P*21/n	*P*21/n	*P*21/n
Unit cell dimensions *a*, *b*, *c* (Å)	28.5577(5),15.9841(2), 39.9615(6)	28.5003(6),15.9301(3), 39.8630(7)	28.4973(7),15.9022(3) 39.7702(8)
α, *β*, *γ*	90°, 103.3460(16)°, 90°	90°, 103.1188(19)°, 90°	90°, 103.219(2)°, 90°
Volume	17748.6(5) Å^3	17626.0(6) Å^3	17545.1(7) Å^3
Z	2	2	2
Density (calculated)	1.198 mg/cm^3	1.218 mg/cm^3	1.258 mg/cm^3
Absorption coefficient	15.446 mm^{-1}	14.873 mm^{-1}	6.187 mm^{-1}
F(000)	6408	6432	6560
Crystal size, mm^3	0.18 × 0.11 × 0.03	0.18 × 0.14 × 0.02	0.18 × 0.15 × 0.04
Theta range for data collection	3.181 to 76.454°	3.589 to 76.473°	3.597 to 43.217°
Index ranges	-35 ≤ *h* ≤ 34, -20 ≤ *k* ≤ 9, -49 ≤ *l* ≤ 50	-35 ≤ *h* ≤ 33, -16 ≤ *k* ≤ 20, -50 ≤ *l* ≤ 42	-25 ≤ *h* ≤ 25, - 14 ≤ *k* ≤ 14, -34 ≤ *l* ≤ 35
Reflections collected	105177	106251	158465
Independent reflections	36621 [*R*(int) = 0.068]	36489 [*R*(int) = 0.080]	12717 [*R*(int) = 0.110]
Completeness to theta	73.396°, 99.7 %	74.179°, 99.6 %	41.921°, 99.6 %
Absorption correction	Semi-empirical from equivalents	Semi-empirical from equivalents	Semi-empirical from equivalents
Max. and min. transmission	0.63 and 0.02	0.74 and 0.09	0.78 and 0.26
Refinement method	Full-matrix least-squares on F^2	Full-matrix least-squares on F^2	Full-matrix least-squares on F^2
Data/restraints/ parameters	36617/0/1486	36473/0/1486	12655/244/1512
Goodness of fit on F^2	1.0191	0.9991	1.0303
Final *R* indices [$I > 2\sigma(I)$]	R_1 = 0.1126, wR_2 = 0.2713	R_1 = 0.0762, wR_2 = 0.1892	R_1 = 0.0701, wR_2 = 0.1987
R indices (all data)	R_1 = 0.1305, wR_2 = 0.3036	R_1 = 0.0998, wR_2 = 0.2187	R_1 = 0.0851, wR_2 = 0.2144
Largest diff. peak and hole	5.22 and -1.07 e.Å^{-3}	3.45 and -1.00 e.Å^{-3}	1.86 and -1.73 e.Å^{-3}

Table C6. Crystal data and structure refinement for $[Yb_2(DO3A)_2C\text{-}3(2F)]^{2-}$

Structure located in Chapter-II, Figure 2.38

Identification code	7538	
Empirical formula	$C_{31}H_{58}F_2K_1N_8O_{16}Yb_2$	
Formula weight	1222.02	
Temperature	150 K	
Wavelength	1.54184 Å	
Crystal system	Triclinic	
Space group	*P*-1	
Unit cell dimensions	a = 12.6782(2) Å	α = 94.8655(15)°
	b = 13.2543(2) Å	β = 102.8002(15)°
	c = 17.7146(3) Å	γ = 108.0577(16)°
Volume	2721.73(8) $Å^3$	
Z	2	
Density (calculated)	1.491 mg/cm^3	
Absorption coefficient	7.456 mm^{-1}	
F(000)	1210	
Crystal size	0.18 × 0.10 × 0.08 mm^3	
Theta range for data collection	3.557 to 76.293°	
Index ranges	$-15 \le h \le 13$, $-16 \le k \le 16$, $-21 \le l \le 22$	
Reflections collected	49071	
Independent reflections	11279 [R(int) = 0.030]	
Completeness to theta = 74.767°	99.6 %	
Absorption correction	Semi-empirical from equivalents	
Max. and min. transmission	0.55 and 0.11	
Refinement method	Full-matrix least-squares on F^2	
Data/restraints/parameters	11277/0/544	
Goodness-of-fit on F^2	1.0117	
Final R indices [$I > 2\sigma(I)$]	R_1 = 0.0548, wR_2 = 0.1571	
R indices (all data)	R_1 = 0.0565, wR_2 = 0.1598	
Largest diff. peak and hole	2.88 and -2.05 e.$Å^{-3}$	

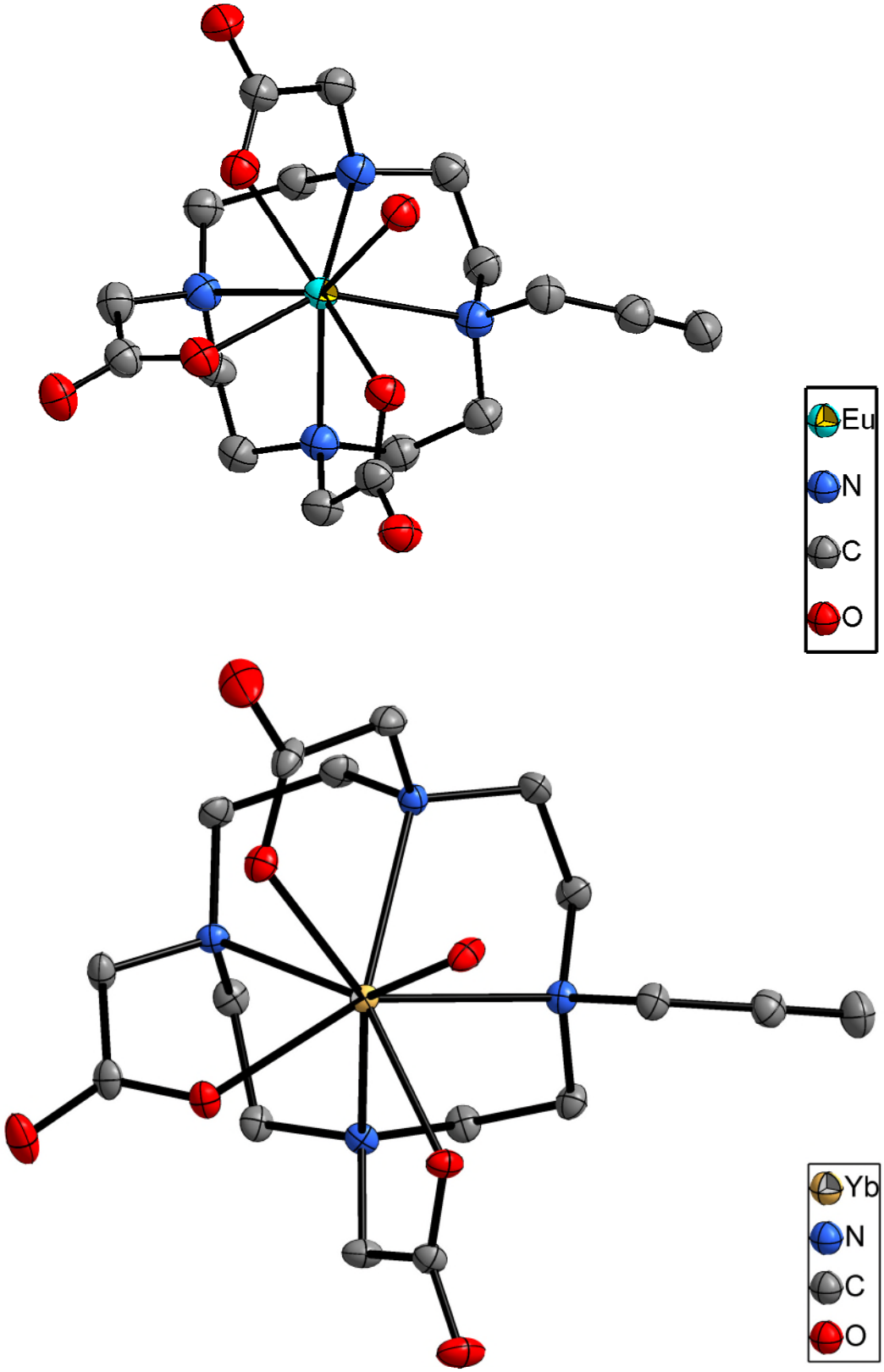


Figure C2. Single crystal X-ray structure of [Eu(**pDO3A**)] (top) and [Yb(**pDO3A**)] (bottom). H atoms and water omitted for clarity. Thermal ellipsoid drawn at 30% probability level. Structure solved by Dr. Kirsten Christensen at Chemical Crystallography, University of Oxford.

Table C7. Crystal data and structure refinement for [Ln(pDO3A)] (Ln = Eu(III) and Yb(III))

Identification code	7626	7630
Empirical formula	$C_{17}H_{31}EuN_4O_9$	$C_{17}H_{31}N_4O_9Yb$
Formula weight	587.41	608.49
Temperature	150 K	150 K
Wavelength	1.54184 Å	1.54184 Å
Crystal system	Monoclinic	Monoclinic
Space group	*P*21/n	*P*21/n
Unit cell dimensions *a, b, c* (Å)	10.79910(10), 18.3916(2), 11.20760(10)	10.8216(2), 18.3994(3), 11.1809(2)
α, β, γ	90°, 106.5527(13)°, 90°	90°, 106.757(2)°, 90°
Volume	2133.72(4) Å^3	2131.71(7) Å^3
Z	4	4
Density (calculated)	1.828 mg/cm^3	1.896 mg/cm^3
Absorption coefficient	21.554 mm^{-1}	8.627 mm^{-1}
F(000)	1184	1212
Crystal size	0.29 × 0.15 × 0.02 mm^3	0.50 × 0.20 × 0.05 mm^3
Theta range for data collection	4.767 to 76.441°	4.779 to 76.317°
Index ranges	-13 ≤ h ≤ 13, -23 ≤ k ≤ 23, -13 ≤ l ≤ 14	-12 ≤ h ≤ 13, -23 ≤ k ≤ 22, -13 ≤ l ≤ 13
Reflections collected	52630	12304
Independent reflections	4458 [*R*(int) = 0.043]	4418 [*R*(int) = 0.024]
Completeness to theta	74.912° 99.8 %	74.790° 99.5 %
Absorption correction	Semi-empirical from equivalents	Semi-empirical from equivalents
Max. and min. transmission	0.65 and 0.02	0.65 and 0.06
Refinement method	Full-matrix least-squares on F^2	Full-matrix least-squares on F^2
Data/restraints/parameters	4450/0/288	4417/0/288
Goodness-of-fit on F^2	1.0350	1.0237
Final *R* indices [$I > 2\sigma(I)$]	R_1 = 0.0734, wR_2 = 0.1999	R_1 = 0.0251, wR_2 = 0.0648
R indices (all data)	R_1 = 0.0738, wR_2 = 0.2017	R_1 = 0.0258, wR_2 = 0.0653
Largest diff. peak and hole	4.10 and -0.85 e.Å^{-3}	1.13 and -0.96 e.Å^{-3}

Table C8. Crystal data and structure refinement for [Eu(DO3A)benzyl-*m*-B]

Structure located in Chapter-IV, Figure 4.3

Identification code	7456	
Empirical formula	$C_{84}H_{154.44}B_4Eu_4N_{16}O_{45.22}$	
Formula weight	2763.44	
Temperature	150 K	
Wavelength	1.54184 Å	
Crystal system	Monoclinic	
Space group	*P*21/n	
Unit cell dimensions	a = 18.0238(5) Å	α = 90°
	b = 17.3266(4) Å	β = 111.948(3)°
	c = 18.5898(4) Å	γ = 90°
Volume	5384.7(3) Å^3	
Z	2	
Density (calculated)	1.704 mg/cm^3	
Absorption coefficient	17.247 mm^{-1}	
F(000)	2808.584	
Crystal size	0.10 × 0.05 × 0.04 mm^3	
Theta range for data collection	3.616 to 76.240°	
Index ranges	$-21 \le h \le 22$, $-21 \le k \le 21$, $-23 \le l \le 20$	
Reflections collected	65291	
Independent reflections	11205 [R(int) = 0.044]	
Completeness to theta = 73.461°	100.0 %	
Absorption correction	Semi-empirical from equivalents	
Max. and min. transmission	0.50 and 0.03	
Refinement method	Full-matrix least-squares on F^2	
Data/restraints/parameters	11196/72/712	
Goodness-of-fit on F^2	1.0539	
Final R indices [$I > 2\sigma(I)$]	R_1 = 0.0953, wR_2 = 0.2257	
R indices (all data)	R_1 = 0.1000, wR_2 = 0.2387	
Largest diff. peak and hole	4.16 and -0.95 e.Å^{-3}	

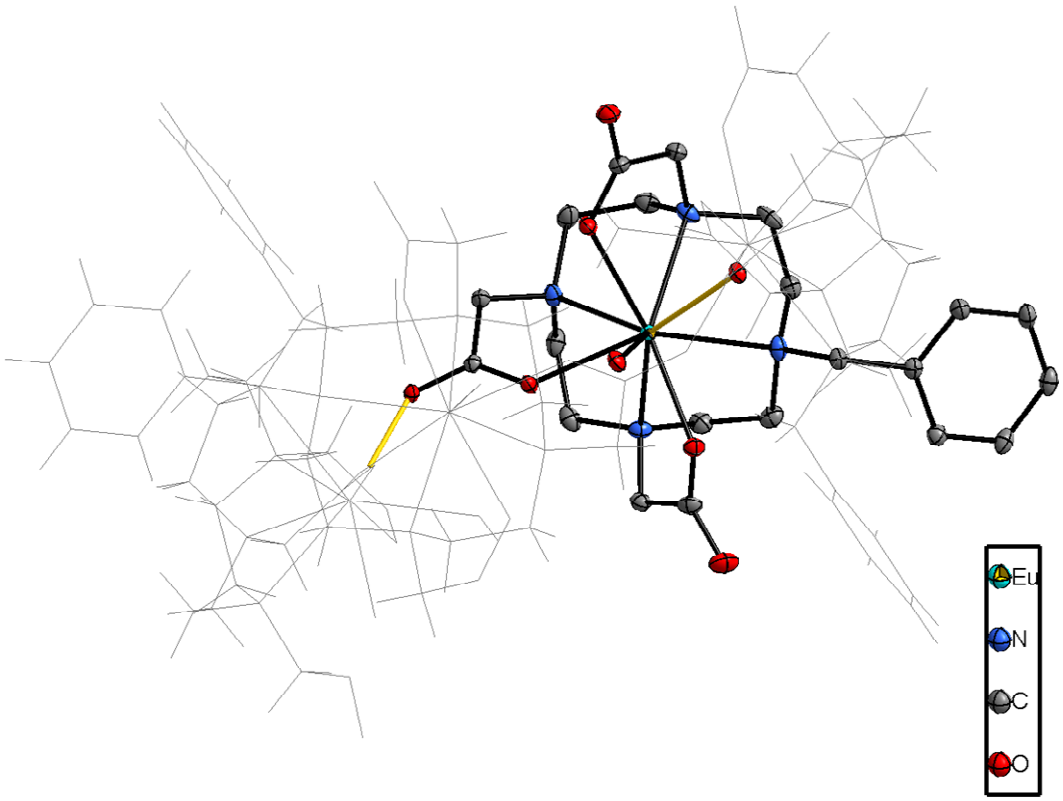


Figure C3. Single crystal X-ray structure of [Eu(**DO3A**)**benzyl**)]. Except selected structure, the rest are shown in wireframe format, H atoms and water are omitted for clarity. Thermal ellipsoid drawn at 30% probability level. μ-oxo bridging bond is shown in yellow. This crystal was obtained from the crude that was obtained from reacting $Eu(OTf)_3$ with DO3A(*p*-PBA). Structure solved by Dr. Kirsten Christensen at Chemical Crystallography, University of Oxford.

Table C9. Crystal data and structure refinement for [Eu(DO3A)benzyl]

Identification code	7693	
Empirical formula	$C_{84}H_{128}Eu_4N_{16}O_{30}$	
Formula weight	2449.87	
Temperature	150 K	
Wavelength	1.54184 Å	
Crystal system	Monoclinic	
Space group	*P*21/n	
Unit cell dimensions	a = 17.5961(2) Å	α = 90°
	b = 17.7957(2) Å	β = 112.1887(13)°
	c = 18.5322(2) Å	γ = 90°
Volume	5373.33(11) Å^3	
Z	2	
Density (calculated)	1.514 mg/cm^3	
Absorption coefficient	17.104 mm^{-1}	
F(000)	2472	
Crystal size	0.20 × 0.18 × 0.11 mm^3	
Theta range for data collection	3.578 to 76.181°	
Index ranges	$-21 \leq h \leq 21$, $-22 \leq k \leq 22$, $-17 \leq l \leq 23$	
Reflections collected	44154	
Independent reflections	11117 [R(int) = 0.046]	
Completeness to theta = 73.896°	99.6 %	
Absorption correction	Semi-empirical from equivalents	
Max. and min. transmission	0.15 and 0.02	
Refinement method	Full-matrix least-squares on F^2	
Data/restraints/parameters	11117/0/604	
Goodness-of-fit on F^2	1.0148	
Final R indices [$I > 2\sigma(I)$]	R_1 = 0.0612, wR_2 = 0.1504	
R indices (all data)	R_1 = 0.0652, wR_2 = 0.1582	
Largest diff. peak and hole	3.02 and -0.84 e.Å^{-3}	

Table C10. Crystal data and structure refinement for [Lu(DO3A)*o*-PBA]

Structure located in Chapter-IV, Figure 4.2

Identification code	7655
Empirical formula	$C_{21}H_{34}BLuN_4O_{10}$
Formula weight	688.30
Temperature	150 K
Wavelength	1.54184 Å
Crystal system	Orthorhombic
Space group	*P*212121
Unit cell dimensions	a = 10.40020(10) Å α = 90°
	b = 10.81180(10) Å β = 90°
	c = 21.7181(2) Å γ = 90°
Volume	2442.09(4) Å^3
Z	4
Density (calculated)	1.872 mg/cm^3
Absorption coefficient	8.302 mm^{-1}
F(000)	1376
Crystal size	0.08 × 0.06 × 0.02 mm^3
Theta range for data collection	4.071 to 74.821°
Index ranges	$-13 \leq h \leq 12$, $-13 \leq k \leq 10$, $-27 \leq l \leq 26$
Reflections collected	42587
Independent reflections	4969 [*R*(int) = 0.043]
Completeness to theta = 74.821°	99.8 %
Absorption correction	Semi-empirical from equivalents
Max. and min. transmission	0.85 and 0.61
Refinement method	Full-matrix least-squares on F^2
Data/restraints/parameters	4969/0/335
Goodness-of-fit on F^2	0.9976
Final *R* indices [$I > 2\sigma(I)$]	R_1 = 0.0220, wR_2 = 0.0528
R indices (all data)	R_1 = 0.0231, wR_2 = 0.0534
Absolute structure parameter	-0.034(4)
Largest diff. peak and hole	0.53 and -0.61 e.Å^{-3}

Table C11. Crystal data and structure refinement for compound 5.9

Structure located in Chapter-V, Figure 5.2

Identification code	7343	
Empirical formula	$C_{28}H_{53}BrKN_4O_7$	
Formula weight	676.75	
Temperature	150 K	
Wavelength	0.71073 Å	
Crystal system	Monoclinic	
Space group	*I*a	
Unit cell dimensions	a = 12.6123(2) Å	α = 90°
	b = 18.8949(2) Å	β = 92.1318(17)°
	c = 16.1231(3) Å	γ = 90°
Volume	3839.60(11) Å^3	
Z	4	
Density (calculated)	1.171 mg/cm^3	
Absorption coefficient	1.220 mm^{-1}	
F(000)	1436	
Crystal size	0.21 × 0.20 × 0.16 mm^3	
Theta range for data collection	1.661 to 29.759°	
Index ranges	$-17 \leq h \leq 17$, $0 \leq k \leq 26$, $-21 \leq l \leq 22$	
Reflections collected	9359	
Independent reflections	9359 [R(int) = 0.0245]	
Completeness to theta = 25.295°	99.3%	
Absorption correction	Semi-empirical from equivalents	
Max. and min. transmission	0.82 and 0.81	
Refinement method	Full-matrix least-squares on F^2	
Data/restraints/parameters	9357/2/371	
Goodness-of-fit on F^2	1.0227	
Final R indices [$I > 2\sigma(I)$]	R_1 = 0.0484, wR_2 = 0.1318	
R indices (all data)	R_1 = 0.0572, wR_2 = 0.1422	
Absolute structure parameter	0.4970(12)	
Largest diff. peak and hole	0.42 and -1.36 e.Å^{-3}	

Table C12. Crystal data and structure refinement for compound 5.11

Structure located in Chapter-V, Figure 5.3

Identification code	7694
Empirical formula	$C_{16}H_{15}BN_2O_4S$
Formula weight	342.18
Temperature	150 K
Wavelength	1.54184 Å
Crystal system	Monoclinic
Space group	*P*21/n
Unit cell dimensions	
	a = 14.3466(3) Å $\quad \alpha = 90°$
	b = 7.68020(10) Å $\quad \beta = 110.957(2)°$
	c = 14.3803(3) Å $\quad \gamma = 90°$
Volume	1479.67(5) $Å^3$
Z	4
Density (calculated)	1.536 mg/cm^3
Absorption coefficient	2.169 mm^{-1}
$F(000)$	712
Crystal size	0.26 × 0.21 × 0.13 mm^3
Theta range for data collection	3.735 to 76.349°
Index ranges	$-17 \le h \le 17, -9 \le k \le 9, -18 \le l \le 17$
Reflections collected	15879
Independent reflections	3097 [R(int) = 0.024]
Completeness to theta = 74.822°	99.8 %
Absorption correction	Semi-empirical from equivalents
Max. and min. transmission	0.75 and 0.62
Refinement method	Full-matrix least-squares on F^2
Data/restraints/parameters	3097/0/218
Goodness-of-fit on F^2	1.0042
Final R indices [$I > 2\sigma(I)$]	R_1 = 0.0310, wR_2 = 0.0831
R indices (all data)	R_1 = 0.0320, wR_2 = 0.0840
Extinction coefficient	19(3)
Largest diff. peak and hole	0.51 and -0.35 e.$Å^{-3}$

Table C13. Crystal data and structure refinement for compound 3.4

Structure located in Chapter-III, Figure 3.2

Identification code	7514
Empirical formula	$C_{16}H_{28.39}Cl_2N_4O_{2.20}$
Formula weight	382.86
Temperature	150 K
Wavelength	1.54180 Å
Crystal system	Orthorhombic
Space group	$P2_12_12_1$
Unit cell dimensions	a = 8.29030(10) Å α = 90°
	b = 10.78030(10) Å β = 90°
	c = 21.4734(2) Å γ = 90°
Volume	1919.12(3) Å^3
Z	4
Density (calculated)	1.325 mg/cm^3
Absorption coefficient	3.188 mm^{-1}
F(000)	815.850
Crystal size	0.20 × 0.16 × 0.03 mm^3
Theta range for data collection	4.117 to 76.225°
Index ranges	$-10 \leq h \leq 10$, $-9 \leq k \leq 13$, $-26 \leq l \leq 26$
Reflections collected	21043
Independent reflections	3989 [R(int) = 0.038]
Completeness to theta = 76.225°	99.6%
Absorption correction	Semi-empirical from equivalents
Max. and min. transmission	0.91 and 0.55
Refinement method	Full-matrix least-squares on F^2
Data/restraints/parameters	3989/210/253
Goodness-of-fit on F^2	1.0048
Final R indices [$I > 2\sigma(I)$]	$R1$ = 0.0379, w$R2$ = 0.1006
R indices (all data)	$R1$ = 0.0391, w$R2$ = 0.1022
Absolute structure parameter	0.010(4)
Largest diff. peak and hole	0.42 and -0.23 e.Å^{-3}

Table C14. Crystal data and structure refinement for [Eu(DO3A)benzyl]

Structure located in Chapter-IV, Figure 4.4

Identification code	7702	
Empirical formula	$C_{84}H_{144}Eu_4N_{16}O_{38}$	
Formula weight	2593.99	
Temperature	100 K	
Wavelength	1.54184 Å	
Crystal system	Monoclinic	
Space group	*P*21/n	
Unit cell dimensions	a = 17.6470(2) Å	$\alpha = 90°$
	b = 17.7412(2) Å	$\beta = 112.4904(15)°$
	c = 18.5622(2) Å	$\gamma = 90°$
Volume	5369.44(12) $Å^3$	
Z	2	
Density (calculated)	1.604 mg/cm^3	
Absorption coefficient	17.207 mm^{-1}	
F(000)	2632	
Crystal size	0.06 × 0.03 × 0.02 mm^3	
Theta range for data collection	3.584 to 76.335°	
Index ranges	$-21 \le h \le 22$, $-22 \le k \le 22$, $-23 \le l \le 21$	
Reflections collected	162784	
Independent reflections	11066 [*R*(int) = 0.052]	
Completeness to theta = 74.045°	99.7 %	
Absorption correction	Semi-empirical from equivalents	
Max. and min. transmission	0.71 and 0.55	
Refinement method	Full-matrix least-squares on F^2	
Data/restraints/parameters	11062/0/645	
Goodness-of-fit on F^2	1.0218	
Final *R* indices [$I > 2\sigma(I)$]	R_1 = 0.0382, wR_2 = 0.0864	
R indices (all data)	R_1 = 0.0400, wR_2 = 0.0874	
Extinction coefficient	12(2)	
Largest diff. peak and hole	1.01 and -0.73 e.$Å^{-3}$	

Table C15. Crystal data and structure refinement for $[Eu_2(DO3A)_2C\text{-}2(CO_3)]^{2-}$

Structure located in Chapter-II, Figure 2.39

Identification code	7610	
Empirical formula	$C_{31}H_{48}Eu_2K_2N_8O_{15}$	
Formula weight	1154.88	
Temperature	150 K	
Wavelength	1.54184 Å	
Crystal system	Monoclinic	
Space group	*P*21/c	
Unit cell dimensions	a = 13.5279(4) Å	α = 90°
	b = 25.1029(11) Å	β = 94.891(3)°
	c = 16.3284(5) Å	γ = 90°
Volume	5524.8(3) Å^3	
Z	4	
Density (calculated)	1.388 mg/cm^3	
Absorption coefficient	17.924 mm^{-1}	
F(000)	2296	
Crystal size	0.07 × 0.06 × 0.03 mm^3	
Theta range for data collection	3.279 to 76.057°.	
Index ranges	$-10 \leq h \leq 16$, $-31 \leq k \leq 31$, $-20 \leq l \leq 20$	
Reflections collected	66722	
Independent reflections	11296 [R(int) = 0.091]	
Completeness to theta = 72.254°	99.6 %	
Absorption correction	Semi-empirical from equivalents	
Max. and min. transmission	0.58 and 0.03	
Refinement method	Full-matrix least-squares on F^2	
Data/restraints/parameters	7878/160/523	
Goodness-of-fit on F^2	0.9714	
Final R indices [$I > 2\sigma(I)$]	R_1 = 0.1385, wR_2 = 0.0840	
R indices (all data)	R_1 = 0.1557, wR_2 = 0.0901	
Largest diff. peak and hole	5.83 and -0.99 e.Å^{-3}	

Table C16. Crystal data and structure refinement for [Eu(pDO3A)2F]$^{2-}$

Structure located in Chapter-II, Figure 2.40

Identification code	7711	
Empirical formula	$C_{17}H_{21}EuF_2K_2N4O_7$	
Formula weight	667.58	
Temperature	100 K	
Wavelength	1.54180 Å	
Crystal system	Triclinic	
Space group	*P* -1	
Unit cell dimensions	*a* = 8.4765(5) Å	α = 100.978(6)°
	b = 8.8557(6) Å	β = 95.512(5)°
	c = 19.1797(12) Å	γ = 94.301(5)°
Volume	1400.42(16) Å^3	
Z	2	
Density (calculated)	1.583 mg/cm^3	
Absorption coefficient	19.160 mm^{-1}	
F(000)	664	
Crystal size	0.11 × 0.08 × 0.05 mm^3	
Theta range for data collection	4.727 to 67.680°.	
Index ranges	-10 ≤ h ≤ 10, -11 ≤ k ≤ 10, -23 ≤ l ≤ 23	
Reflections collected	26089	
Independent reflections	5635 [*R*(int) = 0.175]	
Completeness to theta = 64.023°	99.5 %	
Absorption correction	Semi-empirical from equivalents	
Max. and min. transmission	0.38 and 0.17	
Refinement method	Full-matrix least-squares on F^2	
Data/restraints/parameters	5042/0/298	
Goodness-of-fit on F^2	1.0083	
Final *R* indices [$I > 2\sigma(I)$]	R_1 = 0.1034, wR_2 = 0.2538	
R indices (all data)	R_1 = 0.1228, wR_2 = 0.2670	
Largest diff. peak and hole	5.45 and -3.93 e.Å^{-3}	

APPENDIX-D

Appendix D: DYNAFIT input scripts

D1. A typical DYNAFIT script for a single binding event

```
[task]
   task = fit
   data = equilibria
[mechanism]
   Eu + Cl <==> EuCl : K1 assoc
[constants]
   K1 = 10E4??
[concentrations]
   Eu = 1.00E-03?
[data]
   variable Cl
file
.\CA_E71_01_Eu_PB_titration_Cl\CA_E71_01_PB_titration_Cl.tx
t |response Eu = 1.19E+04?, EuCl = 1.48E+04?
 [output]
directory .\Desktop\DYNAFIT4\Results
[end]
```

Note: The '?' must be present in the script for K1 to get the binding constant value. For the rest, during the final fitting of the data, they must be removed.

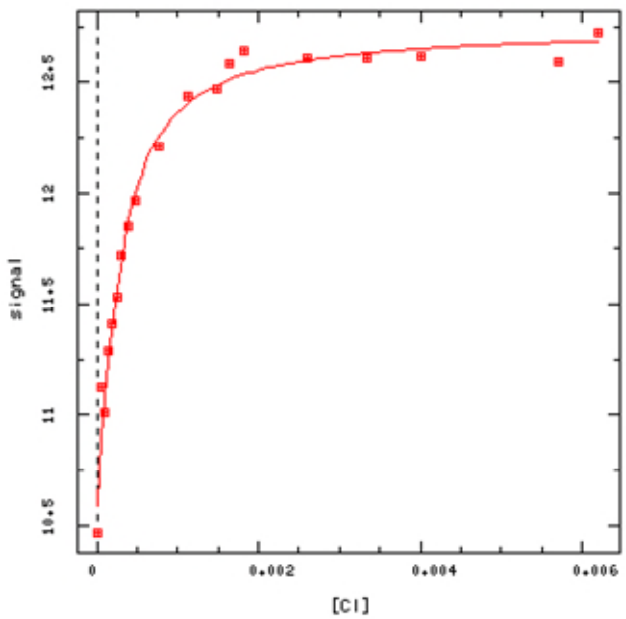


Figure D1. A typical binding isotherm generated from DYNAFIT® software for a single binding event.

D2. A typical DYNAFIT script for a two-binding event

```
Two event binding – peak sum
[task]
   data = equil
   task = fit
[mechanism]
   Eu + F <==> EuF : K1 assoc
   EuF + F <==> EuFF : K2 assoc
[constants]
   K1 = 100000??
   K2 = 10000??
[concentrations]
   Eu = 9.99E-04?
[equil]
   variable F
file
.\CA_E71_01_Eu_water_titration_F\CA_E71_01_Eu_water_titrati
on_F.txt |response Eu = 1.21E+04?, EuF = 1.14E+04?, EuFF =
1.08E+04?
[output]
directory .\DYNAFIT4\Results
[end]
```

Note: The '?' must be present in the script for K1 and K2 to get the binding constant value. For the rest, during the final fitting of the data, they must be removed.

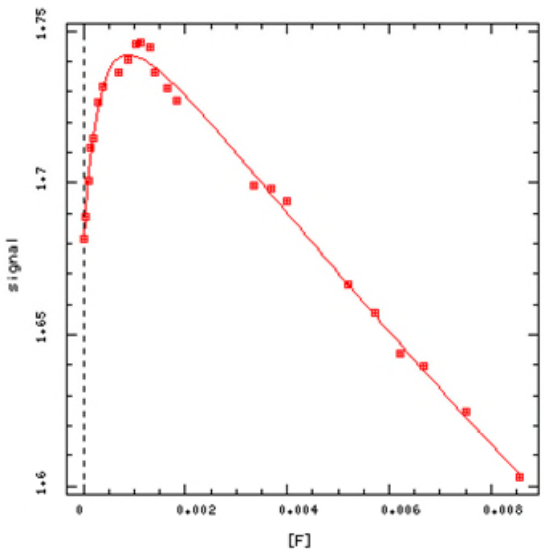


Figure D2. A typical binding isotherm generated from DYNAFIT® software for a two-binding event.

D3. A typical DYNAFIT script for a three-binding event

```
Three event binding – peak sum
[task]
   data = equil
   task = fit
[mechanism]
   Eu + F <==> EuF : K1 assoc
   EuF + F <==> EuFF : K2 assoc
   EuFF + F <==> EuFFF : K3 assoc
[constants]
   K1 = 100000??
   K2 = 10000??
   K3 = 1000??
[concentrations]
   Eu = 9.99E-04?
[equil]
   variable F
file
.\CA_E71_01_Eu_water_titration_F\CA_E71_01_Eu_water_titrati
on_F.txt | response Eu = 4.83e7? , EuF = 4.41e7? ,  EuFF  =
4.18e7?    , EuFFF = 2.01e7?     |     label 580nm
response Eu = 4.45e7? , EuF = 4.52e7? , EuFF = 6.54e7?    ,
EuFFF = 2.47e7? |     label 589nm
response Eu = 7.52e7? , EuF = 5.5e7?  , EuFF = 5.93e7?    ,
EuFFF = 2.68e7  |     label 591nm
response Eu = 4.31e7? , EuF = 2.95e7? ,  EuFF  =  6.16e7?  ,
EuFFF = 2.27e7  |     label 593nm
response Eu = 4.01e7? , EuF = 2.88e7? ,  EuFF = 5.3e7?    ,
EuFFF = 1.91e7? |     label 597nm
[output]
directory
D:\CA_luminescence_data\CA_E71_01_Eu_water_titration_F_tria
l_2\Results
[output]
directory .\DYNAFIT4\Results
[end]
```

Note: The '?' must be present in the script for K1, K2, and K3 to get the binding constant value. For the rest, during the final fitting of the data, they must be removed.

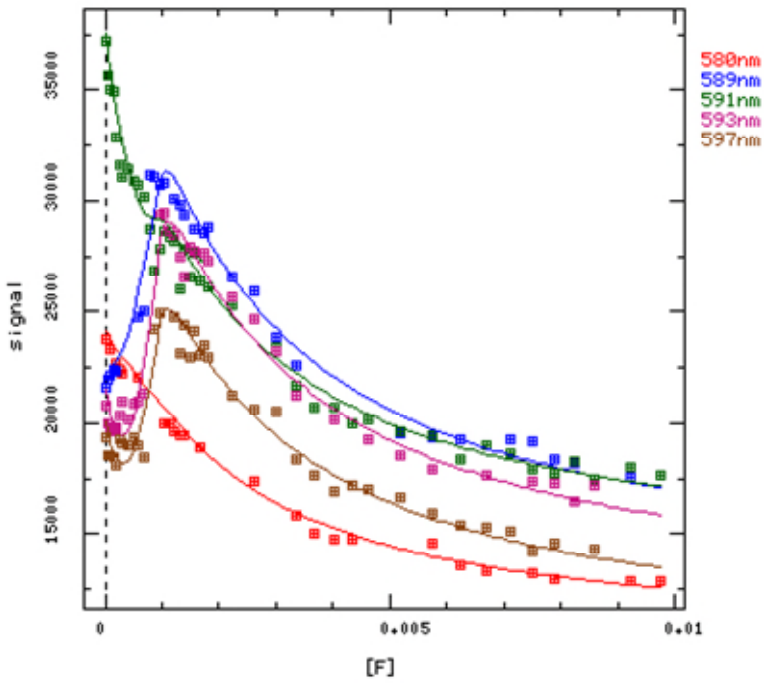


Figure D3. A typical binding isotherm generated from DYNAFIT® software for a three-binding event, generated from multiple data sets as per the script mentioned above.

Note: During the determination of binding events, the plot of change in guest concentration against change in luminescence emission was subjected to a model discrimination analysis using DYNAFIT® which shortlists the possible binding events from the given data.

Parameters

Trust Region Algorithm

Optimized Parameters

No.	Par#Set	Initial	Final	Std. Error	CV (%)	Low[a]	High[a]	Note
#1	K1	10000	**6640**	490	7.3	5710	7760	

[a] Confidence intervals at **95 %** probability level.

All Model Parameters

Optimized *and* fixed model parameters: [TAB-DELIMITED TEXT]

100 × Correlation Matrix

No.	Par#Set	#1
#1	K1	*

Condition Indices and Redundancy Matrix

No.	Par#Set	0.0
#1	K1	100

Confidence Interval Profiles

Combined confidence interval plot: EPS

Confidence interval for **K1**

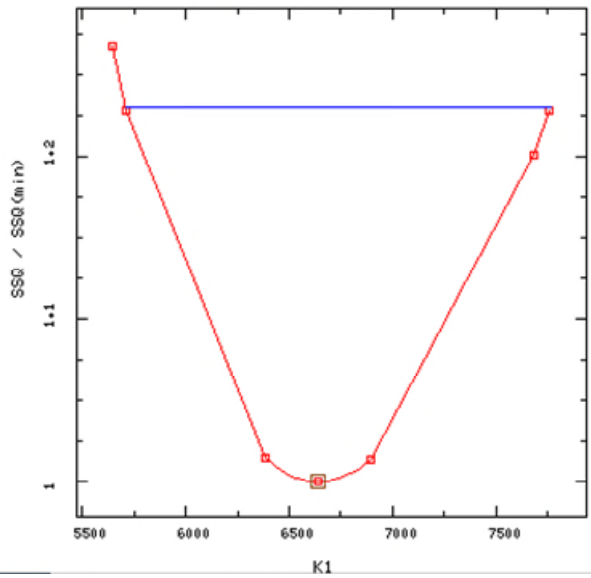


Figure D4. A screenshot of the result for a single binding event plotted using DYNAFIT®. Initial represents the guess made during fitting the data (which contains '?'); final is the binding constant generated by the software; std. error is the standard error for the fitted data; CV is the coefficient of variation expressed in percentage, low and high are the confidence interval range for the given 'final' value generated from the fitting.

D4. A typical DYNAFIT script for a speciation modelling of a three-binding event

```
[task]
   task = fit
   data = equilibria
[mechanism]
   Eu + F <===> EuF      :       K1     assoc
   EuF + F <===> EuFF      :       K2    assoc
   EuFF + F <===> EuFFF      :       K3     assoc
[constants]
   K1 = 4.9e+010
   K2 = 65000
   K3 = 557
[concentrations]
   Eu = 5.00e-4
[data]
   variable F
set 589nm_1 | response Eu = 2e3         , EuF = 1
     , EuFF = 0          , EuFFF = 0
set 589nm_1 | response Eu = 0           , EuF = 2e3
     , EuFF = 1          , EuFFF = 0
set 589nm_1 | response Eu = 0           , EuF = 0
     , EuFF = 2e3        , EuFFF = 1
set 589nm_1 | response Eu = 0           , EuF = 0
     , EuFF = 1          , EuFFF = 2e3
[output]
   directory
D:\CA_luminescence_data\CA_E71_01_Eu_water_titration_F
_trial_2\Results_speciation_trial
```

Note: The data on the y-axis must be normalised; K1, K2, and K3 are obtained from DYNAFIT® during binding isotherm generation; responses for each event must be set such that except for the set speciation (eg. Eu to EuF), the rest must be set to zero. Response is achieved by the ratio of unity to the concentration of the host used in the titration.

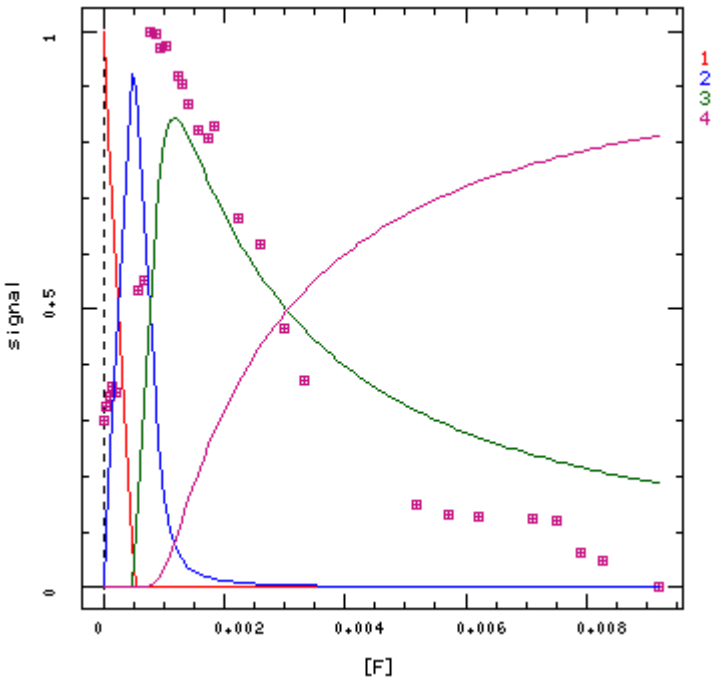


Figure D5. A typical speciation plot generated from DYNAFIT® for a three-binding event. The points are the normalised data points which is removed when the data is transported to a software which can plot graphs.